FROM STRUCTURE TO FUNCTION IN NEURONAL NETWORKS: EFFECTS OF ADAPTATION, TIME-DELAYS, AND NOISE

EDITED BY: Serhiy Yanchuk, Viktor Jirsa, Joana Cabral, Oleksandr Popovych and Alessandro Torcini

PUBLISHED IN: Frontiers in Systems Neuroscience, Frontiers in Applied Mathematics and Statistics and Frontiers in Computational Neuroscience

frontiers Research Topics

ISSN 1664-8714
ISBN 978-2-88976-138-8
DOI 10.3389/978-2-88976-138-8

About Frontiers

Frontiers is more than just an open-access publisher of scholarly articles: it is a pioneering approach to the world of academia, radically improving the way scholarly research is managed. The grand vision of Frontiers is a world where all people have an equal opportunity to seek, share and generate knowledge. Frontiers provides immediate and permanent online open access to all its publications, but this alone is not enough to realize our grand goals.

Frontiers Journal Series

The Frontiers Journal Series is a multi-tier and interdisciplinary set of open-access, online journals, promising a paradigm shift from the current review, selection and dissemination processes in academic publishing. All Frontiers journals are driven by researchers for researchers; therefore, they constitute a service to the scholarly community. At the same time, the Frontiers Journal Series operates on a revolutionary invention, the tiered publishing system, initially addressing specific communities of scholars, and gradually climbing up to broader public understanding, thus serving the interests of the lay society, too.

Dedication to Quality

Each Frontiers article is a landmark of the highest quality, thanks to genuinely collaborative interactions between authors and review editors, who include some of the world's best academicians. Research must be certified by peers before entering a stream of knowledge that may eventually reach the public - and shape society; therefore, Frontiers only applies the most rigorous and unbiased reviews.
Frontiers revolutionizes research publishing by freely delivering the most outstanding research, evaluated with no bias from both the academic and social point of view. By applying the most advanced information technologies, Frontiers is catapulting scholarly publishing into a new generation.

What are Frontiers Research Topics?

Frontiers Research Topics are very popular trademarks of the Frontiers Journals Series: they are collections of at least ten articles, all centered on a particular subject. With their unique mix of varied contributions from Original Research to Review Articles, Frontiers Research Topics unify the most influential researchers, the latest key findings and historical advances in a hot research area! Find out more on how to host your own Frontiers Research Topic or contribute to one as an author by contacting the Frontiers Editorial Office: frontiersin.org/about/contact

FROM STRUCTURE TO FUNCTION IN NEURONAL NETWORKS: EFFECTS OF ADAPTATION, TIME-DELAYS, AND NOISE

Topic Editors:
Serhiy Yanchuk, Potsdam Institute for Climate Impact Research (PIK), Germany
Viktor Jirsa, Aix-Marseille Université, France
Joana Cabral, University of Minho, Portugal
Oleksandr Popovych, Julich Research Center, Helmholtz Association of German Research Centres (HZ), Germany
Alessandro Torcini, CY Cergy Paris Université, France

Citation: Yanchuk, S., Jirsa, V., Cabral, J., Popovych, O., Torcini, A., eds. (2022). From Structure to Function in Neuronal Networks: Effects of Adaptation, Time-Delays, and Noise. Lausanne: Frontiers Media SA.
doi: 10.3389/978-2-88976-138-8

Table of Contents

frontiers | Frontiers in Systems Neuroscience

EDITORIAL
published: 21 April 2022
doi: 10.3389/fnsys.2022.871165

Editorial: From Structure to Function in Neuronal Networks: Effects of Adaptation, Time-Delays, and Noise

Joana Cabral[1,2,3], *Viktor Jirsa*[4], *Oleksandr V. Popovych*[5], *Alessandro Torcini*[6] *and Serhiy Yanchuk*[7,8]*

[1] *Life and Health Sciences Research Institute, School of Medicine, University of Minho, Braga, Portugal,* [2] *Centre for Eudaimonia and Human Flourishing, Linacre College, University of Oxford, Oxford, United Kingdom,* [3] *Center for Music in the Brain, Department of Clinical Medicine, Aarhus University, Aarhus, Denmark,* [4] *Aix Marseille University, INSERM, INS, Institut de Neurosciences des Systèmes, Marseille, France,* [5] *Institute of Neuroscience and Medicine, Brain and Behaviour (INM-7), Research Centre Jülich, Jülich, Germany,* [6] *CY Cergy Paris Université, Laboratoire de Physique Théorique et Modélisation, CNRS, UMR 8089, Cergy, France,* [7] *Research Department Complexity Science, Potsdam Institute for Climate Impact Research, Potsdam, Germany,* [8] *Department of Mathematics, Faculty of Mathematics and Natural Sciences, Humboldt-Universität zu Berlin, Berlin, Germany*

Keywords: neuronal networks, adaptation, structure and function, noise, time-delay, neuronal activity patterns, multi-scale

Editorial on the Research Topic

From Structure to Function in Neuronal Networks: Effects of Adaptation, Time-Delays, and Noise

OPEN ACCESS

Edited by:
Paolo Massobrio, University of Genoa, Italy

Reviewed by:
Mikail Rubinov, Vanderbilt University, United States

***Correspondence:**
Serhiy Yanchuk
yanchuk@pik-potsdam.de

Received: *07 February 2022*
Accepted: *28 February 2022*
Published: *21 April 2022*

Citation:
Cabral J, Jirsa V, Popovych OV, Torcini A and Yanchuk S (2022) Editorial: From Structure to Function in Neuronal Networks: Effects of Adaptation, Time-Delays, and Noise. Front. Syst. Neurosci. 16:871165. doi: 10.3389/fnsys.2022.871165

It is a fundamental challenge to understand how brain function is related to its functional and structural organization, i.e., what shapes the neuronal activity patterns observed across scales that define cognitive and behavioral processes, as well as their breakdown in mental health disorders (Park and Friston, 2013). Few theories integrate the various dimensions in this ambitious endeavor [such as Free Energy Principle (Friston et al., 2006) and Structured Flows on Manifolds (Jirsa and Sheheitli, 2022)], but all acknowledge the multi-scale organization of brain function. Investigation of the complex structure-function relationship can be performed at the macro- and meso-scopic levels (Messé, 2020; Suárez et al., 2020), where dynamical modeling at large scales constitutes one of the promising methodologies (Ghosh et al., 2008; Deco et al., 2009; Honey et al., 2009). At the microscopic level, the dynamics of neuronal networks strongly depends on intrinsic properties of the neuro-anatomical connectome and the functional relationships among neurons, and this goes beyond the connectivity matrix. In particular, the adaptation of the strengths of the synaptic connections through synaptic plasticity (Markram et al., 1997; Abbott and Nelson, 2000; Dan and Poo, 2004), the evolution of the functional connectivity in time, the inevitable time delays resulting from both neurophysiological time constants and finite propagation velocity, noise, and inherent inhomogeneities play key roles in the emergent behavior of neuronal systems across spatial and temporal scales (Deco et al., 2009). A detailed characterization of these effects on the collective dynamics of neuronal networks is an important contemporary problem, which may thus provide the means for studying the link between functional and structural connectivity and brain function in health and disease (Cabral et al., 2017; Jirsa et al., 2017; McIntosh and Jirsa, 2019; Popovych et al., 2019).

This Research Topic focuses on the structure-function relationship in neuronal networks at different temporal and spatial scales. The latter range from fast-spiking and bursting dynamics of individual neurons organized in recurrent networks (Berner and Yanchuk; Protachevicz et al.; Rongala et al.; Sawicki and Schöll; Sánchez-Claros at al.), to neuronal populations' activity examined in terms of neural mass or neural field models (Al-Darabsah et al.; Bi et al.; Hutt et al.; Laing et al.; Tavakoli and Longtin) and to slow and ultra-slow fluctuations of neuronal and metabolic activity at the whole-brain scale (Coronel-Oliveros et al.; Gerster et al.).

Special attention is paid to the modeling of neuronal plasticity (Berner and Yanchuk), to the impact of time delays in coupling and intrinsic activity (Protachevicz et al.; Rongala et al., Sánchez-Claros at al.; Tavakoli and Longtin), and to the effects of noise or stochastic perturbations (Rongala et al.; Sánchez-Claros at al.; Tavakoli and Longtin), as well as to heterogeneity of individual and collective neuronal dynamics (Berner and Yanchuk; Bi et al.; Coronel-Oliveros at al.; Gerster et al.; Laing et al.; Tavakoli and Longtin; Zhou et al.).

A brief description of the contributions is reported below.

The experimental work of Zhou et al. investigates the properties of the local field potential (LFP) in the hippocampus and its spectra as energy is quenched from the system. The authors examine rat LFPs recorded from the hippocampus and entorhinal cortex during barbiturate overdose euthanasia. The data obtained in this study support the energy cascade theory where the energy flows from large cortical populations to smaller loops.

All other contributions report numerical or theoretical studies based on mean-field or network descriptions of neural systems. In particular, the following papers deal with neural mass and field models.

Laing et al. present a powerful method for studying the influence of a network structure on its dynamics by employing the reduction technique by Ott and Antonsen (2008). In particular, the authors investigate large heterogeneous networks of Winfree oscillators with various correlations in (meta-) parameters, such as degree or parameter assortativity.

Gerster et al. exploit the predictive power of personalized brain network models. The authors build multi-population neural mass models for a cohort of 20 healthy subjects and 15 epileptic patients, implementing next generation neural masses (Montbrió et al., 2015; Taher et al., 2020) for each brain region. As paradigms for testing the spatio-temporal organization, the authors systematically simulate the individual seizure-like propagation patterns.

Al-Darabsah et al. investigate the impacts of delays by modeling large interacting neural populations as neural-field systems. Using a master stability function analysis and numerical simulations, they find that delays can (1) stabilize brain dynamics by temporarily preventing the onset to oscillatory and pathologically synchronized dynamics and (2) enhance or weaken synchronization depending on the underlying eigenvalue spectrum of the connectivity matrix.

Bi et al. show that the E-I balance can cause various regimes observable in the brain. The authors classify the possible dynamical behaviors emerging in balanced E-I networks with structural heterogeneity. Analytic results show that both supra- and sub-threshold balanced asynchronous regimes are observable in the limit of large in-degrees. The coherent rhythms observed in the system can range from periodic and quasi-periodic collective oscillations to coherent chaos. These rhythms are characterized by regular or irregular temporal fluctuations joined to spatial coherence, similar to coherent fluctuations observed in the cortex over multiple spatial scales.

Hutt et al. derive a closed-form mean-field representation for an Erdös-Rényi network with two populations of interconnected neurons driven by additive noise. Considering Gaussian and Poissonian stimulation to excitatory neurons, they observe coherence resonance and show that partial stochastic stimulation promotes coherence resonance compared to global stimulation.

Coronel-Oliveros et al. consider a whole-brain model based on the Jasen and Rit neural mass Jansen and Rit (1995) and a human structural connectivity matrix, to find out which structural features of the human connectome network define the optimal neuromodulatory effects. They simulate the effect of the noradrenergic system as changes in filter gain, and studied its effects related to the global-, local-, and meso-scale features of the connectome.

Tavakoli and Longtin explore conditions under which additional delays in high-dimensional chaotic neural networks lead to a reduction in dynamic complexity, a phenomenon recently described as multi-delay complexity collapse. In particular, they observe that a global delayed inhibitory feedback can induce such a collapse.

The following contributions deal with recurrent networks based on spiking neurons or phase oscillators.

Protachevicz et al. study the effect of autapses by examining a random network with adaptive exponential integrate-and-fire neurons. They found that autapses can influence synchronous behavior in neural networks with excitatory synapses by either increasing or decreasing synchrony, depending on the parameters. However, when only inhibitory synapses are considered, synchronization does not suffer significant changes.

Rongala et al. explore noise and stability issues arising in recurrent neuronal networks. Their findings show that neuronal dynamic leak protects recurrent neuronal circuits from self-induction of spurious high-frequency signals. The authors test a range of models, from a linear non-spiking summation model to fully connected recurrent networks of excitatory and inhibitory neurons with randomly distributed weights and random sensory inputs.

Sawicki and Schöll discuss a minimal model that explains the modalities of the influence of music on the human brain. They report synchronization patterns induced by the sound frequency in a network of FitzHugh-Nagumo oscillators with empirically measured structural connectivity. The sound stimulus is modeled by an input to brain areas related to the auditory cortex. It is shown that the synchrony can be increased by properly adjusting the frequency and amplitude of the sound.

Sánchez-Claros et al. study the information flows in a canonical motif that mimics a cortico-thalamo-cortical circuit

with three neuronal populations (V-motif). Through numerical simulations, the authors determine how the amount of information transferred between the populations depends on the connection delays and frequency detuning. The results highlight the role of the transthalamic V-motif in binding spatially separated cortical computations and suggest an important regulatory role of the direct cortico-cortical connection.

Berner and Yanchuk introduce a methodology for studying synchronization in adaptive networks with heterogeneous adaptation rules. The authors consider a network of phase oscillators with distance-dependent adaptations. For such system, the master stability function approach (Berner et al., 2021) is extended to networks with heterogeneous adaptation. Utilizing the proposed methodology, they explain mechanisms leading to synchronization or desynchronization by enhanced long-range connections.

The presented collection of papers in this Research Topic is united by the common theme of how the structure-function relationship contributes to our better understanding of this complex issue and can inspire further investigations in this direction.

AUTHOR CONTRIBUTIONS

All authors contributed to the article and approved the submitted version.

FUNDING

This work was funded through the European Union's Horizon 2020 Framework Programme for Research and Innovation under the Specific Grant Agreement No. 945539 (Human Brain Project SGA3) and No. 826421 (VirtualBrainCloud). SY was supported by the German Research Foundation DFG, Project No. 411803875. JC was funded by the Portuguese Foundation for Science and Technology grants UIDB/50026/2020, UIDP/50026/2020, and CEECIND/03325/2017.

REFERENCES

Abbott, L. F., and Nelson, S. B. (2000). Synaptic plasticity: taming the beast. *Nat. Neurosci.* 3, 1178–1183. doi: 10.1038/81453

Berner, R., Vock, S., Schöll, E., and Yanchuk, S. (2021). Desynchronization transitions in adaptive networks. *Phys. Rev. Lett.* 126:028301. doi: 10.1103/PhysRevLett.126.028301

Cabral, J., Kringelbach, M. L., and Deco, G. (2017). Functional connectivity dynamically evolves on multiple time-scales over a static structural connectome: models and mechanisms. *NeuroImage* 160, 84–96. doi: 10.1016/j.neuroimage.2017.03.045

Dan, Y., and Poo, M.-M. (2004). Spike timing-dependent plasticity of neural circuits. *Neuron* 44, 23–30. doi: 10.1016/j.neuron.2004.09.007

Deco, G., Jirsa, V., McIntosh, A. R., Sporns, O., and Kotter, R. (2009). Key role of coupling, delay, and noise in resting brain fluctuations. *Proc. Natl. Acad. Sci. U.S.A.* 106, 10302–10307. doi: 10.1073/pnas.0901831106

Friston, K., Kilner, J., and Harrison, L. (2006). A free energy principle for the brain. *J. Physiol. Paris* 100, 70–87. doi: 10.1016/j.jphysparis.2006.10.001

Ghosh, A., Rho, Y., McIntosh, A. R., Kötter, R., and Jirsa, V. K. (2008). Noise during rest enables the exploration of the brain's dynamic repertoire. *PLoS Comput. Biol.* 4:e1000196. doi: 10.1371/journal.pcbi.1000196

Honey, C. J., Sporns, O., Cammoun, L., Gigandet, X., Thiran, J. P., Meuli, R., and Hagmann, P. (2009). Predicting human resting-state functional connectivity from structural connectivity. *Proc. Natl. Acad. Sci. U.S.A.* 106, 2035–2040. doi: 10.1073/pnas.0811168106

Jansen, B. H., and Rit, V. G. (1995). Electroencephalogram and visual evoked potential generation in a mathematical model of coupled cortical columns. *Biol. Cybern.* 73, 357–366. doi: 10.1007/BF00199471

Jirsa, V., and Sheheitli, H. (2022). Entropy, free energy, symmetry and dynamics in the brain. *J. Phys.* 3:015007. doi: 10.1088/2632-072X/ac4bec

Jirsa, V. K., Proix, T., Perdikis, D., Woodman, M. M., Wang, H., Bernard, C., et al. (2017). The virtual epileptic patient: individualized whole-brain models of epilepsy spread. *NeuroImage* 145, 377–388. doi: 10.1016/j.neuroimage.2016.04.049

Markram, H., Lübke, J., Frotscher, M., and Sakmann, B. (1997). Regulation of synaptic efficacy by coincidence of postsynaptic APs and EPSPs. *Science* 275, 213–215. doi: 10.1126/science.275.5297.213

McIntosh, A. R., and Jirsa, V. K. (2019). The hidden repertoire of brain dynamics and dysfunction. *Netw. Neurosci.* 3, 994–1008. doi: 10.1162/netn_a_00107

Messé, A. (2020). Parcellation influence on the connectivity-based structure‐function relationship in the human brain. *Hum. Brain Mapp.* 41, 1167–1180. doi: 10.1002/hbm.24866

Montbrió, E., Pazó, D., and Roxin, A. (2015). Macroscopic description for networks of spiking neurons. *Phys. Rev. X* 5:021028. doi: 10.1103/PhysRevX.5.021028

Ott, E., and Antonsen, T. M. (2008). Low dimensional behavior of large systems of globally coupled oscillators. *Chaos* 18:037113. doi: 10.1063/1.2930766

Park, H. J., and Friston, K. (2013). Structural and functional brain networks: from connections to cognition. *Science* 342:6158. doi: 10.1126/science.1238411

Popovych, O. V., Manos, T., Hoffstaedter, F., and Eickhoff, S. B. (2019). What can computational models contribute to neuroimaging data analytics? *Front. Syst. Neurosci.* 12:68. doi: 10.3389/fnsys.2018.00068

Suárez, L. E., Markello, R. D., Betzel, R. F., and Misic, B. (2020). Linking structure and function in macroscale brain networks. *Trends Cogn. Sci.* 24, 302–315. doi: 10.1016/j.tics.2020.01.008

Taher, H., Torcini, A., and Olmi, S. (2020). Exact neural mass model for synaptic-based working memory. *PLoS Comput. Biol.* 16:e1008533. doi: 10.1371/journal.pcbi.1008533

Conflict of Interest: The authors declare that the research was conducted in the absence of any commercial or financial relationships that could be construed as a potential conflict of interest.

Publisher's Note: All claims expressed in this article are solely those of the authors and do not necessarily represent those of their affiliated organizations, or those of the publisher, the editors and the reviewers. Any product that may be evaluated in this article, or claim that may be made by its manufacturer, is not guaranteed or endorsed by the publisher.

frontiers in Systems Neuroscience

ORIGINAL RESEARCH
published: 30 November 2020
doi: 10.3389/fnsys.2020.604563

Influence of Autapses on Synchronization in Neural Networks With Chemical Synapses

Paulo R. Protachevicz[1], Kelly C. Iarosz[2,3], Iberê L. Caldas[1], Chris G. Antonopoulos[4], Antonio M. Batista[1,5] and Jurgen Kurths[6,7,8]*

[1] Institute of Physics, University of São Paulo, São Paulo, Brazil, [2] Faculdade de Telêmaco Borba, FATEB, Telêmaco Borba, Brazil, [3] Graduate Program in Chemical Engineering, Federal University of Technology Paraná, Ponta Grossa, Brazil, [4] Department of Mathematical Sciences, University of Essex, Colchester, United Kingdom, [5] Department of Mathematics and Statistics, State University of Ponta Grossa, Ponta Grossa, Brazil, [6] Department Complexity Science, Potsdam Institute for Climate Impact Research, Potsdam, Germany, [7] Department of Physics, Humboldt University, Berlin, Germany, [8] Centre for Analysis of Complex Systems, Sechenov First Moscow State Medical University, Moscow, Russia

A great deal of research has been devoted on the investigation of neural dynamics in various network topologies. However, only a few studies have focused on the influence of autapses, synapses from a neuron onto itself via closed loops, on neural synchronization. Here, we build a random network with adaptive exponential integrate-and-fire neurons coupled with chemical synapses, equipped with autapses, to study the effect of the latter on synchronous behavior. We consider time delay in the conductance of the pre-synaptic neuron for excitatory and inhibitory connections. Interestingly, in neural networks consisting of both excitatory and inhibitory neurons, we uncover that synchronous behavior depends on their synapse type. Our results provide evidence on the synchronous and desynchronous activities that emerge in random neural networks with chemical, inhibitory and excitatory synapses where neurons are equipped with autapses.

Keywords: synchronization, neural dynamics, integrate-and-fire model, excitatory and inhibitory neural networks, synapses, autapses

OPEN ACCESS

Edited by:
Serhiy Yanchuk, Technical University of Berlin, Germany

Reviewed by:
Eckehard Schöll, Technical University of Berlin, Germany
Sajad Jafari, Amirkabir University of Technology, Iran

****Correspondence:***
Kelly C. Iarosz
kiarosz@gmail.com

Received: *09 September 2020*
Accepted: *05 November 2020*
Published: *30 November 2020*

Citation:
Protachevicz PR, Iarosz KC, Caldas IL, Antonopoulos CG, Batista AM and Kurths J (2020) Influence of Autapses on Synchronization in Neural Networks With Chemical Synapses. Front. Syst. Neurosci. 14:604563. doi: 10.3389/fnsys.2020.604563

1. INTRODUCTION

An important research subject in neuroscience is to understand how cortical networks avoid or reach states of high synchronization (Kada et al., 2016). In normal activity, excitatory and inhibitory currents are well balanced (Tatti et al., 2018; Zhou and Yu, 2018), while in epileptic seizures, high synchronous behavior has been related to unbalanced current inputs (Drongelen et al., 2005; Avoli et al., 2016). Nazemi and Jamali (2018) showed that the structural coupling strength is important for the appearance of synchronized activities in excitatory and inhibitory neural populations. Various studies discuss the relation between structure and function in microscale and macroscale brain networks (Sporns, 2013a; DeBello et al., 2014; Sporns, 2016; Suárez et al., 2020). In a microscale organization, local excitatory and inhibitory connections are responsible for a wide range of neural interactions (Sporns, 2012; Feng et al., 2018). Bittner et al. (2017) investigated population activity structure as a function of neuron types. They verified that the population activity structure depends on the ratio of excitatory to inhibitory neurons sampled. The pyramidal cell (excitatory neuron) exhibit spike adaptation, while the fast spiking cell (inhibitory neuron) have a small or inexistent spike adaptation (Neske et al., 2015; Descalzo, 2005).

The excitatory to inhibitory and inhibitory to excitatory connections can change firing rates, persistent activities and synchronization of the population of postsynaptic neurons (Börgers and Kopell, 2003; Han et al., 2018; Hayakawa and Fukai, 2020; Kraynyukova and Tchumatchenko, 2018; Mahmud and Vassanelli, 2016). Deco et al. (2014) analyzed the effect of control in the inhibitory to excitatory coupling on the neural firing rate. Mejias et al. (2018) proposed a computational model for the primary cortex in which different layers of excitatory and inhibitory connections were considered.

A number of studies reported that excitatory synapses facilitate neural synchronization (Borges et al., 2017; Breakspear et al., 2003), while inhibitory synapses have an opposite effect (Kada et al., 2016; Ostojic, 2014; Protachevicz et al., 2019). The time delay related to excitatory and inhibitory synapses influences the neural synchronization (Gu and Zhou, 2015; Protachevicz et al., 2020). Further on, there is a strong research interest in the investigation of how excitatory and inhibitory synapses influence synchronization in neural networks (Ge and Cao, 2019). On the other hand, different types of networks have been used to analyse neural synchronization, such as random (Bondarenko and Chay, 1998; Gray and Robinson, 2008), small-world (Antonopoulos et al., 2015, 2016; Hizanidis et al., 2016; Kim and Lim, 2013; Li and Zheng, 2010; Qu et al., 2014), regular (Santos et al., 2019; Wang et al., 2007), and scale-free (Lombardi et al., 2017; Wang et al., 2011).

Experiments showed that autapses are common in the brain and that they play an important role in neural activity (Bekkers, 1998; Pouzat and Marty, 1998; Wang and Chen, 2015). An autapse is a synaptic contact from a neuron to itself via a closed loop (Bekkers, 2009; van der Loos and Glaser, 1972), i.e., an auto-connection with a time delay on signal transmission (Ergin et al., 2016). Although, autaptic connections are anatomically present *in vivo* and in the neocortex, their functions are not completely understood (Bacci et al., 2003). Experimental and theoretical studies on excitatory and inhibitory autapses have been carried out (Tamás et al., 1997; Saada-Madar et al., 2012; Suga et al., 2014; Szegedi et al., 2020) and the results have demonstrated that autaptic connections play a significant role in normal and abnormal brain dynamics (Wyart et al., 2005; Valente et al., 2016; Wang et al., 2017; Yao et al., 2019). The effects of autapses on neural dynamics were studied for single neurons (Heng-Tong and Yong, 2015; Herrmann and Klaus, 2004; Jia, 2018; Kim, 2019) and for neural networks (HuiXin et al., 2014). It has been shown that excitatory autapses contribute to a positive feedback (Zhao and Gu, 2017) and can maintain persistent activities in neurons (Bekkers, 2009). It was also found that they promote burst firing patterns (Wiles et al., 2017; Ke et al., 2019). The inhibitory autapses contribute to a negative feedback (Bacci et al., 2003; Zhao and Gu, 2017) and to the reduction of neural excitability (Bekkers, 2003; Qin et al., 2014; Szegedi et al., 2020). Guo et al. (2016) analyzed chemical and electrical autapses in the regulation of irregular neural firing. In this way, autaptic currents can modulate neural firing rates (Bacci et al., 2003). Wang et al. (2014) demonstrated that chemical autapses can induce a filtering mechanism in random synaptic inputs. Interestingly, inhibitory autapses can favor synchronization during cognitive activities (Deleuze et al., 2019). Short-term memory storage was observed by Seung et al. (2000) in a neuron with autapses submitted to excitatory and inhibitory currents. Finally, a study on epilepsy has exhibited that the number of autaptic connections can be different in her epileptic tissue (Bacci et al., 2003).

Here, we construct a random network with adaptive exponential integrate-and-fire (AEIF) neurons coupled with chemical synapses. The model of AEIF neurons was proposed by Brette and Gerstner (2005) and has been used to mimic neural spike and burst activities. Due to the fact that the chemical synapses can be excitatory and inhibitory, we build a network with excitatory synapses and autapses, a network with inhibitory synapses and autapses, and a network with both types of synapses and autapses. In the mixed network, we consider 80% of excitatory and 20% of inhibitory synapses and autapses. In this work, we focus on the investigation of the influence of autapses on neural synchronization. Ladenbauer et al. (2013) studied the role of adaptation in excitatory and inhibitory populations of AEIF neurons upon synchronization, depending on whether the recurrent synaptic excitatory or inhibitory couplings dominate. In our work, we show that not only the adaptation, but also the autapses can play an important role in the synchronous behavior. To do so, we compute the order parameter to quantify synchronization, the coefficient of variation in neural activity, firing rates and synaptic current inputs. In our simulations, we observe that autapses can increase or decrease synchronous behavior in neural networks with excitatory synapses. However, when only inhibitory synapses are considered, synchronization does not suffer significant alterations in the presence of autapses. Interestingly, in networks with excitatory and inhibitory synapses, we show that excitatory autapses can give rise to synchronous or desynchronous neural activity. Our results provide evidence how synchronous and desynchronous activities can emerge in neural networks due to autapses and contribute to understanding further the relation between autapses and neural synchronization.

The paper is organized as follows: in section 2, we introduce the neural network of AEIF neurons and the diagnostic tools that will be used, such as the order parameter for synchronization, the coefficient of variation, the firing rates and synaptic current inputs. In section 3, we present the results of our study concerning the effects of autapses in neural synchronization, and in section 4, we draw our conclusions.

2. METHODS

2.1. The AEIF Model With Neural Autapses and Network Configurations

The cortex comprises mainly excitatory pyramidal neurons and inhibitory interneurons (Atencio and Schreiner, 2008). Inhibitory neurons have a relatively higher firing rate than excitatory ones (Wilson et al., 1994; Inawashiro et al., 1999; Baeg et al., 2001). In the mammalian cortex, the firing pattern of excitatory neurons corresponds to regular spiking (Neske et al., 2015), while inhibitory neurons exhibit fast spiking activities (Wang et al., 2016). Furthermore, excitatory neurons show

adaptation properties in response to depolarizing inputs and the inhibitory adaptation current is negligible or nonexistent (Foehring et al., 1991; Mancilla et al., 1998; Hensch and Fagiolini, 2004; Destexhe, 2009; Masia et al., 2018; Borges et al., 2020). The fast spiking interneurons are the most common inhibitory neurons in the cortex (Puig et al., 2008).

In the neural networks considered in this work, the dynamics of each neuron j, where $j = 1, \ldots, N$, is given by the adaptive exponential integrate-and-fire model. In this framework, N denotes the total number of neurons in the network. The AEIF model is able to reproduce different firing patterns, including regular and fast spiking (di Volo et al., 2019). The network dynamics is given by the following set of coupled, nonlinear, ordinary differential equations

$$\begin{aligned} C_{\mathrm{m}}\frac{dV_j}{dt} &= -g_{\mathrm{L}}(V_j - E_{\mathrm{L}}) + g_{\mathrm{L}}\Delta_{\mathrm{T}}\exp\left(\frac{V_j - V_{\mathrm{T}}}{\Delta_{\mathrm{T}}}\right) \\ &\quad - w_j + I + I_j^{\mathrm{chem}}(t), \\ \tau_w\frac{dw_j}{dt} &= a_j(V_j - E_{\mathrm{L}}) - w_j, \\ \tau_{\mathrm{s}}\frac{dg_j}{dt} &= -g_j, \end{aligned} \tag{1}$$

where V_j is the membrane potential, w_j the adaptation current and g_j the synaptic conductance of neuron j. k and j identify the pre and postsynaptic neurons. When the membrane potential of neuron j is above the threshold V_{thres}, i.e., when $V_j > V_{\mathrm{thres}}$ (Naud et al., 2008), the state variables are updated according to the rules

$$\begin{aligned} V_j &\to V_{\mathrm{r}}, \\ w_j &\to w_j + b_j, \\ g_j &\to g_j + g_{\mathrm{s}}, \end{aligned} \tag{2}$$

where g_{s} assumes the value $g_{\mathrm{e}}^{\mathrm{aut}}$ for excitatory autapses, g_{e} for synapses among excitatory neurons, g_{ei} for synapses from excitatory to inhibitory neurons, $g_{\mathrm{i}}^{\mathrm{aut}}$ for inhibitory autapses, g_{i} for synapses among inhibitory neurons and g_{ie} for synapses from inhibitory to excitatory neurons. We consider a neuron is excitatory (inhibitory) when it is connected to another neuron with an excitatory (inhibitory) synapse. The initial conditions of V_j are randomly distributed in the interval $V_j = [-70, -50]$ mV. The initial values of w_j are randomly distributed in the interval $w_j = [0, 300]$ pA for excitatory and $w_j = [0, 80]$ pA for inhibitory neurons. We consider the initial value of g_j equal to zero for all neurons. **Table 1** summarizes the description and values of the parameters used in the simulations.

The synaptic current arriving at each neuron depends on specific parameters, including the connectivity encoded in the adjacency matrices M^{exc} and M^{inh}, i.e., in the excitatory and inhibitory connectivity matrices. In particular, the input current I_j^{chem} arriving at each neuron j, is calculated by

$$I_j^{\mathrm{chem}}(t) = I_j^{\mathrm{exc}}(t) + I_j^{\mathrm{inh}}(t), \tag{3}$$

TABLE 1 | Description and values of the parameters in the AEIF system (1) and (2) used in the simulations.

Parameter	Description	Value
N	Number of AEIF neurons	1,000 neurons
C_{m}	Membrane capacitance	200 pF
g_{L}	Leak conductance	12 nS
E_{L}	Leak reversal potential	−70 mV
I	Constant input current	270 pA
Δ_{T}	Slope factor	2 mV
V_{T}	Potential threshold	−50 mV
τ_w	Adaptation time constant	300 ms
τ_{s}	Synaptic time constant	2.728 ms
V_{r}	Reset potential	−58 mV
M_{jk}^{exc}	Adjacency matrix elements	0 or 1
M_{jk}^{inh}	Adjacency matrix elements	0 or 1
t_{ini}	Initial time in the analyses	10 s
t_{fin}	Final time in the analyses	20 s
a_j	Subthreshold adaptation	[1.9, 2.1] nS •
		0 nS ⋆
b_j	Triggered adaptation	70 pA •
		0 pA ⋆
V_{REV}	Synaptic reversal potential	$V_{\mathrm{REV}}^{\mathrm{exc}} = 0$ mV •
		$V_{\mathrm{REV}}^{\mathrm{inh}} = -80$ mV ⋆
g_{s}	Chemical conductances	g_{e}, $g_{\mathrm{e}}^{\mathrm{aut}}$, g_{ei} •
		g_{i}, $g_{\mathrm{i}}^{\mathrm{aut}}$, g_{ie} ⋆
g_{e}	Excitatory to excitatory	[0,0.5] nS •
$g_{\mathrm{e}}^{\mathrm{aut}}$	Excitatory autaptic	[0,35] nS •
g_{ei}	Excitatory to inhibitory	[0,5] nS •
g_{i}	Inhibitory to inhibitory	[0,2] nS ⋆
$g_{\mathrm{i}}^{\mathrm{aut}}$	Inhibitory autaptic	[0,100] nS ⋆
g_{ie}	Inhibitory to excitatory	[0,3] nS ⋆
d_j	Time delay	$d_{\mathrm{exc}} = 1.5$ ms •
		$d_{\mathrm{inh}} = 0.8$ ms ⋆

Values for parameters for excitatory and inhibitory connections are denoted by • and ⋆, respectively.

where

$$\begin{aligned} I_j^{\mathrm{exc}}(t) &= I_j^{\mathrm{ee}}(t) + I_j^{\mathrm{ei}}(t) + I_j^{\mathrm{e,aut}}(t) \\ &= (V_{\mathrm{REV}}^{\mathrm{exc}} - V_j(t))\sum_{k=1}^{N} M_{jk}^{\mathrm{exc}} g_k(t - d_{\mathrm{exc}}) \end{aligned}$$

and

$$\begin{aligned} I_j^{\mathrm{inh}}(t) &= I_j^{\mathrm{ii}}(t) + I_j^{\mathrm{ie}}(t) + I_j^{\mathrm{i,aut}}(t) \\ &= (V_{\mathrm{REV}}^{\mathrm{inh}} - V_j(t))\sum_{k=1}^{N} M_{jk}^{\mathrm{inh}} g_k(t - d_{\mathrm{inh}}). \end{aligned}$$

In this framework, the type of synapse (excitatory or inhibitory) depends on the synaptic reversal potential V_{REV}. We consider $V_{\mathrm{REV}}^{\mathrm{exc}} = 0$ mV for excitatory and $V_{\mathrm{REV}}^{\mathrm{inh}} = -80$ mV for inhibitory synapses. The time delay in the conductance of the pre-synaptic

neuron k (g_k) assumes $d_{\text{exc}} = 1.5$ ms for excitatory and $d_{\text{inh}} = 0.8$ ms for inhibitory connections (Borges et al., 2020). The influence of delayed conductance on neural synchronization was studied in Protachevicz et al. (2020). There are no spike activities in the time interval $t = [-d_j, 0]$.

The first N_{exc} neurons are excitatory and the last N_{inh} inhibitory. The connections that depart from excitatory and inhibitory neurons are associated with the excitatory and inhibitory matrices, M^{exc} and M^{inh}, where each entry is denoted M^{exc}_{jk} and M^{inh}_{jk}, respectively. These adjacency matrices are binary and have entries equal to 1 when there is a connection from neuron k to neuron j, or 0 otherwise, as shown in **Figure 1**.

We consider $P_{\text{exc}} = 80\%$ excitatory and $P_{\text{inh}} = 20\%$ inhibitory neural populations following di Volo et al. (2019) and Noback et al. (2005), where the numbers of excitatory and inhibitory neurons are given by $N_{\text{exc}} = P_{\text{exc}}N$ and $N_{\text{inh}} = P_{\text{inh}}N$, respectively. The connectivity probabilities are set to $p_{\text{e}}^{\text{aut}} = p_{\text{i}}^{\text{aut}} = 0.25$ for excitatory and inhibitory autapses, to $p_{\text{e}} = 0.05$ and $p_{\text{i}} = 0.2$ for connectivity within the same neural population and to $p_{\text{ei}} = p_{\text{ie}} = 0.05$ for connectivity among different neural populations (di Volo et al., 2019). The subscripts "e" and "i" stand for "excitatory" and "inhibitory", respectively and the superscript "aut" stands for "autapses." The terms p_{ei} and p_{ie} represent the probabilities of connections from excitatory to inhibitory and from inhibitory to excitatory neurons, respectively.

The probabilities of excitatory and inhibitory autapses are defined by

$$p_{\text{e}}^{\text{aut}} = \frac{N_{\text{e}}^{\text{aut}}}{N_{\text{exc}}} \quad \text{and} \quad p_{\text{i}}^{\text{aut}} = \frac{N_{\text{i}}^{\text{aut}}}{N_{\text{inh}}},$$

where $N_{\text{e}}^{\text{aut}}$ and $N_{\text{i}}^{\text{aut}}$ are the number of autapses in the excitatory and inhibitory populations, respectively. For a network with only excitatory (inhibitory) neurons, the number of excitatory (inhibitory) neurons is $N_{\text{exc}} = N$ ($N_{\text{inh}} = N$). For connections within the excitatory and inhibitory populations, the corresponding probabilities p_{e} and p_{i} are given by

$$p_{\text{e}} = \frac{N_{\text{e}}}{N_{\text{exc}}(N_{\text{exc}} - 1)} \quad \text{and} \quad p_{\text{i}} = \frac{N_{\text{i}}}{N_{\text{inh}}(N_{\text{inh}} - 1)},$$

where N_{e} and N_{i} are the number of synaptic connections in the excitatory and inhibitory populations, respectively. For connections among different populations, the corresponding probabilities are given by

$$p_{\text{ei}} = \frac{N_{\text{ei}}}{N_{\text{exc}}N_{\text{inh}}} \quad \text{and} \quad p_{\text{ie}} = \frac{N_{\text{ie}}}{N_{\text{exc}}N_{\text{inh}}},$$

where N_{ei} and N_{ie} are the number of synaptic connections from the excitatory to the inhibitory and from the inhibitory to the excitatory populations, respectively. Therefore, when only one neural population is considered, p_{ei} and p_{ie} cannot be defined. The resulting six connectivity probabilities are represented in the connectivity matrix in **Figure 1**, where k and j denote the pre- and post-synaptic neurons, respectively. **Figure 1** shows the connections associated to probabilities: (**Figure 1A**) in the same population (p_{e} and p_{i}), (**Figure 1B**) for autapses ($p_{\text{e}}^{\text{aut}}$ and $p_{\text{i}}^{\text{aut}}$) and (**Figure 1C**) among different populations (p_{ei} and p_{ie}).

Finally, we associate the conductances g_{e}, g_{i}, $g_{\text{e}}^{\text{aut}}$, $g_{\text{i}}^{\text{aut}}$, g_{ei}, and g_{ie} to the corresponding connectivity probabilities discussed before. To solve the set of ordinary differential equations in system (1), we used the 4th order Runge-Kutta method with the integration time-step equal to 10^{-2} ms.

2.2. Computation of Neural Synchronization

Synchronous behavior in neural networks can be quantified by means of the order parameter R (Kuramoto, 1984)

$$R(t) = \left| \frac{1}{N} \sum_{j=1}^{N} \exp\left(\text{i}\psi_j(t)\right) \right|,$$

where $R(t)$ is the amplitude of a centroid phase vector over time, i the imaginary unit, satisfying $\text{i}^2 = -1$, and $|\cdot|$, the vector-norm of the argument. The phase of each neuron j in time is obtained by means of

$$\psi_j(t) = 2\pi m + 2\pi \frac{t - t_{j,m}}{t_{j,m+1} - t_{j,m}}, \tag{4}$$

where $t_{j,m}$ is the time of the m-th spike of neuron j, where $t_{j,m} < t < t_{j,m+1}$ (Rosenblum et al., 1997). We consider that spikes occur whenever $V_j > V_{\text{thres}}$ (Naud et al., 2008). $R(t)$ takes values in $[0, 1]$ and, is equal to 0 for completely desynchronized neural activity and 1 for fully synchronized neural behavior. We compute the time-average order parameter $\overline{R}$ (Batista et al., 2017), given by

$$\overline{R} = \frac{1}{t_{\text{fin}} - t_{\text{ini}}} \int_{t_{\text{ini}}}^{t_{\text{fin}}} R(t)dt, \tag{5}$$

where $(t_{\text{fin}} - t_{\text{ini}})$ is the length of the time window $[t_{\text{ini}}, t_{\text{fin}}]$. Here, we have used $t_{\text{ini}} = 10$ s and $t_{\text{fin}} = 20$ s. Similarly, we calculate the synchronization of the non-autaptic neurons

$$R_{\text{non}}(t) = \left| \frac{1}{N^{\text{non}}} \sum_{j=1}^{N^{\text{non}}} \exp\left(\text{i}\psi_j^{\text{non}}(t)\right) \right|$$

and autaptic neurons

$$R_{\text{aut}}(t) = \left| \frac{1}{N^{\text{aut}}} \sum_{j=1}^{N^{\text{aut}}} \exp\left(\text{i}\psi_j^{\text{aut}}(t)\right) \right|,$$

where N^{non} and N^{aut} are the number of non-autaptic and autaptic neurons, respectively. In this context, ψ_j^{non} and ψ_j^{aut} are the phases of the non-autaptic and autaptic neuron j and both terms are computed using Equation (4) for the times of spiking of the non-autaptic and autaptic neurons, respectively. $\overline{R}_{\text{non}}$ and $\overline{R}_{\text{aut}}$ are then obtained according to Equation (5).

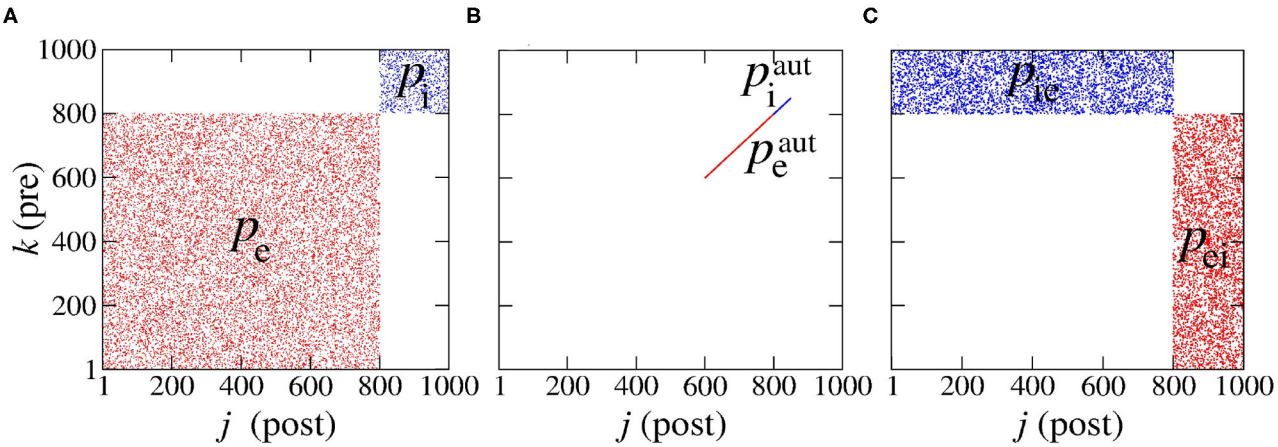

FIGURE 1 | Representation of the connections: **(A)** in the same population, **(B)** for autapses, and **(C)** among different neural populations. Here, "pre" stands for "pre-synaptic" and "post" for "post-synaptic." We note that we have used $P_{exc} = 80\%$ excitatory (denoted red) and $P_{inh} = 20\%$ inhibitory (denoted blue) neural populations which amounts to a total of $N = 1,000$ neurons.

2.3. Mean Coefficient of Variation of Interspike Intervals

We calculate the interspike intervals of each neuron to obtain the mean coefficient of variation. In particular, the m-th interspike interval of neuron j, ISI_j^m, is defined as the difference between two consecutive spikes,

$$\mathrm{ISI}_j^m = t_{j,m+1} - t_{j,m} > 0,$$

where $t_{j,m}$ is the time of the m-th spike of neuron j. Using the mean value of ISI_j over all m, $\overline{\mathrm{ISI}}_j$ and its standard deviation σ_{ISI_j}, we can compute the coefficient of variation (CV) of neuron j,

$$\mathrm{CV}_j = \frac{\sigma_{\mathrm{ISI}_j}}{\overline{\mathrm{ISI}}_j}.$$

The average CV over all neurons in the network, $\overline{\mathrm{CV}}$, can then be computed by

$$\overline{\mathrm{CV}} = \frac{1}{N}\sum_{j=1}^{N} \mathrm{CV}_j.$$

We use the value of $\overline{\mathrm{CV}}$ to identify spikes whenever $\overline{\mathrm{CV}} < 0.5$ and burst firing patterns whenever $\overline{\mathrm{CV}} \geq 0.5$ (Borges et al., 2017; Protachevicz et al., 2018) in neural activity.

2.4. Firing Rates in Neural Populations

The mean firing-rate of all neurons in a network is computed by means of

$$\overline{F} = \frac{1}{N(t_{\mathrm{fin}} - t_{\mathrm{ini}})}\sum_{j=1}^{N}\left(\int_{t_{\mathrm{ini}}}^{t_{\mathrm{fin}}} \delta(t' - t_j)dt'\right),$$

where t_j is the firing time of neuron j. In some occasions, we calculate the mean firing frequency of neurons with and without autapses,

$$\overline{F}_{\mathrm{aut}} = \frac{1}{N_{\mathrm{x}}^{\mathrm{aut}}(t_{\mathrm{fin}} - t_{\mathrm{ini}})}\sum_{j=1}^{N_{\mathrm{x}}^{\mathrm{aut}}}\left(\int_{t_{\mathrm{ini}}}^{t_{\mathrm{fin}}} \delta(t' - t_j^{\mathrm{aut}})dt'\right)$$

and

$$\overline{F}_{\mathrm{non}} = \frac{1}{N_{\mathrm{x}}^{\mathrm{non}}(t_{\mathrm{fin}} - t_{\mathrm{ini}})}\sum_{j=1}^{N_{\mathrm{x}}^{\mathrm{non}}}\left(\int_{t_{\mathrm{ini}}}^{t_{\mathrm{fin}}} \delta(t' - t_j^{\mathrm{non}})dt'\right),$$

where $N_{\mathrm{x}}^{\mathrm{aut}}$ and $N_{\mathrm{x}}^{\mathrm{non}}$ are the number of neurons with and without autapses, and t_j^{aut} and t_j^{non} the firing times of neurons with and without autapses. The subscript "x" denotes the population of excitatory ("e") or inhibitory ("i") neurons.

Similarly, we calculate the firing rate of excitatory and inhibitory neurons by means of

$$\overline{F}_{\mathrm{exc}} = \frac{1}{N_{\mathrm{exc}}(t_{\mathrm{fin}} - t_{\mathrm{ini}})}\sum_{j=1}^{N_{\mathrm{exc}}}\left(\int_{t_{\mathrm{ini}}}^{t_{\mathrm{fin}}} \delta(t' - t_j^{\mathrm{exc}})dt'\right)$$

and

$$\overline{F}_{\mathrm{inh}} = \frac{1}{N_{\mathrm{inh}}(t_{\mathrm{fin}} - t_{\mathrm{ini}})}\sum_{j=1}^{N_{\mathrm{inh}}}\left(\int_{t_{\mathrm{ini}}}^{t_{\mathrm{fin}}} \delta(t' - t_j^{\mathrm{inh}})dt'\right),$$

where t_j^{exc} and t_j^{inh} are the firing times of the excitatory and inhibitory neurons, respectively.

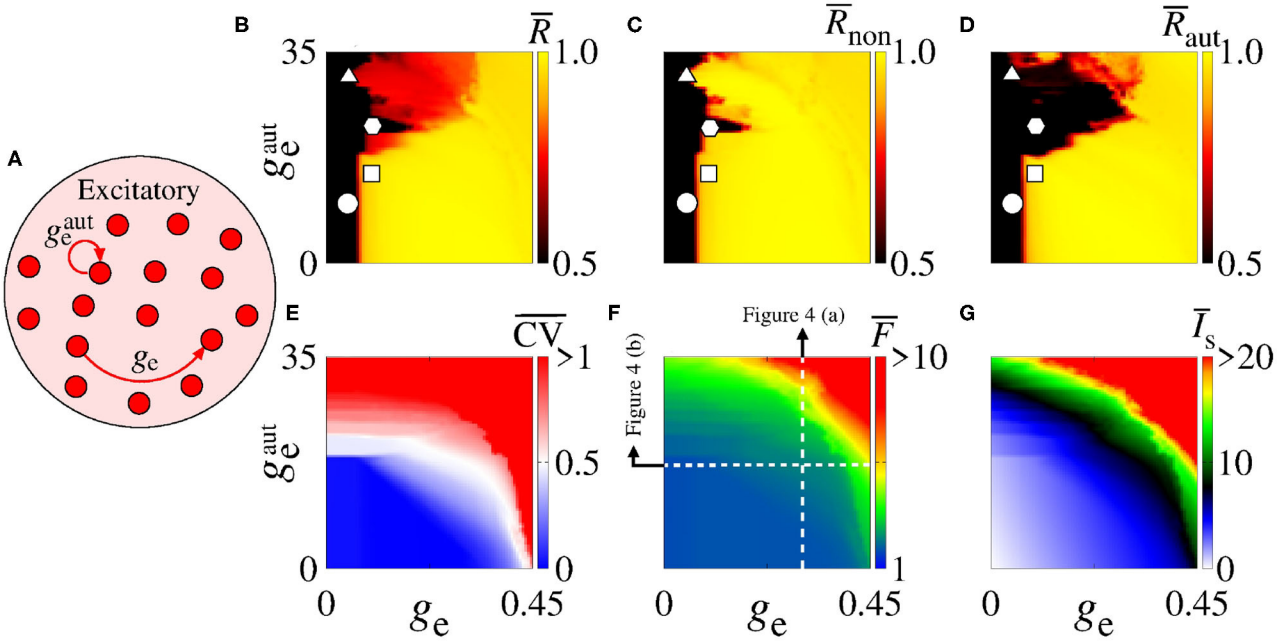

FIGURE 2 | (A) Schematic representation of the neural network where g_e is the intensity of excitatory synaptic conductance and g_e^{aut} of the excitatory autaptic conductance. Parameter space $g_e \times g_e^{aut}$, where the color bars correspond to **(B)** $\overline{R}$, **(C)** $\overline{R}_{non}$, **(D)** $\overline{R}_{aut}$, **(E)** $\overline{CV}$, **(F)** $\overline{F}$, and **(G)** $\overline{I}_s$. The raster plots of the parameters indicated in **(B–D)** (circle, square, triangle, and hexagon) are shown in **Figure 3**. The vertical and horizontal white, dash, lines in **(F)** are used to vary g_e^{aut} and g_e in the computations in **Figures 4A,B**, respectively. The closed loop in **(A)** corresponds to an autapse of excitatory autaptic conductance g_e^{aut}.

2.5. Synaptic Current Inputs

In our work, we calculate the mean instantaneous input $I^{chem}(t)$ and the time average of the synaptic input $\overline{I}_s$ (pA) in the network by

$$I^{chem}(t) = \frac{1}{N}\sum_{j=1}^{N} I_j^{chem}(t)$$

and

$$\overline{I}_s = \frac{1}{t_{fin} - t_{ini}} \int_{t_{ini}}^{t_{fin}} I^{chem}(t)dt,$$

respectively, where $I_j^{chem}(t)$ is given by Equation (3). In this respect, the values of I^{chem} change over time due to excitatory and inhibitory inputs received by neuron j, where $j = 1, \ldots, N$.

3. RESULTS AND DISCUSSION

3.1. Network With Excitatory Neurons Only

Networks with excitatory neurons were studied previously by Borges et al. (2017) and Protachevicz et al. (2019). These studies showed that excitatory neurons can change firing patterns and improve neural synchronization. Fardet et al. (2018) and Yin et al. (2018) reported that excitatory autapses with few milliseconds time delay can change neural activities from spikes to bursts. Wiles et al. (2017) demonstrated that excitatory autaptic connections contribute more to bursting firing patterns than inhibitory ones.

In **Figure 2**, we consider a neural network with excitatory neurons only, where g_e corresponds to the intensity of excitatory synaptic conductance and g_e^{aut} to the intensity of excitatory autaptic conductance. In our neural network, a neuron receives many connections from other neurons with small intensity of synaptic conductances. For the autaptic neurons, only one synaptic contact from a neuron to itself via a closed loop is considered. Due to this fact, to study the autaptic influence on the high synchronous activities, we consider values of g_e^{aut} greater than g_e. **Figure 2A** shows a schematic representation of a neural network of excitatory neurons only with a single autapse represented by the closed loop with excitatory autaptic conductance g_e^{aut}. **Figures 2B–D** give the mean order parameter in the parameter space $g_e \times g_e^{aut}$. We see that excitatory autapses can increase or reduce the synchronization in a population of excitatory neurons when the intensity of the excitatory synaptic conductance is small. In these panels, the circle ($g_e = 0.05$ nS and $g_e^{aut} = 10$ nS), triangle ($g_e = 0.05$ nS and $g_e^{aut} = 31$ nS), square ($g_e = 0.1$ nS and $g_e^{aut} = 15$ nS), and hexagon ($g_e = 0.1$ nS and $g_e^{aut} = 22$ nS) symbols indicate the values of the parameters shown in **Figure 3**. We observe that desynchronous firing patterns as seen in **Figure 3A** can become more synchronous, as it can be seen in **Figure 3B**, due the increase of the excitatory autaptic conductance. On the other hand, the increase of the autaptic conductance can decrease the level of synchronization in the network, i.e., from high in **Figure 3C** to low synchronous activities in **Figure 3D**. However,

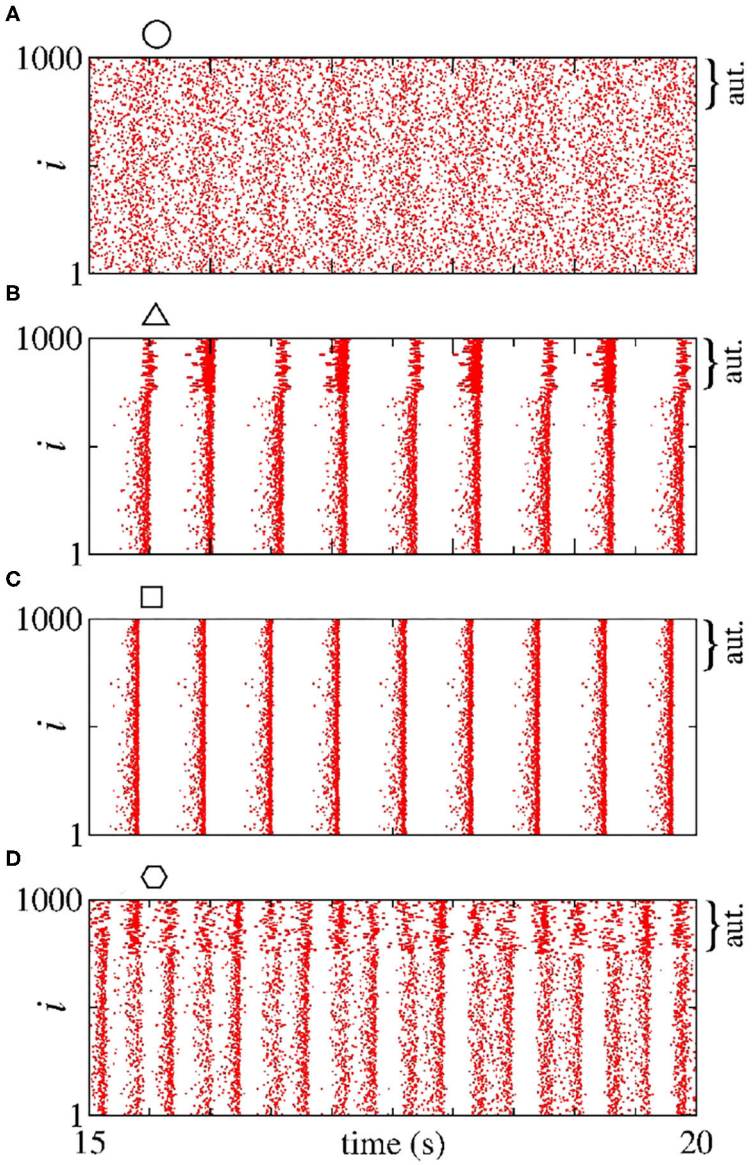

FIGURE 3 | (A–D) Raster plots for the neural network with excitatory neurons only. The values of the parameters g_e and g_e^{aut} are indicated in **Figures 2B–D** by circle, triangle, square, and hexagon symbols, respectively. The curly brackets in the upper right corner of the plots denote the autaptic neurons considered.

as shown in **Figure 2D**, the autaptic connections affect mainly the synchronization of autaptic neurons.

For a strong excitatory synaptic coupling ($g_e \geq 0.3$), autapses do not reduce neural synchronization significantly. **Figures 2E–G** show the mean coefficient of variation ($\overline{CV}$), firing frequency ($\overline{F}$), and synaptic current ($\overline{I}_s$), respectively. We verify that the excitatory autaptic neurons promote the increase of $\overline{CV}$, $\overline{F}$ and $\overline{I}_s$ in the network. In **Figure 2E**, we find that both synaptic and autaptic couplings can lead to burst activities, as reported by Borges et al. (2017) and Fardet et al. (2018). The burst and spike activities are characterized by $\overline{CV} \geq 0.5$ (red region) and $\overline{CV} < 0.5$ (blue region), respectively. In addition, excitatory autaptic neurons can change the firing patterns of all neurons in the network from spike to burst activities. In **Figures 2F,G**, we observe that excitatory autapses contribute to the increase of the mean firing frequency and synaptic current.

Next, we analyse the influence of autaptic connections on neural firing frequency. **Figure 4** shows the mean firing frequency of neurons without ($\overline{F}_{non}$) and with autapses ($\overline{F}_{aut}$), as well as of all neurons in the excitatory network ($\overline{F}$). In **Figure 4A**, we consider $g_e = 0.3$ nS varying g_e^{aut}, while in **Figure 4B**, we use $g_e^{aut} = 20$ nS varying g_e, as shown in **Figure 2F** with white, dash, lines. We find that the autaptic connections increase the firing frequency of all neurons in the network and mainly those with autaptic connections. In our simulations, neurons with excitatory autapses exhibit the highest firing rate.

3.2. Network With Inhibitory Neurons Only

Synaptic inhibition regulates the level of neural activity and can prevent hyper excitability (Fröhlich, 2016). Studies have shown that neural networks can exhibit synchronous activities due to inhibitory synapses (van Vreeswijk et al., 1994; Elson et al., 2002; Franović and Miljković, 2010; Chauhan et al., 2018). Here, we analyse the influence of inhibitory synapses and autapses by varying g_i and g_i^{aut}, as shown in **Figure 5A**. **Figure 5B** shows that inhibitory synapses and autapses do not give rise to the increase of neural synchronization in the network. Actually, neural synchronization due to inhibition is possible when it is considered together with other mechanisms related to neural interactions (Bartos et al., 2002), e.g., with gap junctions associated to inhibitory synapses (Bou-Flores and Berger, 2000; Beierlein et al., 2000; Kopell and Ermentrout, 2004; Bartos et al., 2007; Pfeuty et al., 2007; Guo et al., 2012; Reimbayev et al., 2017).

In our simulations, we do not observe that inhibitory interactions promote synchronization in the network. Although this is not surprising, it helps to identify the role of inhibitory autapses in neural synchronization. **Figure 5C** shows that there is no change from spike to burst patterns, either. In **Figure 5D**, we verify that both inhibitory synapses and autapses increase the intensity of the mean negative synaptic current.

In **Figure 5E**, we see that inhibitory synapses contribute to the decrease of $\overline{F}$, while **Figures 5F,G** show the mean firing rate for non-autaptic neurons, i.e., neurons without autapses ($\overline{F}_{non}$) and for autaptic neurons ($\overline{F}_{aut}$), respectively. The autapses reduce the firing-rate of the autaptic neurons, what can lead to an increase of the firing rate of the non-autaptic neurons. This can be better observed in **Figure 6A**, which shows the values of $\overline{F}_{non}$, $\overline{F}_{aut}$, and $\overline{F}$ as a function of g_i^{aut} for $g_i = 0.1$ nS. **Figure 6B** shows the mean

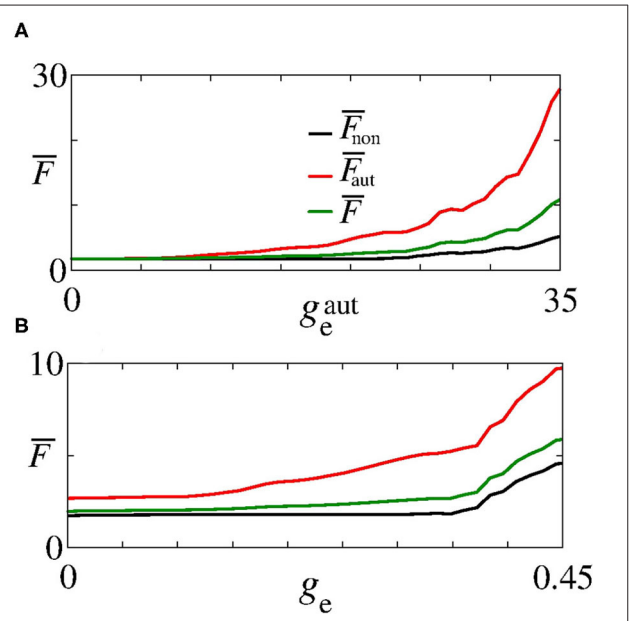

FIGURE 4 | Plot of $\overline{F}_{non}$ (black curve), $\overline{F}_{aut}$ (red curve), and $\overline{F}$ (green curve) for **(A)** $g_e = 0.3$ nS varying g_e^{aut} and **(B)** $g_e^{aut} = 20$ nS varying g_e. Here, g_e^{aut} and g_e vary along the white, dash, lines in **Figure 2F**.

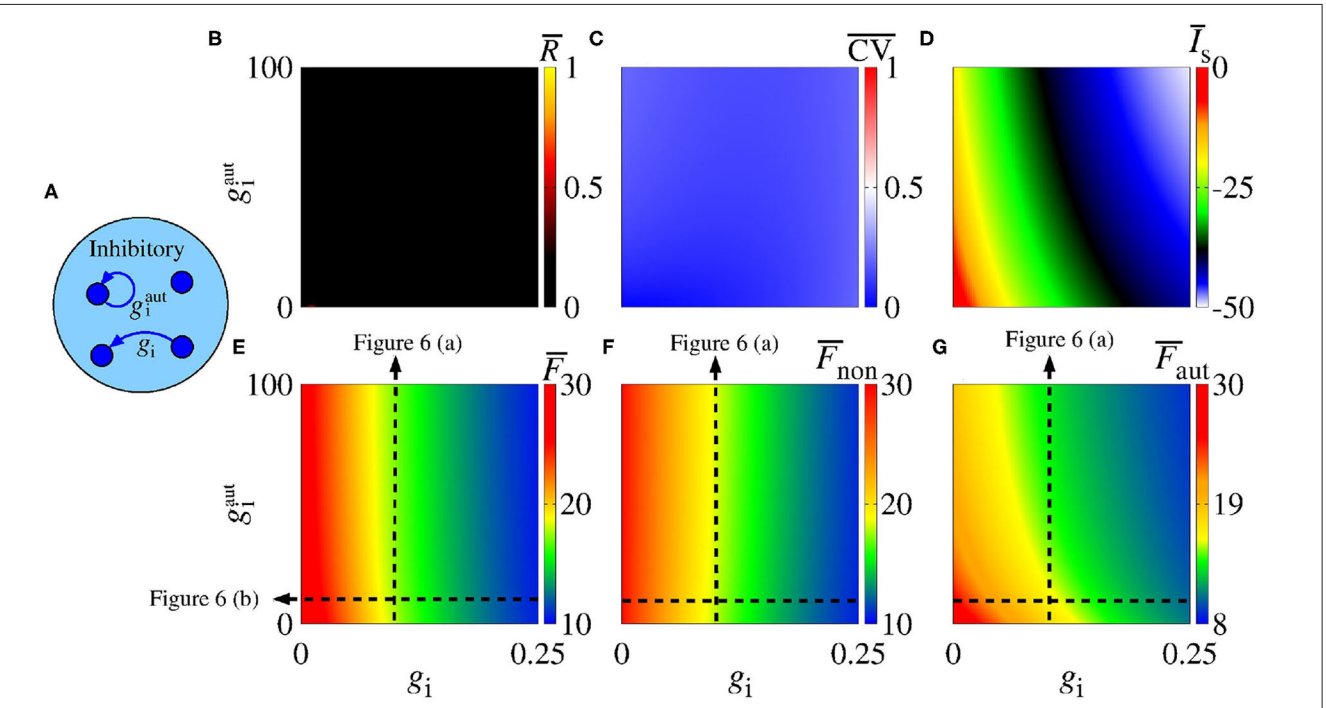

FIGURE 5 | (A) Schematic representation of an inhibitory neural population connected with inhibitory synapses and autapses. Parameter space $g_i \times g_i^{aut}$, where the color bars encode the values of **(B)** $\overline{R}$, **(C)** $\overline{CV}$, **(D)** $\overline{I}_s$, **(E)** $\overline{F}$, **(F)** $\overline{F}_{non}$, and **(G)** $\overline{F}_{aut}$. The vertical and horizontal black, dash, lines in **(E–G)** are used to vary the corresponding parameters in the computations in **Figures 6A,B**. The closed loop in **(A)** corresponds to an autapse of conductance intensity g_i^{aut}.

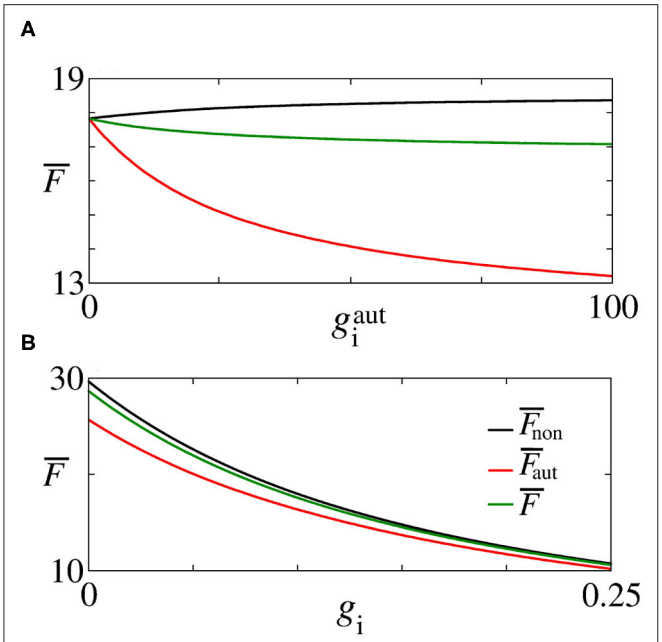

FIGURE 6 | Plot of $\overline{F}_{non}$ (black line), $\overline{F}_{aut}$ (red line), and $\overline{F}$ (green line) for **(A)** $g_i = 0.1$ nS varying g_i^{aut} and **(B)** $g_i^{aut} = 10$ nS varying g_i, indicated in **Figure 5** by the black, dash, lines.

firing rates as a function of g_i for $g_i^{aut} = 10$ nS. The neurons with inhibitory autapses have lower firing rates.

3.3. Network With a Mix of Excitatory and Inhibitory Neurons

Desynchronous neural activities in balanced excitatory/inhibitory regimes have been reported in Borges et al. (2020) and Ostojic (2014). Based on these results, here we study different combinations of g_e, g_i, g_e^{aut}, and g_i^{aut} values in the parameter space $g_{ei} \times g_{ie}$ (see **Figure 7**). The existence of synchronous and desynchronous activities depend on the values of these parameters which are related to the conductances. We focus on a set of parameters for which synchronous activities appear. Firstly, we consider $g_e = 0.5$ nS and $g_i = 2$ nS in a neural network without autaptic connections.

Figure 7A shows a schematic representation of excitatory (red circles) and inhibitory (blue circles) neurons, where g_{ei} (g_{ie}) correspond to the conductance from excitatory to inhibitory (from inhibitory to excitatory) neurons in the absence of autapses. **Figure 7B** presents the mean order parameter ($\overline{R}$) and the circle, square and triangle symbols indicate the values of the parameters considered in the computation of the raster plots shown in the right hand-side. The values of the conductances used to compute the raster plots are given by $g_{ei} = 0.5$ nS and $g_{ie} = 1.5$ nS for the circle, $g_{ei} = 1.8$ nS and $g_{ie} = 1.5$ nS for the square, and $g_{ei} = 4.5$ nS and $g_{ie} = 0.5$ nS for the triangle symbols. The blue and red points in the raster plots represent the firing of the inhibitory and excitatory neurons over time, respectively. Kada et al. (2016) reported that synchronization can be suppressed by means of inhibitory to excitatory or excitatory to inhibitory connection heterogeneity. Here, we observe that a minimal interaction between the excitatory and inhibitory neurons is required to suppress high synchronous patterns. In **Figure 7C**, we verify that $\overline{F}$ decreases when g_{ie} increases. **Figures 7D,E** show that $\overline{F}_{exc}$ and $\overline{F}_{ini}$ can decrease when g_{ie} increases. In addition, $\overline{F}_{exc}$ decreases and $\overline{F}_{ini}$ increases when g_{ei} increases. When the neural populations are uncoupled ($g_{ei} = g_{ie} = 0$), the firing rate difference in the excitatory and inhibitory neurons are mainly due to the adaptation properties of these cells.

Figure 8A shows a schematic representation of a network with a mix of excitatory and inhibitory neurons in the presence of excitatory autapses. In **Figure 8B**, we present the parameter space $g_{ei} \times g_{ie}$ for $g_e^{aut} = 30$ nS, where the color bar corresponds to $\overline{R}$. The white solid line in the parameter space indicates the transition from desynchronous to synchronous behavior in the network without excitatory autaptic conductance ($g_e^{aut} = 0$), as shown in **Figure 7B**. The raster plots in the right hand-side of the figure are computed using the values of the parameters indicated by the circle, square, and triangle symbols in **Figure 7B**. In **Figures 8C–E**, we see that excitatory autapses can increase the firing rate of all neurons, changing the mean firing rate dependence on g_{ei} and g_{ie}.

4. CONCLUSIONS

In this paper, we investigated the influence of autapses on neural synchronization in networks of coupled adaptive exponential integrate-and-fire neurons. Depending on the parameters of the system, the AEIF model exhibits spike or burst activity. In our simulations, we considered neurons randomly connected with chemical synapses in the absence or presence of autapses.

We verified that the type of synaptic connectivity plays a different role in the dynamics in the neural network, especially with regard to synchronization. It has been reported that excitatory synapses promote synchronization and firing pattern transitions. In our simulations, we found that excitatory autapses can generate firing pattern transitions for low excitatory synaptic conductances. The excitatory autaptic connections can promote desynchronization of all neurons or only of the autaptic ones in a network with neurons initially synchronized. The excitatory autapses can also increase the firing rate of all neurons. In a network with only inhibitory synapses, we did not observe inhibitory synapses and autapses promoting synchronization. We saw a reduction and increase of the firing rate of the autaptic and non-autaptic neurons, respectively, due to inhibitory autapses.

Finally, in a network with a mix of excitatory and inhibitory neurons, we saw that the interactions among the populations are essential to avoid high synchronous behavior. The excitatory to inhibitory synaptic connectivities promote the increase (decrease) of the firing rate of the inhibitory (excitatory) populations. On the other hand, the inhibitory to excitatory synaptic connectivities give rise to the decrease of the firing rate of both populations. We observed that the excitatory autapses can reduce the synchronous activities, as well as induce neural

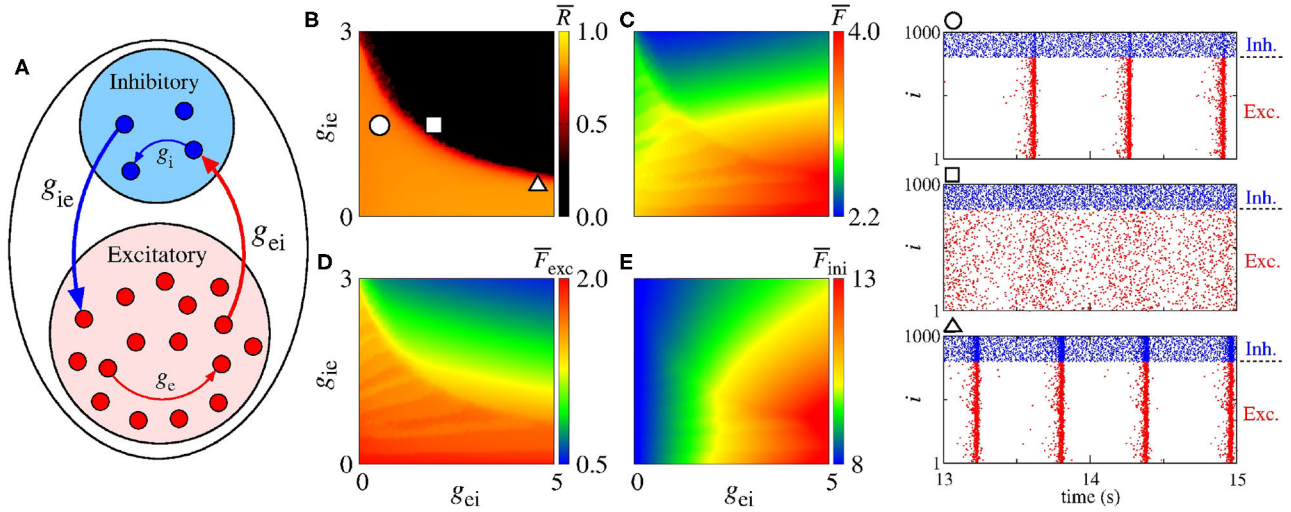

FIGURE 7 | (A) Schematic representation of a neural network with a mix of excitatory and inhibitory neurons without autapses. Parameter spaces $g_{ei} \times g_{ie}$ for $g_e = 0.5$ nS and $g_i = 2$ nS, where the color bars correspond to **(B)** $\overline{R}$, **(C)** $\overline{F}$, **(D)** $\overline{F}_{exc}$, and **(E)** $\overline{F}_{inh}$. The circle, square, and triangle symbols in **(B)** represent the values of the parameters considered in the computation of the raster plots shown in the right side. The blue and red points in the raster plots indicate the firing of the inhibitory and excitatory neurons over time, respectively.

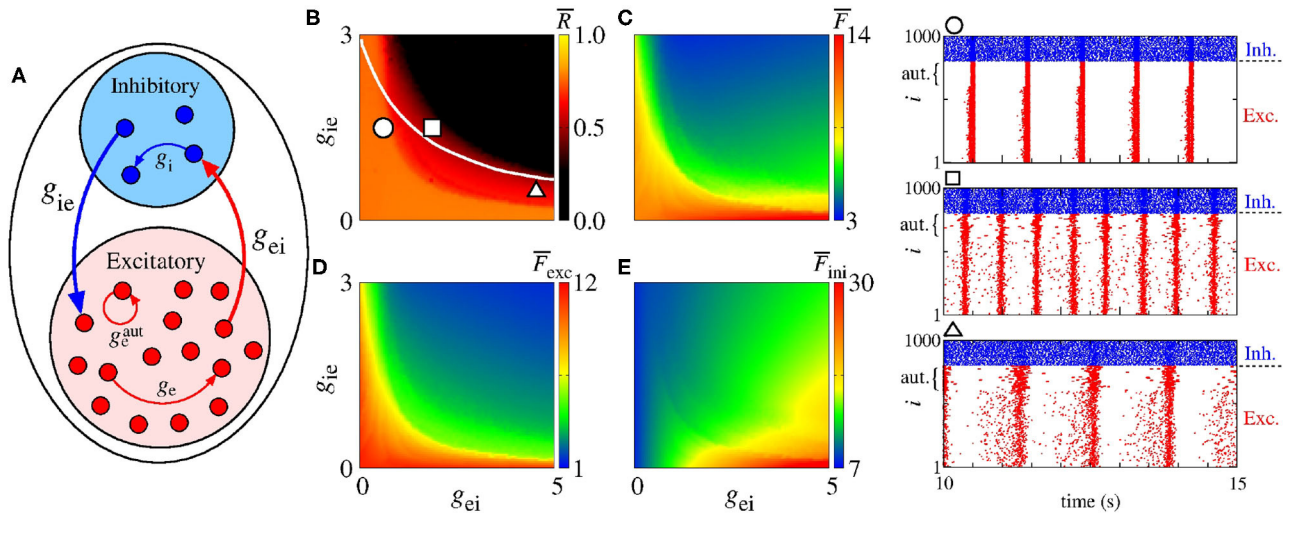

FIGURE 8 | (A) Schematic representation of a neural network with a mix of excitatory and inhibitory neurons with excitatory autapses. Parameter spaces $g_{ei} \times g_{ie}$ for $g_e = 0.5$ nS, $g_i = 2$ nS and $g_e^{aut} = 30$ nS, where the color bars correspond to **(B)** $\overline{R}$, **(C)** $\overline{F}$, **(D)** $\overline{F}_{exc}$, and **(E)** $\overline{F}_{inh}$. The circle, square, and triangle symbols in **(B)** represent the values of the parameters considered in the computation of the raster plots shown in the right side. The blue and red points in the raster plots indicate the firing of the inhibitory and excitatory neurons over time, respectively. The curly brackets in the upper left corner of the plots denote the autaptic neurons considered.

synchronization. For small conductances, excitatory autapses can not change synchronization significantly. Consequently, our results provide evidence on the synchronous and desynchronous activities that emerge in random neural networks with chemical, inhibitory and excitatory, synapses where some neurons are equipped with autapses.

In a more general context, the role of network structure upon synchronicity in networks with delayed coupling and delayed feedback was studied, and very general classifications of the network topology for large delay were given by Flunkert et al. (2010, 2014), e.g., it was shown that adding time-delayed feedback loops to a unidirectionally coupled ring enables stabilization of the chaotic synchronization, since it changes the network class. We believe that the absence or presence of autapses has similar effects upon synchronization. In future works, we plan to compute the master stability function of networks with autapses to compare with the stability of synchronization in delay-coupled networks.

DATA AVAILABILITY STATEMENT

The raw data supporting the conclusions of this article will be made available by the authors, without undue reservation.

AUTHOR CONTRIBUTIONS

PRP and KCI designed the work, developed the theory, and performed the numerical simulations. AMB wrote the manuscript with support from ILC and JK. The authors revised the manuscript several times and gave promising suggestions. All authors also contributed to manuscript revision, read, and approved the submitted version.

FUNDING

This study was possible by partial financial support provided by the following Brazilian government agencies: Fundação Araucária, National Council for Scientific and Technological Development (CNPq), Coordenação de Aperfeiçoamento de Pessoal de Nível Superior-Brasil (CAPES), and São Paulo Research Foundation (FAPESP) (2020/04624-2). We also wish to thank Newton Fund, IRTG 1740/TRP 2015/50122-0 funded by DFG/FAPESP and the RF Government Grant 075-15-2019-1885. Support from Russian Ministry of Science and Education Digital biodesign and personalized healthcare.

REFERENCES

Antonopoulos, C. G., Fokas, A. S., and Bountis, T. C. (2016). Dynamical complexity in the C. elegans neural network. *Eur. Phys. J.* 225, 1255–1269. doi: 10.1140/epjst/e2016-02670-3

Antonopoulos, C. G., Srivastava, S., Pinto, S. E. D. S., and Baptista, M. S. (2015). Do brain networks evolve by maximizing their information flow capacity? *PLoS Comput. Biol.* 11:e1004372. doi: 10.1371/journal.pcbi.1004372

Atencio, C. A., and Schreiner, C. E. (2008). Spectrotemporal processing differences between auditory cortical fast-spiking and regular-spiking neurons. *J. Neurosci.* 28, 3897–3910. doi: 10.1523/JNEUROSCI.5366-07.2008

Avoli, M., Curtis, M., Gnatkovsky, V., Gotman, J., Köhling, R. Lévesque, M., et al. (2016). Specific imbalance of excitatory/inhibitory signaling establishes seizure onset pattern in temporal lobe epilepsy. *J. Neurophysiol.* 115, 3229–3237. doi: 10.1152/jn.01128.2015

Bacci, A., Huguenard, J. R., and Prince, D.A. (2003). Functional autaptic neurotransmission in fast-spiking interneurons: a novel form of feedback inhibition in the neocortex. J. Neurosci. 23, 859–866. doi: 10.1523/JNEUROSCI.23-03-00859.2003

Baeg, E. H., Kim, Y. B., Jang, J., Kim, H. T., Mook-Jung, I., and Jung, M. W. (2001). Fast spiking and regular spiking neural correlates of fear conditioning in the medial prefrontal cortex of the rat. *Cereb. Cortex* 11, 441–451. doi: 10.1093/cercor/11.5.441

Bartos, M., Imre. V., Michael, F., Axel, M., Hannah, M., Geiger, J. R. P., et al. (2002). Fast synaptic inhibition promotes synchronized gamma oscillations in hippocampal interneuron networks. *Proc. Natl. Acad. Sci.* 99, 13222–13227. doi: 10.1073/pnas.192233099

Bartos, M., Vida, I., and Jonas, P. (2007). Synaptic mechanisms of synchronized gamma oscillations in inhibitory interneuron networks. *Nat. Rev.* 8, 45–56. doi: 10.1038/nrn2044

Batista, C. A. S., Szezech, J. D. Jr, Batista, A. M., Macau, E. E. N., and Viana, R. L. (2017). Synchronization of phase oscillators with coupling mediated by a diffusing substance. *Phys. A* 470, 236–248. doi: 10.1016/j.physa.2016.11.140

Beierlein, M., Gibson, J. R., and Connors, B. W. (2000). A network of electrically coupled interneurons drives synchronized inhibition in neocortex. *Nat. Neurosci.* 3, 904–910. doi: 10.1038/78809

Bekkers, J. M. (2003). Synaptic transmission: functional autapses in the cortex. *Curr. Biol.* 13, R443–R435. doi: 10.1016/S0960-9822(03)00363-4

Bekkers, J. M. (2009). Synaptic transmission: excitatory autapses find a function? *Curr. Biol.* 19:R296. doi: 10.1016/j.cub.2009.02.010

Bekkers, J. M. (1998). Neurophysiology: are autapses prodigal synapses? *Curr. Biol.* 8, R52–R55. doi: 10.1016/S0960-9822(98)70033-8

Bittner, S. R., Williamson, R. C., Snyder, A. C., Litwin-Kumar, A., Doiron, B., Chase, S. M., et al. (2017). Population activity structure of excitatory and inhibitory neurons. *PLoS ONE* 12:e181773. doi: 10.1371/journal.pone.0181773

Bondarenko, V. E., and Chay, T. R. (1998). Desynchronization and synchronization processes in a randomly coupled ensemble of neurons. *Phys. Rev. E* 58, 8036–8040. doi: 10.1103/PhysRevE.58.8036

Börgers, C., and Kopell, N. (2003). Synchronization in networks of excitatory and inhibitory neurons with sparse, random connectivity. *Neural Comput.* 15, 509–538. doi: 10.1162/089976603321192059

Borges, F. S., Protachevicz, P. R., Lameu, E. L., Bonetti, R. C., Iarosz, K. C., Caldas, I. L., et al. (2017). Synchronised firing patterns in a random network of adaptive exponential integrate-and-fire neuron model. *Neural Netw.* 90, 1–7. doi: 10.1016/j.neunet.2017.03.005

Borges, F. S., Protachevicz, P. R., Pena, R. F. O., Lameu, E. L., Higa, G. S. V., Kihara, A. H., et al. (2020). Self-sustained activity of low firing rate in balanced networks. *Phys. A* 537:122671. doi: 10.1016/j.physa.2019.122671

Bou-Flores, C., and Berger, A. (2000). Gap junction and inhibitory synapses modelated inspiratory motoneuron synchronization. *Am. Physiol. Soc.* 85, 1543–1541. doi: 10.1152/jn.2001.85.4.1543

Breakspear, M., Terry, J. R., and Friston, K. J. (2003). Modulation of excitatory synaptic coupling facilitates synchronization and complex dynamics in a nonlinear model of neural dynamics. *Neurocomputing* 52–54, 151–158. doi: 10.1016/S0925-2312(02)00740-3

Brette, R., and Gerstner, W. (2005). Adaptive exponential integrate-and-fire model as an effective description of neural activity. *J. Neurophysiol.* 94, 3637–3642. doi: 10.1152/jn.00686.2005

Chauhan, A. S., Taylor, J. D., and Nogaret, A. (2018). Dual mechanism for the emergence of synchronization in inhibitory neural networks. *Sci. Rep.* 8:11431. doi: 10.1038/s41598-018-29822-8

DeBello, W. M., McBride, T. J., Nichols, G. S., Pannoni, K. E., Sanculi, D., and Totten, D. J. (2014). Input clustering and the microscale structure of local circuits. *Front. Neural Circ.* 8:112. doi: 10.3389/fncir.2014.00112

Deco, G., Ponce-Alvarez, A., Hagmann, P., Romani, G. L., Mantini, D., Corbetta, M. (2014). How local excitatory-inhibition ratio impact the whole brain dynamics. *J. Neurosci.* 34, 7886–7998. doi: 10.1523/JNEUROSCI.5068-13.2014

Deleuze, C., Bhumbra, G. S., Pazienti, A., Lourenco, J., Mailhes, C., Aguirre, A., et al. (2019). Strong preference for autaptic self-connectivity of neocortical PV interneurons facilitates their tuning to γ-oscillations. *PLoS Biol.* 17:e3000419. doi: 10.1371/journal.pbio.3000419

Descalzo, V. F., Nowak, L. G., Brumberg, J. C., McCormick, D. A., and Sanchez-Vives, M.V. (2005). Slow adaptation in fast-spiking neurons of visual cortex. *J. Neurophysiol.* 93, 1111–1118. doi: 10.1152/jn.00658.2004

Destexhe, A. (2009). Self-sustained asynchronous irregular states and up-down states in thalamic, cortical and thalamocortical networks of nonlinear integrate-and-fire neurons. *J. Comput. Neurosci.* 27, 493–506. doi: 10.1007/s10827-009-0164-4

di Volo, M., Romagnoni, A., Capone, C., and Destexhe, A. (2019). Biologically realistic mean-field models of conductance-based networks of spiking neurons with adaptation. *Neural Comput.* 31, 653–680. doi: 10.1162/neco_a_01173

Drongelen, W., Lee, H. C., Hereld, M., Chen, Z., Elsen, F. P., and Stevens, R. L. (2005). Emergent epileptiform activity in neural networks with weak excitatory synapses. *IEEE Trans. Neural Syst. Rehabil. Eng.* 13, 236–242. doi: 10.1109/TNSRE.2005.847387

Elson, R. C., Selverston, A. I., Abarbanel, H. D., and Rabinovich, M. I. (2002). Inhibitory synchronization of bursting in biological neurons:

dependence on synaptic time constant. *J. Neurophysiol.* 88, 1166–1176. doi: 10.1152/jn.2002.88.3.1166

Ergin, Y., Veli, B., Matjaž, P., and Mahmut, O. (2016). Enhancement of pacemaker induced stochastic resonance by an autapse in a scale-free neural network. *Sci. China Technol. Sci.* 59, 364–370. doi: 10.1007/s11431-015-5984-z

Fardet, T., Ballandras, M., Bottani, S., Métens, S., and Monceau, P. (2018). Understanding the generation of network bursts by adaptive oscillatory neurons. *Front. Neurosci.* 2:41 doi: 10.3389/fnins.2018.00041

Feng, Z., Zheng, M., Chen, X., and Zhang, M. (2018). neural synapses: microscale signal processing machineries formed by phase separation? *Biochemistry* 57, 2530–2539. doi: 10.1021/acs.biochem.8b00313

Flunkert, V., Yanchuk, S. Dahms, T., and Schöll, E. (2010). Synchronizing distant nodes: a universal classification of networks. *Phys. Rev. Lett.* 105:254101. doi: 10.1103/PhysRevLett.105.254101

Flunkert, V., Yanchuk, S., Dahms, T., and Schöll, E. (2014). Synchronizability of networks with strongly delayed links: a universal classification. *J. Math. Sci.* 202, 809–824. doi: 10.1007/s10958-014-2078-6

Foehring, R. C., Lorenzon, N. M., Herron, P., and Wilson, C. J. (1991). Correlation of physiologically and morphologically identified neural types in human association cortex *in vitro*. *J. Neurophysiol.* 66, 1825–1837. doi: 10.1152/jn.1991.66.6.1825

Franović, I., and Miljković, V. (2010). Phase plane approach to cooperative rhythms in neuron motifs with delayed inhibitory synapses. *Europhys. Lett.* 92:68007. doi: 10.1209/0295-5075/92/68007

Fröhlich, F. (2016). *Microcircuits of the Neocortex in Network Neuroscience.* Academic Press-Elsevier Inc., 85–95. doi: 10.1016/B978-0-12-801560-5.00007-0

Ge, P., and Cao, H. (2019). Synchronization of Rulkov neuron networks coupled by excitatory and inhibitory chemical synapses. *Chaos* 29:023129. doi: 10.1063/1.5053908

Gray, R. T., and Robinson, P. A. (2008). Stability and synchronization of random brain networks with a distribution of connection strengths. *Neurocomputing* 71, 1373–1387. doi: 10.1016/j.neucom.2007.06.002

Gu, H., and Zhao, Z. (2015). Dynamics of time delay-induced mutiple synchronous behaviors in inhibitory coupled neurons. *PLoS ONE* 10:e0138593. doi: 10.1371/journal.pone.0138593

Guo, D., Wang, Q., and Perc, M. (2012). Complex synchronous behavior in interneural networks with delayed inhibitory and fast electrical synapses. *Phys. Rev. E* 85:06190 5. doi: 10.1103/PhysRevE.85.061905

Guo, D., Wu, S., Chen, M., Perc, M., Zhang, Y., Ma, J., et al. (2016). Regulation of irregular neural firing by autaptic transmission. *Sci. Rep.* 6:26096. doi: 10.1038/srep26096

Han, F., Gu, X., Wang, Z., Fan, H., Cao, J., and Lu, Q. (2018). Global firing rate contrast enhancement in E/I neural networks by recurrent synchronized inhibition. *Chaos* 28:106324. doi: 10.1063/1.5037207

Hayakawa, T., and Fukai, T. (2020). Spontaneous and stimulus-induced coherent states of critically balanced neural networks. *Phys. Rev. Res.* 2:013253. doi: 10.1103/PhysRevResearch.2.013253

Heng-Tong, W., and Yong, C. (2015). Firing dynamics of an autaptic neuron. *Chin. Phys. B* 24:128709. doi: 10.1088/1674-1056/24/12/128709

Hensch, T. K., and Fagiolini, M. (2004). *Excitatory-Inhibitory Balance, Synapses, Circuits, Systems.* New York, NY: Springer Science+Bussiness Media, 155–172. doi: 10.1007/978-1-4615-0039-1

HuiXin, Q., Jun, M., WuYin, J., and ChunNi, W. (2014). Dynamics of electric activities in neuron and neurons of network induced by autapses. *Sci. China Technol. Sci.* 57, 936–946. doi: 10.1007/s11431-014-5534-0

Herrmann, C. S., and Klaus, A. (2004). Autapse turns neuron into oscillator. *Int. J. Bifurc. Chaos* 14, 623–633. doi: 10.1142/S0218127404009338

Hizanidis, J., Kouvaris, N. E., Zamora-López, G., Díaz-Guilera, A., and Antonopoulos, C. G. (2016). Chimera-like states in modular neural networks. *Sci. Rep.* 6:19845. doi: 10.1038/srep22314

Inawashiro, S., Miyake, S., and Ito, M. (1999). "Spiking neuron models for regular-spiking, intrinsically bursting and fast-spiking neurons," in *6th International Conference on Neural Information Processing* (Perth, WA: IEEE), 32–36. doi: 10.1109/ICONIP.1999.843957

Jia, B. (2018). Negative feedback mediated by fast inhibitory autapse enhances neural oscillations near a hopf bifurcation point. *Int. J. Bifur. Chaos* 28:1850030. doi: 10.1142/S021812741850030X

Kada, H., Teramae, J.-N., and Tokuda, I. T. (2016). Effective suppression of pathological synchronization in cortical networks by highly heterogeneous distribution of inhibitory connections. *Front. Comput. Neurosci.* 10:109. doi: 10.3389/fncom.2016.00109

Ke,W., He, Q., and Shu, Y. (2019). Functional self-excitatory autapses (auto-synapses) on neocortical pyramidal cells. *Neurosci. Bull.* 35, 1106–1109. doi: 10.1007/s12264-019-00391-8

Kim, S.-Y., and Lim, W. (2013). Sparsely-synchronized brain rhythm in a small-world neural network. *J. Korean Phys. Soc.* 63, 104–113. doi: 10.3938/jkps.63.104

Kim, Y. (2019). Autaptic effects on synchronization and phase response curves of neurons with a chemical synapse. *Korean Phys. Soc.* 75, 167–175. doi: 10.3938/jkps.75.167

Kraynyukova, N., and Tchumatchenko, T. (2018). Stabilized supralinear network can give rise to bistable, oscillatory and persistent activity. *Proc. Natl. Acad. Sci. U.S.A.* 115, 3464–3469. doi: 10.1073/pnas.1700080115

Kuramoto, Y. (1984). *Chemical Oscillations, Waves and Turbulence.* Berlin: Springer-Verlag.

Kopell, N., and Ermentrout, B. (2004) Chemical and electrical synapses perform complementary roles in the synchronization of interneural networks. *Proc. Natl. Acad. Sci. U.S.A.* 101, 15482–15487. doi: 10.1073/pnas.0406343101

Ladenbauer, J., Lehnert, J., Rankoohi, H., Dahms, T., Schöll, E., and Obermayer, K. (2013). Adaptation controls synchrony and cluster states of coupled threshold-model neurons. *Phys. Rev. E* 88:042713. doi: 10.1103/PhysRevE.88.042713

Li, C., and Zheng, Q. (2010). Synchronization of the small-world neural network with unreliable synapses. *Phys. Biol.* 7:036010. doi: 10.1088/1478-3975/7/3/036010

Lombardi, F., Herrmann, H. J., and Arcangelis, L. (2017). Balance of excitation and inhibition determines 1/f power spectrum in neural networks. *Chaos* 27:047402. doi: 10.1063/1.4979043

Mahmud, M., and Vassanelli, S. (2016). Differential modulation of excitatory and inhibitory neurons during periodic stimulation. *Front. Neurosci.* 10:62. doi: 10.3389/fnins.2016.00062

Mancilla, J. G., Fowler, M., and Ulinski, P. S. (1998). Responses of regular spiking and fast spiking cells in turtle visual cortex light flashed. *Vis. Neurosci.* 15, 979–993. doi: 10.1017/S0952523898155190

Masia, L., Micera, Silvestro, M., Akay, M., and Pons, J. L. (2018). "Converging clinical and engineering research on neurorehabilitation III," in *Proceeings of 4th International Coneference on NeuroRehabilitation* (ICNR2018) (Pisa), 21, 58–63.

Mejias, J. F., Murray, J. D., Kennedy, H., and Wang, X.-J. (2016). Feedforward and feedback frequency-dependent interactions in a large-scale laminar network of the primate cortex. *Sci. Adv.* 2:e1601335. doi: 10.1126/sciadv.1601335

Naud, R., Marcille, N., Clopath, C., and Gerstner, W. (2008). Firing patterns in the adaptive exponential integrate-and-fire model. *Biol. Cybern.* 99, 335–347. doi: 10.1007/s00422-008-0264-7

Nazemi, P. S., and Jamali, Y. (2018). On the influence of structural connectivity on the correlation patterns and network synchronization. *Front. Comput. Neurosci.* 12:105. doi: 10.3389/fncom.2018.00105

Neske, G. T., Patrick, S. L., and Connors, B. W. (2015). Contributions of diverse excitatory and inhibitory neurons to recurrent network activity in cerebral cortex. *J. Neurosci.* 35, 1089–1105. doi: 10.1523/JNEUROSCI.2279-14.2015

Noback, C. R., Strominger, N. L., Demarest, R. J., and Ruggiero, D. A. (2005). *The Human Nervous System: Structure and Function, 6th Edn.* Totowa, NJ: Humana Press.

Ostojic, S. (2014). Two types of asynchronous activity in networks of excitatory and inhibitory spiking neurons. *Nat. Neurosci.* 17, 594–600. doi: 10.1038/nn.3658

Pfeuty, B., Golomb, D., Mato, G., and Hansel, D. (2007). Inhibition potentiates the synchronizing action of electrical synapses. *Front. Comput. Neurosci.* 1:2007. doi: 10.3389/neuro.10.008.2007

Pouzat, C., and Marty, A. (1998). Autaptic inhibitory currents recorder from interneurones in rat cerebellar slices. *J. Physiol.* 509, 777–783. doi: 10.1111/j.1469-7793.1998.777bm.x

Protachevicz, P. R., Borges, R. R., Reis, A. S., Borges, F. S., Iarosz, K. C., Caldas, I. L., et al. (2018). Synchronous behaviour in network model

based on human cortico-cortical connections. *Physiol. Measure.* 39:074006. doi: 10.1088/1361-6579/aace91

Protachevicz, P. R., Borges, F. S., Lameu, E. L., Ji, P., Iarosz, K. C., Kihara, A. H., et al. (2019). Bistable firing pattern in a neural network model. *Front. Comput. Neurosci.* 13:19. doi: 10.3389/fncom.2019.00019

Protachevicz, P. R., Borges, F. S., Iarosz, K. C., Baptista, M. S., Lameu, E. L., Hansen, M., et al. (2020). Influence of delayed conductance on neural synchronisation. *Front. Physiol.* 11:1053. doi: 10.3389/fphys.2020.01053

Puig, M. V., Ushimaru, M., and Kawaguchi, Y. (2008). Two distinct activity patterns of fast-spiking interneurons during neocortical UP states. *Proc. Natl. Acad. Sci. U.S.A.* 105, 8428–8433. doi: 10.1073/pnas.0712219105

Qin, H., Wu, Y., Wang, C., and Ma, J. (2014). Emitting waves from defects in network with autapses. *Commun. Nonlin. Sci. Numer. Simul.* 23, 164–174. doi: 10.1016/j.cnsns.2014.11.008

Qu, J., Wang, R., Yan, C., and Du, Y. (2014). Oscillations and synchrony in a cortical neural network. *Cogn. Neurodyn.* 8, 157–166. doi: 10.1007/s11571-013-9268-7

Reimbayev, R., Daley, K., and Belykh, I. (2017). When two wrongs make aright: synchronized neural bursting from combined electrical and inhibitory coupling. *Phylos. Trans. A* 375:20160282. doi: 10.1098/rsta.2016.0282

Rosenblum, M. G., Pikowsky, A. S., and Kurths, J. (1997). From phase to lag synchronization in coupled chaotic oscillators. *Phys. Rev. Lett.* 78, 4193–4196. doi: 10.1103/PhysRevLett.78.4193

Saada-Madar, R., Miller, N., and Susswein, A. J. (2012). Autaptic Muscarinic self-excitation and nitrergic self-inhibition in neurons initiating Aplysia feeding are revealed when the neurons are cultured in isolation. *J. Mol. Histol.* 43, 431–436. doi: 10.1007/s10735-012-9418-y

Santos, M. S., Protachevicz, P. R., Iarosz, K. C., Caldas, I. L, Viana, R. L., Borges, F. S, et al. (2019). Spike-burst chimera states in an adaptive exponential integrate-and-fire neural network. *Chaos* 29:043106. doi: 10.1063/1.5087129

Seung, H. S., Lee, D. D., Reis, B. Y., and Tank, D. W. (2000). The autapse: A simple illustration of short-term analog memory storage by tuned synaptic feedback. *J. Comput. Neurosci.* 9, 171–185. doi: 10.1023/A:1008971908649

Sporns, O. (2012). *Discovering the Human Connectome.* Cambridge, MA: MIT Press, 63–84.

Sporns, O. (2013). Structure and function of complex brain networks. *Dialog. Clin. Neurosci.* 15, 247–262. doi: 10.31887/DCNS.2013.15.3/osporns

Sporns, O. (2016). "Connectome networks: from cells to systems," in *Micro-, Meso- and Macro-Connectomics of the Brain, Vol. 216*, eds H. Kennedy, D. C. Van Essen, and Y. Christen (Cham: Springer), 108–128.

Suárez, L. E., Markello, R. D., Betzel, R. F., and Misic, B. (2020). Linking structure and function in macroscale brain networks. *Trends Cogn. Sci.* 24, 302–315. doi: 10.1016/j.tics.2020.01.008

Suga, K. (2014). Isoproterenol facilitates GABAergic autapses in fast-spiking cells of rat insular cortex. *J. Oral Sci.* 56, 41–47. doi: 10.2334/josnusd.56.41

Szegedi, V., Paizs, M., Baka, J., Barzó, P., Molnár, G., Tamas, G., et al. (2020). Robust perisomatic GABAergic self-innervation inhibits basket cells in the human and mouse supragranullar neocortex. *eLife* 9:e51691. doi: 10.7554/eLife.51691

Tamás, G., Buhl, E. H., and Somogyi, P. (1997). Massive autaptic self-innervation of GABAergic neurons in cat visual cortex. *J. Neurosci.* 17, 6352–6364. doi: 10.1523/JNEUROSCI.17-16-06352.1997

Tatii, R., Haley, M. S., Swanson, O., Tselha, T., and Maffei, A. (2018). Neurophysiology and regulation of the balance between excitation and inhibition in neocortical circuits. *Biol. Psychiatry* 15, 821–831. doi: 10.1016/j.biopsych.2016.09.017

Valente, P., Orlando, M., Raimondi, A., Benfenati, F., and Baldelli, P. (2016). Fine tuning of synaptic plasticity and filtering by GABA released from hippocampal autaptic granule cells. *Cereb. Cortex* 26, 1149–1167. doi: 10.1093/cercor/bhu301

van der Loos, H., and Glaser, E. M. (1972). Autapses in neocortex cerebri: synaptic between a pyramidal cell's axon and its own dendrites. *Brain Res.* 48, 355–360. doi: 10.1016/0006-8993(72)90189-8

Vreeswijk, C. V., Abbot, L. F., and Ermentrout, G. B. (1994). When inhibition not excitation synchronizes neural firing. *J. Comput. Neurosci.* 1, 313–321. doi: 10.1007/BF00961879

Wang, Q. Y., Lu, Q. S., and Chen, G. R. (2007). Ordered bursting synchronized and complex wave propagation in a ring neural network. *Phys. A* 374, 869–878. doi: 10.1016/j.physa.2006.08.062

Wang, Q., Chen, G., and Perc, M. (2011). Synchronous bursts on scale-free neural networks with attractive and repulsive coupling. *PLoS ONE* 6:e15851. doi: 10.1371/journal.pone.0015851

Wang, H., Wang, L., Chen, Y., and Chen, Y. (2014). Effect of autaptic activity on the response of a Hodgkin-Huxley neuron. *Chaos* 24:033122. doi: 10.1063/1.4892769

Wang, H., and Chen, Y. (2015). Firing dynamics of an autaptic neuron. *Chin. Phys. B* 24:128709. doi: 10.1088/1674-1056/24/12/128709

Wang, B., Ke, W., Guang, J., Chen G., Yin, L., Deng, S., et al. (2016). Firing frequency maxima of fast-spiking neurons in human, monkey and mouse neocortex. *Front. Cell. Neurosci.* 10:239. doi: 10.3389/fncel.2016.00239

Wang, C., Guo, S., Xu, Y., Ma, J., Tang, J., Alzahrani, F., et al. (2017). Formation of autapse connected to neuron and it biological function. *Res. Article* 2017:5436737. doi: 10.1155/2017/5436737

Wiles, L., Gu. S., Pasqueletti, F., Parvesse, B., Gabrieli, D. Basset, D. S., et al. (2017). Autaptic connections shitf network excitability and bursting. *Sci. Rep.* 7:44006. doi: 10.1038/srep44006

Wilson, F. A. W., O'Scalaidhe, S. P., and Goldman-Rakic, P. S. (1994). Functional synergism between putative γ-aminobutyrate-containing neurons and pyramidal neurons in prefrontal cortex. *Proc. Natl. Acad. Sci. U.S.A.* 91, 4009–4013. doi: 10.1073/pnas.91.9.4009

Wyart, C., Cocco, S., Bourdieu, L., Léger, J.-F., Herr, C., and Chatenay, D. (2005). Dynamics of excitatory synaptic components in sustained firing at low rates. *J. Neurosci.* 93, 33700–3380. doi: 10.1152/jn.00530.2004

Yao, C., He, Z., Nakano, T., Qian, Y., and Shuai, J. (2019). Inhibitory-autapse-enhanced signal transmission in neural networks. *Nonlin. Dyn.* 97, 1425–1437. doi: 10.1007/s11071-019-05060-z

Yin, L., Zheng, R., Ke, W., He, Q., Zhang, Y., Li, J., et al. (2018). Autapses enhance bursting and coincidence detection in neocortical pyramidal cells. *Nat. Commun.* 9:4890. doi: 10.1038/s41467-018-07317-4

Zhao, Z., and Gu, H. (2017). Transitions between classes of neural excitability and bifurcations induced by autapse. *Sci. Rep.* 7:6760. doi: 10.1038/s41598-017-07051-9

Zhou, S., and Yu, Y. (2018). Synaptic E-I balance underlies efficient neural coding. *Front. Neurosci.* 12:46. doi: 10.3389/fnins.2018.00046

Conflict of Interest: The authors declare that the research was conducted in the absence of any commercial or financial relationships that could be construed as a potential conflict of interest.

frontiers in Systems Neuroscience

ORIGINAL RESEARCH
published: 10 February 2021
doi: 10.3389/fnsys.2021.631377

Dynamics of Structured Networks of Winfree Oscillators

Carlo R. Laing, Christian Bläsche and Shawn Means*

School of Natural and Computational Sciences, Massey University, Auckland, New Zealand

Winfree oscillators are phase oscillator models of neurons, characterized by their phase response curve and pulsatile interaction function. We use the Ott/Antonsen ansatz to study large heterogeneous networks of Winfree oscillators, deriving low-dimensional differential equations which describe the evolution of the expected state of networks of oscillators. We consider the effects of correlations between an oscillator's in-degree and out-degree, and between the in- and out-degrees of an "upstream" and a "downstream" oscillator (degree assortativity). We also consider correlated heterogeneity, where some property of an oscillator is correlated with a structural property such as degree. We finally consider networks with parameter assortativity, coupling oscillators according to their intrinsic frequencies. The results show how different types of network structure influence its overall dynamics.

Keywords: Winfree oscillators, coupled oscillators, neuronal networks, degree, assortativity, copula, Ott/Antonsen

1. INTRODUCTION

The behavior of networks of coupled oscillators is a topic of ongoing interest (Strogatz, 2000; Pikovsky et al., 2001; Arenas et al., 2008). While an individual oscillator may have very simple behavior, it is the emergent behavior such as synchronization that has gained much attention (Winfree, 2001; Strogatz, 2003). Networks of coupled oscillators provide insights into physiological systems such as neuronal or cardiac systems, where synchrony or lack thereof can have profound implications (Fenton et al., 2002; Milton and Jung, 2013).

One of the first models for interacting oscillators was the Winfree model (Winfree, 1967; Ariaratnam and Strogatz, 2001; Pazó and Montbrió, 2014; Ha et al., 2015; Gallego et al., 2017; Pazó et al., 2019; Pazó and Gallego, 2020). Each Winfree oscillator is described by a single angular variable and when uncoupled is assumed to undergo periodic oscillations. Each oscillator is assumed to have a phase response curve, a function of its own phase, which can be measured from individual neurons, for example Schultheiss et al. (2011) and Netoff et al. (2005). This describes how an oscillator's phase changes as the result of input from other oscillators. The output from an oscillator is assumed to be in the form of a non-negative pulsatile function of its own phase, and the inputs to an oscillator are assumed to be additive.

A number of authors have studied networks of Winfree oscillators, but as far as we are aware, only in the all-to-all coupled case. Although straightforward to assemble, such networks do not reproduce complex network structures observed in real-world systems such as assortativities between individual neurons (de Santos-Sierra et al., 2014; Teller et al., 2014). We are interested in networks with far more varied structure, not just randomly connected. These networks are *directed*, i.e., edges connect one oscillator to another, without necessarily having a reciprocal connection, as occurs in networks of neurons. There are many ways to create structured networks and here we consider the following: correlating the in- and out-degrees of an oscillator (i.e., the number of inputs and the number of outputs of an oscillator, section 3), inducing degree assortativity

OPEN ACCESS

Edited by:
Oleksandr Popovych, Helmholtz-Verband Deutscher Forschungszentren (HZ), Germany

Reviewed by:
Denis Goldobin, Institute of Continuous Media Mechanics (RAS), Russia
Ernest Montbrio, Pompeu Fabra University, Spain

****Correspondence:***
Carlo R. Laing
c.r.laing@massey.ac.nz

Received: *20 November 2020*
Accepted: *18 January 2021*
Published: *10 February 2021*

Citation:
Laing CR, Bläsche C and Means S (2021) Dynamics of Structured Networks of Winfree Oscillators. Front. Syst. Neurosci. 15:631377. doi: 10.3389/fnsys.2021.631377

(i.e., connecting two oscillators based on their in- and out-degrees, section 4), correlating some local property of an oscillator with either its in- or out-degree (section 5), and inducing parameter assortativity (i.e., connecting two oscillators based on the similarities of an intrinsic property of the two oscillators, such as their free-running frequency, section 6).

Our main tool is the derivation and then numerical analysis of moderately large sets of coupled ordinary differential equations (ODEs). The derivation utilizes the Ott/Antonsen ansatz (Ott and Antonsen, 2008, 2009), an exact technique for dimension reduction in large networks of sinusoidally coupled phase oscillators, of which Winfree oscillators are an example. Some of the computational techniques used here have been presented before (Bläsche et al., 2020; Laing and Bläsche, 2020) but for networks of theta neurons (Ermentrout and Kopell, 1986) rather than Winfree oscillators. In section 2, we present the general model and its reduction using the Ott/Antonsen ansatz. The results are presented in sections 3–6 and we conclude in section 7.

2. MODEL

We consider the network version of the model as presented in Pazó and Montbrió (2014)

$$\frac{d\theta_j}{dt} = \omega_j + U(\theta_j)\frac{\epsilon}{\langle k\rangle}\sum_{n=1}^{N} A_{jn}T(\theta_n) \tag{1}$$

for $j = 1,\dots N$ where the ω_j are chosen from a distribution $g(\omega)$, ϵ is the strength of coupling, $\langle k\rangle$ is the mean degree of the network, and the connectivity of the network is given by the adjacency matrix A, where $A_{jn} = 1$ if oscillator n connects to oscillator j and zero otherwise. The function U is known as the phase response curve and we choose it to be

$$U(\theta) = \sin\beta - \sin(\theta+\beta) \tag{2}$$

so that $U(0) = 0$. If $\beta < \pi/2$ then this function describes a type-II oscillator whereas $\beta = \pi/2$ describes a type-I oscillator (Tsubo et al., 2007). We consider only type-II oscillators in this work. The pulsatile function T is given by

$$T(\theta) = a_q(1+\cos\theta)^q \tag{3}$$

where q is a positive integer and $a_q = 2^q(q!)^2/(2q)!$ so that $\int_0^{2\pi} T(\theta)d\theta = 2\pi$. The in-degree of oscillator j is

$$k_{in,j} = \sum_{n=1}^{N} A_{jn} \tag{4}$$

and the out-degree of oscillator n is

$$k_{out,n} = \sum_{j=1}^{N} A_{jn} \tag{5}$$

We consider large networks with all oscillators having large in- and out-degrees. Following Chandra et al. (2017) and Laing and Bläsche (2020), we assume that the network can be characterized by two functions: the degree distribution $P(\mathbf{k})$, where $\mathbf{k} = (k_{in}, k_{out})$, and k_{in} and k_{out} are the in- and out-degrees of an oscillator, respectively, and an assortativity function $a(\mathbf{k}' \to \mathbf{k})$ giving the probability that an oscillator with degree $\mathbf{k}'$ connects to one with degree $\mathbf{k}$, given that such oscillators exist. Note that we follow (Chandra et al., 2017; Laing and Bläsche, 2020) and normalize $P(\mathbf{k})$ such that $\sum_{\mathbf{k}} P(\mathbf{k}) = N$.

In the limit $N \to \infty$ the network is described by the probability density function $f(\theta,\omega|\mathbf{k},t)$ where $f(\theta,\omega|\mathbf{k},t)d\theta\ d\omega$ is the probability that an oscillator with degree $\mathbf{k}$ has phase in $[\theta,\theta+d\theta]$ and value of ω in $[\omega,\omega+d\omega]$ at time t. This function satisfies the continuity equation

$$\frac{\partial f}{\partial t} + \frac{\partial}{\partial\theta}(vf) = 0 \tag{6}$$

where

$$v(\theta,\omega,\mathbf{k},t) = \omega + \epsilon U(\theta)R(\mathbf{k},t) \tag{7}$$

where

$$R(\mathbf{k},t) = \frac{1}{\langle k\rangle}\sum_{\mathbf{k}'} P(\mathbf{k}')a(\mathbf{k}'\to\mathbf{k})G(\mathbf{k}',t) \tag{8}$$

and

$$G(\mathbf{k}',t) = \int_{-\infty}^{\infty}\int_0^{2\pi} f(\theta',\omega'|\mathbf{k}',t)T(\theta')d\theta'\ d\omega' \tag{9}$$

The nature of this system [specifically, having $U(\theta)$ being a single sinusoidal function of θ] means that it is amenable to the use of the Ott/Antonsen ansatz (Ott and Antonsen, 2008, 2009). We assume that

$$g(\omega) = \frac{\Delta/\pi}{(\omega-\omega_0)^2+\Delta^2} \tag{10}$$

where Δ is the half-width-at-half-maximum and ω_0 the median of the distribution of intrinsic frequencies. Using standard techniques (Chandra et al., 2017; Laing, 2017) which rely on the Ott/Antonsen theory, one can show that the long-time dynamics of the network is described by

$$\frac{\partial b(\mathbf{k},t)}{\partial t} = \frac{\epsilon e^{-i\beta}R(\mathbf{k},t)}{2} + \left[i\omega_0 - \Delta + i\epsilon\sin\beta R(\mathbf{k},t)\right]b(\mathbf{k},t) - \frac{\epsilon e^{i\beta}R(\mathbf{k},t)}{2}[b(\mathbf{k},t)]^2 \tag{11}$$

where

$$G(\mathbf{k},t) = a_q\left[C_0 + \sum_{j=1}^{q} C_j\left\{[b(\mathbf{k},t)]^j + [\bar{b}(\mathbf{k},t)]^j\right\}\right] \tag{12}$$

where overline indicates complex conjugate and

$$C_j = \sum_{k=0}^{q}\sum_{m=0}^{k}\frac{q!\delta_{k-2m,j}}{2^k(q-k)!m!(k-m)!} \tag{13}$$

The quantity

$$b(\mathbf{k},t)=\int_{-\infty}^{\infty}\int_{0}^{2\pi}f(\theta,\omega|\mathbf{k},t)e^{i\theta}d\theta\,d\omega \tag{14}$$

is the complex-valued order parameter for oscillators with degree $\mathbf{k}$.

Equation (11) is the general equation describing the dynamics of the network and we use it as a base for analysing a number networks with different types of structure. In section 3, we consider correlations between an individual oscillator's in-degree and its out-degree, as described by the degree distribution $P(\mathbf{k})$. In section 4, we consider correlations between the degrees of connected oscillators, effectively modifying the function $a(\mathbf{k}'\to\mathbf{k})$. In section 5, we investigate the results of one of the parameters intrinsic to an oscillator (ω_0,Δ, or β) being correlated with a *network* property of that oscillator (its in- or out-degree). Section 6 considers the case when all oscillators have the same in- and out-degrees, and the assortativity function $a(\mathbf{k}'\to\mathbf{k})$ is replaced by a function describing the probability of connecting oscillators based on the values of one of their intrinsic parameters—in this case, ω_0. We conclude in section 7.

3. WITHIN OSCILLATOR CORRELATIONS

We first consider the effects of correlating an oscillator's in- and out-degree. This general question has been considered by a number of authors studying different types of oscillators (LaMar and Smith, 2010; Vasquez et al., 2013; Martens et al., 2017; Nykamp et al., 2017; Vegué and Roxin, 2019) and experimental evidence for within-neuron degree correlations is given in Vegué et al. (2017). Our derivation follows Laing and Bläsche (2020).

Assuming neutral assortativity we have (Restrepo and Ott, 2014)

$$a(\mathbf{k}'\to\mathbf{k})=\frac{k'_{out}k_{in}}{N\langle k\rangle} \tag{15}$$

where we have assumed that the largest in- and out-degrees are significantly smaller than N, so that $a(\mathbf{k}'\to\mathbf{k})\le 1$. We will write $P(k_{in},k_{out},\hat{\rho})$ instead of $P(\mathbf{k})/N$, where $\hat{\rho}$ is a parameter controlling the correlation between k_{in} and k_{out}, explained in detail below. Substituting (15) into (8) we have

$$\begin{aligned}R(k_{in},k_{out},t)=&\frac{N}{\langle k\rangle}\sum_{k'_{in}}\sum_{k'_{out}}P(k'_{in},k'_{out},\hat{\rho})a(\mathbf{k}'\to\mathbf{k})G(k'_{in},k'_{out},t)\\=&\frac{k_{in}}{\langle k\rangle^2}\sum_{k'_{in}}\sum_{k'_{out}}P(k'_{in},k'_{out},\hat{\rho})k'_{out}G(k'_{in},k'_{out},t)\end{aligned} \tag{16}$$

This is clearly independent of k_{out}, thus ν must also be independent of k_{out}, the state of an oscillator with degree (k_{in},k_{out}) must be independent of k_{out}, and thus G must be independent of k'_{out}. So we can write

$$R(k_{in},t)=\frac{k_{in}}{\langle k\rangle^2}\sum_{k'_{in}}Q(k'_{in},\hat{\rho})G(k'_{in},t) \tag{17}$$

where

$$Q(k'_{in},\hat{\rho})\equiv\sum_{k'_{out}}P(k'_{in},k'_{out},\hat{\rho})k'_{out} \tag{18}$$

Thus, the model equations of interest are

$$\begin{aligned}\frac{\partial b(k_{in})}{\partial t}=&\frac{\epsilon e^{-i\beta}R(k_{in})}{2}+\left[i\omega_0-\Delta+i\epsilon\sin\beta R(k_{in})\right]b(k_{in})\\&-\frac{\epsilon e^{i\beta}R(k_{in})}{2}[b(k_{in})]^2\end{aligned} \tag{19}$$

where G is given by (12) but with the degree dependence being on only k_{in}. Note that the model equations are independent of N, the total number of oscillators.

3.1. Generating Correlated Degrees

The correlations between an oscillator's in- and out-degree are controlled by the function $P(k_{in},k_{out},\hat{\rho})$ and we now describe how to generate these correlations. For simplicity we assume that the distributions of the in- and out-degrees are the same, namely uniform distributions between m and M, i.e.,

$$p(k)=\begin{cases}\frac{1}{M-m} & m\le k\le M\\ 0 & \text{otherwise}\end{cases} \tag{20}$$

We introduce correlations between the in- and out-degree of an oscillator while retaining these marginal distributions, using a Gaussian copula (Nelsen, 2007). The correlated bivariate normal distribution with zero mean is

$$f(x,y,\hat{\rho})=\frac{1}{2\pi\sqrt{1-\hat{\rho}^2}}e^{-(x^2-2\hat{\rho}xy+y^2)/[2(1-\hat{\rho}^2)]} \tag{21}$$

where $\hat{\rho}\in(-1,1)$ is the correlation between x and y. The variables x and y have no physical meaning and we use the copula just as a way of deriving an analytic expression for $P(k_{in},k_{out},\hat{\rho})$ for which the correlations between k_{in} and k_{out} out can be varied systematically. The cumulative distribution function for x is

$$C(x)=[1+\text{erf}(x/\sqrt{2})]/2 \tag{22}$$

and the cumulative distribution function for degree k is

$$C_k(k)=\int_m^k\frac{1}{M-m}ds=\frac{k-m}{M-m} \tag{23}$$

The joint degree distribution for k_{in} and k_{out} is

$$\begin{aligned}P(k_{in},k_{out},\hat{\rho})=&\{C^{-1}[C_k(k_{in})]\}'\{C^{-1}[C_k(k_{out})]\}'f\{C^{-1}[C_k(k_{in})],\\&C^{-1}[C_k(k_{out})],\hat{\rho}\}\end{aligned} \tag{24}$$

where the superscript "−1" indicates the inverse of the corresponding function. Now

$$C^{-1}[C_k(k_{in})]=\sqrt{2}\,\text{erf}^{-1}\left(\frac{2(k-m)}{M-m}-1\right) \tag{25}$$

and

$$\{C^{-1}[C_k(k_{in})]\}' = \sqrt{\frac{\pi}{2}} \exp\left[\left\{\text{erf}^{-1}\left(\frac{2(k-m)}{M-m}-1\right)\right\}^2\right]\frac{2}{M-m}$$
$$= \sqrt{\frac{\pi}{2}}\frac{2}{M-m}\exp\left[\frac{(C^{-1}[C_k(k_{in})])^2}{2}\right] \quad (26)$$

So

$$P(k_{in},k_{out},\hat{\rho}) = \frac{1}{(M-m)^2\sqrt{1-\hat{\rho}^2}}\exp\left\{\frac{\hat{\rho}C^{-1}[C_k(k_{in})]C^{-1}[C_k(k_{out})}{1-\hat{\rho}^2}\right\}$$
$$\times\exp\left[\frac{-\hat{\rho}^2\left(\{C^{-1}[C_k(k_{in})]\}^2+\{C^{-1}[C_k(k_{out})]\}^2\right)}{2(1-\hat{\rho}^2)}\right] \quad (27)$$
$$= \frac{p(k_{in})p(k_{out})}{\sqrt{1-\hat{\rho}^2}}\exp\left\{\frac{\hat{\rho}C^{-1}[C_k(k_{in})]C^{-1}[C_k(k_{out})]}{1-\hat{\rho}^2}\right\}$$
$$\times\exp\left[\frac{-\hat{\rho}^2\left(\{C^{-1}[C_k(k_{in})]\}^2+\{C^{-1}[C_k(k_{out})]\}^2\right)}{2(1-\hat{\rho}^2)}\right] \quad (28)$$

Note the special case $P(k_{in},k_{out},0) = p(k_{in})p(k_{out})$, as expected. Several plots of this function are shown in **Figure 1**.

We also need to relate the parameter $\hat{\rho}$ to ρ, the Pearson correlation coefficient between the in- and out-degrees of a neuron. We have

$$\rho = \frac{\tilde{\Sigma}P(k_{in},k_{out},\hat{\rho})(k_{in}-\langle k\rangle)(k_{out}-\langle k\rangle)}{\sqrt{\tilde{\Sigma}P(k_{in},k_{out},\hat{\rho})(k_{in}-\langle k\rangle)^2}\sqrt{\tilde{\Sigma}P(k_{in},k_{out},\hat{\rho})(k_{out}-\langle k\rangle)^2}} \quad (29)$$

where $\tilde{\Sigma}$ indicates a sum over all k_{in} and k_{out}. This relationship is numerically determined and shown in **Figure 2A**, and it is nearly the identity. Note that the sums in (29) are over $m+1 \le k \le M-1$, since $P(k_{in},k_{out},\hat{\rho})$ is undefined for $k = m, M$.

We can also calculate the function $Q(k_{in},\hat{\rho})$ (Equation 18) where $P(k_{in},k_{out},\hat{\rho})$ is given in (28). This function is shown in **Figure 2B**, where we see that increasing $\hat{\rho}$ gives more weight to high in-degree nodes and less to low in-degree nodes and vice versa. This can be understood by realizing that $Q(k_{in},\hat{\rho})$ is the "weight" given to outputs from oscillators with in-degree k_{in}. If, for example, $\hat{\rho} > 0$, then oscillators with high in-degree will be likely to have high out–degree, and thus their output should be weighted more.

3.2. Results

We set $q = 4$ (so $a_q = 8/35$ and $C_0 = 35/8, C_1 = 7/2, C_2 = 7/4, C_3 = 1/2, C_4 = 1/16$), $\omega_0 = 1$, and consider four different values of β: 0, 0.5, 0.7, and 1 (all corresponding to type-II oscillators). There are two types of behavior typically seen in such a network: synchronous and asynchronous (Pazó and Montbrió, 2014), although the fraction of oscillators actually oscillating can vary in the asynchronous states. Increasing ϵ (the strength of coupling) tends to destroy synchronous behavior through a saddle-node-on-invariant-circle (SNIC) bifurcation, as many of the oscillators "lock" at an approximate fixed point. Increasing Δ (the spread of intrinsic frequencies) tends to destroy synchronous behavior through a Hopf bifurcation, as the oscillators become too dissimilar to synchronize (Pazó and Montbrió, 2014). Examples of typical behavior in a default network are shown in **Figure 3**. The global order parameter for a network of N phase oscillators is a measure of their synchrony, and is defined as (Strogatz, 2000)

$$Z = \frac{1}{N}\sum_{j=1}^{N} e^{i\theta_j}. \quad (30)$$

We see that its magnitude has large, nearly periodic oscillations in the synchronous state, but is approximately constant in the asynchronous state—note the different vertical scales in **Figures 3A,C,E**. Note as well the high $|Z|$ value reflects a large fraction of quiescent oscillators in **Figures 3C,D**—a "trivial synchrony."

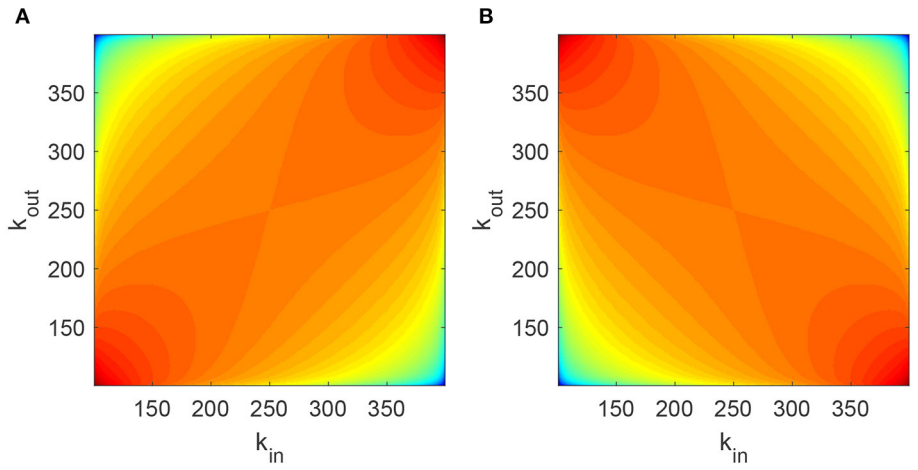

FIGURE 1 | Joint degree distribution $P(k_{in},k_{out},\hat{\rho})$ for **(A)** $\hat{\rho} = 0.5$ and **(B)** $\hat{\rho} = -0.5$. The log of P is shown, with red corresponding to higher values and blue to lower. Parameters: $m = 100, M = 400$.

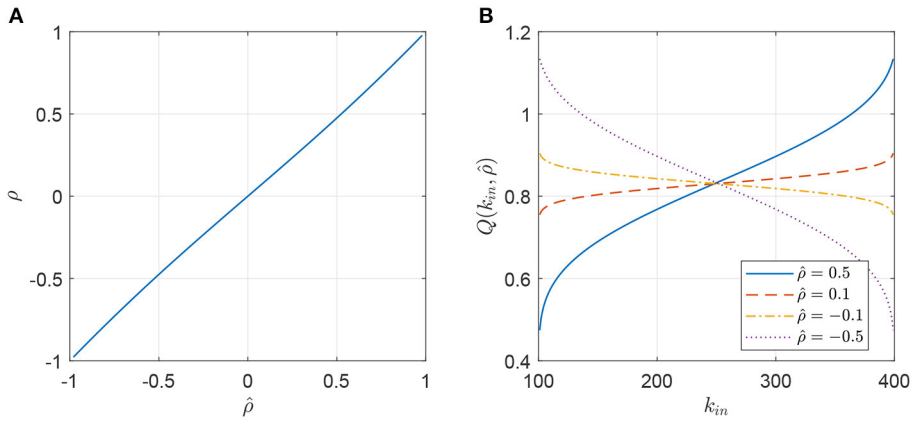

FIGURE 2 | (A) Correlation coefficient between the in- and out-degrees of an oscillator, ρ, as a function of the parameter $\hat{\rho}$ used in the Gaussian copula. **(B)** The function $Q(k_{in}, \hat{\rho})$ (Equation 18) for different values of $\hat{\rho}$. Parameters: $m = 100, M = 400$.

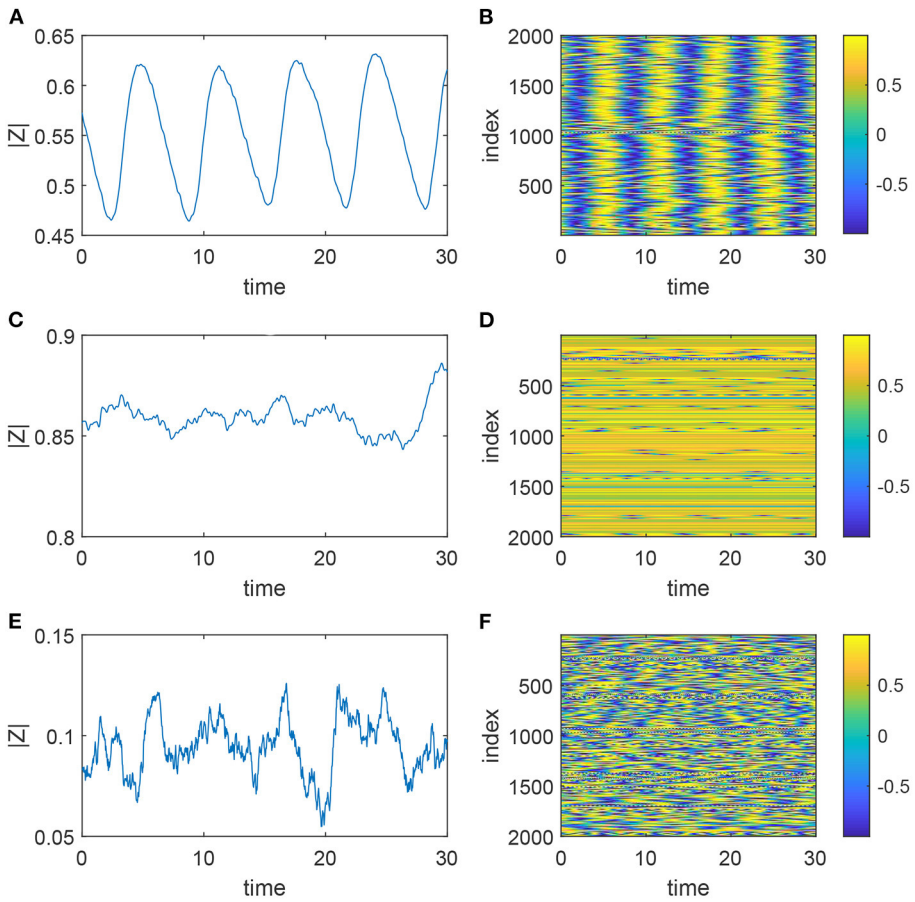

FIGURE 3 | Dynamics of the system (1) with uncorrelated degrees. **(A,B)** Correspond to $(\epsilon, \Delta) = (0.2, 0.05)$ (synchronous state), **(C,D)** to $(\epsilon, \Delta) = (0.8, 0.05)$, and **(E,F)** to $(\epsilon, \Delta) = (0.2, 0.5)$ (asynchronous states). The left panels show the magnitude of the global order parameter, and the right show $\sin\theta_j$. Other parameters: $\omega_0 = 1, \beta = 0, m = 100, M = 400, N = 2000$.

The network whose behavior is shown in **Figure 3** was created using the configuration model (Newman, 2003). Such a network typically has both self-connections (i.e., an oscillator is connected to itself) and multiple connections from one particular oscillator to another. We remove these in a random way as shown in **Figure 4**. For a self-connection we randomly choose

another connection and reconnect as in the top panel. For a double connection we randomly choose another connection and reconnect as in the bottom panel.

We now investigate the effects of varying $\hat{\rho}$ and thus ρ on the dynamics of Equation (19). As mentioned, it is known that increasing Δ (making the intrinsic frequencies more diverse) destroys the synchronous state in a supercritical Hopf bifurcation (Pazó and Montbrió, 2014). In **Figure 5A**, we show how the value of Δ at which this bifurcation occurs varies as a function of ρ, for four different values of β. We vary $\hat{\rho}$ but interpolate the data shown in **Figure 2A** in order to plot the curves in **Figure 5A** as functions of ρ. We see that increasing ρ increases the value of Δ at which the bifurcation occurs, at least for small β, and vice versa, but the effect is small compared with that of varying β. Put another way, for a fixed value of Δ, increasing ρ can cause macroscopic oscillations within the network (at least for β close to zero).

We now fix $\Delta = 0.05$ and consider the effects of varying both ρ and ϵ (the strength of coupling between oscillators). It is known that for an all-to-all coupled network increasing ϵ destroys the synchronous state in a SNIC bifurcation (Pazó and Montbrió, 2014). For our network this is also what happens for $\beta = 0$, as shown in **Figure 5B** (blue circles joined by line). However, for $\beta = 0.5, 0.7$, and 1, there is instead a supercritical Hopf bifurcation as ϵ increases, in contrast with the situation for all-to-all coupled network (for these values of ω_0, β and Δ), illustrating a nontrivial effect of network structure: even the type of bifurcation occurring is changed. These curves of Hopf bifurcations are also shown in **Figure 5B** and we see that increasing ρ decreases the value of ϵ at which the synchronous solution is destroyed and vice versa. Note that between $\beta = 0$ and $\beta = 0.5$, guided by the results for the fully-connected network (Pazó and Montbrió, 2014), we expect there to be several curves of Hopf, homoclinic, and saddle-node bifurcations in **Figure 5B** organized around a Takens-Bogdanov and a saddle-node separatrix-loop point (Gallego et al., 2017), but we have not investigated them here. The results in **Figure 5** have been compared with those from simulation of the full network (Equation 1) and found to agree very well (results not shown).

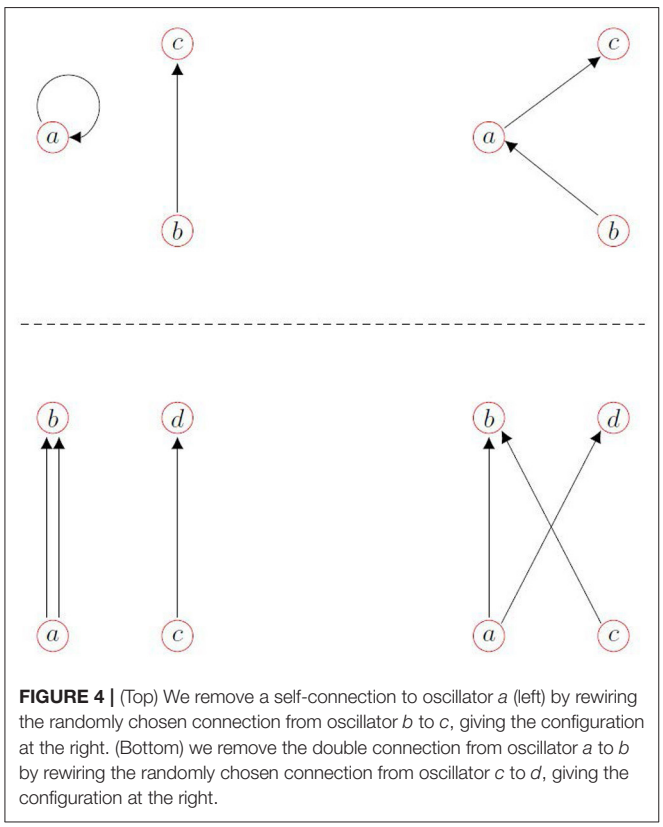

FIGURE 4 | (Top) We remove a self-connection to oscillator *a* (left) by rewiring the randomly chosen connection from oscillator *b* to *c*, giving the configuration at the right. (Bottom) we remove the double connection from oscillator *a* to *b* by rewiring the randomly chosen connection from oscillator *c* to *d*, giving the configuration at the right.

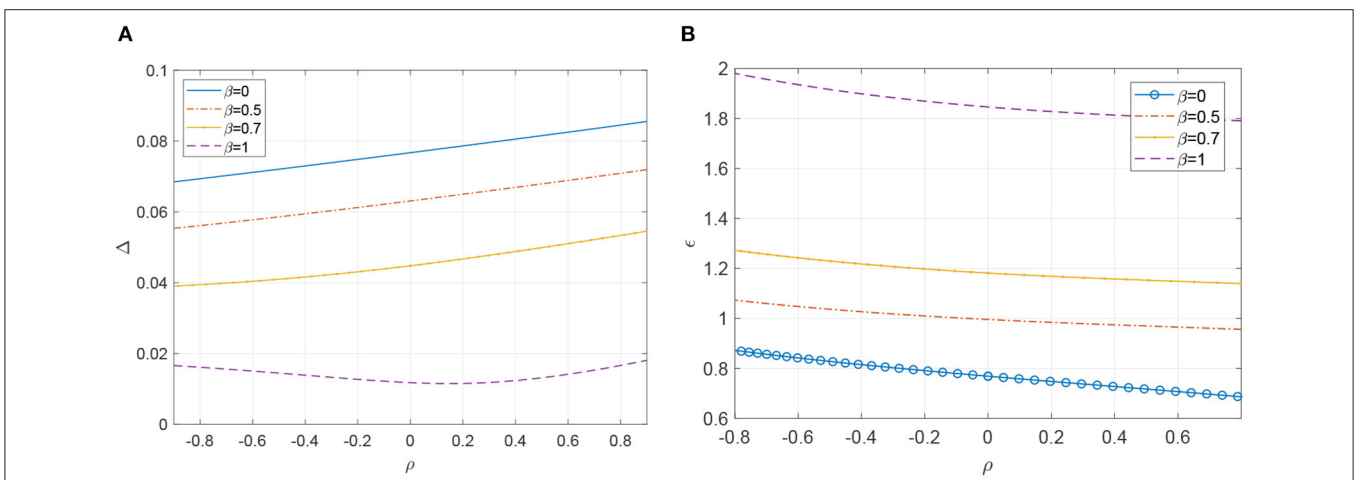

FIGURE 5 | (A) Hopf bifurcation curves of the fixed point of (19). A stable periodic orbit exists below the curve. Other parameters: $\epsilon = 0.2, \omega_0 = 1, m = 100, M = 400$. **(B)** SNIC bifurcation curve ($\beta = 0$, blue circles joined by line) and Hopf bifurcation curves ($\beta = 0.5, 0.7$ and 1) for (19). For each value of β a stable periodic orbit exists below the curve. Other parameters: $\Delta = 0.05, \omega_0 = 1, m = 100, M = 400$.

4. BETWEEN NEURON DEGREE CORRELATIONS

We now turn to the question of correlations between connected oscillators based on their degrees, often referred to as degree assortativity (Foster et al., 2010; Bläsche et al., 2020). Assortativity has often been studied in undirected networks, where a node simply has a degree, rather than in- and out-degrees (Restrepo and Ott, 2014). Here we consider directed networks, which a small number of previous authors have considered (De Franciscis et al., 2011; Avalos-Gaytan et al., 2012; Schmeltzer et al., 2015; Kähne et al., 2017), although they have often imposed other structure on the network such as equal in- and out-degrees for each model neuron.

Because we consider directed networks there are four possible types of degree assortativity, between either the in- or out-degree of the "upstream" (sending) oscillator and either the in- or out-degree of the "downstream" (receiving) oscillator (see **Figure 6**).

Roughly speaking, degree assortativity can be thought of in this way: given an upstream oscillator with specific in- and out-degrees, and a downstream oscillator with specific in- and out-degrees, one can calculate the probability of a connection from the upstream to the downstream oscillator.

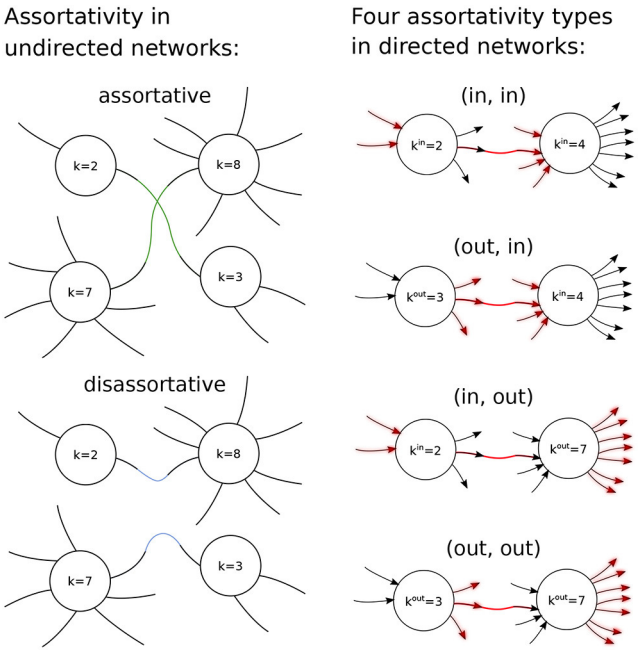

FIGURE 6 | Assortativity in undirected and directed networks. An undirected network (left) is assortative if high degree nodes are more likely to be connected to high degree nodes, and low to low, than by chance (top left). Such a network is disassortative if the opposite occurs (bottom left). (Here, the degree of a node is given by k.) In directed networks (right) there are four possible kinds of assortativity. The probability of a connection (red) depends on the number of red shaded links of the sending (left) and receiving (right) node. (Here, either the in-degree, k^{in}, or out-degree, k^{out}, of a node is the relevant quantity).

If this probability—averaged over the network—is other than that expected by chance, and is further dependent on the degrees of the oscillators, the network shows degree assortativity. One can use this idea to create networks with assortativity, by creating connections where they would typically not occur.

A measure of assortativity for a network with a given connectivity matrix A is by way of calculating the four Pearson correlation coefficients $r(\alpha,\gamma)$ with $\alpha,\gamma \in [\text{in, out}]$ given by

$$r(\alpha,\gamma)=\frac{\sum_{e=1}^{N_e}({}^u k_e^\alpha-\langle {}^u k^\alpha\rangle)({}^d k_e^\gamma-\langle {}^d k^\gamma\rangle)}{\sqrt{\sum_{e=1}^{N_e}({}^u k_e^\alpha-\langle {}^u k^\alpha\rangle)^2}\sqrt{\sum_{e=1}^{N_e}({}^d k_e^\gamma-\langle {}^d k^\gamma\rangle)^2}} \tag{31}$$

where

$$\langle {}^u k^\alpha\rangle=\frac{1}{N_e}\sum_{e=1}^{N_e}{}^u k_e^\alpha \quad \text{and} \quad \langle {}^d k^\gamma\rangle=\frac{1}{N_e}\sum_{e=1}^{N_e}{}^d k_e^\gamma, \tag{32}$$

N_e being the number of edges and the leading superscript u or d refers to the "upstream" or "downstream" oscillator of the respective edge (Bläsche et al., 2020). For example the upstream node's in-degree of the second edge would be ${}^u k_2^{in}$. Note that there are four mean values to compute.

To induce assortativity within a network we start by randomly choosing in-degrees and out-degrees from the distribution given in Equation (20). If the total number of out-degrees does not equal that of the in-degrees (i.e., the network cannot be created; Anstee, 1982) we choose again until it does. We then use the configuration model (Newman, 2003) with these prescribed degrees to create the network, and utilize the same procedure as described earlier for removal of self- and multiple-connections (see **Figure 4**).

To induce assortativity of the form (α,γ) we randomly choose two edges, one connecting oscillator j to oscillator i and another connecting oscillator l to oscillator h. We calculate their contribution to the numerator of (31)

$$c_\parallel=\left(k_j^\alpha-\langle {}^u k^\alpha\rangle\right)\left(k_i^\gamma-\left\langle {}^d k^\gamma\right\rangle\right)+\left(k_l^\alpha-\langle {}^u k^\alpha\rangle\right)\left(k_h^\gamma-\left\langle {}^d k^\gamma\right\rangle\right) \tag{33}$$

and the contribution if we replaced these two edges with one connecting oscillator j to oscillator h and another connecting oscillator l to oscillator i:

$$c_\times=\left(k_l^\alpha-\langle {}^u k^\alpha\rangle\right)\left(k_i^\gamma-\left\langle {}^d k^\gamma\right\rangle\right)+\left(k_j^\alpha-\langle {}^u k^\alpha\rangle\right)\left(k_h^\gamma-\left\langle {}^d k^\gamma\right\rangle\right) \tag{34}$$

If $c_\times > c_\parallel$ we make the swap, otherwise we do not. We then repeat this process many times, storing A, and calculating the value of $r(\alpha,\gamma)$ at regular intervals.

We now discuss how to implement the system Equation (11). Choosing $m = 100, M = 400$, k_{in}, and k_{out} take on values in $\{100, 101, 102, \ldots 400\}$ and thus there are 301×301 possible values of $\mathbf{k}$. Considering that we use a network of size $N = 2,000$ it is clear that there may be many values of $\mathbf{k}$ for which there is not even one oscillator in the network. Thus, we coarse-grain by degree: we divide the interval $[100, 400]$ into 15 equal-size bins with centers $\hat{k}_{in,1}, \hat{k}_{in,2}, \ldots, \hat{k}_{in,15}$ and describe the state of an

oscillator by the value of b associated with the 2D bin it is in (there are 15 × 15 of these 2D bins). We can think of Equation (11) as being a matrix-valued ODE, with the (i,j)th element of the matrix being $b(\hat{k}_{out,i},\hat{k}_{in,j},t)$. We can easily convert this to a vector-valued ODE by stacking the columns of $b(\hat{k}_{out},\hat{k}_{in},t)$, from left to right, into a vector, $\hat{b}(t)$, where the sth entry is $\hat{b}_s(t) = b(\hat{k}_{out,i},\hat{k}_{in,j},t)$ and $s = i + 15(j-1)$. Note that $i,j \in \{1,2,\ldots 15\}$ and $s \in \{1,2,\ldots 225\}$.

Dropping the hat on b we have

$$\frac{db_s(t)}{dt} = \frac{\epsilon e^{-i\beta}R_s(t)}{2} + \left[i\omega_0 - \Delta + i\epsilon \sin\beta R_s(t)\right] b_s(t) - \frac{\epsilon e^{i\beta}R_s(t)}{2}[b_s(t)]^2 \quad (35)$$

for $s \in \{1,2,\ldots 225\}$ where we define

$$G_s(t) = a_n\left[C_0 + \sum_{j=1}^{n} C_j\left\{[b_s(t)]^j + [\bar{b}_s(t)]^j\right\}\right] \quad (36)$$

We need to calculate $R_s(t)$ from $G_s(t)$ using the equivalent of (8). We can write the analog of (8) as

$$R_s(t) = \frac{1}{\langle k\rangle}\sum_{s'=1}^{225} E(s,s')G_{s'}(t) \quad (37)$$

where $E(s,s')$ encodes the connectivity from the 2D bin with index s' to that with index s. Given the connectivity matrix A it is straightforward to calculate $E(s,s')$ as explained in Bläsche et al. (2020). E can be thought of as a 225 × 225 matrix, with (i,j)th entry $E(i,j)$, so we can write Equation (37) as

$$R(t) = \frac{1}{\langle k\rangle}EG(t) \quad (38)$$

where R and G are vector-valued variables and Equation (35) is just the sth component of a vector-valued ODE.

Since we have recorded A at discrete values of the correlation coefficient r, we can also calculate E at these values. To form a parameterized family, $E(r)$, we fit a quadratic to each entry of E as a function of r, i.e., we write $E_{ij}(r) = B_{ij}r^2 + C_{ij}r + D_{ij}$ for $i,j \in [1,225]$, using linear least-squares. We can then efficiently evaluate an approximation of $E(r)$ as

$$E(r) = Br^2 + Cr + D \quad (39)$$

where the (i,j)th entry of B is B_{ij} etc. In summary, we have a parameterized set of ODEs, where r is one of the parameters. Note that we only vary one of the four $r(\alpha,\gamma)$ at a time.

4.1. Results

The results are shown in **Figure 7**, where we vary Δ and the four $r(\alpha,\gamma)$ for four different values of β, and **Figure 8**, where we vary ϵ and the four $r(\alpha,\gamma)$ for the same four values of

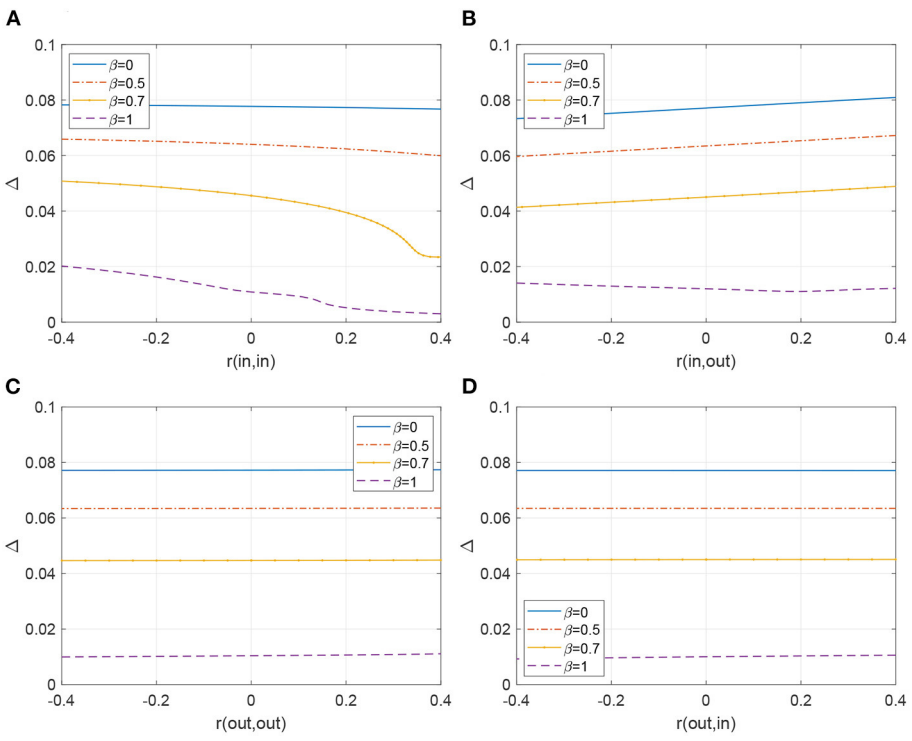

FIGURE 7 | (A–D) Hopf bifurcation curves as both Δ and one of the types of assortativity are varied. A stable periodic orbit exists below the curve. Other parameters: $\epsilon = 0.2, \omega_0 = 1, m = 100, M = 400$.

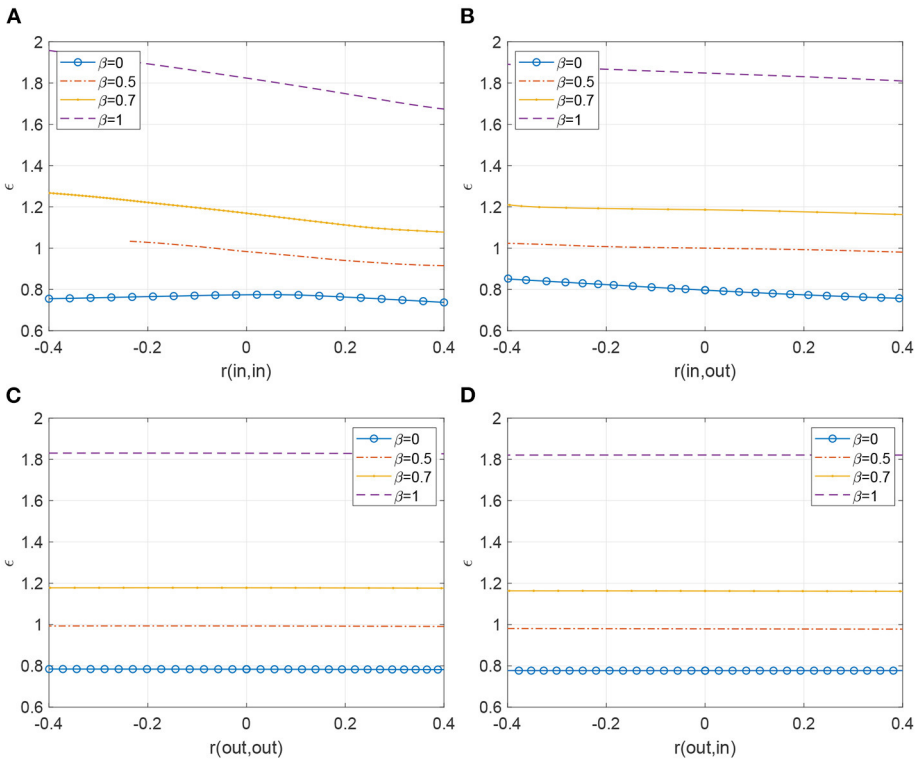

FIGURE 8 | (A–D) SNIC bifurcation curve ($\beta = 0$, blue circles joined by line) and Hopf bifurcation curves ($\beta = 0.5, 0.7$ and 1) as both ϵ and one of the types of assortativity are varied. For each value of β a stable periodic orbit exists below the curve. Other parameters: $\Delta = 0.05, \omega_0 = 1, m = 100, M = 400$. In the top-left panel, for $\beta = 0.5$ the curve terminates as r is decreased.

β. As was seen in Bläsche et al. (2020), assortativities of the type r(out,out) and r(out,in) have no discernable effect on the bifurcations, whereas the other two types do. We can understand this by realizing that the dynamics of an oscillator depend only on its inputs. Since an oscillator's dynamics are independent of its downstream oscillators, neither the r(out,out) nor the r(out,in) assortativities influence the overall network dynamics as shown in all the traces of **Figures 7C,D**. Note, this dynamic interplay is quite different for a network with strong preferential attachment between high in-degree and high out-degree oscillators as when r(in,out) is positive (**Figure 7B**). The influence of the upstream oscillator (with high in-degree, receiving multiple inputs) is amplified or "passed on" to more oscillators via its downstream companion with high out-degree. This pair with high input and high output is thus far more influential than, say, a pair of oscillators preferentially attached according to the upstream node's out-degree. In that scenario, the upstream node of an attached pair may only integrate a small number of inputs (low in-degree), whose behavior is strikingly distinct from an oscillator with many inputs (high in-degree).

Analogously, a positive r(in,in) assortativity demonstrates preferential attachment between high in-degree upstream and downstream pairs of oscillators. In this case, they are relatively potent integrators and concentrators of upstream impulses. We see in **Figure 7A**, the influence of high r(in,in) where the parameter space in which stable periodic orbits exist shrinks, increasing sensitivity to the destructive influence of Δ on synchrony.

5. CORRELATED HETEROGENEITY

We have so far assumed that the parameters ω_0 and Δ (the mean and width, respectively, of the distribution of intrinsic frequencies, see Equation 10) and β (the parameter in the phase response curve, see Equation 2) are the same for each oscillator, but now consider the case of them being correlated with a structural property of an oscillator such as its in-degree or out-degree. Correlating an oscillator's frequency with its degree is known to cause "explosive" synchronization in undirected networks of coupled phase oscillators, for example Liu et al. (2013), Gómez-Gardeñes et al. (2011), and Boccaletti et al. (2016), and we are interested in whether similar effects occur in networks of Winfree oscillators. For simplicity we will use linear relationships between a parameter and its relevant degree.

5.1. In-Degree

We first consider the case of correlation with in-degree. Assuming neutral assortativity and independence between an oscillator's in- and out-degree, following the reasoning in

section 3 the dynamics of b depend only on in-degree and are governed by

$$\frac{\partial b(k_{in})}{\partial t} = \frac{\epsilon e^{-i\beta} R(k_{in})}{2} + \left[i\omega_0 - \Delta + i\epsilon \sin\beta R(k_{in})\right] b(k_{in}) - \frac{\epsilon e^{i\beta} R(k_{in})}{2} [b(k_{in})]^2 \quad (40)$$

for $k_{in} = m, m+1, \ldots M$ where

$$R(k_{in}, t) = \frac{k_{in}}{\langle k\rangle^2} \sum_{k'_{in}} \sum_{k'_{out}} p(k'_{in}) p(k'_{out}) k'_{out} G(k'_{in}, t) = \frac{k_{in}}{\langle k\rangle} \sum_{k'_{in}} p(k'_{in}) G(k'_{in}, t) \quad (41)$$

where G is given by (12) but with the degree dependence being on only k_{in}.

We define a scaled in-degree

$$\hat{k}_{in} = 2\left(\frac{k_{in} - m}{M - m}\right) - 1 \quad (42)$$

which varies linearly from -1 to 1 as k_{in} goes from m to M, respectively. We first consider the case where ω_0 is a function of k_{in}. We write $\omega_0(k_{in}) = 1 + \sigma\hat{k}_{in}$ where σ controls the strength of dependence between k_{in} and ω_0. (Recall that we previously set $\omega_0 = 1$.) Setting $\beta = 0, \epsilon = 0.2$, and $\Delta = 0.05$ we find that when $\sigma = 0$ the network is attracted to a stable periodic orbit. However, increasing or decreasing σ causes the oscillations to cease through a Hopf bifurcation as shown in **Figure 9A**. To visualize the oscillations we define the complex order parameter for (40) as

$$Z(t) = \frac{1}{M - m + 1} \sum_{k_{in}=m}^{M} b(k_{in}, t). \quad (43)$$

This is an appropriate definition since the distribution of in-degrees is uniform; if it were not we would have to weight the contributions from different k_{in} values. **Figure 9A** shows the maximum and minimum over one period of Im(Z) for oscillatory solutions, and just Im(Z) for fixed points. Simulations of a finite network are shown in the lower panels of **Figure 9** (transients not shown) which confirm the results in **Figure 9A**. The small amplitude oscillations seen in **Figures 9A,C** are a result of finite size fluctuations about the fixed point of Equation (40), the linearization about which has complex eigenvalues. The amplitude of these oscillations decreases as the number of oscillators used increases (not shown).

One might think that having ω_0 depend on in-degree broadens the distribution of intrinsic frequencies in the network, which is equivalent in some sense to increasing Δ. However, it is not completely equivalent for several reasons. Firstly, the distribution of all intrinsic frequencies is no longer Lorentzian (although for each oscillator we choose the frequency from a Lorentzian), and depends on both the form of dependence of ω_0 on k_{in} (linear in this case) and the distribution of the k_{in} (uniform in this case). Secondly, the intrinsic frequency of each oscillator now depends on a structural property: its in-degree. But for comparison, the oscillations seen in **Figure 9** for $\sigma = 0$ are destroyed in a Hopf bifurcation as Δ is increased through ~ 0.085 (not shown).

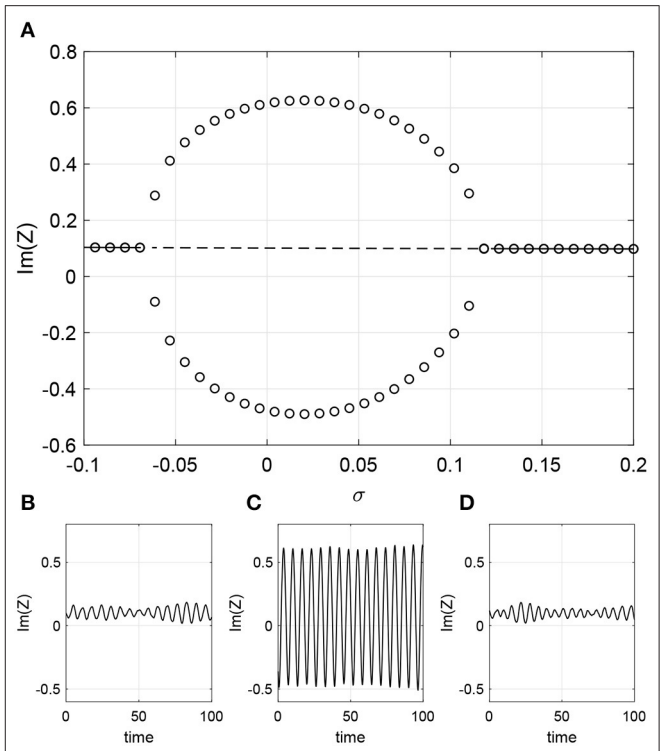

FIGURE 9 | Intrinsic frequency dependence $\omega_0(k_{in}) = 1 + \sigma\hat{k}_{in}$. **(A)** Solid line: stable fixed point of Equation (40); dashed line: unstable fixed point. Circles: maximum and minimum over one period of Im(Z). Im(Z) calculated using (30) for **(B)** $\sigma = -0.1$, **(C)** $\sigma = 0$, and **(D)** $\sigma = 0.2$. Other parameters: $\Delta = 0.05, \beta = 0, \epsilon = 0.2, m = 100, M = 400, N = 2,000$.

Next consider β being a function of k_{in}. In order to not have negative β we set $\beta = \sigma(\hat{k}_{in} + 1)$. We choose $\omega_0 = 1, \epsilon = 0.8, \Delta = 0.05$. For these parameters the network is attracted to a stable fixed point. However, increasing σ first induces oscillations through a SNIC bifurcation and then destroys them through a Hopf bifurcation, as shown in **Figure 10A**. Simulations of a finite network are shown in the lower panels of **Figure 10** and these are consistent with the results in **Figure 10A**.

As a third possibility we let Δ depend on k_{in}. Δ (the width of the distribution of intrinsic frequencies) cannot be negative so we set $\Delta = 0.09 + \sigma\hat{k}_{in}$ and consider only $-0.09 \le \sigma \le 0.09$. We set other parameters $\omega_0 = 1, \beta = 1$ and $\epsilon = 0.6$. A Hopf bifurcation occurs as σ is increased as shown in **Figure 11A**. Simulations of a finite network are shown in the lower panels of **Figure 11**. Significant oscillations are seen for $\sigma = 0$, and the amplitude of oscillations for $\sigma = 0.09$ is less than expected. However, we repeated this type of simulation with $N = 5,000$ and found that the amplitude of oscillations with $\sigma = 0.09$ better matched the results in **Figure 11A** (i.e., were bigger than seen for $N = 2,000$) and that the amplitude of oscillations for $\sigma = 0$ were slightly

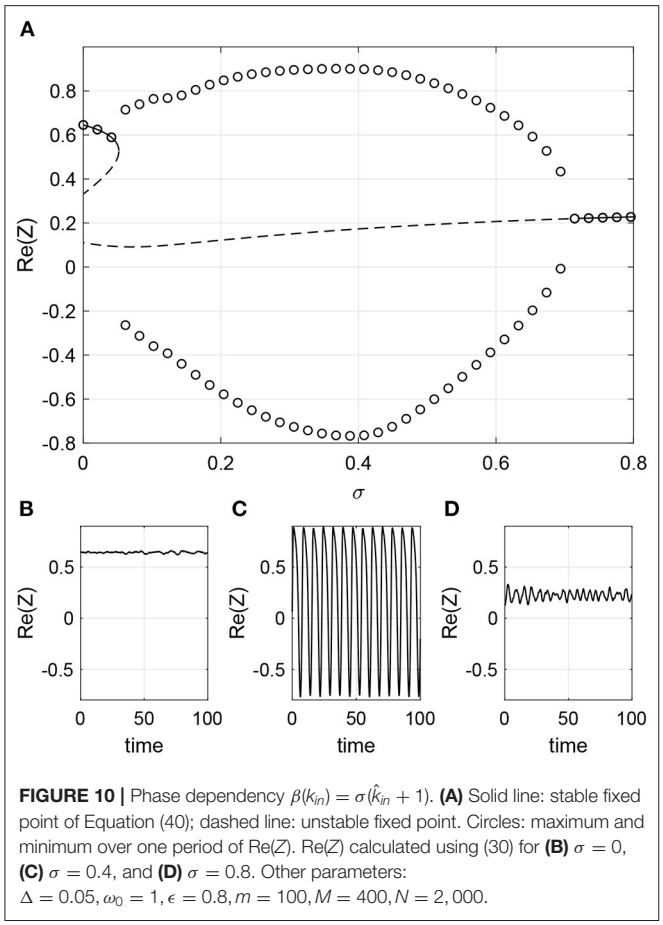

FIGURE 10 | Phase dependency $\beta(k_{in}) = \sigma(\hat{k}_{in} + 1)$. **(A)** Solid line: stable fixed point of Equation (40); dashed line: unstable fixed point. Circles: maximum and minimum over one period of Re(*Z*). Re(*Z*) calculated using (30) for **(B)** $\sigma = 0$, **(C)** $\sigma = 0.4$, and **(D)** $\sigma = 0.8$. Other parameters: $\Delta = 0.05, \omega_0 = 1, \epsilon = 0.8, m = 100, M = 400, N = 2,000$.

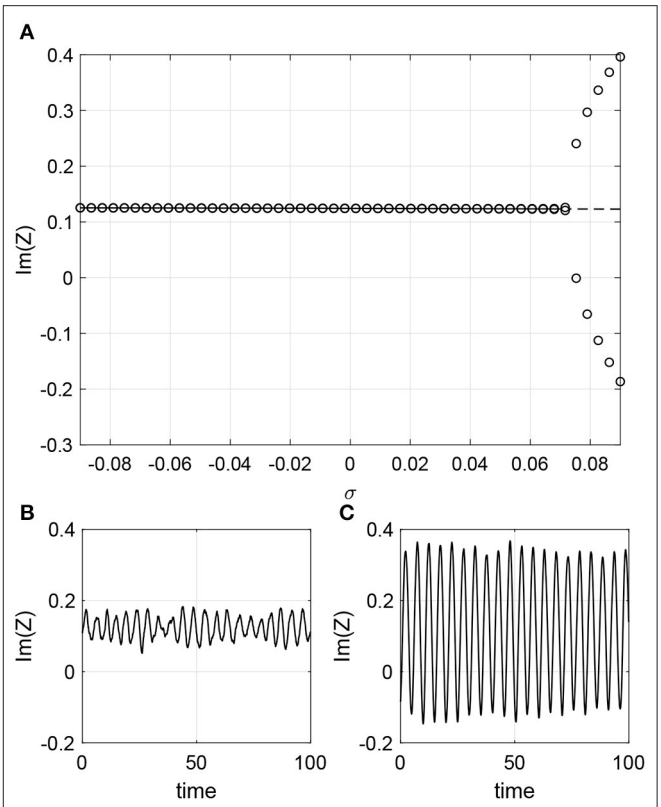

FIGURE 11 | Heterogeneity dependency $\Delta = 0.09 + \sigma\hat{k}_{in}$. **(A)** Solid line: stable fixed point of (40); dashed line: unstable fixed point. Circles: maximum and minimum over one period of Im(*Z*). Im(*Z*) calculated using (30) for **(B)** $\sigma = 0$ and **(C)** $\sigma = 0.09$. Other parameters: $\beta = 1, \omega_0 = 1, \epsilon = 0.6, m = 100, M = 400, N = 2,000$.

smaller than seen for $N = 2,000$ (results not shown), suggesting that this apparent disagreement is a finite-size effect.

5.2. Out-Degree

Now consider the possibility that one of ω_0, Δ, and β are correlated with an oscillator's out-degree. From Equation (11), it is clear that even for neutral assortativity, b will depend on both k_{in} and k_{out}. Thus, the relevant equations are

$$\frac{\partial b}{\partial t} = \frac{\epsilon e^{-i\beta} R}{2} + [i\omega_0 - \Delta + i\epsilon \sin\beta R]\, b - \frac{\epsilon e^{i\beta} R}{2} b^2 \qquad (44)$$

where b is a function of both k_{in} and k_{out}, but R is a function of k_{in} only:

$$R(k_{in}, t) = \frac{k_{in}}{\langle k \rangle^2} \sum_{k'_{in}} \sum_{k'_{out}} p(k'_{in}) p(k'_{out}) k'_{out} G(k'_{in}, k'_{out}, t) \qquad (45)$$

where G is given by Equation (12).

5.2.1. Computational Approach

If $J = M - m + 1$ is the number of distinct in-degrees (and out-degrees) then b can be thought of as a $J \times J$ matrix with J^2 entries. This is too many to deal with computationally, so we discretize in degree space. In the same way that one can approximate a definite integral using Gaussian quadrature, it is possible to approximate a double sum like that in (45) using a double sum over far fewer points (Engblom, 2006). The theory is explained in Laing and Bläsche (2020), but put briefly we define an inner product on either degree space

$$(f, g) = \sum_{k=m}^{M} f(k) g(k) \qquad (46)$$

and assume that there is a corresponding set of orthogonal polynomials $\{q_n(k)\}_{0 \le n}$ associated with this product. We choose a positive integer s and let $\{k_i\}_{i=1,\ldots s}$ be the roots of q_s, found using the Golub-Welsch algorithm, and $\{w_i\}$ be the weights associated with these roots. The approximation of the double sum in (45) is then

$$\sum_{k'_{in}} \sum_{k'_{out}} p(k'_{in}) p(k'_{out}) k'_{out} G(k'_{in}, k'_{out}, t) \approx \sum_{i=1}^{s} \sum_{j=1}^{s} w_i w_j k_j G(k_i, k_j, t) \qquad (47)$$

Note that the k_i are not integer-valued. We thus solve (44) on the non-uniform 2D grid of s^2 "virtual" degree. An example for $s = 10$ is shown in **Figure 12**.

The convergence with s is observed to be geometric (not shown) and we use $s = 20$ to calculate the results below.

5.2.2. Results

We write

$$\hat{k}_{out} = 2\left(\frac{k_{out} - m}{M - m}\right) - 1. \tag{48}$$

Setting $\omega_0(k_{out}) = 1 + \sigma\hat{k}_{out}$ and varying σ we obtain the results in **Figure 13**. Two Hopf bifurcations are seen, as in **Figure 9A** but at different values of σ from in that figure. Writing $\beta(k_{out}) = \sigma(\hat{k}_{out} + 1)$ and varying σ we obtain the results in **Figure 14**. The bifurcations are the same as in **Figure 10A**, but again, at different values of σ. Using the parameters shown in **Figure 11A**, setting $\Delta = 0.09 + \sigma\hat{k}_{out}$ and varying $\sigma \in [-0.09, 0.09]$ (as Δ cannot be negative) the fixed point was always stable (not shown). Simulations of a discrete network of $N = 2,000$ oscillators confirmed all of the results in this section (not shown).

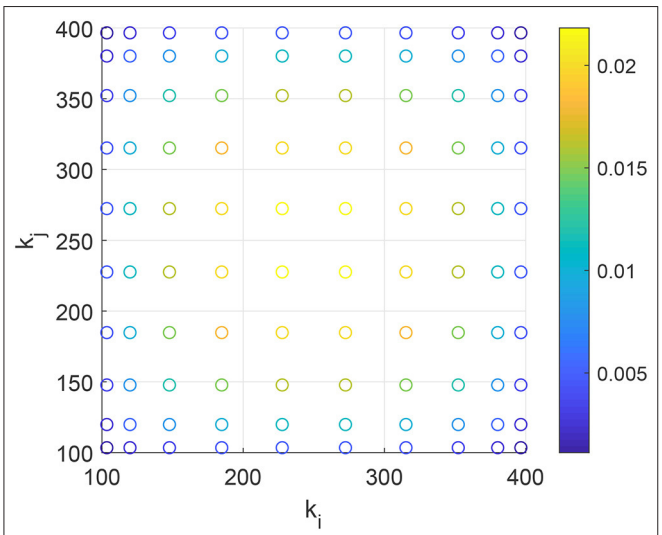

FIGURE 12 | Non-uniform 2D grid of degrees as explained in section 5.2.1 with $m = 100, M = 400, s = 10$. The color shows the weight, $w_i w_j$, associated with each point.

6. PARAMETER ASSORTATIVITY

We now consider assortativity by a parameter other than degree, in this case ω_0 value. We first describe how to create a network with such assortativity, then derive the relevant continuum equations. We follow Skardal et al. (2015) in our derivation.

To create a particular network we first create a network where the in- and out-degrees of all oscillators are the same, in order that degree not affect the dynamics. To do this we use the configuration model (Newman, 2003), then remove all self-connections and multi-edges as before. With N oscillators we randomly choose N *target* values of ω_0 from a distribution $p(\omega_0)$, which is non-zero only if $\omega_0 \in [\underline{\omega}_0, \overline{\omega}_0]$, i.e., $\underline{\omega}_0$ is the minimum value of ω_0 and $\overline{\omega}_0$ is the maximum, and assign these to oscillators. We can calculate the assortativity of the network using similar ideas as those in section 4. We calculate the Pearson correlation coefficient

$$r = \frac{\sum_{e=1}^{N_e}(\omega'_{0,e} - \langle\omega'_0\rangle)(\omega_{0,e} - \langle\omega_0\rangle)}{\sqrt{\sum_{e=1}^{N_e}(\omega'_{0,e} - \langle\omega'_0\rangle)^2}\sqrt{\sum_{e=1}^{N_e}(\omega_{0,e} - \langle\omega_0\rangle)^2}} \tag{49}$$

where $\omega'_{0,e}$ is the value of the target ω_0 associated with the oscillator at the start of edge e and $\omega_{0,e}$ is the value of the target

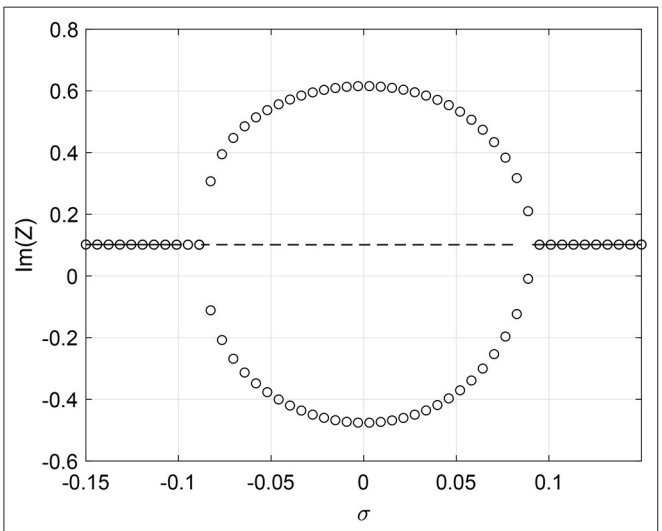

FIGURE 13 | Intrinsic frequency dependence $\omega_0(k_{out}) = 1 + \sigma\hat{k}_{out}$. Solid line: stable fixed point of (44); dashed line: unstable fixed point. Circles: maximum and minimum over one period of Im(Z). Other parameters: $\Delta = 0.05, \beta = 0, \epsilon = 0.2, m = 100, M = 400$.

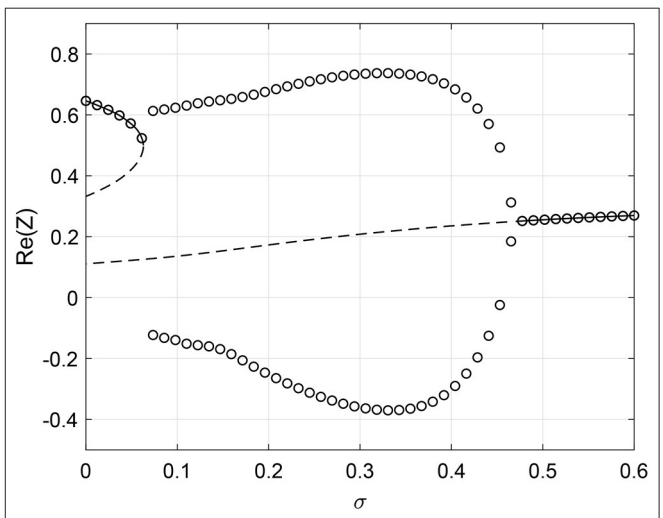

FIGURE 14 | Phase shift dependence $\beta(k_{out}) = \sigma(\hat{k}_{out} + 1)$. Solid line: stable fixed point of (44); dashed line: unstable fixed point. Circles: maximum and minimum over one period of Re(Z). Other parameters: $\Delta = 0.05, \omega_0 = 1, \epsilon = 0.8, m = 100, M = 400$.

ω_0 associated with the oscillator at the end of edge e, and N_e is the number of edges. The means are

$$\langle \omega_0' \rangle = \frac{1}{N_e}\sum_{e=1}^{N_e} \omega_{0,e}' \qquad \langle \omega_0 \rangle = \frac{1}{N_e}\sum_{e=1}^{N_e} \omega_{0,e} \tag{50}$$

Initially the network will have $r \approx 0$. We induce assortativity in a similar way to that described in section 4. We randomly chose two edges, one connecting oscillator j to oscillator i and another connecting oscillator l to oscillator h. We calculate their contribution to the numerator of Equation (49) and the contribution if we replaced these two edges with one connecting oscillator j to oscillator h and another connecting oscillator l to oscillator i. If performing this swap increases r we make the swap, otherwise we do not. We then repeat this process many times, storing A and calculating the value of r at regular intervals. (To decrease r from its initial value of 0 we just consider whether making the swap decreases r). As a last step, in order to use the Ott/Antonsen ansatz, we then randomly assign to oscillator i a value of ω_i chosen from a Lorentzian with mean equal to the *target* ω_0 for that oscillator and with half-width-at-half-maximum Δ. This will result in the creation of a network in which all oscillators have the same in- and out-degree, but those with high ω_0 are more likely to connect to those also having high ω_0 and vice versa.

To derive the continuum equations we see that the state of an oscillator can only depend on its ω_0 value. We discretize the range of ω_0 values, $[\underline{\omega}_0, \overline{\omega}_0]$, into m equal-sized bins, and thus we have

$$\frac{db_s(t)}{dt} = \frac{\epsilon e^{-i\beta} R_s(t)}{2} + \left[i\omega_s - \Delta + i\epsilon \sin\beta R_s(t)\right] b_s(t) - \frac{\epsilon e^{i\beta} R_s(t)}{2}[b_s(t)]^2 \tag{51}$$

for $s = 1, 2, \ldots m$, where ω_s is the value of ω_0 in the center of the sth bin. The analog of Equation (8) is

$$R_s(t) = \frac{1}{\langle k \rangle}\sum_{u=1}^{m} E_{su} G_u(t) \tag{52}$$

where $\langle k \rangle$ is the degree of each oscillator,

$$G_s(t) = a_q\left[C_0 + \sum_{j=1}^{q} C_j\left\{[b_s(t)]^j + [\bar{b}_s(t)]^j\right\}\right] \tag{53}$$

and the matrix E encodes the connectivity of the network, i.e., E_{su} is proportional to the number of oscillators in the uth bin which connect to oscillators in the sth bin, which can be determined from the connectivity matrix A. As in section 4, we record A at discrete values of the correlation coefficient r, so can construct $E(r)$ at those values. We fit a quadratic through each entry of E as a function of r and thus write

$$E(r) = Br^2 + Cr + D \tag{54}$$

where B, C, and D are $m \times m$ constant matrices.

As an example we choose $\beta = 0, \Delta = 0.01$, and $p(\omega_0)$ to be the uniform distribution on $[0, 2]$. ($p(\omega_0)$ must have bounded support so we can discretize its domain into a finite number of bins.) We compare the results of simulating a full network from Equation (1) with those from the reduced model in Equation (51). We use a network of $N = 2,000$ with each oscillator having degree $\langle k \rangle = 100$. We have stored the connectivity matrix A at 101 values of r, and vary both ϵ and r. At each point in this parameter space we solve Equation (1) for 100 time units, discard the first 50 as transients, then calculate the order parameter using Equation (30). The difference between the maximum of $|Z|$ over the final 50 time units and the minimum of $|Z|$ over this time is shown in **Figure 15**.

When this difference is close to zero, most of the oscillators are "locked" at zero frequency, but for $\epsilon = 0.8$ there is a transition at $r \approx 0$ where some the oscillators start unlocking, with those having largest ω_0 unlocking first. Note that this is not a "classical" bifurcation, as the system is not at fixed point before this transition. However, solving the reduced Equations (51) we find that there is a stable fixed point to the left of the red curve in **Figure 15** which is destroyed in a Hopf bifurcation, leading to periodic and then quasiperiodic behavior as r is increased. Thus the reduced model provides an explanation for the observed behavior of the full model (1).

The results in **Figure 15** are an example of the types of results we can obtain using the framework presented here. We could vary parameters other than ϵ, or introduce assortativity by another intrinsic parameter, β. In this case we would have to use a different measure of correlation between the β values for connected oscillators, as β is an angular variable (Fisher and Lee, 1983).

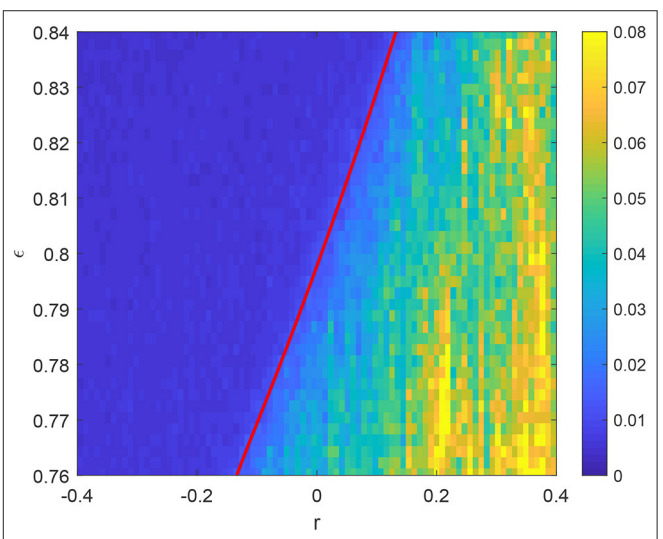

FIGURE 15 | Difference between the maximum of $|Z|$ over the last 50 time units out of 100 and the minimum, having already discarded the first 50 as transient. $p(\omega_0)$ is uniform on [0, 2]. The red curve shows the Hopf bifurcation of the steady state of (51) which is stable to the left of this curve. Other parameters: $\beta = 0, \Delta = 0.01, \langle k \rangle = 100, N = 2,000$. We use $m = 20$ bins to calculate the blue curve.

7. CONCLUSION

We studied large directed networks of Winfree oscillators under the assumption that the expected dynamics of an oscillator in such a network is determined by its degree: either its in-degree, out-degree, or both (apart from the homogenous degree networks in section 6). Using the Ott/Antonsen ansatz we find that the dynamics are given by Equation (11). Correlations between the in- and out-degree of an oscillator were introduced using a Gaussian copula in section 3, where we investigated the influence of these correlations on the position of bifurcations destroying stable periodic orbits. In section 4, we investigated four types of degree assortativity, as in Bläsche et al. (2020), and found similar results, viz. two types of assortativity have no effect on the network dynamics, while the other two do. Correlations between an oscillator's intrinsic parameter and either its in- or out-degree were examined in section 5. Parameter assortativity was considered in section 6. The framework presented here is quite general, and we believe it to be a powerful method for investigating the general issue of the influence of a network's structure on its dynamics.

The main tool used was numerical continuation and bifurcation analysis of a large number of coupled ODEs (Laing, 2014), which enabled the determination of bifurcation points as parameters were varied—including correlations between various network properties. Following such bifurcations shows the influence of network properties in their dynamics.

The influence of these correlations and assortativities on network synchrony is complex, nuanced, and multi-faceted. Introducing degree correlations within oscillators subtly shapes sensitivity of the network to oscillator parameters such as variability of intrinsic frequencies, Δ, and coupling strength, ϵ. Assortativities between the degrees of connected oscillators can have similar effects for in-degree correlations—r(in,·)—or none at all—r(out,·). More dramatically, for the parameters considered, inducing correlations between oscillator degree (in or out) and intrinsic frequency, ω, destroys oscillatory synchrony. Similarly, if the degree and phase offset, β, are correlated, this may cause or destroy synchronized oscillations. The theme continues with assortativities between intrinsic frequencies, where if they are excessively assortative, oscillators in the network unlock from the population—requiring a higher coupling level to stay locked. Conversely, correlating an oscillator's degree with the width of the distribution from which its intrinsic frequency is chosen, Δ, has little effect.

Network structure such as preferential attachment between similar (or dissimilar) oscillators and the influence we have observed here in idealized systems may reflect structural influences in physiological networks of neurons. Intrinsic connectivity preferences observed of neurons grown in culture—e.g., similar numbers of synaptic or dendritic processes connected to each other in groups—results in strong assortativity patterns (de Santos-Sierra et al., 2014; Teller et al., 2014) further inferred in the human cerebral cortex (Hagmann et al., 2008). Our observations of network structure influencing the overall synchrony of a network may be a structural means of calibrating the dynamics of physiological neurons.

Regarding section 5, correlating degree with intrinsic frequency is known to cause explosive synchronization, characterized by bistability between asynchronous and partially synchronized states, in undirected networks of Kuramoto phase oscillators (Gómez-Gardeñes et al., 2011; Liu et al., 2013). We did not observe such behavior but we only considered uniform degree distributions (not power law; Gómez-Gardeñes et al., 2011; Liu et al., 2013) and have directed connections, not undirected. Also, there are many ways to correlate an intrinsic parameter with a degree (Skardal et al., 2013); our form of modification keeps the parameter for nodes with mean degree the same and increases/decreases the parameter for those with degrees above/below mean (or vice versa) in a linear way.

We certainly do not yet have a full understanding of the possible dynamics of the network (1). Possible extensions of the work here include simultaneously having more than one type of structure present in the network (for example, both within-oscillator degree correlations *and* degree assortativity) or correlating an oscillator's intrinsic parameter with some other network property such as the oscillator's centrality (Newman, 2018) or local clustering coefficient (Watts and Strogatz, 1998). More detailed knowledge about the connectivity in networks of neurons of interest would provide motivation to study these extensions, and help verify some of our results.

DATA AVAILABILITY STATEMENT

The raw data supporting the conclusions of this article will be made available by the authors, without undue reservation.

AUTHOR CONTRIBUTIONS

All authors listed have made a substantial, direct and intellectual contribution to the work, and approved it for publication.

FUNDING

This work was partially supported by the Marsden Fund Council from Government funding, managed by Royal Society Te Aparangi, grant number 17-MAU-054.

REFERENCES

Anstee, R. (1982). Properties of a class of (0, 1)-matrices covering a given matrix. *Can. J. Math*. 34, 438–453. doi: 10.4153/CJM-1982-029-3

Arenas, A., Díaz-Guilera, A., Kurths, J., Moreno, Y., and Zhou, C. (2008). Synchronization in complex networks. *Phys. Rep*. 469, 93–153. doi: 10.1016/j.physrep.2008.09.002

Ariaratnam, J. T., and Strogatz, S. H. (2001). Phase diagram for the winfree model of coupled nonlinear oscillators. *Phys. Rev. Lett*. 86:4278. doi: 10.1103/PhysRevLett.86.4278

Avalos-Gaytan, V., Almendral, J. A., Papo, D., Schaeffer, S. E., and Boccaletti, S. (2012). Assortative and modular networks are shaped by adaptive synchronization processes. *Phys. Rev. E* 86:015101. doi: 10.1103/PhysRevE.86.015101

Bläsche, C., Means, S., and Laing, C. R. (2020). Degree assortativity in networks of spiking neurons. *J. Comput. Dyn.* 7, 401–423. doi: 10.3934/jcd.2020016

Boccaletti, S., Almendral, J., Guan, S., Leyva, I., Liu, Z., Sendi na-Nadal, I., et al. (2016). Explosive transitions in complex networks' structure and dynamics: percolation and synchronization. *Phys. Rep.* 660, 1–94. doi: 10.1016/j.physrep.2016.10.004

Chandra, S., Hathcock, D., Crain, K., Antonsen, T. M., Girvan, M., and Ott, E. (2017). Modeling the network dynamics of pulse-coupled neurons. *Chaos* 27:033102. doi: 10.1063/1.4977514

De Franciscis, S., Johnson, S., and Torres, J. J. (2011). Enhancing neural-network performance via assortativity. *Phys. Rev. E* 83:036114. doi: 10.1103/PhysRevE.83.036114

de Santos-Sierra, D., Sendi na-Nadal, I., Leyva, I., Almendral, J. A., Anava, S., Ayali, A., et al. (2014). Emergence of small-world anatomical networks in self-organizing clustered neuronal cultures. *PLoS ONE* 9:e85828. doi: 10.1371/journal.pone.0085828

Engblom, S. (2006). *Gaussian Quadratures With Respect to Discrete Measures*. Technical report, Uppsala University.

Ermentrout, G. B., and Kopell, N. (1986). Parabolic bursting in an excitable system coupled with a slow oscillation. *SIAM J. Appl. Math.* 46, 233–253. doi: 10.1137/0146017

Fenton, F. H., Cherry, E. M., Hastings, H. M., and Evans, S. J. (2002). Multiple mechanisms of spiral wave breakup in a model of cardiac electrical activity. *Chaos* 12, 852–892. doi: 10.1063/1.1504242

Fisher, N. I., and Lee, A. (1983). A correlation coefficient for circular data. *Biometrika* 70, 327–332. doi: 10.1093/biomet/70.2.327

Foster, J. G., Foster, D. V., Grassberger, P., and Paczuski, M. (2010). Edge direction and the structure of networks. *Proc. Natl. Acad. Sci. U.S.A.* 107, 10815–10820. doi: 10.1073/pnas.0912671107

Gallego, R., Montbrió, E., and Pazó, D. (2017). Synchronization scenarios in the winfree model of coupled oscillators. *Phys. Rev. E* 96:042208. doi: 10.1103/PhysRevE.96.042208

Gómez-Garde nes, J., Gómez, S., Arenas, A., and Moreno, Y. (2011). Explosive synchronization transitions in scale-free networks. *Phys. Rev. Lett.* 106:128701. doi: 10.1103/PhysRevLett.106.128701

Ha, S.-Y., Park, J., and Ryoo, S. W. (2015). Emergence of phase-locked states for the winfree model in a large coupling regime. *Discrete Contin. Dyn. Syst. A* 35:3417. doi: 10.3934/dcds.2015.35.3417

Hagmann, P., Cammoun, L., Gigandet, X., Meuli, R., Honey, C., Van Wedeen, J., et al. (2008). Mapping the structural core of human cerebral cortex. *PLoS Biol.* 6:e052306. doi: 10.1371/journal.pbio.0060159

Kähne, M., Sokolov, I., and Rüdiger, S. (2017). Population equations for degree-heterogenous neural networks. *Phys. Rev. E* 96:052306. doi: 10.1103/PhysRevE.96.052306

Laing, C. R. (2014). Numerical bifurcation theory for high-dimensional neural models. *J. Math. Neurosci.* 4:1. doi: 10.1186/2190-8567-4-13

Laing, C. R. (2017). "Phase oscillator network models of brain dynamics," in *Computational Models of Brain and Behavior*, ed A. A. Moustafa (Hoboken, NJ: Wiley Online Library), 505–517. doi: 10.1002/9781119159193.ch37

Laing, C. R., and Bläsche, C. (2020). The effects of within-neuron degree correlations in networks of spiking neurons. *Biol. Cybern.* 114, 337–347. doi: 10.1007/s00422-020-00822-0

LaMar, M. D., and Smith, G. D. (2010). Effect of node-degree correlation on synchronization of identical pulse-coupled oscillators. *Phys. Rev. E* 81:046206. doi: 10.1103/PhysRevE.81.046206

Liu, W., Wu, Y., Xiao, J., and Zhan, M. (2013). Effects of frequency-degree correlation on synchronization transition in scale-free networks. *Europhys. Lett.* 101:38002. doi: 10.1209/0295-5075/101/38002

Martens, M. B., Houweling, A. R., and Tiesinga, P. H. (2017). Anti-correlations in the degree distribution increase stimulus detection performance in noisy spiking neural networks. *J. Comput. Neurosci.* 42, 87–106. doi: 10.1007/s10827-016-0629-1

Milton, J., and Jung, P. (2013). *Epilepsy as a Dynamic Disease*. Berlin; Heidelberg: Springer Science & Business Media.

Nelsen, R. B. (2007). *An Introduction to Copulas*. New York, NY: Springer Science & Business Media.

Netoff, T. I., Banks, M. I., Dorval, A. D., Acker, C. D., Haas, J. S., Kopell, N., et al. (2005). Synchronization in hybrid neuronal networks of the hippocampal formation. *J. Neurophysiol.* 93, 1197–1208. doi: 10.1152/jn.00982.2004

Newman, M. (2003). The structure and function of complex networks. *SIAM Rev.* 45, 167–256. doi: 10.1137/S003614450342480

Newman, M. (2018). *Networks*. New York, NY: Oxford University Press. doi: 10.1093/oso/9780198805090.001.0001

Nykamp, D. Q., Friedman, D., Shaker, S., Shinn, M., Vella, M., Compte, A., et al. (2017). Mean-field equations for neuronal networks with arbitrary degree distributions. *Phys. Rev. E* 95:042323. doi: 10.1103/PhysRevE.95.042323

Ott, E., and Antonsen, T. (2008). Low dimensional behavior of large systems of globally coupled oscillators. *Chaos* 18:037113. doi: 10.1063/1.2930766

Ott, E., and Antonsen, T. (2009). Long time evolution of phase oscillator systems. *Chaos* 19:023117. doi: 10.1063/1.3136851

Pazó, D., and Gallego, R. (2020). The winfree model with non-infinitesimal phase-response curve: Ott-antonsen theory. *Chaos* 30:073139. doi: 10.1063/5.0015131

Pazó, D., and Montbrió, E. (2014). Low-dimensional dynamics of populations of pulse-coupled oscillators. *Phys. Rev. X* 4:011009. doi: 10.1103/PhysRevX.4.011009

Pazó, D., Montbrió, E., and Gallego, R. (2019). The winfree model with heterogeneous phase-response curves: analytical results. *J. Phys. A* 52:154001. doi: 10.1088/1751-8121/ab0b4c

Pikovsky, A., Rosenblum, M., and Kurths, J. (2001). *Synchronization*. Cambridge: Cambridge University Press. doi: 10.1017/CBO9780511755743

Restrepo, J. G. and Ott, E. (2014). Mean-field theory of assortative networks of phase oscillators. *Europhys. Lett.* 107:60006. doi: 10.1209/0295-5075/107/60006

Schmeltzer, C., Kihara, A. H., Sokolov, I. M., and Rüdiger, S. (2015). Degree correlations optimize neuronal network sensitivity to sub-threshold stimuli. *PLoS ONE* 10:e0121794. doi: 10.1371/journal.pone.0121794

Schultheiss, N. W., Prinz, A. A., and Butera, R. J. (2011). *Phase Response Curves in Neuroscience: Theory, Experiment, and Analysis*. New York, NY: Springer. doi: 10.1007/978-1-4614-0739-3

Skardal, P. S., Restrepo, J. G., and Ott, E. (2015). Frequency assortativity can induce chaos in oscillator networks. *Phys. Rev. E* 91:060902. doi: 10.1103/PhysRevE.91.060902

Skardal, P. S., Sun, J., Taylor, D., and Restrepo, J. G. (2013). Effects of degree-frequency correlations on network synchronization: universality and full phase-locking. *Europhys. Lett.* 101:20001. doi: 10.1209/0295-5075/101/20001

Strogatz, S. (2000). From Kuramoto to Crawford: exploring the onset of synchronization in populations of coupled oscillators. *Phys. D* 143, 1–20. doi: 10.1016/S0167-2789(00)00094-4

Strogatz, S. (2003). *Sync: The Emerging Science of Spontaneous Order*. Hyperion.

Teller, S., Granell, C., De Domenico, M., Soriano, J., Gómez, S., and Arenas, A. (2014). Emergence of assortative mixing between clusters of cultured neurons. *PLoS Comput. Biol.* 10:e1003796. doi: 10.1371/journal.pcbi.1003796

Tsubo, Y., Teramae, J.-N., and Fukai, T. (2007). Synchronization of excitatory neurons with strongly heterogeneous phase responses. *Phys. Rev. Lett.* 99:228101. doi: 10.1103/PhysRevLett.99.228101

Vasquez, J., Houweling, A., and Tiesinga, P. (2013). Simultaneous stability and sensitivity in model cortical networks is achieved through anti-correlations between the in- and out-degree of connectivity. *Front. Comput. Neurosci.* 7:156. doi: 10.3389/fncom.2013.00156

Vegué, M., Perin, R., and Roxin, A. (2017). On the structure of cortical microcircuits inferred from small sample sizes. *J. Neurosci.* 37, 8498–8510. doi: 10.1523/JNEUROSCI.0984-17.2017

Vegué, M., and Roxin, A. (2019). Firing rate distributions in spiking networks with heterogeneous connectivity. *Phys. Rev. E* 100:022208. doi: 10.1103/PhysRevE.100.022208

Watts, D. J., and Strogatz, S. H. (1998). Collective dynamics of 'small-world' networks. *Nature* 393, 440–442. doi: 10.1038/30918

Winfree, A. (2001). *The Geometry of Biological Time*. New York, NY: Springer. doi: 10.1007/978-1-4757-3484-3

Winfree, A. T. (1967). Biological rhythms and the behavior of populations of coupled oscillators. *J. Theor. Biol.* 16, 15–42. doi: 10.1016/0022-5193(67)90051-3

Conflict of Interest: The authors declare that the research was conducted in the absence of any commercial or financial relationships that could be construed as a potential conflict of interest.

frontiers in Applied Mathematics and Statistics

ORIGINAL RESEARCH
published: 22 April 2021
doi: 10.3389/fams.2021.662221

Influence of Sound on Empirical Brain Networks

Jakub Sawicki[1,2]* *and Eckehard Schöll*[1,2]

[1]*Potsdam Institute for Climate Impact Research, Potsdam, Germany,* [2]*Institut für Theoretische Physik, Technische Universität Berlin, Berlin, Germany*

We analyze the influence of an external sound source in a network of FitzHugh–Nagumo oscillators with empirical structural connectivity measured in healthy human subjects. We report synchronization patterns, induced by the frequency of the sound source. We show that the level of synchrony can be enhanced by choosing the frequency of the sound source and its amplitude as control parameters for synchronization patterns. We discuss a minimum model elucidating the modalities of the influence of music on the human brain.

Keywords: synchronization, coupled oscillators, neuronal network dynamics, pattern formation, external driven

1 INTRODUCTION

Synchronization phenomena are well-known regarding dynamical activities of the brain. A high degree of synchronization is related to (slow-wave) sleep [1, 2] or transitions from wakefulness to sleep [3, 4]. Recently, partial synchronization has become a clue to explain the first-night effect [5] and unihemispheric sleep [1, 6–8]. Moreover, synchronized dynamics play an important role in the dynamics of epileptic seizures [9], where the synchronization of a part of the brain causes dangerous consequences for the persons concerned. In contrast, synchronization is also used to explain brain processes which subserve for development of syntax and its perception [10–12]. In general, synchronization theory is highly important to analyze and understand musical acoustics and music psychology [13–17]. While the neurophysiological processes when listening to music remain ongoing research, it is presumed that a certain degree of synchrony can be observed while listening to music and building up expectations. Event-related potentials (ERPs), measured by electroencephalography (EEG) of participants while listening to music, show synchronized dynamics between different brain regions [18, 19]. These studies indicate that the increase of synchronization represents musical large-scale form perception. Moreover, it has been observed that areas of the whole brain are involved regarding neuronal dynamics during perception [10]. Therefore, we propose to investigate the general influence of sound on empirical brain networks. We model the spiking dynamics of the neurons by the paradigmatic FitzHugh–Nagumo model, and investigate possible partial synchronization patterns induced by an external sound source, which is connected to the auditory cortex of the human brain. Furthermore, It is a well-known fact that an important feature of musical sound perception is tonal fusion [20]. Although sound has in general a rich overtone spectrum, subjects perceive only one musical pitch which is a fusion of all partials of the spectrum. Against this background, we concentrate our general study on an external sound source with an amplitude and a single frequency, neglecting the complexity of music and its distinct effects in different frequency bands within the brain oscillations. Within the scope of this work, we have restricted ourselves to a minimal model with no node-specific behavior to reveal the impact of a periodic perturbation.

An intriguing synchronization phenomenon in networks is relay (or remote) synchronization between layers which are not directly connected, and interact *via* an intermediate (relay) layer [21]. The simplest realization of such a system is a triplex network where a relay layer in the

OPEN ACCESS

Edited by:
Alessandro Torcini,
Université de Cergy-Pontoise, France

Reviewed by:
Spase Petkoski,
INSERM U1106 Institut de Neurosciences des Systèmes, France
Kanika Bansal,
Columbia University, United States

***Correspondence:**
Jakub Sawicki
zergon@gmx.net

Specialty section:
This article was submitted to Dynamical Systems, a section of the journal Frontiers in Applied Mathematics and Statistics

Received: *31 January 2021*
Accepted: *26 March 2021*
Published: *22 April 2021*

Citation:
Sawicki J and Schöll E (2021) Influence of Sound on Empirical Brain Networks. Front. Appl. Math. Stat. 7:662221. doi: 10.3389/fams.2021.662221

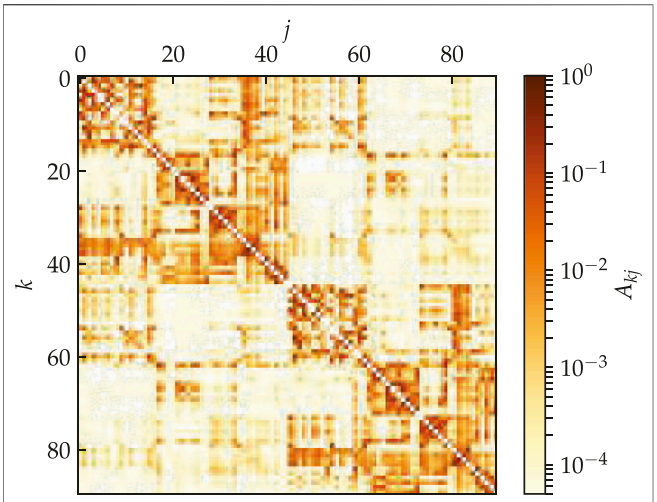

FIGURE 1 | (color online) Model for the hemispheric brain structure: Weighted adjacency matrix A_{kj} of the averaged empirical structural brain network derived from twenty healthy human subjects by averaging over the coupling between two brain regions k and j. The brain regions k, j are taken from the Automated Anatomic Labeling atlas [36], but re-labeled such that $k = 1, \ldots, 45$ and $k = 46, \ldots, 90$ correspond to the left and right hemisphere, respectively. After [9].

middle acts as a transmitter between the two outer layers. Remote synchronization, a regime where pairs of nodes synchronize despite their large distances on the network graph, has been shown to depend on the network symmetries [22–26]. Recently the notion of relay synchronization has been extended from completely synchronized states to partial synchronization patterns in the individual layers of a three-layer multiplex network. It has been shown that the three-layer structure of the network allows for (partial) synchronization of chimera states in the outer layers *via* the relay layer [27–31]. Going towards more realistic models, time-delay plays an important role in the modeling of the dynamics of complex networks. In brain networks, the communication speed will be affected by the distance between regions and therefore a stimulation applied to one region needs time to reach a different region. In such delayed system, it is possible to predict if the effects of stimulation remain focal or spread globally [32]. More generally, time delays due to propagation over the white-matter tracts have been shown to organize the brain network synchronization dynamics for different types of oscillatory nodes [33]. Within the scope of this paper, we focus on the requirements for a simple model to exhibit partial synchronization patterns, which have been experimentally observed [18, 19]. Therefore, we defer the consideration of time delays for now.

2 MODEL

We consider an empirical structural brain network shown in **Figure 1** where every region of interest is modeled by a single FitzHugh–Nagumo (FHN) oscillator.

The weighted adjacency matrix $A = \{A_{kj}\}$ of size 90×90, with node indices $k \in N = \{1, 2, \ldots, 90\}$ was obtained from averaged diffusion-weighted magnetic resonance imaging data measured in 20 healthy human subjects. For details of the measurement procedure including acquisition parameters, see [34], for previous utilization of the structural networks to analyze chimera states see [7, 9, 35]. The data were analyzed using probabilistic tractography as implemented in the FMRIB Software Library, where FMRIB stands for Functional Magnetic Resonance Imaging of the Brain (www.fmrib.ox.ac.uk/fsl/). The anatomic network of the cortex and subcortex is measured using Diffusion Tensor Imaging (DTI) and subsequently divided into 90 predefined regions according to the Automated Anatomical Labeling (AAL) atlas [36]. Each node of the network corresponds to a brain region. Note that in contrast to the original AAL indexing, where sequential indices correspond to homologous brain regions, the indices in **Figure 1** are rearranged such that $k \in N_L = \{1, 2, \ldots, 45\}$ corresponds to left and $k \in N_R = \{46, \ldots, 90\}$ to the right hemisphere. Thereby the hemispheric structure of the brain, i.e., stronger intra-hemispheric coupling compared to inter-hemispheric coupling, is highlighted (**Figure 1**).

The structural connectivity matrices serve as a realistic input for modeling, rather than as exact information concerning the existence and strength of each connection in the human brain. The pipeline for constructing such connectivity information using diffusion tractography is known to face a range of challenges [37]. While some estimates of the strength and direction of structural connections from measurements of brain activity can in principle be attempted, the relation of these can vary dramatically with (experimentally unknown) parameters of the local dynamics and coupling function [38].

The auditory cortex is the part of the temporal lobe that processes auditory information in humans. It is a part of the auditory system, performing basic and higher functions in hearing and is located bilaterally, roughly at the upper sides of the temporal lobes, i.e., corresponding to the AAL indexing $k = 41, 86$ (temporal sup L/R). The auditory cortex takes part in the spectrotemporal analysis of the inputs passed on from the ear.

Each node corresponding to a brain region is modeled by the FitzHugh–Nagumo (FHN) model with external stimulus, a paradigmatic model for neuronal spiking [39–41]. Note that while the FitzHugh-Nagumo model is a simplified model of a single neuron, it is also often used as a generic model for excitable media on a coarse-grained level [42, 43]. Thus the dynamics of the network reads:

$$\varepsilon \dot{u}_k = u_k - \frac{u_k^3}{3} - v_k + \sigma \sum_{j=1}^{N} A_{kj}\left[B_{uu}\left(u_j - u_k\right) + B_{uv}\left(v_j - v_k\right)\right] + C_k \gamma \cos \omega t \quad (1a)$$

$$\dot{v}_k = u_k + a + \sigma \sum_{j=1}^{N} A_{kj}\left[B_{vu}\left(u_j - u_k\right) + B_{vv}\left(v_j - v_k\right)\right], \quad (1b)$$

where $\varepsilon = 0.05$ describes the timescale separation between the fast activator variable (neuron membrane potential) u and the slow inhibitor (recovery variable) v [40]. Depending on the threshold parameter a, the FHN model may exhibit excitable behavior ($|a| > 1$) or self-sustained oscillations ($|a| < 1$). We use the FHN model in the oscillatory regime and thus fix the threshold parameter at $a = 0.5$ sufficiently far from the Hopf bifurcation point. The external stimulus is modeled by a trigonometric function with frequency ω and amplitude γ and is applied to the brain areas $k = 41, 86$ associated with the auditory cortex, i.e. $C_k = 1$ if $k = 41$ or 86 and zero otherwise. The coupling between the single regions is given by the coupling strength σ. As we are looking for partial synchronization patterns we fix $\sigma = 0.6$ similar to numerical studies of synchronization phenomena during unihemispheric sleep [7] and epileptic seizures [9] where partial synchronization patterns have been observed. The interaction scheme between nodes is characterized by a rotational coupling matrix:

$$B = \begin{pmatrix} B_{uu} & B_{uv} \\ B_{vu} & B_{vv} \end{pmatrix} = \begin{pmatrix} \cos\phi & \sin\phi \\ -\sin\phi & \cos\phi \end{pmatrix}, \quad (2)$$

with coupling phase $\phi = \frac{\pi}{2} - 0.1$, causing primarily an activator-inhibitor cross-coupling. This particular scheme was shown to be crucial for the occurrence of partial synchronization patterns in ring topologies [44] as it reduces the stability of the completely synchronized state. Also in the modeling of epileptic-seizure-related synchronization phenomena [9], where a part of the brain synchronizes, it turned out that such a cross-coupling is important. The subtle interplay of excitatory and inhibitory interaction is typical of the critical state at the edge of different dynamical regimes in which the brain operates [45], and gives rise to partial synchronization patterns which are not found otherwise.

3 METHODS

We explore the dynamical behavior by calculating the mean phase velocity $\omega_k = 2\pi M_k/\Delta T$ for each node k, where ΔT denotes the time interval during which M complete rotations are realized. Throughout the paper we use $\Delta T = 10,000$. For all simulations we use initial conditions randomly distributed on the circle $u_k^2 + v_k^2 = 4$. In case of an uncoupled system ($\sigma = 0$), the mean phase velocity (or natural frequency) of each node is $\omega_k = \omega_{FHN} \approx 2.6$. Furthermore we introduce hemispheric measures that characterize the degree of synchronization of the sub-networks and give complementary information. First, the spatially averaged mean phase velocity is:

$$\overline{\omega} = \frac{1}{90} \sum_{k=1}^{N} \omega_k, \quad (3)$$

Thus $\overline{\omega}$ corresponds to the mean phase velocity averaged over the left and right hemisphere. Second, the Kuramoto order parameter:

$$R(t) = \frac{1}{90} \left| \sum_{k=1}^{N} \exp\left[i\theta_k(t)\right] \right|, \quad (4)$$

is calculated by means of an abstract dynamical phase θ_k that can be obtained from the standard geometric phase $\tilde{\phi}_k(t) = \arctan(v_k/u_k)$ by a transformation which yields constant phase velocity $\dot{\theta}_k$. For an uncoupled FHN oscillator the function $t(\tilde{\phi}_k)$ is calculated numerically, assigning a value of time $0 < t(\tilde{\phi}_k) < T$ for every value of the geometric phase, where T is the oscillation period. The dynamical phase is then defined as $\theta_k = 2\pi t(\tilde{\phi}_k)/T$, which yields $\dot{\theta}_k = const$. Thereby identical, uncoupled oscillators have a constant phase relation with respect to the dynamical phase. Fluctuations of the order parameter R caused by the FHN model's slow-fast time scales are suppressed and a change in R indeed reflects a change in the degree of synchronization. The Kuramoto order parameter may vary between 0 and 1, where $R = 1$ corresponds to complete phase synchronization, and small values characterize spatially desynchronized states. Additionally, we calculate the temporal mean of the Kuramoto order parameter

$$\langle R(t) \rangle = \frac{1}{\Delta T} \int_0^{\Delta T} R(t) \mathrm{d}t \quad (5)$$

to estimate the general dynamical behavior of the system over time. Similarly, the temporal mean $\langle \Omega(t) \rangle$ of the collective frequency Ω of the mean field [46], defined by

$$\Omega(t) \equiv \dot{\psi}(t), \quad R(t)e^{i\psi(t)} = \frac{1}{90} \sum_{k=1}^{N} \exp\left[i\theta_k(t)\right] \quad (6)$$

can be considered, and compared with the spatially averaged mean phase velocity.

4 SYNCHRONIZATION REGIONS

We investigate synchronization scenarios emerging from an external periodic stimulus in the auditory cortices of both hemispheres ($k = 41, 86$). **Figure 2** shows synchronization scenarios of an empirical structural brain network in dependence of the frequency ω and amplitude γ of the external stimulus. The light colored regions in **Figure 2A** indicates synchronized dynamics, whereas the darker colors indicate desynchronized dynamics. There is a light colored stripe for $\omega = 2.6$ which indicates a Kuramoto order parameter $\langle R \rangle \approx 0.8$ and a light colored tongue starting at $\omega = 2.4, \gamma = 0.04$. The hatched region in **Figure 2A** stands for a low standard deviation < 0.1 of the

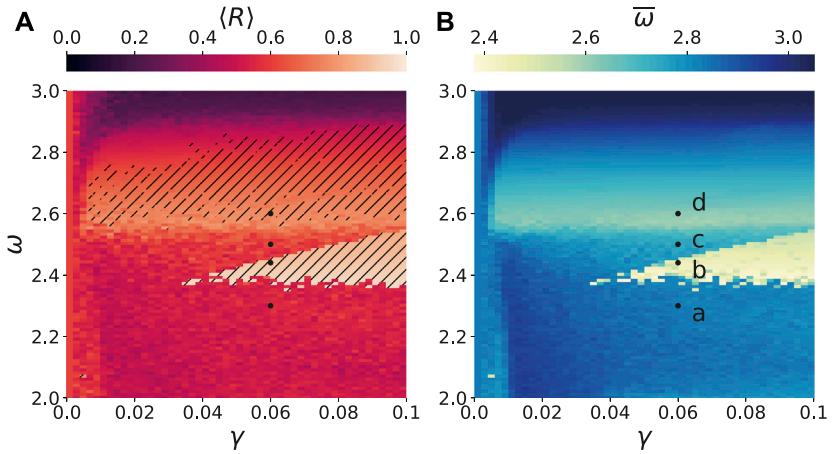

FIGURE 2 | (color online) Synchronization tongues in brain network with external stimulus: **(A)** The temporal mean of the Kuramoto order parameter $\langle R \rangle$ for simulation time $\Delta T = 10,000$ and **(B)** the spatially averaged mean phase velocity $\overline{\omega}$ in the parameter plane of the frequency ω of the external stimulus and its amplitude γ. The light color in panel **(A)** stands for synchronization and the darker color for desynchronization. In the hatched region the standard deviation of $\langle R \rangle$ is less than 0.1, which indicates the absence of strong fluctuations of R in time. The dynamics of the four marked dots in each panel are shown in **Figures 3A–D**, **4A–D**. Other parameters are given by $\sigma = 0.6$, $\epsilon = 0.05$, $a = 0.5$, and $\phi = \frac{\pi}{2} - 0.1$.

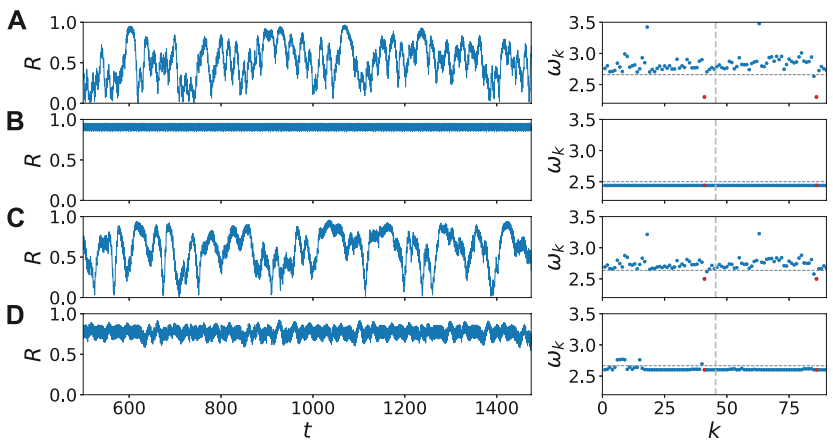

FIGURE 3 | (color online) Dynamical scenarios: dynamics inside and outside the synchronization regions (marked as black dots in **Figure 2**) by the Kuramoto order parameter R (left column) and the mean phase velocities ω_k (right column) for increasing values of the frequency ω of the external stimulus $\omega = 2.30$ **(A)**, $\omega = 2.44$ **(B)**, $\omega = 2.50$ **(C)**, and $\omega = 2.60$ **(D)** for fixed amplitude $\gamma = 0.06$. The vertical dashed line in the right column separates the left and right hemisphere; the horizontal grey dotted line indicates the temporal average of the mean-field frequency ω. The red dots mark the nodes of the auditory cortical regions ($k = 41, 86$). Other parameters are as in **Figure 2**.

temporal mean of the Kuramoto order parameter $\langle R \rangle$. It indicates the absence of strong fluctuations of $R(t)$ and therefore a constant high level of synchrony in time. **Figure 2B** shows the drop of the spatially averaged mean phase velocity $\overline{\omega}$ in case of coherent dynamics in the synchronization regions of **Figure 2A**. In the upper region, $\overline{\omega}$ takes over the value of the frequency ω of the external stimulus, whereas in the synchronization tongue $\overline{\omega}$ keeps its value of $\overline{\omega} = 2.4$.

It turns out that by taking the frequency ω of the external stimulus as a control parameter, one can change the level of synchrony of the system. **Figure 3** depicts the details of the transition to synchronization for increasing values of the frequency ω of the external stimulus. Fixing the amplitude $\gamma = 0.06$, we take a closer look on the temporal evolution of R and the mean phase velocities in the system for different regions in **Figure 2**: In **Figure 3A** the temporal evolution of the Kuramoto order parameter is similar to the system behavior without external stimulus, i.e., it exhibits large temporal fluctuations. In the right column the phase velocities of all nodes are plotted, the horizontal grey dotted line indicates the temporal average of the collective mean-field frequency Ω. Only the phase velocity of the auditory cortex follows the frequency of the external driving stimulus $\omega = 2.3$ and therefore is lower than the frequency of the other nodes $\omega_k \approx 2.8$. Increasing the external frequency to $\omega = 2.4$ yields an

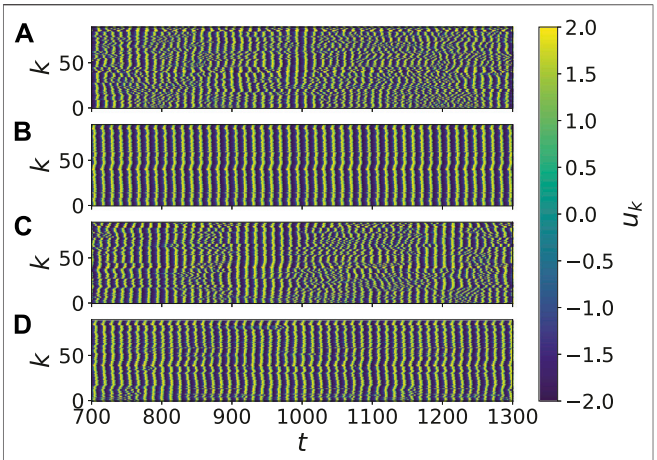

FIGURE 4 | (color online) Synchronized and desynchronized dynamics: Shown are the space-time plot of the variable u_k inside and outside the synchronization regions (marked as black dots in **Figure 2**) for increasing values of the frequency ω of the external stimulus $\omega = 2.30$ **(A)**, $\omega = 2.44$ **(B)**, $\omega = 2.50$ **(C)**, and $\omega = 2.60$ **(D)** for fixed amplitude $\gamma = 0.06$. The panels correspond to the panels in **Figure 3**. Other parameters are as in **Figure 2**.

abrupt transition to a synchronized state. In **Figure 3B** the Kuramoto order parameter $R \approx 0.95$ and the mean phase velocities indicate a synchronous dynamical behavior, which agrees with the collective frequency Ω of the mean-field (grey dotted horizontal line). With a further increment to $\omega = 2.5$, the system loses synchrony (see **Figure 3C**) and enters the region between the two synchronization regions in **Figure 2A**. For $\omega = 2.6$ in **Figure 3D**, which corresponds to the natural frequency of the uncoupled oscillators, the system regains synchronization, though the Kuramoto order parameter with $R \approx 0.8$ is lower than in the synchronization tongue. Remarkable is the fact of a dynamical asymmetry shown by the mean phase velocities. While the nodes of the right hemisphere exhibit an equal mean phase velocity, a part of the left hemisphere exhibits a faster dynamic similar to dynamics of unihemispheric sleep studied in [7]. In such states one hemisphere is synchronized, whereas the other hemisphere is partly desynchronized.

For a better insight, **Figure 4** shows the space-time plot of the variable u_k for the corresponding parameter values in **Figure 3**. In **Figures 4B,D**, the dynamics inside the two synchronization regions is depicted. The perturbation in the mean phase velocity profile in the right panel of **Figure 3D**, can be detected also in the corresponding perturbations in **Figure 4D**. Comparing **Figures 4A,C**, we can see an increase of synchronized time segments. This increase will be analyzed quantitatively in more detail in the inset of **Figure 5**.

5 TRANSITION TO SYNCHRONIZATION

There are two frequencies which play an important role for the dynamics of the system. On the one hand, in **Figure 2A** a broad synchronization region is located at a frequency $\omega \approx 2.6$, which is the frequency of the uncoupled FHN oscillator ω_{FHN}. Although the external stimulus effects only the two auditory nodes (k = 41,86), we can observe a transition to synchronization of the whole system approaching $\omega \approx 2.6$ already for small values of the amplitude $\gamma > 0.004$. On the other hand, we can detect a synchronization tongue with a lower boundary at $\omega \approx 2.4$ and an upper boundary increasing linearly with the amplitude γ. In contrast to the first, smooth transition, we can find here a sharp transition to synchronized dynamics, similar to a first order transition, depicted by the high contrast of the boarder of the synchronization tongue in **Figure 2A**. In this synchronization tongue, the nodes oscillate with an equal mean phase velocity (see **Figure 3B**), but there are phase differences between them, as indicated by $0.95 < R(t) < 1$ and shown in the phase-time plot in **Figure 4B**. Using the fact that u_j/v_j and u_k/v_k are on the same limit cycle in the phase space and have the same mean phase velocity, the phase differences in the coupling term of **Eq. 1** can be effectively summed up in following way:

$$\sum_j A_{kj} \mathrm{B}\begin{pmatrix} u_j - u_k \\ v_j - v_k \end{pmatrix} \approx \Delta t_{\mathrm{eff}} \mathrm{B}\begin{pmatrix} \dot{u}_k \\ \dot{v}_k \end{pmatrix}, \tag{7}$$

where $\Delta t_{eff} \ll 1$ denotes the effective sum of the time intervals of all phase differences. Neglecting $\cos\phi \ll 1$ and setting $\sin\phi \approx 1$, **Eq. 1** reads for $k \neq 41, 86$:

$$\begin{aligned} \varepsilon \dot{u}_k &= u_k - \frac{u_k^3}{3} - v_k - \sigma \Delta t_{\mathrm{eff}}\, \dot{v}_k \\ \dot{v}_k &= u_k + a + \sigma \Delta t_{\mathrm{eff}}\, \dot{u}_k \end{aligned} \tag{8}$$

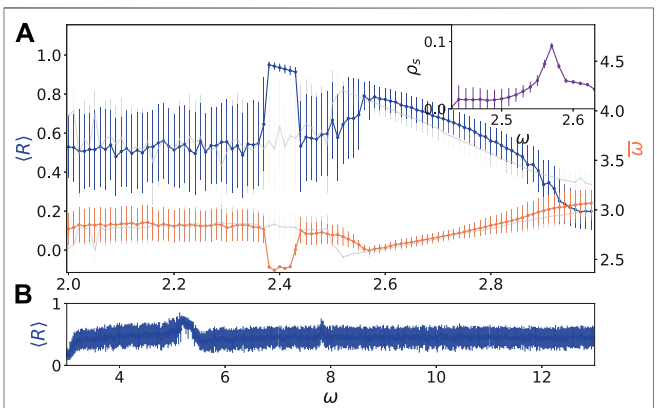

FIGURE 5 | (color online) Transition scenarios: **(A)** temporal mean of the Kuramoto order parameter ⟨R⟩ (dark blue) and the spatially averaged mean phase velocities $\overline{\omega}$ (light orange) in dependence on the frequency ω of the external stimulus for a fixed amplitude $\gamma = 0.052$. The vertical bars indicate the standard deviation of the temporal mean of the Kuramoto order parameter and the spatially averaged mean phase velocities, respectively. As input nodes, the auditory cortices k = 41, 86 are chosen. In case of a different input (k = 1, 45) the corresponding light grey curves are shown in panel **(A)**. The inset in panel **(A)** depicts $\rho_s = \frac{N_s}{\Delta T_L}$, the number N_s of synchronized time intervals ($R(t) > 0.8 \forall t$) divided by a simulation time of $\Delta T_L = 30,000$ for values of the frequency ω between the two synchronization regions. The vertical bars denote the standard deviation of the length of these synchronized time intervals. **(B)** ⟨R⟩ for a larger range of driving frequencies ω, showing higher resonance tonges. Other parameters are as in **Figure 2**.

The local dynamics of **Eq. 1** is governed by a slow-fast system (FitzHugh-Nagumo oscillator), where the slow part essentially determines the period of the oscillations. Hence, considering the slow motion on the falling branches of the u-nullcline ($\dot{u}_k = 0$) by inserting the second equation into the first one

$$v_k = u_k - \frac{u_k^3}{3} - \sigma\Delta t_{eff}\ (u_k + a), \tag{9}$$

the time derivative of the falling branches yields with $\dot{v}_k$ from **Eq. 8**

$$v_k = u_k - \frac{u_k^3}{3} - \sigma\Delta t_{\mathrm{eff}}\ (u_k + a), \tag{10}$$

The separation of the variables gives

$$dt = \frac{1 - u_k^2 - 2\sigma\Delta t_{eff}}{u_k + a}\ du_k, \tag{11}$$

where dt can be integrated over one oscillation period T. As shown in [47], this leads in case of synchronization to a linear dependence of the oscillation period $T_{sync} = \int_0^T dt$ on the effective sum of the phase differences proportional to Δt_{eff} . For incoherent distribution of the phases of each node k (see **Figure 4D**), the phase differences between the single nodes are also strongly distributed and thus $\Delta t_{eff} \approx 0$. In this case, the natural frequency of the uncoupled system plays an important role, provided that the mean phase velocity of all oscillators is still almost equal as in case of **Figure 2D**.

This could explain on one side the fact that we observe a synchronization tongue at $\omega \approx 2.4$ (which is smaller than the frequency of an uncoupled oscillator $\omega_{FHN} \approx 2.6$), and on the other side, the linear boundaries of the synchronization tongue for increasing amplitude γ. The increase of γ yields an increase of the sum of the phase differences in the coupling term of **Eq.1** and therefore an increase of the effective sum of the time intervals Δt_{eff} .

In **Figure 5A**, both transitions are depicted in dependence on the frequency ω for a fixed amplitude $\gamma = 0.052$. We can see an abrupt increase and decrease of the temporal mean of the Kuramoto order parameter $\langle R \rangle$ before and after $\omega \approx 2.4$, respectively. In contrast, in approaching the upper synchronization region starting from $\omega \approx 2.6$, $\langle R \rangle$ increases more slowly than at the transition to the synchronization tongue ($\omega \approx 2.4$). In case of synchronization the standard deviation of $\langle R \rangle$, displayed by the vertical bars, is smaller than in case of desynchronized dynamics. That holds also for the spatially averaged mean phase velocities $\overline{\omega}$, which in case of synchronization takes over the lower value of the frequency ω of the external stimulus. Also for $\omega > 2.6$, $\overline{\omega}$ is equal to ω, whereas the standard deviation of $\overline{\omega}$ increases linearly with ω. In contrast, there is no effect on the system for $\omega < 2.4$. Neither $\langle R \rangle$ nor $\overline{\omega}$ show a different behavior for such values of ω. The high value of the standard deviation of $\langle R \rangle$ stands for dynamics as shown in **Figure 3A**, where the Kuramoto order parameter $R(t)$ is fluctuating over its whole bandwidth $R \in [0, 1]$. Simulations show that for $\omega > 3.0$ the dynamical behavior of the system becomes similar to that with $\omega = 2.3$. For both parameter intervals of ω, there is no effect on the system. Simulations show also that a similar transition to synchronization at $\omega = 2.6$ can be found for higher harmonics, i.e., multiple values of $\omega = 2.6$. In **Figure 5B**, we can identify synchronization regions for $\omega = 5.2, 7.8$, and 10.4 becoming less pronounced for increasing ω, i.e., having a smaller extension in the plane of ω and γ. In contrast, we could not detect repeated synchronization tongues of ω for multiple values of $\omega = 2.4$. This indicates the existence of two different synchronization mechanisms.

The existence of two synchronization regions depends on the choice to which nodes the external stimulus is supplied. In case of a different input, for instance $k = 1,45$ in contrast to $k = 41,86$, the light grey curves in **Figure 5A** depict the corresponding dependence of the Kuramoto order parameter $\langle R \rangle$ and the

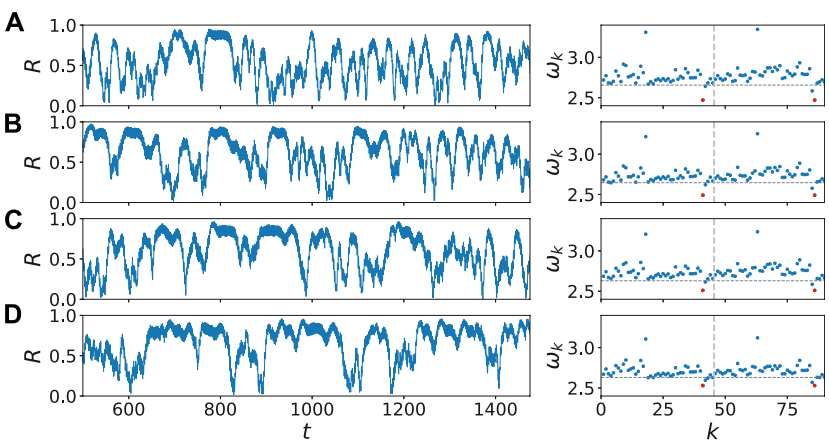

FIGURE 6 | (color online) Transition scenarios: The increase of the regularity and duration of synchronized time intervals shown by the temporal evolution of the Kuramoto order parameter R (left column) and the mean phase velocities ω_k (right column) for increasing values of the frequency ω of the external stimulus $\omega = 2.47$ **(A)**, $\omega = 2.49$ **(B)**, $\omega = 2.51$ **(C)**, and $\omega = 2.53$ **(D)** for fixed amplitude $\gamma = 0.06$. The vertical dashed line in the right column separates the left and right hemisphere, and the horizontal grey dotted line indicates the temporal average of the mean-field frequency Ω. The red colored dots indicate the nodes of the auditory cortical regions ($k = 41,86$). Other parameters as in **Figure 2**.

spatially averaged mean phase velocities $\overline{\omega}$ upon the frequency ω of the external stimulus. The synchronization region at $\omega \approx 2.4$ is missing here and only one synchronization region remains ($\omega > 2.5$).

In the following, we analyze the region between the two synchronization areas in more detail. **Figure 6** depicts the dynamical behavior when we approach the synchronization region by increasing the frequency ω of the external stimulus in the neighborhood of the synchronization region at $\omega = 2.6$. For $\omega = 2.47$ in **Figure 6A**, the time series of the Kuramoto order parameter shows familiar temporal fluctuations with only short episodes of synchronization ($R(t) > 0.8$). In [9] the authors define the threshold $R = 0.8$ as the onset of an epileptic seizure. By increasing the frequency ω, one can increase the quantity of these episodes, as well as their duration. **Figure 6D** with $\omega = 2.51$ features much longer duration of synchronized episodes, moreover the duration of the single episodes are comparable in length. This transition in **Figures 6A–D** can be also seen in **Figure 5A**. The inset of **Figure 5A** confirms the increasing regularity between the two synchronization regions by depicting $\rho_s = \frac{N_s}{\Delta T_L}$ vs. ω, where N_s is the number of synchronized time intervals ($R(t) > 0.8 \,\forall\, t$) and $\Delta T_L = 30,000$ is the simulation time. The vertical bars denote the standard deviation of the length of these synchronized time intervals. With increasing ω not only the number of synchronized time intervals is increasing, but the standard deviation of their duration is decreasing. For $\omega = 2.6$ we enter the synchronization region, where the value of ρ_s drops due to the nearly consistently synchronized dynamics.

Finally, the mean phase velocities in the right column of **Figure 6** display the transition to frequency synchronization. While the frequency of the two driven nodes ($k = 41, 86$) converges to the frequency of an uncoupled FHN oscillator $\omega_{FHN} \approx 2.6$, also the frequencies of all the other nodes are adjusted, especially those with a much higher frequency ($k = 18, 63$).

6 CONCLUSION

We have investigated the influence of an external sound source on the dynamics of a network with empirical structural connectivity. It has been found that depending on the frequency and amplitude of the sound source, synchronization can be induced in the dynamics of the system. We have shown that two frequencies play an important role for synchronization, particularly the natural frequency of the uncoupled oscillator and the frequency of the coupled system. Moreover, the degree of synchronization is gradually increased when the frequency of the uncoupled oscillator or multiple values of it are approached. Furthermore, we have analyzed the linear dependence of the synchronization borders upon the amplitude of the external sound, which can also be characterized as the volume of the sound. This has resulted in the observation that the synchronization region can be enlarged by increasing volume. We have demonstrated the dynamical behavior of the system in the transition to synchronization. By tuning the frequency of the external sound appropriately, we have shown that the level of synchrony can be increased.

These results are in accordance with experiments of Bader's group [18, 19] that music induces a certain degree of synchrony in the human brain. This group has shown that listening to music can have remarkable influence on the brain dynamics, in particular, a periodic alternation between synchronization and desynchronization. Moreover, such an alternation reflects the variability of the system; this can be seen as a critical state between a fully synchronized and a desynchronized state. It is known that the brain is operating in a critical state at the edge of different dynamical regimes [45], exhibiting hysteresis and avalanche phenomena as seen in critical phenomena and phase transitions [48–50]. By choosing appropriate parameters, we have reported an intriguing dynamical behavior regarding the transition to synchronization, and have observed the induced alternation between high and low degrees of synchronization. To sum up, an external sound source connected to the brain allows for synchronization dynamics, which may be used to model the effect of music on the human brain.

DATA AVAILABILITY STATEMENT

The original contributions presented in the study are included in the article, further inquiries can be directed to the corresponding author.

AUTHOR CONTRIBUTIONS

JS did the numerical simulations and the theoretical analysis. ES supervised the study. All authors designed the study and contributed to the preparation of the article. All the authors have read and approved the final article.

FUNDING

This work was supported by the Deutsche Forschungsgemeinschaft (DFG, German Research Foundation, project No. 429685422).

ACKNOWLEDGMENTS

We are grateful to Antonín Škoch and Jaroslav Hlinka (National Institute of Mental Health, Klecany, Czech Republic) for providing the sample structural connectivity matrices, and to Rolf Bader and Lenz Hartmann (University of Hamburg) for stimulating discussions.

REFERENCES

1. Rattenborg NC, Amlaner CJ, and Lima SL. Behavioral, neurophysiological and evolutionary perspectives on unihemispheric sleep. *Neurosci Biobehav Rev* (2000) 24:817–42. doi:10.1016/s0149-7634(00)00039-7
2. Steriade M, McCormick DA, and Sejnowski TJ. Thalamocortical oscillations in the sleeping and aroused brain. *Science* (1993) 262:679–85. doi:10.1126/science.8235588
3. Moroni F, Nobili L, De Carli F, Massimini M, Francione S, Marzano C, et al. Slow eeg rhythms and inter-hemispheric synchronization across sleep and wakefulness in the human hippocampus. *Neuroimage* (2012) 60:497–504. doi:10.1016/j.neuroimage.2011.11.093
4. Schwartz JRL, and Roth T. Neurophysiology of sleep and wakefulness: basic science and clinical implications. *Curr Neuropharmacol* (2008) 6:367–78. doi:10.2174/157015908787386050
5. Tamaki M, Bang JW, Watanabe T, and Sasaki Y. Night watch in one brain hemisphere during sleep associated with the first-night effect in humans. *Curr Biol* (2016) 26:1190–4. doi:10.1016/j.cub.2016.02.063
6. Mascetti GG. Unihemispheric sleep and asymmetrical sleep: behavioral, neurophysiological, and functional perspectives. *Nat Sci Sleep* (2016) 8:221. doi:10.2147/NSS.S71970
7. Ramlow L, Sawicki J, Zakharova A, Hlinka J, Claussen JC, and Schöll E. Partial synchronization in empirical brain networks as a model for unihemispheric sleep. *EPL* (2019) 126:50007. doi:10.1209/0295-5075/126/50007
8. Rattenborg NC, Voirin B, Cruz SM, Tisdale R, Dell'Omo G, Lipp HP, et al. Evidence that birds sleep in mid-flight. *Nat Commun* (2016) 7:12468. doi:10.1038/ncomms12468
9. Gerster M, Berner R, Sawicki J, Zakharova A, Skoch A, Hlinka J, et al. FitzHugh-Nagumo oscillators on complex networks mimic epileptic-seizure-related synchronization phenomena. *Chaos* (2020) 30:123130. doi:10.1063/5.0021420
10. Bader R.. *Neural coincidence detection strategies during perception of multi-pitch musical tones*. arXiv:2001 (2020) (Accessed Jan 17, 2020). 06212v1
11. Koelsch S, Rohrmeier M, Torrecuso R, and Jentschke S. Processing of hierarchical syntactic structure in music. *Proc Natl Acad Sci U.S.A* (2013) 110:15443. doi:10.1073/pnas.1300272110
12. Large EW, Herrera JA, and Velasco MJ. Neural networks for beat perception in musical Rhythm. *Front Syst Neurosci* (2015) 9:159. doi:10.3389/fnsys.2015.00159
13. Bader R.. *Nonlinearities and synchronization in musical acoustics and music psychology*. Berlin, BE: Springer (2013) p. 458.
14. Hou YS, Xia GQ, Jayaprasath E, Yue DZ, and Wu ZM. Parallel information processing using a reservoir computing system based on mutually coupled semiconductor lasers. *Appl Phys B* (2020) 126:40. doi:10.1007/s00340-019-7351-
15. Joris PX, Carney LH, Smith PH, and Yin TCT. Enhancement of neural synchronization in the anteroventral cochlear nucleus. I. responses to tones at the characteristic frequency. *J Neurophysiol* (1994) 71:1022. doi:10.1152/jn.1994.71.3.1022
16. Sawicki J, Omelchenko I, Zakharova A, and Schöll E. Delay controls chimera relay synchronization in multiplex networks. *Phys Rev E* (2018a) 98:062224. doi:10.1103/physreve.98.062224
17. Shainline JM. Fluxonic processing of photonic synapse events. *IEEE J Sel Top Quan Electron.* (2020) 26:7700315. doi:10.1109/jstqe.2019.2927473
18. Hartmann L, and Bader R. Neuronal synchronization of musical large scale form: an eeg-study. *Proc Meetings Acoust* (2014) 22:1.
19. Hartmann L, and Bader R.. *Neural synchronization of music large-scale form.*arXiv:2005 (2020) (Accessed May 14 2020). 06938v1
20. Schneider A.. *Pitch and Pitch Perception*. 1st ed. Heidelberg, HH: Springer HandbooksSpringer (2018)
21. Leyva I, Sendiña-Nadal I, Sevilla-Escoboza R, Vera-Avila VP, Chholak P, and Boccaletti S. Relay synchronization in multiplex networks. *Sci Rep* (2018) 8:8629. doi:10.1038/s41598-018-26945-w
22. Bergner A, Frasca M, Sciuto G, Buscarino A, Ngamga EJ, Fortuna L, et al. Remote synchronization in star networks. *Phys Rev E* (2012) 85:026208. doi:10.1103/physreve.85.026208
23. Gambuzza LV, Cardillo A, Fiasconaro A, Fortuna L, Gómez-Gardeñes J, and Frasca M. Analysis of remote synchronization in complex networks. *Chaos* (2013) 23:043103. doi:10.1063/1.4824312
24. Nicosia V, Valencia M, Chavez M, Díaz-Guilera A, and Latora V. Remote synchronization reveals network symmetries and functional modules. *Phys Rev Lett* (2013) 110:174102. doi:10.1103/physrevlett.110.174102
25. Zhang L, Motter AE, and Nishikawa T. Incoherence-mediated remote synchronization. *Phys Rev Lett* (2017) 118:174102. doi:10.1103/physrevlett.118.174102
26. Zhang Y, Nishikawa T, and Motter AE. Asymmetry-induced synchronization in oscillator networks. *Phys Rev E* (2017) 95:062215. doi:10.1103/physreve.95.062215
27. Drauschke F, Sawicki J, Berner R, Omelchenko I, and Schöll E. Effect of topology upon relay synchronization in triplex neuronal networks. *Chaos* (2020) 30:051104. doi:10.1063/5.0008341
28. Sawicki J, Abel M, and Schöll E. Synchronization of organ pipes. *Eur Phys J B* (2018) 91:24. doi:10.1140/epjb/e2017-80485-8
29. Sawicki J, Omelchenko I, Zakharova A, and Schöll E. Synchronization scenarios of chimeras in multiplex networks. *Eur Phys J Spec Top* (2018b) 227:1161. doi:10.1140/epjst/e2018-800039-y
30. Sawicki J.. *Delay controlled partial synchronization in complex networks*. Heidelberg, HH: Springer ThesesSpringer (2019) doi:10.1007/978-3-030-34076-65
31. Winkler M, Sawicki J, Omelchenko I, Zakharova A, Anishchenko V, and Schöll E. Relay synchronization in multiplex networks of discrete maps. *EPL* (2019) 126:50004. doi:10.1209/0295-5075/126/50004
32. Muldoon SF, Pasqualetti F, Gu S, Cieslak M, Grafton ST, Vettel JM, et al. Stimulation-based control of dynamic brain networks. *Plos Comput Biol* (2016) 12:e1005076. doi:10.1371/journal.pcbi.1005076
33. Petkoski S, and Jirsa VK. Transmission time delays organize the brain network synchronization. *Phil Trans R Soc A* (2019) 377:20180132. doi:10.1098/rsta.2018.0132
34. Melicher T, Horacek J, Hlinka J, Spaniel F, Tintera J, Ibrahim I, et al. White matter changes in first episode psychosis and their relation to the size of sample studied: a DTI study. *Schizophr Res* (2015) 162:22–8. doi:10.1016/j.schres.2015.01.029
35. Chouzouris T, Omelchenko I, Zakharova A, Hlinka J, Jiruska P, and Schöll E. Chimera states in brain networks: empirical neural *vs.* modular fractal connectivity. *Chaos* (2018) 28:045112. doi:10.1063/1.5009812
36. Tzourio-Mazoyer N, Landeau B, Papathanassiou D, Crivello F, Etard O, Delcroix N, et al. Automated anatomical labeling of activations in SPM using a macroscopic anatomical parcellation of the MNI MRI single-subject brain. *Neuroimage* (2002) 15:273–89. doi:10.1006/nimg.2001.0978
37. Schilling KG, Daducci A, Maier-Hein K, Poupon C, Houde J-C, Nath V, et al. Challenges in diffusion MRI tractography - Lessons learned from international benchmark competitions. *Magn Res Imaging* (2019) 57:194–209. doi:10.1016/j.mri.2018.11.014
38. Hlinka J, and Coombes S. Using computational models to relate structural and functional brain connectivity. *Eur J Neurosci* (2012) 36:2137–45. doi:10.1111/j.1460-9568.2012.08081.x
39. Bassett DS, Zurn P, and Gold JI. On the nature and use of models in network neuroscience. *Nat Rev Neurosci* (2018) 19:566–78. doi:10.1038/s41583-018-0038-8
40. FitzHugh R. Impulses and physiological states in theoretical models of nerve membrane. *Biophys J* (1961) 1:445–66. doi:10.1016/s0006-3495(61)86902-6
41. Nagumo J, Arimoto S, and Yoshizawa S. An active pulse transmission line simulating nerve axon. *Proc IRE* (1962) 50:2061–70. doi:10.1109/jrproc.1962.288235
42. Chernihovskyi A, and Lehnertz K. Measuring synchronization with nonlinear excitable media. *Int J Bifurc Chaos* (2007) 17:3425–9. doi:10.1142/s0218127407019159
43. Chernihovskyi A, Mormann F, Müller M, Elger CE, Baier G, and Lehnertz K. EEG analysis with nonlinear excitable media. *J Clin Neurophysiol* (2005) 22:314–29. doi:10.1097/01.wnp.0000179968.14838.e7
44. Omelchenko I, Omel'chenko OE, Hövel P, and Schöll E. When nonlocal coupling between oscillators becomes stronger: patched synchrony or multichimera states. *Phys Rev Lett* (2013) 110:224101. doi:10.1103/physrevlett.110.224101
45. Massobrio P, de Arcangelis L, Pasquale V, Jensen HJ, and Plenz D. Criticality as a signature of healthy neural systems. *Front Syst Neurosci* (2015) 9:22. doi:10.3389/fnsys.2015.00022

46. Petkoski S, Iatsenko D, Basnarkov L, and Stefanovska A. Mean-field and mean-ensemble frequencies of a system of coupled oscillators. *Phys Rev E* (2013) 87: 032908. doi:10.1103/physreve.87.032908
47. Sawicki J, Omelchenko I, Zakharova A, and Schöll E. Delay-induced chimeras in neural networks with fractal topology. *Eur Phys J B* (2019) 92:54. doi:10.1140/epjb/e2019-90309-6
48. Kim H, Moon J-Y, Mashour GA, and Lee U. Mechanisms of hysteresis in human brain networks during transitions of consciousness and unconsciousness: theoretical principles and empirical evidence. *Plos Comput Biol* (2018) 14:e1006424. doi:10.1371/journal.pcbi.1006424
49. Ribeiro TL, Copelli M, Caixeta F, Belchior H, Chialvo DR, Nicolelis MA, et al. Spike avalanches exhibit universal dynamics across the sleep-wake cycle. *PLoS One* (2010) 5:e14129. doi:10.1371/journal.pone.0014129
50. Steyn-Ross A, and Steyn-Ross M. Modeling phase transitions in the brain, Vol. 509. Berlin, BE: Springer (2010) doi:10.1007/978-1-4419-0796-7

Conflict of Interest: The authors declare that the research was conducted in the absence of any commercial or financial relationships that could be construed as a potential conflict of interest.

frontiers in Systems Neuroscience

ORIGINAL RESEARCH
published: 23 April 2021
doi: 10.3389/fnsys.2021.647011

Spectrum Degradation of Hippocampal LFP During Euthanasia

Yuchen Zhou[1], *Alex Sheremet*[1,2], *Jack P. Kennedy*[2], *Nicholas M. DiCola*[2], *Carolina B. Maciel*[3], *Sara N. Burke*[4] *and Andrew P. Maurer*[1,2,4]*

[1] *Engineering School of Sustainable Infrastructure and Environment, University of Florida, Gainesville, FL, United States,* [2] *Department of Neuroscience, McKnight Brain Institute, University of Florida, Gainesville, FL, United States,* [3] *Division of Neurocritical Care, Department of Neurology, University of Florida, Gainesville, FL, United States,* [4] *Department of Biomedical Engineering, University of Florida, Gainesville, FL, United States*

The hippocampal local field potential (LFP) exhibits a strong correlation with behavior. During rest, the theta rhythm is not prominent, but during active behavior, there are strong rhythms in the theta, theta harmonics, and gamma ranges. With increasing running velocity, theta, theta harmonics and gamma increase in power and in cross-frequency coupling, suggesting that neural entrainment is a direct consequence of the total excitatory input. While it is common to study the parametric range between the LFP and its complementing power spectra between deep rest and epochs of high running velocity, it is also possible to explore how the spectra degrades as the energy is completely quenched from the system. Specifically, it is unknown whether the 1/f slope is preserved as synaptic activity becomes diminished, as low frequencies are generated by large pools of neurons while higher frequencies comprise the activity of more local neuronal populations. To test this hypothesis, we examined rat LFPs recorded from the hippocampus and entorhinal cortex during barbiturate overdose euthanasia. Within the hippocampus, the initial stage entailed a quasi-stationary LFP state with a power-law feature in the power spectral density. In the second stage, there was a successive erosion of power from high- to low-frequencies in the second stage that continued until the only dominant remaining power was <20 Hz. This stage was followed by a rapid collapse of power spectrum toward the absolute electrothermal noise background. As the collapse of activity occurred later in hippocampus compared with medial entorhinal cortex, it suggests that the ability of a neural network to maintain the 1/f slope with decreasing energy is a function of general connectivity. Broadly, these data support the energy cascade theory where there is a cascade of energy from large cortical populations into smaller loops, such as those that supports the higher frequency gamma rhythm. As energy is pulled from the system, neural entrainment at gamma frequency (and higher) decline first. The larger loops, comprising a larger population, are fault-tolerant to a point capable of maintaining their activity before a final collapse.

Keywords: local field potential, hippocampus, euthanasia, spectrum evolution, power law spectrum

OPEN ACCESS

Edited by:
Joana Cabral,
University of Minho, Portugal

Reviewed by:
Antonio Fernández-Ruiz,
New York University, United States
Viktor Varga,
Institute of Experimental Medicine (MTA), Hungary

***Correspondence:**
Andrew P. Maurer
drewmaurer@ufl.edu

Received: *28 December 2020*
Accepted: *23 March 2021*
Published: *23 April 2021*

Citation:
Zhou Y, Sheremet A, Kennedy JP, DiCola NM, Maciel CB, Burke SN and Maurer AP (2021) Spectrum Degradation of Hippocampal LFP During Euthanasia. Front. Syst. Neurosci. 15:647011. doi: 10.3389/fnsys.2021.647011

1. INTRODUCTION

For over five decades, it has been evident that hippocampal local-field potential (LFP) activity is strongly correlated with behavior (Vanderwolf, 1969; Buzsaki, 2005). The most prominent feature of hippocampal LFP, the 8–9 Hz theta rhythm, is reported to increase in power with increasing running speed (Whishaw and Vanderwolf, 1973; Morris and Hagan, 1983) and change its shape from sinusoidal to sawtooth waves (Green and Petsche, 1961; Stumpf, 1965; Buzsaki et al., 1983; Terrazas et al., 2005) associated with the development of high order theta harmonics during faster movement (Leung, 1982; Leung et al., 1982; Sheremet et al., 2016; Zhou et al., 2019). Apart from theta, the power of the higher frequency gamma rhythm (60–120 Hz) also increases with respect to running speed (Chorbak and Buzsaki, 1998; Chen et al., 2011; Ahmed and Mehta, 2012; Kemere et al., 2013). The increase in gamma power at faster running speeds is also associated with enhanced theta-gamma coupling (Sheremet et al., 2018). These studies imply that when the rat is in an active behaving state, the hippocampus receives strong barrages of synaptic input (Shu et al., 2003), giving rise to an organization of activity across all spatial and temporal scales (Sheremet et al., 2020).

The hippocampal LFP is often decomposed through Fourier analysis, providing the power spectral density. The power spectra density takes the form of Amplitude = 1/frequency^α, where alpha falls is a value between zero and two (characteristic of a pink noise spectra; Buzsaki, 2006). While this decomposition treats different frequency bands as independent signals, the theta and gamma oscillations are not isolated rhythms. In addition to being coupled to each other, theta and gamma also exist against a "background" of activity. The nature of this background is not well-understood, it is often attributed to either the result of interacting oscillators (Buzsaki, 2006) or the consequence of a broadband, arrhythmic activity that is distinct from oscillations (Hesse and Thilo, 2014). Importantly, similar to theta and gamma, the slope of the spectra that is attributed to the background has also been found to change with increasing running speed (Sheremet et al., 2019b), suggesting that it is sensitive to increased synaptic currents and may be interrelated with the rhythms that are often ascribed as being independent from the background spectra.

One explanation for why power is lower at higher frequencies is the energy cascade across multiple oscillators. Precisely, axonal conduction delay and synaptic time constants determine the frequency in which the populations of neurons can rhythmically engage. Faster oscillations require rapid communication, suggesting that a rhythm like gamma would be local, generated by a small population of neurons. The organization of a larger pool of neurons is rate-limited by communication. Global oscillations, like the theta rhythm which engages a larger pool of neurons, will take the form of reciprocal volleys or traveling waves at a slower frequency. As theta engages a larger neuronal population relative to the mechanisms that support gamma, the slow rhythm is approximately one order of magnitude larger than gamma (Buzsaki and Draguhn, 2004). Importantly, these oscillators—among many others- are not independent but one and the same as synapses do not segregate transmembrane currents to specific frequencies but contribute to many bands simultaneously (Bullock et al., 1995; Sheremet et al., 2019a). The intertwining of the rhythmic mechanism, with the large loops (low frequency) providing then energy for the smaller loops (high frequency), gives rise to spatio-temporal interactions that manifest as a 1/f "pink" power spectral density (Buzsaki, 2006). This "energy cascade" hypothesis has roots in self-organized criticality (Bak et al., 1988) and was formalized by Buzsaki concerning mammalian LFP. Within the last few years, the energy cascade hypothesis has been recovered in terms of the classical physics description of turbulence (Sheremet et al., 2019b; Deco and Kringelbach, 2020) which has been cleverly wrangled into a simple verse: *Big whorls have little whorls Which feed on their velocity, And little whorls have lesser whorls And so on to viscosity* (Richardson, 2007). However, other theories regarding the organization of the power spectra suggest that there are two independent biological processes that support aperiodic noise (the 1/f slope) and the rhythmic frequencies, the "peaks" above the slope (He, 2014; Donoghue et al., 2020). These studies consider the log-log linear components of the power spectra where no clear peak above the slope is evident as being carried by either the occurrence of spikes relative to non-preferred LFP oscillation phases (Tort et al., 2010; Lepage et al., 2011) or the desynchronization of spikes within a population of cells (Pozzorini et al., 2013; Voytek and Knight, 2015; Voytek et al., 2015). In sorting out these theories, it should be considered that perhaps the field has placed too much emphasis on the literal interpretation of the power spectral density (calculated by Fourier, Wavelet, or otherwise), which ascribes a single power-to-frequency value suggesting an independence between sinusoidal oscillations of different frequencies. Rather, we should be reminded that the LFP represents the propagation and distribution of activity into densely recurrent networks of neurons, generating the spatial-temporal dynamics responsible for the organization of behavior (Hebb, 1949; Northoff et al., 2019; Atasoy et al., 2020; Nadel and Maurer, 2020). As the nervous system does not work in the currency of pure rhythms vs. noise, but rather dynamics spatio-temporal patterns, this challenges the degree to which we can interpret and make divisions of neurobiological processes based on parameterizing power spectral densities.

Nevertheless, both visual observations and power spectral densities reveal that low-frequency rhythms are larger in amplitude than higher frequency oscillations. Moreover, the 1/f slope of the spectra is a consistent feature of the LFP with the 1/f slope present during sleep and quiescent periods (for instance, see Figure 4 of Buzsáki et al., 2003). The persistence of the 1/f slope across all behavioral states suggests that the nervous system is constantly propagating activity, with large populations of reentrantly connected populations perpetually cascading activity into smaller recurrent networks. Thus, manipulating the spectra require approaches that alter a large swath of synaptic inputs, such as localized cooling (Petersen and Buzsáki, 2020), focal brain lesion (Mitchell et al., 1982; Buzsaki et al., 1987; Bragin et al., 1995; Fyhn et al., 2004), and study the dying brain. In the current study, we investigated the spectra against the background of

euthanasia by barbiturate overdose, in which the spectra degrades to a complete collapse.

Prior studies on LFP changes with euthanasia have observed a surge of global and highly coherent gamma oscillation after cardiac arrest (Borjigin et al., 2013). This has led to studies exploring hippocampal physiology in the context of near-death experience (Parnia and Fenwick, 2002), theoretically supported by bursts of high-frequency activity (Zhang et al., 2019). While near-death experience is interesting, this topic is beyond the scope of the present study. Rather, we explored the changes from the perspective of the turbulence hypothesis (Sheremet et al., 2019b; Deco and Kringelbach, 2020). If slow frequency perturbations provide the energy to drive higher frequency oscillations, then we predicted that when the system is significantly challenged, the high-frequency rhythms and the 1/f slope will be the first to be compromised. Low frequency activities, being generated by larger more distributed populations, will be more robust, maintaining power for an extended period of time. In accord with this, we observed a steepening of the 1/f carried by a recession of high-frequency power. At end stage, the LFP was mainly characterized by low frequency, high amplitude activity prior to the final collapse of all activity. This phenomenon was observed across the hippocampus and entorhinal cortex, although the spectral integrity persisted in the hippocampus for relatively longer.

2. MATERIALS AND METHODS

2.1. Subjects and Behavioral Training

All behavioral procedures were performed following protocols approved by the Institutional Animal Care and Use Committee at the University of Florida as well as those set forth by the National Institute of Health. The present study consisted of five male hybrid Fisher344-Brown Norway rats (Taconic) ranging from 4 to 10 months of age (r730, r782, r829, r889, and r1074). Animals were singly housed and allowed to acclimate for 1 week after arrival. The colony room maintained a reversed 12–12 h light-dark cycle with all behavior taking place during the dark period. Behavioral shaping began with training animals to run counterclockwise on a circular track one meter in diameter for a food reward (pieces of cereal marshmallow, Medley Hills Farm, Ohio). During this time, the animal's weights were slowly reduced to 85% of their ad lib. weight. Once a criterion of at least 30 laps in 15 min was reached, animals were implanted unilaterally with silicon probes. One probe was implanted in the dorsal hippocampus (HPC) in all the three rats. As to rat 730 and rat 782, another probe was implanted in the medial entorhinal cortex (MEC). The probes used for r730, r782, r829, and r889 were custom single shank, 32 channel probes (NeuroNexus; Ann Arbor, MI) with an area of 177 μ m^2 and a site spacing of 60 μ m. Rat 1074 received single shank 64 channel probe (L3 series; Cambridge NeuroTech; Cambridge, UK) with an area of 165 μ m^2 and a site spacing of 50 μ m. Prior to surgery, all probes were cleaned by soaking in a solution of 7% detergent (Contrad 70 Liquid Detergent; Decon Labs; King of Prussia, PA) in deionized water followed by rinsing with deionized water.

2.2. Surgical Procedures

All surgical procedures were performed following protocols approved by the Institutional Animal Care and Use Committee at the University of Florida as well as those set forth by the National Institute of Health. Animals were placed in an induction chamber and sedated with 3–5% Isoflurane. After loss of muscle tone, they were moved to a nose cone and the top portion of the head was carefully shaved to avoiding cutting any whiskers. Next, the animal was transferred to the nose cone of the stereotaxic frame, where the head was gently secured with using ear and incisor bars. During this portion and for the remainder of the procedure, anesthesia was maintained using an Isoflurane dose between 1 and 2.5% while periodically monitoring respiration. Body temperature was maintained using an electric heating pad with feedback via rectal thermometer. The eyes were protected by applying ophthalmic ointment and shielding from direct light. Prior to the initial incision, the top of the head was cleaned using several cycles of povidone-Iodine and alcohol. An incision was made starting just behind the eyes and continuing to the back of the skull. The skin was retracted, and blunt dissection was used to expose the surface of the skull. Bleeding was managed using a cautery pen (Bovie Medical; Clearwater, FL). After thoroughly cleaning the skull, measurements from a stereotaxic arm were used to ensure that the skull was leveled. Next, bregma and the electrode implant locations were marked on the skull with the cautery pen for visual reference. A total of seven anchor screws were placed into the skull to serve as attachment points for the headcap. One screw over the cerebellum and one screw over the cortex were attached to wires that would serve as the reference and ground locations, respectively. A small amount of luting cement (C&B Metabond; Parkell Inc; Edgewood, NY) was applied to the screws to provide a foundation for the rest of the headcap. Care was taken to avoid covering bregma and the implant sites. Craniotomies were drilled at the implant sites and the dura was removed, taking care to not damage the cortex. Bleeding was managed using saline irrigation or sterile gauze. Probes targeting the dorsal HPC were implanted at −3.2 mm AP; 1.5 mm ML to bregma; −3.7 mm DV to dura. Coordinates targeting the MEC were −0.5 mm AP to the transverse sinus, 4.6 mm ML to bregma, angled 30° posteriorly, and −5.78 mm DV to dura. After implantation, the craniotomies were sealed with a surgical silicone adhesive (Kwik-Sil; World Precision Instruments; Sarasota, FL). Dental acrylic [Grip Cement, 675571 (powder) and 675572 (solvent); Dentsply Caulk; Milford, DE] was then applied to secure the probes and connectors in place. The ground and reference wires were soldered to the appropriate wires on the probe connectors and the reference wire was isolated using dental acrylic. Lastly, copper mesh was shaped into a small bowl around the headcap to serve as physical protection and secured with dental acrylic. The ground wires were soldered to the copper mesh to minimize the danger of electrostatic discharge. Immediately following the removal of the anesthetic, 10 ml of sterile saline and a dose of 1.0 mg/kg meloxicam (Boehringer Ingelheim Vetmedica, Inc; St. Joseph, MO) were administered subcutaneously. The animals were placed on a heating pad and monitored until fully mobile and capable of eating. Post-surgical care included a second dose of meloxicam

24 h later as well as 5 ml of oral antibiotics (40 mg/ml Sulfamethoxazole and 8 mg/ml Trimethoprim Oral Suspension; Aurobindo Pharma Inc; Dayton, NJ) mixed into their food for 7 days. Animals were monitored for 1 week following surgery to ensure no physical or behavioral abnormalities were observed before testing began.

2.3. Euthanasia Electrophysiology

After completing all other behavioral experiments, animals were recorded from for 15 min in the usual resting container to establish a baseline for the LFP data and then received a lethal dose of SomnaSol (390 mg/ml pentobarbital sodium, 50 mg/ml phenytoin sodium; Henry Schein; Melville, NY) injected intraperitoneally. LFP recording continued throughout the injection and for 10–15 min after the animal no longer exhibited a nociceptive withdrawal reflex. The animal was then immediately perfused with 4% paraformaldehyde, and the brain extracted and prepared for histology to verify electrode locations.

2.4. Data Process and Spectral Analysis

The LFP data were analyzed in MATLAB (The MathWorks, Natick, MA) using custom-written code as well as code imported from the HOSAtoolbox (Swami et al., 2000). Raw LFP records sampled at 24 kHz (Tucker-Davis system) were low-pass filtered down to 1 kHz. The spectrogram were calculated based on discrete Fourier transform with window length of 1 s and 50% overlap. The power correlograms for each evolution stage were obtained by estimating the correlation coefficients between all the frequency pairs in the result of spectrogram. The power spectra during the euthanasia were estimated for every 100 s. Within each LFP interval, the power spectrum was obtained via the standard Welch's method (Welch, 1967) with window length of 1 s and 50% overlap. The power law exponential was obtained by linearly fit the log-log power spectrum in the frequency range from 20 to 80 Hz to diminish the influence of EMG noise.

The coherence between two time series is the modulus of their cross-spectrum normalized by their power spectra. The cross-spectrum and power spectra were estimated with window length of 1 s and 50% overlap. To demonstrate the time evolution of coherence, a sliding window with a length of 20 s and a step increment of 5 s was applied. In each window, the coherence between two time series in frequency range from 2 to 128 Hz were estimated.

The asymmetry and skewness of LFP were obtained from the bispectral analysis with a window length of 1 s and 50% overlap. The bispectrum (the Fourier transform of the third-order cumulant) has been thoroughly reviewed in terms of both statistical and mathematical background (Harris, 1967) as well as its application to non-linear wave interaction (Kim and Powers, 1979). In the field of neuroscience, bispectral analysis was used to quantify the degree of phase coupling between the frequencies of the LFP, whereas the bicoherence quantifies the degree of cross-frequency coupling independent from the amplitude (Barnett et al., 1971; Ning and Bronzino, 1989; Sigl and Chamoun, 1994; Bullock et al., 1997; Muthuswamy et al., 1999; Hagihira et al., 2001; Li et al., 2009; Sheremet et al., 2016; Wang et al., 2017; Avarvand et al., 2018). The cross-bispectrum analysis is similar with the bispectrum analysis but the frequency components are from two time series (Lii and Helland, 1981; Sheremet et al., 2020). In our study, as the lengths of stage 2 differ across regions, the cross-bicoherence between HPC and MEC were estimated over the shorter stage length.

The decay rate of each frequency component was derived from the power time series. Power time series of frequency component ω was defined as the variance of filtered LFP in the frequency band $[\omega - 0.5\text{Hz}, \omega + 0.5\text{Hz}]$. The power time series was calculated with a window length of 10 s and a step increment of 2 s (**Figure 3C**). The decay/grow constant was defined as the ratio of the time derivative of the power time series to the power time series itself. The obtained result was smoothed with the time window of 20 s to eliminate fast power oscillations, and was plotted every 5 s. The transition period from the first to the second stage is defined as the moment with the fastest averaged decay rate over 100 Hz. The transition period from the second to the third stage is defined as the moment with the fastest averaged decay rate from 4 to 60 Hz.

3. RESULTS

3.1. Three Stages During Spectrum Degradation

After the injection of SomnaSol, LFP exhibited three distinguishable stages with two rapid transition periods between these stages in all the animals.

3.1.1. Pre-effective Stage

The first stage (marked as blue box in **Figure 2**) was described as the pre-effective stage,or stage 1. This stage was indistinguishable from baseline (pre-injection).Thus in **Figures 1**, **3**, both the pre-injection ($t < 0$) and the pre-effective stages were marked as stage 1. In this stage, LFP was dependent on the behaving state of the rat where there were strong theta and gamma rhythms at high running velocity (Whishaw and Vanderwolf, 1973; Morris and Hagan, 1983; Chen et al., 2011; Ahmed and Mehta, 2012; Kemere et al., 2013; Zheng et al., 2015; Sheremet et al., 2019a). A sample of hippocampal LFP from stage 1 (**Figure 1B**) reveals that theta can express significant deviations from a sinusoid (Buzsaki et al., 1983; Terrazas et al., 2005). This non-sinusoidal waveform is related to high order theta harmonics due to the non-linearity of hippocampal LFP (Scheffer-Teixeira and Tort, 2016; Sheremet et al., 2016; Zhou et al., 2019). In statistical analysis, the lowest order non-linear character of the system can be described by bispectrum (Hasselmann et al., 1963). The real and imaginary part of the bispectrum characterizes the skewness (an example being a cnoidal wave) and the asymmetry ("sawtooth" shaped wave) of the distribution. The sawtooth aspect of the theta wave, with steep wave front (from trough to peak), corresponded to the negative asymmetry (**Figure 1C**) at the [8, 8, 16 Hz] frequency triad (8 Hz at x-axis, 8 Hz at y-axis and their sum 16 Hz). Apart from that strong negative asymmetry region, the [8, 16, 24 Hz] frequency triad exhibited strong positive asymmetry and supported the existence of third-order theta harmonic (Schomburg et al., 2014; Zhou et al., 2019; Cowen et al., 2020).

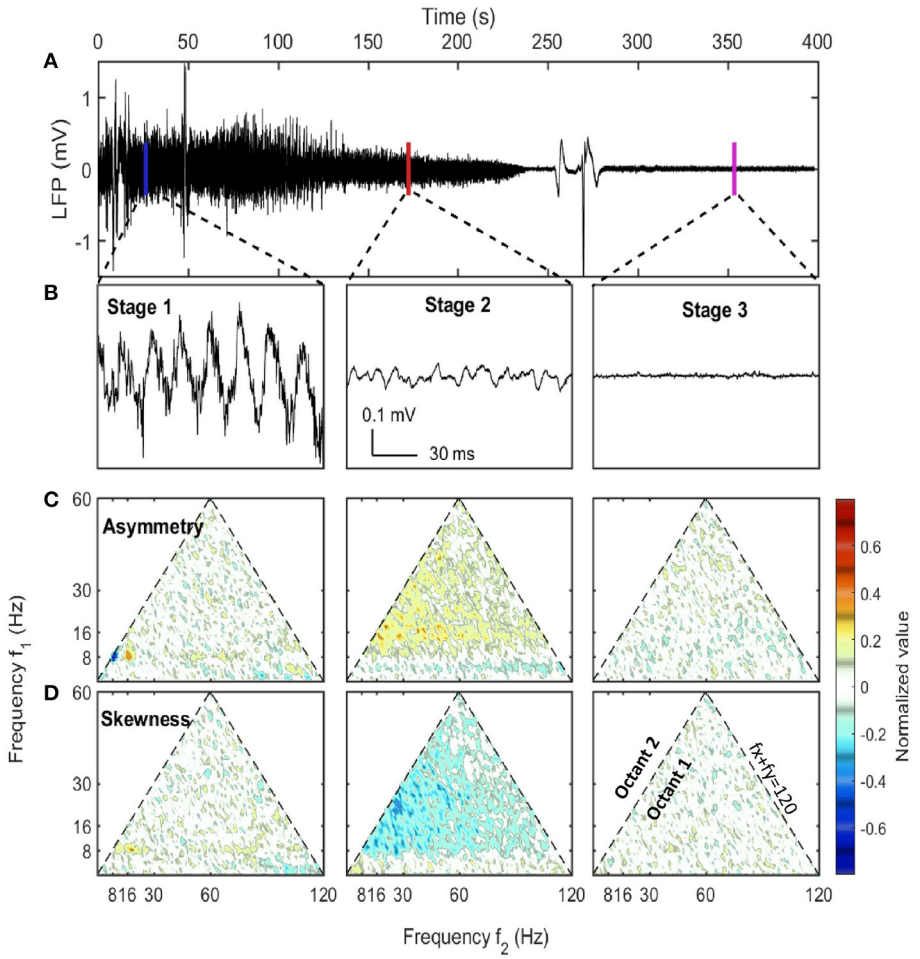

FIGURE 1 | LFP examples at different stages along with their asymmetry and skewness. **(A)** The raw LFP trace recorded in CA1 pyramidal layer after the injection ($t = 0$) which showed the overall neural activity evolution during euthanasia. **(B)** LFP samples of 1 s selected from three stages. The corresponding windows were indicated in **(A)**. **(C,D)** The asymmetry and the skewness of LFP at three stages obtained from bispectral analysis (Haubrich and MacKenzie, 1965; Masuda and Kuo, 1981; Sheremet et al., 2016). Both the horizontal axis and the vertical axis represent frequency. Each point in the plot was the asymmetry or skewness estimated for the frequency triad $(f_x, f_y, f_x + f_y)$. Only the first octant ($f_x \geq 0$, $f_y \geq 0$, $f_x \geq f_y$) is presented as it contained all the non-redundant information due to the symmetry of bispectrum. The first octant is bounded by the dashed line $f_x + f_y = 120$ Hz indicating the upper bound of frequency range of interest. An oscillation has asymmetry if the wave peak or trough doesn't stand at the center of adjacent zero-across points. An oscillation has skewness if the wave height distribution is not symmetric about its mean value. Both asymmetry and skewness indicate cross-frequency coupling. Data from rat 782.

In the spectrogram of hippocampal LFP (**Figure 1B**) during stage 1, there was a strong theta oscillation along with intermittent but distinguishable second and third harmonics. Apart from high power activities in theta and its harmonics bands, intermittent high-frequency events were identified by looking at spectrogram at frequency range over 128 Hz (marked as blue asterisks in **Figures 2B,C**). Although the frequency range overlaps with *epsilon* rhythms described by others Canolty et al., 2006; Freeman, 2007; Sullivan et al., 2011; Belluscio et al., 2012, we make the conservative interpretations that is it caused by abnormal muscle contractions. High-frequency neural events tend to be local as they are supported by interactions within a specific brain region (Buzsaki and Draguhn, 2004; Buzsaki, 2006; Sheremet et al., 2019a), but the high-frequency intermittent bursts during stage 1 were highly coherent and had almost zero phase lag between HPC and MEC regions (**Supplementary Figure 3**). Therefore, the intermittent high-frequency bursts are plausibly related to muscle activities (EMG noise; Muthukumaraswamy, 2013; Nottage and Horder, 2015) as pentobarbital is known to include abnormal contractile activity (Nayler and Szeto, 1972; Khan, 1980; Taylor et al., 1984; Eikermann et al., 2009). This activity subsided after stage 1 due to pentobarbital sodium injection (Altura and Altura, 1975).

3.1.2. Quasi-Stationary Decay Stage

The second stage (marked as red box in **Figure 2**) was described as the quasi-stationary decay stage, or stage 2, after the sudden disappearance of theta and >128 Hz bursts (at 100 ± 33 s after SomnaSol administration). The hippocampal LFP in this quasi-stationary stage exhibited slow power decay over a period

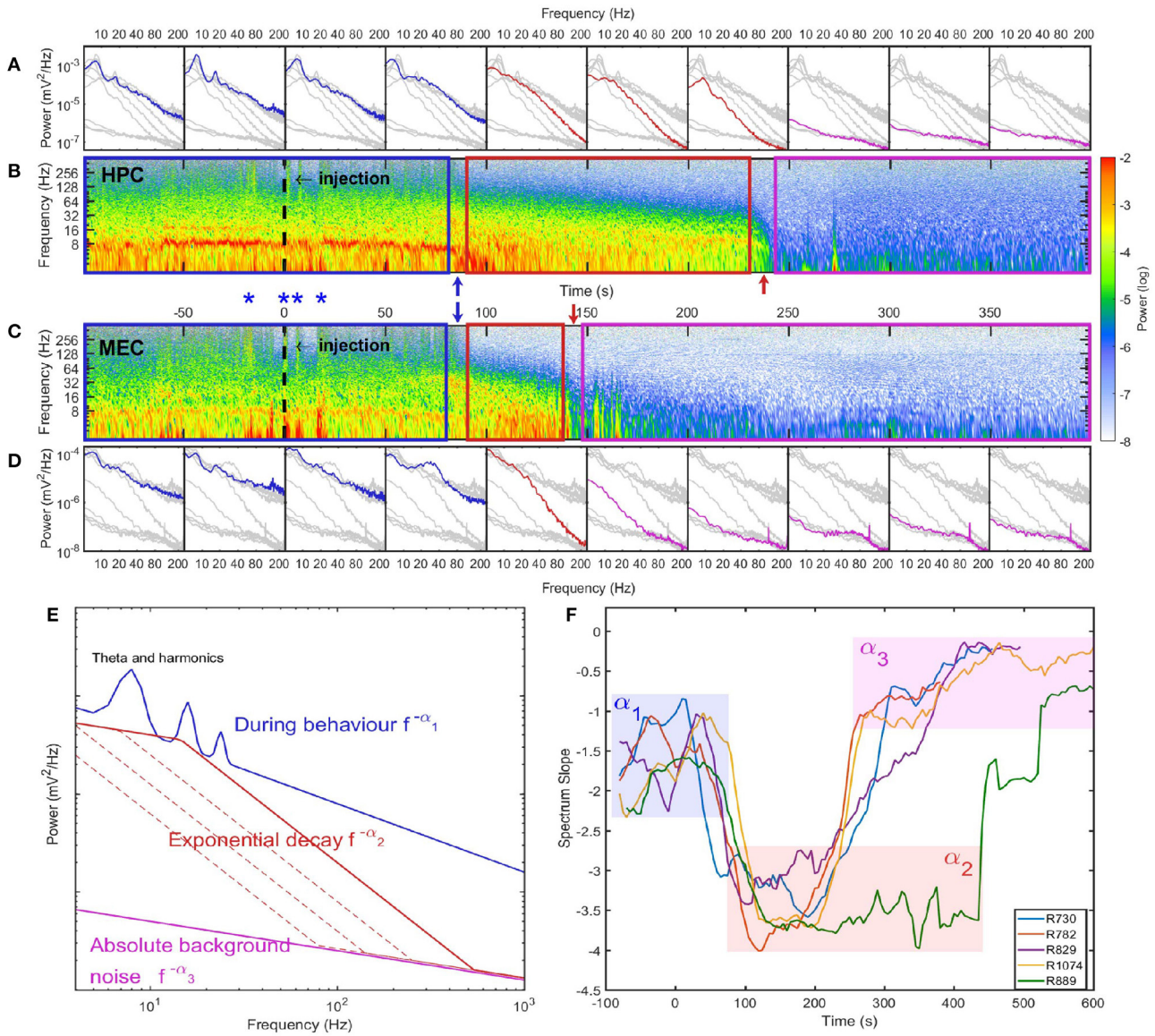

FIGURE 2 | Spectrum evolution during barbiturate overdose euthanasia. **(A)** The development of spectra estimated every 50 s. Spectra estimated within other time intervals were indicated as gray lines for comparison. **(B)** The spectrogram of hippocampal LFP where the injection time was marked as a dashed line at 0 s. The power in spectrogram was normalized by the maximum power during the euthanasia process. Based on the spectrogram and the development of power spectrum, we identified three stages during euthanasia: stage 1 was the pre-effective stage which included the pre-injection period and a short period after injection. This demarcated in the spectrogram as a blue box and in spectra, blue lines; stage 2 was the quasi-stationary decay stage marked as a red box in spectrogram and red lines in spectra; stage 3 was the quasi-white noise stage marked as a magenta box in spectrogram and magenta lines in spectra. Between these stages there were two rapid transition periods marked with blue and red arrows. **(C)** The spectrogram of LFP recorded in MEC. During stage 1, there were instances with strong high-frequency power (>128 Hz) both can be observed in HPC and MEC. Four of these instances were marked as blue asterisks. Given the consistency across regions, these high frequency bursts are most-likely related to sodium pentobarbital related muscle contractions (EMG artifact, see **Supplementary Figure 3**). **(D)** The development of spectra in MEC. Data from rat 782. **(E)** Cartoon illustrate the spectrum evolution during euthanasia. The spectra from the first to the third stages were marked as blue, red and magenta lines. The power spectra exhibits different slopes across stages. **(F)** Power-law exponents evolution of five rats estimated with window length of 40 s and time increment of 5 s. The spectrum slopes were estimated for the frequency range from 20 to 80 Hz in the log-log plot. Three stages can be identified with $\alpha_1 \approx 1.5$, $\alpha_2 \approx 3.5$, and $\alpha_3 \approx 0.5$. Note that rat 889 had longer stage 2 compared with other rats (see **Supplementary Figure 6**).

of ∼100 s without obvious intermittent structures (**Figure 1A**). Within a narrow time frame, the LFP appeared to be nearly stationary, although of lower amplitude compared with stage 1. Traditional 8 Hz theta activity was no longer evident via visual inspection. Rather, a surge in lower frequency band activity (1–4 Hz) occurred and this event has been reported previously (Schramm et al., 2020). As the power in this lower frequency, 1–4 Hz activity dissipated, a 10 Hz oscillation became prominent,

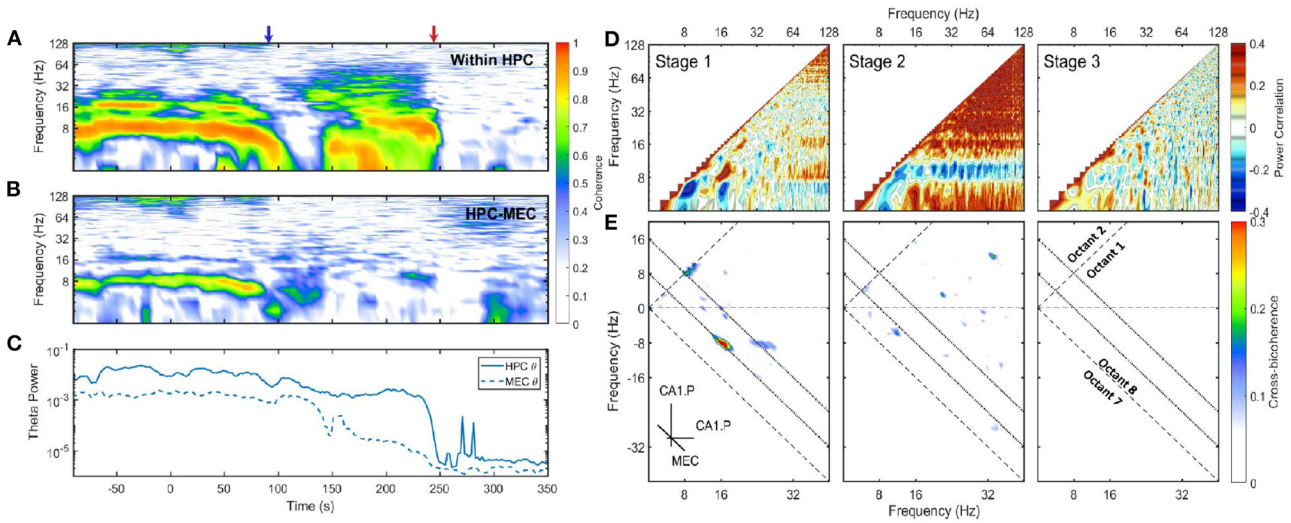

FIGURE 3 | (A) Coherence between CA1.Pyr and LM in HPC. The x-axis was the time and the y-axis was the frequency. Two transition periods were marked with blue and red arrows in the plot. Coherence is the modulus of the normalized cross-spectrum with a value between 0 and 1. High coherence indicates there is a consistent phase difference between two time series at that frequency. In terms of spectral analysis of LFP, high coherence within a narrow frequency band is a sign of the existence of oscillatory rhythm, and there is a phase difference either because the rhythm is a traveling wave or due to the bipolar nature of neurons. **(B)** The development of coherence between HPC and MEC. **(C)** The energy evolution of theta band in HPC and MEC, the variances were calculated with a window length of 10 s and a step increment of 2 s. **(D)** Average auto-correlation coefficients of Fourier transform estimated at three stages. As the auto-correlations are symmetric, only one half was presented. Positive correlation indicates the power of those two frequency components tend to grow or decay simultaneously, while negative correlation demonstrates that the power in some frequencies is lost as others increase (see Masimore et al., 2004, 2005). During stage 1, the positive correlation can be identified in three regions: The correlation between theta and theta harmonics represented by significant dots with frequency under 32 Hz; The correlation between gamma (>60 Hz) and theta (or theta harmonics) represented by horizontal strips. During stage 2, the power of 10 Hz frequency components was negatively correlated with other frequency components, while all other frequency components had positive power correlation. **(E)** Cross-bicoherence between HPC and MEC. Each point in the plot represented the cross-frequency coupling of the frequency triad $(f_x, f_y, f_x + f_y)$ where f_x and f_y were frequency components in HPC and $f_x + f_y$ was frequency component in MEC. Octant 1 and Octant 8 contained all the non-redundant information. Two inclined dotted lines indicated 8 and 16 Hz in MEC. During the stage 1, there were significant regions representing cross-region cross-frequency coupling of theta and its harmonics between HPC and MEC [(8, 8, 16) Hz, (16, −8, 8) Hz and (24, −8, 16)Hz]. Data from r782.

characterized by a wide-flat peak and narrow-deep trough (**Figure 1B**). This waveform expressed a negative skewness in the frequency region from 10 to 30 Hz via bispectrum analysis (**Figure 1D**).

The spectrogram of LFP during stage 2 was consistent with observations of the time-series. There were no intermittent high-frequency structures (EMG artifacts), but there was the development of a 10 Hz oscillation at the end of stage 2. In terms of the spectrum evolution, except for the frequency components <10 Hz, there was a structured power decay over a wide frequency band.The power-law distribution persisted over the entire stage with a slope of $-\alpha_2 \approx -3.3$, but with a decaying total variance (**Figures 2E,F**). There was a progressive recession of power, where the power in the 20–120 Hz decreased at the same logarithmic rate. This degradation is evident in the straight power contour lines in the spectrogram plot (contour lines were not directly plotted but can be identified from the transition of colors) (**Figure 2B**). As a result, during stage 2 the spectrum experienced a "parallel" evolution that can be interpreted as the entire spectrum having a decay in power along with a shift toward lower frequency. By comparing across animals, we observed a "parallel" spectrum evolution in HPC and MEC regions (**Figure 2** and **Supplementary Figures 4–7**). However, although the onsets of stage 2 were synchronized, their lengths varied between HPC and MEC. In the HPC region, the power-law spectrum kept evolving after the LFP spectrum in MEC had collapsed to a low power-containing state.

3.1.3. Collapse Stage

In the HPC region, the LFP collapsed at 320 ± 101 seconds after SomnaSol administration, marking the spectral transition into stage 3, or collapse stage (marked as a magenta box in **Figure 2**). Oscillation amplitude was small (**Figure 1B**) with occasional large "LFP-spikes" (**Figures 1A**, **2B**). This oscillation has been described previously as the "wave of death" (WoD; Kaminogo et al., 1998; Van Rijn et al., 2011; Zandt et al., 2011), which is proposed to reflect the massive and simultaneous depolarization of a large number of neurons. This phenomenon most-likely shares a high degree of similarity with cortical spreading depression (Dreier and Reiffurth, 2015), accounting for why the event was not highly correlated between brain regions (**Figures 2B,C**). Pani et al. (2018) reported this brain activity could persist for about 120 min after cardiac arrest, maintained by a slow spreading depolarization caused by irreversible degenerative processes at the cellular level. Apart from the transient spikes, LFP in stage 3 did not show significant

asymmetry or skewness in the bispectral analysis (**Figures 1C,D**). The power spectrum during stage 3 was flat with a slope of $-\alpha_3 \approx -0.75$ and represented the least power containing state of our LFP measurement (**Figures 1E,F**). Given the low power level during stage 3, it is possible that the spectrum reflected more of the electro-thermal noise in the physical recording environment surrounding the data acquisition system than neural activities.

3.2. Degradation of Theta After the First Stage

In the previous section, we stated the stage 1 of spectrum degradation ended with the erosion of observable theta and the disappearance of the intermittent high-frequency activity. Comparing HPC and MEC spectrograms, we observed that the transition from stage 1 to stage 2 was synchronized across these regions (**Figure 2**, **Supplementary Figures 4B,C**). Although the typical theta oscillation along with its harmonics was no longer visually observable in the raw LFP after stage 1 (**Figures 2B,C**), the power in theta band (6–10 Hz) only exhibited a limited decrease from stage 1 to stage 2 in the HPC and MEC regions (**Figure 3C** and **Supplementary Figures 8–11**). Therefore, to determine if the 6–10 Hz frequency component is a degenerate form of theta or due to a different mechanism, we sought to determine if the band shared features generally associated with theta.

A linear and non-linear spectral analysis was conducted to investigate the coupling in theta band within HPC and across regions. During stage 1, strong coherence existed at theta and theta harmonics frequency range across HPC layers (**Figure 3A**). The high coherence was consistent with the observation that the hippocampal LFP was dominated by theta waves, and the theta oscillation experienced a phase reversal at hippocampal fissure (Winson, 1974). The coherence at theta rhythm can also be observed between HPC and MEC regions, which was expected given the strong reciprocal connections between these structures and the observation of traveling theta waves in both regions (Lubenov and Siapas, 2009; Hernández-Pérez et al., 2020). To identify the fundamental frequencies of the LFP and determine any potential interactions across different oscillatory bands, a power correlation analysis (Masimore et al., 2004, 2005) was conducted. The analysis revealed that during stage 1, the power of theta, the power of theta harmonics, and the gamma rhythm (60–120 Hz) were all positively correlated (**Figure 3D**). In terms of non-linear cross-frequency coupling. the non-linearity of theta can be investigated through the use of the bispectrum, expressed as a significant region at the frequency triad (8, 8, 16) Hz (**Figure 1**). The cross-frequency coupling existed not only within the hippocampal region, but also between HPC and MEC regions. **Figure 3E** showed the cross-region cross-frequency coupling for the frequency triad $(f_x, f_y, f_x + f_y)$ where f_x, f_y belonged to CA1.Pyr and f_{x+y} belonged to MEC. The cross-bispectral analysis revealed that theta and theta harmonics were cross-frequency coupled across HPC and MEC regions during stage 1. To summarize, theta rhythm in stage 1 had the following features: (1) The oscillations at theta range were coherent within HPC, and between HPC and MEC. (2) The power of theta is positively correlated with power of gamma. (3) When the power of theta was strong, theta was phase-coupled with high order theta harmonics.

After stage 1, there was considerable power persisting in the 6-10 Hz frequency band at the end of stage 2. Specifically, there was high coherence around 10 Hz within the hippocampus (**Figure 3A**). However, the across region coherence was weak (**Figure 3B**). Moreover, as the majority of frequencies degraded together, the power correlation during the second stage- except for the 10 Hz oscillation- were positive. That was consistent with the "parallel" spectrum degradation where all the frequency components experienced power decay. The 10 Hz oscillation, however, had a negative power correlation due to the power increase at the end of stage 2 (**Figure 3D**). The cross-bicoherence also showed that the cross-frequency coupling between HPC and MEC was weak during stage 2 compared with stage 1 (**Figure 3E**). Although the oscillation had a frequency close to theta and high coherence within HPC region, it was not coherent between HPC and MEC, nor correlated with other frequency bands. Therefore, it is most-likely distinct from theta as it does not engage a large population of neurons across brain regions, but is perhaps related to a local hippocampal network dynamic (e.g., O'Keefe and Recce, 1993).

3.3. Uniform Exponential Power Decay in the Second Stage

In the previous section we have shown that during stage 2, except for the 10 Hz oscillation, the power of all the frequency components were positively correlated in that their power receded together. In this section, we investigated how power of different frequency components evolved during the entire euthanasia process (**Figure 4A**). According to the power evolution plot there are two periods of rapid change: (1) In the transition from stage 1 to stage 2, there was a marked divergence between low and high frequencies, potentially carried by the development of 10 Hz power and the loss of power in higher frequencies. (2) From stage 2 to stage 3, low frequency components experienced another rapid decay because of the collapse of power-law spectrum (red arrow in **Figure 4A**). Between these two transition periods, the power evolution of frequency components from 20 to 120 Hz can be approximated as straight lines. In the semi-log plot the straight line evolution can be interpreted as exponential decay (stage 2 indicated as red box in **Figures 4A,B**). The slopes of these power lines reflected the decay rates of corresponding frequency components, and during stage 2 the power evolution were almost parallel which indicated that frequency components shared a similar decaying rate.

The decaying rate (in the unit of Hz) can be quantified by differentiating power time-series with respect to time, and normalizing the time derivative by the power (**Figure 4B**). During stage 2 of spectrum degradation, the frequency components over 20 Hz decayed at similar rate with a decay constant around 0.03 Hz. This exponential decay of high-frequency components lasted shorter amounts of time as their power reached the low background energy plateau and experienced limited power decay afterwards. Stage 2 ended with

a rapid decay of low frequency components with decaying rat of 0.06 Hz corresponding to the collapse of the power-law spectrum.

Similar rates of power decay during stage 2 were observed across animals and regions (**Figure 4C**). The decay rates of frequency components lower than 20 Hz were small due to the development of a 10 Hz rhythm at the end of stage 2. The spectrogram in **Figure 2** indicated that the 10 Hz frequency was a degraded form of a 20 Hz rhythm presented earlier in the degradation process. In the spectra evolution (**Figure 2A** and **Supplementary Figures 4**–**7**) the 10 to 20 Hz oscillation acted as a spectrum front, but the reason of its generation and development is unknown. Apart from that, other frequency components had a exponential decay with decay constant at the magnitude of 0.03 Hz in HPC in MEC. One exception is rat 889 which had a longer stage 2 and the decay rates were significantly lower than other rats.

The exponential decay occurred within the gamma range (Bragin et al., 1995; Chorbak and Buzsaki, 1998), defined here as 60–120 Hz based on the power-power couplings observed in **Figure 3D** and based on prior publications (Sheremet et al., 2019a; Zhou et al., 2019). As the gamma oscillations are short-lived and typically emerge from the coordinated interaction of excitation and inhibition (Buzsaki and Wang, 2012), the patterns of gamma rhythm is closely related to local circuit connections and thus have layer specification. To investigate whether the development of gamma rhythm during barbiturate overdose euthanasia is dependent on layers, the evolution of gamma power in layer pyramidal layer (Pyr), radiatum (Rad), lacunosum-moleculare (LM), and MEC layer were plotted (**Figure 5A**). The hippocampal electrode location was confirmed by current source density (CSD) analysis of hippocampal sharp-wave ripple events (**Supplementary Figure 2**). During stage 2, MEC gamma rhythm experienced a faster decay compared with that in HPC strata, which was reflected as a steeper slope in the semi-log gamma power plot. Within the HPC region, however, the degradation of the gamma rhythm did not exhibit strong layer dependence. The gamma power curves were almost parallel during stage 2, with the initial gamma power being the primary difference. The power decay rates of frequency components in gamma range also exhibits strong correlation within and across layers (**Figure 5B**). Apart from the low frequency range which was influenced by the development of 10 Hz oscillation during stage 2, most of the frequency pairs had a correlation coefficient in decay rate over 0.4, and the correlation coefficients grow as approaching the diagonal. The strong correlated decay rates across frequency pairs implied that during stage 2, the frequency components in gamma band experienced a uniform power deprivation. As the cross layer decay rate correlation had similar magnitude with same layer correlation, we reported that no significant layer dependence of gamma evolution was observed during stage 2 of barbiturate overdose euthanasia.

4. DISCUSSION

The current manuscript investigated the degradation of the hippocampal power spectral density over the course of euthanasia. Perhaps the most outstanding result is the magnitude of power loss across all frequency bands. Comparisons of power spectral densities between sleep and wake states (e.g., Figure 4 of Buzsáki et al., 2003; **Supplementary Figure 1**) reveal that the overall "1/f" is well-preserved even in quiescence. The dramatic collapse over euthanasia suggests that the brain is in a persistent state of near-maximal activity, a conclusion arrived upon in perhaps the earliest characterization of the 1/f power spectral density: "*Our theory outlined above claims that the sum of energy is held at the maximum even in the passive state of consciousness...*" (Motokawa, 1949). This is to emphasize that, as the LFP is primarily shaped by synaptic transmembrane current (Buzsaki et al., 2012), the normal functioning brain is constantly maintaining baseline activity far from equilibrium. And although the slope of the spectra has been known to change as a function of running speed (Sheremet et al., 2019b), the parametric space in which the 1/f slope changes is small relative to power in specific frequency bands, such as theta. Therefore, examining the LFP over the course of euthanasia offers a larger parametric space to explore the mechanisms that support the 1/f spectra.

We observed three states of spectral degradation. Stage 1, or pre-effective stage, can be described as a typical "active," theta-dominate state where the 7–10 Hz rhythm is readily identifiable in the LFP and the power spectrum. In stage 2, or the quasi-stationary decay stage, the theta peak above the 1/f slope degraded. This was associated with a reduced theta coherence between the medial entorhinal cortex and hippocampus. This suggests that, in the early part of stage two, the ability of the medial entorhinal cortex and hippocampus to interact is impaired but not absent. As stage two progressed, the spectrum displayed a "parallel" degradation that can be interpreted as the entire spectrum having a decay in power along with a shift toward lower frequency. Interestingly, the erosion in higher frequency bands (including the 60–120 Hz gamma band) was accompanied by the appearance of a 10 Hz peak in the power spectral density. The duration of stage 2 persisted longer in the hippocampus relative to the medial entorhinal cortex (which did not exhibit a 10 Hz peak). The end of stage 2 and start of stage 3 was marked by a complete collapse of the power in all spectral bands, with low activity in nearly all bands and occasional large spikes that plausibly related to spreading depolarization (Pani et al., 2018). Finally, the activity reached a minimum, credibly being the electro-thermal noise in the physical recording environment surrounding the data acquisition system.

As it would be a rare instance for a single experiment to comprise a full test of any hypothesis, it is first necessary to discuss the limitations of the current study before making theoretical extensions. The most-outstanding limitation of the study was the use of the pharmacological agent to induce euthanasia. The action of SomnaSol is systemic, making it difficult to infer the spectral decline mechanism. We cannot expressly state that the lack of perfusion, the action of the barbiturate on the GABAergic system, the combination thereof, etc., is exclusively responsible for the recession in power seen in specific frequency bands. Furthermore, pentobarbital is known to augment the contractile activity of muscle fibers and reduce the cells' ability to maintain appropriate calcium homeostasis,

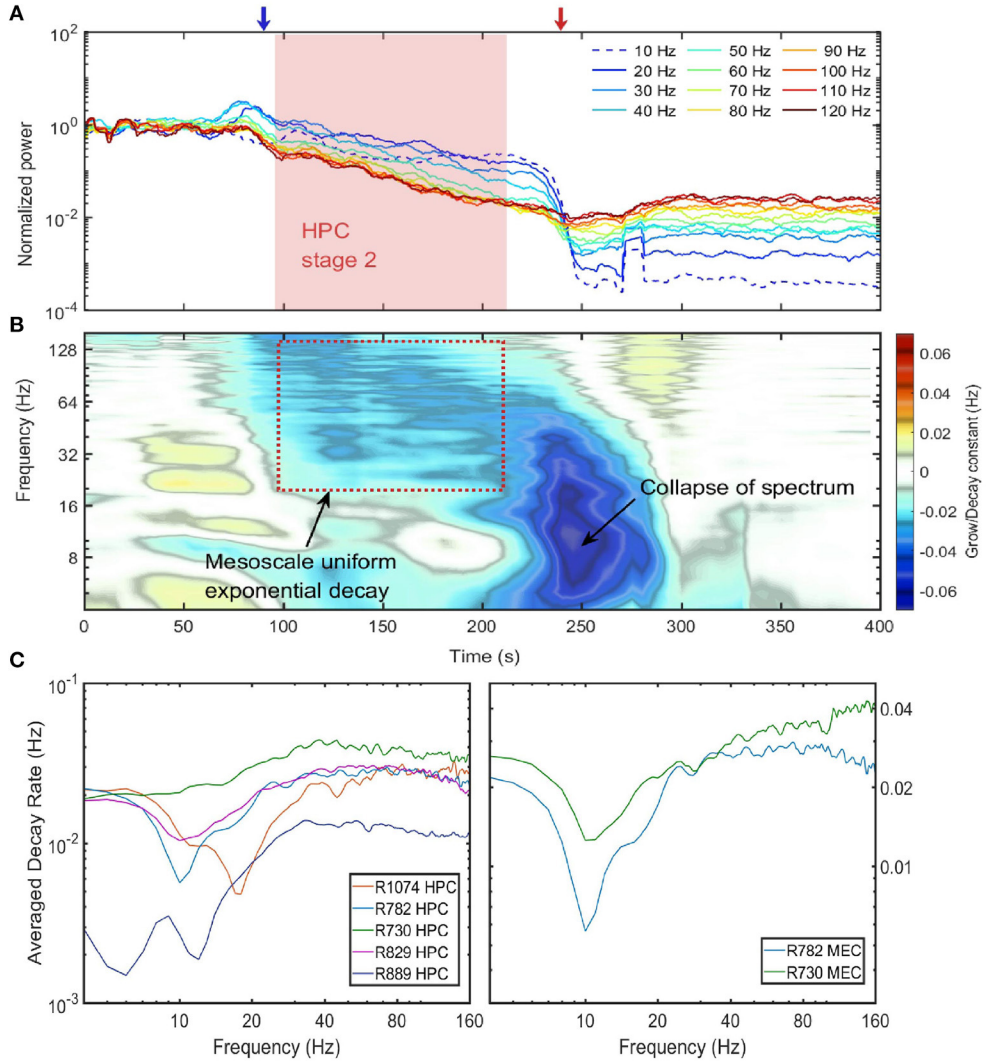

FIGURE 4 | Power decay of frequency components over the euthanasia process. **(A)** The power evolution for frequency component from 10 to 120 Hz. Each line corresponded to the power decay of one frequency component. Low frequency components were indicated by cold colors and high-frequency components by warm colors. Note the power were normalized by their value at the time of injection ($t = 0$), and the 10 Hz frequency component experienced a growth at the end of stage 2. Data from rat 782. **(B)** The percentage power change rates of different frequency components over the entire spectrum degradation process. To obtain the percentage power change rate, the power time series for each frequency component was first estimated and the percentage power change rate was defined as the ratio of the time derivative of power time series to the power time series. If a frequency component experiences a exponential decay or grow $e^{\alpha t}$, the percentage power change rate will be a constant with value α. Data from rat 782. **(C)** The decay constant vs. the frequency during the exponential decay stage. The left panel were the decay constants in HPC among rats and the right panel were decay constants in MEC. The decay constant were estimated by averaging over the entire stage 2 period. Note that the overall decay rate of rat 889 was smaller compared with other rats because rat 889 had a longer stage 2 (see **Supplementary Figure 6**).

thus initiating a contracted state (Nayler and Szeto, 1972; Khan, 1980; Taylor et al., 1984; Eikermann et al., 2009). We observed high-frequency bursts above 128 Hz, most-likely being an EMG artifact as the rhythm is phase-locked across regions (see **Supplementary Figure 9**). Unfortunately, this precludes the ability to either examine high-frequency rhythms or action potential activity of the neurons. Moreover, the large LFP spikes between stages 2 and 3 could be a filtered version of cortical spreading depression due to AC-coupled amplifiers. Future studies should address these limitations by using alternative forms of euthanasia, attempt to minimize EMG artifacts, and implement a DC-coupled recording to explore the cortical spreading depression.

Nevertheless, the use of SomnaSol resulted in a total spectral collapse, with a recession in power from high to low frequencies. We interpret these results from the perspective of the energy cascade hypothesis, where low frequency, high power rhythms are a function of large-scale activity extending beyond a single brain region and high-frequency, low amplitude oscillations are small-scale interactions (Buzsaki and Draguhn,

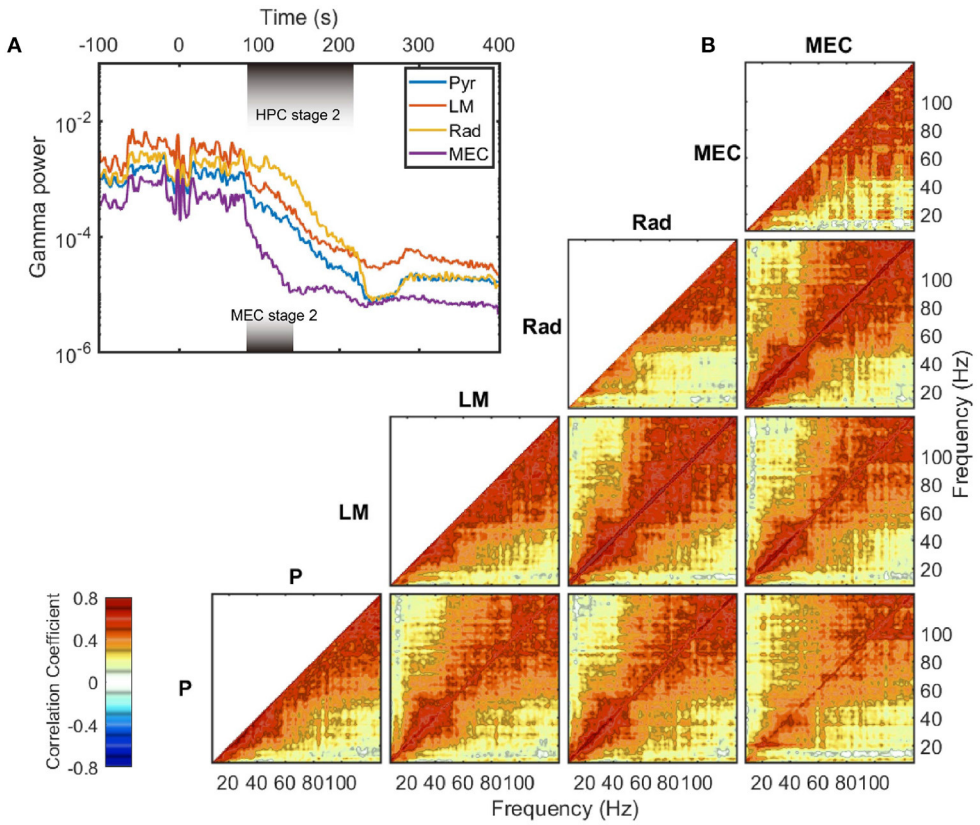

FIGURE 5 | Gamma decay during stage 2. **(A)** The evolution of LFP variance band-passed in gamma range (60–120 Hz) in different layers. The durations of stage 2 are different in HPC and MEC regions, and are marked with shaded rectangles in the plot. Data from rat 782. **(B)** Averaged auto- and cross correlation coefficient of decay rate during stage 2. The decay rate (defined as in **Figure 4B**) of each frequency component was computed and treated as a time series. Then the correlation coefficients were estimated for time series pairs from either the same layer or different layers. Within a region, the correlation of a frequency's decay rate with itself is equal to one. Furthermore, as the autocorrelations are symmetric, only one half is presented. The cross-correlation of decay rate, however, can vary across unity and is not necessarily symmetric. For instance, the bottom right panel represents the correlation of the decay rates in pyramidal (y axis) to that in MEC layer (x axis). Note that for the MEC-related panels (the rightmost column), the data were averaged between rat 730 and rat 782, and the decay rates were estimated over the MEC stage 2 period. For other panels, the results were averaged across all the five rats. P, pyramidal layer; Rad, radiatum; LM, lacunosum-moleculare; MEC, medial entorhinal cortex.

2004; Buzsaki, 2006; Sheremet et al., 2019a). Relative to the more extensive networks, smaller networks are less fault-tolerant as they are fewer in number and have fewer supporting synaptic connections. Thus, as there is less degeneracy/redundancy in small networks, compromising the function of a few neurons would be more catastrophic. The large number of neurons and extensive connectivity in a network supporting slower frequency rhythms would be more fault-tolerant, allowing it the ability to suffer a more significant loss prior to collapsing. This idea is supported by the observation of a progressive recession of power throughout stage 2. As more neurons succumb, there is a progressive loss of power from high to low frequencies that continues until the final remnants of rhythmic activity is supported by the most robust network.

At the end of stage 2, the erosion of high-frequency power appears to temporarily stop at ∼10 Hz in the hippocampus. Theoretically, this "last stop" in rhythmicity may be a function of the dense anatomical connectivity within the hippocampus (Lorente de No, 1938), with a frequency that reflects the intrinsic membrane resonance properties of the pyramidal cells and a subpopulation of interneurons (O'Keefe and Recce, 1993; Kamondi et al., 1998; Yamaguchi and McNaughton, 1998; Bose et al., 2000; Magee, 2001; Lengyel et al., 2003; Maurer et al., 2005, 2006; Geisler et al., 2007). Finally, when either there is a critical loss of hippocampal neuron function or the excitatory input into the hippocampus declines to the point that it is no longer able to excite a sufficient proportion of the hippocampal population, there is a complete collapse of the spectrum to quiescent levels. Notably, the medial entorhinal cortex exhibited a collapse in the faster rhythms prior to the collapse of the same frequencies across the hippocampal layers. This suggests that the mechanisms that support the higher-frequency rhythms in the hippocampus, such as gamma, are not necessarily relayed into the hippocampus but are most-likely generated locally (Buzsaki and Wang, 2012). As interneurons are prevalent across hippocampal layers (Klausberger and Somogyi, 2008), it is tenable that GABAergic circuits support the gamma rhythm observed across layers, with oriens lacunosum moleculare interneurons plausibly

playing a major role in shaping the high frequency power in the lacunosum moleculare layer of CA1.

Up to this point, we have used a heuristic in which specific bands are described as "rhythms" or "oscillations," which implies the converse features "noise" and "arrhythmia" exist. While there has been immense utility in using this approach, there are distinct differences between biology and the imperfect analogy that leads to ambiguity or misunderstanding in the scientific interpretation of the results (Chapter 2 of Başar 2012). This has been briefly mentioned before by Wang and Buzsaki "…although the word 'rhythm' readily conjures up the picture of a clock, gamma rhythms occur in relatively short bursts and are quite variable in frequency…" (Buzsaki and Wang, 2012). The notion of a rhythm-to-clock relationship is most likely tied to the power-frequency representation in time-series decompositions. This was initially described as the "Fourier Fallacy" in which one assumes, based on the power spectra, that all the necessary frequencies in the power spectra occur as periodic sine waves in the brain (Jasper, 1948; n.b., this applies to any method which provides a "one power to one frequency" relationship). Indeed, the concept of a unique neurobiological generator ascribed to each Fourier frequency is more magic than reality (He, 2014). However, the gap between the abstract representation of a spectral decomposition and neurobiology has yet to be fully fleshed out. Therefore, the field reaches a crossroads where we are either left to (1) expand on the notion of Wang and Buzsaki (2012) and explore the idea that the interrelated frequencies in the LFP are primarily the consequence of synaptic transmembrane currents from a local network when receiving a barrage of input or (2) whole-heartedly buy into the idea that there are divisions to be made between neural rhythms and neural noise.

The power spectral density is a low-dimensional abstraction of the actual raw time series, collapsing the underlying time-series to a decimation of sine waves. Any such transformation requires significant consideration regarding the relationship of the raw data to the algorithmic lens (Rosen, 1991). One hypothesis suggests the peaks above the 1/f slope are true neurobiological oscillators, whereas the slope itself is the consequence of a distinct broadband, arrhythmic activity (He, 2014) or similarly, rhythmicity superimposed onto a wide-band, noisy background (Bullock et al., 2003). Along these lines, analytical toolboxes have been released that claim to dissect the periodic components from the aperiodic components of the LFP (Donoghue et al., 2020). However, this perspective falls to a different sort of Fourier Fallacy in which a dichotomous "periodic" vs. "aperiodic" division based on the idea that the underlying neurobiology has two opposing physiological patterns: one that makes a pure rhythm (peaks in the power spectra) and another that makes noise (the 1/f slope; Voytek et al., 2015). The major flaw in this perspective is that it over interprets the abstract representation of a power spectral density plot, assuming that it provides more information than what can be observed in the raw LFP trace. Specifically, any measure of "rhythmicity" in the nervous system should not only measure power, but the degree to which their phase assignment of each sine wave aligns. As an exercise, conduct a Fourier decomposition on a musical concerto, maintain the power across each sine wave but randomize their phases and listen to the time-series recovered using the inverse Fourier transform. The composition falls into discord. Any rhythmicity in the musical time-series is effectively destroyed while the power spectral density retains the same exact form. Therefore, it becomes evident that the power spectral density is an incomplete tool to make a rhythm vs. noise division in any time series. With respect to neurophysiology, the division misinterprets the abstract decomposition for a literal representation, obfuscating the biophysics of the system.

Wang and Buzsaki provided a glimpse into an alternative hypothesis in which the nervous system works through evolving unique spatio-temporal patterns (Buzsaki and Wang, 2012). These spatio-temporal patterns may sometimes manifest as easy-to-identify rhythms. However, the nervous system did not evolve to perfect "clockwork operations". It should be appreciated that a single synaptic event can have rhythmic entrainment to both "theta" and "gamma" bands, challenging the heuristic of independence across rhythms. Instead, the dynamic patterns in the LFP are closely related to how the activity spatio-temporally evolves a reentrant network (Berg et al., 2019; Maurer and Nadel, 2021). While there is comfort in giving independence to specific patterns like theta and gamma, neurobiology makes no such distinction. To the neuroscientist, the Greek letters have meaning with respect to biophysical scale and the neurotransmitter shaping their interactions (among other features). The nervous system however is not self-aware of actions within a single frequency band. To relate a specific band to a behavior or cognitive function first and foremost requires a neurobiological description (what neurobiological or synaptic events lead to the increase in 80 Hz activity?) rather than a psychological, correlational answer (attention caused the increase in the 80 Hz band). The Greek letter-defined rhythms, while helpful in colloquial discussion, gave a platform to assign them individual tasks, such as synchronizing, entraining, buffering memory, and/or being a physiological readout of psychological function—a personification of sorts that speaks to the danger of taking the "rhythm" heuristic too far. Instead, it should be appreciated that the LFP is related to the non-linear spatio-temporal patterns that occur within a network of densely interconnected neurons, or more specifically, the LFP is primarily a biophysical product of the synaptic transmembrane currents associated with these dynamic patterns. In this reinterpretation, theta is the propagation of activity along a large "macroscale" loop. Nested within this large loop are many smaller loops in which the activity can be reciprocally coordinated on the mesoscale, supporting faster rhythms, such as gamma (Buzsaki and Draguhn, 2004; Buzsaki, 2006). The scales—and the names that define them-are not orthogonal but intricately coupled. The nervous system, however, does not care should a "peak" appear in the power spectra of the LFP.

Therefore, we offer to replace one heuristic ("rhythms," "oscillators," "noise," "arrhythmia") with another system defined by forcing and nested loops of multiple scales: the cardiovascular system. Should one measure the velocity of a red blood cell in a capillary, the time-series itself will exhibit the dominant frequency of the heartbeat (macroscale forcing event). As

heartbeats are "slow charge, rapid discharge" event, the large amplitude changes in velocity will exhibit a significant deviation from a sinusoid. Furthermore, this forcing occurs as a cascade from macro to micro scale, from arteries through arterioles to capillaries. Thus, blood cell velocity will be subjected to other influences, such as friction as a result of running into the other blood cells or the vascular walls or even form high-frequency turbulent eddies (e.g., partial occlusion). This jostling can be identified in the velocity profile as being a repeatable, low amplitude-high-frequency event coupled to the macroscale heartbeat frequency. Finally, decomposing the red blood cell velocity would reveal a power spectra density eerily similar to the hippocampus, complete with a fundamental frequency, harmonics, and a 1/f background (see Figure 2B of Harlepp et al., 2017). In fact, one may suspect that the influence of pentobarbital on the power spectra of red blood cell velocity would parallel the degradation observed in the LFP, with the highest frequencies succumbing first. Therefore, while Fourier decomposition is certainly a useful tool in time-series analysis, defining the presence of an oscillation as a peak above the background and the absence as having no peak along the 1/f background as "aperiodic" from the power spectra has a peculiar and contracted relevance. The cardiovascular system never evolved to make rhythms or arrhythmic activity but takes advantage of a turbulent energy cascade across scales to move blood cells (Saqr et al., 2020).

As "...the EEG reflects the 'average' behavior of neurons" (Buzsaki, 2006, p. 129), the analogy above has a direct relation to neurophysiological theories incorporating the classical physics theory of turbulence into the description of the LFP (Sheremet et al., 2019b; Deco and Kringelbach, 2020). An action potential of a single neuron represents the smallest spatio-temporal event, the microscale component, that resides in nested loops of multiple scales. The LFP is the aggregate activity related to activity moving through multiple loops of different scales simultaneously. The movement of the activity through the nervous system is, from this perspective, a unitary process where activity "chases is own tail" through reentrant loops (Hebb, 1958). Cross-frequency dependence becomes the rule rather than the exception. Certainly, there may be activity that expresses as a peak above the 1/f background, such as theta, which comprises the movement of activity on the macroscale. However, oscillations like gamma rarely peak above the background (Zhou et al., 2019) and yet also describe the mesoscale volleys of activity governed by interneurons. Rather than making false dichotomies between "non-rhythm/rhythm,""present/absent,""periodic/aperiodic" a new appreciation is required in which the LFP is a reflection of the underlying evolution of spatio-temporal patterns within a densely interconnected network of neurons.

DATA AVAILABILITY STATEMENT

The raw data supporting the conclusions of this article are available for download without reservation here: https://datadryad.org/stash/dataset/doi:10.5061/dryad.vmcvdncs6.

ETHICS STATEMENT

The animal study was reviewed and approved by University of Florida Institute of Animal Care and Use Committee.

AUTHOR CONTRIBUTIONS

AS and AM came up with the idea of investigating the spectrum evolution with decreasing energy and participated in the entire process of this study. JK and ND performed the surgery, conducted experiments, and collected the data. YZ conducted the data analysis and made the figures. CM and SB provided insights into the interpretation of the results. All authors made contributions to writing the manuscript.

FUNDING

This work was supported by the McKnight Brain Research Foundation, and NIH grants—Grant Sponsor: National Institute on Aging; Grant number: AG055544 and Grant Sponsor: National Institute of Mental Health; Grant Number: MH109548 and a Diversity Supplement to NIH grant R01MH109548 (JK).

SUPPLEMENTARY MATERIAL

The Supplementary Material for this article can be found online at: https://www.frontiersin.org/articles/10.3389/fnsys.2021.647011/full#supplementary-material

Supplementary Figure 1 | Background spectrum of hippocampal LFP. The background spectrum is indicated as the gray dashed line. Theta, theta harmonics, gamma, and ripple will develop on the background spectrum at different behaving states.

Supplementary Figure 2 | Hippocampal lamination of five rats with current source density (CSD) analysis. The CSD analyses were triggered on the maximum positive-going ripple in the pyramidal cell layer. DOF, Degree of freedom, indicating the number of ripple events. Strong sharp wave sources and sinks can be observed at pyramidal layer (Pyr), stratum radiatum (Rad), lacunosum-moleculare (LM), and upper granule layer (G). Embedded high-frequency ripples can be spotted at strata Pyr and Rad.

Supplementary Figure 3 | Coherent high-frequency bursts (>128 Hz) during stage 1. **(A)** Power evolution of frequency components over 128 Hz during early stage of euthanasia. Four instances with strong (2nd and 3rd) or weak (1st and 4th) high-frequency power were marked with dashed lines. **(B)** Raw LFPs of four layers (Pyr, Rad, LM, and MEC) at instances marked by dashed lines in **(A)**. **(C)** LFPs band-pass filtered in frequency range 140–160 Hz at instances marked by dashed lines in **(A)**. At instances with strong high-frequency power (2nd and 3rd columns), synchronized wave envelopes can be observed across layers. **(D)** Evolution of coherence between Pyr and LM. **(E)** Evolution of coherence between Pyr and MEC layer. **(F)** Evolution of phase lag between Pyr and LM. **(G)** Evolution of phase lag between Pyr and MEC layer. According to **(D–G)**, during the stage 1 of degradation, the cross-spectrum at high-frequency range (>128 Hz) is dominated by zero phase-lag high-coherent events.

Supplementary Figure 4 | Similar with **Figure 2**. Data from rat 730.

Supplementary Figure 5 | Similar with **Figure 2**. Spectrum degradation in hippocampus. Data from rat 829.

Supplementary Figure 6 | Similar with **Figure 2**. Spectrum degradation in hippocampus. Data from rat 889.

Supplementary Figure 7 | Similar with **Figure 2**. Spectrum degradation in hippocampus. Data from rat 1074.

Supplementary Figure 8 | Similar with **Figure 3**. Data from rat 730.

Supplementary Figure 9 | Similar with **Figure 3** without cross region coherence and bicoherence. Data from rat 829.

Supplementary Figure 10 | Similar with **Figure 3** without cross region coherence and bicoherence. Data from rat 889.

Supplementary Figure 11 | Similar with **Figure 3** without cross region coherence and bicoherence. Data from rat 1074.

REFERENCES

Ahmed, O., and Mehta, M. (2012). Running speed alters the frequency of hippocampal gamma oscillations. *J. Neurosci.* 32, 7373–7383. doi: 10.1523/JNEUROSCI.5110-11.2012

Altura, B. T., and Altura, B. M. (1975). Pentobarbital and contraction of vascular smooth muscle. *Am. J. Physiol.* 229, 1635–1640. doi: 10.1152/ajplegacy.1975.229.6.1635

Atasoy, S., Deco, G., and Kringelbach, M. L. (2020). Harmonic waves as the fundamental principle underlying temporo-spatial dynamics of brain and mind. Comment on "is temporo-spatial dynamics the" common currency "of brain and mind? in quest of "spatiotemporal neuroscience"" Georg Northoff et al. *Phys. Life Rev.* 33, 67–69. doi: 10.1016/j.plrev.2019.10.001

Avarvand, F. S., Bartz, S., Andreou, C., Samek, W., Leicht, G., Mulert, C., et al. (2018). Localizing bicoherence from EEG and MEG. *Neuroimage* 174, 352–363. doi: 10.1016/j.neuroimage.2018.01.044

Bak, P., Tang, C., and Wiesenfeld, K. (1988). Self-organized criticality. *Phys. Rev. A* 38, 364–375. doi: 10.1103/PhysRevA.38.364

Barnett, T., Johnson, L., Naitoh, P., Hicks, N., and Nute, C. (1971). Bispectrum analysis of electroencephalogram signals during waking and sleeping. *Science* 172, 401–402. doi: 10.1126/science.172.3981.401

Başar, E. (2012). *Chaos in Brain Function: Containing Original Chapters By E. Basar and T. H. Bullock and Topical Articles Reprinted From the Springer Series in Brain Dynamics*. Berlin; Heidelberg: Springer Science & Business Media.

Belluscio, M. A., Mizuseki, K., Schmidt, R., and Buzsaki, G. (2012). Cross-frequency phase-phase coupling between theta and gamma oscillations in the hippocampus. *J. Neurosci.* 32, 423–435. doi: 10.1523/JNEUROSCI.4122-11.2012

Berg, R. W., Willumsen, A., and Lindén, H. (2019). When networks walk a fine line: balance of excitation and inhibition in spinal motor circuits. *Curr. Opin. Physiol.* 8, 76–83. doi: 10.1016/j.cophys.2019.01.006

Borjigin, J., Lee, U., Liu, T., Pal, D., Huff, S., Klarr, D., et al. (2013). Surge of neurophysiological coherence and connectivity in the dying brain. *Proc. Natl. Acad. Sci. U.S.A.* 110, 14432–14437. doi: 10.1073/pnas.1308285110

Bose, A., Booth, V., and Recce, M. (2000). A temporal mechanism for generating the phase precession of hippocampal place cells. *J. Comput. Neurosci.* 9, 5–30. doi: 10.1023/A:1008976210366

Bragin, A., Jandó, G., Nádasdy, Z., Hetke, J., Wise, K., and Buzsáki, G. (1995). Gamma (40–100 Hz) oscillation in the hippocampus of the behaving rat. *J. Neurosci.* 15, 47–60. doi: 10.1523/JNEUROSCI.15-01-00047.1995

Bullock, T., Achimowicz, J., Duckrow, R., Spencer, S., and Iragui-Madoz, V. (1997). Bicoherence of intracranial EEG in sleep, wakefulness and seizures. *Electroencephalogr. Clin. Neurophysiol.* 103, 661–678. doi: 10.1016/S0013-4694(97)00087-4

Bullock, T., McClune, M., Achimowicz, J., Iragui-Madoz, V., Duckrow, R., and Spencer, S. (1995). Temporal fluctuations in coherence of brain waves. *Proc. Natl. Acad. Sci. U.S.A.* 92, 11568–11572. doi: 10.1073/pnas.92.25.11568

Bullock, T., McClune, M., and Enright, J. (2003). Are the electroencephalograms mainly rhythmic? Assessment of periodicity in wide-band time series. *Neuroscience* 121, 233–252. doi: 10.1016/S0306-4522(03)00208-2

Buzsaki, G. (2005). Theta rhythm of navigation: link between path integration and landmark navigation, episodic and semantic memory. *Hippocampus* 15, 827–840. doi: 10.1002/hipo.20113

Buzsaki, G. (2006). *Rhythms of the Brain*. Oxford: Oxford University Press.

Buzsaki, G., Anastassiou, C., and Koch, C. (2012). The origin of extracellular fields and currents—EEG, ECoG, LFP and spikes. *Nat. Rev. Neurosci.* 13, 407–420. doi: 10.1038/nrn3241

Buzsáki, G., Buhl, D. L., Harris, K. D., Csicsvari, J., Czéh, B., and Morozov, A. (2003). Hippocampal network patterns of activity in the mouse. *Neuroscience* 116, 201–211. doi: 10.1016/S0306-4522(02)00669-3

Buzsaki, G., and Draguhn, A. (2004). Neuronal oscillations in cortical networks. *Science* 304, 1926–1929. doi: 10.1126/science.1099745

Buzsaki, G., Gage, F., Kellenyi, L., and Björklund, A. (1987). Behavioral dependence of the electrical activity of intracerebrally transplanted fetal hippocampus. *Brain Res.* 400, 321–333. doi: 10.1016/0006-8993(87)90631-7

Buzsaki, G., Leung, W., and Vanderwolf, C. (1983). Cellular bases of hippocampal EEG in the behaving rat. *Brain Res.* 287, 139–171. doi: 10.1016/0165-0173(83)90037-1

Buzsaki, G., and Wang, X.-J. (2012). Mechanisms of gamma oscillations. *Annu. Rev. Neurosci.* 35, 203–225. doi: 10.1146/annurev-neuro-062111-150444

Canolty, R. T., Edwards, E., Dalal, S. S., Soltani, M., Nagarajan, S. S., Kirsch, H. E., et al. (2006). High gamma power is phase-locked to theta oscillations in human neocortex. *Science* 313, 1626–1628. doi: 10.1126/science.1128115

Chen, Z., Resnik, E., McFarland, J., Sakmann, B., and Mehta, M. (2011). Speed controls the amplitude and timing of the hippocampal gamma rhythm. *PLoS ONE* 6:e21408. doi: 10.1371/journal.pone.0021408

Chorbak, J., and Buzsaki, G. (1998). Gamma oscillations in the entorhinal cortex of the freely behaving rat. *J. Neurosci.* 18, 388–398. doi: 10.1523/JNEUROSCI.18-01-00388.1998

Cowen, S. L., Gray, D. T., Wiegand, J.-P. L., Schimanski, L. A., and Barnes, C. A. (2020). Age-associated changes in waking hippocampal sharp-wave ripples. *Hippocampus* 30, 28–38. doi: 10.1002/hipo.23005

Deco, G., and Kringelbach, M. L. (2020). Turbulent-like dynamics in the human brain. *Cell Rep.* 33:108471. doi: 10.1016/j.celrep.2020.108471

Donoghue, T., Haller, M., Peterson, E. J., Varma, P., Sebastian, P., Gao, R., et al. (2020). Parameterizing neural power spectra into periodic and aperiodic components. *Nat. Neurosci.* 23, 1655–1665. doi: 10.1038/s41593-020-00744-x

Dreier, J. P., and Reiffurth, C. (2015). The stroke-migraine depolarization continuum. *Neuron* 86, 902–922. doi: 10.1016/j.neuron.2015.04.004

Eikermann, M., Fassbender, P., Zaremba, S., Jordan, A. S., Rosow, C., Malhotra, A., et al. (2009). Pentobarbital dose-dependently increases respiratory genioglossus muscle activity while impairing diaphragmatic function in anesthetized rats. *J. Am. Soc. Anesthesiol.* 110, 1327–1334. doi: 10.1097/ALN.0b013e3181a16337

Freeman, W. J. (2007). Definitions of state variables and state space for brain-computer interface: part 1. Multiple hierarchical levels of brain function. *Cogn. Neurodyn.* 1, 3–14. doi: 10.1007/s11571-006-9001-x

Fyhn, M., Molden, S., Witter, M. P., Moser, E. I., and Moser, M. B. (2004). Spatial representation in the entorhinal cortex. *Science* 305, 1258–1264. doi: 10.1126/science.1099901

Geisler, C., Robbe, D., Zugaro, M., Sirota, A., and Buzsáki, G. (2007). Hippocampal place cell assemblies are speed-controlled oscillators. *Proc. Natl. Acad. Sci. U.S.A.* 104, 8149–8154. doi: 10.1073/pnas.0610121104

Green, J. D., and Petsche, H. (1961). Hippocampal electrical activity ii. Virtual generators. *Electroencephalogr. Clin. Neurophysiol.* 13, 847–853. doi: 10.1016/0013-4694(61)90063-3

Hagihira, S., Takashina, M., Mori, T., Mashimo, T., and Yoshiya, I. (2001). Practical issues in bispectral analysis of electroencephalographic signals. *Anesth. Analges.* 93, 966–970. doi: 10.1097/00000539-200110000-00032

Harlepp, S., Thalmann, F., Follain, G., and Goetz, J. G. (2017). Hemodynamic forces can be accurately measured *in vivo* with optical tweezers. *Mol. Biol. Cell* 28, 3252–3260. doi: 10.1091/mbc.e17-06-0382

Harris, B. (1967). *Spectral Analysis of Time Series*. New York, NY: Wiley.

Hasselmann, K., Munk, W., and McDonald, G. (1963). "Bispectra of ocean waves," in *Proceedings of Symposium on Time Series Analysis* (New York, NY), 125–139.

Haubrich, R. A., and MacKenzie, G. S. (1965). Earth noise 5 to 500 millicycles per second: 2. Reaction of the Earth to oceans and atmosphere. *J. Geophys. Res.* 70, 1429–1440. doi: 10.1029/JZ070i006p01429

He, B. J. (2014). Scale-free brain activity: past, present, and future. *Trends Cogn. Sci.* 18, 480–487. doi: 10.1016/j.tics.2014.04.003

Hebb, D. (1949). *The Organization of Behavior: A Neuropsychological Theory*. New York, NY: Wiley.

Hebb, D. (1958). *A Textbook of Psychology*. Philadelphia, PA: W. B. Saunders.

Hernández-Pérez, J. J., Cooper, K. W., and Newman, E. L. (2020). Medial entorhinal cortex activates in a traveling wave in the rat. *Elife* 9:e52289. doi: 10.7554/eLife.52289

Hesse, J., and Thilo, G. (2014). Self-organized criticality as a fundamental property of neural systems. *Front. Syst. Neurosci*. 8:166. doi: 10.3389/fnsys.2014.00166

Jasper, H. H. (1948). Charting the sea of brain waves. *Science* 108, 343–347. doi: 10.1126/science.108.2805.343

Kaminogo, M., Suyama, K., Ichikura, A., Onizuka, M., and Shibata, S. (1998). Anoxic depolarization determines ischemic brain injury. *Neurol. Res*. 20, 343–348. doi: 10.1080/01616412.1998.11740529

Kamondi, A., Acsady, L., Wang, X., and Buzsaki, G. (1998). Theta oscillations in somata and dendrites of hippocampal pyramidal cells *in vivo*: activity-dependent phase-precession of action potentials. *Hippocampus* 8, 244–261. doi: 10.1002/(SICI)1098-1063(1998)8:3<244::AID-HIPO7>3.0.CO;2-J

Kemere, C., Carr, M. F., Karlsson, M. P., and Frank, L. M. (2013). Rapid and continuous modulation of hippocampal network state during exploration of new places. *PLoS ONE* 8:e73114. doi: 10.1371/journal.pone.0073114

Khan, A. R. (1980). Mechanism of action of pentobarbital on the contractile system of isolated frog muscle fibres. *Acta Physiol. Scand*. 108, 405–409. doi: 10.1111/j.1748-1716.1980.tb06551.x

Kim, Y. C., and Powers, E. J. (1979). Digital bispectral analysis and its applications to nonlinear wave interactions. *IEEE Trans. Plasma Sci*. 7, 120–131. doi: 10.1109/TPS.1979.4317207

Klausberger, T., and Somogyi, P. (2008). Neuronal diversity and temporal dynamics: the unity of hippocampal circuit operations. *Science* 321, 53–57. doi: 10.1126/science.1149381

Lengyel, M., Szatmáry, Z., and Érdi, P. (2003). Dynamically detuned oscillations account for the coupled rate and temporal code of place cell firing. *Hippocampus* 13, 700–714. doi: 10.1002/hipo.10116

Lepage, K. Q., Kramer, M. A., and Eden, U. T. (2011). The dependence of spike field coherence on expected intensity. *Neural Comput*. 23, 2209–2241. doi: 10.1162/NECO_a_00169

Leung, L. (1982). Nonlinear feedback model of neuronal populations in hippocampal CAl region. *J. Neurophysiol*. 47, 845–868. doi: 10.1152/jn.1982.47.5.845

Leung, L. W. S., Da Silva, F. L., and Wadman, W. (1982). Spectral characteristics of the hippocampal EEG in the freely moving rat. *Electroencephalogr. Clin. Neurophysiol*. 54, 203–219. doi: 10.1016/0013-4694(82)90162-6

Li, X., Li, D., Voss, L. J., and Sleigh, J. W. (2009). The comodulation measure of neuronal oscillations with general harmonic wavelet bicoherence and application to sleep analysis. *Neuroimage* 48, 501–514. doi: 10.1016/j.neuroimage.2009.07.008

Lii, K., and Helland, K. (1981). Cross-bispectrum computation and variance estimation. *ACM Trans. Math. Softw*. 7, 284–294. doi: 10.1145/355958.355961

Lorente de No, R. (1938). "Cerebral cortex: architecture, intracortical connections, motor projections," in *Physiology of the Nervous System, 2nd Edn*, ed J. F. Fulton (New York, NY: Oxford University Press), 274–301.

Lubenov, E., and Siapas, A. (2009). Hippocampal theta oscillations are travelling waves. *Nature* 459, 534–539. doi: 10.1038/nature08010

Magee, J. C. (2001). Dendritic mechanisms of phase precession in hippocampal ca1 pyramidal neurons. *J. Neurophysiol*. 86, 528–532. doi: 10.1152/jn.2001.86.1.528

Masimore, B., Kakalios, J., and Redish, A. (2004). Measuring fundamental frequencies in local field potentials. *J. Neurosci. Methods* 138, 97–105. doi: 10.1016/j.jneumeth.2004.03.014

Masimore, B., Schmitzer-Torbert, N. C., Kakalios, J., and Redish, A. D. (2005). Transient striatal γ local field potentials signal movement initiation in rats. *Neuroreport* 16, 2021–2024. doi: 10.1097/00001756-200512190-00010

Masuda, A., and Kuo, Y.-Y. (1981). A note on the imaginary part of bispectra. *Deep Sea Res*. 28, 213–222. doi: 10.1016/0198-0149(81)90063-7

Maurer, A., Vanrhoads, S. R., Sutherland, G., Lipa, P., and McNaughton, B. (2005). Self-motion and the origin of differential spatial scaling along the septo-temporal axis of the hippocampus. *Hippocampus* 15, 841–852. doi: 10.1002/hipo.20114

Maurer, A. P., Cowen, S. L., Burke, S. N., Barnes, C. A., and McNaughton, B. L. (2006). Organization of hippocampal cell assemblies based on theta phase precession. *Hippocampus* 16, 785–794. doi: 10.1002/hipo.20202

Maurer, A. P., and Nadel, L. (2021). The continuity of context: a role for the hippocampus. *Trends Cogn. Sci*. 25, 187–199. doi: 10.1016/j.tics.2020.12.007

Mitchell, S., Rawlins, J., Steward, O., and Olton, D. (1982). Medial septal area lesions disrupt theta rhythm and cholinergic staining in medial entorhinal cortex and produce impaired radial arm maze behavior in rats. *J. Neurosci*. 2, 292–302. doi: 10.1523/JNEUROSCI.02-03-00292.1982

Morris, R. G. M., and Hagen J. J. (1983). "Hippocampal electrical activity and ballistic movement," in *Neurobiology of the Hippocampus*, ed W. Seifert (Göttingen: Academic Press), 321–331.

Motokawa, K. (1949). Energy of brain waves and energetics of the brain. *Tohoku J. Exp. Med*. 51, 119–129. doi: 10.1620/tjem.51.119

Muthukumaraswamy, S. (2013). High-frequency brain activity and muscle artifacts in meg/eeg: a review and recommendations. *Front. Hum. Neurosci*. 7:138. doi: 10.3389/fnhum.2013.00138

Muthuswamy, J., Sherman, D. L., and Thakor, N. V. (1999). Higher-order spectral analysis of burst patterns in EEG. *IEEE Trans. Biomed. Eng*. 46, 92–99. doi: 10.1109/10.736762

Nadel, L., and Maurer, A. (2020). Recalling lashley and reconsolidating Hebb. *Hippocampus* 30, 776–793. doi: 10.1002/hipo.23027

Nayler, W. G., and Szeto, J. (1972). Effect of sodium pentobarbital on calcium in mammalian heart muscle. *Am. J. Physiol*. 222, 339–344. doi: 10.1152/ajplegacy.1972.222.2.339

Ning, T., and Bronzino, J. D. (1989). Bispectral analysis of the rat EEG during various vigilance states. *IEEE Trans. Biomed. Eng*. 36, 497–499. doi: 10.1109/10.18759

Northoff, G., Wainio-Theberge, S., and Evers, K. (2019). Is temporo-spatial dynamics the "common currency" of brain and mind? in quest of "spatiotemporal neuroscience". *Phys. Life Rev*. 33, 34–54. doi: 10.1016/j.plrev.2019.05.002

Nottage, J. F., and Horder, J. (2015). State-of-the-art analysis of high-frequency (gamma range) electroencephalography in humans. *Neuropsychobiology* 72, 219–228. doi: 10.1159/000382023

O'Keefe, J., and Recce, M. L. (1993). Phase relationship between hippocampal place units and the EEG theta rhythm. *Hippocampus* 3, 317–330. doi: 10.1002/hipo.450030307

Pani, P., Giarrocco, F., Giamundo, M., Brunamonti, E., Mattia, M., and Ferraina, S. (2018). Persistence of cortical neuronal activity in the dying brain. *Resuscitation* 130, e5–e7. doi: 10.1016/j.resuscitation.2018.07.001

Parnia, S., and Fenwick, P. (2002). Near death experiences in cardiac arrest: visions of a dying brain or visions of a new science of consciousness. *Resuscitation* 52, 5–11. doi: 10.1016/S0300-9572(01)00469-5

Petersen, P. C., and Buzsáki, G. (2020). Cooling of medial septum reveals theta phase lag coordination of hippocampal cell assemblies. *Neuron* 107, 731–744.e3. doi: 10.1016/j.neuron.2020.05.023

Pozzorini, C., Naud, R., Mensi, S., and Gerstner, W. (2013). Temporal whitening by power-law adaptation in neocortical neurons. *Nat. Neurosci*. 16, 942–948. doi: 10.1038/nn.3431

Richardson, L. F. (2007). *Weather Prediction by Numerical Process*. Cambridge: Cambridge University Press.

Rosen, R. (1991). *Life Itself: A Comprehensive Inquiry Into the Nature, Origin, and Fabrication of Life*. New York, NY: Columbia University Press.

Saqr, K. M., Tupin, S., Rashad, S., Endo, T., Niizuma, K., Tominaga, T., et al. (2020). Physiologic blood flow is turbulent. *Sci. Rep*. 10:15492. doi: 10.1038/s41598-020-72309-8

Scheffer-Teixeira, R., and Tort, A. B. (2016). On cross-frequency phase-phase coupling between theta and gamma oscillations in the hippocampus. *Elife* 5:e20515. doi: 10.7554/eLife.20515

Schomburg, E., Fernandez-Ruiz, A., Mizuseki, K., Berenyi, A., Anastassiou, C., Koch, C., et al. (2014). Theta phase segregation of input-specific gamma patterns in entorhinal-hippocampal networks. *Neuron* 84, 470–485. doi: 10.1016/j.neuron.2014.08.051

Schramm, A. E., Carton-Leclercq, A., Diallo, S., Navarro, V., Chavez, M., Mahon, S., et al. (2020). Identifying neuronal correlates of dying and resuscitation in a model of reversible brain anoxia. *Prog. Neurobiol*. 185:101733. doi: 10.1016/j.pneurobio.2019.101733

Sheremet, A., Burke, S., and Maurer, A. (2016). Movement enhances the nonlinearity of hippocampal theta. *J. Neurosci*. 36, 4218–4230. doi: 10.1523/JNEUROSCI.3564-15.2016

Sheremet, A., Kennedy, J., Qin, Y., Zhou, Y., Lovett, S. D., Burke, S. N., et al. (2019a). Theta-gamma cascades and running speed. *J. Neurophysiol.* 121, 444–458. doi: 10.1152/jn.00636.2018

Sheremet, A., Qin, Y., Kennedy, J. P., Zhou, Y., and Maurer, A. P. (2019b). Wave turbulence and energy cascade in the hippocampus. *Front. Syst. Neurosci.* 12:62. doi: 10.3389/fnsys.2018.00062

Sheremet, A., Zhou, Y., Kennedy, J., Qin, Y., Burke, S., and Maurer, A. (2018). Theta-gamma coupling: a nonlinear dynamical model. *bioRXiv*. doi: 10.1101/304238

Sheremet, A., Zhou, Y., Qin, Y., Kennedy, J. P., Lovett, S. D., and Maurer, A. P. (2020). An investigation into the nonlinear coupling between ca1 layers and the dentate gyrus. *Behav. Neurosci.* 134, 491–515. doi: 10.1037/bne0000366

Shu, Y., Hasenstaub, A., Badoual, M., Bal, T., and McCormick, D. A. (2003). Barrages of synaptic activity control the gain and sensitivity of cortical neurons. *J. Neurosci.* 23, 10388–10401. doi: 10.1523/JNEUROSCI.23-32-10388.2003

Sigl, J. C., and Chamoun, N. G. (1994). An introduction to bispectral analysis for the electroencephalogram. *J. Clin. Monit.* 10, 392–404. doi: 10.1007/BF01618421

Stumpf, C. (1965). The fast component in the electrical activity of rabbit's hippocampus. *Electroencephalogr. Clin. Neurophysiol.* 18, 477–486. doi: 10.1016/0013-4694(65)90128-8

Sullivan, D., Csicsvari, J., Mizuseki, K., Montgomery, S., Diba, K., and Buzsáki, G. (2011). Relationships between hippocampal sharp waves, ripples, and fast gamma oscillation: influence of dentate and entorhinal cortical activity. *J. Neurosci.* 31, 8605–8616. doi: 10.1523/JNEUROSCI.0294-11.2011

Swami, A., Mendel, C., and Nikias, C. (2000). *Higher-Order Spectral Analysis (HOSA) Toolbox*. Version 2, 3. (The Mathworks). Available online at: https://labcit.ligo.caltech.edu/∼rana/mat/HOSA/HOSA.PDF

Taylor, R. G., Abresch, R. T., Lieberman, J. S., Fowler Jr, W. M., and Portwood, M. M. (1984). Effect of pentobarbital on contractility of mouse skeletal muscle. *Exp. Neurol.* 83, 254–263. doi: 10.1016/S0014-4886(84)90096-7

Terrazas, A., Krause, M., Lipa, P., Gothard, K. M., Barnes, C. A., and McNaughton, B. L. (2005). Self-motion and the hippocampal spatial metric. *J. Neurosci.* 25, 8085–8096. doi: 10.1523/JNEUROSCI.0693-05.2005

Tort, A. B., Komorowski, R., Eichenbaum, H., and Kopell, N. (2010). Measuring phase-amplitude coupling between neuronal oscillations of different frequencies. *J. Neurophysiol.* 104, 1195–1210. doi: 10.1152/jn.00106.2010

Van Rijn, C. M., Krijnen, H., Menting-Hermeling, S., and Coenen, A. M. (2011). Decapitation in rats: latency to unconsciousness and the "wave of death". *PLoS ONE* 6:e16514. doi: 10.1371/journal.pone.0016514

Vanderwolf, C. H. (1969). Hippocampal electrical activity and voluntary movement in the rat. *Electroencephalogr. Clin. Neurophysiol.* 26, 407–418. doi: 10.1016/0013-4694(69)90092-3

Voytek, B., and Knight, R. T. (2015). Dynamic network communication as a unifying neural basis for cognition, development, aging, and disease. *Biol. Psychiatry* 77, 1089–1097. doi: 10.1016/j.biopsych.2015.04.016

Voytek, B., Kramer, M. A., Case, J., Lepage, K. Q., Tempesta, Z. R., Knight, R. T., et al. (2015). Age-related changes in 1/f neural electrophysiological noise. *J. Neurosci.* 35, 13257–13265. doi: 10.1523/JNEUROSCI.2332-14.2015

Wang, J., Fang, Y., Wang, X., Yang, H., Yu, X., and Wang, H. (2017). Enhanced gamma activity and cross-frequency interaction of resting-state electroencephalographic oscillations in patients with Alzheimer's disease. *Front. Aging Neurosci.* 9:243. doi: 10.3389/fnagi.2017.00243

Welch, P. D. (1967). The use of fast fourier transform for the estimation of power spectra: a method based on time averaging over short, modified periodograms. *IEEE Trans. Audio Electroacoust.* 15, 70–73. doi: 10.1109/TAU.1967.1161901

Whishaw, I., and Vanderwolf, C. H. (1973). Hippocampal EEG and behavior: change in amplitude and frequency of RSA (theta rhythm) associated with spontaneous and learned movement patterns in rats and cats. *Behav. Biol.* 8, 461–484. doi: 10.1016/S0091-6773(73)80041-0

Winson, J. (1974). Patterns of hippocampal theta rhythm in the freely moving rat. *Electroencephalogr. Clin. Neurophysiol.* 36, 291–301. doi: 10.1016/0013-4694(74)90171-0

Yamaguchi, Y., and McNaughton, B. L. (1998). "Non-linear dynamics generating theta phase precession in hippocampal closed circuit and generation of episodic memory," in *ICONIP* (Kitakyushu), Vol. 98, 781–784.

Zandt, B.-J., ten Haken, B., van Dijk, J. G., and van Putten, M. J. (2011). Neural dynamics during anoxia and the "wave of death". *PLoS ONE* 6:e22127. doi: 10.1371/journal.pone.0022127

Zhang, Y., Li, Z., Zhang, J., Zhao, Z., Zhang, H., Vreugdenhil, M., et al. (2019). Near-death high-frequency hyper-synchronization in the rat hippocampus. *Front. Neurosci.* 13:800. doi: 10.3389/fnins.2019.00800

Zheng, C., Bieri, K. W., Trettel, S. G., and Colgin, L. L. (2015). The relationship between gamma frequency and running speed differs for slow and fast gamma rhythms in freely behaving rats. *Hippocampus* 25, 924–938. doi: 10.1002/hipo.22415

Zhou, Y., Sheremet, A., Qin, Y., Kennedy, J., DiCola, N., Burke, S., et al. (2019). Methodological considerations on the use of different spectral decomposition algorithms to study hippocampal rhythms. *Eneuro* 6:ENEURO.0142-19.2019. doi: 10.1523/ENEURO.0142-19.2019

Conflict of Interest: The authors declare that the research was conducted in the absence of any commercial or financial relationships that could be construed as a potential conflict of interest.

frontiers in Computational Neuroscience

ORIGINAL RESEARCH
published: 20 May 2021
doi: 10.3389/fncom.2021.656401

A Non-spiking Neuron Model With Dynamic Leak to Avoid Instability in Recurrent Networks

Udaya B. Rongala[1], Jonas M. D. Enander[1], Matthias Kohler[2], Gerald E. Loeb[3] and Henrik Jörntell[1]*

[1] Department of Experimental Medical Science, Faculty of Medicine, Lund University, Lund, Sweden, [2] Department of Informatics, Technical University of Munich, Munich, Germany, [3] Department of Biomedical Engineering, Viterbi School of Engineering, University of Southern California, Los Angeles, CA, United States

Recurrent circuitry components are distributed widely within the brain, including both excitatory and inhibitory synaptic connections. Recurrent neuronal networks have potential stability problems, perhaps a predisposition to epilepsy. More generally, instability risks making internal representations of information unreliable. To assess the inherent stability properties of such recurrent networks, we tested a linear summation, non-spiking neuron model with and without a "dynamic leak", corresponding to the low-pass filtering of synaptic input current by the RC circuit of the biological membrane. We first show that the output of this neuron model, in either of its two forms, follows its input at a higher fidelity than a wide range of spiking neuron models across a range of input frequencies. Then we constructed fully connected recurrent networks with equal numbers of excitatory and inhibitory neurons and randomly distributed weights across all synapses. When the networks were driven by pseudorandom sensory inputs with varying frequency, the recurrent network activity tended to induce high frequency self-amplifying components, sometimes evident as distinct transients, which were not present in the input data. The addition of a dynamic leak based on known membrane properties consistently removed such spurious high frequency noise across all networks. Furthermore, we found that the neuron model with dynamic leak imparts a network stability that seamlessly scales with the size of the network, conduction delays, the input density of the sensory signal and a wide range of synaptic weight distributions. Our findings suggest that neuronal dynamic leak serves the beneficial function of protecting recurrent neuronal circuitry from the self-induction of spurious high frequency signals, thereby permitting the brain to utilize this architectural circuitry component regardless of network size or recurrency.

Keywords: neuron model, recurrent networks, dynamic leak, spurious high frequency signals, non-spiking, excitation, inhibition

OPEN ACCESS

Edited by:
Viktor Jirsa,
Aix-Marseille Université, France

Reviewed by:
Qing Yun Wang,
Beihang University, China
Spase Petkoski,
INSERM U1106 Institut de Neurosciences des Systèmes, France

****Correspondence:***
Udaya B. Rongala
udaya_bhaskar.rongala@med.lu.se

Received: *20 January 2021*
Accepted: *19 April 2021*
Published: *20 May 2021*

Citation:
Rongala UB, Enander JMD, Kohler M, Loeb GE and Jörntell H (2021) A Non-spiking Neuron Model With Dynamic Leak to Avoid Instability in Recurrent Networks. Front. Comput. Neurosci. 15:656401. doi: 10.3389/fncom.2021.656401

INTRODUCTION

Recurrent excitatory loops are a common feature in the central nervous system, such as in neocortical circuits (Binzegger et al., 2004; Song et al., 2005; Koestinger et al., 2018; Kar and DiCarlo, 2020), thalamocortical loops (Steriade, 1997; Hooks et al., 2013), cerebrocerebellar and spinocerebellar loops (Allen and Tsukahara, 1974; Jörntell, 2017). Inhibitory interneurons have

been described to provide lateral inhibition (Zhu and Lo, 2000; Douglas and Martin, 2009; Obermayer et al., 2018; Rongala et al., 2018) and feed-forward inhibition (Swadlow, 2003; Isaacson and Scanziani, 2011), but they also make synapses on other inhibitory neurons, thereby potentially forming recurrent disinhibitory loops as well (Jörntell and Ekerot, 2003; Pi et al., 2013; Sultan and Shi, 2018). Furthermore, such excitatory and inhibitory connectivity has been reported to be balanced (Anderson et al., 2000; Wehr and Zador, 2003; Okun and Lampl, 2008). Functionally, recurrent connections enable a network to use preceding states to impact the processing of the present state. Such state memory can, for example, improve learning performance (Sutskever et al., 2014). However, due to the many potential positive feedback loops in larger networks with extensive recurrent connections, imbalances in excitatory (E) and inhibitory (I) synaptic activity could lead to activity saturation (Brunel, 2000; Vogels and Abbott, 2005), such as observed in epilepsy (Chakravarthy et al., 2009; Liou et al., 2020), or, in milder cases, a noise-like perturbation of the information content of internal signals, which would be disadvantageous for learning.

We explored potential noise and stability issues that could arise in recurrent neuronal networks. In order to focus on the network architecture aspect of this problem, we used a non-spiking neuron model designed to be simple and computationally efficient, while embodying fundamental properties of Hodgkin-Huxley conductance-based models. The relevance of a non-spiking neuron model stems from the stochasticity inherent in neuronal spike generation (Naundorf et al., 2006; Saarinen et al., 2008; Spanne et al., 2014; Nilsson and Jörntell, 2021), which renders the spiking output of the individual neuron to some degree unreliable in terms of information content. To compensate for such unreliability, the brain could encode each representation across a population of neurons (below referred to as an ensemble of redundant neurons), as has been observed in the brain *in vivo* (Spanne and Jörntell, 2015). The input-output relationships across a range of neuron types in the central nervous system *in vivo* indicate that overall, each neuron's spike output is a probability density function (PDF) of the underlying membrane potential of the neuron (Spanne et al., 2014). That PDF thereby approximates the membrane potential and could be considered to correspond to the spike output of an ensemble of neurons with similar inputs. Thus, simulating a non-spiking neuron and providing the PDF of the neuron as its output avoids the extreme resource demands of both simulating the highly complex spike generation stochasticity (Saarinen et al., 2008) and compensating for that stochasticity by simulating large populations of redundant neurons. Synaptic input creates modulation of the neuronal membrane potential, hence its PDF, by temporarily activating conductances that are added to the static leak conductances. The synaptic conductances and currents can modulate very rapidly but the membrane capacitance together with the static leak channels forms an RC circuit that constitutes a low-pass filter (herein, dynamic leak) for the resultant membrane potential. We hypothesized that this dynamic leak would improve network stability without compromising information transfer.

To test this hypothesis, we constructed a highly recurrent, two-layer neuronal network, with five excitatory and five inhibitory neurons in the first layer and four excitatory and four inhibitory neurons in the second layer. All neurons in both layers were reciprocally connected with randomized gains. All first layer neurons were provided with six randomized and broadly distributed input signals. A striking finding was that for all tested network configurations, synaptic weight distributions, various conduction delays and input density of sensory inputs, recurrent networks tended to generate high frequency components that were not present in the sensory input data. In all cases these transients were eliminated by incorporating a dynamic leak in the neuron models without compromising the representation of the input signals.

We note that the fully reciprocal connectivity employed in the networks described herein encompasses the wide range of connectivity that has been identified experimentally in cortical and other central neural structures (see above). The strictly layered connectivity of many popular neural network models for deep learning reflects only a small subset of the known complexity of biological networks. Attempts to add limited recurrency into such models have encountered stability problems (Brunel, 2000; Vogels and Abbott, 2005), for which dynamic leak appears to offer substantial mitigation. Chowdhury et al. (2020) demonstrated that a leaky component (a low-pass filter effect) in a spiking neuron model (Leaky-Integrate and Fire, LIF, model) eliminates the high-frequency components from the input, which resulted in improved robustness against random noise in a multi-layer feed forward network trained with back-propagation.

MATERIALS AND METHODS

Neuron Model

Linear Summation Neuron Model (LSM)

The neuron model implemented for this study was a non-spiking, linear input summation model with an additional dynamic leak component. For the version without dynamic leak, the activity ($\mathbf{A}_{\mathbf{N}o\mathbf{D}_{yn}}$) was given by the total weighted input activity ($\mathbf{w}*\mathbf{a}$) (where $\mathbf{a}$ is the activity of each individual input and $\mathbf{w}$ is the weight of that input) across all individual synapses ($\mathbf{i}$) (Eq. 1). Electrotonic compactness in the neuron is assumed, so that all synapses have equal impact on the activity of the neuron. This simplified model of synaptic input activity integration can be shown to be closely related to a Hodgkin-Huxley (H-H) model (see **Appendix 1**), for example resulting in the preservation of two key dependencies of EPSPs and IPSPs on membrane biophysics: (i) input response magnitude depends on the difference between the membrane potential and the reversal potentials for the relevant corresponding "ion channels" (i.e., depending on if the input is provided through an excitatory or an inhibitory synapse); (ii) input response magnitude depends on relative shunting of synaptic currents by conductances resulting from the background of synaptic input activity (Eq. 1). The responsive properties of the LSM and the H-H neuron model are shown to be highly similar in **Supplementary Figure 1**.

The LSM implemented a degree of activity normalization (denominator of Eq. 1) by introducing a static leak, which was calculated as the product of a constant (k_{static}) multiplied by the number of synapses on the neuron, plus a term reflecting the total number of open channels, which is activity dependent.

To mimic the effect of the RC circuit created by the ion channels and the capacitance of the membrane, we added a dynamic leak function to the neuron. To test the impact of the dynamic leak on network dynamics, we compared the networks composed of neurons with the dynamic leak with the same network when the neuron model did not include this dynamic leak. The neuron activity for the neuron model variant with dynamic leak (A_{Dyn}) is given by the linear summation model with an additional leak time constant (τ_{Dyn}). Larger neurons with more synapses tend to have longer time constants (Zhang, 2004), so we tried various ways of scaling τ_{Dyn} with number of synapses i. Thereby, the dynamic leak integrates the function of the capacitance in the RC circuit of the biological neuron into the LSM (Eq. 2). The neuron activity of this model is given by the following equations,

$$\mathbf{A_{No_{Dyn}}} = \frac{\sum(\mathbf{w_i}*\mathbf{a_i})}{(\mathbf{k_{static}}*\mathbf{i}) + \sum|\mathbf{w_i}*\mathbf{a_i}|} \quad (1)$$

$$\frac{\tau_{\mathbf{D}yn}* \mathbf{d}A_{\mathbf{D}yn}}{\mathbf{d}t} = -\mathbf{A}_{\mathbf{D}yn}(\mathbf{t}) + \mathbf{A}_{\mathbf{No}_{\mathbf{Dyn}}}(\mathbf{t}) \quad (2)$$

$$0 \leq \mathbf{A}_{\mathbf{No}_{\mathbf{Dyn}}} and\, 0 \leq \mathbf{A}_{\mathbf{D}yn} \quad (3)$$

Figure 1 illustrates the output activity of individual LSM neurons (Eqs. 1–3), which were isolated in the sense that they were not connected to any neuronal network other than the provided inputs, for different input combinations (from left to right in **Figure 1**) of emulated excitatory and inhibitory synaptic inputs (**Figures 1A,B**). The input spike trains were convoluted using a kernel function in order to emulate post-synaptic-potential inputs (detailed below, Eq. 6), that were fed to the LSM neuron (**Figures 1C–E**). The LSM activity without dynamic leak ($A_{No_{Dyn}}$, **Figure 1F**) shows the activity normalization resulting from the static leak constant ($k_{static} = 1$, for this illustration), along with the effect of the neuron output activity threshold at zero (Eq. 3). The activity of the LSM neuron would also be expected to fall back toward this zero level of activity without any external or internal input. This level hence corresponds to a threshold for spike initiation among a population of similarly connected neurons that are typically represented by the one modeled neuron. The output activity for the LSM neuron with dynamic leak (A_{Dyn}, **Figure 1G**) exhibits a low pass filtering effect on the output activity, which is reflective of the effect of the RC component integrated in the LSM neuron model with the dynamic leak.

Figure 2 illustrates the impact of various static and dynamic leaks. As indicated in **Figure 2A**, the static leak constant acts as a normalization factor for the total neuron activity, without diminishing the underlying dynamics of that activity (**Supplementary Figure 2**). At very low values of the static leak constant, the mean activity reached sufficiently high levels for the reversal potential to start having a significant dampening effect on the activity dynamics (see uppermost trace in **Figure 2A**), substantially reducing the coefficient of variation (CV in **Figure 2B**). **Figures 2C,D** illustrates the additional impact of various values of the dynamic leak constant. **Figure 2C** and **Supplementary Figure 3** demonstrate the filtering effect of the dynamic leak constant on the total neuron activity. A high value of this dynamic leak constant substantially smoothens the activity dynamics, which was reflected in the resulting low CV value (**Figure 2D**). The dynamic leak constant (τ_{Dyn}) was set to 1/100 for the rest of this study, unless otherwise specified.

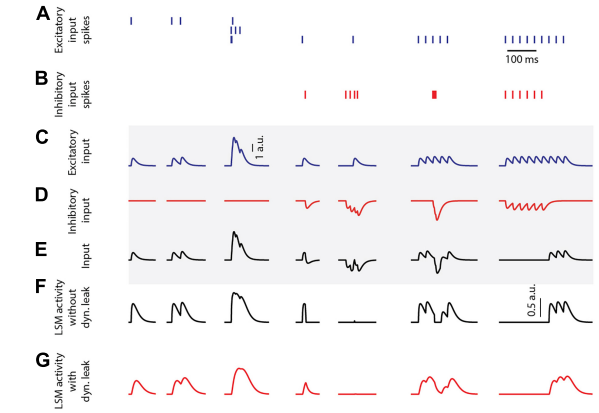

FIGURE 1 | LSM responses to emulated synaptic inputs. **(A)** The activation times of three different excitatory synaptic inputs are indicated as spike trains. **(B)** The activation times of one inhibitory synaptic input. **(C,D)** The excitatory and inhibitory sensory input spike trains were convoluted using a kernel function (see section "Materials and Methods") to create input that resembles post-synaptic potentials. Note that the input to the LSM neuron can exceed 1 a.u., while the output of the LSM neuron cannot. Calibration applies to **(C–E)** (traces in the shaded region). **(E)** The input from summation of the excitatory and inhibitory inputs. **(F)** LSM (without dynamic leak, $\mathbf{k_{static} = 1}$) output activity for the given PSP inputs. Calibration applies to **(F–G)**. **(G)** LSM (with dynamic leak, $\mathbf{k_{static} = 1}$, $\boldsymbol{\tau_{dyn} = 1/100\ s}$) output activity for the given PSP inputs.

In **Appendix 1**, we show that the LSM neuron model can be derived from a simplified H-H type conductance-based neuron model. In the H-H model, the leak is proportional to the membrane voltage and the synaptic currents are scaled depending on the membrane voltage, so that the voltage is limited to a fixed range. The differential equation describing this model suffers from numerical instability, therefore we solve it with the implicit Euler method. The model is simple enough so that an analytical solution can be obtained. Key H-H model features that are captured by the LSM neuron: (*i*) the response to a given input scales with the difference between the current activity level (membrane potential, V) and the reversal potentials of the excitatory/inhibitory inputs (which have been normalized to +1 and -1, respectively); and (*ii*) the impact of a given input is scaled by the degree of the shunting caused by the total synaptic activity the neuron receives at that time.

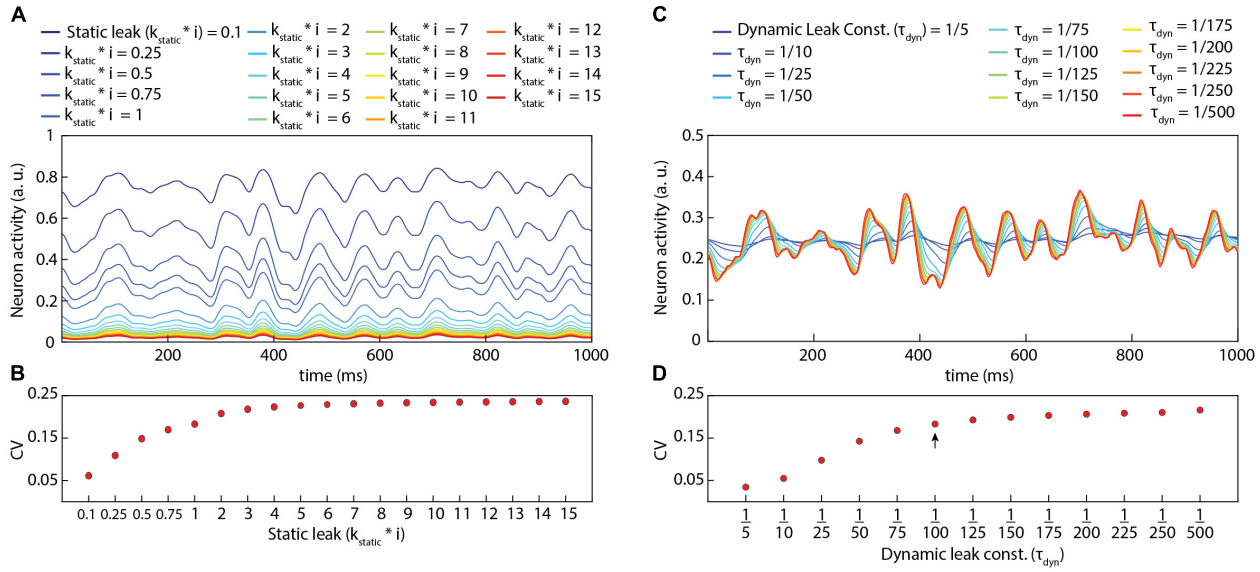

FIGURE 2 | Impact of static leak ($\mathbf{k_{static}}$) and dynamic leak constant ($\boldsymbol{\tau_{dyn}}$) in LSM. **(A)** Impact of the value of $\mathbf{k_{static}}$ in the LSM (for $\boldsymbol{\tau_{dyn}}$ = **1/100**) for a given pseudo-random sensory input at 50 Hz for each of six sensors (see **Figure 3**). **(B)** The perseverance of dynamics in the neuron activity **(A)** for varying $\mathbf{k_{static}}$ value as assessed by the coefficient of variation [CV = σ(A)/Ā]. A higher value of CV indicates a higher activity variance relative to the mean activity. **(C)** Impact of the value of $\boldsymbol{\tau_{dyn}}$ in the LSM (for $\mathbf{k_{static}}$ = **1**) for the same pseudo-random sensory input as in **(A)**. **(D)** The CV as a function of the value of the dynamic leak ($\boldsymbol{\tau_{dyn}}$) in the LSM. The arrow indicates the value of $\boldsymbol{\tau_{dyn}}$ used in rest of this paper unless otherwise specified.

Izhikevich Neuron Model (IZ)

For the Izhikevich neuron model (Izhikevich, 2003), the membrane potential (IZ_v) and the adaptation variable (IZ_u) were updated via the following nonlinear differential equations discretized using Euler's method.

$$\dot{IZ_v} = IZ_A IZ_v^2 + IZ_B IZ_v + IZ_C - IZ_u + (IZ_{input} * IZ_k) \quad (4)$$

$$\dot{IZ_u} = IZ_a(IZ_b IZ_v - IZ_u)$$

When the membrane potential reached the spike depolarization threshold of 30 mV, one spike was produced followed by a reset:

$$if\, IZ_v \geq 30mV, then \begin{cases} IZ_v \leftarrow IZ_c \\ IZ_u \leftarrow IZ_u + IZ_d \end{cases} \quad (5)$$

The IZ_A, IZ_B, andIZ_C parameters and the spiking threshold were the standard ones of the Izhikevich artificial neuron model, whereas the parameters IZ_a, IZ_b, IZ_c, and IZ_d were selected (**Table 1** and **Figures 3E,F**) to mimic a regular spiking behavior (Izhikevich, 2003, 2004). IZ_{input} was the input current to the neuron model, that was weighted synaptic activity ($\mathbf{w}*\mathbf{a}$) in this article and IZ_k is the input gain factor.

Further, to analyze the IZ model behavior across different spiking and bursting behaviors, we have explored the parametric space (**Table 2** and **Figure 3G**) of IZ_a, IZ_b, IZ_c, IZ_d, and IZ_k (parameters in Eqs. 4, 5) within the boundaries identified in Izhikevich, 2003. We investigated the IZ neuron model responses (**Figure 3G**) across 405 different parameter settings for each given input spike frequency. The parameter space was defined by the possible combinations of parameters listed in **Table 2**.

Network Connectivity

Our network was a two-layer fully connected neuronal network that comprised both inhibitory neurons (*IN*) and excitatory neurons (*EN*) (**Figure 4A**). This network configuration provides a simple system that includes the critical element of recurrency. The network architecture is defined based on the following two rules: (*a*) The sensory inputs are projected as excitatory synapses to all neurons in layer 1 only; (*b*) All excitatory and inhibitory neurons were fully reciprocally connected both within and between layers. Most of the analysis reported here utilized a "5 × 4" network architecture (five ENs and five INs in layer 1 and four ENs and four INs in layer 2). In the analysis of **Figure 8**, where different network sizes were explored, we simply scaled up the number of neurons in each layer using the same connectivity rules (**Figure 8**).

A two-layer, fully reciprocally connected neuronal network architecture with self-recurrent connections (autapses) was also investigated. In this specific network architecture, in addition to the network connectivity defined above, the excitatory neurons

TABLE 1 | Izhikevich neuron model parameters used in the evaluation of this study (for the IZ model responses presented in **Figures 3EâĂŞ-F** and **Supplementary Figure 3)**.

IZ_A	IZ_B	IZ_C	IZ_a	IZ_b	IZ_c	IZ_d	IZ_k
0.04	5	140	0.02	0.2	−65	8	300

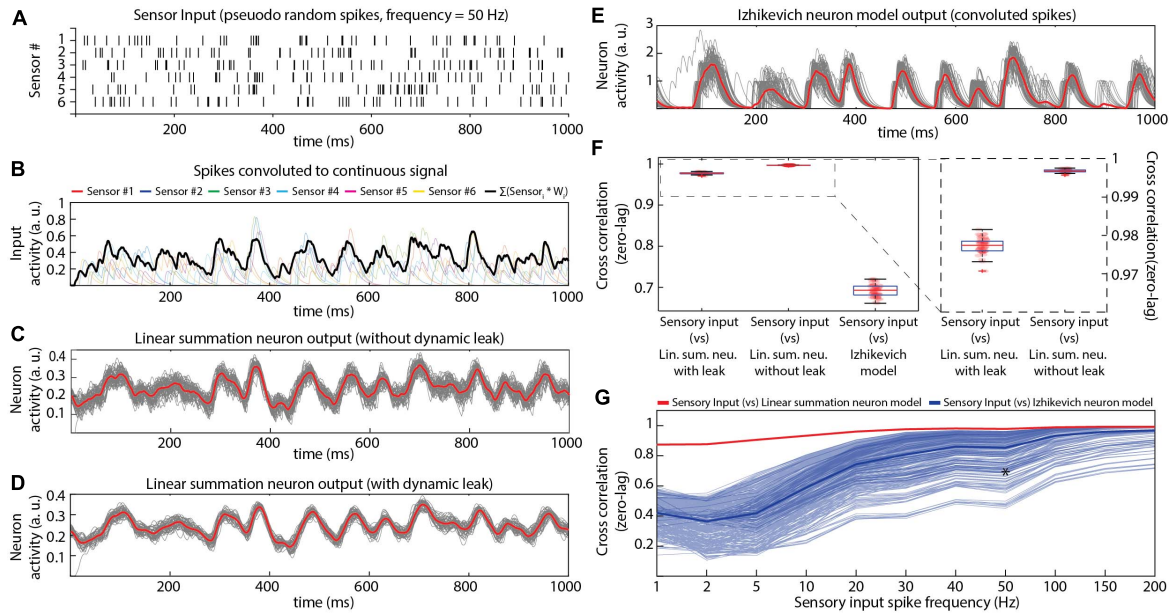

FIGURE 3 | Comparing the properties of different neuron models in isolation. **(A)** Pseudo-random input spike trains (six spike trains corresponding to the six sensory inputs, with an average spike frequency of 50 Hz in each sensor). **(B)** The sensory input spike trains were convoluted using a kernel function (see section "Materials and Methods"). The convoluted input responses were fed as weighted (randomly generated, mu = 0.4) EPSP inputs to the neuron model. **(C)** Output responses of the LSM without dynamic leak. The red line is the mean across 50 presentations (each presentation made different by adding Gaussian noise, black lines). In this and all panels below, tests were made for the neuron in isolation, without network connections. **(D)** Similar display as in **(C)**, but for LSM with dynamic leak. **(E)** Similar display as in **(C)**, but for output responses of Izhikevich neuron model. The spike output of the Izhikevich neuron model were convoluted using a kernel function (same kernel parameters setting as in **(B)**. **(F)** Cross-correlations between the sensory input and the output responses of neuron models (illustrated in **C–E**). **(G)** Cross-correlation between different sensory input frequencies and neuron model outputs across a range of IZ model settings, compared to the LSM with dynamic leak. Thin blue lines indicate the cross-correlation with the sensory input for the IZ neuron model responses for each of the 405 IZ model parameter settings ($\mathbf{IZ_a}$, $\mathbf{IZ_b}$, $\mathbf{IZ_C}$, $\mathbf{IZ_d}$, and $\mathbf{IZ_k}$; see section "Materials and Methods") tested. Thick blue line indicates the mean of those cross-correlations. The red line indicates the cross-correlation between the sensory inputs and the LSM outputs. Asterisk indicates the cross-correlation measure for the parameters chosen in **Figure 3F**.

projected excitatory synaptic connections onto themselves, and inhibitory neurons projected inhibitory synaptic connections onto themselves (**Supplementary Figure 7A**).

Sensory Inputs

In this article, we investigated the individual neuron responses (**Figures 2**, **3** and **Supplementary Figures 1–4**) and network dynamics (**Figures 4–8** and **Supplementary Figures 6**, **7**, except **Figures 7C,D**) based on six sensory inputs. These sensory inputs were pseudo-randomly generated (see below) and provided as excitatory input to both excitatory and inhibitory neurons. We also tested our recurrent networks with higher input sensor density (#sensors = 6, 15, 30, and 50, **Figures 7C,D**), the inputs of which were also pseudo-randomly generated.

Pseudo-Random Inputs

For the sensory inputs to the LSM and the IZ neurons, we generated pseudorandom spike trains for several different average frequencies (50, 100, 150, and 200 Hz, **Figure 3A** and **Supplementary Figure 4**) with uniform normal distributions. We used an inbuilt MATLAB function "*randi*" to generate the spike time distributions in these spike trains. Furthermore, these spikes were convoluted to resemble post-synaptic-potentials

TABLE 2 | Izhikevich neuron model parametric space explored in the evaluation of this study (for the IZ model presented in **Figure 3G**).

IZ_a	0.02	0.07	0.1	–	–
IZ_b	0.2	0.225	0.25	–	–
IZ_c	−65	−55	-50	–	–
IZ_d	2	4	8	–	–
IZ_k	100	200	300	400	500

(time continuous activity) using the following kernel equation (Mazzoni et al., 2008),

$$\mathbf{a_i} = \frac{\tau_{km}}{\tau_{kd}-\tau_{kr}} * \left[exp\left(\frac{-t-\tau_{kl}-t^*}{\tau_{kd}}\right) - exp\left(\frac{-t-\tau_{kl}-t^*}{\tau_{kr}}\right)\right] \quad (6)$$

Where, t^* is the input spike time,τ_{kd} is the decay time (4 ms),τ_{kr} is the rise time (12.5 ms) and τ_{km} is the constant to calculate ration between rise time and decay time (21.3 ms), and τ_{kl} is the latency time which is zero in this case. These values were chosen based on the previous work (Rongala et al., 2018). The convoluted sensor signal was then provided as synaptic input to the neuronal network.

In order to analyze the network dynamics, we provided 50 presentations of the same pseudorandom spike trains

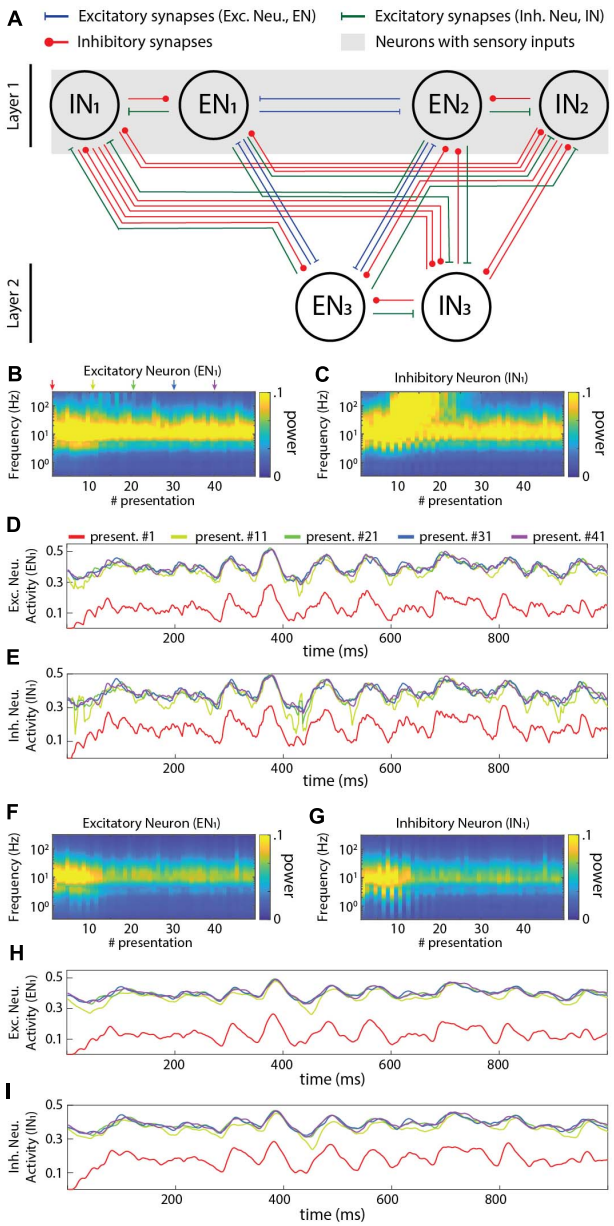

FIGURE 4 | Activity dynamics in a sample recurrent network. **(A)** Principles of the connectivity structure in the recurrent network studied. Note that the default network, and the one used in panels **(B–I)** of this figure, contained excitatory neurons (five in the input layer, four in the output layer) and inhibitory neurons (same numbers) with the same connectivity, whereas only the neurons in layer 1 also received sensory inputs (the same six sensory inputs to each neuron) with all synapses having randomly generated Gaussian weights (mu = 0.4). **(B)** Frequency plot of the activity in an excitatory neuron. **(C)** Similar plot for an inhibitory neuron. **(D)** Raw data plots for sample signals in the excitatory neuron generated at the indicated presentation #. **(E)** Similar plot for the inhibitory neuron. **(F–I)** Similar plots as in **(B–E)** but when all the neurons were modeled to include the neuronal dynamic leak.

(for each given average frequency). Each input presentation differed by an addition of random noise of ±10 ms to individual spike times (**Figures 3C–E**, black lines) to the reference pseudorandom spike train (**Figure 3A**, for spike frequency of 50 Hz). These presentations were concatenated without pause or reset between them, so the input subdivided into 50 presentations was in effect one long presentation lasting for 50,000 ms.

To allow a comparison with the output of the LSM, we convoluted the output spike trains also of the spiking neuron model (IZ). The process of convolution emulated a post synaptic response that would have been generated in a receiving neuron, whereas the LSM output itself directly corresponded to such a signal.

Synaptic Weights

All excitatory and inhibitory synaptic weights in the network were randomly distributed, including the excitatory sensory inputs to only the layer 1 neurons. The synaptic weight distributions were either normal, lognormal or binary. The normal and the log-normal distributions were generated for different mean weights (μ) (values between 0.1 and 0.5) each with a fixed coefficiency of variation (cv) of 20% [where sigma (σ) $=$ (cv / 100)*μ]. For binary distributions, we tested different probabilities of high weight synapses ($w = 1$) (probability varied between 10 and 50%), whereas the remainder of the synapses were set to zero weight (**Figures 5A–C**).

Statistical Analysis

Cross-Correlation

The correlation index measure was used to compute the similarity of the responses of the neuron models (**Figures 3F,G** and **Supplementary Figure 4E**). The correlation between two signals was computed with an inbuilt MATLAB function "*xcorr*" (with zero lag), which produces values from 0 (uncorrelated) to 1 (identical).

Frequency Analysis

We performed a continuous wavelet transform (using an inbuilt MATLAB function "*cwt*") in order to define the frequency composition of the input signal over time. The wavelet transform was used to extract the power of each frequency band as a function of time for the continuous neuron activity signal. Here, we reported (**Figures 4–8** and **Supplementary Figures 5–7**), for each frequency band, the maximum power of the signal within each input presentation time window (1 s).

In **Supplementary Figure 5**, the frequency analysis was performed on the sensory input signals (on the convoluted signal for each given average spiking frequency) across all the 6 sensory inputs for all 50 presentations (see section "Materials and Methods"). The maximum power was computed for each sensory input and each presentation, and the average across all six input sensors was reported in this figure.

In **Figure 4**, the frequency analysis was performed on the activity of one excitatory and one inhibitory neuron in layer 1 (**Figures 4B,C,F,G**) across all frequencies and presentations. **Supplementary Figure 6** display the frequency analysis performed on the activity of all excitatory and inhibitory neurons in the network of **Figure 4A**. A similar frequency analysis was carried out in **Figures 5–8** and **Supplementary Figure 5**, which show the average maximum power calculated across all neurons in all layers and across all 50 presentations.

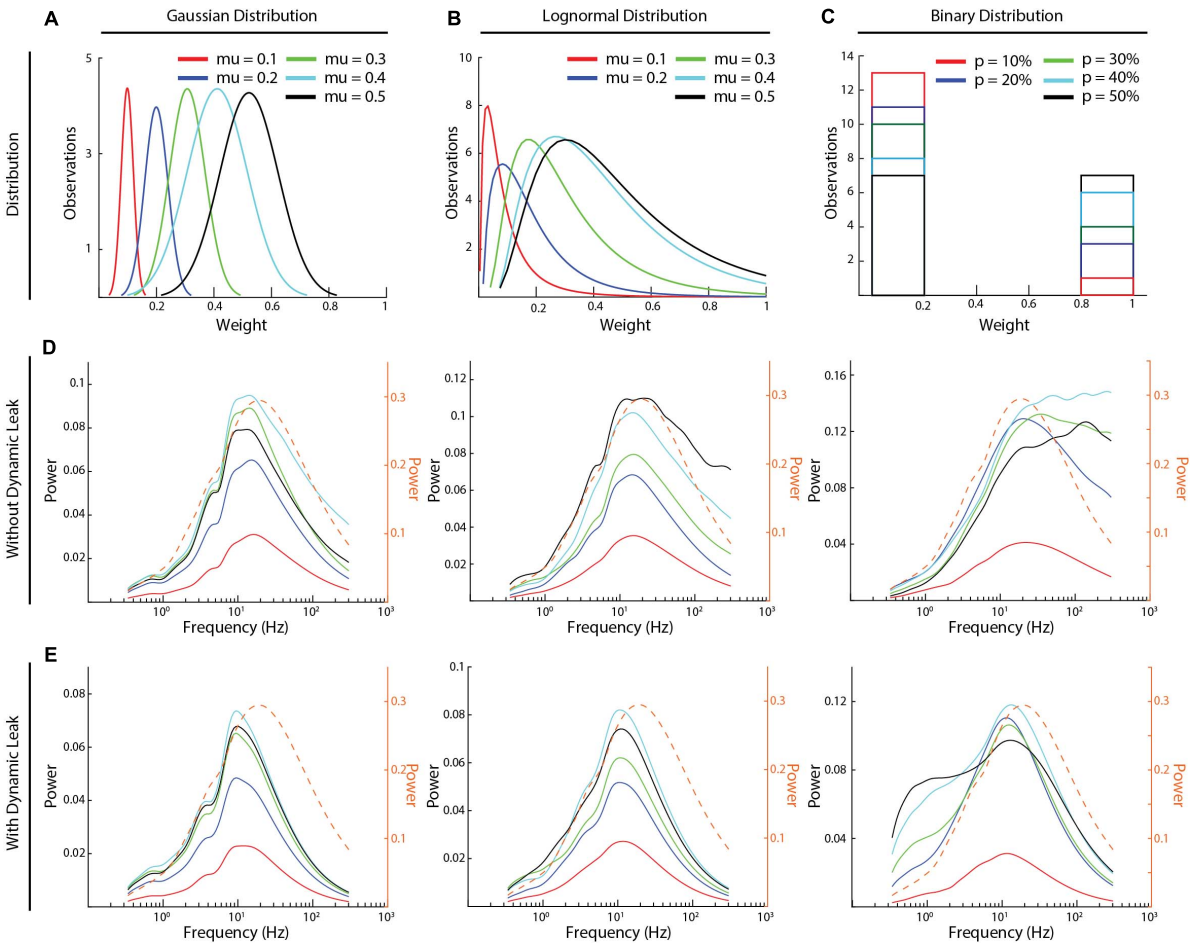

FIGURE 5 | High frequency components and the effect of dynamic leak across different synaptic weight distributions. **(A–C)** The three types of synaptic weight distributions that were explored (Gaussian, Log-Normal, and Binary) and the average weight distributions for each mean weight value (five weight distributions were generated for each mean weight). **(D)** The frequency power distributions across all the above synaptic weight distributions. Color keys for the different average synaptic weights are in **(A–C)**. **(E)** Similar display as in **(C)**, for the same networks but with the neuron model with dynamic leak. Dashed orange traces in **(D,E)** show the corresponding frequency power distribution for the sensory inputs at 50 Hz, averaged across the six sensory inputs, for comparison.

RESULTS

Comparison to Spiking Neuron Models

We first characterized the input-output relationship of the neuron model in isolation (**Figure 3**) for a standardized sensor input, consisting of randomized spike times in six sensor neurons that were convoluted to time-continuous input signals. These were synaptically integrated by a single modeled neuron (**Figures 3A,B**). The activity of the non-spiking LSM (linear summation neuron model) was compared with that of a spiking neuron model (Izhikevich, IZ), in terms of how well their output (**Figures 3C–E**) correlated with the input (**Figure 3F**). The IZ neuron model was chosen for this comparison, as it was created to mimic a rich neuronal response dynamics with computational efficiency (Izhikevich, 2003). The spikes generated by the IZ neuron model were convoluted (see section "Materials and Methods") to a time continuous signal (**Figure 3E**) in order for it to be comparable with the output of the LSM.

Both neuron models (LSM and IZ) were provided with the same pseudo-random sensory inputs (average firing frequency of 50 Hz in each of six sensors, see section "Materials and Methods") connected via six different synapses (**Figure 3B**). The IZ neuron model parameters for this particular comparison (**Figures 3E,F**) were chosen to mimic the regular spiking behavior (hypothesized to be a common neuron behavior in cortex; Izhikevich, 2003, 2004). The LSM neuron without dynamic leak reproduced on average a close representation of the source convolution signal for the input but the individual traces were considerably noisier without dynamic leak (**Figure 3C**) than with dynamic leak (**Figure 3D**). The main difference between the LSM and the IZ neuron model responses was that the IZ neuron model tended to create output dynamic behavior that was not present in the input signal (**Figures 3B,E**), a consequence of the binary nature of the spike output. A cross-correlation analysis between the neurons' responses (**Figure 3F**) showed that the IZ neuron model reflected the input signal less faithfully than the LSM. Note that

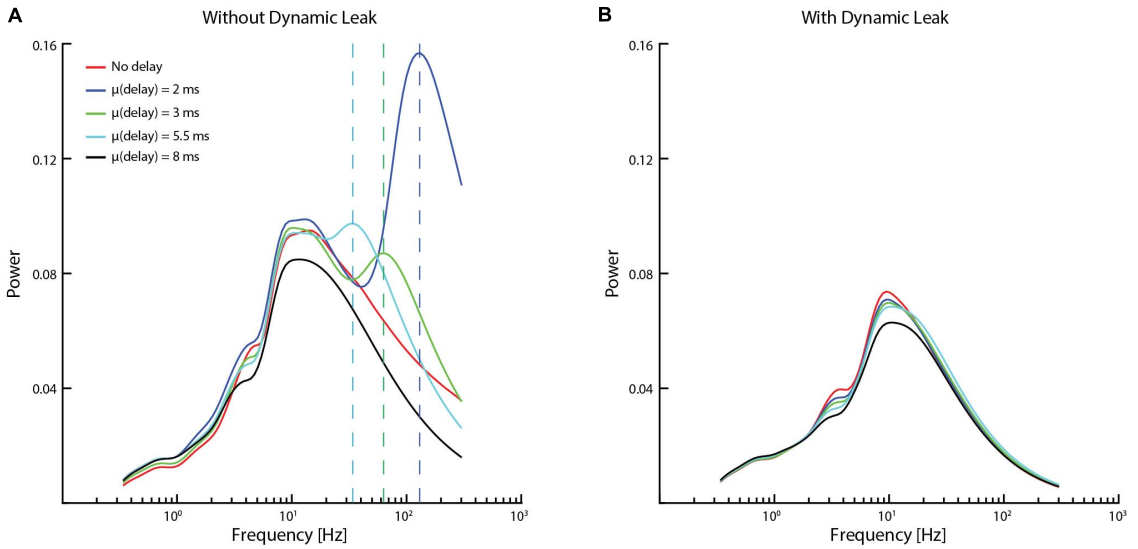

FIGURE 6 | Impact of conduction delays on the frequency distribution. **(A)** Frequency distributions for the same network (network settings as in **Figure 4**) with different average conduction delays between neurons. The vertical dashed lines indicate the supplementary frequency peaks (frequency peaks that were not present in the input sensory data / network dynamics without conduction delays) of the high-frequency component for addition of a mean conduction delay to the network. **(B)** Data for the same networks and delays when the neuron model included dynamic leak.

the cross-correlation is slightly poorer for the LSM with dynamic leak than without, which is due to that the some of the fine-timing details of the high frequency components of the underlying convoluted signal is slightly filtered by the dynamic leak.

We tested if this observation depended on the frequency of the spiking in the sensory inputs. The LSM consistently showed a higher correlation with the input signal than the IZ neuron model across a range of input spike frequencies (**Supplementary Figure 3**). Next we tested if the specific parameters chosen for the IZ neuron model (**Figure 3E**, also indicated by an asterisk in **Figure 3G**) were responsible for these results (**Figure 3F**). Therefore, we tested a range of parameter settings (405 different parameter combinations), which are known to reproduce specific output dynamics (bursting, for example) observed in a variety of neuron types *in vitro* (Izhikevich, 2003). The correlation analysis showed that LSM was more consistent than the IZ model in maintaining high correlation with the sensory inputs across the full range of sensory input spike frequencies (**Figure 3G**). The exception was the highest sensory input frequencies, but that can be explained by that the dynamics of the sensory input diminishes due to the density of the inputs (**Supplementary Figures 3A–D**), as previously described also for neurons *in vivo* (Bengtsson et al., 2011). This effect, which we will refer to as the input density problem, is also evident in **Figure 3G**.

Network Dynamics (With and Without Neuronal Dynamic Leak)

We next investigated the activity dynamics of a standardized recurrent neuronal network implemented using the LSM (**Figure 4A**). The sensory input was fed as excitatory input to both the excitatory and inhibitory neurons of the first layer for 50 presentations, where the sequential presentation differed by added Gaussian noise to the sensory signal (see section "Materials and Methods"). In the network with the neuron model without dynamic leak, there was initially a gradual increase in the power across the higher frequency components of the activity in both excitatory and inhibitory neurons (**Figures 4B,C**) (more extensively illustrated in **Supplementary Figure 6**, where the first few presentations of sensory input evoked a lower power response). These high frequency components were not present in the sensory input (**Supplementary Figure 5A**) and were therefore generated by the network, most likely as a consequence of the parallel excitatory and inhibitory connections, which would be expected to lead to some degree of signal derivation (Wehr and Zador, 2003). Interestingly, in the illustrated IN1 the high frequency components gradually built up (until presentation #10, approximately) and then faded away (after presentation #20, approximately), despite that the average intensity of the sensory input did not vary over time, which suggests a relatively rich internal dynamics in this type of recurrent network, despite its limited size. In neurons of the second layer, high frequency components typically faded away more slowly (**Supplementary Figure 6**). The appearance of these high frequency components was sometimes associated with the appearance of transients in the neuron activity (**Figures 4D,E**). In contrast, in the same network but with the neuron model including the dynamic leak, the transients and the high-frequency components of the neuron activity disappeared (**Figures 4F–I**). Hence, the low-pass filtering effect of the dynamic leak "rescued" the recurrent network from generating spurious high-frequency components.

The recurrent connections of the network were likely strongly contributing to these high-frequency components. An extreme case of recurrent connectivity is when a neuron

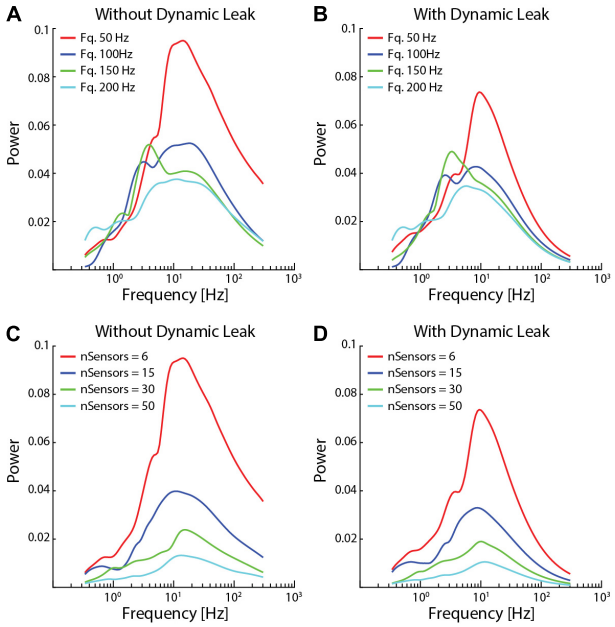

FIGURE 7 | Network activity dynamics increased when sensor input density decreased. **(A)** The high frequency components became more prominent with lower average spike frequencies in the sensor input. **(B)** Neuronal dynamic leak resulted in disappearance of the high-frequency components across all input spike frequencies. **(C)** The high frequency components also became more prominent with lower number of sensory inputs, while a very high number of sensor inputs substantially reduced overall neuron activity dynamics. **(D)** Introduction of neuronal dynamic leak resulted in disappearance of the high-frequency components irrespective of the number of sensory inputs. The network settings for this analysis were similar to **Figure 4**, except for sensory input.

makes synapse on itself (autapse). It is not clear to what extent autapses exist in adult neuronal circuitry, but they have been shown to be present in early development (Lübke et al., 1996; Tamás et al., 1997) and they are widely used in the field of RNN/computational neuroscience (Graves, 2012). To explore the impact of autapses we used the exact same network architecture used in **Figure 4** but added autapses to all neurons (**Supplementary Figure 7A**). In this scenario, the high-frequency components were strongly amplified (**Supplementary Figures 7B–E**). However, in the same network with the neuron model with the dynamic leak, the transients and the high-frequency components of the neuron activity were again effectively removed (**Supplementary Figures 7F–I**). We did not explore networks with autapses any further.

We next compared the frequency power distributions of the neuronal activity in this recurrent network across a range of different synaptic weight distributions (**Figure 5**). We studied three different types of synaptic weight distributions (Gaussian, log-normal, and binary distributions). For each type of distribution, we tested five different mean synaptic weights (**Figures 5A–C**). Moreover, for each given synaptic weight distribution and mean weight, we generated five random weight distributions. The average signal of these five random weight distributions was used to calculate each frequency power distribution illustrated (**Figures 5D,E**), where each line represents the average activity across all the neurons of the network (**Figures 5D,E**). In the network with the neuron model without dynamic leak (**Figure 5D**), the relative power of the high-frequency components was amplified for synaptic weight distributions at mean synaptic weights of 0.3–0.4 or above ($\mu \geq 0.4$ for Gaussian and $\mu \geq 0.3$ for log-normal distributions) and for $p > 10\%$ for binary distribution, compared to the sensory input (**Supplementary Figure 5**). For other synaptic weight distributions ($\mu = 0.1$ for Gaussian and log-normal distributions and for $p = 10\%$ for binary distributions, for example), there was much lower overall activity in the network, which could be the reason why the high frequency components were not induced in these networks. In the network with the neuron model with the dynamic leak component, the transients and the high-frequency components of the neuron activity disappeared for all settings (**Figure 5E**), though the setting of the dynamic leak component used also appeared to over-dampen the sensory input dynamics between 20 and 200 Hz. Note that each curve in **Figures 5D,E** represents the mean across five randomized repetitions. **Supplementary Figure 8** instead shows the frequency power distribution of the neuronal activity for each individual network sorted by synaptic weight distribution. The overlap between these frequency power distribution curves across randomized weights and different distribution means implies that there was no simple linear relationship between the network structure and the spurious high frequency components.

To further explore if the high-frequency components observed were induced by the recurrent network, we tested if we could affect the "center of gravity" of the high-frequency components by introducing different conduction delays in signal transmission between the neurons (**Figure 6**). In the brain *in vivo*, these would correspond to the axonal conduction delays and synaptic delays combined. The delays were randomized between all the neurons, and several different mean delays were tested in different simulations. Interestingly, a supplementary frequency peak component (frequency peaks that were not present in the input sensory data / network dynamics without conduction delays, indicated with dashed vertical lines in **Figure 6A**) was observed without dynamic leak. These supplementary frequency peaks were approximately inversely proportional to the mean conduction delay. From previous studies (Jirsa and Stefanescu, 2011; Petkoski et al., 2018) we know that conduction delays could introduce such additional dynamics into the recurrent networks. These peaks were removed by adding dynamic leak (**Figure 6B**).

The high frequency components also appeared for lower average sensor input spike frequency (50 and 100 Hz, **Figure 7A**) and for lower number of sensory inputs per neuron (nSensors = 6 and 15, **Figure 7C**). In contrast, for higher input spike frequencies (150 and 200 Hz) and higher number of sensory inputs (nSensors = 30 and 50) the increased density of the inputs resulted in a paradoxical decrease in the power of the neuron activity across all frequencies analyzed (i.e., as shown in **Supplementary Figure 1**), most likely due to the large number of randomized inputs regressing toward the constant mean frequency of each sensory signal. In each case, in the network

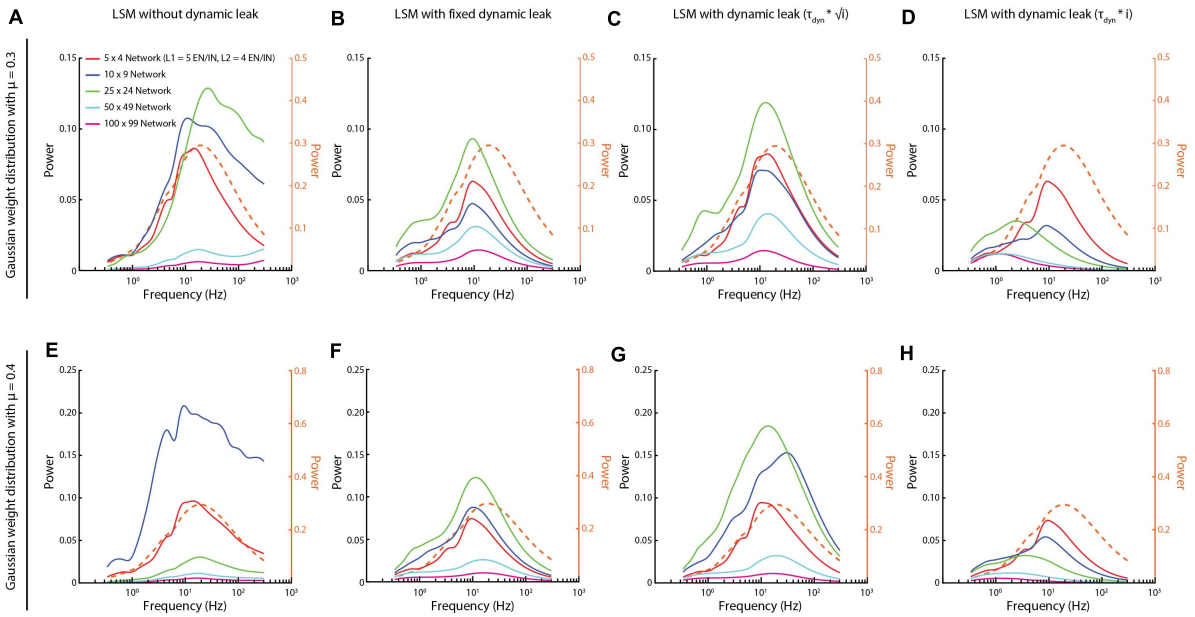

FIGURE 8 | Activity frequency distributions altered with the scale of the networks. **(A,E)** For networks with Gaussian synaptic weight distribution of mean weight mu = 0.3 and 0.4, respectively, the high frequency components could appear without dynamic leak, regardless of network size. **(B,F)** Introduction of the neuronal dynamic leak (τ_{dyn} = **1/100**) "rescued" the networks from these high-frequency components. **(C,G)** The dynamic leak constant was adapted based on the square root of number of synapses (i). **(D,H)** The dynamic leak constant was adapted based on the total number of synapses (i). Dashed orange traces in all plots show the corresponding frequency power distribution for the sensory inputs at 50 Hz, averaged across the six sensory inputs, for comparison.

with the neuron model with the dynamic leak component, the high-frequency components of the neuron activity disappeared for the sensor input configurations where it had been present (**Figures 7B,D**).

We also explored if the size of the network could be a factor for the appearance of the high frequency components. We found that these high frequency components appeared for different network sizes and that in those cases the network activity was "rescued" when the LSM was implemented with the dynamic leak (**Figure 8**). Depending on the specific synaptic weight distribution, the high frequency components became unequally dominant for different network sizes (**Figures 8A,E**) according to unclear relationships. The largest network as a rule had the weakest overall dynamics, which could be due to the same input density problem discussed above, where the density of synaptic input increased as the larger network has a higher number of recurrent synaptic inputs per neuron, which caused the dynamics of the neuron activity to go down. As there is a tendency for membrane time constants to grow with the size of the neuron (Zhang, 2004), we scaled the τ_{Dyn} with the network size (as the neurons of the larger networks had a higher number of synapses) (**Figures 8C,D,G,H**, for two different weight distributions). A moderate scaling of the τ_{Dyn} (with the square root of the number of synapses, **Figures 8C,G**) actually increased the dynamics of some network sizes, while eliminating high frequency components. In contrast, a linear scaling (**Figures 8D,H**) instead appeared to dampen such dynamics and, unsurprisingly, low pass-filtered also signals well below 100 Hz for the largest networks.

DISCUSSION

We explored the properties of a non-spiking neuronal model derived from the differential conductance-based H-H model when deployed in various recurrent neuronal networks. We found that in these recurrent networks, many different factors would tend to trigger network induction of high frequency signal components of a somewhat unpredictable magnitude and distribution (i.e., **Figures 5–8** and **Supplementary Figure 8**). These signal components were not present in the input data (**Supplementary Figure 5**) and sometimes peaked to create overt spurious transients (**Figures 4B,C**). The dynamic leak in our neuron model invariably "rescued" the recurrent networks from their tendency to self-generate these high-frequency signal components (**Figures 4–8** and **Supplementary Figure 7**). Corresponding to the capacitive component and the ion channels of the membrane circuit, dynamic leak is an inevitable feature of real neurons. Furthermore, this low-pass filter component made the behavior of recurrent networks more predictable for networks of different sizes.

We worked under the scenario that neuronal networks in the brain are recurrent and that excitatory and inhibitory connections are both pervasive, without any a priori assumed structure. Our network architecture contained the circuitry elements of previously reported "classical" network connectivity patterns (feedback and feedforward inhibition, for example). Feed-forward and feedback inhibition running in parallel with excitatory connections was likely the main network feature that caused the signal derivation effects/the high frequency

components in the networks without the dynamic leak. The inclusion of autapses in the recurrent network strongly amplified these high frequency components (**Supplementary Figure 7**), presumably primarily through self-amplification of excitatory neurons. But note that in a recurrent network, any local circuity feature will at the global level automatically result in other functional network features as well. Hence, in contrast to a non-recurrent, feed forward neuronal network, in a recurrent network these circuitry features will hence become less clear-cut from a functional point of view, which could cause additional dynamic network effects that for example could explain our observations of gradual build-up of high frequency power components (**Figure 4** and **Supplementary Figure 5**) while there was steady sensory input level to keep the network activity up. However, understanding such network dynamics at a deeper level was outside the scope of this paper, but would need to be addressed if such networks are to be used in a functional setting.

In our recurrent networks, apparently spurious high frequency components could be induced for different types of synaptic weight distributions, delays between neurons, sensory input densities and network sizes. It was hard to predict under what exact conditions such high frequency components would become more or less dominant (i.e., **Figure 8** and **Supplementary Figure 8**), but in each case the dynamic leak effectively canceled them out. From the point of view of the functionality of a processing recurrent network, the fact that the frequency distribution of any given network did not match that of the sensory input is not automatically to be considered a disadvantage because the goal of a processing network would not be to perfectly replicate the sensory input. However, the fact that these high frequency components sometimes took the shape of clear-cut transients with no obvious counterpart in the sensor signal suggests that, at least in part, they should be considered spurious, i.e., noise injected into the signal due to the dynamics of the specific network.

In some cases, the activity of the network became highly suppressed relative to the sensory input (i.e., for low mean weights in **Figure 5** and for the largest network in **Figure 8**). This effect can be ascribed to the input density problem, i.e., when too many unrelated but continuously active synaptic inputs converge on the same neuron, their signal dynamics would tend to cancel out, leaving the neuron with very little signal dynamics (Bengtsson et al., 2011). As these signals, due to the network structure, are paralleled by inhibitory connections, when the signal dynamics is lost, inhibition and excitation cancel each other out and the activity dynamics is lost in the network as a whole.

How would spiking neuron networks fare with respect to rescuing a recurrent network from spurious high frequency components? The phasic nature of discrete spike output would be expected to worsen the problem, whereas refractoriness would tend to dampen it. Refractoriness could certainly rescue the system from the extreme transients observed in networks that included autapses. Refractoriness, however, would not rescue the system from high frequency components generated through longer range recurrent excitatory loops.

Global stability has long been a concern in recurrent neural networks (RNNs) due to the non-linear dynamics that can arise within such networks due to the recurrency and the resulting feedback loops (Shen and Wang, 2011; Zhu and Shen, 2013). Periodic oscillations and stability issues in RNNs can arise, for example, as a consequence of input noise (Pham et al., 1998) and neuron activation delays (Gopalsamy and Leung, 1996). Moreover, such oscillations are inherent to any dynamical system with recurrency and amplification, such as parasitic oscillations in electronics and steady-state error in control theory. Apparently, the central nervous system, with prodigious recurrent loops (see section "Introduction") and intrinsic noise, found a way to avoid such oscillations. In this study we explored the possibility that neuronal leak dampens such oscillations in a recurrent neuronal network.

Recurrent neuronal networks with balanced excitatory and inhibitory synaptic connections have been extensively studied previously (Brunel, 2000; Vogels and Abbott, 2005; Vogels et al., 2011; Rubin et al., 2017), using spiking neuron models (employing integrate-and-fire or related mechanisms for the spike generation). In these studies, the recurrent connections were sparsely distributed with an overall connection probability of 1–2%, and a ratio of 4:1 excitatory to inhibitory interneurons. These studies point out that factors such as high connection probability and unbalanced excitation-inhibition tend to produce network instability (Rubin et al., 2017) and in some cases failure in signal propagation across the layers of those neuronal networks (Vogels and Abbott, 2005). From the stability we observed across a wide range of recurrent network configurations, always at 100% connection probability (though weighted), it would seem that the LSM with dynamic leak would be beneficial for ensuring stable recurrent neuronal network behavior across a range of network sizes and density of connectivity.

The present findings suggest that the biological feature of neuronal dynamic leak, which causes the polarization (i.e., the activity) of the neuron to settle toward resting potential with a time constant, is an important functional feature. It allows brain networks to fully utilize recurrent neuronal network architectures with variable numbers of participating neurons without risking self-generated noise embodied as high frequency components and spurious transients.

DATA AVAILABILITY STATEMENT

The original contributions presented in the study are publicly available. This data can be found here: https://figshare.com/projects/Non-Spiking_Neuron_Model_With_Dynamic_Leak_Rongala_et_al_2021_/112854. Further inquiries can be directed to the corresponding author/s.

AUTHOR CONTRIBUTIONS

UR: design of study, design of model, data analysis, and writing the manuscript. JE and MK: design of model. GL: design of model and writing the manuscript. HJ: design of study, design of model, and writing the manuscript. All authors contributed to the article and approved the submitted version.

FUNDING

This work was supported by the EU Grant FET 829186 ph−coding (Predictive Haptic COding Devices In Next Generation interfaces), the Swedish Research Council (Project Grant No. K2014-63X-14780-12-3).

SUPPLEMENTARY MATERIAL

The Supplementary Material for this article can be found online at: https://www.frontiersin.org/articles/10.3389/fncom.2021.656401/full#supplementary-material

Supplementary Figure 1 | Signal similarity between the LSM and H-H model. A comparison between the output responses for LSM (green line is the mean across 50 presentations) and the H-H (derived using backward Euler method, blue line is the mean across 50 presentations), for a given pseudo-random sensory input at 50 Hz for each of six sensors (see **Figure 3**). The responses of the LSM output were offset by 0.1 activity (a.u.) in order to visualize the coherence between the responses of both neuron models. The cross correlation (with zero lag) was 0.99.

Supplementary Figure 2 | Impact of the value of k_{static} on the internal activity of the LSM for a given sensory input.

Supplementary Figure 3 | Impact of the value of τ_{dyn} on the internal activity of the LSM for a given sensory input.

Supplementary Figure 4 | Comparison of the non-spiking and the spiking neuron model outputs for different sensory input frequencies. **(A–D)** Neuron outputs in response to different sensory input frequencies. **(E)** Cross-correlation between sensory inputs and the neuron model outputs.

Supplementary Figure 5 | Frequency analysis of the sensory inputs. **(A)** Time-continuous frequency power analysis for each of the six sensory inputs (spike frequency = 50 Hz) across the 50 presentations used in the analysis of the network activity. **(B)** Frequency power analysis (using continuous wavelet transform, see section "Materials and Methods"), of sensory inputs. The plots show the average power of the activity across all the six sensors, for each of the four mean sensor firing frequencies, across all 50 presentations used in the analysis of the network activity.

Supplementary Figure 6 | Frequency analysis plots of the activity in all excitatory neurons ($EN_1 - EN_9$) and inhibitory neurons ($IN_1 - IN_9$) for the network shown in **Figure 4A**.

Supplementary Figure 7 | Activity in recurrent networks with autapses. **(A)** Principles of the connectivity structure in the recurrent network studied. The network presented here is a fully connected network as in **Figure 4**, with the addition of self-recurrent excitatory and inhibitory synapses (in excitatory and inhibitory neurons, respectively). **(B)** Frequency plot of the activity in an excitatory neuron. **(C)** Similar plot for an inhibitory neuron. **(D)** Raw data plots for sample signals in the excitatory neuron generated at the indicated presentation #. **(E)** Similar plot for the inhibitory neuron. **(F–I)** Similar plots as in **(B–E)** but when all the neurons were modeled with the dynamic leak.

Supplementary Figure 8 | High frequency components and the effect of dynamic leak across different specific synaptic weight distributions. The synaptic weight distributions used were as shown in **Figures 5A–C**, but instead of representing the five random simulations for each setting as an average, we here show them individually. **(A)** The frequency power distributions across all indicated synaptic weight distributions for five randomized repetitions each. Color keys for the different average synaptic weights are the same as in **Figures 5A–C**. **(B)** Similar display as in **(A)**, for the same networks but with the neuron model with dynamic leak.

Supplementary Table 1 | H-H Model variable definitions (for the H-H neuron model derivation, presented in **Appendix 1**).

REFERENCES

Allen, G. I., and Tsukahara, N. (1974). Cerebrocerebellar communication systems. *Physiol. Rev.* 54, 957–1006. doi: 10.1152/physrev.1974.54.4.957

Anderson, J. S., Carandini, M., and Ferster, D. (2000). Orientation tuning of input conductance, excitation, and inhibition in cat primary visual cortex. *J. Neurophysiol.* 84, 909–926. doi: 10.1152/jn.2000.84.2.909

Bengtsson, F., Ekerot, C. F., and Jörntell, H. (2011). In vivo analysis of inhibitory synaptic inputs and rebounds in deep cerebellar nuclear neurons. *PLoS One* 6:e18822. doi: 10.1371/journal.pone.0018822

Binzegger, T., Douglas, R. J., and Martin, K. A. C. (2004). A quantitative map of the circuit of cat primary visual cortex. *J. Neurosci.* 24, 8441–8453. doi: 10.1523/JNEUROSCI.1400-04.2004

Brunel, N. (2000). Dynamics of sparsely connected networks of excitatory and inhibitory spiking neurons. *J. Comput. Neurosci.* 8, 183–208. doi: 10.1023/A:1008925309027

Chakravarthy, N., Tsakalis, K., Sabesan, S., and Iasemidis, L. (2009). Homeostasis of brain dynamics in epilepsy: A feedback control systems perspective of Seizures. *Ann. Biomed. Eng.* 37, 565–585. doi: 10.1007/s10439-008-9625-6

Chowdhury, S. S., Lee, C., and Roy, K. (2020). Towards understanding the effect of leak in spiking neural networks. *arXiv* [Preprint]. arXiv2006.08761.

Douglas, R. J., and Martin, K. A. C. (2009). Inhibition in cortical circuits. *Curr. Biol.* 19, R398–R402. doi: 10.1016/j.cub.2009.03.003

Gopalsamy, K., and Leung, I. (1996). Delay induced periodicity in a neural netlet of excitation and inhibition. *Phys. D Nonlinear Phenom.* 89, 395–426.

Graves, A. (2012). "Supervised sequence labelling," in *Supervised Sequence Labelling with Recurrent Neural Networks.*, (Berlin, Heidelberg: Springer), 5–13.

Hodgkin, A. L., and Huxley, A. F. (1952). A quantitative description of membrane current and its applicaiton to conduction and excitation in nerve. *J. Physiol.* 117, 500–544. doi: 10.1016/S0092-8240(05)80004-7

Hooks, B. M., Mao, T., Gutnisky, D. A., Yamawaki, N., Svoboda, K., and Shepherd, G. M. G. (2013). Organization of cortical and thalamic input to pyramidal neurons in mouse motor cortex. *J. Neurosci.* 33, 748–760. doi: 10.1523/JNEUROSCI.4338-12.2013

Isaacson, J. S., and Scanziani, M. (2011). How inhibition shapes cortical activity. *Neuron* 72, 231–243. doi: 10.1016/j.neuron.2011.09.027

Izhikevich, E. M. (2003). Simple model of spiking neurons. *IEEE Trans. Neural Netw.* 14, 1569–1572. doi: 10.1109/TNN.2003.820440

Izhikevich, E. M. (2004). Which model to use for cortical spiking neurons? *IEEE Trans. Neural Netw.* 15, 1063–1070. doi: 10.1109/TNN.2004.832719

Jirsa, V. K., and Stefanescu, R. A. (2011). Neural population modes capture biologically realistic large scale network dynamics. *Bull. Math. Biol.* 73, 325–343.

Jörntell, H. (2017). Cerebellar physiology: links between microcircuitry properties and sensorimotor functions. *J. Physiol.* 595, 11–27. doi: 10.1113/JP272769

Jörntell, H., and Ekerot, C. F. (2003). Receptive field plasticity profoundly alters the cutaneous parallel fiber synaptic input to cerebellar interneurons in vivo. *J. Neurosci.* 23, 9620–9631. doi: 10.1523/jneurosci.23-29-09620.2003

Kar, K., and DiCarlo, J. J. (2020). Fast recurrent processing via ventral prefrontal cortex is needed by the primate ventral stream for robust core visual object recognition. *bioRxiv* [Preprint]. doi: 10.1101/2020.05.10.086959

Koestinger, G., Martin, K. A. C., and Rusch, E. S. (2018). Translaminar circuits formed by the pyramidal cells in the superficial layers of cat visual cortex. *Brain Struct. Funct.* 223, 1811–1828. doi: 10.1007/s00429-017-1588-7

Lindner, B. (2014). "Low-pass filtering of information in the leaky integrate-and-fire neuron driven by white noise," in *Understanding Complex Systems*, eds V. A. Palacios and P. Longhini (Cham: Springer). doi: 10.1007/978-3-319-02925-2_22

Liou, J. Y., Smith, E. H., Bateman, L. M., Bruce, S. L., McKhann, G. M., Goodman, R. R., et al. (2020). A model for focal seizure onset, propagation, evolution, and progression. *Elife* 9:e50927. doi: 10.7554/eLife.50927

Lübke, J., Markram, H., Frotscher, M., and Sakmann, B. (1996). Frequency and dendritic distribution of autapses established by layer 5 pyramidal neurons in the developing rat neocortex: Comparison with synaptic innervation of adjacent neurons of the same class. *J. Neurosci.* 16, 3209–3218. doi: 10.1523/jneurosci.16-10-03209.1996

Mazzoni, A., Panzeri, S., Logothetis, N. K., and Brunel, N. (2008). Encoding of naturalistic stimuli by local field potential spectra in networks of excitatory and inhibitory neurons. *PLoS Comput. Biol.* 4:239. doi: 10.1371/journal.pcbi.1000239

Naundorf, B., Wolf, F., and Volgushev, M. (2006). Unique features of action potential initiation in cortical neurons. *Nature* 440, 1060–1063. doi: 10.1038/nature04610

Nilsson, M. N. P., and Jörntell, H. (2021). Channel current fluctuations conclusively explain neuronal encoding of internal potential into spike trains. *Phys. Rev. E* 103:22407.

Obermayer, J., Heistek, T. S., Kerkhofs, A., Goriounova, N. A., Kroon, T., Baayen, J. C., et al. (2018). Lateral inhibition by Martinotti interneurons is facilitated by cholinergic inputs in human and mouse neocortex. *Nat. Commun.* 9:4101. doi: 10.1038/s41467-018-06628-w

Okun, M., and Lampl, I. (2008). Instantaneous correlation of excitation and inhibition during ongoing and sensory-evoked activities. *Nat. Neurosci.* 11, 535–537. doi: 10.1038/nn.2105

Petkoski, S., Palva, J. M., and Jirsa, V. K. (2018). Phase-lags in large scale brain synchronization: Methodological considerations and in-silico analysis. *PLoS Comput. Biol.* 14:e1006160.

Pham, J., Pakdaman, K., and Vibert, J.-F. (1998). Noise-induced coherent oscillations in randomly connected neural networks. *Phys. Rev. E* 58: 3610.

Pi, H. J., Hangya, B., Kvitsiani, D., Sanders, J. I., Huang, Z. J., and Kepecs, A. (2013). Cortical interneurons that specialize in disinhibitory control. *Nature* 503, 521–524. doi: 10.1038/nature12676

Rongala, U. B., Spanne, A., Mazzoni, A., Bengtsson, F., Oddo, C. M., and Jörntell, H. (2018). Intracellular dynamics in cuneate nucleus neurons support self-stabilizing learning of generalizable tactile representations. *Front. Cell. Neurosci.* 12:210. doi: 10.3389/fncel.2018.00210

Rubin, R., Abbott, L. F., and Sompolinsky, H. (2017). Balanced excitation and inhibition are required for high-capacity, noise-robust neuronal selectivity. *Proc. Natl. Acad. Sci. U.S.A.* 114, E9366–E9375. doi: 10.1073/pnas.1705841114

Saarinen, A., Linne, M. L., and Yli-Harja, O. (2008). Stochastic differential equation model for cerebellar granule cell excitability. *PLoS Comput. Biol.* 4:e1000004. doi: 10.1371/journal.pcbi.1000004

Shen, Y., and Wang, J. (2011). Robustness analysis of global exponential stability of recurrent neural networks in the presence of time delays and random disturbances. *IEEE Trans. Neur. Netw. Learn. Syst.* 23, 87–96.

Song, S., Sjöström, P. J., Reigl, M., Nelson, S., and Chklovskii, D. B. (2005). Highly nonrandom features of synaptic connectivity in local cortical circuits. *PLoS Biol.* 3:e68. doi: 10.1371/journal.pbio.0030068

Spanne, A., and Jörntell, H. (2015). Questioning the role of sparse coding in the brain. *Trends Neurosci.* 38, 417–427. doi: 10.1016/j.tins.2015.05.005

Spanne, A., Geborek, P., Bengtsson, F., and Jörntell, H. (2014). Spike generation estimated from stationary spike trains in a variety of neurons In vivo. *Front. Cell. Neurosci.* 8:199. doi: 10.3389/fncel.2014.00199

Steriade, M. (1997). Synchronized activities of coupled oscillators in the cerebral cortex and thalamus at different levels of vigilance. *Cereb. Cortex.* 7, 583–604. doi: 10.1093/cercor/7.6.583

Sultan, K. T., and Shi, S. H. (2018). Generation of diverse cortical inhibitory interneurons. *Wiley Interdiscip. Rev. Dev. Biol.* 7:e306. doi: 10.1002/wdev.306

Sutskever, I., Vinyals, O., and Le, Q. V. (2014). Sequence to sequence learning with neural networks. *Adv. Neur. Inform. Proces. Syst.*

Swadlow, H. A. (2003). Fast-spike interneurons and feedforward inhibition in awake sensory neocortex. *Cerebral Cortex* 13, 25–32. doi: 10.1093/cercor/13.1.25

Tamás, G., Buhl, E. H., and Somogyi, P. (1997). Massive autaptic self-innervation of GABAergic neurons in cat visual cortex. *J. Neurosci.* 17, 6352–6364. doi: 10.1523/jneurosci.17-16-06352.1997

Tougaard, J. (2002). Signal detection theory, detectability and stochastic resonance effects. *Biol. Cybern.* 87, 79–90. doi: 10.1007/s00422-002-0327-0

Vogels, T. P., and Abbott, L. F. (2005). Signal propagation and logic gating in networks of integrate-and-fire neurons. *J. Neurosci.* 25, 10786–10795. doi: 10.1523/JNEUROSCI.3508-05.2005

Vogels, T. P., Sprekeler, H., Zenke, F., Clopath, C., and Gerstner, W. (2011). Inhibitory plasticity balances excitation and inhibition in sensory pathways and memory networks. *Science* 1569:334. doi: 10.1126/science.1211095

Wehr, M., and Zador, A. M. (2003). Balanced inhibition underlies tuning and sharpens spike timing in auditory cortex. *Nature* 426, 442–446. doi: 10.1038/nature02116

Zhang, Z. W. (2004). Maturation of layer V pyramidal neurons in the rat prefrontal cortex: intrinsic properties and synaptic function. *J. Neurophysiol.* 91, 1171–1182. doi: 10.1152/jn.00855.2003

Zhu, J. J., and Lo, F. S. (2000). Recurrent inhibitory circuitry in the deep layers of the rabbit superior colliculus. *J. Physiol.* 523(Pt 3), 731–740. doi: 10.1111/j.1469-7793.2000.00731.x

Zhu, S., and Shen, Y. (2013). Robustness analysis for connection weight matrices of global exponential stability of stochastic recurrent neural networks. *Neur. Netw.* 38, 17–22.

Conflict of Interest: The authors declare that the research was conducted in the absence of any commercial or financial relationships that could be construed as a potential conflict of interest.

APPENDIX 1

Neuron Model Derivation From H-H Model

We first describe the rationale for our Linear Summation neuron model (LSM). In brief, the LSM aims to provide a simple and computationally efficient neuron model, while capturing important characteristics of H-H conductance models (Hodgkin and Huxley, 1952; Rongala et al., 2018). The membrane potential in the LSM model is normalized between +1 and -1 with a resting potential of zero. The output of an LSM neuron is a continuous, non-spiking signal that reflects the portion of the membrane potential that exceeds some threshold, which we assumed to be the zero resting potential. This would be suitable to represent one neuron or a population of similarly connected neurons that is biased by background activity to be at or near spontaneous activity (such as is hypothesized for stochastic resonance to prevent dead bands) (Tougaard, 2002). This continuous output signal is intended to reflect the mean spike rate that a population of similarly connected neurons would transmit to other centers in the nervous system.

In H-H models the various ion channels associated with ionic pumps and leaks define a resting membrane potential where there are no net currents. Any change in membrane potential away from this resting potential will settle back to the resting potential according to the combined conductance of all of these ion channels, which is called the static leak. Synaptic activation leads to opening of specific ion channels, which in the H-H models as a change of synaptic conductance. The ion(s) that are made permeable by the synapse have a reversal potential that is different from the resting membrane potential. When the ion channels of a particular synapse are open, the membrane potential will be driven toward that reversal potential, with a strength that depends on the strength of the synaptic conductance relative to the static leak conductance.

The synaptic currents charge the neuron, which is modeled as a single capacitor (assuming that the electrotonic distances between different parts of the neuron are negligible). Various synaptic signals are thus integrated and converted into a dynamically changing membrane potential. The static leak is in parallel with this capacitor, thereby defining a time-constant τ for these dynamic changes. The effect is that of low-pass filtering of the integrated synaptic currents (Lindner, 2014) to produce the membrane potential that defines the output state of the neuron. In an H-H model, the output state is created by converting the membrane voltage into patterns of spike output, with the help of a threshold for spike generation. Spike generation is omitted in the LSM model and the output of the neuron is instead the part of the membrane potential that exceeds some threshold (herein equal to the resting membrane potential).

First, we describe a conductance-based model similar to previously presented models (Hodgkin and Huxley, 1952; Rongala et al., 2018) and then show how a model similar to the LSM model can be derived. In this category of ion channel conductance-based models, the dynamics of one type of ion channel is lumped together into one single conductance. Compared to other conductance-based models, no spike generation is modeled and the neurons resting potential is set to zero. The neuron is modeled as a capacitor with capacitance (C) and is charged by excitatory ($I_{syn,exc}$) and inhibitory synaptic currents ($I_{syn,inh}$) and discharged by a leak current (I_{leak}). Therefore, the neurons membrane potential (V) measured across the capacitor follows the following equation.

$$\mathbf{C}\frac{\mathbf{d}V}{\mathbf{d}t} = \mathbf{I}_{leak} + \mathbf{I}_{syn,exc} + \mathbf{I}_{syn,inh} \qquad (A1)$$

The leak current is set proportional to the membrane potential by constant conductance g_L according to Ohm's law:

$$\mathbf{I}_{leak} = -\mathbf{g}_{\mathbf{L}}\mathbf{V} \qquad (A2)$$

If the synaptic currents are zero, the neuron's membrane potential will decay to zero. Therefore, this model neuron's resting membrane potential is zero. At each excitatory synapse i the firing rate of the presynaptic neuron (v_i^+) produces a current. The synapse has a baseline conductance (w_i^+), called synaptic weight. This conductance is scaled by the presynaptic neuron's firing rate. The direction and magnitude of the current is determined by the difference between the constant reversal potential (E_{exc}) and the neuron's membrane potential. For an excitatory synapse, the current would reverse if the membrane potential rose above the positive reversal voltage, so synaptic activity can never produce a membrane potential about the reversal potential. Therefore if the neuron has already reached this voltage, the neuron's voltage cannot increase further. The current contributed by an individual synapse can be modeled as

$$\mathbf{I}_{syn,exc_i} = -(\mathbf{V}-\mathbf{E}_{exc})\mathbf{w}_\mathbf{i}^+\mathbf{v}_\mathbf{i}^+ \qquad (A3)$$

The same model is applied for the current generated by an inhibitory synapse i, with reversal potential (E_{inh}), synaptic weight (w_i^-) and presynaptic firing rate (v_i^-). The reversal potential of an inhibitory synapse is set so that the neurons potential cannot decrease below this potential.

$$\mathbf{I}_{syn,inh_i} = -(\mathbf{V}-\mathbf{E}_{inh})\mathbf{w}_\mathbf{i}^-\mathbf{v}_\mathbf{i}^- \qquad (A4)$$

Summing all synaptic currents and plugging in the current equations into the membrane potential equation we obtain

$$\mathbf{C}\frac{\mathbf{d}V}{\mathbf{d}t} = -\mathbf{g_L}\mathbf{V} - \sum_{\mathbf{i}} (\mathbf{V} - \mathbf{E}_{exc})\, \mathbf{w_i^+ v_i^+} + \sum_{\mathbf{i}} (\mathbf{V} - \mathbf{E}_{inh})\, \mathbf{w_i^- v_i^-} \tag{A5}$$

where the first sum is over all excitatory synapses and the second sum over all inhibitory synapses. In order, to show the relationship of this equation to the LSM model, we set the leak conductance to one and replace leak conductance and membrane capacitance by a time constant τ. The reversal potentials are set to +1 and -1 for the excitatory and the inhibitory synapses, respectively. Hence the range of possible membrane potential is between +1 and -1, assuming that the initial voltage is also in that range.

The resulting differential equation is

$$\tau\frac{\mathbf{d}V}{\mathbf{d}t} = -\mathbf{V} + (\mathbf{1} - \mathbf{V}) \sum \mathbf{w_j^+ v_j^+} + (\mathbf{1} + \mathbf{V}) \sum \mathbf{w_k^- v_k^-} \tag{A6}$$

This equation can be solved by applying the implicit Euler method. Let V_t be the membrane voltage in timestep t and h the stepsize. The following equation must be solved for V_{t+1}

$$\mathbf{V_{t+1}} = \mathbf{V_t} + \mathbf{h}\frac{\mathbf{1}}{\tau}\left(-\mathbf{V_{t+1}} + (\mathbf{1} - \mathbf{V_{t+1}}) \sum \mathbf{w_j^+ v_j^+} + (\mathbf{1} + \mathbf{V_{t+1}}) \sum \mathbf{w_k^- v_k^-}\right) \tag{A7}$$

In this case an analytic solution is possible:

$$\mathbf{V_{t+1}} = \frac{\mathbf{V_t} + \frac{\mathbf{h}}{\tau} \sum \mathbf{w_i v_i}}{\mathbf{1} + \frac{\mathbf{h}}{\tau} + \frac{\mathbf{h}}{\tau} \sum |\mathbf{w_i}|\, \mathbf{v_i}} \tag{A8}$$

where both sums are over all synapses.

The parameters of this model are also listed in **Supplementary Table 1**. This new system has components not commonly found in neuron models. The reason is that usually the differential equation describes an instantaneous effect of the inputs and the state of the neuron. In this system the effect of the input on how the input is processed by the neuron in a future time step is already considered.

From the above derivation (Eq. A8) we could observe that the excitatory ($I_{syn,exc}$) and inhibitory ($I_{syn,inh}$) synaptic currents from a conductance based neuron model (Eq. A1), can be reduced to a total synaptic weight summation $\left(\frac{\sum wV}{1+\sum |w| V}\right)$, and that the leak current (I_{leak}) (Eq. A1), which is a dynamic leak because it occurs across capacitor, can be reduced to h/τ (a dynamic leak constant, Eq. A8; if this constant is larger than zero and smaller than one, it can be disregarded in this expression). Based on this neuron model derivation, we propose the simplified linear summation neuron model (LSM, A10) to capture the essential dynamics of the original H-H conductance-based model (**Supplementary Figure 1**). The LSM is given by two equations: LSM without dynamic leak (Eq. A9) and LSM with dynamic leak (Eq. A10).

$$\mathbf{A_{NoDyn}} = \frac{\sum (\mathbf{w_i a_i})}{\mathbf{1} + \sum |\mathbf{w_i a_i}|} \tag{A9}$$

$$\frac{\tau_{\mathbf{D}yn} * \mathbf{d}A_{\mathbf{D}yn}}{\mathbf{d}t} = -\mathbf{A}_{\mathbf{D}yn}\,(\mathbf{t}) + \mathbf{A_{NoDyn}}\,(\mathbf{t}) \tag{A10}$$

frontiers in Systems Neuroscience

ORIGINAL RESEARCH
published: 05 July 2021
doi: 10.3389/fnsys.2021.688517

The Impact of Small Time Delays on the Onset of Oscillations and Synchrony in Brain Networks

Isam Al-Darabsah[1], *Liang Chen*[2], *Wilten Nicola*[3] *and Sue Ann Campbell*[2]*

[1] Department of Mathematics, University of Manitoba, Winnipeg, MB, Canada, [2] Department of Applied Mathematics, Centre for Theoretical Neuroscience, University of Waterloo, Waterloo, ON, Canada, [3] Hotchkiss Brain Institute, Cumming School of Medicine, University of Calgary, Calgary, AB, Canada

The human brain constitutes one of the most advanced networks produced by nature, consisting of billions of neurons communicating with each other. However, this communication is not in real-time, with different communication or time-delays occurring between neurons in different brain areas. Here, we investigate the impacts of these delays by modeling large interacting neural circuits as neural-field systems which model the bulk activity of populations of neurons. By using a Master Stability Function analysis combined with numerical simulations, we find that delays (1) may actually stabilize brain dynamics by temporarily preventing the onset to oscillatory and pathologically synchronized dynamics and (2) may enhance or diminish synchronization depending on the underlying eigenvalue spectrum of the connectivity matrix. Real eigenvalues with large magnitudes result in increased synchronizability while complex eigenvalues with large magnitudes and positive real parts yield a decrease in synchronizability in the delay vs. instantaneously coupled case. This result applies to networks with fixed, constant delays, and was robust to networks with heterogeneous delays. In the case of real brain networks, where the eigenvalues are predominantly real, owing to the nearly symmetric nature of these weight matrices, biologically plausible, small delays, are likely to increase synchronization, rather than decreasing it.

Keywords: synchronization, time delay, Wilson-Cowan network, homeostatic synaptic plasticity, master stability function, network neuroscience, connectomes

OPEN ACCESS

Edited by:
Serhiy Yanchuk, Technical University of Berlin, Germany

Reviewed by:
Konstantin B. Blyuss, University of Sussex, United Kingdom
Stefan Ruschel, University of Auckland, New Zealand

***Correspondence:**
Sue Ann Campbell
sacampbell@uwaterloo.ca

Received: *31 March 2021*
Accepted: *31 May 2021*
Published: *05 July 2021*

Citation:
Al-Darabsah I, Chen L, Nicola W and Campbell SA (2021) The Impact of Small Time Delays on the Onset of Oscillations and Synchrony in Brain Networks. Front. Syst. Neurosci. 15:688517. doi: 10.3389/fnsys.2021.688517

1. INTRODUCTION

Biological systems often form intricate and highly interconnected networks. Examples include the chemical reaction networks present within a single cell at the small scale (Kitano, 2002), the spread of disease through social networks (Keeling and Eames, 2005) or ecological networks across entire biomes or even the planet itself at the large scale (Montoya et al., 2006). Yet, one of the critical defining features in these networks is that communication from putative nodes is seldom instantaneous, and is often plagued by delays. Nowhere is this clearer than in the human brain, an intricate network of neurons limited by the slow propagation speed of action potentials or spikes, which can take up to milliseconds to transmit information across areas (Roxin et al., 2005; Ghosh et al., 2008; Deco et al., 2009).

This seems unusual when we consider the readily synchronizable nature of brain matter. For example, pathologically strong synchrony exists in neurological disorders such as epilepsy despite the presence of time-delays (Uhlhaas and Singer, 2006). Beyond pathological states, weakly synchronized brain areas are normal and even necessary states for the functioning of brain networks during a variety of tasks (Varela et al., 2001). Indeed, the presence of delays alone can have variable impacts on synchronization with synchronizability determined by (1) the topology of the network, (2) the dynamics of the nodes, and (3) the nature of the delays.

We investigated how these three forces would interact with computational modeling in networks of homeostatically-coupled Wilson-Cowan (WC) nodes (Wilson and Cowan, 1972; Destexhe and Sejnowski, 2009; Vogels et al., 2011; Cowan et al., 2016; Hellyer et al., 2016; Nicola et al., 2018). In this model, each node can be interpreted as a population of excitatory and inhibitory neurons. The nodes are stabilized onto a steady-state equilibrium with a homeostatic, dynamically adjusted weight which strives to maintain a stable firing rate in each population (Nicola et al., 2018; Nicola and Campbell, 2021). However, the homeostatic adjustment of weights can also lead to more complex dynamics, such as mixed mode oscillations and chaos, which and lead to desynchronization of the nodes (Nicola et al., 2018; Nicola and Campbell, 2021). Here, we show how the presence of small time delays in the coupling influences dynamic behavior and synchronization in comparison to the instantaneously coupled networks.We limit our study to delay magnitudes that are biologically relevant; these are small in comparison with other time scales in the model. First, we find that the induction of oscillations (via a Hopf bifurcation) requires larger global coupling strengths in the delay coupled network vs. the instantaneously coupled system. Second, we find that for a sufficiently large delay, the system readily loses all non-relaxation oscillator solutions (period doubling cascades, mixed-mode dynamics, chaos) past the Hopf-bifurcation. Third, by applying a master-stability formalism to these networks, we find that synchronization is dependent on the underlying graph and the nature of the time-varying synchronized solutions. The delays decreased the synchronizability of graphs with large complex eigenvalues (with postive real parts) while increasing the synchronizability of graphs with purely real eigenvalues, as in the case of DTI-derived connectomes (Bullmore and Sporns, 2009). For small delays, synchronization could occur for chaotic or other complex solutions as in the nondelayed case. For sufficiently large delays, however, synchronization was always associated with oscillatory solutions. This general portrait of the interactions between network topology, dynamics, and delays was also robust to delay heterogeneity throughout the network. Thus, we find that rich dynamics and variable synchronizability with different graph structures.

2. MATERIALS AND METHODS

2.1. Model Equations

To model the system we use a Wilson-Cowan network with homeostatic regulation of the inhibitory connection weight due to Vogels et al. (2011), Hellyer et al. (2016), Nicola et al. (2018), and Nicola and Campbell (2021). We introduce a time delay in the excitatory connections between the nodes (**Figure 1A**).

$$\begin{aligned} \tau_1 \frac{dE_k}{dt} &= -E_k + \phi\left(\sum_{j=1}^{N} \boldsymbol{W}_{kj}^{EE} E_j(t-\epsilon_{kj}) - W_k^{EI} I_k\right) \\ \frac{dI_k}{dt} &= -I_k + \phi(W^{IE} E_k) \\ \tau_2 \frac{dW_k^{EI}}{dt} &= I_k(E_k - p) \end{aligned} \tag{1}$$

E_k is the activity of the excitatory population of neurons within the kth node, I_k is the activity of the inhibitory population in the kth node, W_k^{EI} is the homeostatically adjusted inhibitory weight of the kth node and W^{IE} is the fixed excitatory weight of the kth node. $\boldsymbol{W}_{kj}^{EE} > 0$ are the (fixed) excitatory weights and ϵ_{kj} is the time delay between nodes. The function ϕ is a sigmoidal transfer function which we take to be the logistic function:

$$\phi(x) = \frac{1}{1+\exp(-ax)} \tag{2}$$

where a controls the steepness of the sigmoid, while the sigmoid itself determines the proportion of the population of neurons which is active in node k.

We use the parameter values as described in Nicola et al. (2018): $p = 0.2$, $a = 5$, $\tau_1 = 1$, $\tau_2 = 5$. The values of W^{IE} and $\boldsymbol{W}_{kj}^{EE}$ are varied. To choose an appropriate value for the time delay, ϵ, note that in Equation (1) time has already been scaled by the timescale of the inhibitory population, τ_I (Nicola et al., 2018). This means that the delays are also scaled $\epsilon_{ij} = \frac{T_{ij}}{\tau_I}$. From Hellyer et al. (2016) we find values of T_{ij} in the range $1 - 14$ ms and $\tau_I = 20$ ms, which yields ϵ_{ij} in the range $0.05 - 0.7$.

In our work, we consider two primary constraints on this system (**Figure 1B**). First, the row-sum of the weight matrix $\boldsymbol{W}^{EE}$ is constant:

$$\sum_{j=1}^{N} \boldsymbol{W}_{kj}^{EE} = W^E, \quad k = 1, 2, \ldots N \tag{3}$$

where the parameter W^E acts as the global coupling strength of the entire system. The second constraint is that the delays are homogeneous throughout the network:

$$\epsilon_{kj} = \epsilon, \quad \forall k, j \tag{4}$$

However, in **Figure 4** we consider the impact of heterogeneous delays by choosing the delays ϵ_{kj} value from a Beta distribution with an average of ϵ.

2.2. The Synchronous Solution and the Single, Self-Coupled Node

The model (Equation 1) with the constraints (Equations 3, 4) admits a synchronous solution $(E_k, I_k, W_k^{EI}) = (E_s(t), I_s(t), W_s^{EI}(t))$, $k = 1, \ldots, N$. The functions $(E_s(t), I_s(t), W_s^{EI}(t))$

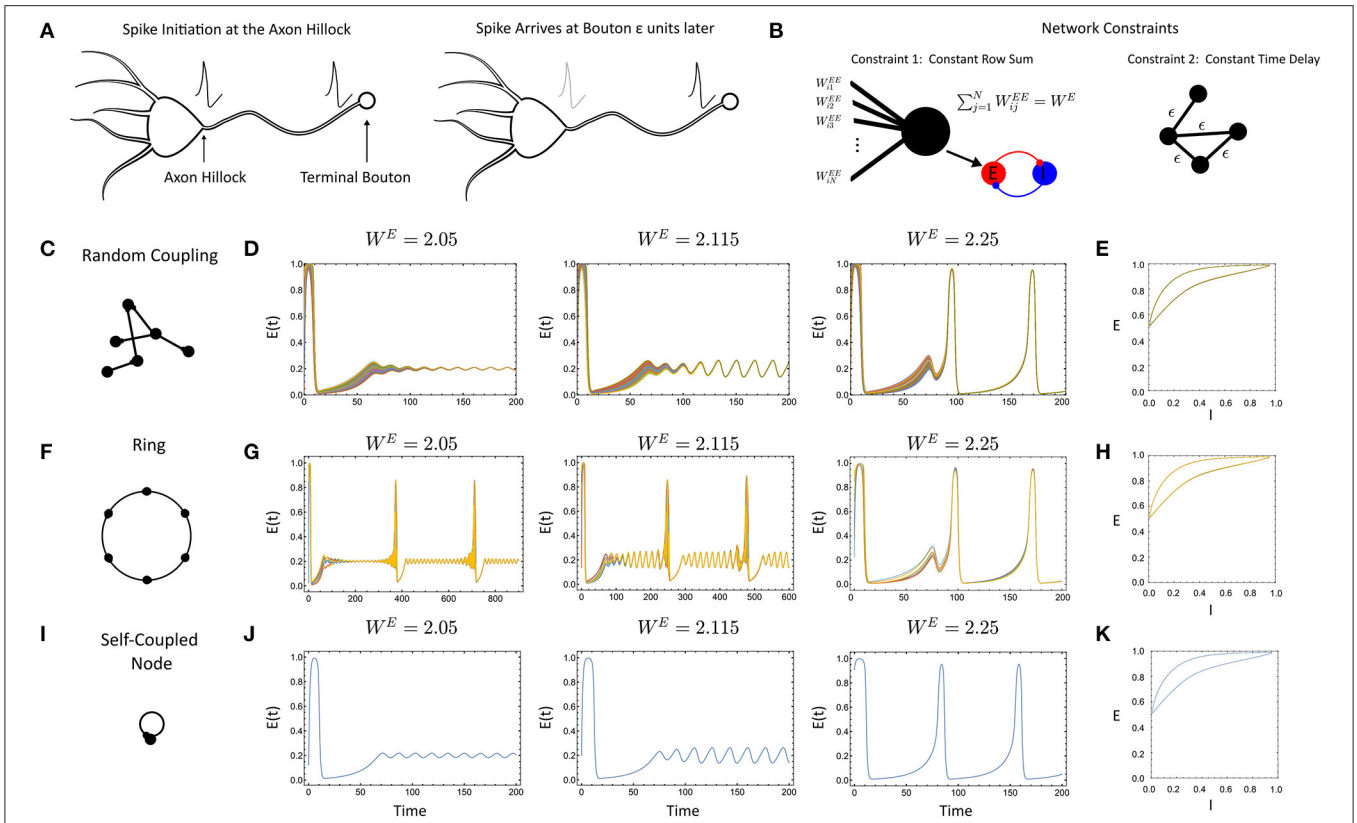

FIGURE 1 | (A) Communication delays in neural networks are caused by the non-instantaneous transmission of an action potential down an axon. The spike is initiated at the axon hilock and arrives at the terminal bouton after a period of time. **(B)** The primary constraints in system (Equation 1), the row-sum of the weights normalizes to W^E and all the delays are constant. **(C)** Randomly-coupled networks with constant delay. **(D)** Simulation for increasing W^E **(E)** Phase portrait of $[E(t), I(t)]$ for the network after synchronization for $W^E = 2.25$. **(F)** Ring networks. **(G)** Simulated ring network with $N = 8$ nodes for increasing W^E **(H)** Same as **(E)** except for ring topology. **(I)** The single, delay coupled node. **(J)** Simulations of the single, delay coupled node. **(K)** Same as **(E,H)** only for the single, delay coupled node. For all simulations, the parameter values were: $\epsilon = 0.1$, $p = 0.2$, $\tau_1 = 1$, $\tau_2 = 5$, $W^{IE} = 1$, and $a = 5$.

satisfy the equations for a single, isolated node with delayed, self-coupling

$$\tau_1 \frac{dE}{dt} = -E + \phi\left(W^E E(t-\epsilon) - W^{EI} I\right) \tag{5}$$

$$\frac{dI}{dt} = -I + \phi\left(W^{IE} E\right) \tag{6}$$

$$\tau_2 \frac{dW^{EI}}{dt} = I(E - p) \tag{7}$$

The self-coupling arises from the analysis of the synchronous solution and is independent of whether there is self-coupling in the full model. See **Supplementary Materials Section 1** for details.

Thus, the synchronous solution of Equation 1 can be described by analyzing the behavior of model for a single, self-coupled node (Equations 5–7). For example, this model has an equilibrium solution which yields the following equilibrium solution of the full model

$$(\bar{E}_k, \bar{I}_k, \bar{W}_k^{EI}) = \left(p, \phi(W^{IE}p), \frac{W^E p - \phi^{-1}(p)}{\phi(W^{IE}p)}\right),\ k = 1, \ldots N.$$

Analysis of the linearization of Equation 1 about this equilibrium point shows that a Hopf bifurcation occurs for a sufficiently strong global coupling strength, W^E, as a function of the excitatory-to-inhibitory coupling parameter W^{IE},

$$W^E_{Hopf} = g(W^{IE})$$

This Hopf-bifurcation curve can be approximated via a perturbation analysis in the limit of small delays ($\epsilon \ll 1$, see **Supplementary Materials Section 2**).

2.3. Master Stability Function

The Master stability function was first developed to study synchronization in large networks of coupled oscillators without time delay (Pecora and Carroll, 1990). The derivation for systems with time delays has been described in Dhamala et al. (2004), Choe et al. (2010), and Flunkert et al. (2010). The application to the model (Equation 1) is almost identical to that described in Nicola and Campbell (2021) (see **Supplementary Materials Section 3**).

Assuming that W^{EE} is diagonalizable, the linear (local) stability of the synchronized solution $(E_k, I_k, W_k^{EI}) =$

$(E_s(t), I_s(t), W_s^{EI}(t))$, $k = 1, \ldots, N$ of the model (Equation 1) can be determined by studying the three dimensional linear system

$$\begin{aligned}\tau_1 \frac{d\eta_x}{dt} &= -\eta_x + M_{s1}(t)\left(\hat{r}\eta_x(t-\epsilon) - I_s(t)\eta_z - W_s^{EI}(t)\eta_y\right)\\ \frac{d\eta_y}{dt} &= -\eta_y + M_{s2}(t)\eta_x\\ \tau_2 \frac{d\eta_z}{dt} &= (E_s(t) - p)\eta_y + I_s(t)\eta_x\end{aligned} \tag{8}$$

where $M_{s1}(t) = \phi'(W^E E_s(t-\epsilon) - W_s^{EI}(t)I_s(t))$ and $M_{s2}(t) = W^{IE}\phi'(W^{IE}E_s(t))$, and $\hat{r}$ is an eigenvalue of W^{EE}. The Master stability function, $\lambda(r)$ is typically defined as follows. For a given $r \in \mathbb{C}$ if the trivial solution of (Equation 8) asymptotically stable, then $\lambda(r) < 0$. If it is unstable then $\lambda(r) > 0$. A standard approach is to define $\lambda(r)$ be the maximal Lyapunov exponent of the system (Equation 8). The MSF is then used to define a *region of stability* in the complex plane, corresponding to all values of r for which $\lambda(r) < 0$. If all eigenvalues of W^{EE} lie inside this region then the synchronous solution of Equation 1 is locally asymptotically stable. Finally, we remark that we primarily consider the scaled eigenvalues, $r_k = \frac{\hat{r}_k}{W^E}$ for all numerical simulations and plots, thereby allowing us to compare eigenvalues on the unit circle across global coupling strengths.

2.4. Numerical Methods

We use the commands ParametricNDSolveValue in *Wolfram Mathematica* and NDSolveValue to simulate the system (1) with homogeneous and heterogeneous delays. We used the numerical continuation package DDE-Biftool (Engelborghs et al., 2001) to compute Hopf bifurcation curves and period doubling curves for the model (Equations 5–7) in the W^{IE}, W^E parameter space.

Numerically Implementing the Master Stability Function for a Delay Differential System

The Master Stability Function (MSF) approach for a generic delay differential system

$$\frac{dx}{dt} = F(\boldsymbol{x}(t-\epsilon), \boldsymbol{x}(t)) \tag{9}$$

is performed by first discretizing the delay-differential system:

$$\frac{d\boldsymbol{x}_1}{dt} = F(\boldsymbol{x}_m, \boldsymbol{x}_1) \tag{10}$$

$$\frac{d\boldsymbol{x}_n}{dt} = (\boldsymbol{x}_{n+1}(t) - \boldsymbol{x}_{n-1}(t)) \cdot \frac{m}{2\epsilon}, \quad n = 1, 2, \ldots m-1 \tag{11}$$

$$\frac{d\boldsymbol{x}_m}{dt} = (\boldsymbol{x}_{m-1}(t) - \boldsymbol{x}_m(t)) \cdot \frac{m}{\epsilon}, \tag{12}$$

as in Farmer (1982) and Lakshmanan and Senthilkumar (2011).

This approximation is applied to the linearized system with delays (Equation 8) which reduces the original system of $3N$ delay differential equations to a system of $3Nm$ ordinary differential equations. Then, the classical MSF approach via computing the Lyapunov exponents of the reduced variational equations is now immediately applicable as the resulting network consists of coupled ordinary differential equations. Details of the implementation can be found online (see Code Availability Statement). The value of $m = 10$ discretization points was taken.

To supplement this approach, we performed numerical simulations of the linear delay differential equation system (Equation 8) and tracked whether solutions decayed to zero or not. This was then used to define the MSF. This yielded results consistent with those from the discretized DDE.

3. RESULTS

Delay Coupled Wilson-Cowan Systems Can Still Synchronize

With the initial network constructed, we first sought to determine what impacts the delay would have, if any, by comparison with results for the instantaneously coupled network. To assess this, we conducted an initial barrage of simulations with randomly-coupled networks (**Figures 1C–E**), ring networks (**Figures 1F–H**), and the single, self-coupled node with delay (**Figures 1I–K**). Simulations for larger delay ($\epsilon = 0.3, 0.5$) showed similar behavior. First, we found that when the networks did synchronize, they synchronized to solutions of the self-coupled node with delay with an identical W^E value (**Figures 1J,K**), given by Equations 5–7. This is indeed, similar to the instantaneously coupled network case where networks with a coupling strength of W^E can synchronize to solutions of Equations 5–7 with $\epsilon = 0$ (Nicola et al., 2018; Nicola and Campbell, 2021).

However, the delay-coupled network did exhibit differences from the instantaneously coupled network, in both the synchronization and the nature of the attractors. For example, the ring network considered in **Figures 1F–H** would desynchronize at different parameter values (e.g., smaller rings) in the delay-coupled case vs. the instantaneous case. As the delay was increased further, smaller networks could desynchronize. In contrast, the randomly-coupled networks remained synchronized for all parameter values and delay values we considered. Thus, the preliminary simulations display some link to qualitative behaviors of the instantaneous case (synchronization to the self-coupled node) but with differences in the behavior of the delayed vs. non-delayed networks for otherwise identical parameter values.

The Single, Delay Coupled Node

Given the synchronization to the delayed, self-coupled node in **Figure 1**, we sought to investigate the bifurcation structure of the corresponding model (Equations 5–7). First, we found that as in the instantaneously coupled case, the self-coupled node displayed a supercritical Hopf bifurcation at a critical value of the coupling strength parameter W^E (**Figure 2A**). As W^E is increased, this Hopf bifurcation is followed by a period-doubling cascade to chaos (**Figures 2B–D**) provided that the delay is not too large. These results were confirmed using numerical simulation, numerical bifurcation analysis and

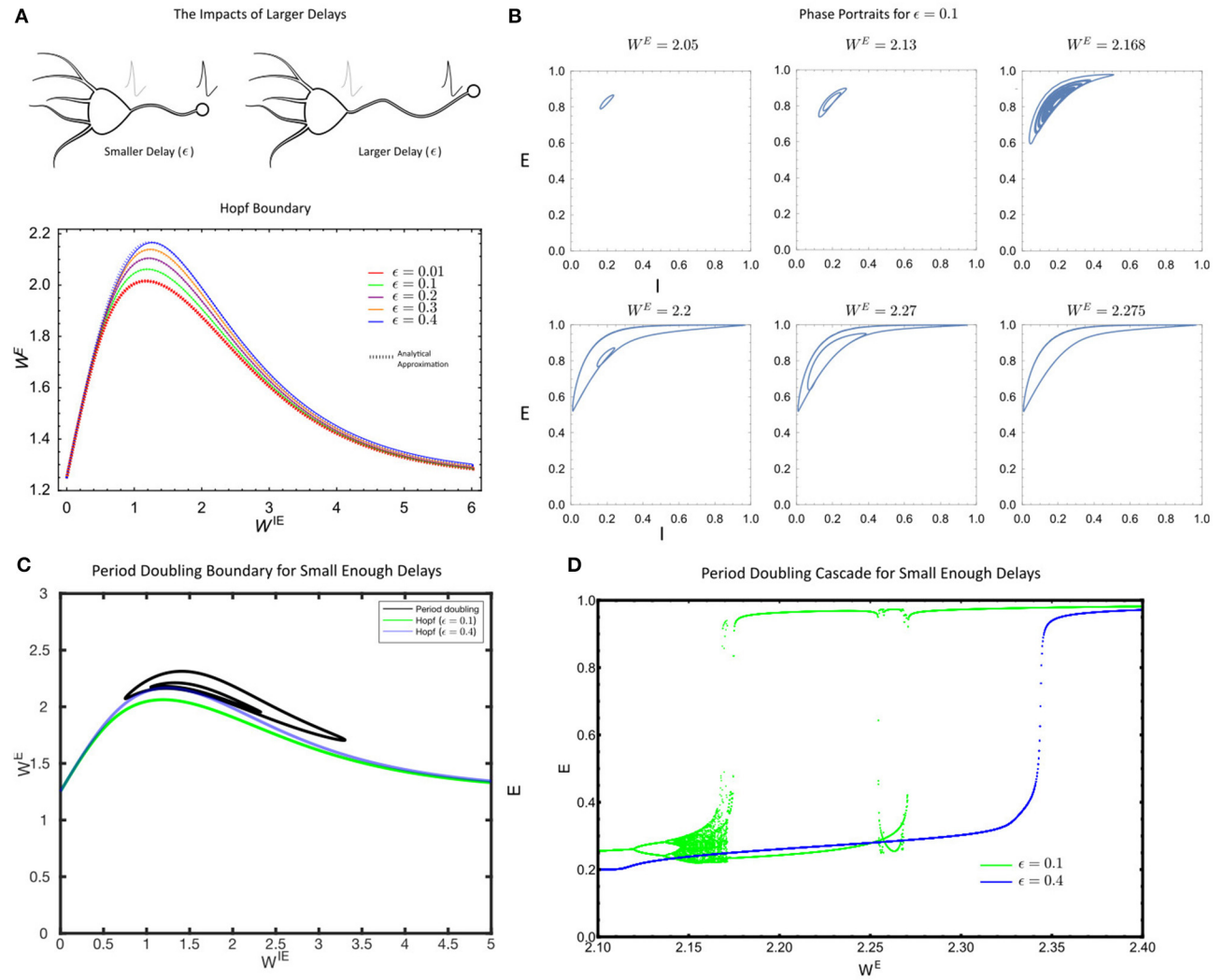

FIGURE 2 | (A) The Hopf bifurcation boundary for the single, delayed self-coupled node, estimated analytically (dashed coloured lines) via a perturbation theory and numerically (solid lines, DDE-Biftool). **(B)** The phase portraits in the $(E(t), I(t))$ space for the single node for increasing values of W^E. **(C)** The single self-coupled node undergoes period-doubling bifurcations for sufficiently small delay, ($\epsilon = 0.1$). **(D)** A period-doubling cascade is present for small delays ($\epsilon = 0.1$, green) but not large delays ($\epsilon = 0.4$, blue). For all simulations, the parameter values were: $p = 0.2$, $\tau_1 = 1$, $\tau_2 = 5$, $W^{IE} = 1$ and $a = 5$.

by analytically approximating the Hopf-bifurcation curve (see **Supplementary Materials Section 2**).

As the delay, ϵ, in Equation 5–7 increased, we found that the critical value of the coupling strength W^E required to induce a Hopf bifurcation increased, thereby pushing the system into the more strongly coupled regime (**Figure 2A**). At the level of the single node, this is the primary factor that can eliminate the rich single node dynamics. In particular, for sufficiently large delays, the period doubling cascade is eliminated (**Figure 2D**), with the only remaining dynamics being a putative Canard-type explosion in limit cycle amplitude (see Nicola et al., 2018). Thus, for small delays, the single self-coupled node maintains many of the rich dynamical states of the instantaneously coupled system. However, for sufficiently large delay in the self-coupling, the rich-dynamical repertoire of the single node system is largely eliminated as the Hopf-bifurcation is only induced at strong coupling (W^E) values.

Master Stability Function Analysis of the System With Delays

With the dynamics of the single self-coupled node largely resolved, we sought to determine how networks would synchronize to non-equilibrium (e.g., limit cycle or chaotic attractor) solutions. First, we applied the Master Stability Function approach (MSF) for the system with a constant fixed delay (**Figure 3A**, see Methods). Briefly, the Master Stability Function, $\lambda(r)$, is a function which is evaluated at the eigenvalues of a connectivity matrix. If $\lambda(r_i) < 0$ for all $i = 1, 2, \ldots N$

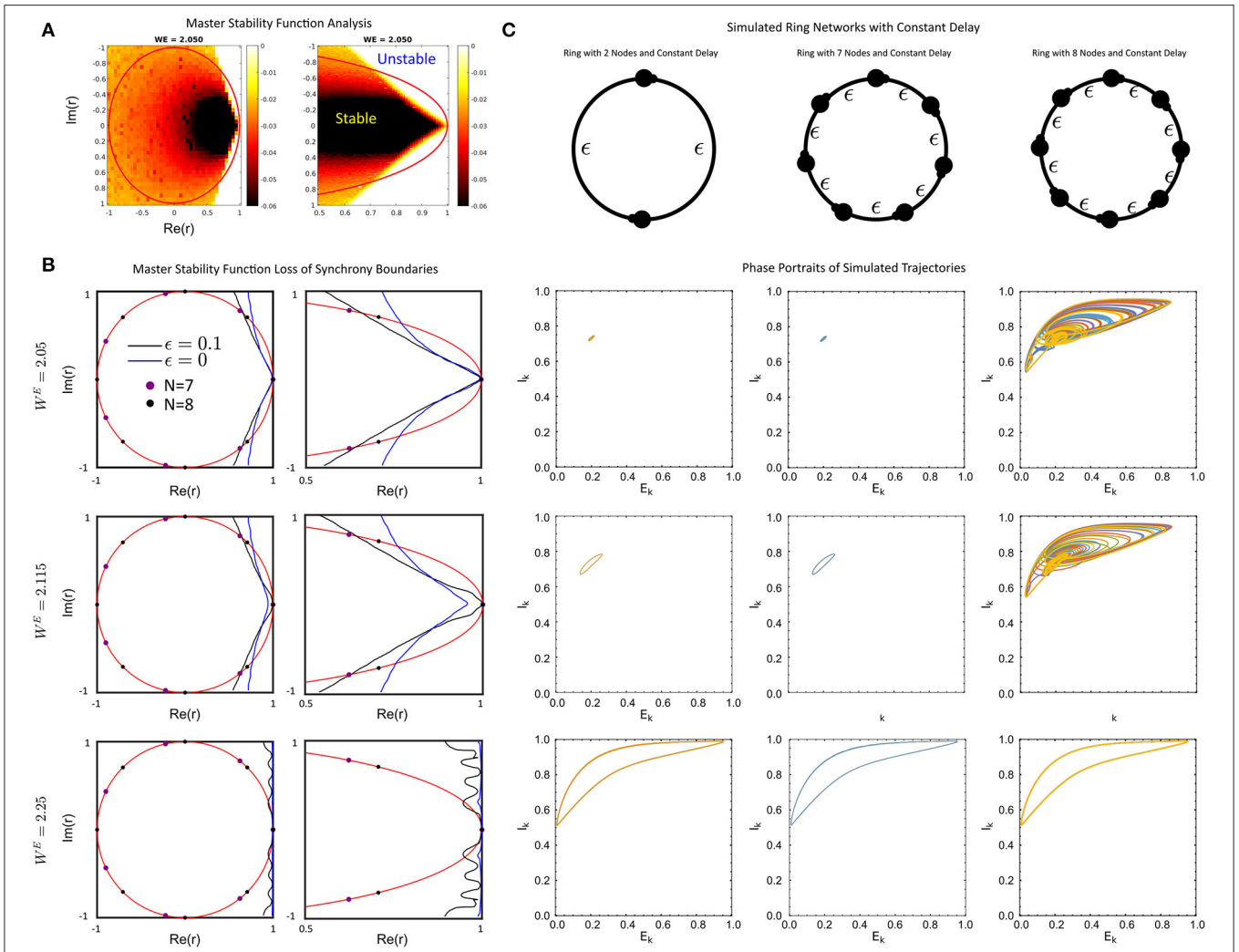

FIGURE 3 | (A) The full Master-Stability Function (MSF) computed for $W^E = 2.05$ and $\epsilon = 0.1$. **(B)** The sign-change boundaries for the MSF for no delay (blue) and delay $\epsilon = 0.1$ (black) with $W^E = 2.05$ (top), $W^E = 2.115$ (middle), $W^E = 2.25$ (bottom) for the full unit-circle region (left) and a zoom (right). **(C)** Simulated ring networks for $N = 2$ (left), $N = 7$ (middle) and $N = 8$ (right) rings with the values of W^E as in **(B)**. For all simulations, the parameter values were: $\epsilon = 0.1$, $p = 0.2$, $\tau_1 = 1$, $\tau_2 = 5$, $W^{IE} = 1$, and $a = 5$.

eigenvalues, then synchronized solutions are stable for any matrix with eigenvalues $r_1, r_2, \ldots r_N$. If, however, $\lambda(r_i) > 0$ for any i, then the synchronized solution is unstable.

First, we find that for a fixed delay, the change in the MSF in the delay-coupled vs instantaneously coupled case is dependent on the connectivity matrix and global coupling strength W^E. In particular, connectivity matrices with complex-eigenvalues that are large in magnitude with postive real parts are likely to lose stability of the synchronized solution when the network communication is delayed, as opposed to when it is instantaneous (**Figure 3B** top, middle). In contrast, connectivity matrices with purely real eigenvalues, as is the case with symmetric matrices, can gain stability (**Figure 3B**, middle). This is the differential impact of the delay on the connectivity.

An example of the former situation is a uni-directional ring. The spectrum of the connectivity matrix in this case lies on the unit circle and the second largest eigenvalue increases as the size of the ring increases. Thus delay will tend to destabilize larger networks before smaller networks. This can be seen in **Figure 3B** where the eigenvalues for unidirectional rings with $N = 7$ and $N = 8$ are displayed with the MSF. The MSF analysis predicts that both networks will be synchronized for $\epsilon = 0$, but the larger network can be desynchronized for large enough delay. This was verified using numerical simulations of the full network (**Figure 3C**), where the ring of $N = 8$ nodes is desynchronized by the delay while that with $N = 7$ is not. Networks with random coupling also have complex eigenvalues, but the distribution tends to be clustered near the origin, especially for larger networks. See **Figure 4E** for some example distributions. Thus, for our model, these networks should exhibit synchronized solutions, largely unaffected by the presence of delays. Numerical

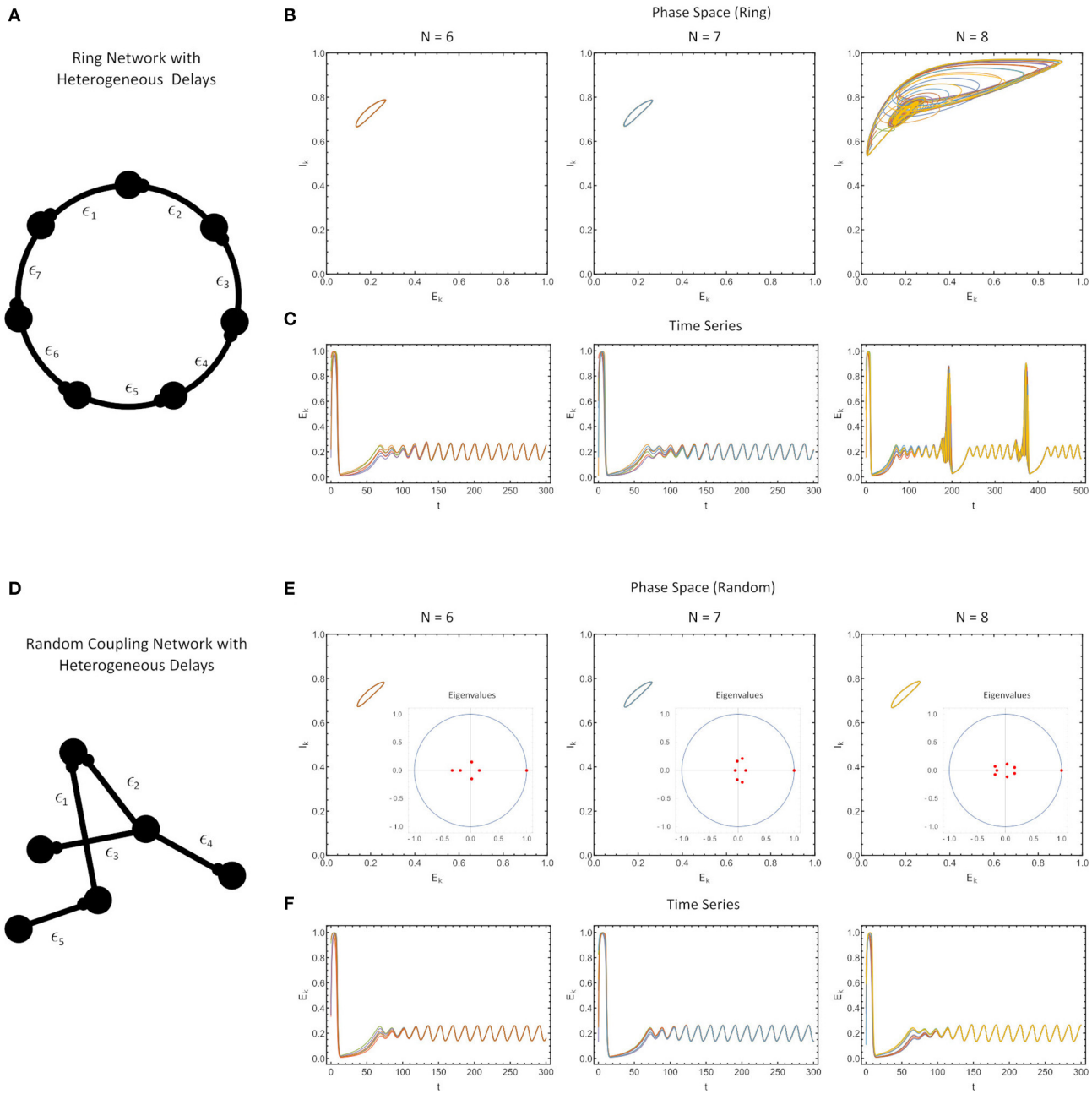

FIGURE 4 | (A) Ring network with heterogeneous delays, where each delay is drawn from a beta-distribution (see Methods) with the finite sample also renormalized to have a sample mean of $\epsilon = 0.1$. **(B)** Phase portrait of the ring in $[E(t), I(t)]$ space, for $N = 6$ (left), $N = 7$ (middle) and $N = 8$ (right). **(C)** The time series of simulations. **(D)** A randomly-coupled network with heterogeneous delays, drawn as in **(A–C)**. **(E)** The phase portrait in the $[E(t), I(t)]$ space with the eigenvalue spectrum of the sample-weight matrix drawn as an inset for randomly-coupled networks with $N = 6$ (left), $N = 7$ (middle) and $N = 8$ (right). **(F)** Time series of the simulations. For all simulations, the parameter values were: $W^E = 2.115$, $p = 0.2$, $\tau_1 = 1$, $\tau_2 = 5$, $W^{IE} = 1$, and $a = 5$.

simulations of some specific networks confirm this (see **Supplementary Figure 1**).

An example of a symmetric network is a lattice. Here the size of the second largest eigenvalue increases with the size of the network N. It was shown in Nicola and Campbell (2021) that for the model (Equation 1) with no delay ($\epsilon = 0$) and $W^E = 2.115$ a lattice of $N = 15$ nodes is synchronized while that with $N = 16$ is desynchronized. **Figure 3B** indicates that with delay $\epsilon = 0.1$ and the same value of W^E the lattice will be synchronized up to much larger values of N.

Heterogeneous Delays Largely Mirror Homogeneous Delay Case

Finally, we investigated how robust our results would be if the delays in our network were not homogeneous, but different for each connection. Here, the MSF approach does not extend, and thus, we opted to use numerical simulations for certain simple connectivity matrices (**Figure 4**). The only constraints in constructing these networks were that 1) all delays generated were positive and drawn from a beta-distribution and 2) the delays were re-scaled to force the sample mean of the delay to exactly match the nominal delay value we considered in **Figures 1–3** ($\epsilon = 0.1$).

First, we found that for ring networks, heterogeneity in the delays does not appreciably alter the synchronization characteristics of the network for the same fixed value of the coupling strength (W^E) as in the homogeneous delay network (**Figures 4A–C**). In fact, even the attractors themselves were minimally altered (compare **Figures 3C**, **4B**).

Second, we found that for all-to-all connected, row-sum normalized randomly-coupled networks, the solutions once again synchronized to identical attractors as for the ring networks (**Figures 4C,F**). Note that for systems which are all-to-all coupled, and with randomly chosen, row-sum normalized, the eigenvalues of the connectivity matrix shrink with the network size (aside from the dominant eigenvalue), which is a consequence of random matrix theory (Pastur and Shcherbina, 2011).

Of course the solutions cannot be perfectly synchronized since the delays are different. Close inspection shows that the different nodes have phase differences on the order of the size of the delay. Since the timescale of the delay is much smaller than the timescale of the oscillations in the WC system, these difference are not apparent in longer simulations. This can be explained by the analysis of Lücken et al. (2013) which determines conditions under which the distribution of delays in a network may be changed but still give equivalent dynamical behavior. The results of Lücken et al. (2013) apply directly to our ring networks and indicate that the system with heterogeneous delays will have the same attractor as that with homogeneous delays, but the phase relationships between the neurons will be different. A synchronized solution for the system with homogeneous delays becomes desynchronized in the system with heterogeneous delays, with the timescale of the desynchronization between neurons determined by the size of the delays.

Thus, numerically we find that the MSF results are robust for this WC system even with a heterogeneous distribution of delays, so long as the system with heterogeneous delays is compared to the homogeneous system with a delay equal to the sample mean of the heterogeneous system.

4. DISCUSSION

The impact of delays on a network cannot be readily disentangled without simultaneously considering both the network topology, and the dynamics of individual nodes. Here, we considered all three in networks of delay-coupled, homoeostatically controlled Wilson-Cowan nodes with the Master Stability Function formalism. First, we find that when networks do synchronize, they synchronize to the single self-delay coupled node. The single node itself undergoes a Hopf-bifurcation to induce oscillations which requires a stronger global strength with larger delay. For small delays, the behavior of the network is similar to the non-delay coupled case, and to the behavior of other neural systems (see Keane et al., 2012 for example). For larger delays, the shift in the Hopf-bifurcation to stronger coupling values has a secondary impact: all mixed-mode, period doubled, and chaotic solutions are no longer present. Next, by applying the MSF approach, we found that the impacts of a delay are dependent on the network structure. Networks with large magnitude, complex eigenvalues (like rings) are likely to lose stability in their synchronous solution(s) while networks with large magnitude, purely real eigenvalues are likely to gain stability in their synchronous solutions. For a sufficiently large delay, which pushes up the global coupling strength necessary to induce oscillations, synchrony is the norm.

The size of delay in our study was chosen so that the ratio of the delay (ϵ) to the synaptic time constants was < 1, as synaptic delays are typically in the sub-millisecond to millisecond range (Roxin et al., 2005; Ghosh et al., 2008; Deco et al., 2009). Nevertheless, delays in this biologically plausible range could still be large enough to induce the effects discussed above.

Our work highlights the importance of considering the network structure when considering the effect of time delay on synchronization behavior. In all cases we considered, the delay decreases the size of the region where synchronization is stable, however the region of stability also changes shape. In general, the region of stability near the right half of the unit circle decreases. This means that structured networks (such as unidirectional rings) are easier to desynchronize with larger delay. This is consistent with studies of structured networks that show that increasing the delay can lead to desynchronized cluster-like solutions (Choe et al., 2010; Kyrychko et al., 2014; Wang and Campbell, 2017; Kaslik and Mureşan, 2020; Kaslik et al., 2020). However, the synchronization region near the real axis was largely unchanged when the nodes exhibit periodic solutions. This means that networks with symmetric or near symmetric coupling are resistant to desynchronization by the delay. This is consistent with the results of studies across a variety of coupled networks with time delay (Dhamala et al., 2004; Choe et al., 2010; Flunkert et al., 2010, 2014; Kyrychko et al., 2014). For both the delayed and instantaneously coupled networks, the key determining factor for synchronization is the second-largest eigenvalue of the normalized connectivity matrix (Nicola and Campbell, 2021). Networks that generate larger eigenvalue distributions (e.g., more sparsely coupled networks) are more likely to desynchronize than networks that generate smaller eigenvalue distributions (e.g., more densely coupled networks).

A novel observation in our work was the influence of chaotic node behavior on synchronization. For networks

with symmetric or near-symmetric coupling, a region of desychronization occurs when the nodes exhibit chaotic or irregular behavior. As discussed above, delays decrease the size of this region of desynchronization due to the fact that increasing the delay can destroy the chaotic behavior. If one considers coupling strengths were increasing the delay creates or preserves the chaotic behavior of the nodes then the delay can *increase* the size of the region of desynchronization. Nevertheless, we always observe the ultimate loss of the chaotic solutions for sufficiently large delay. This is a subtle effect of the model setup where the type of synchronized solution that occurs depends on the coupling strength.

The fact that time delays can influence synchronization behavior has long been understood (Crook et al., 1997; Ermentrout and Kopell, 1998; Ko and Ermentrout, 2007; Choe et al., 2010; Lehnert et al., 2011; Pérez et al., 2011; Dahms et al., 2012; Panchuk et al., 2013; Sun and Guofang, 2017). Here we have contributed to this understanding through our study of Wilson-Cowan networks with homeostatic adjustment of the inhibitory weight. Our work builds on and extends prior work on Wilson-Cowan networks with time delays, which focussed primarily on small networks (one or two nodes) and/or networks without the homeostatic adjustment (Coombes and Laing, 2009; Pasillas-Lépine, 2013; Kaslik and Mureşan, 2020; Kaslik et al., 2020).

DATA AVAILABILITY STATEMENT

The computer code for this study can be found on: ModelDB (https://senselab.med.yale.edu/modeldb/) Accession Number: 267010.

AUTHOR CONTRIBUTIONS

IA-D, LC, and WN performed the numerical simulations. IA-D and SC performed the analysis. IA-D, LC, WN, and SC wrote the manuscript and **Supplementary Materials**. All authors contributed to the article and approved the submitted version.

FUNDING

WN is supported by an NSERC Discovery Grant, a CIHR Canada Research Chair in Computational Neuroscience, and through the Hotchkiss Brain Institute in the Cumming School of Medicine at the University of Calgary. SC is supported by an NSERC Discovery Grant.

SUPPLEMENTARY MATERIAL

The Supplementary Material for this article can be found online at: https://www.frontiersin.org/articles/10.3389/fnsys.2021.688517/full#supplementary-material

REFERENCES

Bullmore, E., and Sporns, O. (2009). Complex brain networks: graph theoretical analysis of structural and functional systems. *Nat. Rev. Neurosci.* 10, 186–198. doi: 10.1038/nrn2575

Choe, C.-U., Dahms, T., Hövel, P., and Schöll, E. (2010). Controlling synchrony by delay coupling in networks: From in-phase to splay and cluster states. *Phys. Rev. E* 81, 025205. doi: 10.1103/PhysRevE.81.025205

Coombes, S., and Laing, C. (2009). Delays in activity-based neural networks. *Phil. Trans. R. Soc. A Math. Phys. Eng. Sci.* 367, 1117–1129. doi: 10.1098/rsta.2008.0256

Cowan, J. D., Neuman, J., and van Drongelen, W. (2016). Wilson–Cowan equations for neocortical dynamics. *J. Math. Neurosci.* 6, 1–24. doi: 10.1186/s13408-015-0034-5

Crook, S. M., Ermentrout, G. B., Vanier, M. C., and Bower, J. M. (1997). The role of axonal delay in synchronization of networks of coupled cortical oscillators. *J. Comput. Neurosci.* 4, 161–172. doi: 10.1023/A:1008843412952

Dahms, T., Lehnert, J., and Schöll, E. (2012). Cluster and group synchronization in delay-coupled networks. *Phys. Rev. E* 86, 016202. doi: 10.1103/PhysRevE.86.016202

Deco, G., Jirsa, V., McIntosh, A. R., Sporns, O., and Kötter, R. (2009). Key role of coupling, delay, and noise in resting brain fluctuations. *Proc. Natl. Acad. Sci. U.S.A.* 106, 10302–10307. doi: 10.1073/pnas.0901831106

Destexhe, A., and Sejnowski, T. J. (2009). The Wilson–Cowan model, 36 years later. *Biol. Cybern.* 101, 1–2. doi: 10.1007/s00422-009-0328-3

Dhamala, M., Jirsa, V. K., and Ding, M. (2004). Enhancement of neural synchrony by time delay. *Phys. Rev. Lett.* 92, 074104. doi: 10.1103/PhysRevLett.92.074104

Engelborghs, K., Luzyanina, T., and Samaey, G. (2001). *DDE–BIFTOOL v. 2.00: A Matlab Package for Bifurcation Analysis of Delay Differential Equations*. Technical Report TW–330, Department of Computer Science, K.U. Leuven, Leuven, Belgium.

Ermentrout, G. B., and Kopell, N. (1998). Fine structure of neural spiking and synchronization in the presence of conduction delays. *Proc. Natl. Acad. Sci. U.S.A.* 95, 1259–1264. doi: 10.1073/pnas.95.3.1259

Farmer, J. D. (1982). Chaotic attractors of an infinite-dimensional dynamical system. *Physica D* 4, 366–393. doi: 10.1016/0167-2789(82)90042-2

Flunkert, V., Yanchuk, S., Dahms, T., and Schöll, E. (2010). Synchronizing distant nodes: a universal classification of networks. *Phys. Rev. Lett.* 105, 254101. doi: 10.1103/PhysRevLett.105.254101

Flunkert, V., Yanchuk, S., Dahms, T., and Schöll, E. (2014). Synchronizability of networks with strongly delayed links: a universal classification. *J. Math. Sci.* 202, 809–824. doi: 10.1007/s10958-014-2078-6

Ghosh, A., Rho, Y., McIntosh, A. R., Kötter, R., and Jirsa, V. K. (2008). Cortical network dynamics with time delays reveals functional connectivity in the resting brain. *Cogn. Neurodyn.* 2, 115. doi: 10.1007/s11571-008-9044-2

Hellyer, P. J., Jachs, B., Clopath, C., and Leech, R. (2016). Local inhibitory plasticity tunes macroscopic brain dynamics and allows the emergence of functional brain networks. *NeuroImage* 124, 85–95. doi: 10.1016/j.neuroimage.2015.08.069

Kaslik, E., Kokovics, E.-A., and Rădulescu, A. (2020). "Wilson–Cowan neuronal interaction models with distributed delays," in *New Trends in Nonlinear Dynamics* (Cham: Springer), 203–211.

Kaslik, E., and Mureşan, R. (2020). "Dynamics of a homeostatically regulated neural system with delayed connectivity," in *New Trends in Nonlinear Dynamics* (Cham: Springer), 173–182.

Keane, A., Dahms, T., Lehnert, J., Suryanarayana, S. A., Hövel, P., and Schöll, E. (2012). Synchronisation in networks of delay-coupled type-I excitable systems. *Eur. Phys. J. B* 85, 1–9. doi: 10.1140/epjb/e2012-30810-x

Keeling, M. J., and Eames, K. T. D. (2005). Networks and epidemic models. *J. R. Soc. Interface* 2, 295–307. doi: 10.1098/rsif.2005.0051

Kitano, H. (2002). Systems biology: a brief overview. *Science* 295, 1662–1664. doi: 10.1126/science.1069492

Ko, T.-W., and Ermentrout, G. B. (2007). Effects of axonal time delay on synchronization and wave formation in sparsely coupled neuronal oscillators. *Phys. Rev. E* 76, 056206. doi: 10.1103/PhysRevE.76.056206

Kyrychko, Y. N., Blyuss, K. B., and Schöll, E. (2014). Synchronization of networks of oscillators with distributed delay coupling. *Chaos* 24, 043117. doi: 10.1063/1.4898771

Lakshmanan, M., and Senthilkumar, D. V. (2011). *Dynamics of Nonlinear Time-Delay Systems*. Berlin: Springer Science & Business Media.

Lehnert, J., Dahms, T., Hövel, P., and Schöll, E. (2011). Loss of synchronization in complex neuronal networks with delay. *EPL* 96, 60013. doi: 10.1209/0295-5075/96/60013

Lücken, L., Pade, J. P., Knauer, K., and Yanchuk, S. (2013). Reduction of interaction delays in networks. *EPL* 103, 10006. doi: 10.1209/0295-5075/103/10006

Montoya, J. M., Pimm, S. L., and Solé R. V. (2006). Ecological networks and their fragility. *Nature* 442, 259–264. doi: 10.1038/nature04927

Nicola, W., and Campbell, S. A. (2021) Normalized connectomes show increased synchronizability with age through their second largest eigenvalue. *SIAM J. Appl. Dyn. Sys*.

Nicola, W., Hellyer, P. J., Campbell, S. A., and Clopath, C. (2018). Chaos in homeostatically regulated neural systems. *Chaos* 28, 083104. doi: 10.1063/1.5026489

Panchuk, A., Rosin, D. P., Hövel, P., and Schöll, E. (2013). Synchronization of coupled neural oscillators with heterogeneous delays. *Int. J. Bifurc. Chaos* 23:1330039. doi: 10.1142/S0218127413300395

Pasillas-Lépine, W. (2013). Delay-induced oscillations in Wilson and Cowan's model: an analysis of the subthalamo-pallidal feedback loop in healthy and parkinsonian subjects. *Biol. Cybern.* 107, 289–308. doi: 10.1007/s00422-013-0549-3

Pastur, L. A., and Shcherbina, M. (2011). *Eigenvalue Distribution of Large Random Matrices*. Number 171. Providence, RI: American Mathematical Soc.

Pecora, L. M., and Carroll, T. L. (1990). Synchronization in chaotic systems. *Phys. Rev. Lett.* 64, 821. doi: 10.1103/PhysRevLett.64.821

Pérez, T., Garcia, G. C., Eguiluz, V. M., Vicente, R., Pipa, G., and Mirasso, C. (2011). Effect of the topology and delayed interactions in neuronal networks synchronization. *PloS ONE* 6:e19900. doi: 10.1371/journal.pone.0019900

Roxin, A., Brunel, N., and Hansel, D. (2005). Role of delays in shaping spatiotemporal dynamics of neuronal activity in large networks. *Phys. Rev. Lett.* 94, 238103. doi: 10.1103/PhysRevLett.94.238103

Sun, X., and Guofang, L. (2017). Synchronization transitions induced by partial time delay in an excitatory-inhibitory coupled neuronal network. *Nonlinear Dyn.* 89, 2509–2520. doi: 10.1007/s11071-017-3600-4

Uhlhaas, P. J., and Singer, W. (2006). Neural synchrony in brain disorders: relevance for cognitive dysfunctions and pathophysiology. *Neuron* 52, 155–168. doi: 10.1016/j.neuron.2006.09.020

Varela, F., Lachaux, J.-P., Rodriguez, E., and Martinerie, J. (2001). The brainweb: phase synchronization and large-scale integration. *Nat. Rev. Neurosci.* 2, 229–239. doi: 10.1038/35067550

Vogels, T. P., Sprekeler, H., Zenke, F., Clopath, C., and Gerstner, W. (2011). Inhibitory plasticity balances excitation and inhibition in sensory pathways and memory networks. *Science* 334, 1569–1573. doi: 10.1126/science.1211095

Wang, Z., and Campbell, S. A. (2017). Symmetry, Hopf bifurcation, and the emergence of cluster solutions in time delayed neural networks. *Chaos* 27, 114316. doi: 10.1063/1.5006921

Wilson, H. R., and Cowan, J. D. (1972). Excitatory and inhibitory interactions in localized populations of model neurons. *Biophys. J.* 12, 1–24. doi: 10.1016/S0006-3495(72)86068-5

Conflict of Interest: The authors declare that the research was conducted in the absence of any commercial or financial relationships that could be construed as a potential conflict of interest.

frontiers in Computational Neuroscience

ORIGINAL RESEARCH
published: 14 July 2021
doi: 10.3389/fncom.2021.687075

Structural Features of the Human Connectome That Facilitate the Switching of Brain Dynamics via Noradrenergic Neuromodulation

*Carlos Coronel-Oliveros [1,2], Samy Castro [3,4], Rodrigo Cofré [5,6] and Patricio Orio [1,7]**

[1] Instituto Milenio Centro Interdisciplinario de Neurociencia de Valparaíso, Universidad de Valparaíso, Valparaíso, Chile, [2] Programa de Doctorado en Ciencias, Mención Biofísica y Biología Computacional, Universidad de Valparaíso, Valparaíso, Chile, [3] Laboratoire de Neurosciences Cognitives et Adaptatives (LNCA), Faculté de Psychologie, Université de Strasbourg, Strasbourg, France, [4] University of Strasbourg Institute for Advanced Studies (USIAS), Université de Strasbourg, Strasbourg, France, [5] CIMFAV-Ingemat, Facultad de Ingeniería, Universidad de Valparaíso, Valparaíso, Chile, [6] Institute of Neuroscience (NeuroPSI), Paris-Saclay University, Centre National de la Recherche Scientifique (CNRS), Gif-sur-Yvette, France, [7] Facultad de Ciencias, Instituto de Neurociencias, Universidad de Valparaíso, Valparaíso, Chile

The structural connectivity of human brain allows the coexistence of segregated and integrated states of activity. Neuromodulatory systems facilitate the transition between these functional states and recent computational studies have shown how an interplay between the noradrenergic and cholinergic systems define these transitions. However, there is still much to be known about the interaction between the structural connectivity and the effect of neuromodulation, and to what extent the connectome facilitates dynamic transitions. In this work, we use a whole brain model, based on the Jasen and Rit equations plus a human structural connectivity matrix, to find out which structural features of the human connectome network define the optimal neuromodulatory effects. We simulated the effect of the noradrenergic system as changes in filter gain, and studied its effects related to the global-, local-, and meso-scale features of the connectome. At the global-scale, we found that the ability of the network of transiting through a variety of dynamical states is disrupted by randomization of the connection weights. By simulating neuromodulation of partial subsets of nodes, we found that transitions between integrated and segregated states are more easily achieved when targeting nodes with greater connection strengths—local feature—or belonging to the rich club—meso-scale feature. Overall, our findings clarify how the network spatial features, at different levels, interact with neuromodulation to facilitate the switching between segregated and integrated brain states and to sustain a richer brain dynamics.

Keywords: whole brain model, neuromodulation, integration and segregation, network topology, noradrenaline, rich club organization

OPEN ACCESS

Edited by:
Joana Cabral,
University of Minho, Portugal

Reviewed by:
Kelly Shen,
Rotman Research Institute (RRI), Canada
Changsong Zhou,
Hong Kong Baptist University, Hong Kong

***Correspondence:**
Patricio Orio
patrico.orio@uv.cl

Received: *28 March 2021*
Accepted: *11 June 2021*
Published: *14 July 2021*

Citation:
Coronel-Oliveros C, Castro S, Cofré R and Orio P (2021) Structural Features of the Human Connectome That Facilitate the Switching of Brain Dynamics via Noradrenergic Neuromodulation. Front. Comput. Neurosci. 15:687075. doi: 10.3389/fncom.2021.687075

1. INTRODUCTION

The human brain generates a rich repertoire of spatiotemporal dynamics characterized by the *integrated* and *segregated* functional states (Tononi, 2004). Information processed in parallel by domain-specific systems (segregated) is brought together (integrated) to guide adaptive behavior (Dehaene and Changeux, 2011). The balance between segregation and integration is essential to

coordinate the local and global communication of neural information, it is needed to support a wide variety of cognitive functions, and has been proposed as a prominent organizational principle of the brain (Sporns, 2013; Cohen and D'Esposito, 2016; Shine, 2019; Wang et al., 2021). The dynamics and flexibility of brain activity, necessary for the coherent global functioning of the brain, enables the coexistence of segregated and integrated brain states (Kelso, 2012; Tognoli and Kelso, 2014; Wang et al., 2021).

Neuroimaging recording techniques such as electroencephalography (EEG) and functional magnetic resonance imaging (fMRI) allow the characterization of functional connectivity (FC) of the brain, from which the functional integration and segregation can be quantified using network theory tools (Bullmore and Sporns, 2009; González et al., 2016). The observed patterns of FC reflect the diversity of neuronal dynamics that emerge, among others, from the nonlinear dynamics of brain regions interconnected through structural connectivity (SC) (Deco and Jirsa, 2012; Lord et al., 2017; Guan et al., 2020). FC continuously evolves even in resting conditions (Allen et al., 2014; Hansen et al., 2015; Cabral et al., 2017), moreover, it changes across several tasks, highlighting the flexible nature of brain dynamics (Cohen and D'Esposito, 2016; Shine et al., 2016, 2019; Wang et al., 2021).

A plausible mechanism to facilitate—and regulate—transitions between different FC patterns are neuromodulatory systems. Neuromodulators do not directly excite neurons. Instead, they change their excitability and response to neurotransmitters, increasing or decreasing the probability of firing action potentials (Thiele and Bellgrove, 2018). The role of the cholinergic and noradrenergic systems in managing the segregation/integration balance has been evidenced in experimental (Shine et al., 2016, 2018b; Pfeffer et al., 2020), and theoretical frameworks (Shine et al., 2018a; Pfeffer et al., 2020; Coronel-Oliveros et al., 2021).

The noradrenergic system is involved in arousal when subjects engage in high-load cognitive tasks (Aston-Jones and Cohen, 2005; Shine et al., 2016, 2018b). For example, in fMRI recordings during an N-back task (for assessing working memory), the pupil diameter—a marker of noradrenergic tone (Reimer et al., 2016)—increases (Shine et al., 2016, 2018b). The principal source of noradrenaline in the cerebral cortex comes from the locus coeruleus (LC) (Fuxe et al., 2010). The GANE model of gain modulation (Mather et al., 2016; Lee et al., 2018), proposes that the noradrenergic system modulates neural response through an excitatory feedback loop between glutamate receptors on varicosities of LC projections and adrenergic β receptors on presynaptic glutamatergic neurons. At the same time, less activated neurons are suppressed through the action of adrenergic α_2 autoreceptors expressed on the varicosities. The overall result comprises an increase of the neuron responsivity above a threshold, and a decrease of the responsivity below this threshold. This is equivalent to increasing the slope of the input-output sigmoid function, also named filter gain, as proposed in Servan-Schreiber et al. (1990) and Aston-Jones and Cohen (2005).

In a recent article (Shine, 2019), the noradrenergic system was considered to promote an integrated functional network configuration increasing the filter gain (Servan-Schreiber et al., 1990; Aston-Jones and Cohen, 2005; Mather et al., 2016; Thiele and Bellgrove, 2018). Computational studies (Shine et al., 2018a; Coronel-Oliveros et al., 2021) have also shown how the interplay between cholinergic and noradrenergic systems can regulate the segregation/integration balance. While recent theoretical articles point out that a non-uniform neuromodulation can explain better the effects of neuromodulatory systems in brain dynamics (Deco et al., 2018; Kringelbach et al., 2020), most studies so far have considered homogeneous neuromodulation, i.e., acting in all nodes in the same way.

There is evidence about the importance of network properties of the human connectome (Cabral et al., 2014; Zamora-López et al., 2016; Wang et al., 2019; Castro et al., 2020). For example, its hierarchical modular organization is needed to sustain a richer brain dynamics (Zamora-López et al., 2016; Wang et al., 2019). Then, the repertoire of network configurations, as a way to conceptualize the dynamical richness, can be affected by neuromodulation. Using a neural mass model to simulate neural activity, Shine et al. (2018a) showed that rich club regions were strongly neuromodulated compared with non-rich club members, especially between the transition from functional segregation to integration. This work notably suggests that some particular brain regions play a key role in the switching between different functional states via neuromodulation. Here, instead of quantifying what regions would be strongly neuromodulated, we studied how much the impact would be on integration and segregation when neuromodulating specific subsets of nodes, and analyzed the structural features that define the nodes that, upon modulation, have the largest effect on the network dynamics as a whole.

To investigate this issue, we built a whole-brain model based on the Jansen and Rit equations (Jansen et al., 1993; Jansen and Rit, 1995) coupled to a human SC matrix, that allows us to simulate the effect of the noradrenergic system on the functional integration and segregation features of the network (Coronel-Oliveros et al., 2021). The interaction between neuromodulation and structural connectivity was studied at three levels: at the global-scale, we used random surrogate connectomes that preserve the number and strength of connections but disrupt the global patterns. At the meso-scale, we determined whether the modulation of a node subset containing the anatomical rich club (Opsahl et al., 2008; Van Den Heuvel and Sporns, 2011) or the critical *s*-core (Garas et al., 2012; Eidsaa and Almaas, 2013), is optimal to produce a change in network dynamics, compared to randomly chosen subsets. At the local-scale, we explored which local properties define the set of nodes that, when being neuromodulated, maximize the effect on network dynamics.

We found that when we selectively neuromodulated the brain regions by the rich club (meso-scale property) or the high strength criteria (local-scale) the whole-brain network dynamics is most effectively modified. Additionally, we observed that surrogate connectomes reduced FC richness, compared with human SC, when neuromodulated. Overall, our findings clarify how the neuromodulation interacts with the anatomical network features at local-, meso-, and macro-scale levels in a whole-brain

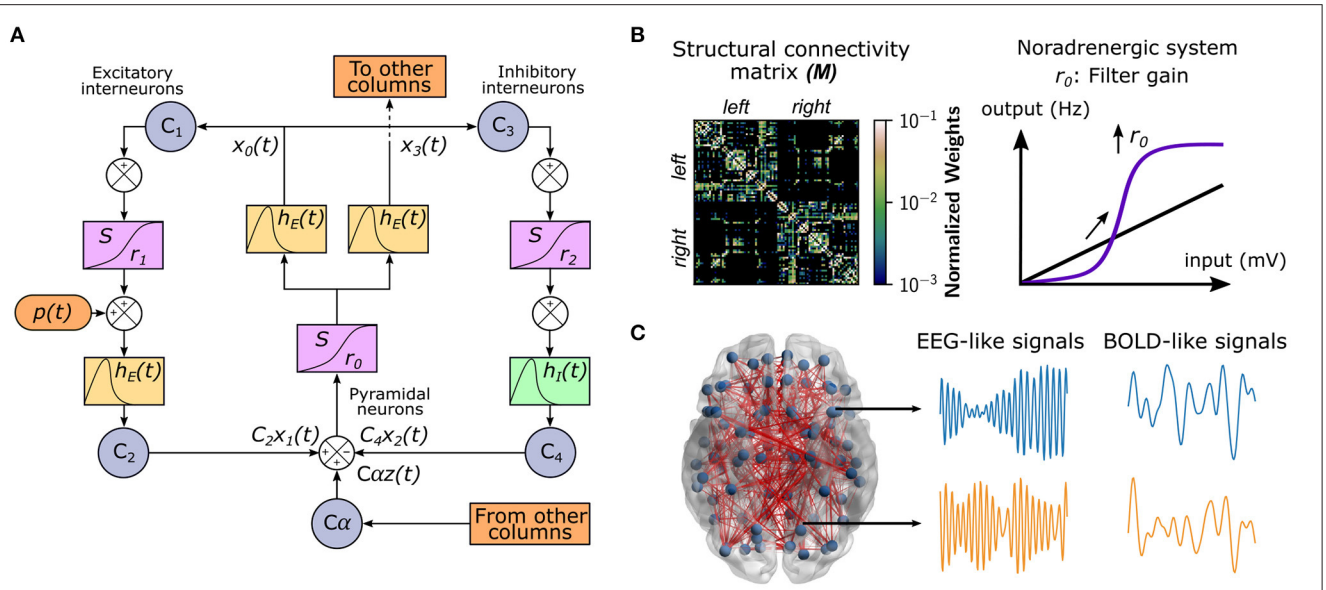

FIGURE 1 | Whole-brain neural mass model with neuromodulation. **(A)** The Jansen and Rit model is composed of a population of pyramidal neurons with excitatory and inhibitory feedback mediated by interneurons. A series of constants C_i connect each population. The outputs are transformed from average pulse density to average postsynaptic membrane potential by an excitatory (inhibitory) impulse response function $h_E(t)$ [$h_I(t)$]. Then, a sigmoid function S performs the inverse operation. Pyramidal neurons project to distant brain areas and receive both uncorrelated Gaussian-distributed inputs $p(t)$ and inputs from other regions $z(t)$, scaled by a global coupling parameter α. **(B)** Each node represents a cortical region, whose dynamics are ruled by the Jansen and Rit equations. The structural connectivity matrix, M, is the map of the connections (and their weights in the color bar) between cortical regions (row and columns of the matrix). The noradrenergic system increments pyramidal neuron responsivity to relevant stimuli with respect to noise, as a filter, by increasing the slope r_0 of their sigmoid function. **(C)** The whole-brain model comprises 90 cortical and subcortical regions linked by a human connectome. For each region, the model produces both EEG-like and BOLD-like signals. The brain figure was obtained using the BrainNet Viewer (Xia et al., 2013).

model to facilitate switching between segregated and integrated brain states.

2. RESULTS

To study the effect of neuromodulatory systems on the integrative/segregative capacities of the human connectome, we used a whole-brain model of brain activity (Coronel-Oliveros et al., 2021). In this model, each node corresponds to a brain area represented by a neural mass, which consists of three populations (Jansen et al., 1993; Jansen and Rit, 1995): pyramidal neurons, excitatory, and inhibitory interneurons (**Figure 1A**). We used the same parameters as in Jansen et al. (1993) and Jansen and Rit (1995), except the connectivity constant from inhibitory interneurons to pyramidal neurons C_4, which we modified to $C_4 = 0.5C$, being C the original intra-area connectivity constant of the model. The nodes are connected through a weighted undirected structural connectivity matrix derived from human MRI data (Deco et al., 2018), parcelated in 90 cortical and sub-cortical regions with the automated anatomical labeling (AAL) atlas (Tzourio-Mazoyer et al., 2002; **Figure 1B**). Pyramidal neurons connect regions (or nodes) because it is considered that long-range projections are mainly excitatory (Gilbert et al., 1990; McGuire et al., 1991). The simulations generate firing rates in each node of the network, which was used as an input to a generalized hemodynamic model (Stephan et al., 2007). In this way, we obtained fMRI BOLD-like signals (**Figure 1C**) from which we built the FC matrices.

We modeled the influence of the noradrenergic system through the manipulation of the filter gain (Aston-Jones and Cohen, 2005; Shine, 2019; **Figure 1B**). The filter gain r_0 modifies the sigmoid function slope of pyramidal neurons, increasing their responsivity to relevant stimuli, decreasing the response to low amplitude stimuli, and boosting the signal-to-noise ratio.

2.1. Human Structural Connectivity Enhances Dynamical Richness

First, we analyzed how neuromodulation depends on the connectivity pattern of the human connectome by using different randomized surrogate connectomes. We employed a degree- and strength-preserving randomization (DSPR), which randomizes the structural connectivity while preserving original degree and strength distributions (**Figure 2B**); in this way we can study the effect of disrupting the global connectivity without altering the local nodal properties. In addition, we employed a complete randomization of the structural connectivity (**Figure 2C**), which does not preserve the degree and strength distributions. Finally, a homogenization (binarization) of the connectome was considered (**Figure 2D**); this surrogate preserves the topology, disrupting the non-uniform weight distribution. We simulated EEG-like and fMRI BOLD-like signals from the Jansen and Rit model at different combinations of $\alpha \in [0, 1]$ and $r_0 \in [0, 1]$

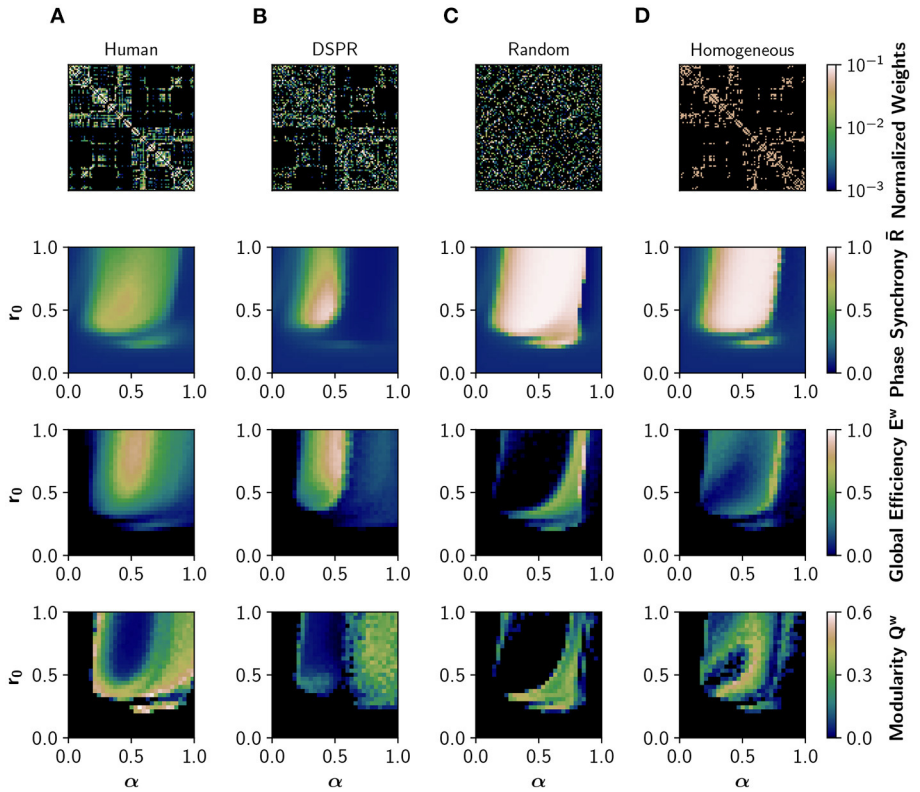

FIGURE 2 | Effects of network structure in neural synchronization and integration. From top to bottom: structural connectivity matrix, phase synchrony $\bar{R}$, global efficiency E^w (a measure of integration), and modularity Q^w (measure of segregation), obtained in the model with different structural connectivities. $\bar{R}$ was obtained from EEG-like simulated activity, while E^w and Q^w were calculated using the FC obtained from the corresponding fMRI BOLD-like traces. **(A)** Human structural connectivity (Human). **(B)** Degree- and strength-preserving randomized version of Human (DSPR). **(C)** Randomized version of Human, where weight values were shuffled across the full matrix (Random). **(D)** Homogeneous version of Human, having the same weight in all connections (Homogeneous).

parameters. Here, the value of the parameters is equal for all the nodes, and we refer to this case as uniform neuromodulation. We computed the mean of the Kuramoto order parameter, also known as phase synchrony $\bar{R}$, the global efficiency, E^w, and the modularity, Q^w, as measures of global phase synchronization, integration, and segregation, respectively. Global efficiency is a measure of integration defined as the inverse of the characteristic path length (Rubinov and Sporns, 2010). High values of E^w represent an efficient coordination between all pairs of nodes in the network, a signature of integration. Modularity is a measure of segregation based on the detection of network communities, or modules (Rubinov and Sporns, 2010); high modularity Q^w is associated with segregation and vice-versa.

Figure 2A shows how neuromodulation of the human connectome causes a shift of the model toward a synchronized and integrated state, with maximum integration observed in an intermediate region of the parameter space, as previously reported in Shine et al. (2018a) and Coronel-Oliveros et al. (2021). The synchrony $\bar{R}$ has an upper bound of 0.76, that is, the network never fully synchronizes. The transition is gradual, with many regions showing an intermediate behavior characterized by higher metastability and richer dynamics (Zamora-López et al., 2016; Shine et al., 2018a; Coronel-Oliveros et al., 2021). Moreover, the region of the parameter space where $\bar{R}$ increases matches the increment in global efficiency, E^w, verifying a link between the fast dynamics of EEG and the slower one of fMRI-BOLD.

We repeated the same exploration using the DSPR surrogate connectome (**Figure 2B**; Rubinov and Sporns, 2011). The area of synchronized activity in the parameter space (r_0, α) is reduced, and a spot of over-synchronized activity can be appreciated. Most importantly, the area of intermediate values of synchrony and integration is largely reduced, suggesting a reduction of dynamical richness. When the connectivity matrix is completely randomized (**Figure 2C**), or made homogeneous by assigning equal weights to all connections (**Figure 2D**), neuromodulation produces a large area of over-synchronized activity in the parameter space and fewer regions with intermediate behavior.

The dramatic decrease in E^w in **Figures 2C,D** is a consequence of the over-synchronization ($\bar{R} \approx 1$) triggered by randomization. When signals are highly synchronized in our model, the envelope in the alpha band of the EEG (between 8 and 13 Hz) becomes flat, and so does the BOLD-like signal calculated with the hemodynamic model (Foster et al., 2016). For this reason, this

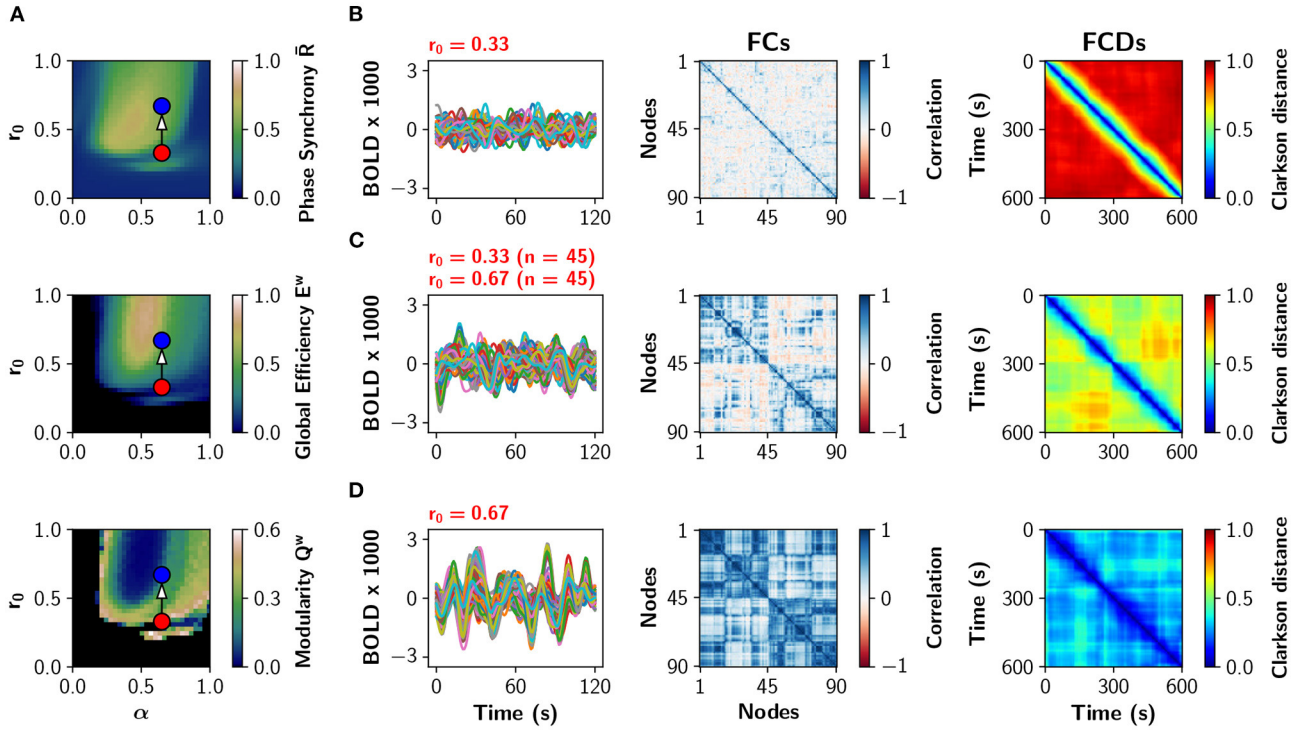

FIGURE 3 | Partial noradrenergic neuromodulation. **(A)** The (α, r_0) parameter space showing phase synchrony $\bar{R}$, global efficiency E^w, and modularity Q^w, for the Human connectome (same as in **Figure 2A**). Blue and red dots are references for **(B–D)**. **(B–D)** BOLD-like signals, FC and FCD matrices obtained when all nodes have $\alpha = 0.65$ and **(B)** $r_0 = 0.33$; **(C)** 45 nodes have $r_0 = 0.33$ and 45 nodes have $r_0 = 0.67$; and **(D)** all nodes have $r_0 = 0.67$. In **(C)**, the 45 nodes with the highest strength were modified to $r_0 = 0.67$.

drop in E^w should not be interpreted as a reduction of integration but a limitation of the hemodynamic model we employed in input simulations. Nevertheless, an over-synchronized regime of activity is a feature never found in the healthy brain (Miron-Shahar et al., 2019).

Thus, in line with several previous reports (Cabral et al., 2014; Zamora-López et al., 2016; Wang et al., 2019; Fukushima and Sporns, 2020), disrupting the organization of the human connectome (or the weight relationships between nodes) causes over-synchronization, and highly metastable regimes can not be easily reached employing neuromodulation.

In the following, we will study which local- or meso-scale organization features are determinant in the effect of neuromodulation of human connectome by evaluating the network behavior when changing the r_0 parameter in subsets of network nodes.

2.2. Neuromodulation of High-Strength Nodes Promotes Better Functional Integration

In this section, we investigate the impact on functional integration when an increasing number of nodes are neuromodulated. The order in which nodes are modulated is defined considering nodal measures obtained from the structural matrix M. We calculated, for each node $i \in [1 \ldots n]$: node strength, K_i^w, nodal efficiency, E_i^w, and clustering coefficient, C_i^w (Rubinov and Sporns, 2010). The superscript w indicates the use of the weighted versions of the measures. Then, for each metric, nodes were ordered either from high to low or from low to high. We fixed the global coupling $\alpha = 0.65$, and swept $r_0 \in [0.33, 1]$ and the number of nodes being neuromodulated in $[0, 90]$ in steps of three. As before, we used the EEG-like and BOLD-like signals to extract synchrony, integration, and segregation.

A particular example of partial neuromodulation is shown with some detail in **Figure 3**. The (α, r_0) parameter space is shown in **Figure 3A** depicting global phase synchrony $\bar{R}$, global efficiency E^w and modularity Q^w in a uniform neuromodulation scenario (all nodes identical). **Figure 3B** shows sample BOLD traces, the functional connectivity (FC) and the functional connectivity dynamics (FCD) matrices for $\alpha = 0.65, r_0 = 0.33$ (red dot in **Figure 3A**). The FCD matrix visually represents the dynamical richness of the network, by computing time-dependent FCs using sliding windows (Cabral et al., 2017; Orio et al., 2018). Then, FCs are vectorized and compared to each other using the Clarkson distance (Clarkson, 1936), resulting in a matrix of time vs. time. At the bottom, **Figure 3D** shows the same analysis for $\alpha = 0.65, r_0 = 0.67$ (blue dot in **Figure 3A**). In the middle, **Figure 3C** shows the results when only half of the nodes have been neuromodulated to $r_0 = 0.67$ while the rest remain with $r_0 = 0.33$. As the number of nodes with $r_0 = 0.67$ increases, the FC matrices become more integrated (high E^w

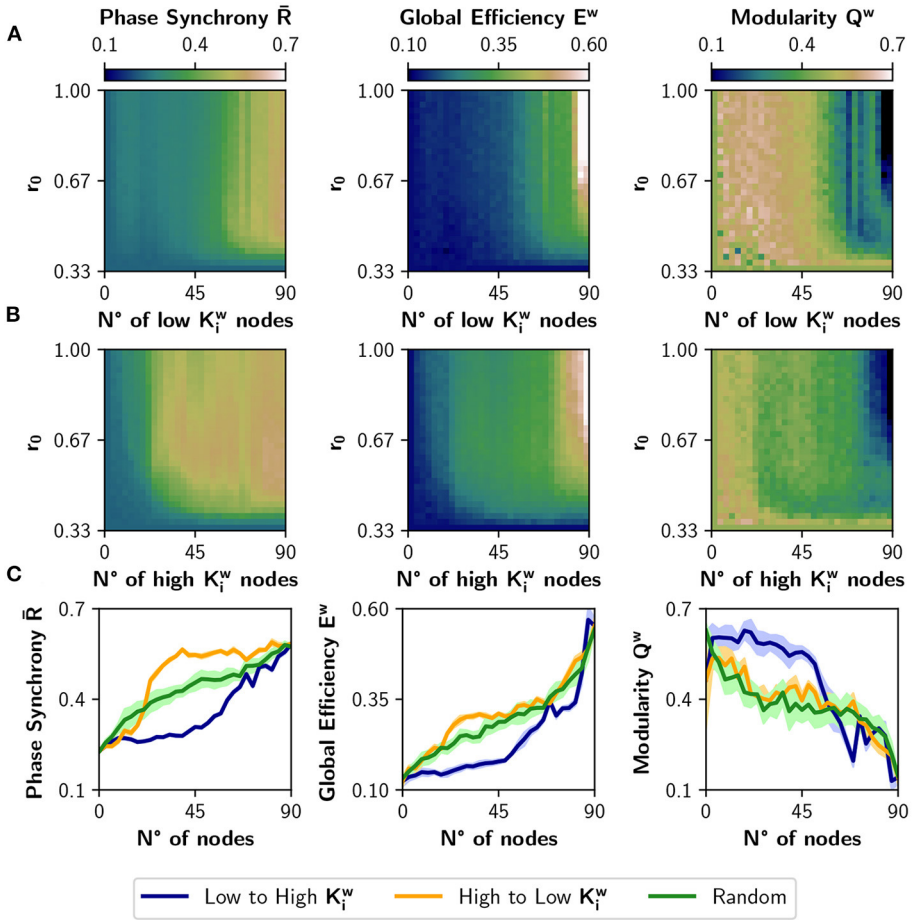

FIGURE 4 | Incremental neuromodulation based on node strength. **(A)** Effect of the neuromodulation on phase synchrony $\bar{R}$, global efficiency E^w, and modularity Q^w, at different combinations of r_0 and number of neuromodulated nodes. Nodes were affected by neuromodulation according to their strength, from low to high. **(B)** Effect of the neuromodulation of nodes sorted from high to low strength. **(C)** Metrics as a function of the number of neuromodulated nodes, for $r_0 = 0.67$ as target value. Blue curves for neuromodulation of nodes with low strength, orange the opposite, and green for a random ordering of the nodes. Shaded areas correspond to 95% confidence intervals, for 10 realizations.

and low Q^w values). Similarly, the FCD matrices change from incoherence (red FCD), to exhibit multi-stable behavior (FCD with yellow-green patches), and finally to show correlated FC patterns (blue FCD). In summary, the increment of the number of neuromodulated nodes increases phase synchrony, functional integration, and the time correlation of FCs captured by the FCD.

Figure 4 shows the result of neuromodulating r_0 with a target value in the $[0.33, 1]$ interval and with the number of neuromodulated nodes ranging from 0 to 90. The order in which nodes are neuromodulated is either from low to high K_i^w (**Figure 4A**) or viceversa (**Figure 4B**). When the number of neuromodulated nodes is large, $\bar{R}$ and E^w raise markedly in both cases; the opposite can be observed for Q^w. However, picking the nodes of high strength first (**Figure 4B**) has greater impact in the change of those metrics. The difference is best appreciated in **Figure 4C**, where we selected a target r_0 value of 0.67. There, the curves for the high to low K_i^w sorting (in orange) present a larger effect at the beginning, compared with the low to high K_i^w sorting (in blue). We can conclude that nodes with higher strength have a greater impact on functional integration, and inspection of the colormaps of **Figures 4A,B** reveals that this is true for almost all values of target r_0. The results were also compared with a random selection of nodes for neuromodulation (green curves). As the blue curve is mainly below the green curve, neuromodulation of nodes with low K_i^w produces less synchronized and integrated dynamics than expected by a random neuromodulation. In contrast, choosing high K_i^w nodes is not different from random selection, when looking at the measures of integration and segregation. In consequence, there is a range (or possibly a set) of nodes that produce a robust integration when neuromodulated, compared to a random choice of nodes.

We compared the results of sorting the nodes based on strength K_i^w, with ranking the nodes based on nodal efficiency E_i^w or clustering coefficient C_i^w (**Figure 5**). A node with a high E_i^w has many short paths to the rest of the nodes of the network, while a high C_i^w is expected for nodes whose neighbors are

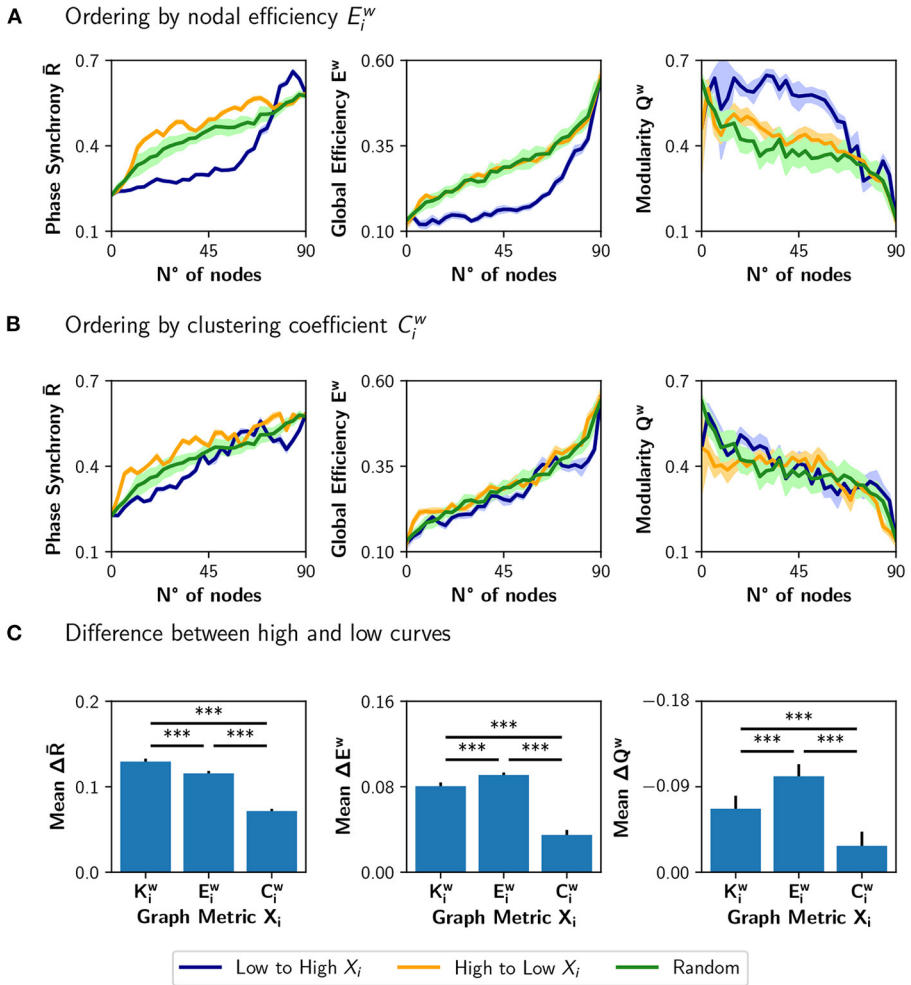

FIGURE 5 | Incremental neuromodulation based on nodal efficiency and clustering coefficient. **(A,B)** Phase synchrony $\bar{R}$, global efficiency E^w, and modularity Q^w as a function of the number of neuromodulated nodes, for $r_0 = 0.67$ as target value. In **(A)**, nodes were sorted according to nodal efficiency, E_i^w, and in **(B)** according to the clustering coefficient, C_i^w. Blue curves for sorting of nodes from low to high (of the particular metric), orange is from high to low, and green for a random sorting of the nodes. **(C)** Difference between the area under the curve (AUC) of high vs. low sorting, averaged over the 10 realizations. Shaded areas in **(A,B)** correspond to 95% confidence intervals, and barplots were built using the mean ± standard deviation. ***$p < 0.001$.

also connected between them. **Figure 5A** shows the result of modulating an increasing number of nodes from a basal $r_0 = 0.33$ to a target $r_0 = 0.67$, when the nodes are ordered from low to high or high to low E_i^w. The results are similar to the ones obtained using the strength K_i^w: neuromodulation of nodes of high E_i^w has a greater impact in synchronization and integration, compared with the nodes of low E_i^w. Here, the random sorting of nodes is similar to the high to low E_i^w. However, when the nodes are sorted according to their clustering coefficient C_i^w (**Figure 5B**), there is little difference compared to random sorting.

When comparing the results in **Figures 5A,B** with the neuromodulation of a random subset of nodes (green curves), there is no clear advantage of selecting the nodes with high E_i^w or C_i^w. Despite the increase in $\bar{R}$ being slightly higher for the orange curves, compared with the green curves, the difference in E^w is unnoticeable, except in Q^w when ordering the nodes from high to low E_i^w. These results contrast with the ones in **Figure 4C**, where the neuromodulation of nodes with high K_i^w produced an increase in synchronization and integration higher than random neuromodulation.

To summarize these results, we computed the difference between the area under the curve (AUC) for the high-to-low minus low-to-high (orange minus blue AUCs; **Figure 5C**). A larger difference implies a higher impact of neuromodulating first the nodes with a higher value of the chosen metric in synchronization, integration, and segregation. The mean difference in the AUCs for the measures $\Delta\bar{R}$, ΔE^w, and $-\Delta Q^w$ (note that the sign is inverted for visualization purposes), is lower for C_i^w than for K_i^w and E_i^w ($p < 0.001$ for all comparisons using Student's t-test).

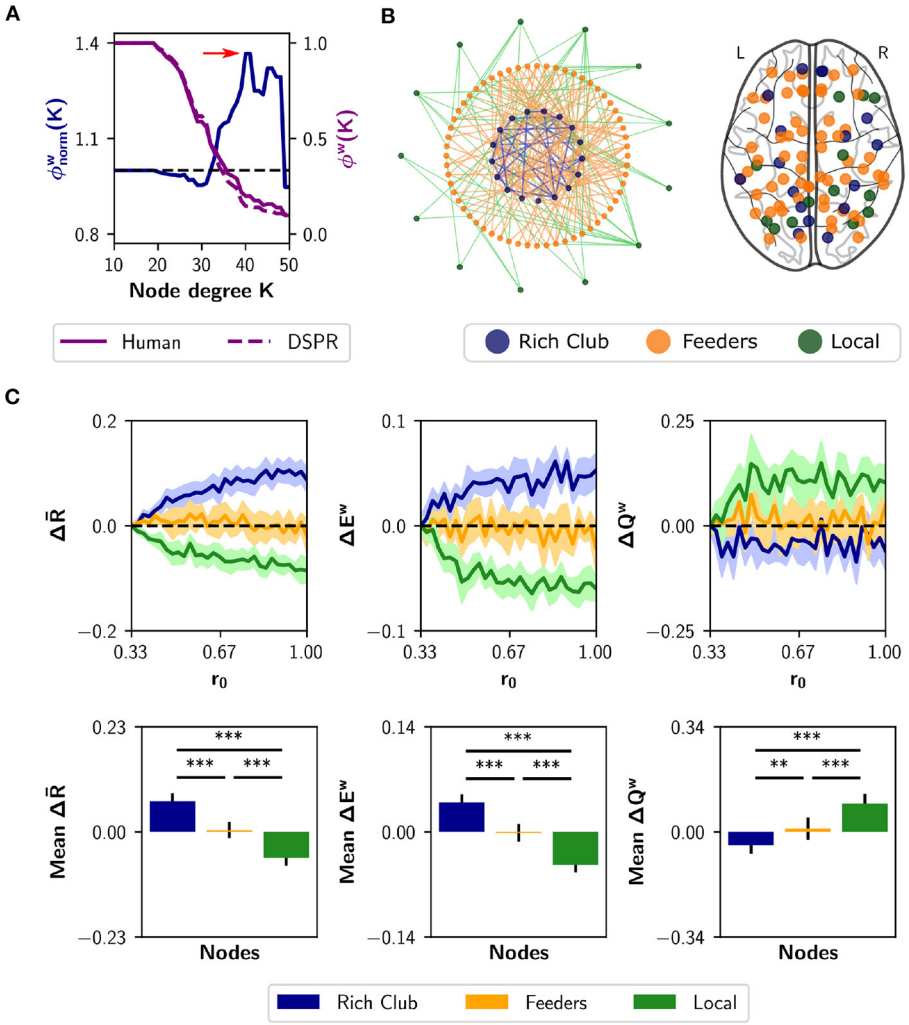

FIGURE 6 | Neuromodulation based on the rich club organization. **(A)** Normalized and weighted rich club coefficient $\phi^w_{norm}(K)$ (blue curve), as a function of the degree-based threshold K. This coefficient was calculated as the ratio between the human rich club coefficient (purple solid curve) and the mean coefficient for random surrogates (DSPR, purple dashed curve). The red arrow marks the point in which $\phi^w_{norm}(K)$ is maximal; rich club nodes were found at that point. **(B)** Schematic depiction of the rich club, feeders (not belonging to the rich club, but connected with it) and local nodes, (connected only to feeders). At the right, we show a glass brain with the nodes identified as rich club (n = 17 nodes), feeders (n = 60), and local (n = 13). **(C)** Changes in synchrony $\bar{R}$, global efficiency E^w and modularity Q^w when neuromodulating 24-node sets containing the rich club (blue), local nodes (green), or only feeders (orange). The results are shown as the difference with respect to a random subset of nodes of equal size (null case). The bottom row summarizes the area under the curve (AUC) for each metric and nodal category, averaged over the 10 realizations. Shaded areas correspond to 95% confidence intervals, and bar plots were built using the mean ± standard deviation. $^{**}p < 0.01$, $^{***}p < 0.001$.

2.3. Neuromodulation of Rich Club Nodes Strongly Impacts Functional Integration

Node strength, nodal efficiency and clustering coefficient are considered local-scale properties, i.e., they belong to each node. Several meso-scale network properties have been described as being determinant for network dynamic too, such as the rich club organization (Van Den Heuvel and Sporns, 2011) and the *s*-core (Hagmann et al., 2008; Garas et al., 2012; Eidsaa and Almaas, 2013; Castro et al., 2020). We identified the nodes belonging to the "rich club," using the weighted rich club coefficient $\phi^w(K)$, where K is a threshold based on degree (Opsahl et al., 2008). The rich club comprises a subset of the graph, thresholded at K, in which nodes are more strongly interconnected than expected by chance (Van Den Heuvel and Sporns, 2011). The coefficient is normalized using random surrogates $\phi^w_{rand}(K)$, in our case DSPR surrogates (Rubinov and Sporns, 2011). If the normalized coefficient $\phi^w_{norm}(K)$ is greater than 1, the network has a rich club organization at threshold K. **Figure 6A** shows a plot of $\phi^w_{norm}(K)$ (blue) as a function of K. The red arrow marks the point in which the normalized coefficient is maximal $[\phi^w_{norm}(K) = 1.367, p < 0.002]$. Then, we identified feeder nodes—nodes that do not belong to the rich club but are connected to at least one of its members—and local nodes—connected to feeders but not to the rich club (**Figure 6B**). We

found 17 nodes belonging to the rich club, 60 feeders and 13 local nodes (**Figure 6B**). The rich club members are the brain regions in **Table 1**.

As the analysis of the rich-club properties of the human SC defines sub-networks, instead of sorting the nodes, we chose a different approach than the neuromodulation of increasing subsets of nodes. Here, we simulated neuromodulation of a fixed-size subset of nodes, that included all nodes belonging to a certain category (rich club, feeders, or local). Because the categories differ in size, we complemented the rich club and local nodes with 7 and 11 nodes, respectively, selected randomly from the feeders. For the last one, we randomly chose 24 feeder nodes. Also, we had a null case, composed of 24 nodes randomly selected from the complete set of nodes. We repeated the random selection of nodes with 10 realizations, always using subsets of 24 nodes. The nodes started with a basal r_0 value of 0.33, and r_0 was swept up to 1 but only in the designated subset of nodes. For each r_0 increment, we measured $\bar{R}$, E^w, and Q^w. Then, we subtracted to each measurement the result of the null case. The results are shown in **Figure 6C**. Neuromodulation of the rich club nodes produces an increase in synchronization and integration, and a decrease in modularity, above chance. The difference becomes more pronounced with further increments of r_0. Opposite results were observed for the subsets containing local nodes. Finally, neuromodulation of subsets containing only feeder nodes produce no difference compared to random selection of nodes. As a summary index, we calculated the AUC for each nodal category (**Figure 6C**). Considering the three measurements, the AUC is higher (lower in the case of modularity Q^w) for the rich club respect to feeders and local, and higher (lower in the case of Q^w) between feeders and local ($p < 0.001$ for all comparisons using Student's t-test). Our results show that noradrenergic neuromodulation of a subset including the rich club nodes has a greater impact on integration compared to the feeders, locals, and a random selection of nodes.

As previously shown, functional integration is also achieved by neuromodulation of highest strength nodes. To highlight the difference between the local and meso-scale approaches, we quantified the overlap between the rich club nodes and the 17 nodes with higher strength. We found that only 8 members of the rich club belong to the subset of 17 nodes with higher strength (**Table 1**). Thus, there are some high-strength key nodes that do not belong to the rich club, that promote functional integration via neuromodulation.

To explore a second meso-scale network organization, we performed a s-core decomposition (Garas et al., 2012; Eidsaa and Almaas, 2013) that classifies nodes according to their core-periphery organization (Hagmann et al., 2008; **Figure 7A**). We defined three categories considering a range of critical s-core values: S_3 with 10 nodes ($1.54 < s < 1.78$), S_2 with 56 nodes ($1.48 < s < 1.54$), and S_1 with 24 nodes ($s < 1.48$; **Figure 7B**). The critical s-core is defined as the maximal value of s at which nodes are still connected to the network. Thus, S_3 are nodes connected within them with highest strength, S_2 middle-strength nodes, and S_1 the nodes with the lowest strength. The S_3 subset comprises the brain regions shown in **Table 1**.

TABLE 1 | List of regions belonging (X) to the rich club, the S_3 category, and the 17 nodes with highest strength.

Brain regions	Rich club	S_3 core	Top strength
Posterior cingulate gyrus (L, R)	X	X	X
Precuneus (L, R)	X	X	X
Calcarine fissure (L, R)		X	X
Cuncus (L, R)		X	
Cuneus (L, R)		X	X
Caudate nucleus (R)	X		
Hippocampus (L, R)	X		
Insula (L)			X
Middle occipital gyrus (L)	X		X
Pallidum (L, R)	X		
Putamen (L, R)	X		X
Rolandic Operculum (L)			X
Superior dorsal gyrus, dorsolateral (L, R)	X		
Superior frontal gyrus, orbital (L)			X
Superior occipital gyrus (L, R)			X
Superior frontal gyrus, medial (L)	X		X
Thalamus (L, R)	X		

*L, left hemisphere; R, right hemisphere. The regions listed here are the same displayed in the glass brains of **Figures 6**, **7**.*

We simulated the neuromodulation in subsets of 24 nodes, containing either the S_3 or the S_1 category, and complementing S_3 with 14 random nodes from S_2 as done with the rich club. A third group was built with 24 nodes randomly selected from S_2, and all groups were compared to a random selection of 24 nodes from the whole set. As shown in **Figure 7C**, the selection of S_2 nodes for neuromodulation shows the largest effect in $\Delta\bar{R}$, ΔE^w, and ΔQ^w, compared with S_1 nodes ($p < 0.001$ using Student's t-test) and compared to the selection of S_3 nodes ($p < 0.001$, except for ΔE^w with $p = 0.106$). Thus, nodes belonging to the highest s-core (nodes of the highest within-strength sub-network) do not behave like the rich club, as their neuromodulation does not have the highest impact on network synchronization and integration/segregation properties.

3. DISCUSSION

In this work, we sought to identify the relationship between structural features of the human connectome and the specific set of regions that, when neuromodulated in a biologically realistic whole-brain model, produce a significant increase in functional integration. We found that the global organization of the connectome sustains rich metastable and partially synchronized states, essential to the effects related to neuromodulation. At the meso- and local-scales, nodes belonging to the anatomical rich club, and those having high nodal strength, produce a marked increase in functional integration (and a decrease in segregation) when neuromodulated.

Our results show that the whole-brain model exhibits over-synchronized behavior when using surrogate connectomes, restricting the dynamic features of the model. This result is in the

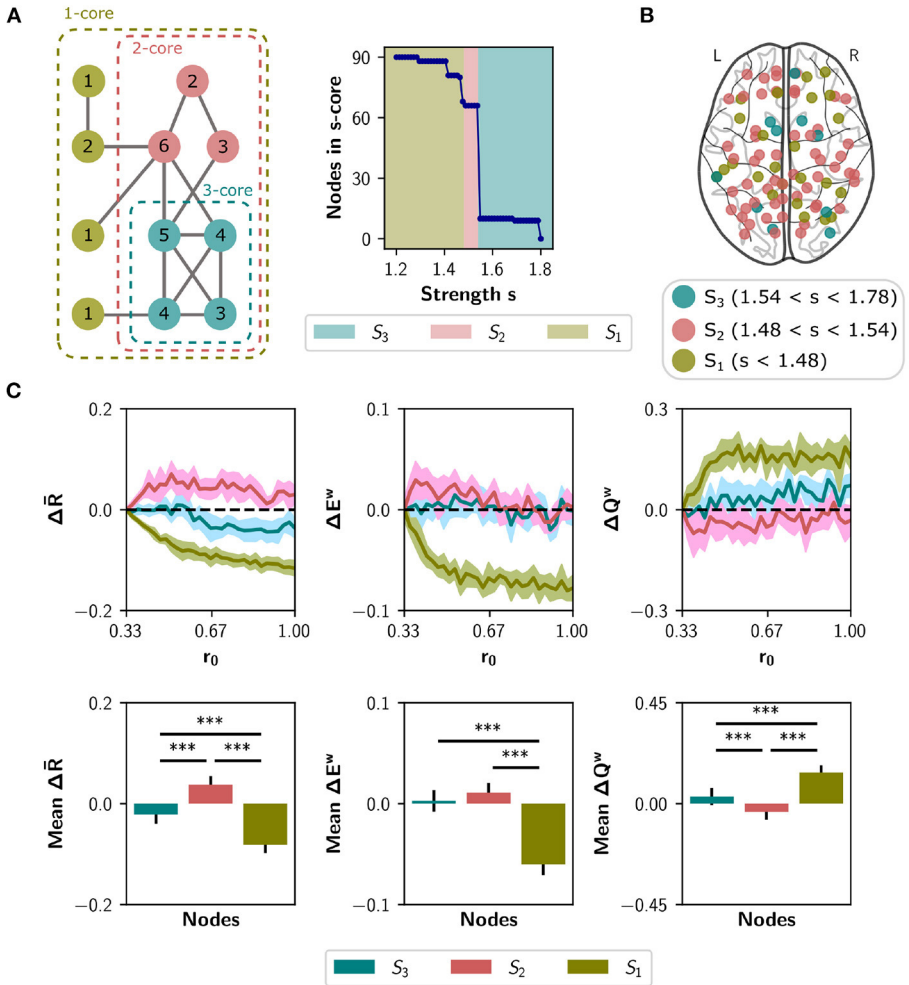

FIGURE 7 | Neuromodulation based on the *s*-core decomposition. **(A)** *s*-core decomposition. At the left, example based on degree (*k*-core). Nodes are recursively removed based on a degree threshold. The remaining nodes form a subgraph or core where all nodes have a within-degree above the threshold. For example, the three-core of the figure corresponds to a subgraph where all nodes have a degree of three or more. The numbers on the circles correspond to nodes' degree. The right plot shows the number of remaining nodes in *s*-core after applying the strength-based threshold *s*. **(B)** Brain regions identified using the *s*-core decomposition. We defined three categories, considering a range of *s* values: S_3 (n = 10 nodes), S_2 (n = 56), and S_1 (n = 24). **(C)** Changes in synchrony $\bar{R}$, global efficiency E^w and modularity Q^w when neuromodulating 24-node sets containing the S_3 nodes (blue), S_1 nodes (olive green), or only S_2 nodes (pink). S_1 and S_3 sets were complemented with random nodes from S_2 to obtain sets of 24. Results are shown as the difference with respect to a random subset of nodes of equal size (null case). The bottom row summarizes the area under the curve (AUC) for each metric and nodal category, averaged over the 10 random seeds. Shaded areas correspond to 95% confidence intervals, and bar plots were built using the mean ± standard deviation. ***$p < 0.001$.

same line as other previous findings (Cabral et al., 2014; Zamora-López et al., 2016; Wang et al., 2019; Fukushima and Sporns, 2020). Here, we show this behavior in the (α, r_0) parameter space, where simulations with randomized connectomes show either incoherent or over-synchronized activity. Using a whole-brain model to simulate and fit magnetoencephalography (MEG) resting-state recordings, Cabral et al. (2014) found not only that randomized and homogenized versions of the human structural connectivity did not fit empirical data; moreover, they found that the fit was maximal in the metastable region of the parameter space, when unsynchronized (segregated) and synchronized (integrated) regimes of activity coexist. In the same way, Fukushima and Sporns (2020) using more complex surrogate data in the context of whole-brain models, found features of the human connectome that better capture the dynamic fluctuations in fMRI resting-state recordings. Additionally, computational studies conducted by Zamora-López et al. (2016) showed that the human connectome better maximizes functional complexity in fMRI recordings, compared with different surrogate connectomes. Finally, Wang et al. (2019) analyzed how the hierarchical modular structure of the human connectome enables the coexistence of segregated and integrated functional states, also with the use of network surrogates in which hierarchical levels were controlled. Our study interpret the explorations of the parameter space as levels of neuromodulation, that allow the brain to tune its integration or segregation levels

to environmental demands. However, neuromodulation cannot bring back a dynamically rich regime to a network without a structural connectome that sustains it.

At the local level, the effects of neuromodulation strongly depend on the characteristics of the nodes in the human connectome. In our model, the nodes with high strength are the ones that better facilitate functional integration when neuromodulated. This result resonates with a recent work by Herzog et al. (2020), who studied a whole-brain model fitted to reproduce the effects of lysergic acid diethylamide (LSD) in resting-state brain dynamics. In their model, the serotonergic-induced changes in nodal entropy correlated positively with node strength. Notably, the correlation disappears when the human connectome was randomized without preserving the strength distribution, emphasizing the importance of the specific organization of the human connectome in shaping brain dynamics. Interestingly, the entropy changes described by Herzog et al. (2020) are poorly explained by the $5HT_{2A}$ receptor density map, obtained by PET (Beliveau et al., 2017), and depends on both node strength and receptor density. Thus, the interaction between the structural connectivity, receptor density, and neuromodulation is not straightforward. A similar complex picture arises when our results are contrasted with receptor maps of noradrenergic receptors (see below).

Network hubs, or nodes belonging to the rich club or network's ignition core, can be critical elements for binding information of segregated brain regions, that is, to integrate information across brain areas (Griffa and Van den Heuvel, 2018; Castro et al., 2020). Considering the relevance of integration for the brain function (Tononi, 2004), and the noradrenergic influence on integration (Shine, 2019), we hypothesized that anatomical network hubs are pivotal elements for promoting functional network integration. Our results confirmed this hypothesis, being the neuromodulation of rich club nodes the one that most effectively facilitates functional integration and synchronization of brain activity. This result agrees with findings reported in a fMRI resting-state model of the brain by Deco et al. (2017), where removing the rich club nodes causes a larger decrease in integration compared to the removal of the non-rich club members. Similar results have been found in computational models of noradrenergic neuromodulation where rich club nodes are strongly neuromodulated causing functional networks to switch from segregation to integration (Shine et al., 2018a).

Notably, neuromodulation of nodes belonging to the critical *s*-core (the maximally inter-connected core) does not promote integration as the rich club nodes do. Both meso-scale analyses rely on sets of nodes organized with strong connection weights. However, they do it differently. The rich club coefficient threshold is based on degree, and rich club members are highly connected between them as well as with the non-rich club members. In contrast, the *s*-core decomposition find subsets of nodes highly interconnected at strength *s*, but not necessarily well connected to the rest of the network. Thus, the whole-network changes are more easily achieved if the set of nodes to be neuromodulated is highly connected both between them and with the rest of the network. The rich-club organization captures additional information that is missing in the local (weight) analysis. For example, the 17 rich club nodes have an overlap of ≈50% with the 17 highest strength nodes. In contrast, nodes belonging to the S_3 category are the nodes of the highest strength in the network; however, they cannot boost functional integration to the same extent as the rich club nodes.

Part of the brain regions we found in the rich club support high order brain functions. For example, frontoparietal regions play an important role in cognition, and are markedly activated when subjects engage in cognitive tasks (Cavanna, 2007). Precuneus has been associated with consciousness, and a decrease in its activity was reported in sleep, anesthesia, and vegetative states (Lückmann et al., 2014). Thalamus, the brain "relay station," strongly connects several networks that comprise multiple cortical regions (Hwang et al., 2017). Multi-task fMRI recordings in humans suggest a robust role of the anatomical rich club as facilitating elements of functional integration in overall tasks (Shine et al., 2019). An extended analysis and discussion about the role of the rich club, in both health and disease, can be found in Griffa and Van den Heuvel (2018).

The non-uniform expression of receptors across several brain areas suggests that the brain uses selective or partial neuromodulation. In this way, the effect of the noradrenergic system on filter gain may be modeled as proportional to adrenergic receptor expression. Experimentally, the optogenetic activation of the LC in mice increased average functional connectivity, which correlates with the expression of α_2, α_1, and β_1 adrenergic receptors (Zerbi et al., 2019). Thus, a future research avenue in computational models may include a density-dependent noradrenergic neuromodulation with the addition of some receptors maps, obtained by positron emission tomography (PET), or even gene expression maps (Shen et al., 2012) that correlate with receptor density maps (Komorowski et al., 2017). Surprisingly, using the Allen Human Brain Atlas database (Shen et al., 2012) we found that some adrenergic receptor genes, i.e., the ADRA2A and ADRB1, are less expressed in the rich club nodes than in feeders and local nodes (**Figure 8**). As a consequence, the noradrenergic-mediated increase in filter gain could have a lower impact on rich club nodes. It is possible that this reduced expression constitutes a compensation for the high connectivity of rich club nodes, specially considering the higher metabolism of rich regions that exposed them to oxidative stress and neuroinflammation (Griffa and Van den Heuvel, 2018). On the other hand, receptor expression can itself be compensated by a specific sub-cellular localization or other excitability factors that may enhance the effect of noradrenaline.

It has been suggested that the effect of noradrenaline in functional connectivity is context-dependent (Shine et al., 2018b; Pfeffer et al., 2020). In that line, modeling the effect of noradrenaline in resting-state and task conditions could untangle the mechanisms behind this context-dependent effect of noradrenaline. The anatomical backbone and other dynamical parameters of this model can be substituted to study the mouse or monkey brain and to any other species for which the whole-brain white-matter connectivity is available.

Our work considers an arbitrary basal value of r_0. Despite this, we reported a clear effect of the selective noradrenergic neuromodulation on functional integration, that is, some brain

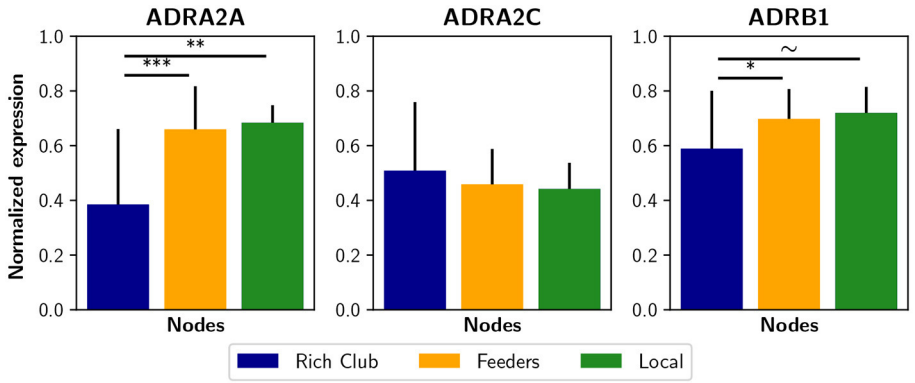

FIGURE 8 | Expression of some noradrenergic receptors genes in brain regions. Genes ADRA2A, ADRA2C, and ADRAB1 are related to noradrenergic receptors α_{2A}, α_{2C}, and β_1, respectively. The normalized expression was obtained from the Allen Human Brain Atlas using the AAL parcelation. Bar plots were built using the mean ± standard deviation. $^{***}p < 0.001$, $^{**}p < 0.01$, $^{*}p < 0.05$, $\sim p < 0.1$.

regions have a greater impact in the noradrenaline-mediated effect on brain function. A further improvement to our approach constitutes the use of a different benchmark, e.g., fitting the model to reproduce the empirical FC in resting-state, and then apply a homogeneoeus or selective neuromodulation. Furthermore, the addition of receptors maps may be considered, as commented above.

Overall, our results offer new insights into the key regions of the human brain that, when neuromodulated via the noradrenergic system, promote transitions to integrated functional states. Our results highlight the importance of the rich club and high-strength connections in producing changes related to neuromodulation. We hope that our theoretical framework inspires new research toward clinical applications or treatments of human brain disorders caused by or associated with changes in functional and structural brain connectivity.

4. METHODS

4.1. Whole-Brain Neural Mass Model

We simulated neuronal activity using the Jansen and Rit neural mass model (Jansen et al., 1993; Jansen and Rit, 1995). In this model, a brain area consists of three populations of neurons: pyramidal neurons, excitatory and inhibitory interneurons. The dynamical evolution of the three populations within the brain area is modeled by two blocks each. The first block transforms the average pulse density in average postsynaptic membrane potential (which can be either excitatory or inhibitory; **Figure 1A**). This block, denominated post synaptic potential (PSP), is represented by an impulse response function. For the excitatory outputs:

$$h_E(t) = \begin{cases} Aate^{-at}, & t \geq 0 \\ 0, & t < 0 \end{cases} \quad (1)$$

and for the inhibitory ones

$$h_I(t) = \begin{cases} Bbte^{-bt}, & t \geq 0 \\ 0, & t < 0, \end{cases} \quad (2)$$

The constants A and B define the maximum amplitude of the PSPs for the excitatory (EPSPs) and inhibitory (IPSPs) cases respectively, while a and b represent the inverse time constants for the excitatory and inhibitory postsynaptic action potentials, respectively. The second block transforms the postsynaptic membrane potential in average pulse density, and is given by a sigmoid function of the form

$$S(v, r) = \frac{\zeta_{max}}{1 + e^{r(v_{th} - v)}}, \quad (3)$$

with ζ_{max} as the maximum firing rate of the neuronal population, r the slope of the sigmoid function, v_{th} the half maximal response of the population, and v their average PSP. Additionally, pyramidal neurons receive an external stimulus $p(t)$, whose values are taken from a Gaussian distribution with mean $\mu = 2$ impulses/s and standard deviation $\sigma = 2$. In this model (**Figure 1A**), each node $i \in [1 \ldots n]$ represents a single brain area. The global coupling is scaled by a parameter α, and nodes are connected by a normalized structural connectivity matrix $\widetilde{M}$ (**Figure 1B**). This matrix is derived from a human connectome (Deco et al., 2018) parcelated in $n = 90$ cortical and subcortical regions with the automated anatomical labeling (AAL) atlas (Tzourio-Mazoyer et al., 2002); the matrix is undirected and takes values between 0 and 1. Because long-range connections are mainly excitatory (Gilbert et al., 1990; McGuire et al., 1991), only links between the pyramidal neurons of a node i with pyramidal neurons of a node j are considered. We applied a global normalization procedure to the structural connectivity matrix M. The normalization consisted of dividing all the values of the matrix by the mean strength of the nodes. The resulting normalized matrix $\widetilde{M}$ is defined as

$$\widetilde{M} = \frac{M}{\frac{1}{n}\sum_{i=1}^{n}\sum_{j=1, j\neq i}^{n} M_{ij}} \quad (4)$$

The set of equations, for a node i, includes the within and between nodes activity

$$\begin{aligned}
\dot{x}_{0,i}(t) =& y_{0,i}(t) \\
\dot{y}_{0,i}(t) =& Aa\left[S(C_2 x_{1,i}(t) - C_4 x_{2,i}(t) + C\alpha z_i(t), r_0)\right] \\
& - 2a y_{0,i}(t) - a^2 x_{0,i}(t) \\
\dot{x}_{1,i}(t) =& y_{1,i}(t) \\
\dot{y}_{1,i}(t) =& Aa\left[p(t) + S(C_1 x_{0,i}(t), r_1)\right] - 2a y_{1,i}(t) - a^2 x_{1,i}(t) \\
\dot{x}_{2,i}(t) =& y_{2,i}(t) \\
\dot{y}_{2,i}(t) =& Bb\left[S(C_3 x_{0,i}(t), r_2)\right] - 2b y_{2,i}(t) - b^2 x_{2,i}(t) \\
\dot{x}_{3,i}(t) =& y_{3,i}(t) \\
\dot{y}_{3,i}(t) =& A\bar{a}\left[S(C_2 x_{1,i}(t) - C_4 x_{2,i}(t) + C\alpha z_i(t), r_0)\right] \\
& - 2\bar{a} y_{3,i}(t) - \bar{a}^2 x_{3,i}(t)
\end{aligned} \tag{5}$$

where x_0, x_1, x_2 correspond to the outputs of the PSP blocks of the pyramidal neurons, and excitatory and inhibitory interneurons, respectively, and x_3 the long-range outputs of pyramidal neurons. The constants C_1, C_2, C_3, and C_4 scale the connectivity between the neural populations (see **Figure 1A**). The first pair of equations, x_0 and y_0, are related to the outputs of pyramidal cells to both interneurons; the second pair, x_1 and y_1, represent all the local excitatory inputs that the pyramidal neurons receive; x_2 and y_2 constitute the inhibitory contribution to pyramidal cells. An additional pair of equations (x_3 and y_3) are introduced to represent long-range (inter-area) connections, as they target the apical dendrites of pyramidal neurons and thus their EPSP have a larger characteristic time constant. We used the original parameter values of Jansen and Rit (Jansen et al., 1993; Jansen and Rit, 1995), except for C_4: $\zeta_{max} = 5\ \mathrm{s}^{-1}$, $\nu_{th} = 6$ mV, $r_0 = r_1 = r_2 = 0.56\ \mathrm{mV}^{-1}$, $a = 100\ \mathrm{s}^{-1}$, $b = 50\ \mathrm{s}^{-1}$, $A = 3.25$ mV, $B = 22$ mV, $C_1 = C$, $C_2 = 0.8C$, $C_3 = 0.25C$, $C_4 = 0.5C$, and $C = 135$. Changing C_4 from 0.25 C to 0.5 C allowed the model to sustain oscillations in a wider range of α values. The parameters A, B, a, and b were selected to produce IPSPs longer in amplitude and latency in comparison with the EPSPs. The inverse of the characteristic time constant for the long-range EPSPs was defined as $\bar{a} = 0.5a$. This choice was based on the fact that long-range excitatory inputs of pyramidal neurons target their apical dendrites, and consequently this slows down the time course of the EPSPs at the soma (Branco and Häusser, 2011).

The input from brain areas $j \neq i$ to the region i is given by

$$z_i(t) = \sum_{j=1, j\neq i}^{n} \widetilde{M}_{ij} x_{3,j}(t) \tag{6}$$

The average PSP of pyramidal neurons in region i characterizes the EEG-like signal in the source space; it is computed as (Jansen et al., 1993; Jansen and Rit, 1995)

$$\nu(t)_i = C_2 x_{1,i}(t) - C_4 x_{2,i}(t) + C\alpha z_i(t) \tag{7}$$

The firing rates of pyramidal neurons $\zeta_i(t) = S[\nu(t)_i, r_0]$ were used to simulate the fMRI-BOLD signals.

4.2. Neuromodulation

The effect of the noradrenergic system was simulated controlling the parameter r_0 (filter gain; **Figure 1B**), which represents the sigmoid function slope of the pyramidal population, and increases the signal-to-noise ratio of pyramidal cells (Servan-Schreiber et al., 1990; Thiele and Bellgrove, 2018). Details about the relationship between the noradrenergic system and filter gain can be found in the Introduction section. Further analysis about this relationship has been presented previously in Mather et al. (2016) and Shine (2019). We analyzed the effect of the noradrenergic neuromodulation in three scenarios:

Macro-scale: Noradrenergic neuromodulation was studied in interaction with the cholinergic system, represented by the parameter α. The parameters were the same for all nodes. We changed the features of the connectivity matrix M (see **Figure 2**) to study the combined effect in neural coordination.

Meso-scale: nodes were classified in different categories, either according to the rich club organization (Van Den Heuvel and Sporns, 2011) or s-core decomposition of the network (see section 4.5; Garas et al., 2012; Eidsaa and Almaas, 2013). Global coupling was fixed in $\alpha = 0.65$, and the basal value of r_0 was 0.33 for all nodes (**Figure 3**). We incremented r_0 in a subset of 24 nodes belonging to a particular category, and compared the results with the neuromodulation of a equal-length random subset of nodes.

Because the categories differ in the number of nodes, a fair comparison must considered subsets of equal size. To achieve that, we complemented the rich club with seven randomly selected feeder nodes, while the local nodes were complemented with 11 randomly selected feeders. Likewise, we complemented the S_3 category with 14 randomly selected S_2 nodes. From both the feeders and S_2 nodes we selected 24 nodes randomly. All subsets consisted on 24 nodes, were generated 10 times with different random seeds and the results averaged.

Local-scale: Nodes were sorted using one of three metrics: node strength K_i^w, nodal efficiency E_i^w, or clustering coefficient C_i^w (Rubinov and Sporns, 2010). We neuromodulated—increasing r_0—node by node in increments of three, considering the metric from high to low and vice-versa (**Figure 3**).

4.3. Simulations

Following Birn et al. (2013), we ran simulations to generate the equivalent of 11 min real-time recordings, discarding the first 60 s. The system of stochastic differential equations (5) was solved with the Euler-Maruyama method, using an integration step of 1 ms. We used 10 random seeds (realizations) which controlled the initial conditions and the stochasticity of the simulations. We simulated neuronal activity sweeping the parameters $\alpha \in [0, 1]$ and $r_0 \in [0, 1]$, for the macro-scale scenario. In the local- and meso-scale scenarios, we swept $r_0 \in [0.33, 1]$ for a susbset of nodes, considering a basal value of $r_0 = 0.33$ and a fixed $\alpha = 0.65$. All the simulations were implemented in Python and the codes are freely available at: https://github.com/vandal-uv/Structural_Neuromod_2021.git. The graph analysis was performed using the Brain Connectivity Toolbox for Python (https://github.com/fiuneuro/brainconn; Rubinov and Sporns, 2010).

4.4. Simulated fMRI-BOLD Signals

We used the firing rates $\zeta_i(t)$ to simulate BOLD-like signals using a generalized hemodynamic model presented in Stephan et al. (2007). In this model, an increment in the firing rate $\zeta_i(t)$ triggers a vasodilatory response s_i, producing blood inflow f_i, changes in the blood volume v_i and deoxyhemoglobin content q_i. The corresponding system of differential equations is

$$\begin{aligned}\dot{s}_i(t) &= \zeta_i(t) - \frac{s_i(t)}{\tau_s} - \frac{f_i(t)-1}{\tau_f}\\ \dot{f}_i(t) &= s_i(t)\\ \dot{v}_i(t) &= \frac{f_i(t) - v_i(t)^{1/\kappa}}{\tau_v}\\ \dot{q}_i(t) &= \frac{\frac{f_i(t)(1-(1-E_0)^{1/f_i(t)})}{E_0} - \frac{q_i(t)v_i(t)^{1/\kappa}}{v_i(t)}}{\tau_q},\end{aligned} \tag{8}$$

where $\tau_s = 0.65$, $\tau_f = 0.41$, $\tau_v = 0.98$, $\tau_q = 0.98$ represent the time constants for the signal decay, blood inflow, blood volume, and deoxyhemoglobin content, respectively. The stiffness constant (resistance of the veins to blood flow) is given by κ, and the resting-state oxygen extraction rate by E_0. We used $\kappa = 0.32$ and $E_0 = 0.4$. The BOLD-like signal of node i, denoted $B_i(t)$, is a non-linear function of $q_i(t)$ and $v_i(t)$

$$B_i(t) = V_0\left[k_1(1-q_i(t)) + k_2\left(1 - \frac{q_i(t)}{v_i(t)}\right) + k_3(1-v_i(t))\right], \tag{9}$$

where $V_0 = 0.04$ represents the fraction of venous blood (deoxygenated) in resting-state, and $k_1 = 2.77$, $k_2 = 0.2$, $k_3 = 0.5$ are kinetic constants.

The system of differential equations (8) was solved using the Euler method with an integration step of 1 ms. The signals were band-pass filtered between 0.01 and 0.1 Hz with a 3rd order Bessel filter. These BOLD-like signals were used to build the functional connectivity (FC) matrices from which the subsequent analysis of functional network properties was performed.

4.5. Structural Metrics

4.5.1. Macro-Scale

To compare different Macro-scale features of the connectome we used four connectivity matrices (see **Figure 2**). The first matrix corresponds to the original human connectome matrix (Human, **Figure 2A**) (Deco et al., 2018). The second to a degree and strength preserving randomization of the matrix (DSPR, **Figure 2B**; Rubinov and Sporns, 2011). The third to a randomization, which only preserves the weight distribution of the original matrix (Random, **Figure 2C**). The fourth matrix was built setting to 0 all entries of $M_{ij} < 0.05$, and 1 otherwise (Homogeneous, **Figure 2D**).

4.5.2. Meso-Scale

We identified the nodes belonging to the "rich club" sub-network of the graph (Van Den Heuvel and Sporns, 2011). Nodes were ranked according to degree, and then a subgraph was built using a threshold K, retaining the nodes with a degree greater than K. For each K value the weighted rich-club coefficient was computed as (Opsahl et al., 2008).

$$\phi^w(K) = \frac{W_{>K}}{\sum_{l=1}^{E_{>K}} w_l^{rank}} \tag{10}$$

where $W_{>K}$ is the sum of the weighted edges of the subgraph of nodes with a degree greater than K, $E_{>K}$ represent the total number of edges of the subgraph, and w_l^{rank} a vector that contains all the weighted edges of the entire network sorted from high to low values. If $\phi^w(K) = 1$, then the sum of the weights of the "rich nodes" is maximal. Otherwise, $\phi^w(K) < 1$ indicates the proportion of the weighted edges of network that are into the sub-network, and then some of the stronger connections were missed when applying the threshold K. The rich club coefficient was normalized in relation to DSPR surrogate graphs.

$$\phi^w_{norm}(K) = \frac{\phi^w(K)}{\phi^w_{rand}(K)} \tag{11}$$

being $\phi^w_{norm}(K)$ the normalized rich club coefficient, and $\phi^w_{rand}(K)$ the mean rich club coefficient for a set of 1,000 random surrogates graphs. Values of $\phi^w_{norm}(K) > 1$ indicates a rich-club organization, and nodes retained at K are defined as "rich club" nodes (**Figure 6A**). The nodes that do not belong to the rich club, but are connected with these nodes are called "feeders." The remaining nodes correspond to "local" nodes (**Figure 6B**). For a maximum $\phi^w_{norm}(K) = 1.367$ ($p < 0.002$), we identified 17 "rich club" nodes, 60 feeder nodes and 13 local nodes (**Figure 6B**). Because the high density of the structural matrix M ($\approx$ 40%) hindered the discerning of the local nodes from feeders, we identify these nodes applying an absolute threshold of 0.05 to M. We selected this value as the maximum threshold that, when applied, preserves the fitting of the model to the empirical resting-state FC matrix.

The core-periphery organization (Hagmann et al., 2008) was analyzed performing a s-core decomposition (Garas et al., 2012; Eidsaa and Almaas, 2013), which identifies the cores of densely interconnected nodes in the network. The method consists in removing recursively a shell of nodes with strength less than s to obtain the network core nodes. The nodes were assigned to a category that corresponded to the maximal s value at which they are still connected to the network, defined as the critical s-core (**Figure 7A**). We defined three categories for different s values: s_1 with 24 nodes ($s < 1.48$), s_2 with 56 nodes ($1.48 < s < 1.54$), and s_3 with 10 nodes ($1.54 < s < 1.78$; **Figure 7B**).

4.5.3. Local-Scale

We employed three different metrics to characterize individual nodes. Node strength (weighted degree) was computed as

$$K_i^w = \sum_{j\in N, j\neq i} w_{ij}, \tag{12}$$

where N is the set of nodes and w_{ij} the weighted edge of the matrix M (Rubinov and Sporns, 2010). We computed the nodal efficiency as

$$E_i^w = \frac{\sum_{j\in N, j\neq i}(d_{ij}^w)^{-1}}{n-1}, \tag{13}$$

where d_{ij}^w is the shortest path between the nodes i and j. Shortest paths were calculated from the sum of the inverse of the weights of M; the shortest path between two nodes (i, j) is the path that minimizes this sum (the distance). Using the shortest paths, nodal efficiency E_i^w was computed. Nodes with high values of E_i^w are those with high proportion of short paths to the rest of the nodes of the network (Rubinov and Sporns, 2010). Finally, we calculated the clustering coefficient for each node (Rubinov and Sporns, 2010)

$$C_i^w = \frac{2t_i^w}{k_i(k_i-1)}, \tag{14}$$

where t_i^w is the proportion of triangles around the node i, calculated as

$$t_i^w = \frac{1}{2}\sum_{j,h\in N}(w_{ij}w_{ih}w_{jh})^{1/3}. \tag{15}$$

A node with a high C_i^w is highly connected with adjacent (local) nodes.

4.6. Phase Synchronization

As a measure of global synchronization, we calculated the Kuramoto order parameter $R(t)$ (Acebrón et al., 2005) of the EEG-like signals $v(t)$ derived from the Jansen and Rit model. First, the raw signals were filtered with a 3rd order Bessel band-pass filter using their frequency of maximum power (usually between 4 and 10 Hz) ±3 Hz. Then, the instantaneous phase $\theta(t)$ was obtained using the Hilbert transform. The global phase synchrony is computed as:

$$\bar{R} = \left\langle \left| \langle e^{j\theta_i(t)} \rangle_N \right| \right\rangle_t, \tag{16}$$

where $\theta_i(t)$ is the phase of the oscillator i over time, $j = \sqrt{-1}$ the imaginary unit, $|\bullet|$ denotes the module, $\langle\rangle_N$ denotes the average over all nodes, and $\langle\rangle_t$ the average over time.

4.7. Functional Integration and Segregation

Functional Connectivity (FC) matrices were built from Pearson correlations of the entire BOLD-like time series. Instead of employing an absolute or proportional thresholding, we thresholded the FC matrices using Fourier transform (FT) surrogate data (Lancaster et al., 2018) to avoid the problem of introducing spurious correlations (Fornito et al., 2013). The FT algorithm uses a phase randomization process to destroy pairwise correlations, preserving the spectral properties of the signals (the surrogates have the same power spectrum as the original data). We generated 500 surrogate time series of the original set of BOLD-like signals, to obtain the surrogate sFCs matrices. For each one of the $(n^2 - n)/2$ possible connectivity pairs (with $n = 90$) we fitted a normal distribution of the surrogate values. Using these distributions, we tested the hypothesis that a pairwise correlation is higher than chance (that is, the value is at the right of the surrogate distribution).

To reject the null hypothesis, we selected a p-value equal to 0.05, and corrected for multiple comparisons with the FDR Benjamini-Hochberg procedure (Benjamini and Hochberg, 1995) to decrease the probability of making type I errors (false positives). The entries of the sFC matrix associated with a $p > 0.05$ were set to 0. The result is a thresholded, undirected, and weighted (with only positive values) sFC matrix.

Integration was evaluated over the thresholded FC matrices. We employed the weighted version of the global efficiency (Latora and Marchiori, 2001). This measure of integration is based on paths over the graph: it is defined as the inverse of the average shortest path length. This metric is computed as

$$E^w = \frac{1}{n}\sum_{i\in N}\frac{\sum_{j\in N, j\neq i}(d_{ij}^w)^{-1}}{n-1}, \tag{17}$$

being N the set of all nodes, n number of nodes, and d_{ij}^w the shortest path between the nodes i and j.

Segregation was quantified using modularity Q^w, a metric for the detection of the network's communities (Rubinov and Sporns, 2010). The detection of so-called communities or network modules in the thresholded FC matrix, was based on the Louvain's algorithm (Newman, 2006; Blondel et al., 2008). We used the weighted version of the modularity (Newman, 2004) defined as

$$Q^w = \frac{1}{l^w}\sum_{i,j\in N}\left[w_{ij} - \frac{k_i^w k_j^w}{l^w}\right]\delta_{m_i,m_j} \tag{18}$$

where w_{ij} is the weight of the link between the nodes i and j, l^w is the total number of weighted links of the network, m_i (m_j) the module of the node i (j), and k_i^w (m_j) the weighted degree (named also strength) of i (j). The algorithm assigns a module to each node in a way that maximizes the modularity (18). The Kronecker delta δ_{m_i,m_j} is equal to 1 when $m_i = m_j$ (that is, when two nodes belongs to the same module), and 0 otherwise.

Because the Louvain's algorithm is stochastic, we employed the consensus-clustering algorithm (Lancichinetti and Fortunato, 2012). We ran the Louvain's algorithm 200 times with the resolution parameter set to 1.0 (this parameter controls the size of the detected modules; larger values of this parameter allows the detection of smaller modules). Then, we built an agreement matrix G, whose entries $G_{ij} \in [0, 1]$ indicates the proportion of partitions in which the pairs of nodes (i, j) share the same module. Then, we applied an absolute threshold of 0.5 to the matrix G, and ran the Louvain's algorithm again 200 times using G as input, producing a new consensus matrix G'. This last step was repeated until convergence to a unique partition.

4.8. Functional Connectivity Dynamics

The FCD matrix captures the evolution of FC patterns and, consequently, the dynamical richness of the network (Hansen et al., 2015; Cabral et al., 2017). We used the sliding window approach (Hansen et al., 2015; Orio et al., 2018), with windows of 100 s length and a displacement of 2 s between consecutive windows. The length was chosen on the basis of the lower limit

of the band-pass filter (0.01 Hz), in order to minimize spurious correlations (Leonardi and Van De Ville, 2015). For each window, a FC matrix was calculated from the Pearson correlation of BOLD-like signals. We obtained 251 weighted and undirected FC matrices from the 600 s simulated BOLD-like signals. The upper triangular of each FC matrix is unfolded to make a vector, and the FCD is built by calculating the Clarkson distance $\lambda(x, y) = \frac{1}{\sqrt{2}} \left|\left| \frac{x}{||x||} - \frac{y}{||y||} \right|\right|$ between each pair of FCs (Clarkson, 1936).

$$FCD_{ij} = \lambda(FC(t_i), FC(t_j)) \tag{19}$$

4.9. Gene Expression Maps

To quantify the expression of some noradrenergic receptor genes in brain regions, we used the microarray expression data of the Allen Human Brain Atlas (Shen et al., 2012). The dataset was processed and normalized employing the Abagen library for Python (https://github.com/rmarkello/abagen/tree/0.1; Arnatkevicute et al., 2019), and then parcellated using the AAL atlas (Tzourio-Mazoyer et al., 2002). We compared the expression of the ADRA2A, ADRA2C, and ADRB1 genes in rich club, feeders and local nodes. Statistical comparison was performed with a Student's *t*-test for independent samples.

DATA AVAILABILITY STATEMENT

The datasets presented in this study can be found in online repositories. The names of the repository/repositories and accession number(s) can be found at: https://github.com/vandal-uv/Structural_Neuromod_2021.

AUTHOR CONTRIBUTIONS

CC-O, SC, RC, and PO contributed to conception and design of the study and wrote the manuscript. CC-O performed the simulations and statistical analysis. All authors contributed to manuscript revision, read, and approved the submitted version.

FUNDING

This work was supported by Fondecyt Grants 1181076 (to PO) and 11181072 (to RC), the Advanced Center for Electrical and Electronic Engineering (ANID FB0008), and ANID—Millennium Science Initiative Program ICN09-022 (Centro Interdisciplinario de Neurociencia de Valparaíso CINV). CC-O was funded by Beca Doctorado Nacional ANID 2018-21180995.

ACKNOWLEDGMENTS

We thank Gustavo Deco for kindly providing the anatomical connectivity matrix used in the model, and Vicente Medel for fruitful and critical discussions of the work.

REFERENCES

Acebrón, J. A., Bonilla, L. L., Vicente, C. J. P., Ritort, F., and Spigler, R. (2005). The kuramoto model: a simple paradigm for synchronization phenomena. *Rev. Modern Phys.* 77:137. doi: 10.1103/RevModPhys.77.137

Allen, E. A., Damaraju, E., Plis, S. M., Erhardt, E. B., Eichele, T., and Calhoun, V. D. (2014). Tracking whole-brain connectivity dynamics in the resting state. *Cereb. Cortex* 24, 663–676. doi: 10.1093/cercor/bhs352

Arnatkevicute, A., Fulcher, B. D., and Fornito, A. (2019). A practical guide to linking brain-wide gene expression and neuroimaging data. *Neuroimage* 189, 353–367. doi: 10.1016/j.neuroimage.2019.01.011

Aston-Jones, G. and Cohen, J. D. (2005). An integrative theory of locus coeruleus-norepinephrine function: adaptive gain and optimal performance. *Annu. Rev. Neurosci.* 28, 403–450. doi: 10.1146/annurev.neuro.28.061604.135709

Beliveau, V., Ganz, M., Feng, L., Ozenne, B., Højgaard, L., Fisher, P. M., et al. (2017). A high-resolution *in vivo* atlas of the human brain's serotonin system. *J. Neurosci.* 37, 120–128. doi: 10.1523/JNEUROSCI.2830-16.2016

Benjamini, Y., and Hochberg, Y. (1995). Controlling the false discovery rate: a practical and powerful approach to multiple testing. *J. R. Stat. Soc. Ser. B* 57, 289–300. doi: 10.1111/j.2517-6161.1995.tb02031.x

Birn, R. M., Molloy, E. K., Patriat, R., Parker, T., Meier, T. B., Kirk, G. R., et al. (2013). The effect of scan length on the reliability of resting-state fMRI connectivity estimates. *Neuroimage* 83, 550–558. doi: 10.1016/j.neuroimage.2013.05.099

Blondel, V. D., Guillaume, J.-L., Lambiotte, R., and Lefebvre, E. (2008). Fast unfolding of communities in large networks. *J. Stat. Mech.* 2008:P10008. doi: 10.1088/1742-5468/2008/10/P10008

Branco, T., and Häusser, M. (2011). Synaptic integration gradients in single cortical pyramidal cell dendrites. *Neuron* 69, 885–892. doi: 10.1016/j.neuron.2011.02.006

Bullmore, E., and Sporns, O. (2009). Complex brain networks: graph theoretical analysis of structural and functional systems. *Nat. Rev. Neurosci.* 10, 186–198. doi: 10.1038/nrn2575

Cabral, J., Kringelbach, M. L., and Deco, G. (2017). Functional connectivity dynamically evolves on multiple time-scales over a static structural connectome: models and mechanisms. *NeuroImage* 160, 84–96. doi: 10.1016/j.neuroimage.2017.03.045

Cabral, J., Luckhoo, H., Woolrich, M., Joensson, M., Mohseni, H., Baker, A., et al. (2014). Exploring mechanisms of spontaneous functional connectivity in MEG: how delayed network interactions lead to structured amplitude envelopes of band-pass filtered oscillations. *Neuroimage* 90, 423–435. doi: 10.1016/j.neuroimage.2013.11.047

Castro, S., El-Deredy, W., Battaglia, D., and Orio, P. (2020). Cortical ignition dynamics is tightly linked to the core organisation of the human connectome. *PLoS Comput. Biol.* 16:e1007686. doi: 10.1371/journal.pcbi.1007686

Cavanna, A. E. (2007). The precuneus and consciousness. *CNS Spectr.* 12, 545–552. doi: 10.1017/S1092852900021295

Clarkson, J. A. (1936). Uniformly convex spaces. *Trans. Am. Math. Soc.* 40, 396–414. doi: 10.1090/S0002-9947-1936-1501880-4

Cohen, J. R., and D'Esposito, M. (2016). The segregation and integration of distinct brain networks and their relationship to cognition. *J. Neurosci.* 36, 12083–12094. doi: 10.1523/JNEUROSCI.2965-15.2016

Coronel-Oliveros, C., Cofré, R., and Orio, P. (2021). Cholinergic neuromodulation of inhibitory interneurons facilitates functional integration in whole-brain models. *PLoS Comput. Biol.* 17:e1008737. doi: 10.1371/journal.pcbi.1008737

Deco, G., Cruzat, J., Cabral, J., Knudsen, G. M., Carhart-Harris, R. L., Whybrow, P. C., et al. (2018). Whole-brain multimodal neuroimaging model using serotonin receptor maps explains non-linear functional effects of LSD. *Curr. Biol.* 28, 3065–3074. doi: 10.1016/j.cub.2018.07.083

Deco, G., and Jirsa, V. K. (2012). Ongoing cortical activity at rest: criticality, multistability, and ghost attractors. *J. neurosci.* 32, 3366–75. doi: 10.1523/JNEUROSCI.2523-11.2012

Deco, G., Van Hartevelt, T. J., Fernandes, H. M., Stevner, A., and Kringelbach, M. L. (2017). The most relevant human brain regions for functional connectivity: evidence for a dynamical workspace of binding nodes from whole-brain computational modelling. *Neuroimage* 146, 197–210. doi: 10.1016/j.neuroimage.2016.10.047

Dehaene, S., and Changeux, J. P. (2011). Experimental and theoretical approaches to conscious processing. *Neuron* 70, 200–227. doi: 10.1016/j.neuron.2011.03.018

Eidsaa, M., and Almaas, E. (2013). S-core network decomposition: a generalization of k-core analysis to weighted networks. *Phys. Rev. E* 88:062819. doi: 10.1103/PhysRevE.88.062819

Fornito, A., Zalesky, A., and Breakspear, M. (2013). Graph analysis of the human connectome: promise, progress, and pitfalls. *Neuroimage* 80, 426–444. doi: 10.1016/j.neuroimage.2013.04.087

Foster, B. L., He, B. J., Honey, C. J., Jerbi, K., Maier, A., and Saalmann, Y. B. (2016). Spontaneous neural dynamics and multi-scale network organization. *Front. Syst. Neurosci.* 10:7. doi: 10.3389/fnsys.2016.00007

Fukushima, M., and Sporns, O. (2020). Structural determinants of dynamic fluctuations between segregation and integration on the human connectome. *Commun. Biol.* 3, 1–11. doi: 10.1038/s42003-020-01331-3

Fuxe, K., Dahlström, A. B., Jonsson, G., Marcellino, D., Guescini, M., Dam, M., et al. (2010). The discovery of central monoamine neurons gave volume transmission to the wired brain. *Prog. Neurobiol.* 90, 82–100. doi: 10.1016/j.pneurobio.2009.10.012

Garas, A., Schweitzer, F., and Havlin, S. (2012). A k-shell decomposition method for weighted networks. *New J. Phys.* 14:083030. doi: 10.1088/1367-2630/14/8/083030

Gilbert, C. D., Hirsch, J. A., and Wiesel, T. N. (1990). Lateral interactions in visual cortex. *Cold Spring Harb. Symp. Quant. Biol.* 55, 663–677. doi: 10.1101/SQB.1990.055.01.063

González, G. F., Van der Molen, M., Žarić, G., Bonte, M., Tijms, J., Blomert, L., et al. (2016). Graph analysis of EEG resting state functional networks in dyslexic readers. *Clin. Neurophysiol.* 127, 3165–3175. doi: 10.1016/j.clinph.2016.06.023

Griffa, A., and Van den Heuvel, M. P. (2018). Rich-club neurocircuitry: function, evolution, and vulnerability. *Dial. Clin. Neurosci.* 20, 121–132. doi: 10.31887/DCNS.2018.20.2/agriffa

Guan, S., Jiang, R., Bian, H., Yuan, J., Xu, P., Meng, C., et al. (2020). The profiles of non-stationarity and non-linearity in the time series of resting-state brain networks. *Front. Neurosci.* 14:493. doi: 10.3389/fnins.2020.00493

Hagmann, P., Cammoun, L., Gigandet, X., Meuli, R., Honey, C. J., Wedeen, V. J., et al. (2008). Mapping the structural core of human cerebral cortex. *PLoS Biol.* 6:e159. doi: 10.1371/journal.pbio.0060159

Hansen, E. C., Battaglia, D., Spiegler, A., Deco, G., and Jirsa, V. K. (2015). Functional connectivity dynamics: modeling the switching behavior of the resting state. *Neuroimage* 105, 525–535. doi: 10.1016/j.neuroimage.2014.11.001

Herzog, R., Mediano, P. A., Rosas, F. E., Carhart-Harris, R., Perl, Y. S., Tagliazucchi, E., et al. (2020). A mechanistic model of the neural entropy increase elicited by psychedelic drugs. *Sci. Rep.* 10, 1–12. doi: 10.1038/s41598-020-74060-6

Hwang, K., Bertolero, M. A., Liu, W. B., and D'esposito, M. (2017). The human thalamus is an integrative hub for functional brain networks. *J. Neurosci.* 37, 5594–5607. doi: 10.1523/JNEUROSCI.0067-17.2017

Jansen, B. H., and Rit, V. G. (1995). Electroencephalogram and visual evoked potential generation in a mathematical model of coupled cortical columns. *Biol. Cybern.* 73, 357–366. doi: 10.1007/BF00199471

Jansen, B. H., Zouridakis, G., and Brandt, M. E. (1993). A neurophysiologically-based mathematical model of flash visual evoked potentials. *Biol. Cybern.* 68, 275–283. doi: 10.1007/BF00224863

Kelso, J. S. (2012). Multistability and metastability: understanding dynamic coordination in the brain. *Philos. Trans. R. Soc. B Biol. Sci.* 367, 906–918. doi: 10.1098/rstb.2011.0351

Komorowski, A., James, G., Philippe, C., Gryglewski, G., Bauer, A., Hienert, M., et al. (2017). Association of protein distribution and gene expression revealed by pet and post-mortem quantification in the serotonergic system of the human brain. *Cereb. Cortex* 27, 117–130. doi: 10.1093/cercor/bhw355

Kringelbach, M. L., Cruzat, J., Cabral, J., Knudsen, G. M., Carhart-Harris, R., Whybrow, P. C., et al. (2020). Dynamic coupling of whole-brain neuronal and neurotransmitter systems. *Proc. Natl. Acad. Sci. U.S.A.* 117, 9566–9576. doi: 10.1073/pnas.1921475117

Lancaster, G., Iatsenko, D., Pidde, A., Ticcinelli, V., and Stefanovska, A. (2018). Surrogate data for hypothesis testing of physical systems. *Phys. Rep.* 748, 1–60. doi: 10.1016/j.physrep.2018.06.001

Lancichinetti, A., and Fortunato, S. (2012). Consensus clustering in complex networks. *Sci. Rep.* 2:336. doi: 10.1038/srep00336

Latora, V., and Marchiori, M. (2001). Efficient behavior of small-world networks. *Phys. Rev. Lett.* 87:198701. doi: 10.1103/PhysRevLett.87.198701

Lee, T.-H., Greening, S. G., Ueno, T., Clewett, D., Ponzio, A., Sakaki, M., et al. (2018). Arousal increases neural gain via the locus coeruleus-noradrenaline system in younger adults but not in older adults. *Nat. Hum. Behav.* 2, 356–366. doi: 10.1038/s41562-018-0344-1

Leonardi, N., and Van De Ville, D. (2015). On spurious and real fluctuations of dynamic functional connectivity during rest. *Neuroimage* 104, 430–436. doi: 10.1016/j.neuroimage.2014.09.007

Lord, L.-D., Stevner, A. B., Deco, G., and Kringelbach, M. L. (2017). Understanding principles of integration and segregation using whole-brain computational connectomics: implications for neuropsychiatric disorders. *Philos. Trans. R. Soc. A* 375:20160283. doi: 10.1098/rsta.2016.0283

Lückmann, H. C., Jacobs, H. I., and Sack, A. T. (2014). The cross-functional role of frontoparietal regions in cognition: internal attention as the overarching mechanism. *Prog. Neurobiol.* 116, 66–86. doi: 10.1016/j.pneurobio.2014.02.002

Mather, M., Clewett, D., Sakaki, M., and Harley, C. W. (2016). Norepinephrine ignites local hotspots of neuronal excitation: how arousal amplifies selectivity in perception and memory. *Behav. Brain Sci.* 39:e200. doi: 10.1017/S0140525X15000667

McGuire, B. A., Gilbert, C. D., Rivlin, P. K., and Wiesel, T. N. (1991). Targets of horizontal connections in macaque primary visual cortex. *J. Compar. Neurol.* 305, 370–392. doi: 10.1002/cne.903050303

Miron-Shahar, Y., Kantelhardt, J. W., Grinberg, A., Hassin-Baer, S., Blatt, I., Inzelberg, R., et al. (2019). Excessive phase synchronization in cortical activation during locomotion in persons with Parkinson's disease. *Parkinsonism Relat. Disord.* 65, 210–216. doi: 10.1016/j.parkreldis.2019.05.030

Newman, M. E. (2004). Analysis of weighted networks. *Phys. Rev. E* 70:056131. doi: 10.1103/PhysRevE.70.056131

Newman, M. E. (2006). Modularity and community structure in networks. *Proc. Natl. Acad. Sci. U.S.A.* 103, 8577–8582. doi: 10.1073/pnas.0601602103

Opsahl, T., Colizza, V., Panzarasa, P., and Ramasco, J. J. (2008). Prominence and control: the weighted rich-club effect. *Phys. Rev. Lett.* 101:168702. doi: 10.1103/PhysRevLett.101.168702

Orio, P., Gatica, M., Herzog, R., Maidana, J. P., Castro, S., and Xu, K. (2018). Chaos versus noise as drivers of multistability in neural networks. *Chaos* 28:106321. doi: 10.1063/1.5043447

Pfeffer, T., Ponce-Alvarez, A., Meindertsma, T., Gahnström, C., van den Brink, R. L., Nolte, G., et al. (2020). Circuit mechanisms for chemical modulation of cortex-wide network interactions and exploration behavior. *bioRxiv*. doi: 10.1101/2020.06.25.171199

Reimer, J., McGinley, M. J., Liu, Y., Rodenkirch, C., Wang, Q., McCormick, D. A., et al. (2016). Pupil fluctuations track rapid changes in adrenergic and cholinergic activity in cortex. *Nat. Commun.* 7, 1–7. doi: 10.1038/ncomms13289

Rubinov, M., and Sporns, O. (2010). Complex network measures of brain connectivity: uses and interpretations. *Neuroimage* 52, 1059–1069. doi: 10.1016/j.neuroimage.2009.10.003

Rubinov, M., and Sporns, O. (2011). Weight-conserving characterization of complex functional brain networks. *Neuroimage* 56, 2068–2079. doi: 10.1016/j.neuroimage.2011.03.069

Servan-Schreiber, D., Printz, H., and Cohen, J. D. (1990). A network model of catecholamine effects: gain, signal-to-noise ratio, and behavior. *Science* 249, 892–895. doi: 10.1126/science.2392679

Shen, E. H., Overly, C. C., and Jones, A. R. (2012). The allen human brain atlas: comprehensive gene expression mapping of the human brain. *Trends Neurosci.* 35, 711–714. doi: 10.1016/j.tins.2012.09.005

Shine, J. M. (2019). Neuromodulatory influences on integration and segregation in the brain. *Trends Cogn. Sci.* 23, 572–583. doi: 10.1016/j.tics.2019.04.002

Shine, J. M., Aburn, M. J., Breakspear, M., and Poldrack, R. A. (2018a). The modulation of neural gain facilitates a transition between functional segregation and integration in the brain. *Elife* 7:e31130. doi: 10.7554/eLife.31130

Shine, J. M., Bissett, P. G., Bell, P. T., Koyejo, O., Balsters, J. H., Gorgolewski, K. J., et al. (2016). The dynamics of functional brain networks: integrated network states during cognitive task performance. *Neuron* 92, 544–554. doi: 10.1016/j.neuron.2016.09.018

Shine, J. M., Breakspear, M., Bell, P. T., Martens, K. A. E., Shine, R., Koyejo, O., et al. (2019). Human cognition involves the dynamic integration of neural activity and neuromodulatory systems. *Nat. Neurosci.* 22, 289–296. doi: 10.1038/s41593-018-0312-0

Shine, J. M., van den Brink, R. L., Hernaus, D., Nieuwenhuis, S., and Poldrack, R. A. (2018b). Catecholaminergic manipulation alters dynamic network topology across cognitive states. *Netw. Neurosci.* 2, 381–396. doi: 10.1162/netn_a_00042

Sporns, O. (2013). Network attributes for segregation and integration in the human brain. *Curr. Opin. Neurobiol.* 23, 162–171. doi: 10.1016/j.conb.2012.11.015

Stephan, K. E., Weiskopf, N., Drysdale, P. M., Robinson, P. A., and Friston, K. J. (2007). Comparing hemodynamic models with DCM. *Neuroimage* 38, 387–401. doi: 10.1016/j.neuroimage.2007.07.040

Thiele, A., and Bellgrove, M. A. (2018). Neuromodulation of attention. *Neuron* 97, 769–785. doi: 10.1016/j.neuron.2018.01.008

Tognoli, E., and Kelso, J. S. (2014). The metastable brain. *Neuron* 81, 35–48. doi: 10.1016/j.neuron.2013.12.022

Tononi, G. (2004). An information integration theory of consciousness. *BMC Neurosci.* 5:42. doi: 10.1186/1471-2202-5-42

Tzourio-Mazoyer, N., Landeau, B., Papathanassiou, D., Crivello, F., Etard, O., Delcroix, N., et al. (2002). Automated anatomical labeling of activations in SPM using a macroscopic anatomical parcellation of the MNI MRI single-subject brain. *Neuroimage* 15, 273–289. doi: 10.1006/nimg.2001.0978

Van Den Heuvel, M. P., and Sporns, O. (2011). Rich-club organization of the human connectome. *J. Neurosci.* 31, 15775–15786. doi: 10.1523/JNEUROSCI.3539-11.2011

Wang, R., Lin, P., Liu, M., Wu, Y., Zhou, T., and Zhou, C. (2019). Hierarchical connectome modes and critical state jointly maximize human brain functional diversity. *Phys. Rev. Lett.* 123:038301. doi: 10.1103/PhysRevLett.123.038301

Wang, R., Liu, M., Cheng, X., Wu, Y., Hildebrandt, A., and Zhou, C. (2021). Segregation, integration and balance of large-scale resting brain networks configure different cognitive abilities. *arXiv preprint arXiv:2103.00475*. doi: 10.1073/pnas.2022288118

Xia, M., Wang, J., and He, Y. (2013). Brainnet viewer: a network visualization tool for human brain connectomics. *PLoS ONE* 8:e68910. doi: 10.1371/journal.pone.0068910

Zamora-López, G., Chen, Y., Deco, G., Kringelbach, M. L., and Zhou, C. (2016). Functional complexity emerging from anatomical constraints in the brain: the significance of network modularity and rich-clubs. *Sci. Rep.* 6:38424. doi: 10.1038/srep38424

Zerbi, V., Floriou-Servou, A., Markicevic, M., Vermeiren, Y., Sturman, O., Privitera, M., et al. (2019). Rapid reconfiguration of the functional connectome after chemogenetic locus coeruleus activation. *Neuron* 103, 702–718. doi: 10.1016/j.neuron.2019.05.034

Conflict of Interest: The authors declare that the research was conducted in the absence of any commercial or financial relationships that could be construed as a potential conflict of interest.

frontiers in Applied Mathematics and Statistics

ORIGINAL RESEARCH
published: 15 July 2021
doi: 10.3389/fams.2021.714978

Synchronization in Networks With Heterogeneous Adaptation Rules and Applications to Distance-Dependent Synaptic Plasticity

Rico Berner[1,2]* *and Serhiy Yanchuk*[1]

[1]*Institut für Mathematik, Technische Universität Berlin, Berlin, Germany,* [2]*Institut für Theoretische Physik, Technische Universität Berlin, Berlin, Germany*

This work introduces a methodology for studying synchronization in adaptive networks with heterogeneous plasticity (adaptation) rules. As a paradigmatic model, we consider a network of adaptively coupled phase oscillators with distance-dependent adaptations. For this system, we extend the master stability function approach to adaptive networks with heterogeneous adaptation. Our method allows for separating the contributions of network structure, local node dynamics, and heterogeneous adaptation in determining synchronization. Utilizing our proposed methodology, we explain mechanisms leading to synchronization or desynchronization by enhanced long-range connections in nonlocally coupled ring networks and networks with Gaussian distance-dependent coupling weights equipped with a biologically motivated plasticity rule.

Keywords: synaptic plasticity, adaptive networks, phase oscillator, synchronization, distance-dependent synaptic plasticity, nonlocally coupled rings, master stability approach

OPEN ACCESS

Edited by:
Jun Ma,
Lanzhou University of Technology, China

Reviewed by:
Syamal Kumar Dana,
Jadavpur University, India
Gopal R.,
SASTRA University, India

***Correspondence:**
Rico Berner
rico.berner@physik.tu-berlin.de

Specialty section:
This article was submitted to Dynamical Systems, a section of the journal Frontiers in Applied Mathematics and Statistics

Received: *26 May 2021*
Accepted: *21 June 2021*
Published: *15 July 2021*

Citation:
Berner R and Yanchuk S (2021) Synchronization in Networks With Heterogeneous Adaptation Rules and Applications to Distance-Dependent Synaptic Plasticity. Front. Appl. Math. Stat. 7:714978. doi: 10.3389/fams.2021.714978

1 INTRODUCTION

In nature and technology, complex networks serve as a ubiquitous paradigm with a broad range of applications from physics, chemistry, biology, neuroscience, socioeconomic, and other systems [1]. Dynamical networks consist of interacting dynamical units, such as neurons or lasers. Collective behavior in dynamical networks has attracted much attention in recent decades. Depending on the network and the specific dynamical system, various synchronization patterns with increasing complexity were explored [2–5]. Even in simple models of coupled oscillators, patterns such as complete synchronization [6, 7], cluster synchronization [8–11], and various forms of partial synchronization have been found, such as frequency clusters [12], solitary [13–15], or chimera states [16–20]. In particular, synchronization is believed to play a crucial role in brain networks, for example, under normal conditions in the context of cognition and learning [21, 22], and under pathological conditions, such as Parkinson's disease [23–25], epilepsy [26–29], tinnitus [30, 31], schizophrenia, to name a few [32].

The powerful methodology of master stability function [33] has been a milestone for the analysis of synchronization phenomena. This method allows for the separation of dynamic and structural features in dynamical networks. It greatly simplifies the problem by reducing the dimension and unifying the synchronization study for different networks. Since its introduction, the master stability approach has been extended and refined for various complex systems [34–42], and methods beyond the local stability analysis have been developed [43–47]. More recently, the master stability approach has been extended to

another class of oscillator networks with high application potential, namely adaptive networks [48].

Adaptive networks are commonly used models for various systems from nature and technology [49–57]. A prominent example are neuronal networks with spike-timing dependent plasticity, in which the synaptic coupling between neurons changes depending on their relative spiking times [58–61]. There are a large number of studies investigating the dynamic properties induced by this form of synaptic plasticity [62]. However, analysis is usually limited to only one or two forms of spike timing-dependent plasticity within a neuronal population. On the other hand, experimental studies indicate that different forms of spike timing-dependent plasticity may be present within a neuronal population, where the form depends on the connection structure between the axons and dendrites [63]. Among all structural aspects, an important factor for the specific form of the plasticity rule is the distance between neurons [64–66]. More specifically, it has been found that the plasticity rule between proximal or distal neurons, respectively, can change from Hebbian-like to anti-Hebbian-like [67, 68].

This work introduces a methodology to study synchronization in adaptive networks with heterogeneous plasticity (adaptation) rules. As a paradigmatic system, we consider an adaptively coupled phase oscillator network [69–75], which is proven to be useful for predicting and describing phenomena occurring in more realistic and detailed models [76–79]. More specifically, in the spirit of the master stability function approach, we consider the synchronization problem as the interplay between network structure and a heterogeneous adaptation rule arising from distance- (or location-)dependent synaptic plasticity. For a given heterogeneous adaptation rule, our master stability function provides synchronization criteria for any coupling configuration. As illustrative examples, we consider a nonlocally coupled ring with biologically motivated plasticity rule, and a network with a Gaussian distance-dependent coupling weights. We explained such intriguing effects as synchronization or desynchronization by enhancement of long-distance links.

We introduce the model in **Section 2**. Building on findings from [48], we develop a master stability approach in **Section 3** that takes a heterogeneous adaptation rule in account. In **Section 4.1**, we provide an approximation of the structural eigenvalues that determine the stability of the synchronous state. We then consider two different setups: a nonlocally coupled ring in **Section 4.2** and a weighted network with Gaussian distance distribution of coupling weights in **Section 4.3**. Both systems are equipped with a biologically motivated plasticity rule. In **Section 5**, we summarize the results.

2 MODEL

In this work, we study the synchronization on networks with adaptive coupling weights, where the adaptation (plasticity) rule depends on the distance between oscillators (neurons). We consider the model of adaptively coupled phase oscillators, which has proven to be useful for understanding dynamics in neuronal systems with spike timing-dependent plasticity [77, 79, 48]. The model reads as follows:

$$\frac{\mathrm{d}}{\mathrm{d}t}\phi_i = \omega + \sum_{j=1}^{N} a_{ij}\kappa_{ij} g\big(\phi_i - \phi_j\big), \tag{1}$$

$$\frac{\mathrm{d}}{\mathrm{d}t}\kappa_{ij} = -\epsilon\big(\kappa_{ij} + h_{ij}\big(\phi_i - \phi_j\big)\big), \tag{2}$$

where $\phi_i \in S^1 = \mathbb{R}/2\pi\mathbb{Z}$ $(i = 1, \ldots, N)$ is the phase of the ith oscillator, κ_{ij} $(i, j = 1, \ldots, N)$ is the dynamical coupling weight from oscillator j to i, ω denotes the natural frequency of each oscillator, and $a_{ij} \in [0, 1]$ are the entries of the weighted adjacency matrix A describing the network connectivity. The time scales of the "fast" phase oscillators and "slow" coupling weights are separated by the parameter ϵ, which we assume to be small $0 < \epsilon \ll 1$. The functions g and h_{ij} denote the coupling and the N^2 plasticity functions, respectively. For illustrative purposes, the coupling function is set throughout the paper to $g(\phi) = -\sin(\phi + \alpha)/N$ with the phase lag parameter α [80]. Such a phase lag can account for a small synaptic propagation delay [81, 48]. For formal derivations, however, a generic coupling function is used. Note that the system **Eqs. 1**, **2** is shift-symmetric, i.e., invariant under the transformation $\phi_i \mapsto \phi_i + \psi$ for any $\psi \in S^1$. This allows us to restrict our consideration to the case $\omega = 0$ by introducing a new "co-rotating" coordinate system $\phi_{i,\mathrm{new}} = \psi_i - \omega t$.

The main difference of system **Eqs. 1**, **2** from the models considered previously in the literature [40, 70, 71, 74, 82], is that the plasticity functions h_{ij} can be different for each network connection $j \to i$.

A solution to **Eqs. 1**, **2** is called *phase-locked* if, for all $i = 1, \ldots, N$, the phases evolve as $\phi_i = \Omega t + \vartheta_i$ with some *collective frequency* $\Omega \in \mathbb{R}$ and $\vartheta_i \in S^1$. If $\vartheta_i = \vartheta$ for all $i = 1, \ldots, N$, the phase-locked state is called *in-phase synchronous* or, short, *synchronous* state.

In the case of in-phase synchronous state, we can set $\vartheta_i = 0$ for each oscillator due to the shift symmetry of **Eqs. 1**, **2**. The in-phase synchronous state is given as

$$\phi^s(t) = -wg(0)t, \tag{3}$$

$$\kappa_{ij}^s = -h_{ij}(0), \tag{4}$$

where we assume that the weighted row sum $w = \sum_{j=1}^{N} a_{ij}h_{ij}(0)$ is constant for all. Such an assumption of constant row sum is necessary for the existence of the synchronous state. Moreover, it is satisfied for commonly considered cases of global or nonlocal shift-invariant coupling.

In the following section, we show how the stability of the synchronous state is determined in a master-stability-like approach.

3 MASTER STABILITY APPROACH

In **Section 2**, we have introduced a general class of models and the synchronous state, that are considered throughout this paper. In this section, we derive a framework for the local stability analysis of the synchronous states. We note that the

master stability approach for homogeneous adaptations $h_{ij} = h$ was introduced in [48, 83]. Here we extend the methodology to heterogeneous adaptation rules.

To describe the local stability, we introduce the variations $\xi_i = \phi_i - \phi^s$ and $\chi_{ij} = \kappa_{ij} - \kappa^s_{ij}$. The linearized equations for these variations can be written in the following matrix form

$$\frac{\mathrm{d}}{\mathrm{d}t}\begin{pmatrix}\boldsymbol{\xi}\\ \boldsymbol{\chi}\end{pmatrix} = J\begin{pmatrix}\boldsymbol{\xi}\\ \boldsymbol{\chi}\end{pmatrix} = \begin{pmatrix}\mathrm{D}g(0)L^h & g(0)B\\ -\epsilon C & -\epsilon\mathbb{I}_{N^2}\end{pmatrix}\begin{pmatrix}\boldsymbol{\xi}\\ \boldsymbol{\chi}\end{pmatrix}, \tag{5}$$

where $\boldsymbol{\xi} = (\xi_1, \ldots, \xi_N)^T$ is N-dimensional vector containing the perturbations $\xi_i = \delta\phi_i$ of the phases and $\boldsymbol{\chi} = (\chi_{11}, \chi_{12}, \ldots, \chi_{NN})^T$ are N^2- dimensional vectorized perturbations of coupling weights $\boldsymbol{\chi} = \mathbf{vec}[\delta\kappa_{ij}]$, respectively. The $N \times N$ weighted Laplacian matrix L^h has the following elements

$$l^h_{ij} = \begin{cases} -\sum_{m=1, m\neq i}^{N} a_{im}h_{im}(0), & i = j,\\ a_{ij}h_{ij}(0), & i \neq j.\end{cases} \tag{6}$$

The time-independent matrices B and C are

$$B = \begin{pmatrix}\boldsymbol{a}_1 & & \\ & \ddots & \\ & & \boldsymbol{a}_N\end{pmatrix},$$
$$C = \begin{pmatrix}(\mathrm{D}h)_1^T & & \\ & \ddots & \\ & & (\mathrm{D}h)_N^T\end{pmatrix} - \begin{pmatrix}\mathrm{diag}\,(\mathrm{D}h)_1\\ \vdots\\ \mathrm{diag}\,(\mathrm{D}h)_N\end{pmatrix},$$

where $\boldsymbol{a}_i = (a_{i1}, \ldots, a_{iN})$, $(\mathrm{D}h)_i = (\mathrm{D}h_{i1}(0), \ldots, \mathrm{D}h_{iN}(0))$, and

$$\mathrm{diag}\,(\mathrm{D}h(0))_i = \begin{pmatrix}\mathrm{D}h_{i1}(0) & & \\ & \ddots & \\ & & \mathrm{D}h_{iN}(0)\end{pmatrix}.$$

Note that due to the shift symmetry of **Eqs. 1**, **2**, the Jacobian J in **Eq. 5** is time independent. Therefore, the real parts of the $N(N+1)$ eigenvalues λ of J are the Lyapunov exponents of the synchronous state and hence determine its local stability. In the following proposition, we exploit the fact that J contains a large diagonal block $-\epsilon\mathbb{I}_{N^2}$ to reduce the dimension of the eigenvalue problem for J.

Proposition 1. *Suppose $\phi_i = \Omega t$ is an in-phase synchronous state of* **Eqs. 1**, **2**. *Then its linear stability is determined by the $2N$-dimensional linear system*

$$\frac{\mathrm{d}}{\mathrm{d}t}\boldsymbol{\nu} = \begin{pmatrix}\mathrm{D}g(0)L^h & g(0)\mathbb{I}_N\\ \epsilon L^{\mathrm{D}h} & -\epsilon\mathbb{I}_N\end{pmatrix}\boldsymbol{\nu}, \tag{7}$$

where $\mathrm{D}g(0)$ and L^h are as in **Eq. 5** *and the $N \times N$ weighted Laplacian matrix $L^{\mathrm{D}h}$ possesses the following elements*

$$l^{\mathrm{D}h}_{ij} = \begin{cases} -\sum_{m=1, m\neq i}^{N} a_{im}\mathrm{D}h_{im}(0), & i = j,\\ a_{ij}\mathrm{D}h_{ij}(0), & i \neq j.\end{cases} \tag{8}$$

Proof. We remind that system **Eq. 5** determines the spectrum (Lyapunov exponents) of the synchronous state. The Jacobian matrix in **Eq. 5** is sparse with a large $N^2 \times N^2$ block given by the simple diagonal matrix $-\epsilon\mathbb{I}_{N^2}$. This implies that **Eq. 5** possess $N^2 - N$ stable directions with Lyapunov exponents $-\epsilon$. To find these directions, we substitute $(\boldsymbol{\xi}, \boldsymbol{\chi}) = e^{-\epsilon t}(\boldsymbol{\xi}_0, \boldsymbol{\chi}_0)$ into **Eq. 5** and obtain the linear system

$$\begin{pmatrix}\mathrm{D}g(0)L^h + \epsilon\mathbb{I}_N & g(0)B\\ -\epsilon C & 0\end{pmatrix}\begin{pmatrix}\boldsymbol{\xi}_0\\ \boldsymbol{\chi}_0\end{pmatrix} = 0. \tag{9}$$

This system has at least $N^2 - N$ linearly independent solutions, since the matrix in **Eq. 9** is degenerate due to the large $N^2 \times N^2$ zero block. The structure of the invariant subspaces in system **Eq. 5** allows for introducing new coordinates, which separate the $N^2 - N$ stable directions (corresponding to the eigenvalues $-\epsilon$) from the remaining $2N$ directions. Explicitly, this transformation is given by

$$\begin{pmatrix}\boldsymbol{\xi}\\ \boldsymbol{\chi}\end{pmatrix} = R\begin{pmatrix}\boldsymbol{\xi}\\ \widehat{\boldsymbol{\chi}}\end{pmatrix}, \quad R = \begin{pmatrix}\mathbb{I}_N & 0 & 0\\ 0 & (1/r)B^T & K\end{pmatrix}$$

with $(N^2+N) \times (N^2+N)$ matrix R. Here K is an $(N^2-N) \times (N^2-N)$ orthogonal matrix with $BK = 0$. Applying this transformation, we obtain the following system

$$\frac{\mathrm{d}}{\mathrm{d}t}\begin{pmatrix}\boldsymbol{\xi}\\ \boldsymbol{\chi}_N\\ \boldsymbol{\chi}_{N^2-N}\end{pmatrix} = \begin{pmatrix}\mathrm{D}g(0)L^h & g(0)\mathbb{I}_N & 0\\ \epsilon L^{\mathrm{D}h} & -\epsilon\mathbb{I}_N & 0\\ -\epsilon K^T C & 0 & -\epsilon\mathbb{I}_{N^2-N}\end{pmatrix}\begin{pmatrix}\boldsymbol{\xi}\\ \boldsymbol{\chi}_N\\ \boldsymbol{\chi}_{N^2-N}\end{pmatrix}, \tag{10}$$

where $(\boldsymbol{\xi}, \boldsymbol{\chi}_N, \boldsymbol{\chi}_{N^2-N})^T = (\boldsymbol{\xi}, \widehat{\boldsymbol{\chi}})^T$, with $\boldsymbol{\chi}_N$ and $\boldsymbol{\chi}_{N^2-N}$ are an N and $N^2 - N$-dimensional vectors, respectively, and the $N \times N$ weighted Laplacian matrix $L^{\mathrm{D}h}$ as given in **Eq. 8**. For more details on the transformation, we refer the reader to [48, 83]. We observe that the variables $(\boldsymbol{\xi}, \boldsymbol{\chi}_N)$ are independent on $\boldsymbol{\chi}_{N^2-N}$. Hence, separating the master from the slave system, the resulting coupled differential equations that determine the stability of the synchronous state are given by system **Eq. 7**. This concludes the proof.

Proposition 1 reduces the problem's dimension significantly from $N(N+1)$ to $2N$. In the spirit of the master stability approach [33], we aim for further decomposition of the $2N$- dimensional coupled system **Eq. 7** into dynamically independent blocks of dimension 2. For this, we restrict our consideration to the case when L^h can be diagonalized $S^h = Q^{-1}L^hQ$ by a nonsingular complex-valued matrix Q. Note that the eigenvalues μ_i of L^h lie on the diagonal of S^h. In general, the matrices L^h and $L^{\mathrm{D}h}$ do not commute. Therefore, $Q^{-1}L^{\mathrm{D}h}Q$ is not necessarily of upper triangular shape. Regardless of this fact, the following proposition provides an explicit form for the eigenvalues of J in **Eq. 5** in the limit of slow adaptation, i.e., $\epsilon \ll 1$.

Proposition 2. *Assume that L^h is diagonalizable, with $S^h = Q^{-1}L^hQ$ being the associated diagonal matrix and Q the corresponding transformation. Let $\phi_i = \Omega t$ be an in-phase synchronous state of* **Eqs. 1**, **2** *Then, the local stability of this state is determined by the solutions of N quadratic equations, which are given up to the first order in ϵ as*

$$\lambda^2 + \left(\epsilon - \mathrm{D}g(0)\mu_i\right)\lambda - \epsilon\left(\mathrm{D}g(0)\mu_i + g(0)\nu_i\right) = 0, \quad i = 1, \ldots, N, \tag{11}$$

where μ_i are the eigenvalues of L^h located on the diagonal of S^h and ν_i are the corresponding diagonal elements of $Q^{-1}L^{\mathrm{D}h}Q$. If L^h and $L^{\mathrm{D}h}$ commute, then **Eq. 11** *is exact, and ν_i are the eigenvalues of $L^{\mathrm{D}h}$.*

Proof. Due to Proposition 1, the eigenvalues of the Jacobian in **Eq. 5** are given by

$$\det\begin{pmatrix} \mathrm{D}g(0)L^h - \lambda\mathbb{I}_N & g(0)\mathbb{I}_N \\ \epsilon L^{\mathrm{D}h} & -(\epsilon+\lambda)\mathbb{I}_N \end{pmatrix} = \det\begin{pmatrix} \mathrm{D}g(0)S^h - \lambda\mathbb{I}_N & g(0)\mathbb{I}_N \\ \epsilon Q^{-1}L^{\mathrm{D}h}Q & -(\epsilon+\lambda)\mathbb{I}_N \end{pmatrix} = 0,$$

where we have used the transformation Q that brings L^h to the diagonal form $S^h = Q^{-1}L^hQ$. Making further use of the Schur complement [84], we obtain

$$\det\begin{pmatrix} \mathrm{D}g(0)S^h - \lambda\mathbb{I}_N & g(0)\mathbb{I}_N \\ \epsilon Q^{-1}L^{\mathrm{D}h}Q & -(\epsilon+\lambda)\mathbb{I}_N \end{pmatrix} = \det\Big((\lambda+\epsilon)\Big(\lambda\mathbb{I}_N - \mathrm{D}g(0)S^h\Big) - \epsilon g(0)Q^{-1}L^{\mathrm{D}h}Q \Big) = 0. \quad (12)$$

The latter equation is almost diagonal. The only off-diagonal components remain from $Q^{-1}L^{\mathrm{D}h}Q$ and scale with ϵ. Let us consider the Leibniz formula for the determinant of an $N\times N$ matrix F with entries f_{ij}, that reads $\det(F) = \sum_{\sigma\in\mathrm{Perm}(N)}\mathrm{sgn}(\sigma)\prod_{i=1}^N f_{i\sigma(i)}$. In the latter expression $\mathrm{Perm}(N)$ denotes the set of all permutations σ of the integer numbers $1,\dots,N$ and $\mathrm{sgn}(\sigma)\in\{-1,1\}$ is the sign of the permutation. Since all off-diagonal terms of the matrix considered in **Eq. 12** scale with ϵ, for any but the identical permutation each term $\prod_{i=1}^N f_{i\sigma(i)}$ scales with ϵ^2 or higher. Hence, we are left with $\det(F) = \prod_{i=1}^N f_{ii} + \mathcal{O}(\epsilon^2)$ and find

$$\begin{aligned}\det&\Big((\lambda+\epsilon)\Big(\lambda\mathbb{I}_N - \mathrm{D}g(0)S^h\Big) - \epsilon g(0)Q^{-1}L^{\mathrm{D}h}Q\Big)\\ &= \prod_{i=1}\big(\lambda^2 + (\epsilon - \mathrm{D}g(0)\mu_i)\lambda - \epsilon\big(\mathrm{D}g(0)\mu_i + g(0)\nu_i\big)\big) + \mathcal{O}(\epsilon^2)\\ &= 0,\end{aligned} \quad (13)$$

where μ_i are the eigenvalues of L^h, ν_i are the diagonal elements of $Q^{-1}L^{\mathrm{D}h}Q$ and $\mathcal{O}(\epsilon^2)$ denotes higher order terms $(\epsilon^m, m>1)$. If L^h and $L^{\mathrm{D}h}$ commute, both matrices share the same set of eigenvectors and hence they can be brought to the diagonal form with the same transformation Q. In this case, the diagonal elements ν_i are the eigenvalues of $L^{\mathrm{D}h}$ and the higher order terms $\mathcal{O}(\epsilon^2)$ in **Eq. 13** vanish.

The $2N$ solutions λ_i of the N **Eq. 11** determine the stability of the synchronous state. More precisely, the real parts of theses solutions determine the Lyapunov exponents. If $\Lambda = \max_i\mathrm{Re}(\lambda_i) < 0$, then the synchronous state is locally stable, while for $\Lambda > 0$ it is locally unstable. The case $\Lambda = 0$ provides the stability boundary.

Note that for a fixed time scale parameter $\epsilon \ll 1$, the **Eq. 11** and hence its solutions depend on the coupling function g, the connectivity, and the adaptation structure. This dependence, however, is only encoded in the two complex parameters $\mathrm{D}g(0)\mu$ and $g(0)\nu$. Therefore, we define the master stability function $\Lambda:\mathbb{C}^2\to\mathbb{R}$ with $\Lambda(\mathrm{D}g(0)\mu, g(0)\nu) = \max_i\mathrm{Re}(\lambda_i(\mathrm{D}g(0)\mu, g(0)\nu))$ that maps each pair of parameters $(\mathrm{D}g(0)\mu, g(0)\nu)$ to the corresponding Lyapunov exponent.

For an illustration, we consider a cross-section of $(\mathrm{D}g(0)\mu, g(0)\nu)$- space by setting $\mathrm{Im}(\mu) = 0$ and $\mathrm{Im}(\nu) = 0$. This cross-section is of particular interest in cases of symmetric matrices L^h and $L^{\mathrm{D}h}$ since their eigenvalues are real. In **Figure 1**, we present the master stability function for the coupling function $g(\phi) = -\sin(\phi+\alpha)/N$ and different values of the parameter α. In case of real μ and ν, we obtain two explicit stability conditions from **Eq. 11**: The synchronous state is locally stable $(\Lambda < 0)$ if

$$c_1(\alpha,\mu) = \cos(\alpha)\mu > -\epsilon, \quad (14)$$

$$c_2(\alpha,\mu,\nu) = \cos(\alpha)\mu + \sin(\alpha)\nu > 0. \quad (15)$$

These conditions agree with the black dashed lines in **Figure 1** and are used subsequently to describe stability for certain network models.

4 SYNCHRONIZATION ON NETWORKS WITH DISTANCE-DEPENDENT PLASTICITY

In the previous section, we established a generic analytic tool for studying stability of synchronous states. In this section, we focus on the application of the tool to certain network models. For the rest of the work, we restrict our attention to the following generalization of the Kuramoto-Sakaguchi system with distance-dependent synaptic plasticity

$$\frac{\mathrm{d}}{\mathrm{d}t}\phi_i = \omega - \frac{1}{N}\sum_{j=1}^N a_{ij}\kappa_{ij}\sin\big(\phi_i - \phi_j + \alpha\big), \quad (16)$$

$$\frac{\mathrm{d}}{\mathrm{d}t}\kappa_{ij} = -\epsilon\big(\kappa_{ij} + h\big(\phi_i - \phi_j, d_{ij}\big)\big). \quad (17)$$

The plasticity function h depends on the phase difference $\phi_i - \phi_j$ and on the distance d_{ij}. In this work, we associate the distance to the difference of indices by $d_{ij} = |j-i|$. For the plasticity function, we consider

$$h_{ij}(\phi) = h\Big(\phi, \frac{d_{ij}}{N}\Big) = \begin{cases} \widehat{h}\Big(\phi, \dfrac{d_{ij}}{N}\Big) & d_{ij} \le N/2, \\ \widehat{h}\Big(\phi, 1 - \dfrac{d_{ij}}{N}\Big) & d_{ij} > N/2. \end{cases} \quad (18)$$

With this form of the adaptation function, we have a symmetric $h_{ij}(\phi) = h_{ji}(\phi)$ and a circulant $h_{i+l,j+l}(\phi) = h_{ij}(\phi)$ structure of the corresponding matrix with entries h_{ij}. Particularly, for the numerical analysis, we use

$$\widehat{h}\big(\phi, d_{ij}/N\big) = \sin\big(\phi + \beta\big(d_{ij}/N\big)\big), \quad (19)$$

where the distance dependence is encoded in the phase shift function

$$\beta\Big(\frac{d_{ij}}{N}\Big) = \begin{cases} \Big(\dfrac{2}{N}d_{ij} - 1\Big)\pi, & N \text{ even}, \\ \Big(\dfrac{2}{(N+1)}d_{ij} - 1\Big)\pi, & N \text{ odd}. \end{cases} \quad (20)$$

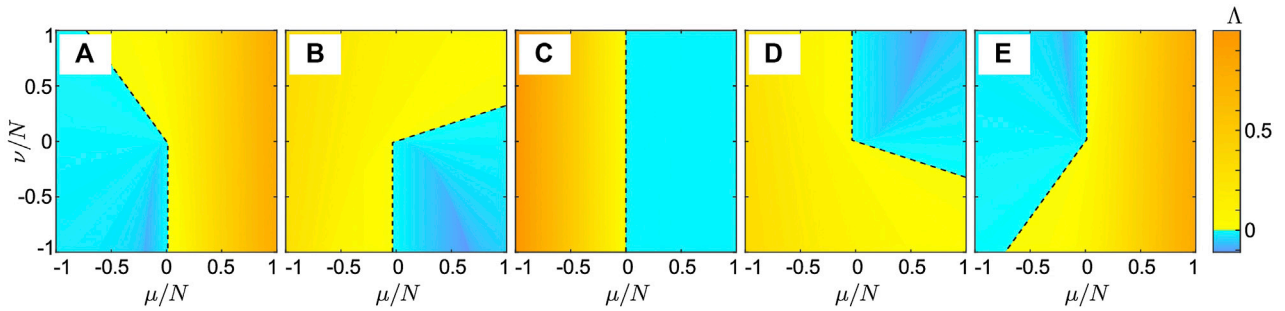

FIGURE 1 | The master stability function $\Lambda(Dg(0)\mu, g(0)\nu)$ for the coupling function $g(\phi) = -\sin(\phi + \alpha)/N$ and real μ and ν ($\mathrm{Im}(\mu) = 0$, $\mathrm{Im}(\nu) = 0$). The values of the master stability function are color-coded in all panels **(A–E)**. The dashed black line describes the border between regions corresponding to local stability and instability, respectively. Parameters: $\epsilon = 0.01$, **(A)** $\alpha = -0.8\pi$, **(B)** $\alpha = -0.4\pi$, **(C)** $\alpha = 0$, **(D)** $\alpha = 0.4\pi$, and **(E)** $\alpha = 0.8\pi$.

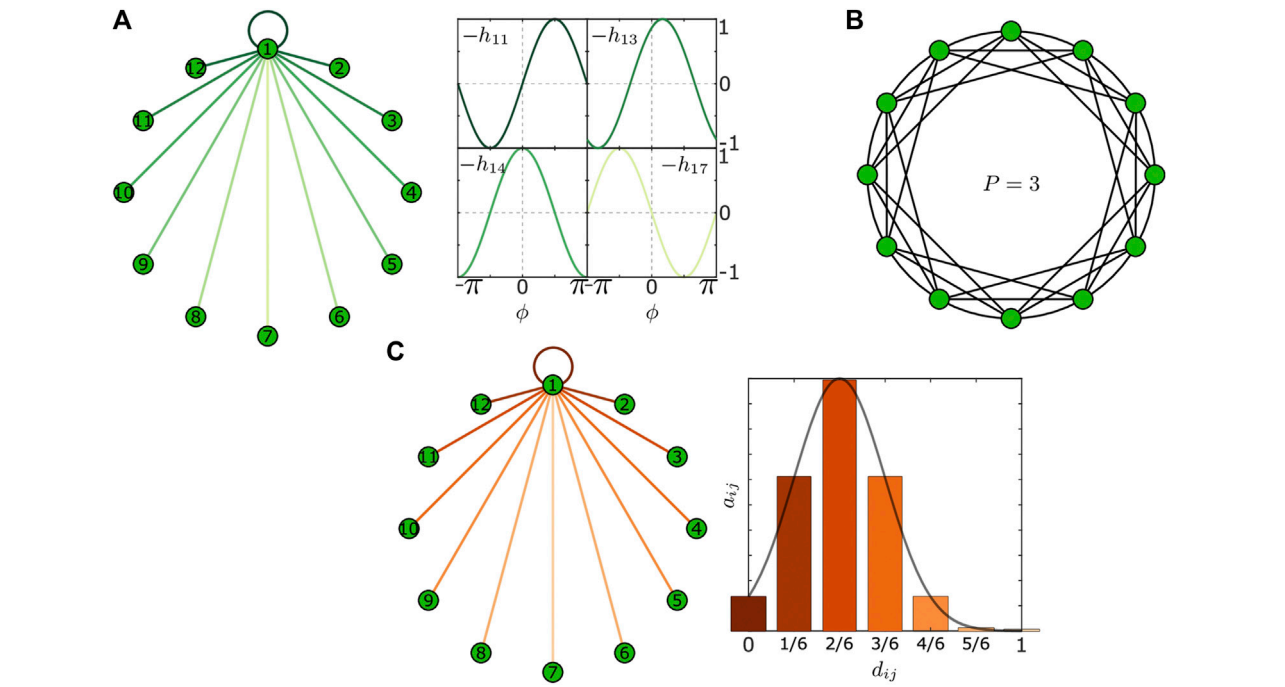

FIGURE 2 | Panel **(A)** shows the plasticity function h_{1j} given in **Eqs. 18–20** depending on the distance d_{1j} exemplified for node $i = 1$ in a network with $N = 12$ nodes. Note that the colors of the links in the network **(left)** correspond to the colors of the depicted plasticity function (right). Panel **(B)** displays the connectivity structure of a nonlocally coupled ring network with $N = 12$ nodes and a coupling range $P = 3$. Panel **(C)** displays the weighted connectivity structure of a network with $N = 12$ nodes **(left)** with distance-dependent Gaussian weight distribution **(right)**. Note that the colors of the links in the network (left) correspond to the colors of the bars in the weight distribution **(right)**.

In **Figure 2A**, we illustrate the distance-dependent plasticity function **Eqs. 18–20** for a network of $N = 12$ nodes. The illustration shows the different plasticity functions depending on the distance between the nodes d_{ij}. The plasticity function changes from a Hebbian to anti-Hebbian rule for proximal and distal node, respectively. This change, particularly in the proximity of $\phi = 0$, is in qualitative agreement with the experimental findings in [67]. Note the symmetry of the plasticity function that renders the matrix with elements h_{ij} circulant.

If not indicated differently, we consider the coupling structure given by

$$a_{ij} = a\left(d_{ij}/N\right), \tag{21}$$

where $a : [0, 1] \to [0, 1]$ is a bounded and piece-wise continuous function. This corresponds to a distant-dependent coupling, and it results to a dihedral symmetry in the coupling structure (ring-like).

In the following section, we provide an approximation for the eigenvalues of L^h and L^{Dh} for large networks with circulant

connectivity and plasticity structure. Using this approximation, we subsequently analyze the stability of the synchronous state on nonlocally coupled networks and on isotropic networks with Gaussian weight distribution.

4.1 Approximation of the Eigenvalues for Large Systems With Circulant Structure

In the previous part, we have defined the plasticity functions h_{ij} in such a way that the structures of L^h and L^{Dh} inherit important properties from the underlying network structure $a(d_{ij}/N)$. In particular, assuming that the adjacency matrix is circulant, renders L^h and L^{Dh} to be circulant, as well.

In this section, we briefly recall how one can derive the eigenvalues μ_k and ν_k $(k = 0, \ldots, N-1)$ in case of a circulant structure. It is well-known that for a circulant matrix the eigenvalues are determined by applying a discrete Fourier approach [85]. More precisely, suppose L is a circulant $N \times N$ matrix where the elements of the first row are given by the entries l_j with $j = 1, \ldots, N$. Then the kth eigenvalue is explicitly given by

$$\mu_k = l_1 + \sum_{j=2}^{N} l_j \exp\Big(\mathrm{i}\frac{2\pi}{N}(j-1)k\Big).$$

For the case of L^h as in **Eq. 6**, a_{ij} and h_{ij} as in **Eqs. 18** and **21**, we obtain

$$\mathrm{Re}(\mu_k) = \mathrm{Re}\big(l^h_{11}\big) + \frac{1}{N}\sum_{j=2}^{N} a\big(x_j\big)h\big(0, x_j\big)\cos\big(2\pi x_j k\big), \tag{22}$$

with $x_j = d_{1j}/N$ and $\mathrm{Re}(l^h_{11}) = -\frac{1}{N}\sum_{j=2}^{N} a(x_j)h(0, x_j)$. Since the adjacency matrix A is assumed to be symmetric, the eigenvalues of L^h are real. Therefore, we omit considering the imaginary part of μ_k. **Eq. 22** provides exact expressions for the eigenvalues. However, the values depend on the total number of oscillators N that makes it harder to study the influence of other system properties, such as the coupling structure or the plasticity function. To remove this N-dependence, we consider the continuum limit $N \to \infty$ (compare with [86]) and obtain

$$\mathrm{Re}(\mu_k) = \mathrm{Re}\big(l^h_{11}\big) + \int_0^1 a(x)h(0, x)\cos(2\pi x k)\mathrm{d}x,$$

Due to the definition of h and the symmetry of $a(x)$, we find

$$\mathrm{Re}(\mu_k) = 2\int_0^{1/2} a(x)h(0, x)\left(\cos(2\pi x k) - 1\right)\mathrm{d}x \tag{23}$$

for any k. This explicit expression allows studying the distribution of the eigenvalues μ_k for a given plasticity function h and coupling structure a. Note that a similar expression as (23) can be analogously derived for the eigenvalues of L^{Dh} and reads

$$\mathrm{Re}(\nu_k) = 2\int_0^{1/2} a(x)\mathrm{D}h(0, x)\left(\cos(2\pi x k) - 1\right)\mathrm{d}x. \tag{24}$$

We note that $\mu_0 = \nu_0 = 0$ due to the Laplacian structure of L^h and L^{Dh}.

The results from **Eqs. 23** and **24** are applied in the next sections to analyze different networks.

4.2 Synchronization on Nonlocally Coupled Ring Networks

In this section, we analyze the effect of long distance connections on the stability of synchronous states in nonlocally coupled ring networks. We consider the coupling structure given by

$$a_{ij} = a\big(d_{ij}/N\big) = \begin{cases} 1 & \text{for } 0 < d_{ij} \le P, \\ 1 & \text{for } 0 < N - d_{ij} \le P, \\ 0 & \text{otherwise.} \end{cases} \tag{25}$$

This means that any two oscillators are coupled if they are separated at most by the coupling range P. The coupling **Eq. 25** defines a nonlocal ring structure with coupling range p to each side and two special limiting cases: local ring for $P = 1$ and globally coupled network for $P = N/2$ (if N is even, else $P = (N+1)/2$). The matrix of the form Eq. 25 is circulant [85] and has constant row sum, i.e., $\sum_{j=1}^{N} a_{ij} = 2P$ for all $i = 1, \ldots, N$. An illustration for $N = 12$ adn $P = 3$ is presented in **Figure 2B**.

In order to study the influence of the coupling range, we use the approximations for the eigenvalues μ_k and ν_k derived in **Section 4.1**. The nonlocally coupled ring structure is expressed by the piecewise continuous function $a(x) = 0$ for $p < x < 1 - p$ and $a(x) = 1$ otherwise with relative coupling range $p = P/N$. Thus, for a nonlocally coupled ring Eq. 25 and plasticity function **Eqs. 18–20**, we find

$$\begin{aligned} \mathrm{Re}(\mu_k) &= -2\int_0^p \sin(2\pi x)\left(\cos(2\pi k x) - 1\right)\mathrm{d}x \\ &= \frac{(1 - \cos(2\pi p))}{\pi} + \frac{1}{\pi}\begin{cases} \frac{1}{2}\left(\cos^2(2\pi p) - 1\right) & k = 1 \\ \frac{1}{(1-k^2)}\left(k\sin(2\pi p)\sin(2\pi k p) + \cos(2\pi p)\cos(2\pi k p) - 1\right) & k \ne 1 \end{cases} \end{aligned} \tag{26}$$

for the eigenvalues μ_k of L^h. Analogously, we obtain

$$\begin{aligned} \mathrm{Re}(\nu_k) &= -2\int_0^p \cos(2\pi x)\left(\cos(2\pi k x) - 1\right)\mathrm{d}x \\ &= \frac{\sin(2\pi p)}{\pi} - \frac{1}{\pi}\begin{cases} p\pi + \frac{\sin(4\pi p)}{4} & k = 1 \\ \frac{1}{(1-k^2)}\left(\sin(2\pi p)\cos(2\pi k p) - k\cos(2\pi p)\sin(2\pi k p)\right) & k \ne 1 \end{cases} \end{aligned} \tag{27}$$

for ν_k of L^{Dh}.

In **Figure 3A**, we provide an error analysis of the approximations **Eqs. 26** and **27** compared to the exact eigenvalues given by **Eq. 22**. As expected, the errors tend to zero as the number of oscillators increases. Additionally in **Figures 3B,C**, we display μ_k and ν_k for several values of k depending on the relative coupling range p. We observe that $\mu_k \ge 0$ for all k. This is due to given plasticity function **Eqs. 18–20**, for which the update is positive (or equal to zero) for all distances at $\phi = 0$, i.e., $h(0, d_{ij}) \ge 0$ for all d_{ij}.

It is important to note, that our choice of the circulant adaptation functions imply that the matrices L^h and L^{Dh} are diagonalizable and commute. Hence, Proposition 2 holds with the

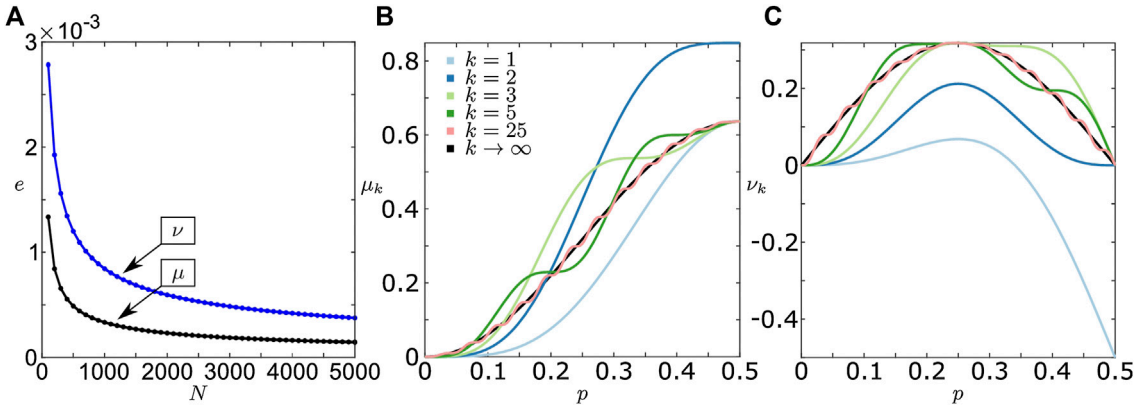

FIGURE 3 | Panel **(A)** shows the errors $e(\mu)$ (black) and $e(\nu)$ (blue) with $e(\gamma) = \sqrt{\frac{\sum_{k=0}^{N-1}(\gamma_k^{\text{exact}} - \gamma_k)^2}{N}}$ of the approximations **Eqs. 26**, **27**, respectively, where γ_k^{exact} are the exact eigenvalues derived by a discrete Fourier transformation, see **Eq. 22**. The errors are displayed in dependence of the system size N (number of oscillators). The relative coupling range is set to $p = 0.1$. Panel **(B)** and **(C)** show the approximated eigenvalues given by **Eqs. 26**, **27**, respectively, depending on the relative coupling range p for different values of k.

master stability **Eq. 11** being exact. Therefore, the stability criterium **Eq. 14** is also exact.

Combining the fact $\mu_k \geq 0$ with the stability criterium **Eq. 14**, we find $\cos(\alpha) > 0$ as a necessary condition for the stability of the synchronous state for $\epsilon \to 0$. This yields, that the synchronous state can be stable only for $\alpha \in (-\pi/2, \pi/2)$. In contrast to L^h, the L^{Dh} is in general neither positive nor negative definite, hence the eigenvalues ν_k may take positive or negative values. This is due to the fact that the plasticity function may change sign at the origin, i.e., Dh_{ij} may change signs depending on the distance d_{ij}. In particular, we find that only the eigenvalue ν_1 changes the sign, see **Figure 3C**. This change may lead to a destabilization of the synchronous states as we show in the subsequent analysis. Finally, note that there exist $\mu_\infty = (1 - \cos(2\pi p))/\pi$ and $\nu_\infty = -\sin(2\pi p)/\pi$ to which the eigenvalues converge for large values of k. These limits are displayed in **Figures 3B,C** as black lines.

In **Figure 4**, we show different scenarios for the stability of the synchronous state depending on the phase lag parameter α and the coupling range p. Due to the necessary condition $\cos(\alpha) > 0$ as $\epsilon \to 0$, we consider $\alpha \in (-\pi/2, \pi, 2)$ only. **Figures 4A,B** show that for $-\pi/2 < \alpha < 0$, the second stability condition Eq. 15 is only fulfilled for p larger than a critical value of the coupling range $p_c(\alpha)$. In these cases, a higher coupling range stabilizes the synchronous state. Note that $p_c(\alpha) \to 0$ as $\alpha \to 0$ with $\alpha < 0$. The results seen in **Figures 4A,B** are in agreement with the results for a network of $N = 200$ coupled phase oscillators. For this network, we calculate the Laplacian eigenvalues and plot them along with the master stability function in **Figures 4E,F**. The outcomes from numerical simulations are presented in **Figures 4I,J**.

The situation changes for $0 < \alpha < \pi/2$, as shown in **Figures 4C,D**. Here, for a large range of α, all nonlocally coupled networks lead to a stable synchronous state. However, closer to $\pi/2$, long distance connections destabilize the synchronous state. In particular, this destabilization can be traced back to the single negative eigenvalue ν_1 of the Laplacian L^{Dh}, see **Figure 4H**. Hence, the unstable manifold of the synchronous state is only one-dimensional. This finding is in agreement with the example of $N = 200$ phase oscillators presented in **Figures 4G,H,K, L**. Particularly in **Figure 4L**, the low dimension of the unstable manifold manifests itself as follows: The black trajectory first tends to the synchronous state along the $N(N+1) - 1$ stable directions before it is repelled along the direction corresponding to ν_1.

We have shown that long distance interactions may stabilize or destabilize the synchronous state depending on the phase lag parameter α. In this section, all links have the same weight independent of the corresponding distance. In the next section, we analyze a network with a more realistic structure with a distance-dependent distribution of weights.

4.3 Synchronization on Isotropic and Homogeneous Network With Gaussian Distance Distribution

In the previous section, we used the prototypical example of a nonlocally coupled rings to study the effects of long-range interaction on synchronization. In this setup, however, all links are equally weighted. In realistic systems, in contrast, the number of links with a certain distance are distributed, see [67] for details. To incorporate this into our network model, we weight the links with respect to a distance distribution. Measurements suggest that the distance distribution can be estimated by a mean and a distribution width [67]. The Gaussian distributions is a paradigmatic distribution that allows for studying effects emanating from the mean and the distribution width. For the remainder of the section, we consider the link distance distribution given by a Gaussian distribution, and weight the links of the network connectivity structure A accordingly, i.e.

$$a_{ij}\left(d_{ij}/N\right) = \begin{cases} e^{-\frac{\left(d_{ij}/N-\xi\right)^2}{2\sigma^2}} & d_{ij} \leq N/2, \\ e^{-\frac{\left(1-d_{ij}/N-\xi\right)^2}{2\sigma^2}} & d_{ij} > N/2. \end{cases} \tag{28}$$

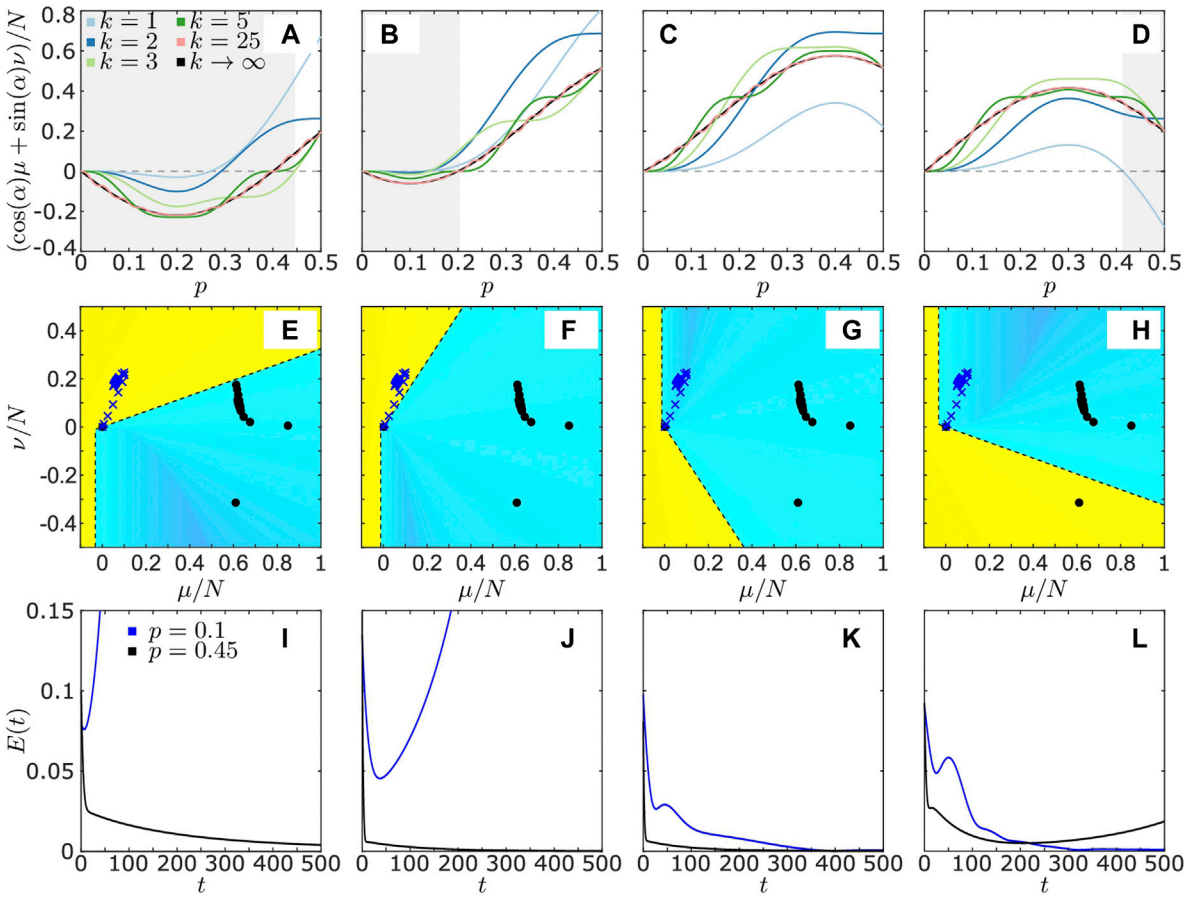

FIGURE 4 | Stability analysis of the synchronous state of system **Eqs. 16**, **17** with plasticity rule **Eqs. 18–20** and coupling structure **Eq. 25**. Panels **(A–D)** show the function $c_2(\alpha,\mu_k(p),\nu_k(p))$ for different α, see **Eq. 15**, calculated with the approximations **Eqs. 26**, **27** depending on the relative coupling range p. In each panel, c_2 is displayed for different values of k. The gray shaded regions refer to unstable synchronous states. Panels (e,f,g,h) show the master stability function $\Lambda(Dg(0)\mu,g(0)\nu)$ for the cross-section $\mathrm{Im}(\mu)=0$ and $\mathrm{Im}(\nu)=0$ for different values of α with color code as in **Figure 1**. The crosses and dots correspond to two sets of eigenvalue pairs (μ_k,ν_k) $(k=0,\ldots,N-1)$ for relative coupling range $p=0.1$ (blue crosses) and $p=0.45$ (black points), respectively. Panels **(I–L)** show the synchronization error $E(t)=\sqrt{\sum_{i=1}^{N}(\phi_i(t)-\phi_1(t))^2}$ for simulations with relative coupling range $p=0.1$ (blue) and $p=0.45$ (black). Each simulation is initialized at a slightly perturbed synchronous state. Parameters: $N=200$, $\epsilon=0.01$, **(A, E, I)** $\alpha=-0.4\pi$, **(B, F, J)** $\alpha=-0.2\pi$, **(C, G, K)** $\alpha=0.2\pi$, **(D, H, L)** $\alpha=0.4\pi$.

where ξ and σ are the mean value and the standard deviation, respectively. Note that the standard deviation characterizes the width of the distribution. For the numerical simulations, we normalize each row of A by $\sum_{j=1}^{N}a_{ij}$. Here, we further make the assumption that the network is homogeneous and isotropic. This means that in any direction from a node and at each node the network looks the same. Hence, we obtain a circulant connectivity structure. An illustration of the weight distribution for $N=12$ is presented in **Figure 2C**.

As we know from **Eqs. 14** and **15**, for $\epsilon\ll 1$, the values of $c_2(\alpha,\mu_k,\nu_k)$ determine the stability of the synchronous state. In particular, the synchronous state is stable if $c_{\min}=\min_{k\in 1,N-1}c_2(\alpha,\mu_k,\nu_k)>0$ for a given N and unstable otherwise. In **Figure 5A**, we display $c_{\min}$ for $\alpha=-0.4\pi$ and different mean values ξ and standard deviations σ of the weight distribution. In agreement with the finding in **Section 4.2**, the synchronized state stabilizes due to an increase of long distance interaction expressed by an increase of σ. Complementing the finding in **Section 4.2**, here, we note that the stability can be also achieved by distributions with peaks at long distance links alone. In this case, the width of the distribution is not important. **Figure 5B** shows how the boundary between regions corresponding to stable and unstable synchronization change for different values of α. As in the case of nonlocally coupled ring networks, with $\alpha\to 0$ (with $\alpha<0$) the boundary tends to the limiting point $(\sigma,\xi)=(0,0)$. On the contrary, if $\alpha\to-\pi/2$ (with $\alpha>-\pi/2$), the width of the distribution has to increase to have stable synchronization for small values of the mean ξ.

An opposite scenario is shown in **Figure 5C** for $\alpha=0.4\pi$. Here, an increase of the weights for long distance links destabilizes the synchronous state, as in **Figures 4D,H,L**. We also note that for small values α, the synchronous state is stable for almost all values of σ and ξ, see **Figure 5D**. Only in cases of distribution sharply peaked at long distances, i.e., ξ close to 1/2 and σ close to 0, the synchronous state is unstable. This effect

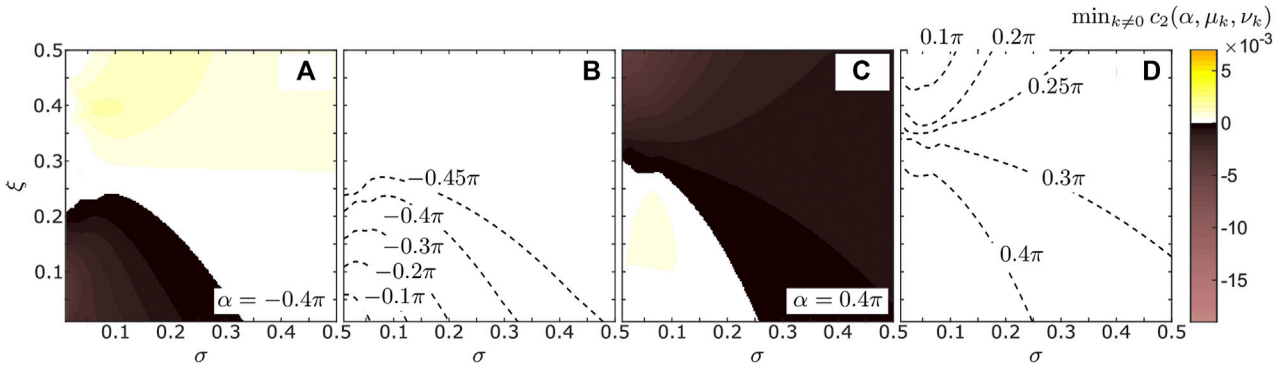

FIGURE 5 | Stability analysis of the synchronous state of system **Eqs. 16**, **17** with plasticity rule **Eqs. 18–20** and coupling structure **Eq. 28**. Panels **(A, C)** show the minimum over all $k \neq 0 < N$ of c_2, se **Eq. 15**, for two different values of α depending on the mean value ξ and the standard deviation σ of the weight distribution. The minima are displayed in color code. Panels **(B, D)** show the boundaries between stable and unstable regions in (σ, ξ)- plane for different values of α as given in the figure. Parameters: **(A)** $N = 400$, $\alpha = -0.4\pi$, **(C)** $N = 400$, $\alpha = 0.4\pi$, **(B, C)** $N = 200$.

could not be found in networks with nonlocally coupled rings, see **Section 4.2**.

5 CONCLUSION

In summary, we have investigated the phenomenon of synchronization on adaptive networks with heterogeneous plasticity rules. In particular, we have modeled systems with distance-dependent plasticity as they have been found in neuronal networks experimentally [64–67] as well as computational models [68]. For the realization, we have used a ring-like network architecture and associated the distance of two nodes with the distance of their placement on the ring.

In **Section 3**, we have developed a generalized master stability approach for phase oscillator models that are adaptively coupled and where each link has its own adaptation rule (plasticity). By using an explicit splitting of the time scales between fast dynamics of the phase oscillators and slow dynamics of the link weights, we have established an explicit stability condition for the synchronous state. More precisely, we found that the stability is governed by the coupling function and the eigenvalues of two structure matrices. These structure matrices L^h and L^{Dh} are determined by the connectivity of the network and the plasticity rules of the link weights. Note that for the structural matrices, the plasticity rule needs only to be known in the vicinity of 0, which greatly facilitates the application of the approach to realistic forms of synaptic plasticity. Thus, we have extended previous work on the master stability function of adaptive networks [48, 83] and broaden the scope of potential future applications for this methodology.

In **Section 4**, we applied the novel technique to a system of adaptively coupled oscillators with distance-dependent plasticity. Here, we have used a ring-like network structure to study the impact of long- and short-distance connections on the stability of synchronization. For this purpose we introduced an approximation of the eigenvalues for the structure matrices in **Section 4.1**. This approximation allows for a comprehensive analysis of the stability as a function of various system parameters. Moreover, it enables us to identify critical eigenvalues that govern the stability of the synchronous state. In **Sections 4.2** and **4.3**, we have brought together all methodological findings and applied them to systems with a nonlocally coupled ring structure and with a Gaussian distribution of link weights. The latter structure accounts for the fact that in realistic neuronal populations the number of links with different distances are not uniformly distributed [67]. We found that long-distance connections can stabilize or destabilize the synchronous state, depending on the coupling function between the oscillators. A remarkable fact with respect to neuronal applications relates to the destabilization scenario. Here we observed that the destabilization can be attributed to the pronounced change of the plasticity rule from Hebbian to anti-Hebbian. For more realistic connectivity structures, we found that weight distributions of the connectivity structure with sharp peaks at long distances lead to destabilization for a wide range of the coupling function.

All in all, in this article, we have provided a general framework to study the emergence of synchronization in neuronal system with a heterogeneous plasticity rule. The developed methodology is not limited to distance-dependent types of plasticity and can also be used for non-symmetric setups. For the latter case, we have provided the necessary analytical result. In this work, we have restricted our attention to the case of phase oscillators, but the methods can be extended to more realistic neuron models by using techniques established, for example, in [48]. Moreover, techniques are available that allow for further generalization toward systems with slightly different local dynamics at each node [87]. On the one hand, the master stability approach offers a great tool to study the stability of the synchronous state depending on the networks structure. On the other hand, this approach allows for characterizing the network structures that are, in some sense, optimal for synchronization [88, 89]. In this regard, it remains an open question as to how plasticity optimizes

the synchronizability of the network in a self-organized way. In addition, recent studies have shown that there is a great interest in synchronization phenomena to understand diseases such as Parkinson's disease [90–92] or epilepsy [29, 93] for the development of proper therapeutic treatments. We believe that our work provides an important step toward understanding synchronization under realistic conditions.

DATA AVAILABILITY STATEMENT

The raw data supporting the conclusions of this article will be made available by the authors, without undue reservation.

AUTHOR CONTRIBUTIONS

RB designed the study and did the numerical simulations. RB and SY developed the analytical results. Both authors contributed to the preparation of the manuscript. Both authors read and approved the final manuscript.

FUNDING

This work was supported by the German Research Foundation DFG, Project Nos. 411803875 and 440145547, and the Open Access Publication Fund of TU Berlin.

REFERENCES

1. Newman MEJ. The Structure and Function of Complex Networks. *SIAM Rev* (2003) 45:167–256. doi:10.1137/s003614450342480
2. Pikovsky A, Rosenblum M, and Kurths J. *Synchronization: A Universal Concept in Nonlinear Sciences*. 1st ed. Cambridge: Cambridge University Press (2001).
3. Strogatz SH. Exploring Complex Networks. *Nature* (2001) 410:268–76. doi:10.1038/35065725
4. Arenas A, Díaz-Guilera A, Kurths J, Moreno Y, and Zhou C. Synchronization in Complex Networks. *Phys Rep* (2008) 469:93–153. doi:10.1016/j.physrep.2008.09.002
5. Boccaletti S, Pisarchik AN, del Genio CI, and Amann A. *Synchronization: From Coupled Systems to Complex Networks*. Cambridge: Cambridge University Press (2018).
6. Kuramoto Y. *Chemical Oscillations, Waves and Turbulence*. Berlin: Springer-Verlag (1984).
7. Pecora LM, Carroll TL, Johnson GA, Mar DJ, and Heagy JF. Fundamentals of Synchronization in Chaotic Systems, Concepts, and Applications. *Chaos* (1997) 7:520–43. doi:10.1063/1.166278 https://doi.org/10.1063/1.166278
8. Yanchuk S, Maistrenko Y, and Mosekilde E. Partial Synchronization and Clustering in a System of Diffusively Coupled Chaotic Oscillators. *Mathematics Comput Simulation* (2001) 54:491–508. doi:10.1016/S0378-4754(00)00276-7
9. Choe C-U, Dahms T, Hövel P, and Schöll E. Controlling Synchrony by Delay Coupling in Networks: from In-phase to Splay and Cluster States. *Phys Rev E* (2010) 81:025205. doi:10.1103/physreve.81.025205
10. Belykh I, and Hasler M. Mesoscale and Clusters of Synchrony in Networks of Bursting Neurons. *Chaos* (2011) 21:016106. doi:10.1063/1.3563581
11. Zhang Y, and Motter AE. Symmetry-independent Stability Analysis of Synchronization Patterns. *SIAM Rev* (2020) 62:817–36. doi:10.1137/19m127358x
12. Berner R, Schöll E, and Yanchuk S. Multiclusters in Networks of Adaptively Coupled Phase Oscillators. *SIAM J Appl Dyn Syst* (2019) 18:2227–66. doi:10.1137/18m1210150
13. Jaros P, Brezetsky S, Levchenko R, Dudkowski D, Kapitaniak T, and Maistrenko Y. Solitary States for Coupled Oscillators with Inertia. *Chaos* (2018) 28:011103. doi:10.1063/1.5019792
14. Teichmann E, and Rosenblum M. Solitary States and Partial Synchrony in Oscillatory Ensembles with Attractive and Repulsive Interactions. *Chaos* (2019) 29:093124. doi:10.1063/1.5118843
15. Berner R, Polanska A, Schöll E, and Yanchuk S. Solitary States in Adaptive Nonlocal Oscillator Networks. *Eur Phys J Spec Top* (2020) 229:2183–203. doi:10.1140/epjst/e2020-900253-0
16. Kuramoto Y, and Battogtokh D. Coexistence of Coherence and Incoherence in Nonlocally Coupled Phase Oscillators. *Nonlin Phen Complex Sys* (2002) 5(4):380–5.
17. Abrams DM, and Strogatz SH. Chimera States for Coupled Oscillators. *Phys Rev Lett* (2004) 93:174102. doi:10.1103/physrevlett.93.174102
18. Schöll E. Synchronization Patterns and Chimera States in Complex Networks: Interplay of Topology and Dynamics. *Eur Phys J Spec Top* (2016) 225:891–919. doi:10.1140/epjst/e2016-02646-3
19. Omel'chenko OE. The Mathematics behind Chimera States. *Nonlinearity* (2018) 31:R121. doi:10.1088/1261-6544/aaaa07
20. Omel'chenko OE, and Knobloch E. Chimerapedia: Coherence-Incoherence Patterns in One, Two and Three Dimensions. *New J Phys* (2019) 21:093034. doi:10.1088/1367-2630/ab3f6b
21. Singer W. Neuronal Synchrony: A Versatile Code for the Definition of Relations? *Neuron* (1999) 24:49–65. doi:10.1016/s0896-6273(00)80821-1
22. Fell J, and Axmacher N. The Role of Phase Synchronization in Memory Processes. *Nat Rev Neurosci* (2011) 12:105–18. doi:10.1038/nrn2979
23. Hammond C, Bergman H, and Brown P. Pathological Synchronization in Parkinson's Disease: Networks, Models and Treatments. *Trends Neurosciences* (2007) 30:357–64. doi:10.1016/j.tins.2007.05.004
24. Goriely A, Kuhl E, and Bick C. Neuronal Oscillations on Evolving Networks: Dynamics, Damage, Degradation, Decline, Dementia, and Death. *Phys Rev Lett* (2020) 125:128102. doi:10.1103/physrevlett.125.128102
25. Pfeifer KJ, Kromer JA, Cook AJ, Hornbeck T, Lim EA, Mortimer BJP, et al. Coordinated Reset Vibrotactile Stimulation Induces Sustained Cumulative Benefits in Parkinson's Disease. *Front Physiol* (2021) 12:624317. doi:10.3389/fphys.2021.624317
26. Jiruska P, de Curtis M, Jefferys JGR, Schevon CA, Schiff SJ, and Schindler K. Synchronization and Desynchronization in Epilepsy: Controversies and Hypotheses. *J Physiol* (2013) 591(4):787–97. doi:10.1113/jphysiol.2012.239590
27. Jirsa VK, Stacey WC, Quilichini PP, Ivanov AI, and Bernard C. On the Nature of Seizure Dynamics. *Brain* (2014) 137:2210–30. doi:10.1093/brain/awu133
28. Andrzejak RG, Rummel C, Mormann F, and Schindler K. All Together Now: Analogies between Chimera State Collapses and Epileptic Seizures. *Sci Rep* (2016) 6:23000. doi:10.1038/srep23000
29. Gerster M, Berner R, Sawicki J, Zakharova A, Škoch A, Hlinka J, et al. FitzHugh-Nagumo Oscillators on Complex Networks Mimic Epileptic-Seizure-Related Synchronization Phenomena. *Chaos* (2020) 30:123130. doi:10.1063/5.0021420
30. Tass PA, Adamchic I, Freund H-J, von Stackelberg T, and Hauptmann C. Counteracting Tinnitus by Acoustic Coordinated Reset Neuromodulation. *Restor Neurol Neurosci* (2012) 30:137–59. doi:10.3233/rnn-2012-110218
31. Tass PA, and Popovych OV. Unlearning Tinnitus-Related Cerebral Synchrony with Acoustic Coordinated Reset Stimulation: Theoretical Concept and Modelling. *Biol Cybern* (2012) 106:27–36. doi:10.1007/s00422-012-0479-5
32. Uhlhaas P, Pipa G, Lima B, Melloni L, Neuenschwander S, Nikolic D, et al. Neural Synchrony in Cortical Networks: History, Concept and Current Status. *Front Integr Neurosci* (2009) 3:17. doi:10.3389/neuro.07.017.2009
33. Pecora LM, and Carroll TL. Master Stability Functions for Synchronized Coupled Systems. *Phys Rev Lett* (1998) 80:2109–12. doi:10.1103/physrevlett.80.2109
34. Flunkert V, Yanchuk S, Dahms T, and Schöll E. Synchronizing Distant Nodes: a Universal Classification of Networks. *Phys Rev Lett* (2010) 105:254101. doi:10.1103/physrevlett.105.254101

35. Dahms T, Lehnert J, and Schöll E. Cluster and Group Synchronization in Delay-Coupled Networks. *Phys Rev E* (2012) 86:016202. doi:10.1103/physreve.86.016202
36. Keane A, Dahms T, Lehnert J, Suryanarayana SA, Hövel P, and Schöll E. Synchronisation in Networks of Delay-Coupled Type-I Excitable Systems. *Eur Phys J B* (2012) 85:407. doi:10.1140/epjb/e2012-30810-x
37. Kyrychko YN, Blyuss KB, and Schöll E. Synchronization of Networks of Oscillators with Distributed Delay Coupling. *Chaos* (2014) 24:043117. doi:10.1063/1.4898771
38. Lehnert J. *Controlling Synchronization Patterns in Complex Networks. Springer Theses*. Heidelberg: Springer (2016).
39. Tang L, Wu X, Lü J, Lu JA, and D'Souza RM. Master Stability Functions for Complete, Intralayer, and Interlayer Synchronization in Multiplex Networks of Coupled Rössler Oscillators. *Phys Rev E* (2019) 99:012304. doi:10.1103/PhysRevE.99.012304
40. Berner R, Sawicki J, and Schöll E. Birth and Stabilization of Phase Clusters by Multiplexing of Adaptive Networks. *Phys Rev Lett* (2020) 124:088301. doi:10.1103/physrevlett.124.088301
41. Börner R, Schultz P, Ünzelmann B, Wang D, Hellmann F, and Kurths J. Delay Master Stability of Inertial Oscillator Networks. *Phys Rev Res* (2020) 2:023409. doi:10.1103/physrevresearch.2.023409
42. Mulas R, Kuehn C, and Jost J. Coupled Dynamics on Hypergraphs: Master Stability of Steady States and Synchronization. *Phys Rev E* (2020) 101:062313. doi:10.1103/physreve.101.062313
43. Belykh VN, Belykh IV, and Hasler M. Connection Graph Stability Method for Synchronized Coupled Chaotic Systems. *Physica D: Nonlinear Phenomena* (2004) 195:159–87. doi:10.1016/j.physd.2004.03.012
44. Belykh I, de Lange E, and Hasler M. Synchronization of Bursting Neurons: What Matters in the Network Topology. *Phys Rev Lett* (2005) 94:188101. doi:10.1103/physrevlett.94.188101
45. Belykh I, Belykh V, and Hasler M. Generalized Connection Graph Method for Synchronization in Asymmetrical Networks. *Physica D: Nonlinear Phenomena* (2006) 224:42–51. doi:10.1016/j.physd.2006.09.014
46. Belykh I, Belykh V, and Hasler M. Synchronization in Asymmetrically Coupled Networks with Node Balance. *Chaos* (2006) 16:015102. doi:10.1063/1.2146180 https://doi.org/10.1063/1.2146180
47. Daley K, Zhao K, and Belykh IV. Synchronizability of Directed Networks: The Power of Non-existent Ties. *Chaos* (2020) 30:043102. doi:10.1063/1.5134920
48. Berner R, Vock S, Schöll E, and Yanchuk S. Desynchronization Transitions in Adaptive Networks. *Phys Rev Lett* (2021) 126:028301. doi:10.1103/physrevlett.126.028301
49. Jain S, and Krishna S. A Model for the Emergence of Cooperation, Interdependence, and Structure in Evolving Networks. *Proc Natl Acad Sci* (2001) 98:543–7. doi:10.1073/pnas.98.2.543
50. Proulx S, Promislow D, and Phillips P. Network Thinking in Ecology and Evolution. *Trends Ecol Evol* (2005) 20:345–53. doi:10.1016/j.tree.2005.04.004
51. Gross T, D'Lima CJD, and Blasius B. Epidemic Dynamics on an Adaptive Network. *Phys Rev Lett* (2006) 96:208701. doi:10.1103/physrevlett.96.208701
52. Martens EA, and Klemm K. Transitions from Trees to Cycles in Adaptive Flow Networks. *Front Phys* (2017) 5:62. doi:10.3389/fphy.2017.00062
53. Kuehn C. Multiscale Dynamics of an Adaptive Catalytic Network. *Math Model Nat Phenom* (2019) 14:402. doi:10.1051/mmnp/2019015
54. Horstmeyer L, and Kuehn C. Adaptive Voter Model on Simplicial Complexes. *Phys Rev E* (2020) 101:022305. doi:10.1103/physreve.101.022305
55. Meisel C, and Gross T. Adaptive Self-Organization in a Realistic Neural Network Model. *Phys Rev E* (2009) 80:061917. doi:10.1103/physreve.80.061917
56. Mikkelsen K, Imparato A, and Torcini A. Emergence of Slow Collective Oscillations in Neural Networks with Spike-Timing Dependent Plasticity. *Phys Rev Lett* (2013) 110:208101. doi:10.1103/physrevlett.110.208101
57. Mikkelsen K, Imparato A, and Torcini A. Sisyphus Effect in Pulse-Coupled Excitatory Neural Networks with Spike-timing-dependent Plasticity. *Phys Rev E* (2014) 89:062701. doi:10.1103/physreve.89.062701
58. Markram H, Lübke J, Frotscher M, and Sakmann B. Regulation of Synaptic Efficacy by Coincidence of Postsynaptic APs and EPSPs. *Science* (1997) 275:213–5. doi:10.1126/science.275.5297.213
59. Abbott LF, and Nelson SB. Synaptic Plasticity: Taming the Beast. *Nat Neurosci* (2000) 3:1178–83. doi:10.1038/81453
60. Caporale N, and Dan Y. Spike Timing-dependent Plasticity: A Hebbian Learning Rule. *Annu Rev Neurosci* (2008) 31:25–46. doi:10.1146/annurev.neuro.31.060407.125639
61. Popovych OV, Yanchuk S, and Tass PA. Self-organized Noise Resistance of Oscillatory Neural Networks with Spike Timing-dependent Plasticity. *Sci Rep* (2013) 3:2926. doi:10.1038/srep02926
62. Zenke F, Agnes EJ, and Gerstner W. Diverse Synaptic Plasticity Mechanisms Orchestrated to Form and Retrieve Memories in Spiking Neural Networks. *Nat Commun* (2015) 6:6922. doi:10.1038/ncomms7922
63. Tazerart S, Mitchell DE, Miranda-Rottmann S, and Araya R. A Spike-timing-dependent Plasticity Rule for Dendritic Spines. *Nat Commun* (2020) 11:4276. doi:10.1038/s41467-020-17861-7
64. Froemke RC, Poo M-m., and Dan Y. Spike-timing-dependent Synaptic Plasticity Depends on Dendritic Location. *Nature* (2005) 434:221–5. doi:10.1038/nature03366
65. Sjöström PJ, and Häusser M. A Cooperative Switch Determines the Sign of Synaptic Plasticity in Distal Dendrites of Neocortical Pyramidal Neurons. *Neuron* (2006) 51:227–38. doi:10.1016/j.neuron.2006.06.017
66. Froemke RC, Letzkus JJ, Kampa BM, Hang GB, and Stuart GJ. Dendritic Synapse Location and Neocortical Spike-timing-dependent Plasticity. *Front.Syna.Neurosci.* (2010) 2:29. doi:10.3389/fnsyn.2010.00029
67. Letzkus JJ, Kampa BM, and Stuart GJ. Learning Rules for Spike Timing-dependent Plasticity Depend on Dendritic Synapse Location. *J Neurosci* (2006) 26:10420–9. doi:10.1523/jneurosci.2650-06.2006
68. Meissner-Bernard C, Tsai MC, Logiaco L, and Gerstner W. Dendritic Voltage Recordings Explain Paradoxical Synaptic Plasticity: A Modeling Study. *Front Synaptic Neurosci* (2020) 12:585539. doi:10.3389/fnsyn.2020.585539
69. Aoki T, and Aoyagi T. Co-evolution of Phases and Connection Strengths in a Network of Phase Oscillators. *Phys Rev Lett* (2009) 102:034101. doi:10.1103/physrevlett.102.034101
70. Kasatkin DV, Yanchuk S, Schöll E, and Nekorkin VI. Self-organized Emergence of Multilayer Structure and Chimera States in Dynamical Networks with Adaptive Couplings. *Phys Rev E* (2017) 96:062211. doi:10.1103/physreve.96.062211
71. Kasatkin DV, and Nekorkin VI. The Effect of Topology on Organization of Synchronous Behavior in Dynamical Networks with Adaptive Couplings. *Eur Phys J Spec Top* (2018) 227:1051–61. doi:10.1140/epjst/e2018-800077-7
72. Berner R, Fialkowski J, Kasatkin D, Nekorkin V, Yanchuk S, and Schöll E. Hierarchical Frequency Clusters in Adaptive Networks of Phase Oscillators. *Chaos* (2019) 29:103134. doi:10.1063/1.5097835
73. Berner R, Yanchuk S, and Schöll E. What Adaptive Neuronal Networks Teach Us about Power Grids. *Phys Rev E* (2021) 103:042315. doi:10.1103/physreve.103.042315
74. Feketa P, Schaum A, and Meurer T. Synchronization and Multi-Cluster Capabilities of Oscillatory Networks with Adaptive Coupling. *IEEE Trans Automat Control* (2020) 66(7):3084. doi:10.1109/tac.2020.3012528
75. Franović I, Yanchuk S, Eydam S, Bačić I, and Wolfrum M. Dynamics of a Stochastic Excitable System with Slowly Adapting Feedback. *Chaos* (2020) 30:083109. doi:10.1063/1.5145176
76. Popovych OV, Xenakis MN, and Tass PA. The Spacing Principle for Unlearning Abnormal Neuronal Synchrony. *PLoS ONE* (2015) 10:e0117205. doi:10.1371/journal.pone.0117205
77. Lücken L, Popovych OV, Tass PA, and Yanchuk S. Noise-enhanced Coupling between Two Oscillators with Long-Term Plasticity. *Phys Rev E* (2016) 93:032210. doi:10.1103/physreve.93.032210
78. Chakravartula S, Indic P, Sundaram B, and Killingback T. Emergence of Local Synchronization in Neuronal Networks with Adaptive Couplings. *PLoS ONE* (2017) 12:e0178975. doi:10.1371/journal.pone.0178975
79. Röhr V, Berner R, Lameu EL, Popovych OV, and Yanchuk S. Frequency Cluster Formation and Slow Oscillations in Neural Populations with Plasticity. *PLoS ONE* (2019) 14:e0225094. doi:10.1371/journal.pone.0225094
80. Sakaguchi H, and Kuramoto Y. A Soluble Active Rotater Model Showing Phase Transitions via Mutual Entertainment. *Prog Theor Phys* (1986) 76:576–81. doi:10.1143/ptp.76.576
81. Madadi Asl M, Valizadeh A, and Tass PA. Dendritic and Axonal Propagation Delays Determine Emergent Structures of Neuronal Networks with Plastic Synapses. *Sci Rep* (2017) 7:39682. doi:10.1038/srep39682

82. Madadi Asl M, Valizadeh A, and Tass PA. Dendritic and Axonal Propagation Delays May Shape Neuronal Networks with Plastic Synapses. *Front Physiol* (2018) 9:1849. doi:10.3389/fphys.2018.01849
83. Vock S, Berner R, Yanchuk S, and Schöll E. Effect of Diluted Connectivities on Cluster Synchronization of Adaptively Coupled Oscillator Networks. *Scientia Iranica D* (2021) 28(3):1669.
84. Liesen J, and Mehrmann V. *Linear Algebra*. Cham: Springer (2015). doi:10.1007/978-3-319-24346-7
85. Gray RM *Toeplitz and Circulant Matrices: A Review*. Found. Trends Commun. Inf. Theory, Hanover, MA, USA: Now Publishers Inc. (2006). p. 155–239.
86. Aoki T, and Aoyagi T. Self-organized Network of Phase Oscillators Coupled by Activity-dependent Interactions. *Phys Rev E* (2011) 84:066109. doi:10.1103/physreve.84.066109
87. Sun J, Bollt EM, and Nishikawa T. Master Stability Functions for Coupled Nearly Identical Dynamical Systems. *Europhys Lett* (2009) 85:60011. doi:10.1209/0295-5075/85/60011
88. Skardal PS, Taylor D, and Sun J. Optimal Synchronization of Complex Networks. *Phys Rev Lett* (2014) 113:144101. doi:10.1103/physrevlett.113.144101
89. Acharyya S, and Amritkar RE. Synchronization of Nearly Identical Dynamical Systems: Size Instability. *Phys Rev E* (2015) 92:052902. doi:10.1103/physreve.92.052902
90. Kromer JA, and Tass PA. Long-lasting Desynchronization by Decoupling Stimulation. *Phys Rev Res* (2020) 2:033101. doi:10.1103/physrevresearch.2.033101
91. Kromer JA, Khaledi-Nasab A, and Tass PA. Impact of Number of Stimulation Sites on Long-Lasting Desynchronization Effects of Coordinated Reset Stimulation. *Chaos* (2020) 30:083134. doi:10.1063/5.0015196
92. Khaledi-Nasab A, Kromer JA, and Tass PA. Long-Lasting Desynchronization of Plastic Neural Networks by Random Reset Stimulation. *Front Physiol* (2021) 11:622620. doi:10.3389/fphys.2020.622620
93. Olmi S, Petkoski S, Guye M, Bartolomei F, and Jirsa V. Controlling Seizure Propagation in Large-Scale Brain Networks. *Plos Comput Biol* (2019) 15: e1006805. doi:10.1371/journal.pcbi.1006805

Conflict of Interest: The authors declare that the research was conducted in the absence of any commercial or financial relationships that could be construed as a potential conflict of interest.

frontiers in Applied Mathematics and Statistics

ORIGINAL RESEARCH
published: 15 July 2021
doi: 10.3389/fams.2021.697904

Coherence Resonance in Random Erdös-Rényi Neural Networks: Mean-Field Theory

A. Hutt[1]*, *T. Wahl*[1], *N. Voges*[2], *Jo Hausmann*[3] and *J. Lefebvre*[4]

[1]Team MIMESIS, INRIA Nancy Grand Est, Strasbourg, France, [2]ILCB and INT UMR 7289, Aix Marseille Université, Marseille, France, [3]R&D Department, Hyland Switzerland Sarl, Geneva, Switzerland, [4]Krembil Research Institute, University Health Network, Toronto, ON, Canada

Additive noise is known to tune the stability of nonlinear systems. Using a network of two randomly connected interacting excitatory and inhibitory neural populations driven by additive noise, we derive a closed mean-field representation that captures the global network dynamics. Building on the spectral properties of Erdös-Rényi networks, mean-field dynamics are obtained via a projection of the network dynamics onto the random network's principal eigenmode. We consider Gaussian zero-mean and Poisson-like noise stimuli to excitatory neurons and show that these noise types induce coherence resonance. Specifically, the stochastic stimulation induces coherent stochastic oscillations in the γ-frequency range at intermediate noise intensity. We further show that this is valid for both global stimulation and partial stimulation, i.e. whenever a subset of excitatory neurons is stimulated only. The mean-field dynamics exposes the coherence resonance dynamics in the γ-range by a transition from a stable non-oscillatory equilibrium to an oscillatory equilibrium via a saddle-node bifurcation. We evaluate the transition between non-coherent and coherent state by various power spectra, Spike Field Coherence and information-theoretic measures.

Keywords: coherence resonance, phase transition, stochastic process, excitable system, mean-field, random networks

OPEN ACCESS

Edited by:
Alessandro Torcini,
Université de Cergy-Pontoise, France

Reviewed by:
Matteo Di Volo,
Université de Cergy-Pontoise, France
Miguel Pineda,
University College London,
United Kingdom

***Correspondence:**
A. Hutt
axel.hutt@inria.fr

Specialty section:
This article was submitted to Dynamical Systems, a section of the journal Frontiers in Applied Mathematics and Statistics

Received: *20 April 2021*
Accepted: *17 June 2021*
Published: *15 July 2021*

Citation:
Hutt A, Wahl T, Voges N, Hausmann J and Lefebvre J (2021) Coherence Resonance in Random Erdös-Rényi Neural Networks: Mean-Field Theory. Front. Appl. Math. Stat. 7:697904. doi: 10.3389/fams.2021.697904

1 INTRODUCTION

Synchronization is a well characterized phenomenon in natural systems [1]. A confluence of experimental studies indicate that synchronization may be a hallmark pattern of self-organization [2–4]. While various mechanisms are possible, synchronization may emerge notably through an enhancement of internal interactions or via changes in external stimuli statistics. A specific type of synchronization can occur due to random external perturbations, leading to a noise-induced coherent activity. Such a phenomenon is called coherence resonance (CR) and has been found experimentally in solid states [5], nanotubes [6] and in neural systems [7, 8]. Theoretical descriptions of CR have been developed for single excitable elements [9, 9, 10], for excitable populations [11] and for clustered networks [12].

In general, stimulus-induced synchronization is well-known in neural systems [2]. Synchronization has been observed intracranially in the presence of noise between single neurons in specific brain areas [13, 14] and between brain areas [15–17]. The source of these random perturbations is still under debate. In this context, it is interesting to mention that [18] have found that the ascending reticular arousal system (ARAS) affects synchronization in the visual

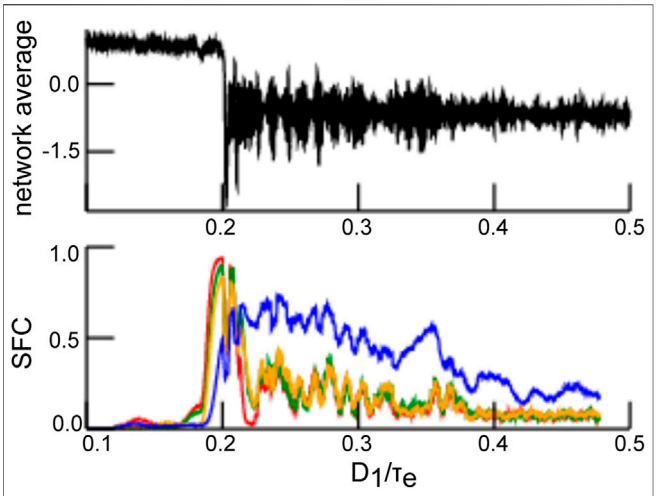

FIGURE 1 | Synchronization dependent on noise intensity as a marker of coherence resonance. The top panel shows the network average of $\boldsymbol{V}$ in **Eq. 1** and the bottom panel provides the Spike Field Coherence (SFC) in the Θ– (red), α– (green), β– (orange) and γ– (blue) frequency range. For low noise intensity D_1/τ_e there is no SFC, intermediate noise intensity yields strong SFC while large noise intensities diminish SFC again. To gain the SFC values, we have integrated in time the model system with 10^4 time steps while increasing the noise variance according to (**Eq. 7**). For illustration reasons, the SFC-values have been averaged by a sliding window of length $\Delta(D_1/\tau_e) = 0.004$. Definitions are given in **section 2** and parameters are the same as in **Figure 4** with $q = 1$.

cortex. The ARAS provides dynamic inputs to many brain areas [19–21]. It has thus been hypothesized that synchronization in the visual system represents a CR effect triggered by ARAS-mediated drive. This hypothesis has been supported recently by [22] showing in numerical simulations that an intermediate intensity of noise maximizes the interaction in a neural network of Hodgkin-Huxley neurons. Furthermore, recent theoretical work [21] has provided key insights on how human occipital electrocorticographic γ-activity (40–120 Hz) commonly observed with open eyes [21] is closely linked to CR. Coherence resonance has further been associated with states of elevated information processing and transfer [22], which are difficult to assess in the absence of mean-field descriptions. For illustration, **Figure 1** (upper panel) shows average network activity for increasing noise intensities D_1 and one observes a jump from non-oscillatory to oscillatory activity. Moreover, the figure presents very low coherence in the network under study for weak and strong noise intensities D_1, whereas high coherence emerges for intermediate noise intensities (bottom panel). In the present work, we will explain this noise-induced coherence by a mean-field description.

To better understand the mechanisms underlying CR and its impact on information processing, we consider a simple two-population Erdös-Rényi network of interconnected McCullogh-Pitts neurons. Our goal is to use this model to provide some insight into the emergence of stimulus-induced synchronization in neural systems and its influence on the neural network's information content. The neural network under study has random connections, a simplification inspired from the lack structure neural circuits possess at microscopic scales. Previous studies [23] have shown that such systems are capable of noise-induced CR. Building on these results, we here provide a rigorous derivation of a mean-field equation based on an appropriate eigenmode decomposition to highlight the role of the network's connectivity–Erdös-Rényi more specifically eigenspectrum in supporting accurate mean-field representations. We extend previous results by further considering both global (all neurons are stimulated) and partial (some neurons are stimulated) stochastic stimulation and its impact on CR similar to some previous studies [24–26]. This partial stimulation is both more general and realistic than global stimulation as considered in most previous studies [11, 23, 27]. We apply our results to both zero-mean Gaussian and Poisson-like stochastic stimuli, and derive the resulting mean-field description. It is demonstrated rigorously that partial stochastic stimulation shifts the system's dynamic topology and promotes CR, compared to global stimulation. We confirm and explore the presence of CR using various statistical measures.

2 MATERIALS AND METHODS

We first introduce the network model under study, motivate the mean-field description, mentions the nonlinear analysis employed and provides details on the statistical evaluation.

2.1 The Network Model

Generically, biological neuronal networks are composed of randomly connected excitatory and inhibitory neurons, which interact through synapses with opposite influence on post-synaptic cells. We assume neural populations of excitatory $\mathcal{E}$ and inhibitory $\mathcal{I}$ neurons with N neurons in each population. Excitatory neurons in $\mathcal{E}$ excite each other through the connectivity matrix $\boldsymbol{F}$, and excite inhibitory neurons in $\mathcal{I}$ through the connectivity matrix $\boldsymbol{M}$. Similarly, neurons in $\mathcal{I}$ inhibit each other by $\boldsymbol{F}$ and inhibit excitatory neurons through the connectivity matrix $\boldsymbol{M}$. Hence, $\boldsymbol{F}$ and $\boldsymbol{M}$ represent the intra-population and inter-population synaptic connections, respectively. Mathematically, such neural population interactions are described by a $2N$ dimensional non-linear dynamical system governing the evolution of the state variable vectors $\mathbf{V}, \mathbf{W} \in \mathbb{R}^N$,

$$\begin{aligned} \tau_e \frac{d\mathbf{V}}{dt} &= -\mathbf{V} + \mathbf{F}\mathbf{S}_1[\mathbf{V}] - \mathbf{M}\mathbf{S}_2[\mathbf{W}] + eI^e + \boldsymbol{\xi}^e(t) \\ \tau_i \frac{d\mathbf{W}}{dt} &= -\mathbf{W} + \mathbf{M}\mathbf{S}_1[\mathbf{V}] - \mathbf{F}\mathbf{S}_2[\mathbf{W}] + eI^i + \boldsymbol{\xi}^i(t). \end{aligned} \tag{1}$$

This formulation is reminiscent of many rate-based models discussed previously [28], where it is assumed that neuronal activity is asynchronous and synaptic response functions are of first order. The state variables $\mathbf{V}$ and $\mathbf{W}$ represent excitatory and inhibitory dendritic currents, respectively. The terms $\boldsymbol{\xi}^{e,i}$ represent respective stochastic inputs from various sources, such as ion channel fluctuations, stochastic input from other brain areas or external stimuli not directly accounted for in the

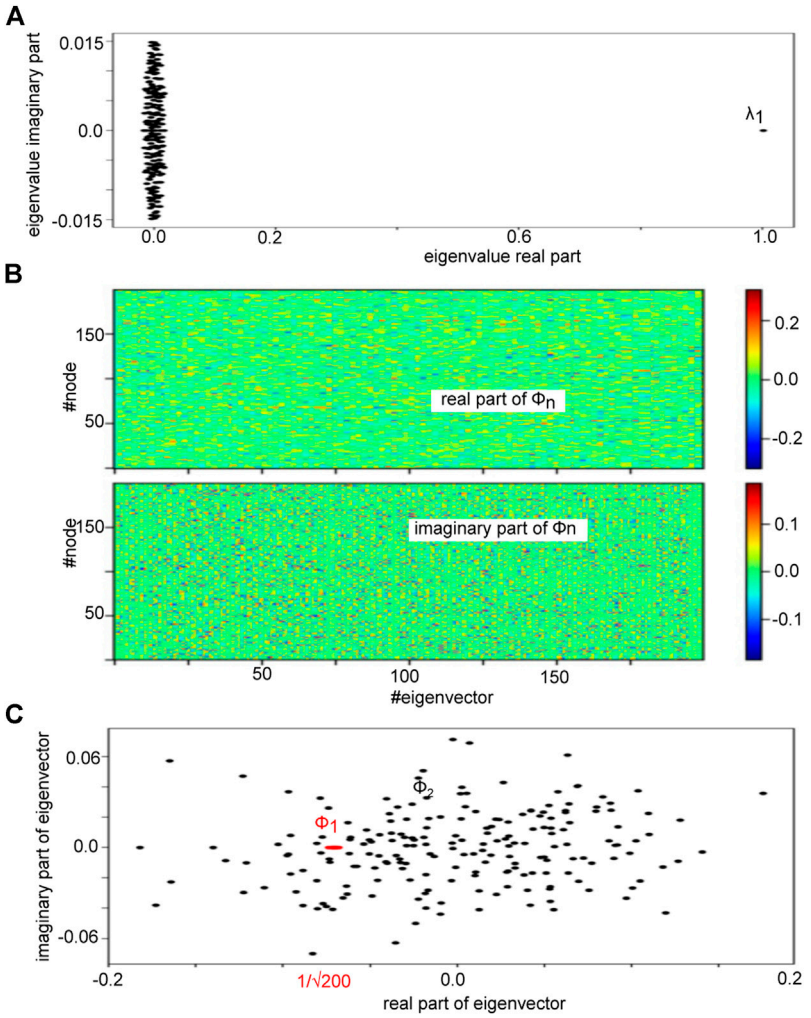

FIGURE 2 | Eigenvalue spectrum of an Erdös-Rényi adjency matrix A under study and its eigenbasis. **(A)** The plot shows the eigenvalues in the complex plane demonstrating a clear spectral gap between the first eigenvalue λ_1 and the other eigenvalues $\lambda_{n>1}$. **(B)** The panels show the real **(top)** and imaginary **(bottom)** part of all unit-normalized eigenvectors for illustration. They appear to be random reflecting the random network topology. **(C)** The normalized eigenvector $\mathbf{\Phi}_1 \approx (1,\ldots,1)/\sqrt{N}$ with maximum eigenvalue $\lambda_1 \approx 1$ plotted in complex plane together with the eigenvector $\mathbf{\Phi}_2$ of the second largest eigenvalue $\lambda_2 = 0.015 + i0.0006$. Each dot corresponds to a complex-numbered vector entry in the complex plane. This result confirms the choice $\mathbf{\Phi}_1 \approx (1,\ldots,1)$ in **Eq. 9**.

model [29]. More specifically, we assume noise $\boldsymbol{\xi}^{e,i} \in \mathbb{R}^N$, constant input $I^{e,i}$ with $e = (1,\ldots,1)^t$. The connectivity matrices are defined by $\mathbf{F}, \mathbf{M} \in \mathbb{R}^{N\times N}$ while the nonlinear transfer function is given by $\mathbf{S}_{1,2}[\mathbf{u}] \in \mathbb{R}^N$ with $(\mathbf{S}_1[\mathbf{u}])_n = H_0 S(u_n)$, $(\mathbf{S}_2[\mathbf{u}])_n = S(u_n)$, $H_0 > 0$ and the scalar transfer function $S(u) > 0\ \forall u \in \mathbb{R}$. Specifically, we will consider the transfer function $S(u) = \Theta(u)$ with the Heaviside function $\Theta(u) = 0\ \forall u < 0, \Theta(u) = 1\ \forall u \geq 0$. In addition, the synaptic time scales are $\tau_{e,i}$.

The present work considers directed Erdös-Rényi networks (ERN) with connection probability density $c = 0.95$, i.e. both neuron populations exhibit intra-population and inter-population non-sparse random connections. Let us assume $\mathbf{F} = \mathbf{A}F_0$, $\mathrm{M} = \mathbf{A}M_0$ and $\mathbf{A}$ is the non-symmetric adjacency matrix of the ERN for which $(\boldsymbol{A})_{nm} = 0$ with probability $1 - c$ and $(\boldsymbol{A})_{nm} = 1/cN$ with probability c. At first, let $\boldsymbol{A} = \boldsymbol{S} + \boldsymbol{U}$ with the symmetric matrix $\boldsymbol{S} = (\boldsymbol{A} + \boldsymbol{A}^t)/2$, the antisymmetric matrix $\boldsymbol{U} = (\boldsymbol{A} - \boldsymbol{A}^t)/2$ and the eigenvalues λ_A and λ_S of the matrix $\boldsymbol{A}$ and $\boldsymbol{S}$, respectively. Then $\mathcal{R}e(\lambda_A) = \lambda_S$, i.e. the real part of the eigenvalue spectrum in the directed (i.e. non-symmetric) and non-directed (i.e. symmetric) random matrix $\boldsymbol{A}$ and $\boldsymbol{S}$ is identical. Moreover, for non-directed ERNs with symmetric adjacency matrix and $N \to \infty$ its edge spectrum contains the maximum eigenvalue $\lambda_1 = 1$ with eigenvector $\boldsymbol{v}_1 = (1,1,\ldots,1)^t$ [30–33] and the bulk spectrum has the maximum eigenvalue

$$\begin{aligned} \lambda_2 &= \frac{2\sigma\sqrt{N}}{cN} \\ &= \frac{2\sqrt{1-c}}{\sqrt{cN}}, \end{aligned} \tag{2}$$

with the corresponding Bernoulli distribution variance $\sigma^2 = c(1-c)$. It is obvious that $\lambda_2 \ll \lambda_1$ and $\lambda_2 \approx 0$ for large mean degree cN. Since $\mathcal{R}e(\lambda_A) = \lambda_S$, the finite-size non-symmetric connectivity matrix $\boldsymbol{F}$ ($\boldsymbol{M}$) has a maximum eigenvalue $\lambda_1 \approx F_0$ and $\lambda_{n>1} \approx 0$ ($\lambda_1 \approx \boldsymbol{M}_0$, $\lambda_{n>1} \approx 0$). If c decreases, then λ_2 increases, i.e. the spectral gap decreases, and this approximation does not hold anymore. The **Supplementary Appendix** illustrates the limits of this approximation in numerical simulations. **Figure 2A** shows the single maximum eigenvalue λ_1 of $\boldsymbol{A}$ representing the edge spectrum and the other very small eigenvalues of the bulk spectrum. Hence, the matrix $\boldsymbol{F}$ has maximum eigenvalue F_0 and the other eigenvalues vanish. The same holds for matrix $\boldsymbol{M} = M_0\boldsymbol{A}$ with a maximum eigenvalue M_0. **Figure 2B** shows the real and imaginary part of the eigenvectors. The eigenvectors of the bulk spectrum ($i > 1$) have uniformly distributed elements in good accordance with theory of symmetric ER networks [34]. The eigenvector of the edge spectrum is $\boldsymbol{\Phi}_1 = (1, \ldots, 1)^t$, see **Figure 2C**.

Moreover, we assume that each noise process at inhibitory neurons $(\boldsymbol{\eta}^i)_n = \eta_n^i$ at network node n is Gaussian distributed with zero mean, noise intensity D_2 and uncorrelated in time

$$\langle \xi_n^i(t)\xi_m^i(\tau)\rangle = 2D_2\delta_{nm}\delta(t-\tau),$$

Conversely each noise process at excitatory neurons ξ_n^e belongs to a certain class $\mathcal{G}_m, m = 1, \ldots, M$ of M classes [23]. Noise processes in a specific class $\mathcal{G}_m$, i.e. $n \in \mathcal{G}_m$, share their mean $\overline{\xi}_m^e$ and variances D_1^m, i.e.

$$\langle \xi_k^e(t)\xi_l^i(\tau)\rangle = 2D_1^m\delta_{kl}\delta(t-\tau), \quad k,l \in \mathcal{G}_m,$$

In the following, we assume two classes $M = 2$ with $\overline{\xi}_1^e \neq 0, D_1^1 = D_1$ and $\overline{\xi}_2^e = 0, D_1^2 = 0$, i.e. only a subset of nodes $n \in \mathcal{G}_1$ are stimulated. Hence we consider a partial stimulation at number of nodes $N_1 = |\mathcal{G}_1|$.

In biological neural systems, the input to a neural population is well-described by incoming spike trains that induce dendritic currents at synaptic receptors. According to renewal theory, neurons emit spike trains whose interspike interval obeys a Poisson distribution [35]. Then incoming spike trains at mean spike rate r induce random responses at excitatory synapses with time constant τ_{in}. This random process $I_{\text{in}}(t)$ has the ensemble mean $\mathrm{E}[I_{\text{in}}] = w_{\text{in}}r\tau_{\text{in}}$ and ensemble variance $\mathrm{Var}[I_{\text{in}}] = w_{\text{in}}^2 r\tau_{\text{in}}/2$ [36] assuming the synaptic coupling weight w_{in}. Since a Poisson distribution converges to a Gaussian distribution for large enough mean, we implement this input current as a Gaussian random process with mean $\mathrm{E}[I_{\text{in}}]$ and variance $\mathrm{Var}[I_{\text{in}}]$ while ensuring the validity of this approximation by a large enough input firing rate λ_{in}. It is important to point out that for Poisson noise, in contrast to the zero-mean Gaussian noise, both mean and variance are proportional to the input firing rate.

2.2 Conventional Mean-Field Analysis

To compare mesoscopic neural population dynamics to macroscopic experimental findings, it is commonplace to describe the network activity by the mean population response, i.e. the mean-field dynamics [37–39]. A naive mean-field approach was performed in early neuroscience studies [40–42], in which one blindly computes the mean network activity to obtain

$$\begin{aligned}\tau_e\frac{dE[V]}{dt} &= -E[V] + \mathbf{f}\mathbf{S}_1[\mathbf{V}] - \mathbf{m}\mathbf{S}_2[\mathbf{W}] + eI^e\\ \tau_i\frac{dE[W]}{dt} &= -E[W] + \mathbf{m}\mathbf{S}_1[\mathbf{V}] - \mathbf{f}\mathbf{S}_2[\mathbf{W}] + eI^i,\end{aligned} \tag{3}$$

with the network average $E[x] = \sum_k x_k/N$ and $(\boldsymbol{f})_k = \sum_l \boldsymbol{F}_{lk}/N$, $(\boldsymbol{m})_k = \sum_l \boldsymbol{M}_{lk}/N$ assuming zero-mean external noise with $\sum_k (\boldsymbol{\xi}^{e,i})_k = 0$. In addition, one may assume identical network interactions with $(f)_k = \boldsymbol{f}_0/N = \text{const}$, $(\boldsymbol{m})_k = m_0/N = \text{const}$ and the simplifying but questionable linear assumption.

$$E\big[S_{1,2}(x)\big] = S_{1,2}(E[x]). \tag{4}$$

Combined, these assumptions lead to mean-field equations.

$$\begin{aligned}\tau_e\frac{dE[V]}{dt} &= -E[V] + f_0S_1[E[V]] - m_0S_2[E[W]]\\ &\quad + \boldsymbol{e}I^e\\ \tau_i\frac{dE[W]}{dt} &= -E[W] + m_0S_1[E[V]] - f_0S_2[E[W]].\\ &\quad + \boldsymbol{e}I^i\end{aligned} \tag{5}$$

In this approximate description, additive noise does not affect the system dynamics. The assumption (**Eq. 4**) is very strong and typically not valid. In a more reasonable ansatz.

$$\begin{aligned}E\big[S_{1,2}(x)\big] &= E\left[S_{1,2}(x_0) + \sum_{n=1}^{\infty}\frac{1}{n!}S_{1,2}^{(n)}(x-x_0)^n\right]\\ &= S_{1,2}(x_0) + \sum_{n=1}^{\infty}\frac{1}{n!}S_{1,2}^{(n)}E[(x-x_0)^n]\\ &= \mathcal{F}\big(E[x], E[x^2], E[x^3], \ldots\big),\end{aligned} \tag{6}$$

with $S_{1,2}^{(n)} = \partial S_{1,2}^n(x)/\partial x^n$ computed at an arbitrary point $x = x_0$ and a function $\mathcal{F}_{1,2} \in \mathbb{R}$. Hence the dynamics of the mean-field $E[V]$ depends on the higher-order statistical orders $E[V^n]$ via the nonlinear function $E[S_{1,2}(V)]$. This is called the closure problem that is solvable in specific cases only [43].

Motivated by previous studies on stochastic bifurcations [44–53], in which additive noise may tune the stability close to the bifurcation point, the present work shows how additive noise strongly impacts the nonlinear dynamics of the system for arbitrary noise intensity and away from the bifurcation. Previous *ad-hoc* studies have already used mean-field approaches [23, 54, 55] which circumvents the closure problem (**Eq. 6**) through a different mean-field ansatz. These motivational studies left open a more rigorous derivation. This derivation will be given in the present work: presenting in more detail its power and its limits of validity.

2.3 Equilibria, Stability and Quasi-Cycles

The dynamic topology of a model differential equation system may be described partially by the number and characteristics of its

TABLE 1 | Parameter set of model (1).

Parameter	Description	Value
τ_e	Exc. synaptic time constant	5 ms
τ_i	Inhib. synaptic time constant	20 ms
F_0	Intra-population conn. weight	2.17
M_0	Inter-population conn. weight	3.87
c	Connection probability	0.95
N	Number of network nodes	200
I_e	Constant exc. Input	1.1
I_i	Constant inhib. Input	0.4
D_2	Inhib. noise variance	0.2
w_{in}	Poisson input weight	2.1
τ_{in}	synaptic time scale of input	5 ms
Δt	Numerical integration step	0.5 ms

equilibria. In general, for the non-autonomous differential equation system

$$\dot{\boldsymbol{z}} = \boldsymbol{A}\boldsymbol{z} + \boldsymbol{N}(\boldsymbol{z}) + \boldsymbol{I}(t),$$

with state variable $\boldsymbol{z} \in \mathbb{R}^N$, the driving force $\boldsymbol{I} \in \mathbb{R}^N$, the nonlinear vector $\boldsymbol{N} \in \mathbb{R}^N$ and the matrix $\boldsymbol{A} \in \mathbb{R}^{N\times N}$, it is insightful to consider the equilibria of the corresponding autonomous system $\boldsymbol{z}_0$ with $\dot{\boldsymbol{z}} = 0$ yielding the implicit condition

$$\boldsymbol{A}\boldsymbol{z}_0 = -\boldsymbol{N}(\boldsymbol{z}_0),$$

The stability of an equilibrium $\boldsymbol{z}_0$ is given by the eigenvalue spectrum of the corresponding Jacobian

$$\boldsymbol{J} = \boldsymbol{A} + \nabla \boldsymbol{N}^0,$$

where $(\nabla \boldsymbol{N}^0)_{ij} = \partial N_i(\boldsymbol{z})/\partial z_j$ computed at $\boldsymbol{z}_0$. The eigenvalues $\{\lambda_k\}$ of $\boldsymbol{J}$ can be written as $\lambda_k = a_k + i2\pi\nu_k$ with the damping a_k and the eigenfrequency ν_k. Asymptotically stable equilibria have $\Re(\lambda_k) < 0$, e.g. stable foci have $a_k < 0, \nu_k \in \mathbb{R}$. Linear response theory tells that noise-driven linear systems, whose deterministic dynamics exhibit a stable focus, exhibit quasi-cycles with a spectral power peak close to the eigenfrequency, see e.g. [51, 56, 57]. The smaller the noise intensity, the closer is the spectral peak frequency to the eigenfrequency. Hence, the eigenfrequency ν_k provides a reasonable estimate of the quasi-cycle spectral peak.

2.4 Numerical Simulations

The Langevin **Eq. 1** have been integrated over time utilizing the Euler-Maruyama scheme [58]. **Table 1** presents the parameters used. In certain cases, the noise variance has been changed over time t according to

$$D_1(t) = D_{\min} + \frac{D_{\max} - D_{\min}}{T}t, \tag{7}$$

with the maximum integration time T and the maximum and minimum noise variance values $D_{\max}$ and $D_{\min}$, respectively.

2.5 Numerical Spectral Data Analysis

Since prominent oscillations of the network mean activity indicates synchronized activity in the population, we have computed the power spectrum of the network mean activity $\overline{V}(t) = \Sigma_{n=1}^{N}(V_n(t)/N)$ employing the Bartlett-Welch method with overlap rate 0.8. To gain a power spectrum with frequency resolution Δf, the Bartlett-Welch segments were chosen to the length $1/\Delta f$ and the time series had a duration of 5 s for the zero-mean Gaussian noise and 8 s for the Poisson noise stimulation.

In addition to the power spectrum, the synchronization between single neuron spike activity and the dendritic current reflects the degree of coherence in the system. To this end, we have computed the Spike Field Coherence (SFC) [59]. To estimate the SFC, we have chosen a time window of 5s for zero-mean Gaussian stimulation and 8s for Poisson stimulation and computed the spike-triggered average and power spectra in these time windows to compute the SFC for each frequency. Then we have averaged the SFC in the Θ– (4–8 Hz), α– (8–12 Hz), β– (12–20 Hz) and γ– (25–60 Hz) frequency band to gain an average SFC in the corresponding band. This standard measure estimates the coherence between spikes, that occur if $H[V_n](t) = 1$, and their corresponding dendritic currents $V_n(t)$ at the same cell averaged over all cells in the excitatory population. Significant differences of SFC at different noise intensities are evaluated by an unpaired Welch t-test with $\alpha = 0.05$.

2.6 Information Measures

Coherence quantifies the degree of mutual behavior of different elements. Interestingly, recent studies of biological neural systems have shown that synchronization and information content are related [60, 61]. For instance, under general anesthesia asynchronous cortical activity in conscious patients is accompanied by less stored information and much available information whereas synchronous cortical activity in unconscious patients exhibits more stored information and less available information [19, 20, 62–64]. We are curious how much information is stored and available in coherence resonance described in the present work. The result may indicate a strong link between coherence and information content. To this end, we compute the amount of stored information in the excitatory population as the predictable information and the amount of available information as the population's entropy, cf [64].

The predictable information in the excitatory population is computed as the Active Information Storage AIS [65, 66] utilizing the Gaussian Copula Mutual Information (GCMI) estimation [67]. Assuming a single time series $V_i(t)$

$$\begin{aligned} \text{AIS}_i &= \text{MI}\left(V_i(t); \mathbf{V}_{\mathbf{i\Delta}}^{(\mathbf{k})}\right), \\ \mathbf{V}_{\mathbf{i\Delta}}^{(\mathbf{k})} &= (V_i(t-\Delta), V_i(t-2\Delta), \ldots V_i(t-k\Delta)), \end{aligned} \tag{8}$$

where MI is the mutual information [64, 68], k is the embedding dimension and Δ is the embedding delay. The value AIS_i describes how much the dendritic current $V_i(t)$ in excitatory neuron i is influenced by its past. To gain an estimate of stored information in the excitatory population, we evaluate the average stored information in the population and its variance

$$\text{AIS} = \frac{1}{N}\sum_{i=1}^{N}\text{AIS}_i$$

$$\sigma_{\text{AIS}}^2 = \frac{1}{N-1}\sum_{i=1}^{N}(\text{AIS}_i - \text{AIS})^2,$$

with $N = 200$. Significant AIS differences at different noise intensities are evaluated by an unpaired Welch t-test with $\alpha = 0.05$.

Moreover, we compute the available information in the excitatory cortex of the dendritic current $V_i(t)$ at excitatory neuron i as its entropy H_i utilizing the GCMI estimation. Its population average and variance reads

$$\mathrm{H} = \frac{1}{N}\sum_{i=1}^{N} \mathrm{H}_i$$
$$\sigma_H^2 = \frac{1}{N}\sum_{i=1}^{N} (\mathrm{H}_i - \mathrm{H})^2,$$

and entropy differences at different noise intensities are evaluated statistically by an unpaired Welch t-test with $\alpha = 0.05$.

In subsequent sections, we have computed AIS and H for embedding dimension $k \in [1; 60]$ and $\Delta \in \{\Delta t, 2\Delta t, 5\Delta t\}$ with $k\Delta = 60$ and find consistent significance test results. Specifically, we have chosen $\Delta = \Delta t$ and $k = 1$ in the shown results.

3 RESULTS

The subsequent section shows the derivation of the mean-field equations, before they are applied to describe network dynamics for two types of partial stimulation.

3.1 Mean-Field Description

To derive the final equations, we first introduce the idea of a mode projection before deriving the mean-field equations as a projection on the principal mode. The extension to partial stimuli extends the description.

Mode Decomposition

In the model (1), the system activity $\mathbf{V} \in \mathcal{U}$ in space $\mathcal{U}$ may be expanded into a mode basis $\{\mathbf{\Phi}_n^e\}, n = 1, \ldots, N, \mathbf{\Phi}_n^e \in \mathbb{C}^N$,

$$\mathbf{V} = \sum_{n=1}^{N} a_n \mathbf{\Phi}_n^e,$$

with complex mode amplitude $a_n \in \mathbb{C}$ and a biorthogonal basis $\{\mathbf{\Psi}_n^e\}, \mathbf{\Psi}_n^e \in \mathbb{C}^N$ and

$$\mathbf{\Psi}_k^{e\dagger}\mathbf{\Phi}_n^e = \delta_{kn}\,, k, n = 1, \ldots, N,$$

Here, † denotes the transpose complex conjugate. The same holds for $\boldsymbol{W}$ with the basis $\{\mathbf{\Phi}_n^i\}, n = 1, \ldots, N, \mathbf{\Phi}_n^i \in \mathbb{C}^N$,

$$\mathbf{W} = \sum_{n=1}^{N} b_n \mathbf{\Phi}_n^i,$$

with the complex mode amplitude $b_n \in \mathbb{C}$ and the biorthogonal basis $\{\mathbf{\Psi}_n^i\}, \mathbf{\Psi}_n^i \in \mathbb{C}^N$ and

$$\mathbf{\Psi}_k^{i\dagger}\mathbf{\Phi}_n^i = \delta_{kn}\,, k, n = 1, \ldots, N,$$

Projecting $\mathbf{V}, \boldsymbol{W}$ onto the respective basis $\{\mathbf{\Psi}_k^e\}$ and $\{\mathbf{\Psi}_k^i\}$, we obtain amplitude equations

$$\tau_e \frac{da_k}{dt} = -a_k + \mathbf{\Psi}_k^{e\dagger}\mathbf{F}\mathbf{S}_1[\mathbf{V}] - \mathbf{\Psi}_k^{e\dagger}\mathbf{M}\mathbf{S}_2[\mathbf{W}] + I^e + \mathbf{\Psi}_k^{e\dagger}\boldsymbol{\xi}^e(t)$$
$$\tau_i \frac{db_k}{dt} = -b_k + \mathbf{\Psi}_k^{i\dagger}\mathbf{M}\mathbf{S}_1[\mathbf{V}] - \mathbf{\Psi}_k^{i\dagger}\mathbf{F}\mathbf{S}_2[\mathbf{W}] + I^i + \mathbf{\Psi}_k^{i\dagger}\boldsymbol{\xi}^i(t),$$

Now let us assume that $\mathbf{\Psi}_k^e, \mathbf{\Phi}_k^e$ are eigenvectors of $\boldsymbol{F}$ with eigenvalue $\lambda_k^e \in \mathbb{C}$

$$\mathbf{F}\mathbf{\Phi}_k^e = \lambda_k^e \mathbf{\Phi}_k^e$$
$$\mathbf{\Psi}_k^{e\dagger}\mathbf{F} = \lambda_k^e \mathbf{\Psi}_k^{e\dagger},$$

and $\mathbf{\Psi}_k^i, \mathbf{\Phi}_k^i$ are eigenvectors of $\boldsymbol{M}$ with eigenvalue $\lambda_k^i \mathbb{C}$

$$\mathbf{M}\mathbf{\Phi}_k^i = \lambda_k^i \mathbf{\Phi}_k^i$$
$$\mathbf{\Psi}_k^{i\dagger}\mathbf{M} = \lambda_k^i \mathbf{\Psi}_k^{i\dagger},$$

Then

$$\begin{aligned} \lambda_1^e &= F_0\,, \mathbf{\Phi}_1^e = e, \mathbf{\Psi}_1^e = \frac{\boldsymbol{e}}{N} \\ \lambda_n^e &\approx 0, n = 2, \ldots, N, \end{aligned} \tag{9}$$

cf. **section 2.1**, where we have utilized the bi-orthogonality of the basis. Equivalently,

$$\lambda_1^i = M_0\,, \mathbf{\Phi}_1^i = \boldsymbol{e}, \mathbf{\Psi}_1^i = \frac{\boldsymbol{e}}{N}$$
$$\lambda_n^i \approx 0, n = 2, \ldots, N,$$

We observe that $\mathbf{\Psi}_1^{i\dagger} = \mathbf{\Psi}_1^{e\dagger}$ and $\mathbf{\Phi}_1^e = \mathbf{\Phi}_1^i$. The vector space $\mathcal{U}$ can be decomposed into complement subspaces $\mathcal{Z}, \mathcal{Z}_\perp$ with $\mathcal{U} = \mathcal{Z} \oplus \mathcal{Z}_\perp$ and $\mathbf{\Psi}_1^e, \mathbf{\Psi}_1^i \in \mathcal{Z}$. Then $\mathbf{\Psi}_{k>1}^e, \mathbf{\Psi}_{k>1}^i \in \mathcal{Z}_\perp$. Each vector $\mathbf{\Psi}_{k>1}^i$ can be described in the basis $\mathbf{\Psi}_{k>1}^e$ in $\mathcal{Z}_\perp$ and one gains

$$\begin{aligned} \mathbf{\Psi}_{k>1}^{i\dagger}F &= \sum_{n=2}^{N} c_n \mathbf{\Psi}_n^{e\dagger}\boldsymbol{F} \\ &= \sum_{n=2}^{N} c_n \lambda_n^e \mathbf{\Psi}_n^{e\dagger} \\ &= 0, \end{aligned}$$

due to (**Eq. 9**) and equivalently

$$\begin{aligned} \mathbf{\Psi}_{k>1}^{e\dagger}\boldsymbol{M} &= \sum_{n=2}^{N} c_n \mathbf{\Psi}_n^{i\dagger}\boldsymbol{M} \\ &= \sum_{n=2}^{N} c_n \lambda_n^i \mathbf{\Psi}_n^{i\dagger} \\ &= 0, \end{aligned}$$

with some coefficients $c_n \in \mathbb{C}$. This yields

$$\tau_e \frac{da_1}{dt} = -a_1 + \frac{\lambda_1^e}{N}\boldsymbol{e}^t\mathbf{S}_1[V] - \frac{\lambda_1^i}{N}\boldsymbol{e}^t\mathbf{S}_2[\mathbf{W}] + I^e + m_e(t) \tag{10}$$

$$\tau_i \frac{db_1}{dt} = -b_1 + \frac{\lambda_1^i}{N} \boldsymbol{e}^t \mathbf{S}_1[\mathbf{V}] - \frac{\lambda_1^e}{N} \boldsymbol{e}^t \mathbf{S}_2[\mathbf{W}] + I^i + m_i(t) \tag{11}$$

$$\tau_e \frac{da_k}{dt} = -a_k + \boldsymbol{\Psi}_k^{e\dagger} \boldsymbol{\xi}^e(t), k = 2, \ldots, N \tag{12}$$

$$\tau_i \frac{db_k}{dt} = -b_k + \boldsymbol{\Psi}_k^{i\dagger} \boldsymbol{\xi}^i(t), k = 2, \ldots, N, \tag{13}$$

with $m_{e,i}(t) = \boldsymbol{e}^t \boldsymbol{\xi}^{e,i}(t)/N$.

The Mean-Field Equations

Equations 12, **13** describe an Ornstein-Uhlenbeck process with solution

$$\begin{aligned} a_k(t) &= \int_{-\infty}^{t} e^{-(t-\tau)/\tau_e} \boldsymbol{\Psi}_k^{e\dagger} \boldsymbol{\xi}^e(\tau) d\tau \\ b_k(t) &= \int_{-\infty}^{t} e^{-(t-\tau)/\tau_i} \boldsymbol{\Psi}_k^{i\dagger} \boldsymbol{\xi}^i(\tau) d\tau, \end{aligned} \tag{14}$$

for $t \to \infty$. In **Eqs 10**, **11** the terms $\boldsymbol{V}, \boldsymbol{W}$ can be written as

$$\begin{aligned} \boldsymbol{V} &= \sum_{n=1}^{N} a_n(t) \boldsymbol{\Phi}_n^e = a_1 \boldsymbol{\Phi}_1^e + \sum_{n=2}^{N} a_n(t) \boldsymbol{\Phi}_n^e \\ \boldsymbol{W} &= \sum_{n=1}^{N} b_n(t) \boldsymbol{\Phi}_n^i = b_1 \boldsymbol{\Phi}_1^i + \sum_{n=2}^{N} b_n(t) \boldsymbol{\Phi}_n^i. \end{aligned} \tag{15}$$

Inserting expressions in **Eq. 14** into these expressions leads to

$$\begin{aligned} \sum_{n=2}^{N} a_n(t) \boldsymbol{\Phi}_n^e &= \int_{-\infty}^{t} e^{-(t-\tau)/\tau_e} \sum_{n=2}^{N} \boldsymbol{\Phi}_n^e \boldsymbol{\Psi}_n^{e\dagger} \boldsymbol{\xi}(\tau) d\tau. \\ \sum_{n=2}^{N} b_n(t) \boldsymbol{\Phi}_n^i &= \int_{-\infty}^{t} e^{-(t-\tau)/\tau_i} \sum_{n=2}^{N} \boldsymbol{\Phi}_n^i \boldsymbol{\Psi}_n^{i\dagger} \boldsymbol{\xi}(\tau) d\tau. \end{aligned} \tag{16}$$

By virtue of the completeness of the basis, it is

$$\begin{aligned} \sum_{n=2}^{N} \boldsymbol{\Phi}_n^e \boldsymbol{\Psi}_n^{e\dagger} &= \mathbf{I} - \boldsymbol{\Phi}_1^e \boldsymbol{\Psi}_1^{e\dagger} \\ \sum_{n=2}^{N} \boldsymbol{\Phi}_n^i \boldsymbol{\Psi}_n^{i\dagger} &= \mathbf{I} - \boldsymbol{\Phi}_1^i \boldsymbol{\Psi}_1^{i\dagger}, \end{aligned}$$

with the unity matrix $\mathbf{I} \in \mathbb{R}^{N \times N}$. Then inserting these identities into (**Eq. 16**)

$$\begin{aligned} \sum_{n=2}^{N} a_n(t) \boldsymbol{\Phi}_n^e &= \int_{-\infty}^{t} e^{-(t-\tau)/\tau_e} \boldsymbol{\xi}^e(\tau) d\tau - \int_{-\infty}^{t} e^{-(t-\tau)/\tau_e} \boldsymbol{\Phi}_1^e m_e(\tau) d\tau \\ \sum_{n=2}^{N} b_n(t) \boldsymbol{\Phi}_n^i &= \int_{-\infty}^{t} e^{-(t-\tau)/\tau_i} \boldsymbol{\xi}^i(\tau) d\tau - \int_{-\infty}^{t} e^{-(t-\tau)/\tau_i} \boldsymbol{\Phi}_1^i m_i(\tau) d\tau, \end{aligned} \tag{17}$$

We define $\boldsymbol{\eta}^{e,i}(t) = \boldsymbol{\xi}^{e,i}(t) - \boldsymbol{\xi}_0^{e,i}$, $\boldsymbol{e}^t \boldsymbol{\eta}^{e,i}(t) = N \rho^{e,i}(t)$ with $\rho^{e,i} \sim \mathcal{N}(0, D_{1,2}/N)$ and temporally constants $\boldsymbol{\xi}_0^{e,i}$, i.e. $\rho^{e,i}$ are finite size fluctuations with variance $D_{1,2}/N$ and $\rho^{e,i} \to 0$ for $N \to \infty$. With the definitions

$$\boldsymbol{w}_{e,i}(t) = \int_{-\infty}^{t} e^{-(t-\tau)/\tau_{e,i}} \boldsymbol{\eta}^{e,i}(\tau) d\tau \tag{18}$$

$$\boldsymbol{s}_{e,i}(t) = \tau_e \left(\boldsymbol{\xi}_0^{e,i} - e \overline{\boldsymbol{\xi}_0}^{e,i} \right) - \boldsymbol{e} \int_{-\infty}^{t} e^{-(t-\tau)/\tau_{e,i}} \rho^{e,i}(\tau) d\tau, \tag{19}$$

with $\overline{\xi}_0^{e,i} = \sum_{n=1}^{N} (\xi_{0,n}^{e,i}/N)$ and inserting **Eq. 17** into **Eq. 15**

$$\begin{aligned} \boldsymbol{V}(t) &= a_1(t) \boldsymbol{e} + \boldsymbol{s}_e(t) + \boldsymbol{w}_e(t) \\ \boldsymbol{W}(t) &= b_1(t) \boldsymbol{e} + \boldsymbol{s}_i(t) + \boldsymbol{w}_i(t) \end{aligned}. \tag{20}$$

and the mean-field equations can the be written as

$$\begin{aligned} \tau_e \frac{da_1}{dt} &= -a_1 + \frac{F_0}{N} \boldsymbol{e}^t \mathbf{S}_1[a_1(t) \boldsymbol{e} + \boldsymbol{s}_e(t) + \boldsymbol{w}_e(t)] \\ &\quad - \frac{M_0}{N} \boldsymbol{e}^t \mathbf{S}_2[b_1(t) \boldsymbol{e} + \boldsymbol{s}_i(t) + \boldsymbol{w}_i(t)] \\ &\quad + I^e + \overline{\xi}_0^e + \rho^e(t) \\ \tau_i \frac{db_1}{dt} &= -b_1 + \frac{M_0}{N} \boldsymbol{e}^t \mathbf{S}_1[a_1(t) \boldsymbol{e} + \boldsymbol{s}_e(t) + \boldsymbol{w}_e(t)] \\ &\quad - \frac{F_0}{N} \boldsymbol{e}^t \mathbf{S}_2[b_1(t) \boldsymbol{e} + \boldsymbol{s}_i(t) + \boldsymbol{w}_i(t)] \\ &\quad + I^i + \overline{\xi}_0^i + \rho^i(t), \end{aligned} \tag{21}$$

By virtue of the finite-size fluctuations over time $\rho^{e,i}(t)$ the system's mean-field obeys stochastic dynamics.

Equation 14 describe an Ornstein-Uhlenbeck process of mode k and thus $\boldsymbol{w}_{e,i}(t)$ describes a multivariate Ornstein-Uhlenbeck process over time. In addition, $\boldsymbol{w}_{e,i}(t)$ is stationary over time and, since all modes k share identical properties, it is stationary over the network. Consequently, the process is ergodic and the stationary probability density function $p(\boldsymbol{w}_{e,i})$ of $\omega_{e,i}$ can be computed over the network yielding

$$\begin{aligned} \frac{1}{N} \boldsymbol{e}^t \mathbf{S}_1[x\boldsymbol{e} + \boldsymbol{w}] &= \frac{1}{N} \sum_{n=1}^{N} S[x + w_n] \\ &\approx \int_{-\infty}^{\infty} S(x + w) p_e(w) dw \\ &= G_1(x), \end{aligned} \tag{22}$$

where the approximation is good for large N. Specifically, for Gaussian zero-mean uncorrelated noise $\boldsymbol{\xi}_e$ with variance D [69]

$$p_e(w) = \frac{1}{\sqrt{2\pi}\sigma} e^{-\omega^2/2\sigma^2}, \sigma^2 = \frac{D}{\tau_e}.$$

Similarly,

$$\begin{aligned} \frac{1}{N} \boldsymbol{e}^t \mathbf{S}_2[x\boldsymbol{e} + \boldsymbol{w}] &\approx \int_{-\infty}^{\infty} S(x + w) p_i(\omega) dw \\ &= G_2(x), \end{aligned} \tag{23}$$

Moreover, if the mean input is $\boldsymbol{\xi}_0^{e,i} = \alpha^{e,i} e$ and $N \to \infty$, then $s_{e,i} = 0$ and $\rho^{e,i} = 0$ and consequently the mean-field equation

$$\begin{aligned}\tau_e\frac{da_1}{dt} &= -a_1 + F_0G_1(a_1) - M_0G_2(b_1) + I^e + \alpha^e \\ \tau_i\frac{db_1}{dt} &= -b_1 + M_0G_1(a_1) - F_0G_2(b_1) + I^i + \alpha^i\end{aligned}, \tag{24}$$

obeys deterministic dynamics. However, the above formulation depends implicitly on the additive noise through the convolution of the transfer function.

Partial Stimuli

Each noise baseline stimulus at inhibitory neurons $(\boldsymbol{\xi}^i)_n = \xi^i_n$ at network node n is Gaussian distributed with zero mean and variance D_2 (cf. **section 2.1**). Then $\overline{\xi}^i_0 = 0$, $\boldsymbol{s}_i(t) = \overline{\rho}^i(t) \sim \mathcal{N}(0, D_2/\tau_i N)$ and, considering **Eq. 18**, the corresponding probability density function in **Eq. 23** is $p_i(w) = \mathcal{N}(0, D_2/\tau_i)$. Here $\mathcal{N}(0,\sigma^2)$ denotes a normal distribution with zero mean and variance σ^2 .Additionally, stochastic stimuli driving excitatory neurons in class $\mathcal{G}_1$ are ergodic (cf. **section 2.1**). Then the mean and variance of class $\mathcal{G}_1$ is

$$\begin{aligned}\overline{\xi}^e_1 &= \frac{1}{N_1}\sum_{n\in\mathcal{G}_1}\xi^e_n \\ D_1 &= \frac{1}{N_1}\sum_{n\in\mathcal{G}_1}(\xi^e_n)^2,\end{aligned} \tag{25}$$

Using **Eq. 18** and **Eq. 19** and assuming $N\to\infty$, then

$$w^e(t) + \boldsymbol{s}^e(t) = \int_{-\infty}^{t} e^{-(t-\tau)/\tau_e}\left(\boldsymbol{\eta}^e(\tau) + \Delta\boldsymbol{\xi}\right)d\tau,$$

whose probability density function $p_e(w)$ is [23].

$$\begin{aligned}p_e(w) &= \sum_{m=1}^{2} q_m\mathcal{N}\left(\overline{\xi}^e_m, D^m_1/\tau_e\right) \\ &= q\mathcal{N}\left(\overline{\xi}^e_1, D_1/\tau_e\right)[w] + (1-q)\delta(w),\end{aligned} \tag{26}$$

with $q = N_1/N$, $q_1 = q, q_2 = 1-q$. Here, $\Delta\boldsymbol{\xi} = (1-q, 1-q, \ldots, -q, -q)\xi^e_1$ with terms $1-q$ of number N_1 and assuming that the nodes $n = 1,\ldots,N_1$ receive stochastic input. In addition the constant input in the mean-field equation is $\overline{\xi}^e_0 = q\xi^e_1$.

Then, utilizing **Eqs 22**, **23** and specifying S to a step function (cf. **section 2.1**), the mean-field transfer functions in **Eq. 24** read

$$\begin{aligned}G_1(a_1) &= \frac{H_0 q}{2}\left[1 - \mathrm{erf}\left(-\frac{a_1}{\sqrt{2D_1/\tau_e}}\right)\right] + (1-q)\Theta(a_1) \\ G_2(b_1) &= \frac{1}{2}\left[1 - \mathrm{erf}\left(-\frac{b_1}{\sqrt{2D_2/\tau_i}}\right)\right],\end{aligned} \tag{27}$$

Here, $\Theta(\cdot)$ denotes the Heaviside step function. **Figure 3** shows examples for p_e and G_1.

Essentially, the mean-field obeys

$$\begin{aligned}\tau_e\frac{da_1}{dt} &= -a_1 + F_0G_1(a_1) - M_0G_2(b_1) + I^e + \rho^e(t) \\ \tau_i\frac{db_1}{dt} &= -b_1 + M_0G_1(a_1) - F_0G_2(b_1) + I^i + \rho^i(t)\end{aligned} \tag{28}$$

utilizing (**Eq. 27**).

3.2 Zero-Mean Gaussian Partial Stimulation

At first, we consider the case of a partial noise stimulation with zero network mean, i.e. $\boldsymbol{e}^t\overline{\boldsymbol{\xi}}^e = 0$ and $\boldsymbol{s}_e(t) \sim \mathcal{N}(0, D_1/\tau_e N_1)$ and $\xi^e_1 = \overline{\xi}^e_0 = 0$. Then D_1 parametrizes the noise intensity only. **Figure 4** shows the network evolution of $\boldsymbol{V}(t)$ for increasing noise intensities, cf. **Equation 7**. Starting from a high activity state, increasing the noise intensity yields a phase transition of the system to a network state at lower activity. This occurs for global ($q = 1.0$) and partial stimulation ($q = 0.8$, $q = 0.6$ and $q = 0.5$). Please re-call that, for instance, $q = 0.5$ reflects a stimulation where 50% of the network nodes are stimulated. These stimulated network nodes have been randomly chosen from a uniform distribution.

Figure 5 shows the respective power spectra of the network mean $\boldsymbol{V}(t)$, which provides insights about the system's synchronization at low and high noise intensity. High noise intensity induces strong oscillations in the γ-frequency band, whereas the low noise intensity states does not - in contrast, this state shows a decaying low-pass power spectral density that is expected from a non-oscillatory stochastic process.

Stronger power spectral density at a given frequency is the signature of a coherent network, as seen in **Figure 5**. Since the neurons in our network model emit spikes and exhibit synaptic input currents, noise-induced coherence may be visible in the coherence between spiking and synaptic activity as well. In fact, in **Figure 6A** one observes a significant strongly enhanced Spike Field Coherence at high noise intensities for both global and partial stimulation. Hence, in sum the system exhibits coherence resonance in the sense that strong noise induces coherent oscillations that are not present at low noise intensities.

Coherence resonance is supposed to be linked to information processing in neural systems. Thus we investigate the relationship between stimulus noise intensity and information in the system across frequency bands. **Figure 6B** shows how much information is stored in the networks (AIS) and how much information is available (H). We observe that significantly more information is stored (AIS) and available (H) at high noise intensities for global stimulation $q = 1.0$, whereas high noise partial stimulation with $q = 0.8$ diminishes the stored active information and available information significantly. For more sparse stimulation with $q = 0.6$ the finding in information measures is heterogeneous and no interpretation consistent with the results for larger q is possible.

To understand this noise-induced coherence, we take a closer look at the dynamic topology of the mean-field **Eq. 28**. Their equilibria (cf. **section 2.3**) for negligible finite-size fluctuations $\rho^{e,i}(t) \ll 1$ are shown in **Figure 7** together with simulated mean-field activity $\overline{V}(t)$ for illustrative purposes. Low noise intensity induces a bistable regime with a stable node as upper equilibrium

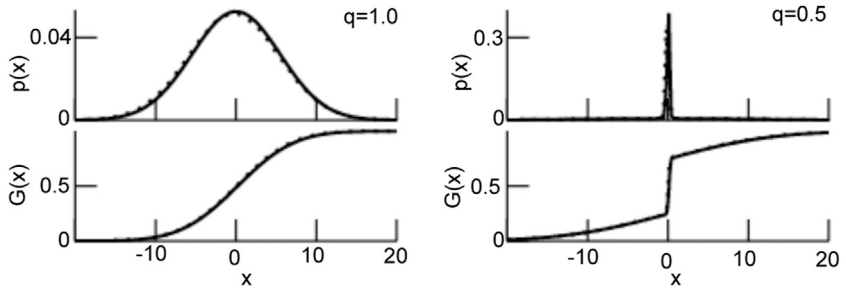

FIGURE 3 | The probability density function p (**Eq. 26**) and the resulting transfer function G (**Eq. 27**). For $q = 1.0$ $D_1/\tau_e = 0.15$ and for $q = 0.5$ $D_1/\tau_e = 0.5$.

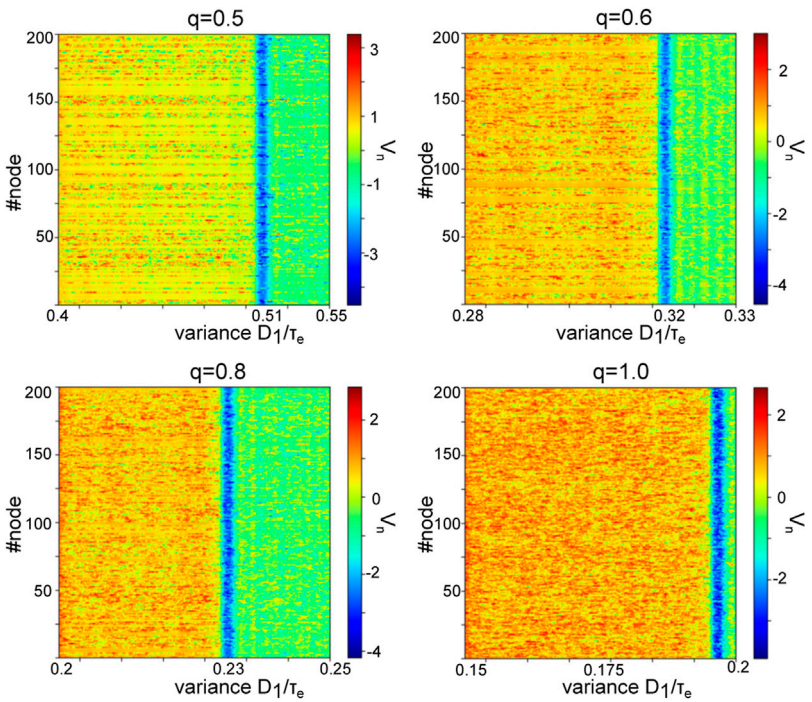

FIGURE 4 | Enhanced zero-mean Gaussian noise induces phase transitions in spatiotemporal dynamics. The panels show the network activity $\mathbf{V}(t)$ according to **Eq. 1** with temporally increasing noise variances D_1/τ_e for different stimulus ratios q.

and a focus as lower equilibrium. For global stimulation ($q = 1.0$), this lower focus is unstable at very low noise intensity and stable at larger noise intensities. Moreover, the lower equilibrium is a stable focus at all noise intensities for partial ($q < 1.0$) stimulation. The center branch is always a saddle node. For larger noise intensity, the upper equilibrium branch merges with the center branch via a saddle-node bifurcation and the lower stable focus is preserved as noise is further increased. This finding remains valid for both global ($q = 1.0$) and partial ($q < 1.0$) stimulation as shown in **Figure 7** for q ranging within the interval $0.5 \leq q \leq 1.0$. One can see that for smaller q (i.e. less excitatory neurons are stimulated) the bifurcation point moves to larger noise intensities. Hence thinning out the stimulation of excitatory neurons increases the noise intensity interval at which bistability occurs. Moreover, we point out that the bifurcation points predicted by the mean-field description and shown in **Figure 7** show very good accordance to the values of D_1/τ_e in **Figure 4**, where the system transitions from the upper to the lower state.

The mean-field solution involves finite-size fluctuations that affect the solutions principal oscillation frequency and magnitude. By construction, these mean-field solutions converge to the network average for increasing network size N. **Figure 8** compares the time series of mean-field solutions and network averages for increasing network sizes and affirms the convergence and thus the validity of the mean-field description. It is interesting to note that, besides the mean-field dynamics, the network's dynamical properties change with increasing N as well. **Figure 8** provides the principal oscillation frequencies for both solutions for the given network size: the network speeds up with

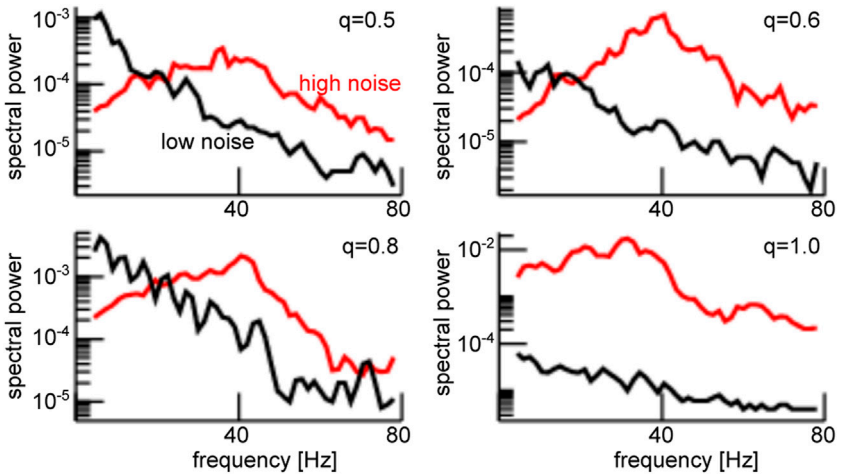

FIGURE 5 | Enhanced noise yields strong power of the global mode $\overline{V}(t)$ in the γ-frequency range. The panels show the power spectra of $\overline{V}$ for the stimulus ratios $q = 0.5$ ($D_1/\tau_e = 0.35$ (black) and $D_1/\tau_e = 0.55$ (red)), $q = 0.6$ ($D_1/\tau_e = 0.25$ (black) and $D_1/\tau_e = 0.33$ (red)), $q = 0.8$ ($D_1/\tau_e = 0.20$ (black) and $D_1/\tau_e = 0.25$ (red)) and $q = 1.0$ ($D_1/\tau_e = 0.15$ (black) and $D_1/\tau_e = 0.20$ (red)). Power spectra at lower noise intensities are computed on the respective upper branch of the bistable system.

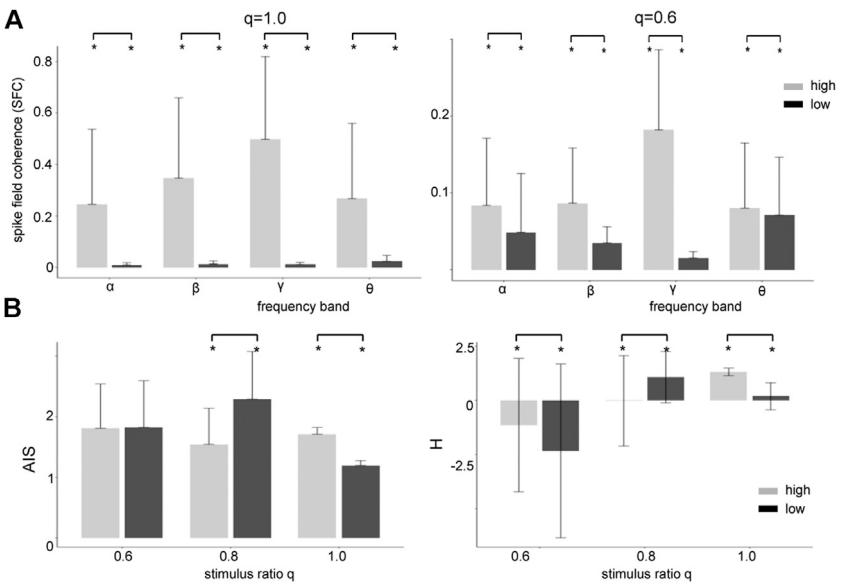

FIGURE 6 | High zero-mean Gaussian noise enhances the Spike Field Coherence in all frequency bands and affects heterogeneously Active Information Storage (AIS) and differential entropy (H). **(A)** The differences between high noise intensity (grey-colored) and low noise intensity (black-colored) is significant ($p < 0.001$) for both global and partial stimulation. **(B)** For global stimulation ($q = 1.0$), high noise intensity induces states of significantly enhanced stored active information (AIS) and available information (H), whereas partial stimulation with $q = 0.8$ diminishes both AIS and H significantly. Results for $q = 0.6$ are not consistent and difficult to interpret. In all panels, vertical bars denote the standard deviation, $p < 0.001$ and parameters are identical to the parameters used in **Figure 5**.

increasing size and its frequency converges to the mean-field principal frequency that remains about the same value. However, we point out that the mean-field solution remains still slightly different even for very large N since it implies the approximation of negligible connectivity matrix bulk spectra. **Figure 9** affirms this finding by comparing simulation trials of the transitions from the non-oscillatory to the oscillatory coherent state. We observe that the transition values of D_1/τ_e of the network mean and the mean-field are closer to each other for larger network size. The mean-field description (**Eq. 28**) with (**Eq. 27**) assumes vanishing finite-size fluctuations and these are reduced for larger network size N, i.e. the effective noise level (the finite-size fluctuations) is reduced and thus deterministic mean-field and stochastic network activity transition are closer to each other.

The frequency range of oscillations observed for steady states located within the lower branch (see **Figure 7**) is a

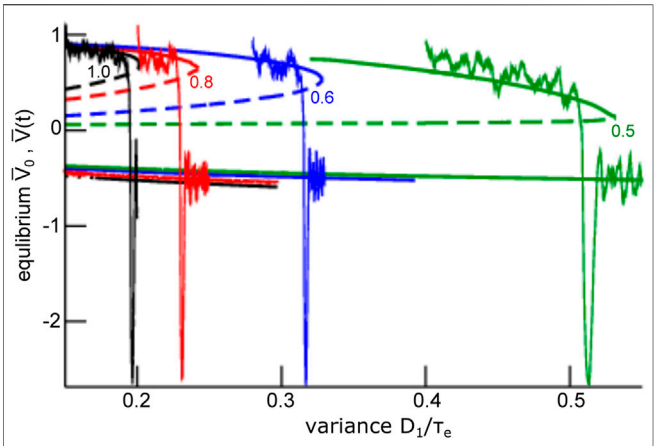

FIGURE 7 | Equilibria and representative time series of the global mode $\overline{V}(t)$ for the zero-mean partial stimulation. There is a bistability and saddle-node bifurcation from a stable node to an stable focus at enhanced noise intensity. The numbers denote the values of the stimulus ratio q. Solid (dashed) lines mark stable (unstable) states. The time series $\overline{V}$ results from the time-varying noise intensity according to **Eq. 7**.

consequence of both network connectivity and neuronal properties and is further tuned by additive noise. **Figure 10** shows the maximum eigenvalue real part for the upper (A) and the lower branch (B, top opanel) and the eigenfrequency (cf. **section 2.3**) of the equilibrium at the lower branch (B, lowel panel). We observe that increasing noise intensity decreases slightly the eigenfrequency in the $\gamma-$ frequency range and decreases the negative maximum eigenvalue real part. This means that additive noise increases the damping of the response of the system to perturbations - including noise. This increased noise-induced damping leads to magnitude changes in quasi-cycle solutions - which is manifested in the power spectral density distribution. Indeed, the power spectral density distribution widens as noise intensity increases, leading to the spectra as seen in **Figure 10C**. This broad spectral power distribution is the signature of suppressed coherence. As a corollary, our analysis demonstrates that coherent band-limited oscillations emerge for intermediate noise intensities only. This is a known feature of coherence resonance. For additional illustration, **Figure 1** shows the typical bell-shape of coherence (here Spike Field Coherence) in different frequency bands. We observe that the coherence effect is strongest in the $\gamma-$ frequency range.

3.3 Poisson Partial Stimulation

Synaptic receptors respond to afferent Poisson-distributed input spike trains, whose properties differ substantially from the Gaussian noise processes we considered so far. To generalize our results to more physiological stimuli statistics, we considered a partial Poisson noise stimulation with dependent mean and variance. Specifically, afferent spike trains at spike rate r_{in} induce random responses at excitatory synapses with time constant τ_{in} and synaptic weight w_{in}. Then

$$\begin{aligned} \boldsymbol{s}^e(t) &= \tau_e \Delta\boldsymbol{\xi} + \overline{\rho}^e(t) \\ \xi_1^e &= w_{\text{in}} r_{\text{in}} \tau_{\text{in}} \\ D_1 &= w_{\text{in}} \xi_0 / 2 \\ \overline{\xi}_0^e &= q\xi_1^e, \end{aligned}$$

and finite-size fluctuations $\overline{\rho}^e(t) \sim \mathcal{N}(0, D_1/N_1)$. **Figure 11A** illustrates the temporal network activity for a low and high stimuli firing rates r_{in}. Increasing r_{in} induces a transition from a high-activity to a low activity state for both global and partial stimulation - similarly as in the Gaussian noise case. The high-activity state is non-oscillatory while the low-activity state is oscillatory, with frequency found in the $\gamma-$ frequency range (**Figure 11B**). In addition, the low-activity state induced by high Poisson input rate exhibits a strong Spike Field Coherence in contrast to the high-activity state (**Figure 11C**). Moreover, high stimulation noise increases the stored information and the available information for global stimulation with $q = 1.0$, cf. **Figure 11D**. Information measures for partial stimulation ($q = 0.6$) are heterogeneous and an interpretation of results for AIS and H is difficult.

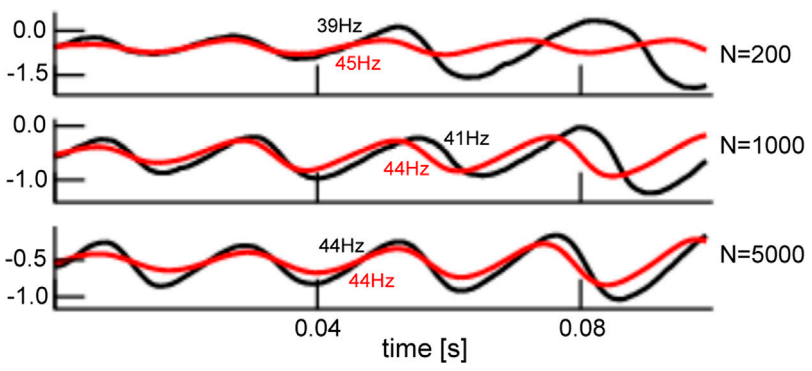

FIGURE 8 | Comparison of network average and mean-field solution for different network sizes. The network average (black) and mean-field solutions (red) resembles more and more the larger the network of size N. This holds for the magnitude and frequency (provided in panels) of both solutions. The initial value of the mean-field activity has been chosen to the initial value of the network average. Simulations consider zero-mean Gaussian simulations with $q = 1$ and $D_1/\tau_e = 0.2$.

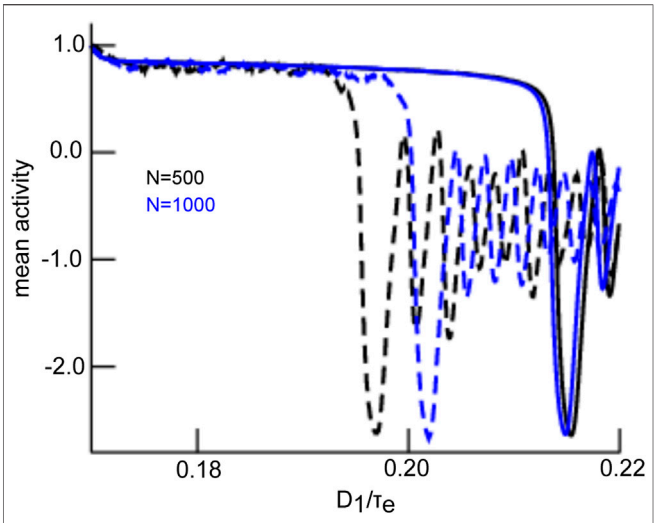

FIGURE 9 | Comparison of transitions in network and mean-field for different network sizes. The network average (dashed line) and mean-field solutions (solid line) resemble more for larger network size N. This is explained by reduced finite-size fluctuations for larger networks. The initial value of the mean-field activity has been chosen to the initial value of the network average. Simulations consider zero-mean Gaussian simulations with $q = 1$.

These results can be understood by taking a closer look at the dynamic topology of the system. **Figure 12** reveals that, for global stimulation ($q = 1.0$), the system has two unstable equilibria and one stable equilibrium at lower noise intensities. The top branch is a stable node, the center branch a saddle node and the lower branch an unstable focus. There is a very small noise intensity interval at which the top and bottom branch are both stable. Increasing the Poisson stimuli firing rate leads to a sudden suppression of high-activity equilibria through a saddle-node bifurcation. Consequently, the transition observed in **Figure 11A** is a jump from the stable node on the top bifurcation branch to the stable focus on the bottom branch similar to the effect shown in **Figure 4**. For partial stimulation ($q = 0.6$), the lower branch exhibits a stable focus for much lower input firing rates. The saddle-node bifurcation is delayed, leading to an increased noise intensity interval of bistability. Hence, the system exhibits coherence resonance for Poisson noise as well.

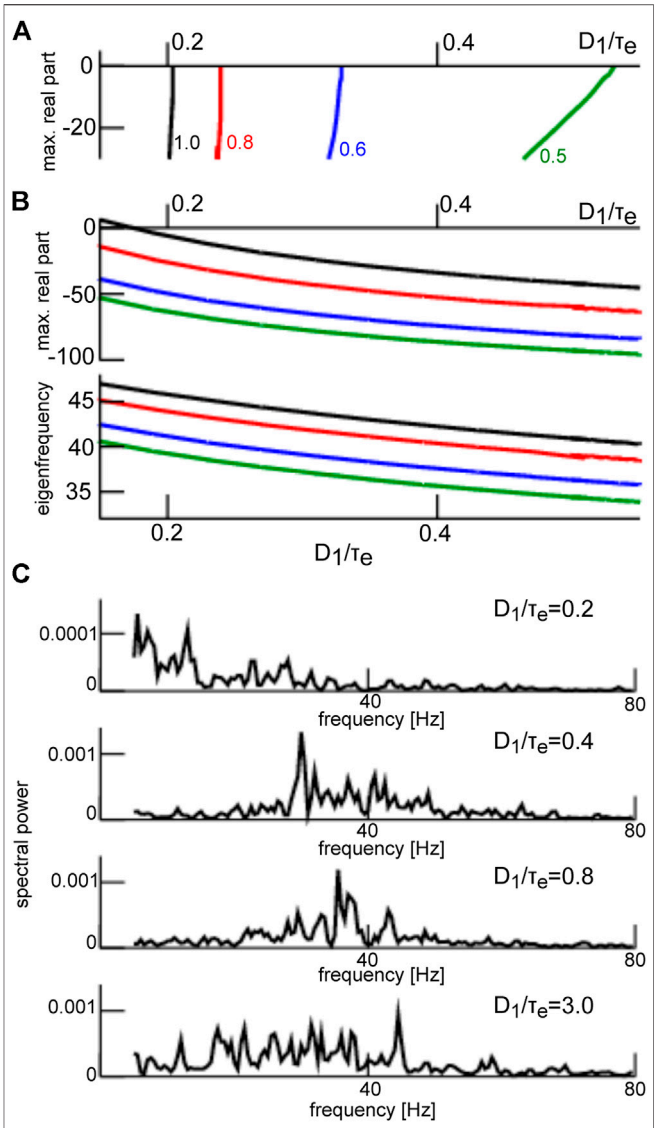

FIGURE 10 | Eigenvalues at the top and bottom branch in **Figure 7** and corresponding power spectra. **(A)** maximum eigenvalue of equilibria on the top branch in **Figure 7**. **(B)** maximum real part r of the eigenvalue $r + i2\pi\nu$ (top panel) and the corresponding eigenfrequency frequency ν. The numbers denote the values of the stimulus ratio q in all panels. **(C)** Power spectra of $\boldsymbol{V}(t)$ about the lower branch for $q = 0.6$ for different noise intensities D_1/τ_e.

4 DISCUSSION

This study presents a rigorous derivation of mean-field equations for two nonlinearly coupled non-sparse Erdös-Rényi networks (ERN) that are stimulated by additive noise. This mean field representation is made possible through spectral separation: the eigenspectrum of ERN networks exhibits a large spectral gap between the eigenvalue with largest real part and the rest of the spectrum. We show that the projection of the network dynamics onto the leading eigenmode represents the mean-field. Its dynamics are shaped by eigenmodes located in the complement subspace spanned by non-leading eigenmodes. In our model, the subspace dynamics are governed and influenced by additive noise statistics and they obey an Ornstein-Uhlenbeck process.

We extended the mean-field derivation to various types of additive noise, such as global and partial noise stimuli (i.e. when only a fraction of the excitatory neurons are stimulated) and for both zero-mean Gaussian and Poisson-like noise. Collectively, our analysis shows that additive noise induces a phase transition from a non-oscillatory state to an oscillatory coherent state. Such noise-induced coherence is known as coherence resonance (CR). This phase transition has been shown to occur not only for Gaussian zero-mean noise but also for Poisson-like noise.

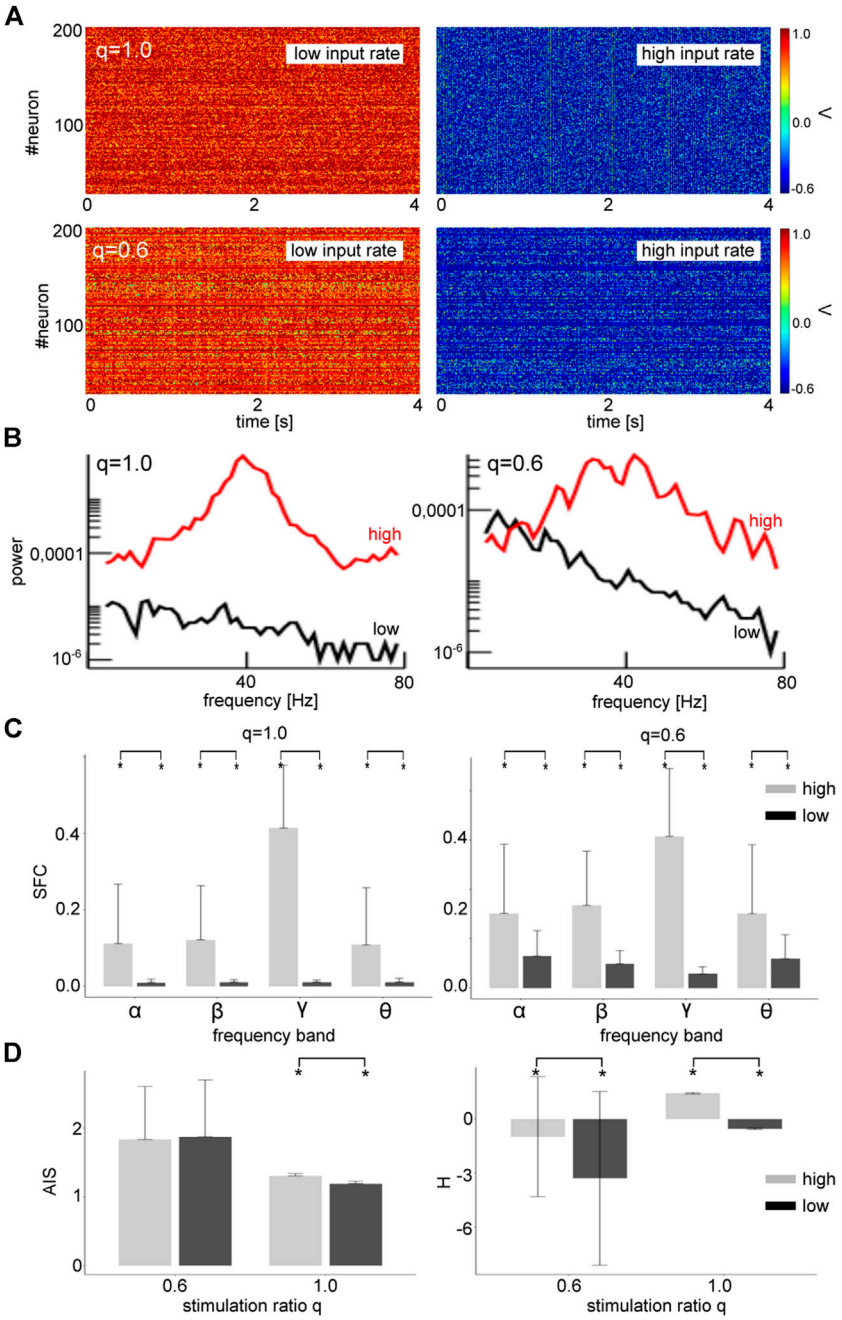

FIGURE 11 | Poisson noise induces transitions from a non-oscillatory to an oscillatory state for both global and partial stimulation. **(A)** Network activity $V_n(t)$ for low input firing rate ($r = 0.04$ for $q = 1.0$ and $r = 0.09$ for $q = 0.6$) and high input firing rate ($r = 0.14$ for $q = 1.0$ and $r = 0.19$ for $q = 0.6$). For the low (high) input rate the system evolves about an upper (lower) state. **(B)** Power spectra of the network mean $\overline{V}(t)$ showing $\gamma-$ activity for the large input rate. **(C)** The high input firing rate (grey-colored) induces a state of large Spike Field Coherence compared to the state for low input firing rate (black-colored) for both global and partial stimulation ($p < 0.01$). **(D)** For global stimulation ($q = 1.0$), high input firing induces a state of significantly enhanced stored active information (*AIS*) and available information (*H*). This is not consistent to results for partial stimulation ($q = 0.6$). Here is $p < 0.01$.

To the best of our knowledge, CR has not been found yet for such Poisson-like noise. The general underlying mechanism is a noise-induced multiplicative impact of additive stimulation via the nonlinear coupling of different modes. This multiplicative effect modifies the net transfer function of the network and thus enlarges its dynamical repertoire. This resembles the impact of additive noise in stochastic bifurcations [51, 52, 70, 71].

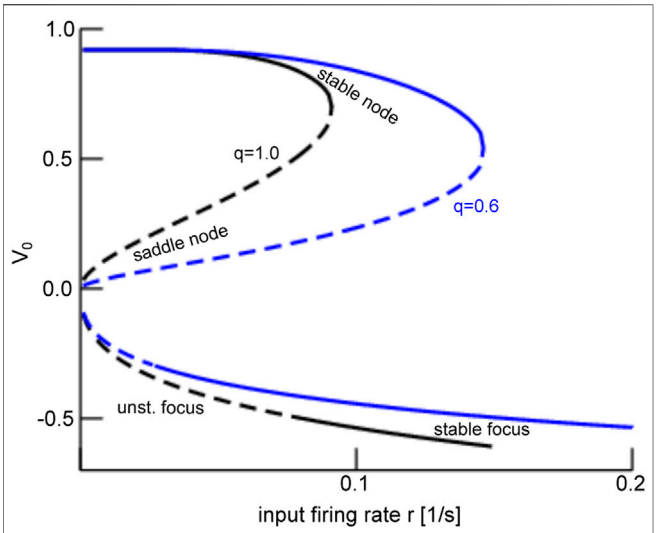

FIGURE 12 | Equilibria of the mean-field $\overline{V}(t)$ for the Poisson partial stimulation. For global stimulation $q = 1.0$, the system is always monostable with three equilibria at low input firing rates and a single equilibrium at large input firing rates. Increasing the input firing rate from low to large firing rates, the system jumps from the upper stationary state (stable node) to a stable focus on the lower stationary state via a saddle-node bifurcation. For partial stimulation $q = 0.6$, the system is monostable with three equilibria at low input firing rates. For larger input rates, the system is bistable and passes a saddle-node bifurcation inducing a transition from a stable node to an stable focus at enhanced input firing rate r. Solid (dashed) lines mark stable (unstable) states, black- and blue-colored lines denote equilibria for global and partial stimulation, respectively. The bifurcation diagram of the mean-field $\overline{W}(t)$ is equivalent.

Embedding into Literature

Our results build on previous studies from the authors [23, 54, 55] to provide a rigorous derivation of the mean-field description, whereas previous work have motivated heuristically the mean-field reduction and, e.g., failed to show in detail whether the mean-field equation is the only solution for any given additive stimuli. Several other previous studies have presented mean-field descriptions in stochastically driven systems. For instance, Bressloff et al. [28] have derived rigorously mean-field equations for stochastic neural fields considering, inter alia, finite-element fluctuations by utilizing a Master equation and van Kampen's volume expansion approach. We note here that we also took into account finite-size fluctuations resulting from a non-negligible variance of statistical mean values. Moreover [28], do not specify the network type and results in a rather opaque description, whereas we assume an ERN and thus exploit its unique eigenspectrum structure. This yields directly to a mean-field description, whose dependence of stochastic forces is obvious and avoids its implicit closure problem known from mean-field theories [43]. This is possible since the ERN considered share many properties with Izing models, that are known to permit an analytically treatable solution of the closure problem, see e.g. [72].

Moreover, several technical analysis steps in the present work have been applied in previous studies in a similar context. In a work on stochastic neural mean-field theory, Faugeras and others [27] have assumed that the system activity fluctuations obey a normal probability distribution and have derived an effective nonlinear interaction in their Proposition 2.1 similar to our **Eq. 22**. Further, the authors have shown how the fluctuation correlation function, i.e. the system activity's second moment, determine the mean-field dynamics. This is in line with our result (**Eq. 22**) showing how the mean and variance of the additive noise tunes the system's stability. However, the authors have not considered in detail the random nature of the system connectivity, whereas we have worked out the interaction of external stimulation and the ERN. This interaction yields directly the mean-field and its dependence of the external stimulus that is not present in [27]. Moreover, the present work also shows how the mean-field fluctuations affect the mean-field dynamics by deriving the fluctuation's probability density function that describes all higher moments.

Noise-induced synchronization has been found recently in a system of stochastically driven linearly coupled FitzHugh-Nagumo neurons by Touboul and others [73]. The authors have found a minimum ratio of activated neurons that are necessary to induce global oscillatory synchronization, i.e. CR in the sense presented in our work. This question has been considered in the present work as well by asking how the mean-field dynamics, and thus how noise-induced synchronization, changes when modifying the ratio of stimulated excitatory neurons q while retaining the stimulation of inhibitory neurons. We find that global stimulation, i.e. stimulation of all excitatory neurons, yields a finite critical noise intensity below which the system is bistable and exhibits CR. Partial stimulation shifts this critical noise intensity to larger values and enlarges the bistability parameter space and thus promotes CR.

Several previous studies of mean-field dynamics in neural systems have applied the master equation formalism [74–76]. This works nicely in completely irregular networks and the asynchronous activity regime and has been applied successfully to neural populations considering biological neuron models [77–80]. However, the analysis of more regular networks will be very difficult to develop with the Master equation since the implicit integration over system states would be more complex. Conversely, our presented approach may consider regular structures by a corresponding matrix eigenvalue decomposition.

At last, we mention the relation to the Master stability function [81, 82]. This function describes the stability of identical synchronization of complex networks in a synchronization manifold and this manifold corresponds to the mean-field in our study. Although the Master stability function has been proven to be powerful, to the best of our knowledge it does not allow to reveal coherence resonance as the current work.

Limits and Outlook

The present work proposes to describe mean-field dynamics in a topological network by projection onto the networks eigenmodes. This works well for non-sparse random ERN with large connectivity probability. This network does not exhibit a spatial structure. However, less connected ERN networks show different dynamics, cf. the **Supplementary Appendix**. Moreover,

biological networks are not purely random but may exhibit distance-dependent synaptic weights [83] or spatial clusters [84]. Our specific analysis applies for networks with a large spectral gap in their eigenspectra and it might fail for biological networks with smaller spectral gaps (as shown in the **Supplementary Appendix**). Future work will attempt to utilize the presented approach to derive mean-field dynamics for heterogeneous networks that exhibit a smaller spectral gap, such as scale-free networks [84].

Moreover, the single neuron model in the present work assumes a simple static threshold firing dynamics (McCullough-Pitts neuron) while neglecting somatic dynamics as described by Hodgkin-Huxley type models or the widely used FitzHugh-Nagumo model [11, 73]. Future work will aim at reinforcing the biological relevance of neurons coupled through ERN. This will be possible by extending the trivial transfer function from a step function to sigmoidal shapes for type I or type II neurons [76, 85, 86].

Our results show that noise-induced CR emerges in the $\gamma-$ frequency range. This frequency band is thought to play an important role in visual information processing [13–17]. Experimental studies have shown that the degree of this γ-synchronization in primary cortical areas may be modulated by attention [59, 87–89]. Since attention is known to affect the ARAS activity [90] and specifically the brain stem as part of the ARAS [91] and ARAS, in turn, provides input to the cortex [92]. We conclude that it is possible that attention modulates the cortical input activity, i.e. the Poisson firing rate in our model. In this picture, attention-modulated enhanced ARAS activity induces $\gamma-$ coherence and may enhance stored information [93], as shown in **Figures 6**, **11**. Future more detailed brain models including the cortico-thalamic feedback and cortical interactions [21, 57] will provide further evidence whether coherence resonance is present in visual processing.

DATA AVAILABILITY STATEMENT

The raw data supporting the conclusion of this article will be made available by the authors, without undue reservation.

AUTHOR CONTRIBUTIONS

AH conceived the work structure motivated by intensive discussions with JL; AH, TW, NV, and JH contributed different work parts and all authors have written the work.

SUPPLEMENTARY MATERIAL

The Supplementary Material for this article can be found online at: https://www.frontiersin.org/articles/10.3389/fams.2021.697904/full#supplementary-material

REFERENCES

1. Pikovsky A, Rosenblum M, and Kurths J. *Synchronization: A Universal Concept in Nonlinear Sciences*. Cambridge University Press (2001).
2. Singer W. The Brain as a Self-Organizing System. *Eur Arch Psychiatr Neurol Sci* (1986) 236:4–9. doi:10.1007/bf00641050
3. Witthaut D, Wimberger S, Burioni R, and Timme M. Classical Synchronization Indicates Persistent Entanglement in Isolated Quantum Systems. *Nat Commun* (2017) 8:14829. doi:10.1038/ncomms14829
4. Hutt A, and Haken H. *Synergetics*. New York: Springer-Verlag (2020).
5. Mompo E, Ruiz-Garcia M, Carretero M, Grahn HT, Zhang Y, and Bonilla LL. Coherence Resonance and Stochastic Resonance in an Excitable Semiconductor Superlattice. *Phys Rev Lett* (2018) 121:086805. doi:10.1103/PhysRevLett.121.086805
6. Lee CY, Choi W, Han J-H, and Strano MS. Coherence Resonance in a Single-Walled Carbon Nanotube Ion Channel. *Science* (2010) 329:1320–4. doi:10.1126/science.1193383
7. Gu H, Yang M, Li L, Liu Z, and Ren W. Experimental Observation of the Stochastic Bursting Caused by Coherence Resonance in a Neural Pacemaker. *Neuroreport* (2002) 13:1657–60. doi:10.1097/00001756-200209160-00018
8. Ratas I, and Pyragas K. Noise-induced Macroscopic Oscillations in a Network of Synaptically Coupled Quadratic Integrate-And-Fire Neurons. *Phys Rev E* (2019) 100:052211. doi:10.1103/PhysRevE.100.052211
9. Pikovsky AS, and Kurths J. Coherence Resonance in a Noise-Driven Excitable System. *Phys Rev Lett* (1997) 78:775–8. doi:10.1103/physrevlett.78.775
10. Gang H, Ditzinger T, Ning CZ, and Haken H. Stochastic Resonance without External Periodic Force. *Phys Rev Lett* (1993) 71:807–10. doi:10.1103/physrevlett.71.807
11. Baspinar E, Schüler L, Olmi S, and Zakharova A. *Coherence Resonance in Neuronal Populations: Mean-Field versus Network Model*. Submitted (2020).
12. Tönjes R, Fiore CE, and Pereira T. Coherence Resonance in Influencer Networks. *Nat Commun* (2021) 12:72. doi:10.1038/s41467-020-20441-4
13. Singer W, and Gray CM. Visual Feature Integration and the Temporal Correlation Hypothesis. *Annu Rev Neurosci* (1995) 18:555–86. doi:10.1146/annurev.ne.18.030195.003011
14. Eckhorn R, Bauer R, Jordan W, Brosch M, Kruse W, Munk M, et al. Coherent Oscillations: A Mechanism of Feature Linking in the Visual Cortex? *Biol Cybern* (1988) 60:121–30. doi:10.1007/bf00202899
15. Castelo-Branco M, Neuenschwander S, and Singer W. Synchronization of Visual Responses between the Cortex, Lateral Geniculate Nucleus, and Retina in the Anesthetized Cat. *J Neurosci* (1998) 18:6395–410. doi:10.1523/jneurosci.18-16-06395.1998
16. Nelson JI, Salin PA, Munk MH-J, Arzi M, and Bullier J. Spatial and Temporal Coherence in Cortico-Cortical Connections: a Cross-Correlation Study in Areas 17 and 18 in the Cat. *Vis Neurosci* (1992) 9:21–37. doi:10.1017/s0952523800006349
17. Bressler SL. Interareal Synchronization in the Visual Cortex. *Behav Brain Res* (1996) 76:37–49. doi:10.1016/0166-4328(95)00187-5
18. Munk MHJ, Roelfsema PR, Konig P, Engel AK, and Singer W. Role of Reticular Activation in the Modulation of Intracortical Synchronization. *Science* (1996) 272:271–4. doi:10.1126/science.272.5259.271
19. Hutt A, Lefebvre J, Hight D, and Sleigh J. Suppression of Underlying Neuronal Fluctuations Mediates EEG Slowing during General Anaesthesia. *Neuroimage* (2018) 179:414–28. doi:10.1016/j.neuroimage.2018.06.043
20. Hutt A. Cortico-thalamic Circuit Model for Bottom-Up and Top-Down Mechanisms in General Anesthesia Involving the Reticular Activating System. *Arch Neurosci* (2019) 6:e95498. doi:10.5812/ans.95498
21. Hutt A, and Lefebvre J. Arousal Fluctuations Govern Oscillatory Transitions between Dominant γ- and α Occipital Activity during Eyes Open/Closed Conditions. *Brain Topography* (2021), in press.
22. Pisarchik AN, Maksimenko VA, Andreev AV, Frolov NS, Makarov VV, Zhuravlev MO, et al. Coherent Resonance in the Distributed Cortical Network during Sensory Information Processing. *Sci Rep* (2019) 9:18325. doi:10.1038/s41598-019-54577-1
23. Hutt A, Lefebvre J, Hight D, and Kaiser HA. Phase Coherence Induced by Additive Gaussian and Non-gaussian Noise in Excitable Networks with

Application to Burst Suppression-like Brain Signals. *Front Appl Math Stat* (2020) 5:69. doi:10.3389/fams.2019.00069
24. Chacron MJ, Longtin A, and Maler L. The Effects of Spontaneous Activity, Background Noise, and the Stimulus Ensemble on Information Transfer in Neurons. *Netw Comput Neural Syst* (2003) 14:803–24. doi:10.1088/0954-898x_14_4_010
25. Chacron MJ, Lindner B, and Longtin A. Noise Shaping by Interval Correlations Increases Information Transfer. *Phys.Rev.Lett.* (2004) 93: 059904. doi:10.1103/physrevlett.93.059904
26. Chacron MJ, doiron B, Maler L, Longtin A, and Bastian J. Non-classical Receptive Field Mediates Switch in a Sensory Neuron's Frequency Tuning. *Nature* (2003) 423:77–81. doi:10.1038/nature01590
27. Faugeras OD, Touboul JD, and Cessac B. A Constructive Mean-Field Analysis of Multi Population Neural Networks with Random Synaptic Weights and Stochastic Inputs. *Front Comput Neurosci* (2008) 3:1. doi:10.3389/neuro.10.001.2009
28. Bressloff PC. Stochastic Neural Field Theory and the System Size Expansion. *SIAM J Appl Math* (2009) 70:1488–521.
29. Terney D, Chaieb L, Moliadze V, Antal A, and Paulus W. Increasing Human Brain Excitability by Transcranial High-Frequency Random Noise Stimulation. *J Neurosci* (2008) 28:14147–55. doi:10.1523/jneurosci.4248-08.2008
30. Erdős L, Knowles A, Yau H-T, and Yin J. Spectral Statistics of Erdős-Rényi Graphs I: Local Semicircle Law. *Ann Probab* (2013) 41:2279–375. doi:10.1214/11-AOP734
31. Ding X, and Jiang T. Spectral Distributions of Adjacency and Laplacian Matrices of Random Graphs. *Ann Appl Prob* (2010) 20:2086–117. doi:10.1214/10-aap677
32. Kadavankandy A. Spectral Analysis of Random Graphs with Application to Clustering and Sampling. In: *Ph.D. Thesis, Université Cote d'Azur*. Nice, France: NNT: 2017AZUR4059 (2017).
33. Füredi Z, and Komlós J. The Eigenvalues of Random Symmetric Matrices. *Combinatorica* (1981) 1:233–41. doi:10.1007/bf02579329
34. O'Rourke S, Vu V, and Wang K. Eigenvectors of Random Matrices: A Survey. *J Comb Theor Ser A* (2016) 144:361–442. doi:10.1016/j.jcta.2016.06.008
35. Koch C. *Biophysics of Computation*. Oxford: Oxford University Press (1999).
36. Ross S. *Stochastic Processes (Probability and Mathemati- Cal Statistics)*. Wiley (1982).
37. Wright JJ, and Kydd RR. The Electroencephalogram and Cortical Neural Networks. *Netw Comput Neural Syst* (1992) 3:341–62. doi:10.1088/0954-898x_3_3_006
38. Nunez PL. Toward a Quantitative Description of Large-Scale Neocortical Dynamic Function and EEG. *Behav Brain Sci* (2000) 23:371–98. doi:10.1017/s0140525x00003253
39. Nunez P, and Srinivasan R. *Electric Fields of the Brain: The Neurophysics of EEG*. New York - Oxford: Oxford University Press (2006).
40. Wilson HR, and Cowan JD. Excitatory and Inhibitory Interactions in Localized Populations of Model Neurons. *Biophysical J* (1972) 12:1–24. doi:10.1016/s0006-3495(72)86068-5
41. Gerstner W, and Kistler W. *Spiking Neuron Models*. Cambridge: Cambridge University Press (2002).
42. Bressloff PC, and Coombes S. Physics of the Extended Neuron. *Int J Mod Phys B* (1997) 11:2343–92. doi:10.1142/s0217979297001209
43. Kuehn C. Moment Closure-A Brief Review. In: Schöll E, Klapp S, and Hövel P, editors. *Control of Self-Organizing Nonlinear Systems*. Heidelberg: Springer (2016). p. 253–71. doi:10.1007/978-3-319-28028-8_13
44. Sri Namachchivaya N. Stochastic Bifurcation. *Appl Math Comput* (1990) 39: 37s–95s. doi:10.1016/0096-3003(90)90003-L
45. Berglund N, and Gentz B. Geometric Singular Perturbation Theory for Stochastic Differential Equations. *J Differential Equations* (2003) 191:1–54. doi:10.1016/s0022-0396(03)00020-2
46. Bloemker D, Hairer M, and Pavliotis GA. Modulation Equations: Stochastic Bifurcation in Large Domains. *Commun Math Phys* (2005) 258:479–512. doi:10.1007/s00220-005-1368-8
47. Boxler P. A Stochastic Version of center Manifold Theory. *Probab Th Rel Fields* (1989) 83:509–45. doi:10.1007/bf01845701
48. Hutt A, and Lefebvre J. Stochastic center Manifold Analysis in Scalar Nonlinear Systems Involving Distributed Delays and Additive Noise. *Markov Proc Rel Fields* (2016) 22:555–72.
49. Lefebvre J, Hutt A, LeBlanc VG, and Longtin A. Reduced Dynamics for Delayed Systems with Harmonic or Stochastic Forcing. *Chaos* (2012) 22: 043121. doi:10.1063/1.4760250
50. Hutt A. Additive Noise May Change the Stability of Nonlinear Systems. *Europhys Lett* (2008) 84:34003. doi:10.1209/0295-5075/84/34003
51. Hutt A, Longtin A, and Schimansky-Geier L. Additive Noise-Induced Turing Transitions in Spatial Systems with Application to Neural fields and the Swift-Hohenberg Equation. *Physica D: Nonlinear Phenomena* (2008) 237:755–73. doi:10.1016/j.physd.2007.10.013
52. Hutt A, Longtin A, and Schimansky-Geier L. Additive Global Noise Delays Turing Bifurcations. *Phys Rev Lett* (2007) 98:230601. doi:10.1103/physrevlett.98.230601
53. Hutt A, and Lefebvre J. Additive Noise Tunes the Self-Organization in Complex Systems. In: Hutt A and Haken H, editors. *Synergetics, Encyclopedia of Complexity and Systems Science Series*. New York: Springer (2020). p. 183–95. doi:10.1007/978-1-0716-0421-2_696
54. Lefebvre J, Hutt A, Knebel J-F, Whittingstall K, and Murray MM. Stimulus Statistics Shape Oscillations in Nonlinear Recurrent Neural Networks. *J Neurosci* (2015) 35:2895–903. doi:10.1523/jneurosci.3609-14.2015
55. Hutt A, Mierau A, and Lefebvre J. Dynamic Control of Synchronous Activity in Networks of Spiking Neurons. *PLoS One* (2016) 11:e0161488. doi:10.1371/journal.pone.0161488
56. Hutt A, Sutherland C, and Longtin A. Driving Neural Oscillations with Correlated Spatial Input and Topographic Feedback. *Phys.Rev.E* (2008) 78: 021911. doi:10.1103/physreve.78.021911
57. Hashemi M, Hutt A, and Sleigh J. How the Cortico-Thalamic Feedback Affects the EEG Power Spectrum over Frontal and Occipital Regions during Propofol-Induced Sedation. *J Comput Neurosci* (2015) 39:155–79. doi:10.1007/s10827-015-0569-1
58. Klöden PE, and Platen E. *Numerical Solution of Stochastic Differential Equations*. Heidelberg: Springer-Verlag (1992).
59. Fries P, Reynolds J, Rorie A, and Desimone R. Modulation of Oscillatory Neuronal Synchronization by Selective Visual Attention. *Science* (2001) 291: 1560–3. doi:10.1126/science.1055465
60. Tononi G. An Information Integration Theory of Consciousness. *BMC Neurosci* (2004) 5:42. doi:10.1186/1471-2202-5-42
61. Alkire MT, Hudetz AG, and Tononi G. Consciousness and Anesthesia. *Science* (2008) 322:876–80. doi:10.1126/science.1149213
62. Lee M, Sanders RD, Yeom S-K, Won D-O, Seo K-S, Kim HJ, et al. Network Properties in Transitions of Consciousness during Propofol-Induced Sedation. *Sci Rep* (2017) 7:16791. doi:10.1038/s41598-017-15082-5
63. Massimini M, Ferrarelli F, Huber R, Esser SK, Singh H, and Tononi G. Breakdown of Cortical Effective Connectivity during Sleep. *Science* (2005) 309: 2228–32. doi:10.1126/science.1117256
64. Wollstadt P, Sellers KK, Rudelt L, Priesemann V, Hutt A, Fröhlich F, et al. Breakdown of Local Information Processing May Underlie Isoflurane Anesthesia Effects. *Plos Comput Biol* (2017) 13:e1005511. doi:10.1371/journal.pcbi.1005511
65. Lizier JT, Prokopenko M, and Zomaya AY. Local Measures of Information Storage in Complex Distributed Computation. *Inf Sci* (2012) 208:39–54. doi:10.1016/j.ins.2012.04.016
66. Wibral M, Lizier JT, Vögler S, Priesemann V, and Galuske R. Local Active Information Storage as a Tool to Understand Distributed Neural Information Processing. *Front Neuroinform* (2014) 8:1. doi:10.3389/fninf.2014.00001
67. Ince RAA, Giordano BL, Kayser C, Rousselet GA, Gross J, and Schyns PG. A Statistical Framework for Neuroimaging Data Analysis Based on Mutual Information Estimated via a Gaussian Copula. *Hum Brain Mapp* (2017) 38: 1541–73. doi:10.1002/hbm.23471
68. Wibral M, Pampu N, Priesemann V, Siebenhühner F, Seiwert H, Lindner RV, et al. Measuring Information-Transfer Delays. *PLoS One* (2013) 8:e55809. doi:10.1371/journal.pone.0055809
69. Risken H. *The Fokker-Planck Equation — Methods of Solution and Applications*. Berlin: Springer (1989).
70. Arnold L. *Random Dynamical Systems*. Berlin: Springer-Verlag (1998).
71. Xu C, and Roberts AJ. On the Low-Dimensional Modelling of Stratonovich Stochastic Differential Equations. *Physica A: Stat Mech its Appl* (1996) 225: 62–80. doi:10.1016/0378-4371(95)00387-8
72. Derrida B, Gardner E, and Zippelius A. An Exactly Solvable Asymmetric Neural Network Model. *Europhys Lett* (1987) 4:187. doi:10.1209/0295-5075/4/2/007

73. Touboul JD, Piette C, Venance L, and Ermentrout GB. Noise-Induced Synchronization and Antiresonance in Interacting Excitable Systems: Applications to Deep Brain Stimulation in Parkinson's Disease. *Phys Rev X* (2019) 10:011073. doi:10.1103/PhysRevX.10.011073
74. El Boustani S, and Destexhe A. A Master Equation Formalism for Macroscopic Modeling of Asynchronous Irregular Activity States. *Neural Comput* (2009) 21:46–100. doi:10.1162/neco.2009.02-08-710
75. Soula H, and Chow CC. Stochastic Dynamics of a Finite-Size Spiking Neural Network. *Neural Comput* (2007) 19:3262–92. doi:10.1162/neco.2007.19.12.3262
76. Montbrio E, Pazo D, and Roxin A. Macroscopic Description for Networks of Spiking Neurons. *Phys Rev X* (2015) 5:021028. doi:10.1103/physrevx.5.021028
77. Brunel N, and Hakim V. Fast Global Oscillations in Networks of Integrate-And-Fire Neurons with Low Firing Rates. *Neural Comput* (1999) 11:1621–71. doi:10.1162/089976699300016179
78. Roxin A, Brunel N, and Hansel D. Rate Models with Delays and the Dynamics of Large Networks of Spiking Neurons. *Prog Theor Phys Suppl* (2006) 161: 68–85. doi:10.1143/ptps.161.68
79. Fourcaud N, and Brunel N. Dynamics of the Firing Probability of Noisy Integrate-And-Fire Neurons. *Neural Comput* (2002) 14:2057–110. doi:10.1162/089976602320264015
80. di Volo M, and Torcini A. Transition from Asynchronous to Oscillatory Dynamics in Balanced Spiking Networks with Instantaneous Synapses. *Phys Rev Lett* (2018) 121:128301. doi:10.1103/physrevlett.121.128301
81. Arenas A, Díaz-Guilera A, Kurths J, Moreno Y, and Zhou C. Synchronization in Complex Networks. *Phys Rep* (2008) 469:93–153. doi:10.1016/j.physrep.2008.09.002
82. Della Rossa F, and DeLellis P. Stochastic Master Stability Function for Noisy Complex Networks. *Phys Rev E* (2020) 101:052211. doi:10.1103/PhysRevE.101.052211
83. Hellwig B. A Quantitative Analysis of the Local Connectivity between Pyramidal Neurons in Layers 2/3 of the Rat Visual Cortex. *Biol Cybern* (2000) 82:111–21. doi:10.1007/pl00007964
84. Yan G, Martinez ND, and Liu Y-Y. Degree Heterogeneity and Stability of Ecological Networks. *J R Soc Interf* (2017) 14:20170189. doi:10.1098/rsif.2017.0189
85. Hutt A, and Buhry L. Study of GABAergic Extra-synaptic Tonic Inhibition in Single Neurons and Neural Populations by Traversing Neural Scales: Application to Propofol-Induced Anaesthesia. *J Comput Neurosci* (2014) 37:417–37. doi:10.1007/s10827-014-0512-x
86. Brunel N. Dynamics of Sparsely Connected Networks of Excitatory and Inhibitory Spiking Neurons. *J Comput Neurosci* (2000) 8:183–208. doi:10.1023/a:1008925309027
87. Steinmetz PN, Roy A, Fitzgerald PJ, Hsiao SS, Johnson KO, and Niebur E. Attention Modulates Synchronized Neuronal Firing in Primate Somatosensory Cortex. *Nature* (2000) 404:187–90. doi:10.1038/35004588
88. Coull J. Neural Correlates of Attention and Arousal: Insights from Electrophysiology, Functional Neuroimaging and Psychopharmacology. *Prog Neurobiol* (2019) 55:343–61. doi:10.1016/s0301-0082(98)00011-2
89. Lakatos P, Szilágyi N, Pincze Z, Rajkai C, Ulbert I, and Karmos G. Attention and Arousal Related Modulation of Spontaneous Gamma-Activity in the Auditory Cortex of the Cat. *Cogn Brain Res* (2004) 19:1–9. doi:10.1016/j.cogbrainres.2003.10.023
90. Kinomura S, Larsson J, Guly s Bz., and Roland PE. Activation by Attention of the Human Reticular Formation and Thalamic Intralaminar Nuclei. *Science* (1996) 271:512–5. doi:10.1126/science.271.5248.512
91. Galbraith GC, Olfman DM, and Huffman TM. Selective Attention Affects Human Brain Stem Frequency-Following Response. *Neuroreport* (2003) 14: 735–8. doi:10.1097/00001756-200304150-00015
92. Koval'zon V. Ascending Reticular Activating System of the Brain. *Transl Neurosci Clin* (2016) 2:275–85. doi:10.18679/CN11-6030/R.2016.034
93. Serences JT. Neural Mechanisms of Information Storage in Visual Short-Term Memory. *Vis Res* (2016) 128:53–67. doi:10.1016/j.visres.2016.09.010

Conflict of Interest: JH was employed by Hyland Switzerland Sarl.

The remaining authors declare that the research was conducted in the absence of any commercial or financial relationships that could be construed as a potential conflict of interest.

frontiers in Systems Neuroscience

ORIGINAL RESEARCH
published: 29 July 2021
doi: 10.3389/fnsys.2021.705371

Information Transmission in Delay-Coupled Neuronal Circuits in the Presence of a Relay Population

Jaime Sánchez-Claros[1], *Aref Pariz*[2,3], *Alireza Valizadeh*[2], *Santiago Canals*[4] and *Claudio R. Mirasso*[1]*

[1] Instituto de Física Interdisciplinar y Sistemas Complejos (IFISC, UIB-CSIC), Campus UIB, Palma de Mallorca, Spain, [2] Institute for Advanced Studies in Basic Sciences, Zanjan, Iran, [3] Department of Biology, University of Ottawa, Ottawa, ON, Canada, [4] Instituto de Neurociencias, Consejo Superior de Investigaciones Científicas, Universidad Miguel Hernández, Sant Joan d'Alacant, Spain

Synchronization between neuronal populations is hypothesized to play a crucial role in the communication between brain networks. The binding of features, or the association of computations occurring in spatially segregated areas, is supposed to take place when a stable synchronization between cortical areas occurs. While a direct cortico-cortical connection typically fails to support this mechanism, the participation of a third area, a relay element, mediating in the communication was proposed to overcome this limitation. Among the different structures that could play the role of coordination during the binding process, the thalamus is the best placed region to carry out this task. In this paper we study how information flows in a canonical motif that mimics a cortico-thalamo-cortical circuit composed by three mutually coupled neuronal populations (also called the V-motif). Through extensive numerical simulations, we found that the amount of information transferred between the oscillating neuronal populations is determined by the delay in their connections and the mismatch in their oscillation frequencies (detuning). While the transmission from a cortical population is mostly restricted to positive detuning, transmission from the relay (thalamic) population to the cortical populations is robust for a broad range of detuning values, including negative values, while permitting feedback communication from the cortex at high frequencies, thus supporting robust bottom up and top down interaction. In this case, a strong feedback transmission between the cortex to thalamus supports the possibility of robust bottom-up and top-down interactions in this motif. Interestingly, adding a cortico-cortical bidirectional connection to the V-motif (C-motif) expands the dynamics of the system with distinct operation modes. While overall transmission efficiency is decreased, new communication channels establish cortico-thalamo-cortical association loops. Switching between operation modes depends on the synaptic strength of the cortico-cortical connections. Our results support a role of the transthalamic V-motif in the binding of spatially segregated cortical computations, and suggest an important regulatory role of the direct cortico-cortical connection.

Keywords: delay-coupled neuronal circuits, information transmission, synchronization, V and circular motifs, feature binding problem, thalamo-cortical circuit

OPEN ACCESS

Edited by:
Serhiy Yanchuk,
Technical University of Berlin,
Germany

Reviewed by:
Rico Berner,
Technische Universität Berlin,
Germany
Otti D'Huys,
Maastricht University, Netherlands

***Correspondence:**
Claudio R. Mirasso
claudio@ifisc.uib-csic.es

Received: *05 May 2021*
Accepted: *30 June 2021*
Published: *29 July 2021*

Citation:
Sánchez-Claros J, Pariz A, Valizadeh A, Canals S and Mirasso CR (2021) Information Transmission in Delay-Coupled Neuronal Circuits in the Presence of a Relay Population. Front. Syst. Neurosci. 15:705371. doi: 10.3389/fnsys.2021.705371

1. INTRODUCTION

The synchronization of neuronal populations is a ubiquitous phenomenon in the brain circuits. The correlated activity of neurons in local networks gives rise to the appearance of brain oscillations over different frequency ranges (Başar et al., 2000; Pfurtscheller et al., 2000; Başar, 2012; Jensen et al., 2019). Based on the coherence and phase relations between oscillations in different brain regions, it has been proposed that information transmission and even directionality can be modulated (Eckhorn et al., 1988; Pfurtscheller et al., 2000; Gross et al., 2001; Fries, 2015; Maris et al., 2016). As a consequence, coherent activity in brain networks is hypothesized to underlie several cognitive phenomena such as features binding (Singer, 2007; Opitz, 2010; Coll et al., 2018), attention (Borisyuk et al., 1999; Niebur, 2002; Doesburg et al., 2008), working memory (Baddeley, 1992, 2010; Baddeley and Hitch, 2010) and motor function (Feige et al., 2000; Baker et al., 2003; Denker et al., 2007), among others.

An interesting case of the synchrony between different brain regions is the zero-lag synchronization, which can be observed even between distant cortical areas (Chawla et al., 2001; Vicente et al., 2008; Viriyopase et al., 2012; Esfahani and Valizadeh, 2014; Gollo et al., 2014), representing a suitable mechanism for the binding of sensory features into integrated and coherent perception. This phenomenon has been subject of controversial debate for many years: how two distant brain areas can synchronize at (almost) zero-lag despite the presence of non-negligible delays in their connections (Vicente et al., 2008; Viriyopase et al., 2012). However, a relatively simple and widespread motif found in neural circuits, a chain of three mutually delay-coupled oscillatory populations has been shown to support zero-lag synchronization (Fischer et al., 2006; Uhlhaas et al., 2009; Gollo et al., 2014). The biological relevance of such connectivity pattern, usually called V-motif, is justified for instance in the cortico-thalamic loops. The V-motif can determine a cortico-thalamo-cortical circuit in which the thalamus plays the role of the intermediate element (higher order relay) indirectly connecting two cortical regions (Save and Poucet, 2000; Uhlhaas et al., 2009; Sherman, 2012; Sysoeva et al., 2016). The V-motif circuit attracted much interest in recent years and several studies have been devoted to the exploration of its dynamical properties, either considering single neurons/oscillators or neural populations (Sporns and Kötter, 2004; Fischer et al., 2006; Esfahani and Valizadeh, 2014; Mirasso et al., 2017).

The addition of a cortico-cortical connection, that is known to play an important role in cortical circuits, transforms the V-motif into a circular motif (C-motif). In fact, this extension of the V-motif finds a counterpart in biological cortico-thalamic circuits (Sherman, 2016). Indeed, interaction between the direct cortico-cortical and the indirect transthalamic pathways, which converge onto individual postsynaptic cells in layer 4 of the cortex (Lee and Sherman, 2008; De Pasquale and Sherman, 2011), is hypothesized to have an important role in information transfer between areas (Sherman, 2016).

Although the structure of the adult brain does not change in short time scales, the efficacy of the synaptic connections and the excitation/inhibition balance are subject to continuous change and can evolve almost instantaneously, enabling the brain to flexibly exploit the fixed structure in a multiplex of tasks (Friston, 1994, 2011; Deco et al., 2008; Hutchison et al., 2013; Avena-Koenigsberger et al., 2018) According to communication through coherence (CTC) theory, the synchrony and phase relationship between neuronal populations can modulate the effective connectivity between brain areas and the direction of the information transfer in brain circuits (Fries, 2015). This means that a change in the phase difference due to changes in the network parameters affects the effective connectivity, a fact that has been shown in several computational studies in two-component networks (Barardi et al., 2014; Sancristóbal et al., 2014; Kirst et al., 2016; Palmigiano et al., 2017; Pariz et al., 2018, 2021). It is natural then to explore the effective connectivity in the proposed cortico-thalamic-cortical circuit since its structure influences the phase relationships between the regions. It is known that the arrangement of the three neural populations in a V-motif favors the state of zero-lag synchronization between outer populations. However, the effective connectivity in this network is poorly understood and we did not find studies that address how information is transmitted in this neural population network, as well as in other three-component networks. In fact, most studies of functional connectivity have focused on two-component motifs, as mentioned before, and the consequences of pairwise communication on patterns transferred in larger networks (Barardi et al., 2014; Sancristóbal et al., 2014; Kirst et al., 2016; Palmigiano et al., 2017; Pariz et al., 2018, 2021). Since the CTC theory predicts the modulation of the effective connectivity due to changes in the phase relationships, we wonder how communication is affected in the V-motif, as well as in the C-motif, due to frequency detuning and communication delays.

In this study, we address the previous question by considering a network of three mutually delay-coupled neural populations arranged in a V-motif. We further analyze how a direct and reciprocal cortico-cortical connection affects on our results. We systematically explored the effect that a change in the connections delay and detuning between the natural oscillation frequencies of the populations have in the transmission of signals in these particular motifs. Our results show in the case of the V-motif that for small delays, an efficient transmission is achieved when the sender population oscillates faster than the receiver ones, in a good agreement with previous results (Barardi et al., 2014; Sancristóbal et al., 2014; Kirst et al., 2016; Pariz et al., 2018, 2021). For intermediate delays and when the sender population is the relaying node, a good transmission quality is obtained even if its oscillation frequency is slower than that of the receiver. However, the picture drastically changes when the signal is added to one of the outer populations. In this case, an efficient transmission only happens, for any delay, for positive values of the detuning, i.e., when the sender population oscillates with a higher frequency than the others. We discuss these results in the context of the known anatomy of the cortico-thalamo-cortical loop and its hypothesized functions.

The paper is organized as follows. In section 2 we present the material and methods used to model our system. In section 3 we describe the tools we used to analyze the results obtained, which

are presented in detail in section 4. Finally, in section 5 we discuss some of the main results and highlight some conclusions.

2. MATERIALS AND METHODS

2.1. Neural Model

Our neural population model is similar to the one used in Pariz et al. (2018) which employs the Hodgkin-Huxley neuron model (Hodgkin and Huxley, 1952). This model describes the evolution of the membrane potential and the gate variables as follows

$$\begin{aligned} C\frac{dv}{dt} &= -g_K n^4(v-E_k) - g_{Na}m^3h(v-E_{Na}) \\ &\quad - g_L(v-E_L) + I_{\text{ext}} + I_{\text{syn}} + I_{\text{noise}}, \\ \frac{dn}{dt} &= \alpha_n(v)(1-n) - \beta_n(v), \\ \frac{dm}{dt} &= \alpha_m(v)(1-m) - \beta_m(v), \\ \frac{dh}{dt} &= \alpha_h(v)(1-h) - \beta_h(v). \end{aligned} \tag{1}$$

The functions α_x and β_x, $x = n, m, h$, are define as

$$\begin{aligned} \alpha_n(v) &= \frac{(v+55)/100}{1-\exp(-(v+55)/100)}, \\ \alpha_m(v) &= \frac{(v+40)/10}{1-\exp(-(v+40)/100)}, \\ \alpha_h(v) &= 0.07\exp\left(\frac{-(v+65)}{20}\right), \\ \beta_n(v) &= \frac{1}{80}\exp\left(\frac{-(v+65)}{80}\right), \\ \beta_m(v) &= 4\exp\left(\frac{-(v+65)}{18}\right), \\ \beta_h(v) &= \frac{1}{1+\exp(-(v+35)/10)}, \end{aligned} \tag{2}$$

where I_{ext}, I_{syn} and I_{noise} are the injected input current, the synaptic current and the gaussian white noise current, respectively. The values the parameters used in our calculations are shown in **Table 1** (Pariz et al., 2021).

The synaptic current $I_{\text{syn},i}$ of the i-th post-synaptic neuron is modeled as

$$\begin{aligned} I_{\text{syn},i} &= \sum_j g_{ij}S_{ij}(t)(v_i - E_{\text{syn},j}), \\ S_{ij}(t) &= \frac{1}{A}\left[\exp\left(\frac{-(t-t_j^*-\tau_{ij})}{\tau_r}\right) - \exp\left(\frac{-(t-t_j^*-\tau_{ij})}{\tau_d}\right)\right], \\ A &= \left(\frac{\tau_r}{\tau_d}\right)^{\frac{\tau_r}{\tau_d-\tau_r}} - \left(\frac{\tau_r}{\tau_d}\right)^{\frac{\tau_d}{\tau_d-\tau_r}}, \end{aligned} \tag{3}$$

where v_i is the membrane potential of the post-synaptic neuron and $E_{\text{syn},j}$ is the reversal synaptic potential of the post-synaptic neuron. The dynamics of S_{ij} is described by a double-exponential function, modeling the efficacy of AMPA and $GABA_a$ chemical synapses (Pariz et al., 2021). Variable t_j^* represents the time at which the j-th pre-synaptic neuron spikes and τ_{ij} is the axonal delay between the pre- and post-synaptic neurons. The values of the synaptic parameters are also given in **Table 1**.

TABLE 1 | Parameters of the model.

C	1 μF/cm^2	Capacitance
g_K	36 μS/cm^2	K conductance
g_{Na}	120 μS/cm^2	Na conductance
g_L	0.3 μS/cm^2	Leak conductance
E_K	–77 mV	K reversal potential
E_{Na}	50 mV	Na reversal potential
E_L	–54.4 mV	Leak reversal potential
$E_{\text{syn},E}$	0 mV	Excitatory reversal potential
$E_{\text{syn},I}$	–80 mV	Inhibitory reversal potential
τ_{inter}	0–14 ms	Inter population delay
τ_{intra}	0.5 ms	Intra population delay
τ_d	3 ms	Synaptic decay time
τ_r	0.5 ms	Synaptic rise time
I_{ext}	10–12 μA/cm^2	Injected current
μ	0 μA/cm^2	Median of the gaussian white noise
σ	0.5 μA/cm^2	Standard Deviation of the gaussian white noise
g_{EE}	3.75 μS/cm^2	Synaptic weight: excitatory → excitatory
g_{EI}	7.5 μS/cm^2	Synaptic weight: excitatory → inhibitory
g_{IE}	15 μS/cm^2	Synaptic weight: inhibitory → excitatory
g_{II}	15 μS/cm^2	Synaptic weight: inhibitory → inhibitory

2.2. Population Architecture

Each population is composed of 100 neurons described by the Hodgkin-Huxley equations, where 80 are considered as excitatory and 20 as inhibitory. Each neuron is randomly connected to 10% (5%) of neurons in the same (different) population. The intra-population delay is set to 0.5 ms and the inter-population delay τ is varied from 0 to 14 ms. While the intra-population connections are both excitatory and inhibitory, the inter-population connections are assumed to be only excitatory. In **Figure 1** we schematically represent the three populations and their connections.

Each neuron receives an external constant injection current, bias current, that varies between 10 and 12 μA/cm^2. Additionally, each neuron receives a Gaussian white noise current with zero mean (μ = 0 μA/cm^2), and standard deviation σ = 0.5 μA/cm^2. Since the level of coherency and synchronization is very high (Pariz et al., 2021) we can consider each population as a collective oscillator with a well-defined frequency. For the values of the parameters we have chosen and depending on the bias current,

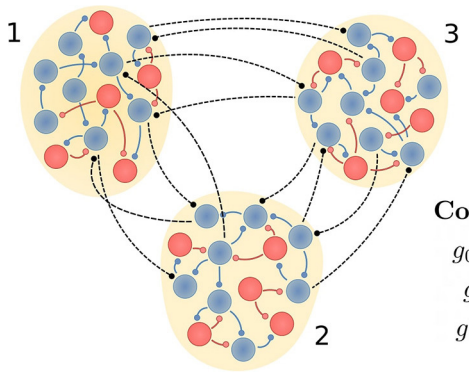

FIGURE 1 | Schematic representation of the circuit. Neural populations 1 and 3 would represent cortical areas and the population 2 the thalamus. Excitatory and inhibitory neurons (as well as their synaptic projections) are shown in blue and red, respectively. Inter-population connections are only excitatory and, depending on the case of interest, their synaptic weights are modified. If the connections between populations 1 and 3 are absent, then we call it a V-motif circuit. Otherwise, the circuit is a circular motif (C-motif).

the oscillation frequency varies linearly from 68 to 73 Hz (see **Supplementary Figure 1**).

We define the detuning or the frequency mismatch as the difference of the natural oscillation frequency of an isolated population with respect to those of the other populations. In our simulations, we drive the sender by external current I, and the other two populations by $I_0 = 11\mu\text{A/cm}^2$, where their difference $\Delta I = I - I_0$, sets the frequency detuning. When we apply a frequency mismatch to a certain population, we do it by changing the bias current of all the neurons in that population and keeping that of the neurons of the other populations fixed at I_0. To measure the transmission of signals we apply two types of perturbations, a slow (5 Hz) aperiodic signal and a fast pulsating signal ($\sim$ 70 Hz).

2.3. Simulations

For the numerical implementation we used the Mil'shtein algorithm (Milshtein, 1975) with a time step Δt = 0.01 ms. The total simulation time used to analyze the transmission quality of a signal was different depending on whether the applied modulation was slow or fast. We used 6 s for the case of the slow signal-modulation and 4.2 s for fast signals. We varied the inter-population delay τ between populations and the detuning or frequency mismatch $\Delta\nu$ (or equivalently ΔI) of the sender population. All the simulations were performed in Brian simulator (Goodman and Brette, 2009) written in the Python programming language.

3. ANALYSIS

Our analysis was done using an approximation of the firing rate $r(t)$. We computed first the multi unit activity $s(t)$ as the total number of spikes that occur between t and $t + \Delta t$. For each neural population, the firing rate r was computed as follows (Dayan and Abbott, 2001),

$$r(t) = \frac{1}{N\Delta t}\int_{-\infty}^{\infty} s(t-t')w(t')dt', \tag{4}$$

where N is the total number of neurons in the population. This integral is called linear filter, and the window function $w(t)$ is called the filter kernel which is considered here as a Gaussian function. We used $\sigma = 2$ ms and $\sigma = 100$ ms when fast and slow signals are injected to the system, respectively. In the absence of an external signal, $\sigma = 2$ ms was also considered to compute the firing rate.

3.1. Phase Difference

The phase of each neural population was computed from its collective oscillatory firing rate by the interpolation

$$\theta(t) = 2\pi\left(\frac{t - t_{\max,k}}{t_{\max,k+1} - t_{\max,k}}\right), \tag{5}$$

for $t_{\max,k} \leq t < t_{\max,k+1}$, where $\{t_{\max,k}, k = 1, ..., k_{\max}\}$ are the relative maxima of the time series. So $t_{\max,k}$ denotes the initial time of the k-th oscillation cycle of the firing rate. This definition works independently of the periodicity of the time series. This approximated phase adapts to possible variations in the cycle duration. The phase difference between two populations, i and j, is then given by

$$\theta_{ij}(t) = \text{mod}[\theta_i(t) - \theta_j(t), 2\pi], \tag{6}$$

which was further shifted to be defined in the interval $[-\pi, \pi)$. Then, the representative phase difference between the oscillations of a given pair of populations was set to be the median of the time series $\theta_{ij}(t)$.

3.2. Phase Locking

To quantify the phase locking between two populations, we estimated how the phase difference distribution $\{p_{\theta_{ij},k}\}$ approximated the perfect locked distribution, *i.e.*, a delta-Dirac function. To this end we computed the Bhattacharyya coefficient (Kailath, 1967). Given two discrete probability distributions $\{q_k\}$ and $\{h_k\}$ $(k = 1, 2, \ldots, n)$, this coefficient is defined by

$$B(\{q_k\}, \{h_k\}) = \sum_{k=1}^{n} \sqrt{q_k h_k}. \tag{7}$$

Note that when the two distributions are identical $B = 1$ while two orthogonal distributions have $B = 0$.

In our analysis, the perfect locked distribution was defined as

$$\delta_k = \begin{cases} 1 & \text{if } k = k^*\text{: } p_{\theta_{ij},k^*} = \max_k\left(p_{\theta_{ij},k}\right) \\ 0 & \text{otherwise} \end{cases} \tag{8}$$

So, considering equation (8), we defined our phase-locking index as

$$\mathcal{D}_{ij} = 1 - B(\{p_{\theta_{ij},k}\}, \{\delta_k\}) = 1 - \sqrt{\max_k\left(\theta_{ij,k}\right)}. \tag{9}$$

Therefore, perfect locking implies $\mathcal{D} = 0$ and the maximum value is $1 - 1/\sqrt{n}$ when the distribution is uniform. This index allowed us to estimate the stable-unstable region frontiers. When $\mathcal{D}$ is approximately 0.35 phase-drift effects start to appear in the dynamics, and so, we used this value to delimit these frontiers.

3.3. Time-Delayed Mutual Information

For slow modulation, we measured the information shared by the populations considering their firing rates. Specifically, this information transfer was computed via the time-delayed mutual information dMI of populations i and j (Kirst et al., 2016; Pariz et al., 2021). The dMI considers the instantaneous firing rates $x_i(t)$ and the lagged firing rate $x_j(t + \delta)$, being δ the time lag. The dMI expression is given by

$$\mathrm{dMI}_{ij}(\delta) = \int\int p_{ij^{(\delta)}}(t) \log\left(\frac{p_{ij^{(\delta)}}(t)}{p_i(t)p_j(t)}\right) dx_i(t)dx_j(t+\delta), \quad (10)$$

where $p_a(t)$ is the probability distribution of $x_a(t)$, with $a = i, j$, and $p_{i,j^{(\delta)}}(t)$ the joint distribution between $x_i(t)$ and $x_j(t + \delta)$. Asymmetries in $\mathrm{dMI}_{i,j}(\delta)$ indicate a dominant direction in which the information is shared or transferred between the populations. Therefore, we quantified these asymmetries by using the difference

$$\begin{aligned} \Delta\mathrm{MI}_{ij} &= \mathrm{MI}_{i\to j} - \mathrm{MI}_{j\to i}, \\ \mathrm{MI}_{i\to j} &= \int_0^\infty \mathrm{dMI}_{ij}(\delta)\mathrm{d}\delta, \\ \mathrm{MI}_{j\to i} &= \int_{-\infty}^0 \mathrm{dMI}_{ij}(\delta)\mathrm{d}\delta. \end{aligned} \quad (11)$$

If $\Delta\mathrm{MI}_{ij}$ is positive, the information is mainly transferred from the population i to j, while a negative value indicates the opposite direction. Additionally, the higher this quantity, the better the transmission, and vice versa.

The number of bins of the probability distributions were computed by the algorithm described in Hacine-Gharbi et al. (2012). The maximum lag we considered for computing the time-delayed mutual information was 200 ms which is the period of the slow modulation (5 Hz).

For each value of the difference $\Delta\mathrm{MI}_{i,j}$ computed, we determined whether or not it is statistically significant. To check this, we obtained the null-hypothesis distribution (lack of functional coupling). We generated 5,000 surrogates by a permutation technique of the time-series to build this distribution. After that, $\Delta\mathrm{MI}_{i,j}$ values whose p-values were more than 0.05 were removed as an indicative of no statistically significance. For plot representation, we further applied a clustering algorithm to remove outliers that appeared.

3.4. Cross-Covariance

The cross-covariance quantifies the similarity between two time series as a function of the relative time distance between them. We used this quantity to determine the similarity between the firing rate of the receiving population with the external slow modulation. We assumed that the quality of the transmission is better if the firing rate follows the signal. We considered the non-normalized zero-lag cross-covariance (ZLC) to also detect differences in amplitude between the signals.

3.5. Phase Response Curve of the Population

When we considered the transmission of a fast signal, we used the phase response curve of the oscillating populations to quantify the quality of the transmitted signal. The phase response curve (PRC) is defined as the phase shift of an oscillation resulting from the application of an external perturbation with respect to the unperturbed case, as a function of the time at which the perturbation is applied (Ko and Ermentrout, 2009). This quantity is usually defined considering an isolated oscillator. However, in our system, each population (a collective oscillator) is coupled to one or two populations. To measure the response of a population to an injected pulse, we should proceed in a different way as it is usually done in the isolated case. Recent studies have proposed to measure information directionality based on the PRCs in a circuit of two mutually coupled oscillators under the weak coupling condition (Dumont and Gutkin, 2019).

The effect of an external perturbation in the sender population is quantified by the local phase response curve (lPRC), while that in the receiver populations is characterized by the non-local phase response curve (nPRC). The nPRC is defined as the response of an oscillator to a non-local perturbation (Schultheiss, 2012; Pariz et al., 2021). The process of finding the nPRC is similar to the PRC process, first we compute the positions of the peaks of the firing rate of all populations before applying the perturbation. Then, the perturbation pulse is applied at different phases (β) on all excitatory neurons of the first population, producing a change in the period of the oscillations. The effect of these phase changes, will propagate to the other populations, affecting the period of their oscillations. An important aspect is the axonal delay time between the populations. The response of the first population to the applied pulse will take an axonal delay time (τ) to reach the second population. By subtracting the periods of oscillation of the second and third populations, with and without the injected perturbation on the first population, gives the nPRC. In our study, we went one step further. Instead of applying the pulse at different phases and repeating the simulation to find the nPRC, we distributed the phase of the injected pulse along the oscillating period of the receiver population, considering the perturbation as a fast applied signal. The width of each pulse was taken as 2 ms and the amplitude as 0.25 μA/cm^2.

We then quantified the information transmission Z_i as

$$Z_i = \int_0^{2\pi} |\mathrm{nPRC}_i(\beta)| d\beta, \quad (12)$$

where the nPRC measurements were first fitted to a 4th-order Fourier series function.

4. RESULTS

In this section we study how a signal injected in population 1 or 2 is transmitted to the rest of the populations in the circuit.

We mainly analyze the transmission when there is a frequency detuning between the oscillation frequencies of the populations and the transmission time of the signal between populations is non-zero. We consider two particular circuits: the V-motif and the C-motif (see **Figure 1**).

4.1. Synchronization and Phase-Locking in the V-Motif Circuit

We start showing our results for the case of the V-motif, i.e., when the cortico-cortical connections were neglected. ($g_{13} = g_{31} = 0$ μS/cm^2). We assume here that the coupling strengths between populations are symmetric, i.e. $g_{12} = g_{21} = g_{23} = g_{32}$ (results for asymmetric cases are shown in the **Supplementary Material**). As we mentioned before (see Methods), each isolated neural population exhibits a high synchronized behavior which is also kept when they are coupled (see Pariz et al., 2018). This fact allows us to determine the phase difference between the oscillations of the populations. Since we are interested in studying the information transmission from one outer population or from the relay population to the others, we must consider two situations for the analysis of the locking regions: when the frequency mismatch is applied to population 1 (or equivalently to population 3) and when it is applied to population 2. When analyzing the phase-locking regions, estimated by computing the phase-locking index (see Methods), with respect to our control parameters (τ and ΔI), three regions are generally found delimited by two non-locked regions (see **Figures 2A,E** and **Supplementary Figures 2–5**). The shape of the non-locked regions (and consequently of the phase-locking regions) changes as a function of the synaptic weight g and the induced frequency mismatch. However, the emergence of these regions is a general property of delay-coupled dynamical systems (Mirasso et al., 2017).

The locking regions between populations 1 and 2 (1 and 3) are shown in the ΔI vs. τ phase space in of **Figure 2E** when the detuning ΔI is applied in the population 1 and in **Figure 4** when applied in population 2. As expected, these locking regions are slightly larger between populations 1 and 2 than between populations 1 and 3 although a high value for the phase index is found in both cases. The phase at which the oscillations of populations 1 and 2 (1 and 3) lock are shown in **Figures 2B**, **4F**. In the absence of frequency mismatch $\Delta I = 0$, we observe the expected zero-lag synchronization between population 1 and 3. Also for small and high (close to the oscillation period) values of the delay, populations 1 and 2 are almost in-phase. However, for intermediate values they exhibit an anti-phase dynamics, as previously observed (Vicente et al., 2008; Esfahani and Valizadeh, 2014; Mirasso et al., 2017). Examples of the activity of the three populations and their firing rates can be seen in **Figures 3A–C** for differents values of the detuning when the connection delay is 6 ms. For $\Delta I \neq 0$ and for small or large delays, the locking phase is no longer zero but it is positive (delayed synchronization) for positive detuning and negative (anticipated synchronization) for negative detuning (Mirasso et al., 2017). It is worth mentioning that analysis considering different values of the coupling strength were undertaken obtaining qualitatively similar results to those shown in **Figure 2** (see **Supplementary Material**).

4.2. Information Transmission in the V-Motif Circuit

Depending on whether we analyze the transmission of a slow (modulation) or fast (chain of pulses) signal, we use different tools. The effect of the slow signal is translated into a modulation of the firing rate, keeping oscillation frequency of the population constant (in those cases where phase locking occurs), while each pulse of the fast signal modifies the period of an oscillation cycle. Therefore, these two effects occur at different time scales that require different tools to quantify them.

For the first case, as explained in the material and methods section, we used two different measurements: the zero-lag cross-covariance (ZLC) between the firing rate of the receiving population and the injected signal, and the difference ΔMI_{ij} computed from the time-delayed mutual information between the firing rates of the sender and receiver populations.

We show in **Figure 2** panels C and G, the results for the ΔMI_{ij} when the population 1 (cortical area) acts as the sender and a slow modulation signal is injected (locking areas from panel A and E are also included here with dashes lines). Also in the **Supplementary Figure 7** we have shown the results for asymmetric cases. The corresponding ZLC results are shown in **Supplementary Figure 6**.

Generally, regions with high values of ΔMI_{ij} in **Figure 2** and with high values of ZLC in **Supplementary Figure 6** qualitatively match despite the fact that they quantify different properties. The covariance determines the similarity of the activity between two populations, while the difference ΔMI_{ij} indicates directionality and strength of the transmission. However, we checked that these two quantities are more correlated the closer the phase-locking index tends to zero, i.e., perfect locking (see **Supplementary Figures 12–14**). Moreover, we found that in the cases where the values of ΔMI_{ij} and cross-covariance are the highest, the phase-locking index is very close or to zero, or equivalently, there is a constant well-defined phase relation. This result is in a good agreement with the Communication Through Coherence hypothesis (Fries, 2015), where a well-defined phase relation is required to enhance the communication between neural populations.

As it can be observed, the optimal way to transmit a slow modulation signal from 1 to 2 and then to 3 is by imposing a positive frequency mismatch (positive ΔI; higher oscillation frequency) in the sender population since for negative values of the frequency mismatch the transmission is very poor. These findings are in a good agreement with previous results (Pariz et al., 2018, 2021). Yellow points in **Figures 2C,G** refer to the selected values of the detuning ΔI which characterize the temporal series shown in **Figures 3D–F** for a delay $\tau = 6$ ms. For those points that lie within the red region in **Figure 3**, the firing rate of the receiver populations follows quite well the injected signal, while those outside the red regions do not. The fact that the $\Delta\text{MI}_{1,2}$ is high reflects the similarity between the slow variations in the firing rates of the two populations,

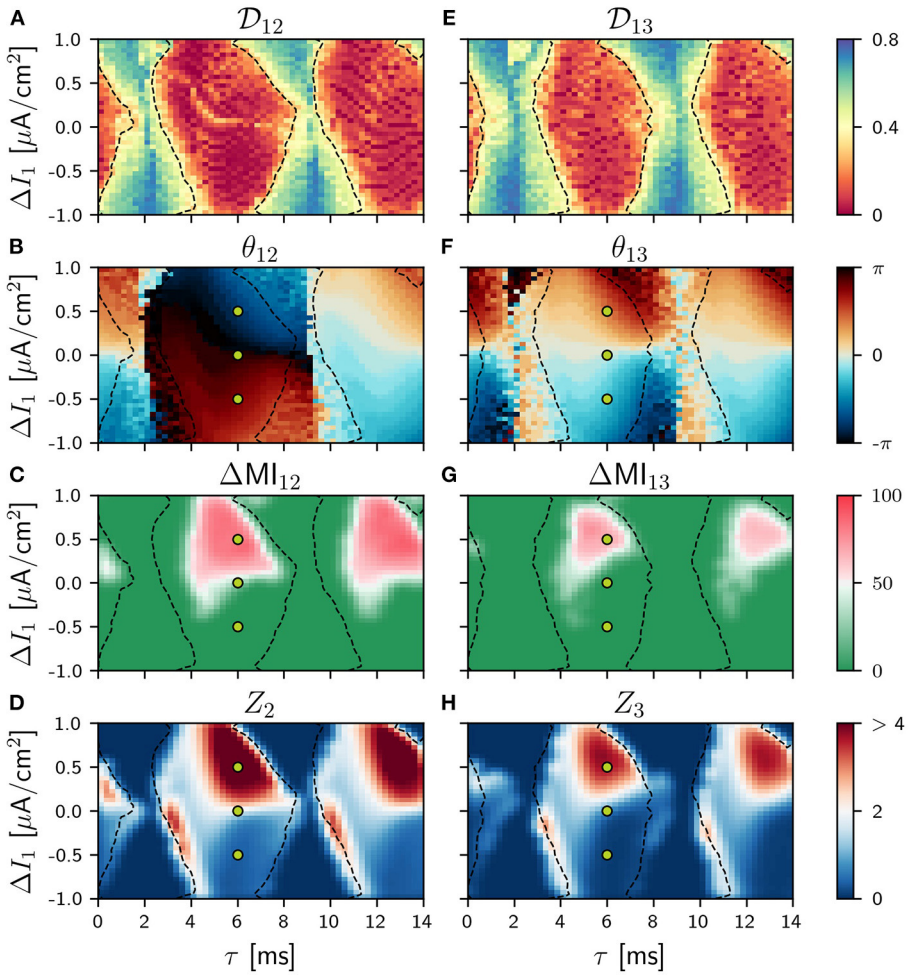

FIGURE 2 | Population 1 as the sender in the V-motif. Phase locking index $\mathcal{D}_{ij}$ **(A,E)**. Phase difference θ_{ij} **(B,F)**. Difference ΔMI_{ij} **(C,G)** when a slow modulation is injected. Integral of the absolute value of the nPRC Z_i **(D,H)** when a fast signal is injected. All of them as a function of the delay and the frequency mismatch ΔI in population 1.

at a time scale which is much longer than that of the gamma oscillations. Interestingly, for some cases of negative detuning the time evolution of the firing rates are quite similar to each other, however, none of them follow the injected signal (not shown).

Similar results were obtained when we injected a fast pulsating signal instead of the slow signal. For the fast signal injection, we computed the integral of the absolute value of the non-local phase response curve (nPRC) of the receiving populations (see Methods). The results are shown in **Figures 2D,H** where it can be observed that the regions where a better transmission occurs match quite well with those of the slow modulation case. For these colormaps, we impose $Z_i = 0$ when the resultant dynamics does not exhibit a PRC shape-like, assuming that there is no signal transmission. We also show some examples in **Figures 3G–I** of the lPRC of the sender population (blue) and the nPRCs of the receiving populations (orange and green) for the values of the parameters indicated in yellow in **Figures 2G,H**. For the points laying outside the locking areas, an analytical expression for the fitting cannot be obtained. In general we observed the information transmission, either rate or spike coding, changes with the strength g, improving as g increases (see **Supplementary Figure 8**).

The situation drastically changes when the sender is population 2 (the thalamus in our cortico-thalamic-cortical assumption) and the system maintains symmetry even when a frequency mismatch is applied.

The information transmission of a slow signal to both populations 1 and 3 are equivalent, as it can be seen in **Figures 4C,G** (see **Supplementary Figure 10** for asymmetric cases and **Supplementary Figure 9** for ZLC). Furthermore, the transmission is possible in this case even for negative values of the frequency mismatch for intermediate and long delays. This result is equivalent to the case of two mutually-coupled neural population reported in Pariz et al. (2021) and is a direct consequence of the symmetry of the system. However, we found that the capability of the signal transmission over this condition

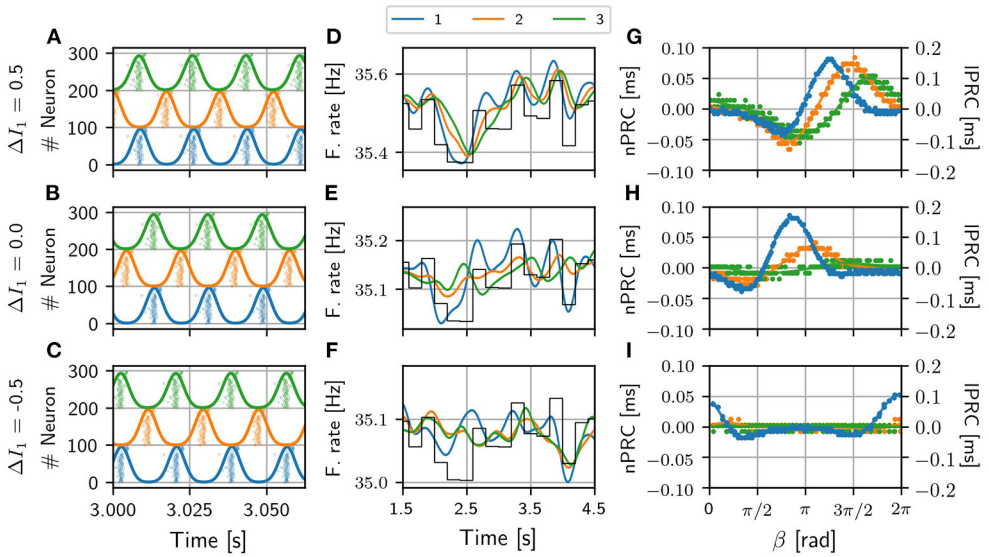

FIGURE 3 | V-motif. Examples of the activity of the three populations and their corresponding firing rate for different values of ΔI in the absence of an external signal **(A–C)**. Examples of firing rates of the three populations for different values of the frequency mismatch ΔI when a slow arbitrary signal (black line, arbitrary units) is applied to population 1 **(D–F)**. Examples of local and non-local phase response curves of the sender and receiving populations, respectively, for the same different values of frequency mismatch ΔI when a fast pulsating signal is applied in population 1 **(G–I)**. Note that the scale of IPRC and nPRC are different for a better visualization. Delay τ = 6 ms in all cases.

is reduced, as expected, as the cortico-thalamic synaptic strength increases (results not shown).

A similar behavior is observed when a fast arbitrary signal is injected, as it can be seen in **Figures 4D,H** where the patterns of Z_i are shown (see **Supplementary Figure 6** for asymmetric cases).

4.3. Synchronization and Phase-Locking in the Circular Motif Circuit

With the addition of a cortico-cortical connection, the circuit has now a ring topology. We considered four different values of the synaptic strength g' between the outer populations (= $g_{13} = g_{31}$): $0.05g_0$, $0.25g_0$, $0.50g_0$, $0.75g_0$, always weaker than the cortico-thalamic and the thalamo-cortical connections. The results presented in this section account only for two of these values, g=0.25 g_0 (low) and g=0.75 g_0 (high). Results for the other g's values are included in the **Supplementary Material**. The strength of the thalamo-cortical and the cortico-thalamic synapses is kept constant and equal to g_0. We proceed in the same way as before, analyzing first the phase differences distributions and the conditions of phase-locking in the parameter space. We show in **Figures 5**, **6** the phase-locking index and the phase differences for low and high values of cortico-cortical synaptic conductance g' when the detuning is applied in population 1 and 2, respectively (see **Supplementary Figures 15–18** for all the different values of g').

According to the coupled oscillators theory, in the absence of frequency mismatch, two identical and mutually coupled oscillators with delay in their connections can only be in two regimes of synchronization: in-phase and anti-phase (DHuys et al., 2008). Consequently, the addition of the third connection to our V-motif rises the competition between the V-motif dynamics and the dynamics preferred by the mutual coupling of the external populations. While the V-motif structure tends to synchronize populations 1 and 3 at zero-phase (or close to zero-phase) independently of the connection delay, the additional direct connection between populations 1 and 3 tends to synchronize them in anti-phase at intermediate delay values.

In our circular motif and for small values of the synaptic strength g' the effect of the new connections is very small, as it can be seen in **Figures 5A,B,E,F,H**. However, as soon as we increase g', its effect becomes noticeable in the phase differences and in the locking regions that reduced their size, as it can be seen in **Figures 5C,D,G,H**. The competition between the zero (or almost zero) phase locking of the V motif and the π (or almost π) phase locking of the mutually coupled populations only occurs in the interval of intermediate values of the delay, since for small and large delay values both systems exhibit in-phase dynamics. We observed, in this delay window, that the phase-locking index increased as the synaptic strength g' was increased (results not shown).

4.4. Information Transmission in the Circular Motif Circuit

As a consequence of the mentioned competition, the efficiency of the information transmission in the circuit is expected to be affected. Again, we explored the propagation of slow and fast signals when the sender was the population 1 or the population 2. The differences ΔMI_{ij} when the slow modulation was injected in population 1 are shown in **Figures 7A,E** for small g' and

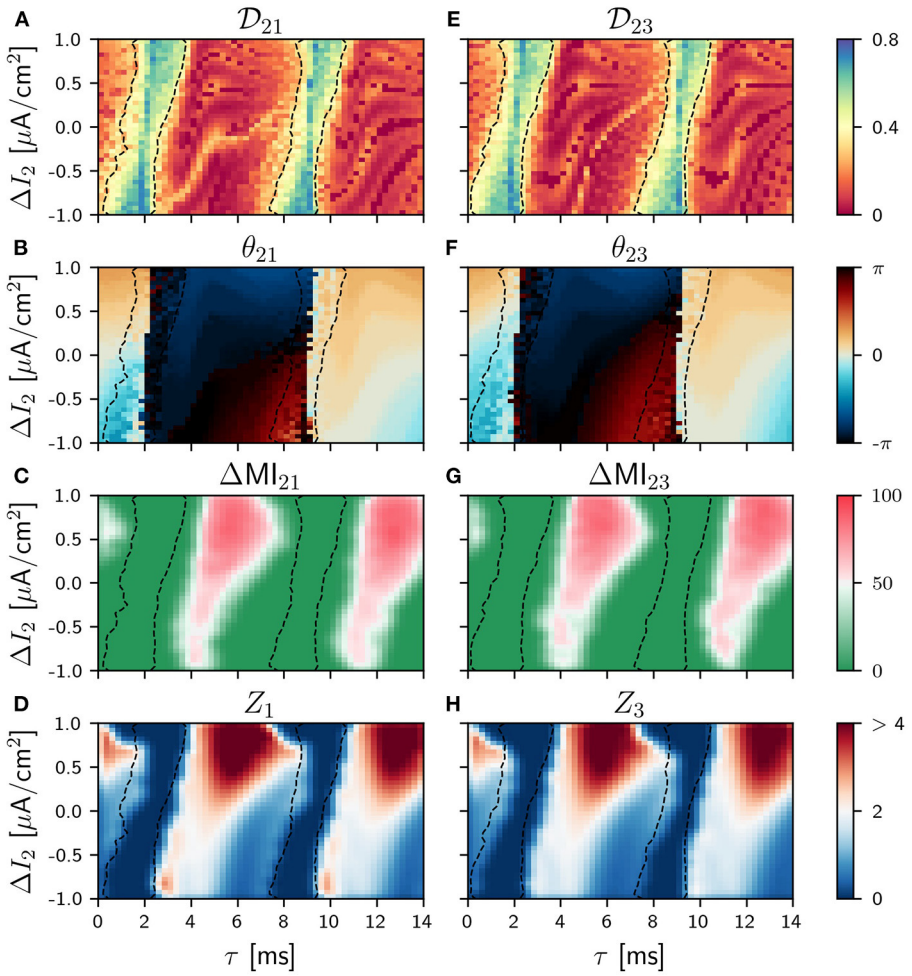

FIGURE 4 | Population 2 as the sender in the V-motif. Phase locking index $\mathcal{D}_{ij}$ **(A,E)**. Phase difference θ_{ij} **(B,F)**. Difference $\Delta\mathrm{MI}_{ij}$ **(C,G)** when a slow modulation is injected. Integral of the absolute value of the nPRC Z_i **(D,H)** when a fast signal is injected. All of them as a function of the delay and the frequency mismatch ΔI in population 2.

Figures 7C,G for large g' (see **Supplementary Figure 20** for all the values considered for g' and **Supplementary Figure 19** for the correspondant ZLC results). As it can be seen, the effect of the cortico-cortical connection is noticeable for $g' = 0.75g_0$. Comparing with the case in which $g' = 0.25g_0$, the shapes of the regions where the transmission is good for the intermediate delay values have changed, and the values of $\Delta\mathrm{MI}_{ij}$ (strength and directionality of the transmission) become smaller. However, the situation is very different with respect to the case of the V-motif, since now the transmission is enhanced for negative detuning (negative values of the current mismatch ΔI) both for populations 1 or 2 and 1 and 3. Furthermore, this effect is also noticeable for high values of delay. We observed in this case that the communication for negative detunings improves as the synaptic weight g' is increased (results not shown).

When we considered the injection of a fast arbitrary signal, the situation was similar to those of the case of slow signals as it can be seen in **Figures 7B,D,F,H** for low an high values of the conductance g', respectively. For $g' = 0.75$ and intermediate values of the delay, the transmission is moderately enhanced for negative values of the detuning in contrast to the V-motif case. Furthermore, for high values of the delay, the transmission in general enhanced but without an important effect for negative values of the frequency mismatch (see **Supplementary Figure 21** for different values of g').

As for the case of slow signal modulation, important changes in the behavior of the system occur in the intermediate region when the sender is the population 2, as it can be seen in **Figure 8** (see **Supplementary Figure 21** for the different values of g'). Again the regions of signal transmission depend less on the detuning and the delay.

In general, our results indicate that the quality of the signal transmission does not depend much on whether the external modulation is slow or fast, neither for the V-motif nor for the circular motif. What significantly affects transmission is the addition of the cortico-cortical link between populations 1 and

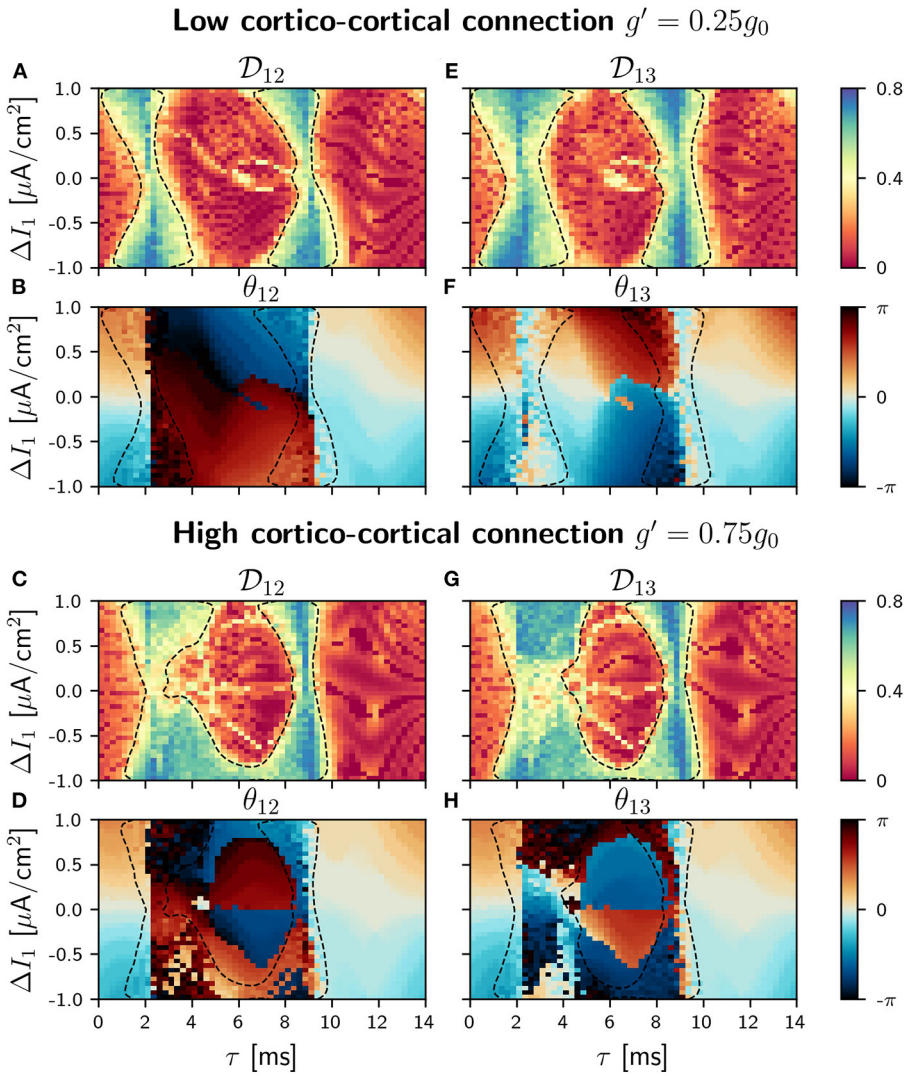

FIGURE 5 | C-motif: Phase locking $\mathcal{D}_{ij}$ for $g' = 0.25g_0$ **(A,E)** and $g' = 0.75g_0$ **(C,G)**. Phase difference θ_{ij} for $g' = 0.25g_0$ **(B,F)** and $g' = 0.75g_0$ **(D,H)**. All of them as a function of the delay τ and the frequency mismatch induced by a change ΔI in population 1.

3. In this case, transmission becomes, unexpectedly, less robust and effective, but allowing information transmission also for negative detunings.

5. DISCUSSION

In this paper we have studied transmission of signals in neuronal circuits considering two different canonical motifs: the V-motif that consists of a chain of three bidirectionally coupled neural populations and the circular motif, which results from adding bidirectional connection between the populations at the end of the chain. These simple neural motifs are inspired in the cortico-thalamo-cortical network and allow us to address open questions about the condition for efficient information transmission in this circuit. We identify two operation modes that can be dynamically switched by modulating the strength of the direct cortico-cortical connection. When this connection is weak, the V-motif dynamics predominate supporting robust transmission from the thalamus to the cortex as well as in feedback cortico-thalamic direction. When the strength of cortico-cortical connection increases, C-motif dynamics facilitate the coexistence of the above canonical thalamo-cortical transmission with a cortico-thalamo-cortical association loop. Thus, direct cortico-cortical and indirect transthalamic communication cooperate in cortical computations. We hypothesize that the first operation mode supports unimodal sensory transmission and the second multimodal integration and feature binding.

To investigate information transmission in the above system, we systematically explored the consequences of varying two important parameters, detuning or frequency mismatch between

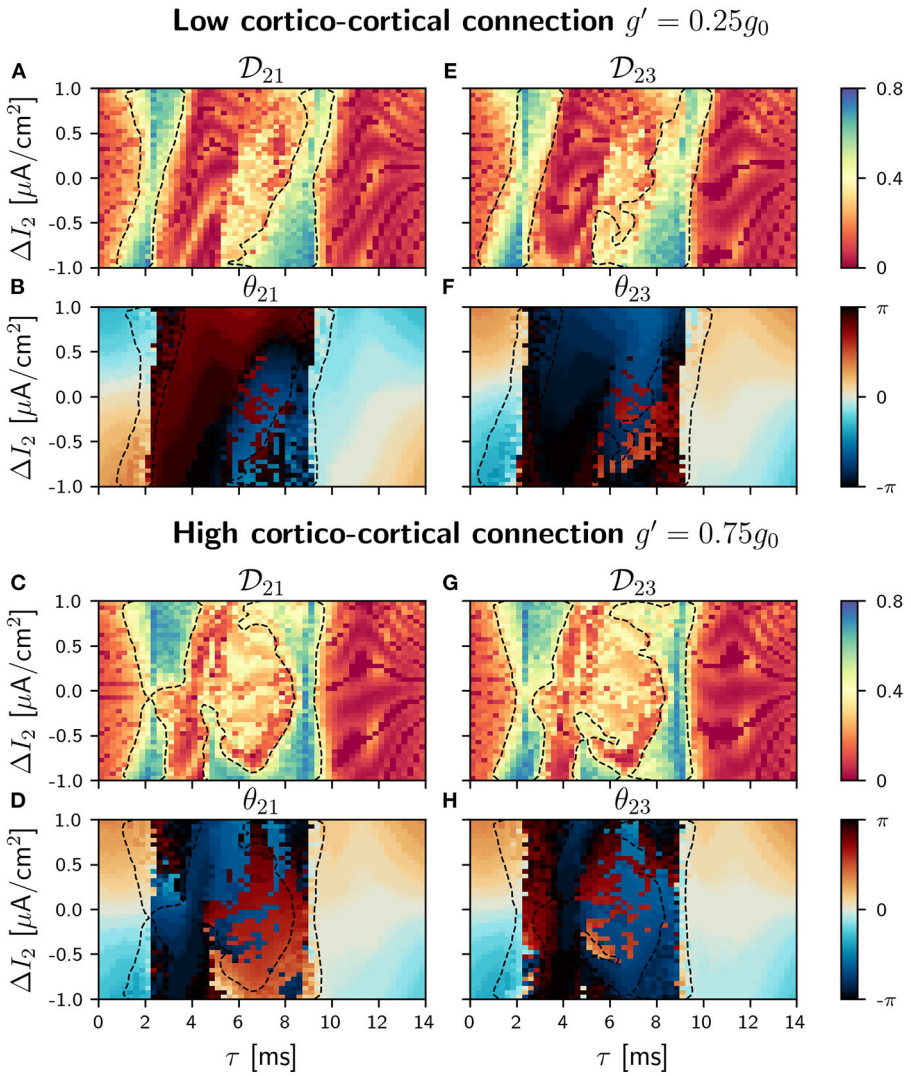

FIGURE 6 | C-motif: Phase locking $\mathcal{D}_{ij}$ for $g' = 0.25g_0$ **(A and E)** and $g' = 0.75g_0$ **(C and G)**. Phase difference θ_{ij} for $g' = 0.25g_0$ **(B and F)** and $g' = 0.75g_0$ **(D and H)**. All of them as a function of the delay τ and the frequency mismatch induced by a change ΔI in population 2.

the populations (produced through a change in the bias current ΔI applied to one population, the sender), and the delay (τ) in the connections between populations. The first would be dynamically controlled by modulating the afferent synaptic strengths, neuronal excitability or the excitation/inhibition balance in the networks, and the second is hardwired in the system and depends on the axonal length and conduction velocities. From previous works, it is known that applying a positive detuning (resulting in a higher oscillation frequency) to the sender population, enhances the communication in the network (Sancristóbal et al., 2014; Kirst et al., 2016; Palmigiano et al., 2017; Pariz et al., 2018, 2021). However, this is true when we consider small values of the delay τ. For larger delay values, it is the combination of the detuning and the delay that determine the efficacy and the preferred direction of the signal transmission (Pariz et al., 2021).

Based on the theory provided by Pariz et al. (2021), phase relations between pair of the bidirectionally coupled oscillators can determine the amount of signal/information transfered between them, once their PRCs are known. For symmetric bidirectionally coupled oscillators both 0 and π phase difference can be stable depending on the delay time and their PRCs. In the three network motifs, the organization of the connections can also affect the phase relation. In the absence of the cortico-cortical connections, and depending on the delay, each pair of adjacent nodes can take 0 or π phase, and in either case the outer populations favor the zero phase lag (Gollo et al., 2010, 2014; Mirasso et al., 2017). In a symmetric circular motif, a new state emerges where the three populations tend to lock at $2\pi/3$ phase difference compatible with the symmetry of the motif. For small values of the cortico-cortical connection the former states have larger basin of attraction while this latter state only appears for

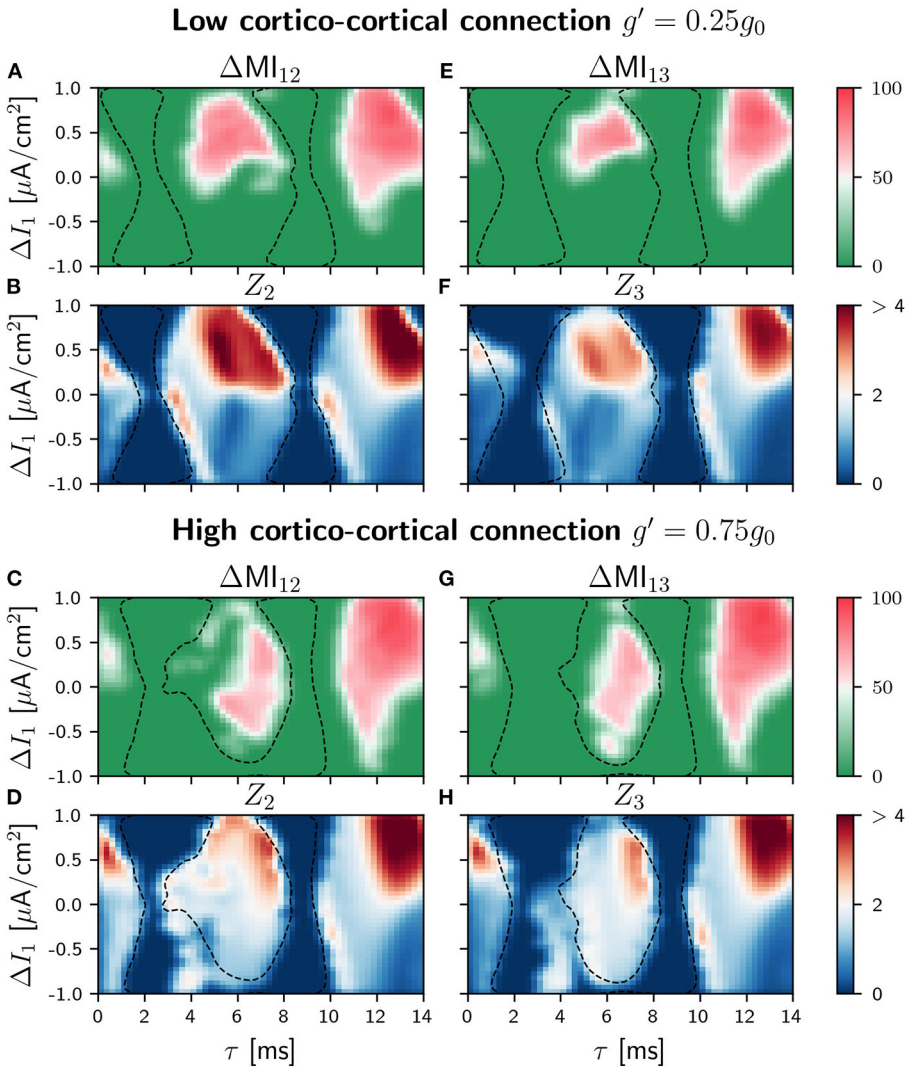

FIGURE 7 | Population 1 as the sender in C-motif: Difference ΔMI_{ij} for $g' = 0.25g_0$ **(A and E)** and $g' = 0.75g_0$ **(C and G)** when a slow modulation is injected. Integral of the absolute value of the nPRC Z_i for $g' = 0.25g_0$ **(B and F)** and $g' = 0.75g_0$ **(D and H)** when a fast signal is injected. All of them as a function of the delay τ and the frequency mismatch induced by a change ΔI in population 1.

large enough values of the cortico-cortical connection strength. In this case, the pattern of information transfer deviates from that of the relay motif.

As it is shown in Pariz et al. (2021), the amount of signal transmission between the neuronal populations depends on the slope of the phase response curve of the receiver population (nPRC) at the time that it receives the spiking activity of the sender population. In this way not only the phase relation between the two populations and the delay time, but also the PRC of the populations are important in the pattern of information transmission between neuronal populations. Population PRCs are shown to depend on the mechanism of the generation of the oscillations in the excitatory-inhibitory networks (Dumont and Gutkin, 2019) and consequently, the internal dynamical properties of the EI networks also affect the information transfer in brain circuits. Moreover, the preference of the system for a positive detuning as compared to the negative one is due to the asymmetric shape of phase response curve of the realistic neurons (Sadeghi and Valizadeh, 2014) and neuronal populations (Dumont and Gutkin, 2019), as is shown in Pariz et al. (2021). The same results seen for the three neurons motifs in this study, confirm that the shape of the PRC and in particular its symmetry properties can fundamentally affect information transfer in the brain.

In agreement with previous findings, our results show that in general positive detuning enhances transmission between populations. However, there are cases in which a good transmission is feasible even for negative detuning values. In the V-motif, this happens when the intermediate population (the thalamic relay) acts as the sender population. When the signal

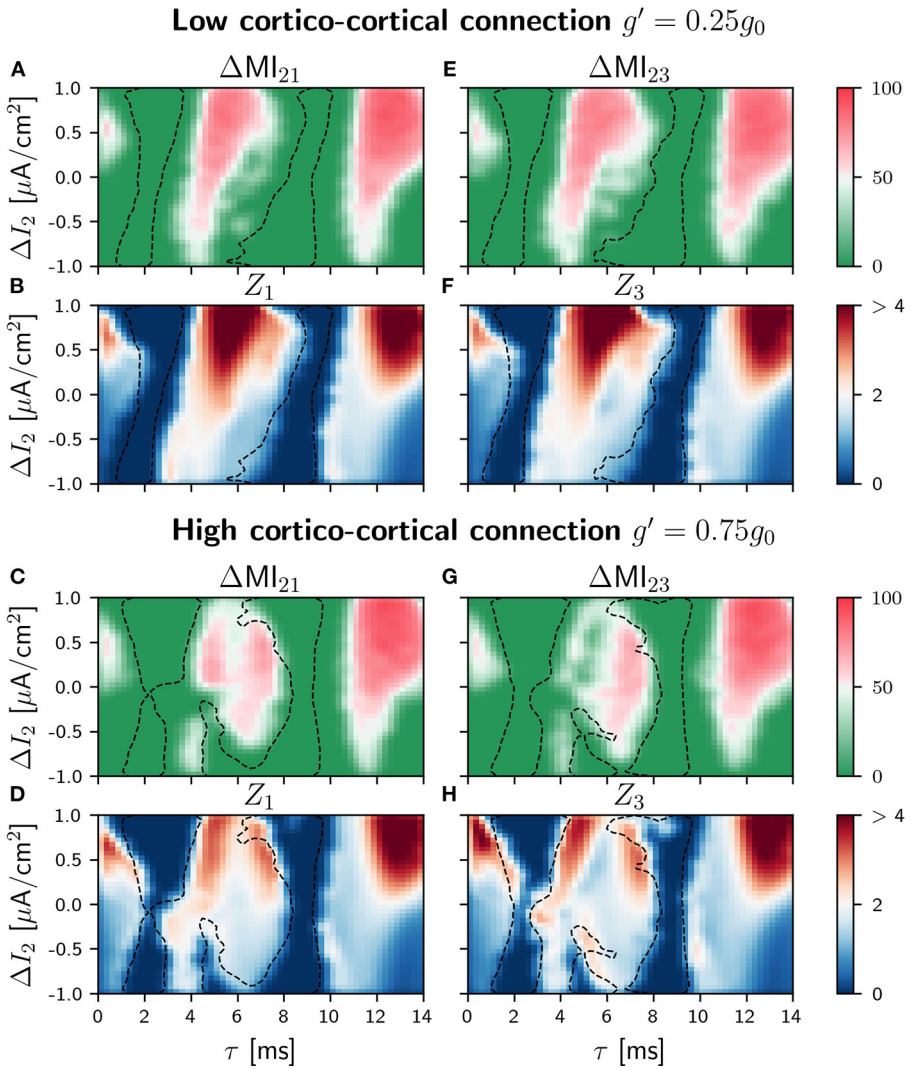

FIGURE 8 | Population 2 as the sender in C-motif: Difference ΔMI_{ij} for $g' = 0.25g_0$ **(A,E)** and $g' = 0.75g_0$ **(C,G)** when a slow modulation is injected. Integral of the absolute value of the nPRC Z_i for $g' = 0.25g_0$ **(B,F)** and $g' = 0.75g_0$ **(D,H)** when a fast signal is injected. All of them as a function of the delay τ and the frequency mismatch induced by a change ΔI in population 2.

is injected in one of the external populations (cortical), good transmission always requires positive values of the detuning, that is, higher frequencies in the cortical vs. the thalamic population. Following the biological analogy, our results suggest that the canonical thalamo-cortical sensory transmission would be preserved for a broad range of thalamic frequencies (positive and negative detuning), thus facilitating the coexistence of top-down and bottom-up computations required for proper sensory integration (Hirsch et al., 2015). Cortico-thalamic transmission (top-down) in the V-motif would be restricted to positive detuning (when cortical frequency is higher than that of the thalamus). This operation mode is compatible with the canonical view of the thalamic function (Sherman, 2016).

Interestingly, different operation modes appear by adding a direct link between the outer populations (cortico-cortical connection generating the C-motif). In this condition, higher cortico-cortical synaptic weights (g') facilitate effective communication in the indirect cortico-thalamo-cortical pathway for negative detuning values, a communication channel that did not exist in the V-motif. Accordingly, for small values of cortico-cortical connection, the dynamics is mainly governed by that of the V-motif. Therefore, the strength of the cortico-cortical connection may control switching between distinct dynamic modes.

Quantitatively, the V-motif (or the C-motif with low cortico-cortical connection strength) is a better configuration for efficient signal transmission but, on the other hand, the circular motif with higher cortico-cortical connectivity allows new channels of communication, although with lower overall efficiency. The later generates cortical associative loops

in which both, the direct cortico-cortical and the indirect transthalamic pathways, play distinct but fundamental roles. We hypothesize that the first operation mode supports the canonical function of the thalamus in sensory transmission and the second would be ideally suited for the integration of cortically segregated computations and feature binding (Singer, 2007; Uhlhaas et al., 2009; Gollo et al., 2010).

Our study has some limitations. All these results have been obtained in a highly coherent and synchronized regime. The intrinsic dynamics of each population exhibited a single oscillation frequency which cannot fully represent the realistic dynamics of cortical networks. It is well known that brain functions are associated with different frequency bands, and synchronization occurs in short periods from a weakly coherent scenario (Xing et al., 2012). Previous studies have proposed neural network models to reproduce this complex dynamics (Tort et al., 2013; Palmigiano et al., 2017) and others suggested the important role of slow synapses (Cannon et al., 2014), not considered in our model. Therefore, further work must be done considering richer neural dynamics which will help to further explain the underlying circuit mechanisms of information transmission between brain areas.

In conclusion, signal propagation in V- and C-motifs resembling those found in the thalamo-cortical system was systematically studied. Complex but distinct operation modes emerge in this relatively simple system with three neuronal populations and two main variables, connection delay and frequency detuning. An important modulatory role was identified for the cortico-cortical connection strength in the selection between operation modes. In a neurobiological thalamo-cortical context, modes switching would flexibly support the alternation between computations with a predominant sensory processing function, with robust thalamo-cortical transmission and top-down cortico-thalamic modulation (i.e., attentional modulation), with feature binding, and cortical integrative computation.

DATA AVAILABILITY STATEMENT

The raw data supporting the conclusions of this article will be made available by the authors under request, without undue reservation.

AUTHOR CONTRIBUTIONS

AV, SC, and CM contributed to conception and design of the study. JS-C and AP performed simulations and prepared the figures. All authors contributed to manuscript revision, read, and approved the submitted version.

FUNDING

JS-C and CM acknowledge support from the Spanish Agency of Research (AEI) through project PID2019-111537GBC22/AEI/10.13039/501100011033. SC was supported by the Spanish Agency of Research (AEI) under Grant no. BFU2015-64380-C2-1-R (AEI/FEDER, UE). JS-C and CM acknowledge the Spanish State Research Agency, through the Severo Ochoa and María de Maeztu Program for Centers and Units of Excellence in R&D (MDM-2017-0711). SC acknowledges the Spanish State Research Agency, through the Severo Ochoa and María de Maeztu Program for Centers and Units of Excellence in R&D (MDM-2017-0711 and SEV-2017-0723).

SUPPLEMENTARY MATERIAL

The Supplementary Material for this article can be found online at: https://www.frontiersin.org/articles/10.3389/fnsys.2021.705371/full#supplementary-material

REFERENCES

Avena-Koenigsberger, A., Misic, B., and Sporns, O. (2018). Communication dynamics in complex brain networks. *Nat. Rev. Neurosci.* 19, 17. doi: 10.1038/nrn.2017.149

Baddeley, A. (1992). Working memory. *Science* 255, 556–559. doi: 10.1126/science.1736359

Baddeley, A. (2010). Working memory. *Curr. Biol.* 20, R136–R140. doi: 10.1016/j.cub.2009.12.014

Baddeley, A., and Hitch, G. J. (2010). Working memory. *Scholarpedia* 5, 3015. doi: 10.4249/scholarpedia.3015

Baker, S. N., Pinches, E. M., and Lemon, R. N. (2003). Synchronization in monkey motor cortex during a precision grip task. ii. effect of oscillatory activity on corticospinal output. *J. Neurophysiol.* 89, 1941–1953. doi: 10.1152/jn.00832.2002

Barardi, A., Sancristóbal, B., and Garcia-Ojalvo, J. (2014). Phase-coherence transitions and communication in the gamma range between delay-coupled neuronal populations. *PLoS Comput. Biol.* 10:e1003723. doi: 10.1371/journal.pcbi.1003723

Başar, E. (2012). *Brain Function and Oscillations, Vol. I, Brain Oscillations. Principles and Approaches*. Berlin Heidelberg: Springer.

Başar, E., Başar-Eroğlu, C., Karakaş, S., and Schürmann, M. (2000). Brain oscillations in perception and memory. *Int. J. Psychophysiol.* 35, 95–124. doi: 10.1016/S0167-8760(99)00047-1

Borisyuk, G., Borisyuk, R., Kazanovich, Y., and Strong, G. (1999). "Oscillatory neural networks: Modeling binding and attention by synchronization of neural activity," in *Oscillations in Neural Systems*, eds D. S. Levine, R. V. Brown and V. Thimoty Shirey (New Jersey, NJ: Lawrence Erlbaum Associated Publishers).

Cannon, J., McCarthy, M. M., Lee, S., Lee, J., Börgers, C., Whittington, M. A., and Kopell, N. (2014). Neurosystems: brain rhythms and cognitive processing. *Eur. J. Neurosci.* 39, 705–719. doi: 10.1111/ejn.12453

Chawla, D., Friston, K. J., and Lumer, E. D. (2001). Zero-lag synchronous dynamics in triplets of interconnected cortical areas. *Neural Netw.* 14, 727–735. doi: 10.1016/S0893-6080(01)00043-0

Coll, S. Y., Ceravolo, L., Fr'uhholz, S., and Grandjean, D. (2018). The behavioral and neural binding phenomena during visuomotor integration of angry facial expressions. *Sci. Rep.* 8, 1–13. doi: 10.1038/s41598-018-25155-8

Dayan, P., and Abbott, L. F. (2001). *Theoretical Neuroscience: Computational and Mathematical Modeling of Neural Systems*. Computational Neuroscience Series. doi: 10.1086/421681

De Pasquale, R., and Sherman, S. M. (2011). Synaptic properties of corticocortical connections between the primary and secondary visual cortical areas in the mouse. *J. Neurosci.* 31, 16494–16506. doi: 10.1523/JNEUROSCI.3664-11.2011

Deco, G., Jirsa, V. K., Robinson, P. A., Breakspear, M., and Friston, K. (2008). The dynamic brain: from spiking neurons to neural masses and cortical fields. *PLoS Comput. Biol.* 4:e1000092. doi: 10.1371/journal.pcbi.1000092

Denker, M., Roux, S., Timme, M., Riehle, A., and Grün, S. (2007). Phase synchronization between lfp and spiking activity in motor cortex during movement preparation. *Neurocomputing* 70, 2096–2101. doi: 10.1016/j.neucom.2006.10.088

DHuys, O., Vicente, R., Erneux, T., Danckaert, J., and Fischer, I. (2008). Synchronization properties of network motifs: Influence of coupling delay and symmetry. *Chaos* 18, 037116. doi: 10.1063/1.2953582

Doesburg, S. M., Roggeveen, A. B., Kitajo, K., and Ward, L. M. (2008). Large-scale gamma-band phase synchronization and selective attention. *Cereb. Cortex* 18, 386–396. doi: 10.1093/cercor/bhm073

Dumont, G., and Gutkin, B. (2019). Macroscopic phase resetting-curves determine oscillatory coherence and signal transfer in inter-coupled neural circuits. *PLoS Comput. Biol.* 15:e1007019. doi: 10.1371/journal.pcbi.1007019

Eckhorn, R., Bauer, R., Jordan, W., Brosch, M., Kruse, W., Munk, M., and Reitboeck, H. (1988). Coherent oscillations: a mechanism of feature linking in the visual cortex? *Biol. Cybern.* 60, 121–130. doi: 10.1007/BF00202899

Esfahani, Z. G., and Valizadeh, A. (2014). Zero-lag synchronization despite inhomogeneities in a relay system. *PLoS ONE* 9:e112688. doi: 10.1371/journal.pone.0112688

Feige, B., Aertsen, A., and Kristeva-Feige, R. (2000). Dynamic synchronization between multiple cortical motor areas and muscle activity in phasic voluntary movements. *J. Neurophysiol.* 84, 2622–2629. doi: 10.1152/jn.2000.84.5.2622

Fischer, I., Vicente, R., Buldú, J. M., Peil, M., Mirasso, C. R., Torrent, M., and García-Ojalvo, J. (2006). Zero-lag long-range synchronization via dynamical relaying. *Phys. Rev. Lett.* 97, 123902. doi: 10.1103/PhysRevLett.97.123902

Fries, P. (2015). Rhythms for cognition: communication through coherence. *Neuron* 88, 220–235. doi: 10.1016/j.neuron.2015.09.034

Friston, K. J. (1994). Functional and effective connectivity in neuroimaging: a synthesis. *Hum. Brain Map.* 2, 56–78. doi: 10.1002/hbm.460020107

Friston, K. J. (2011). Functional and effective connectivity: a review. *Brain Connect.* 1, 13–36. doi: 10.1089/brain.2011.0008

Gollo, L. L., Mirasso, C., Sporns, O., and Breakspear, M. (2014). Mechanisms of zero-lag synchronization in cortical motifs. *PLoS Comput. Biol.* 10:e1003548. doi: 10.1371/journal.pcbi.1003548

Gollo, L. L., Mirasso, C., and Villa, A. E. (2010). Dynamic control for synchronization of separated cortical areas through thalamic relay. *Neuroimage* 52, 947–955. doi: 10.1016/j.neuroimage.2009.11.058

Goodman, D. F., and Brette, R. (2009). The brian simulator. *Front. Neurosci.* 3:26. doi: 10.3389/neuro.01.026.2009

Gross, J., Kujala, J., Hämäläinen, M., Timmermann, L., Schnitzler, A., and Salmelin, R. (2001). Dynamic imaging of coherent sources: studying neural interactions in the human brain. *Proc. Natl. Acad. Sci. U.S.A.* 98, 694–699. doi: 10.1073/pnas.98.2.694

Hacine-Gharbi, A., Ravier, P., Harba, R., and Mohamadi, T. (2012). Low bias histogram-based estimation of mutual information for feature selection. *Pattern Recogn. Lett.* 33, 1302–1308. doi: 10.1016/j.patrec.2012.02.022

Hirsch, J. A., Wang, X., Sommer, F. T., and Martinez, L. M. (2015). How inhibitory circuits in the thalamus serve vision. *Ann. Rev. Neurosci.* 38, 309–329. doi: 10.1146/annurev-neuro-071013-014229

Hodgkin, A. L., and Huxley, A. F. (1952). A quantitative description of membrane current and its application to conduction and excitation in nerve. *J. physiol.* 117, 500. doi: 10.1113/jphysiol.1952.sp004764

Hutchison, R. M., Womelsdorf, T., Allen, E. A., Bandettini, P. A., Calhoun, V. D., Corbetta, M., et al. (2013). Dynamic functional connectivity: promise, issues, and interpretations. *Neuroimage* 80, 360–378. doi: 10.1016/j.neuroimage.2013.05.079

Jensen, O., Spaak, E., and Zumer, J. M. (2019). "Human brain oscillations: from physiological mechanisms to analysis and cognition," in *Magnetoencephalography: From Signals to Dynamic Cortical Networks*, eds S. Supek and C. J. Aine (Heidelberg: Springer), 471–517.

Kailath, T. (1967). The divergence and bhattacharyya distance measures in signal selection. *IEEE Trans. Commun. Technol.* 15, 52–60. doi: 10.1109/TCOM.1967.1089532

Kirst, C., Timme, M., and Battaglia, D. (2016). Dynamic information routing in complex networks. *Nat. Commun.* 7, 1–9. doi: 10.1038/ncomms11061

Ko, T.-W., and Ermentrout, G. B. (2009). Phase-response curves of coupled oscillators. *Phys. Rev. E* 79, 016211. doi: 10.1103/PhysRevE.79.016211

Lee, C. C., and Sherman, S. M. (2008). Synaptic properties of thalamic and intracortical inputs to layer 4 of the first-and higher-order cortical areas in the auditory and somatosensory systems. *J. Neurophysiol.* 100, 317–326. doi: 10.1152/jn.90391.2008

Maris, E., Fries, P., and van Ede, F. (2016). Diverse phase relations among neuronal rhythms and their potential function. *Trends Neurosci.* 39, 86–99. doi: 10.1016/j.tins.2015.12.004

Milshtein, G. (1975). Approximate integration of stochastic differential equations. *Theory Probab. Appl.* 19, 557–562. doi: 10.1137/1119062

Mirasso, C. R., Carelli, P. V., Pereira, T., Matias, F. S., and Copelli, M. (2017). Anticipated and zero-lag synchronization in motifs of delay-coupled systems. *Chaos* 27, 114305. doi: 10.1063/1.5006932

Niebur, E. (2002). Electrophysiological correlates of synchronous neural activity and attention: a short review. *Biosystems* 67, 157–166. doi: 10.1016/S0303-2647(02)00102-8

Opitz, B. (2010). Neural binding mechanisms in learning and memory. *Neurosci. Biobehav. Rev.* 34, 1036–1046. doi: 10.1016/j.neubiorev.2009.11.001

Palmigiano, A., Geisel, T., Wolf, F., and Battaglia, D. (2017). Flexible information routing by transient synchrony. *Nat. Neurosci.* 20, 1014. doi: 10.1038/nn.4569

Pariz, A., Esfahani, Z. G., Parsi, S. S., Valizadeh, A., Canals, S., and Mirasso, C. R. (2018). High frequency neurons determine effective connectivity in neuronal networks. *Neuroimage* 166, 349–359. doi: 10.1016/j.neuroimage.2017.11.014

Pariz, A., Fischer, I., Valizadeh, A., and Mirasso, C. (2021). Transmission delays and frequency detuning can regulate information flow between brain regions. *PLoS Comput. Biol.* 17, e1008129. doi: 10.1371/journal.pcbi.1008129

Pfurtscheller, G., Neuper, C., Pichler-Zalaudek, K., Edlinger, G., and da Silva, F. H. L. (2000). Do brain oscillations of different frequencies indicate interaction between cortical areas in humans? *Neurosci. Lett.* 286, 66–68. doi: 10.1016/S0304-3940(00)01055-7

Sadeghi, S., and Valizadeh, A. (2014). Synchronization of delayed coupled neurons in presence of inhomogeneity. *J. Comput. Neurosci.* 36, 55–66. doi: 10.1007/s10827-013-0461-9

Sancristóbal, B., Vicente, R., and Garcia-Ojalvo, J. (2014). Role of frequency mismatch in neuronal communication through coherence. *J. Comput. Neurosci.* 37, 193–208. doi: 10.1007/s10827-014-0495-7

Save, E., and Poucet, B. (2000). Hippocampal-parietal cortical interactions in spatial cognition. *Hippocampus* 10, 491–499. doi: 10.1002/1098-1063(2000)10:4<491::AID-HIPO16>3.0.CO;2-0

Schultheiss, N. W. (2012). "Continuum of type i somatic to type ii dendritic prcs; phase response properties of a morphologically reconstructed globus pallidus neuron model," in *Phase Response Curves in Neuroscience*, eds N. W. Schultheiss, and A. A. Prinz (New York, NY: Springer), 307–325.

Sherman, S. M. (2012). Thalamocortical interactions. *Curr. Opin. Neurobiol.* 22, 575–579. doi: 10.1016/j.conb.2012.03.005

Sherman, S. M. (2016). Thalamus plays a central role in ongoing cortical functioning. *Nat. Neurosci.* 19, 533–541. doi: 10.1038/nn.4269

Singer, W. (2007). Binding by synchrony. *Scholarpedia.* 2:1657. doi: 10.4249/scholarpedia.1657

Sporns, O., and Kötter, R. (2004). Motifs in brain networks. *PLoS Biol.* 2:e369. doi: 10.1371/journal.pbio.0020369

Sysoeva, M., Sitnikova, E., and Sysoev, I. (2016). Thalamo-cortical mechanisms of initiation, maintenance and termination of spike-wave discharges at wag/rij rats. *Zh. Vyssh. Nerv. Deiat. Im. I. P. Pavlova* 66, 103–112. doi: 10.1016/j.eplepsyres.2010.02.011

Tort, A. B., Scheffer-Teixeira, R., Souza, B. C., Draguhn, A., and Brankačk, J. (2013). Theta-associated high-frequency oscillations (110-160 hz)

in the hippocampus and neocortex. *Progr. Neurobiol.* 100, 1–14. doi: 10.1016/j.pneurobio.2012.09.002

Uhlhaas, P., Pipa, G., Lima, B., Melloni, L., Neuenschwander, S., Nikolić, D., and Singer, W. (2009). Neural synchrony in cortical networks: history, concept and current status. *Front. Integr. Neurosci.* 3:17. doi: 10.3389/neuro.07.017.2009

Vicente, R., Gollo, L. L., Mirasso, C. R., Fischer, I., and Pipa, G. (2008). Dynamical relaying can yield zero time lag neuronal synchrony despite long conduction delays. *Proc. Natl. Acad. Sci. U.S.A.* 105, 17157–17162. doi: 10.1073/pnas.0809353105

Viriyopase, A., Bojak, I., Zeitler, M., and Gielen, S. (2012). When long-range zero-lag synchronization is feasible in cortical networks. *Front. Comput. Neurosci.* 6:49. doi: 10.3389/fncom.2012.00049

Xing, D., Shen, Y., Burns, S., Yeh, C.-I., Shapley, R., and Li, W. (2012). Stochastic generation of gamma-band activity in primary visual cortex of awake and anesthetized monkeys. *J. Neurosci.* 32, 13873–13880a. doi: 10.1523/JNEUROSCI.5644-11.2012

Conflict of Interest: The authors declare that the research was conducted in the absence of any commercial or financial relationships that could be construed as a potential conflict of interest.

Publisher's Note: All claims expressed in this article are solely those of the authors and do not necessarily represent those of their affiliated organizations, or those of the publisher, the editors and the reviewers. Any product that may be evaluated in this article, or claim that may be made by its manufacturer, is not guaranteed or endorsed by the publisher.

frontiers in Systems Neuroscience

ORIGINAL RESEARCH
published: 01 September 2021
doi: 10.3389/fnsys.2021.675272

Patient-Specific Network Connectivity Combined With a Next Generation Neural Mass Model to Test Clinical Hypothesis of Seizure Propagation

*Moritz Gerster[1], Halgurd Taher[2], Antonín Škoch[3,4], Jaroslav Hlinka[3,5], Maxime Guye[6,7], Fabrice Bartolomei[8], Viktor Jirsa[9], Anna Zakharova[1] and Simona Olmi[2,10]**

[1] Institut für Theoretische Physik, Technische Universität Berlin, Berlin, Germany, [2] Inria Sophia Antipolis Méditerranée Research Centre, MathNeuro Team, Valbonne, France, [3] National Institute of Mental Health, Klecany, Czechia, [4] MR Unit, Department of Diagnostic and Interventional Radiology, Institute for Clinical and Experimental Medicine, Prague, Czechia, [5] Institute of Computer Science of the Czech Academy of Sciences, Prague, Czechia, [6] Faculté de Médecine de la Timone, Centre de Résonance Magnétique et Biologique et Médicale (CRMBM, UMR CNRS-AMU 7339), Medical School of Marseille, Aix-Marseille Université, Marseille, France, [7] Assistance Publique -Hôpitaux de Marseille, Hôpital de la Timone, Pôle d'Imagerie, Marseille, France, [8] Assistance Publique - Hôpitaux de Marseille, Hôpital de la Timone, Service de Neurophysiologie Clinique, Marseille, France, [9] Aix Marseille Université, Inserm, Institut de Neurosciences des Systèmes, UMRS 1106, Marseille, France, [10] Consiglio Nazionale delle Ricerche, Istituto dei Sistemi Complessi, Sesto Fiorentino, Italy

Dynamics underlying epileptic seizures span multiple scales in space and time, therefore, understanding seizure mechanisms requires identifying the relations between seizure components within and across these scales, together with the analysis of their dynamical repertoire. In this view, mathematical models have been developed, ranging from single neuron to neural population. In this study, we consider a neural mass model able to exactly reproduce the dynamics of heterogeneous spiking neural networks. We combine mathematical modeling with structural information from non invasive brain imaging, thus building large-scale brain network models to explore emergent dynamics and test the clinical hypothesis. We provide a comprehensive study on the effect of external drives on neuronal networks exhibiting multistability, in order to investigate the role played by the neuroanatomical connectivity matrices in shaping the emergent dynamics. In particular, we systematically investigate the conditions under which the network displays a transition from a low activity regime to a high activity state, which we identify with a seizure-like event. This approach allows us to study the biophysical parameters and variables leading to multiple recruitment events at the network level. We further exploit topological network measures in order to explain the differences and the analogies among the subjects and their brain regions, in showing recruitment events at different parameter values. We demonstrate, along with the example of diffusion-weighted magnetic resonance imaging (dMRI) connectomes of 20 healthy subjects and 15 epileptic patients, that individual variations in structural connectivity, when linked with mathematical dynamic models, have the capacity to explain changes in spatiotemporal organization of brain dynamics, as observed in network-based brain disorders. In particular, for epileptic patients, by means of the integration of the clinical hypotheses on the epileptogenic zone (EZ), i.e., the local network where highly synchronous seizures originate, we have identified the

OPEN ACCESS

Edited by:
James W. Grau,
Texas A&M University, United States

Reviewed by:
David B. Grayden,
The University of Melbourne, Australia
Marc Goodfellow,
University of Exeter, United Kingdom

***Correspondence:**
Simona Olmi
simona.olmi@inria.fr

Received: *02 March 2021*
Accepted: *07 July 2021*
Published: *01 September 2021*

Citation:
Gerster M, Taher H, Škoch A, Hlinka J, Guye M, Bartolomei F, Jirsa V, Zakharova A and Olmi S (2021) Patient-Specific Network Connectivity Combined With a Next Generation Neural Mass Model to Test Clinical Hypothesis of Seizure Propagation. Front. Syst. Neurosci. 15:675272. doi: 10.3389/fnsys.2021.675272

sequence of recruitment events and discussed their links with the topological properties of the specific connectomes. The predictions made on the basis of the implemented set of exact mean-field equations turn out to be in line with the clinical pre-surgical evaluation on recruited secondary networks.

Keywords: neural mass model, quadratic integrate-and-fire neuron, patient-specific brain network model, epileptic seizure-like event, topological network measure

1. INTRODUCTION

Epilepsy is a chronic neurological disorder characterized by the occurrence and recurrence of seizures and represents the third most common neurological disorder affecting more than 50 million people worldwide (World Health Organization, 2005). Anti-epileptic drugs are the first line of treatment for epilepsy, and they provide sufficient seizure control in around two-thirds of cases (Kwan and Brodie, 2000). However, about 30–40% of epilepsy patients do not respond to drugs, a percentage that has remained relatively stable despite significant efforts to develop new anti-epileptic medication over the past decades. For drug-resistant patients, a possible treatment is the surgical resection of the brain tissue responsible for the generation of seizures.

As a standard procedure, epilepsy surgery is preceded by a qualitative assessment of different brain imaging modalities to identify the brain tissue responsible for seizure generation, i.e., the epileptogenic zone (EZ) (Rosenow and Lüders, 2001), which in general represents a localized region or a network where seizures arise, before recruiting secondary networks, called the propagation zone (PZ) (Talairach and Bancaud, 1966; Bartolomei et al., 2001; Spencer, 2002; Richardson, 2012). Outcomes are positive whenever the patient has become seizure-free after surgical operation.

Intracranial electroencephalography (iEEG) is commonly used during the presurgical assessment to find the seizure onset zone (Rosenow and Lüders, 2001; David et al., 2011; Duncan et al., 2016), the assumption being that the region where seizures emerge, is at least part of the brain tissue responsible for seizure generation. As a part of the standard presurgical evaluation with iEEG, stereotactic EEG (SEEG) is used to help correctly delineating the EZ (Bartolomei et al., 2002). SEEG employs penetrating depth electrodes that are implanted through small burr holes in the skull and are positioned using stereotactic guidance (Talairach and Bancaud, 1966), thus allowing for the measurement of neural activity in deeper structures of the brain. Alternative imaging techniques such as structural Magnetic Resonance Imaging (MRI), magneto- or electro-encephalography (M/EEG), and positron emission tomography (PET) help the clinician estimate the position of the EZ. Recently, diffusion MRI (dMRI) started being evaluated as well, thus giving the possibility to infer the connectivity between different brain regions by computing *in-vivo* fiber tract trajectories incoherently organized brain white matter pathways (Basser et al., 2000). dMRI has revealed a quantitative decrease of regional connectivity around the EZ that is associated with a network reorganization and cognitive impairment (Leyden et al., 2015). In particular, it has revealed reduced fractional anisotropy (Ahmadi et al., 2009; Bernhardt et al., 2013) and structural alterations in the connectome of epileptic patients (Bonilha et al., 2012; Besson et al., 2014; DeSalvo et al., 2014). However, epilepsy surgery is often unsuccessful and the long-term positive outcome may be lower than 25% in extra-temporal cases (De Tisi et al., 2011; Najm et al., 2013), thus meaning that the EZ has not been correctly identified or that the EZ and the seizure onset zone may not coincide (Lopes et al., 2019).

To quantitatively examine clinical data and to determine targets for surgery, many computational models have been recently proposed (Freestone et al., 2013; Hutchings et al., 2015; Goodfellow et al., 2016; Khambhati et al., 2016; Lopes et al., 2017; Sinha et al., 2017; Karoly et al., 2018), that use MRI or iEEG data acquired during presurgical workup to infer structural or functional brain networks. Taking advantages of recent advances in the understanding of epilepsy, that indicate that seizures may arise from distributed ictogenic networks (Richardson, 2012; Bartolomei et al., 2017; Besson et al., 2017), phenomenological models of seizure transitions are used to compute the escape time, i.e., the time that each network node takes to transit from a normal state to a seizure-like state. Nodes with the lowest escape time are then considered as representative of the seizure onset zone and, therefore, candidates for surgical resection, by assuming seizure onset zone as a proxy for the EZ (Hutchings et al., 2015; Sinha et al., 2017). Alternatively, different possible surgeries are simulated *in silico* to predict surgical outcomes (Goodfellow et al., 2017; Lopes et al., 2017, 2019) by making use of synthetic networks and phenomenological network models of seizure generation. Further attention has been paid to studying how network structure and tissue heterogeneities underpin the emergence of focal and widespread seizure dynamics in synthetic networks of phase oscillators (Lopes et al., 2019, 2020).

More in general there is a vast and valuable literature on computational modeling in epilepsy, where two classes of models are used: (1) mean-field (macroscopic) models and (2) detailed (microscopic) network models. Mean-field models are often preferred over the more detailed models since they have fewer parameters and, thus, simplify the study of transitions from interictal to ictal states and the subsequent EEG analysis of data from patients with epilepsy. This is justified as the macroelectrodes used for EEG recordings represent the average local field potential arising from neuronal populations. Indeed, much effort has been made so far to explain the biophysical and dynamical nature of seizure onsets and offsets by employing neural mass models (Da Silva et al., 1974; Wendling et al., 2002; Kalitzin et al., 2010; Touboul et al., 2011; Baier et al.,

2012; Goodfellow et al., 2012; Kramer et al., 2012; Jirsa et al., 2014; Karoly et al., 2018). Mechanistic interpretability of the mean-field parameters is lost, as many physiological details are absorbed in few degrees of freedom. Since the mean-field models remain relatively simple, they can also be employed to describe epileptic processes occurring in "large-scale" systems, e.g., the precise identification of brain structures that belong to the seizure-triggering zone (epileptic activity often spreads over quite extended regions and involves several cortical and subcortical structures). However, only recently, the propagation of epileptic seizures was started to be studied using brain network models and was limited to a small number of populations (Terry et al., 2012) or absence seizures (Taylor et al., 2013), while partial seizures have been reported to propagate at the mesoscopic scale through cortical columns (Kramer et al., 2007; Goodfellow et al., 2011) and at the macroscopic scale through large-scale networks in humans (Bartolomei et al., 2013) and animal models (Toyoda et al., 2013). All in all, even though neural mass models are in general easier to analyze numerically because relatively few variables and parameters are involved, they drastically fail to suggest molecular and cellular mechanisms of epileptogenesis.

On the other hand, detailed network models are best suited for understanding the molecular and cellular bases of epilepsy and, thus, they may be used to suggest therapeutics targeting molecular pathways (Destexhe and Sejnowski, 1995; Van Drongelen et al., 2005; Turrigiano, 2008; Cressman et al., 2009; Ullah et al., 2009). Due to the substantial complexity of neuronal structures, relatively few variables and parameters can be accessed at any time experimentally. Although biophysically explicit modeling is the primary technique to look into the role played by experimentally inaccessible variables in epilepsy, the usefulness of detailed biophysical models is limited by constraints in computational power, uncertainties in detailed knowledge of neuronal systems, and the required simplification for the numerical analysis. Therefore, an intermediate "across-scale" approach, establishing relationships between sub-cellular/cellular variables of detailed models and mean-field parameters governing macroscopic models, might be a promising strategy to cover the gaps between these two modeling approaches (Brocke et al., 2016; Lindroos et al., 2018; Schirner et al., 2018).

In view of developing a cross-scale approach, it is important to point out that a large-scale brain network models emphasize the network character of the brain and merge structural information of individual brains with mathematical modeling, thus constituting *in-silico* approaches for the exploration of causal mechanisms of brain function and clinical hypothesis testing (Proix et al., 2017, 2018; Olmi et al., 2019). In particular, in brain network models, a network region is a neural mass model of neural activity, connected to other regions *via* a connectivity matrix representing fiber tracts of the human brain. This form of virtual brain modeling (Fuchs et al., 2000; Jirsa et al., 2002, 2010) exploits the explanatory power of network connectivity imposed as a constraint upon network dynamics and has provided important insights into the mechanisms underlying the emergence of asynchronous and synchronized dynamics of wakefulness and slow-wave sleep (Goldman et al., 2020) while revealing the whole-brain mutual coupling between the neuronal and the neurotransmission systems to understand the flexibility of human brain function despite having to rely on fixed anatomical connectivity (Kringelbach et al., 2020). Recent studies have pointed out the influence of individual structural variations of the connectome upon the large-scale brain network dynamics of the models, by systematically testing the virtual brain approach along with the example of epilepsy (Proix et al., 2017, 2018; Olmi et al., 2019). The employment of patient-specific virtual brain models derived from dMRI may have a substantial impact on personalized medicine, allowing for an increase in predictivity concerning the pathophysiology of brain disorders, and their associated abnormal brain imaging patterns. More specifically a personalized brain network model derived from non-invasive structural imaging data would allow for testing of clinical hypotheses and exploration of novel therapeutic approaches.

To exploit the predictive power of personalized brain network models, we have implemented, on subject-specific connectomes, a next-generation neural mass model that, differently from the previous applied heuristic mean-field models (Proix et al., 2017, 2018; Olmi et al., 2019), is exactly derived from an infinite size network of quadratic integrate-and-fire neurons (Montbrió et al., 2015), that represent the normal form of Hodgkin's class I excitable membranes (Ermentrout and Kopell, 1986). This next generation neural mass model can describe the variation of synchrony within a neuronal population, which is believed to underlie the decrease or increase of power seen in given EEG frequency bands while allowing for a more direct comparison with the results of electrophysiological experiments like local field potential, EEG, and event-related potentials (ERPs), thanks to its ability to capture the macroscopic evolution of the mean membrane potential. Most importantly, the exact reduction dimension techniques at the basis of the next-generation neural mass model have been developed for coupled phase oscillators (Ott and Antonsen, 2008) and allow for an exact (analytical) moving upward through the scales: While keeping the influence of smaller scales on larger ones, they level out their inherent complexity. In this way it is, therefore, possible to develop an intermediate "across-scale" approach exploiting the 1:1 correspondence between the microscopic and mesoscopic level that allows for more detailed modeling parameters and for mapping the microscopic results to the relative ones in the regional mean-field parameters.

The next-generation neural mass model developed by Montbrió et al. (2015), has been recently extended to take into account time-delayed synaptic coupling (Pazó and Montbrió, 2016; Devalle et al., 2018), and when integrated with a large-scale brain network, time delays in the interaction between the different brain areas, due to the finite conduction speed along fiber tracts of different lengths (Rabuffo et al., 2020). The time delay, together with the effective stochasticity of the investigated dynamics give rise, both on structural connectivity matrices of mice and healthy subjects, to preferred spatiotemporal pattern formation (Jirsa, 2008; Petkoski and Jirsa, 2020) and short-lived neuronal cascades that form spontaneously and

propagate through the network under conditions of near-criticality (Rabuffo et al., 2020). The largest neuronal cascades produce short-lived but robust co-fluctuations at pairs of regions across the brain, thus contributing to the organization of the slowly evolving spontaneous fluctuations in brain dynamics at rest. The introduction of extrinsic or endogenous noise sources in the framework of exact neural mass models is possible in terms of (pseudo)-cumulants expansion in Tyulkina et al. (2018) and Goldobin et al. (2021).

In this paper, we have built brain network models for a cohort of 20 healthy subjects and 15 epileptic patients, implementing for each brain region the neural mass model developed by Montbrió et al. (2015). As paradigms for testing the spatiotemporal organization, we have systematically simulated the individual seizure-like propagation patterns, looking for the role played by the individual structural topologies in determining the recruitment mechanisms. Specific attention has been devoted to the analogies and differences among the self-emergent dynamics in healthy and epilepsy-affected subjects. Furthermore, for epileptic patients, we have validated the model against the presurgical SEEG data and the standard-of-care clinical evaluation. More specifically the Methods section is devoted to the description of the implemented model and the applied methods. In section Healthy Subjects are reported the results specific for healthy subjects, while in section Epileptic Patients is reported a detailed analysis performed on epileptic patients. Finally, a discussion on the presented results is reported in section Discussion.

2. METHODS

2.1. Network Model

The membrane potential dynamics of the i-th quadratic integrate-and-fire (QIF) neuron in a network of size N can be written as

$$\tau_m \dot{V}_i = V_i^2(t) + \eta_i + I_B + I_S(t) + \tau_m \frac{1}{N}\sum_{j=1}^{N} \tilde{J}_{ij}(t) S_j(t) \quad , \qquad i = 1, \ldots, N \quad (1)$$

where $\tau_m = 20$ ms is the membrane time constant and $\tilde{J}_{ij}(t)$ the strength of the direct synapse from neuron j to i that we assume to be constant and all identical, i.e., $\tilde{J}_{ij}(t) = J$. The sign of J determines if the neuron is excitatory ($J > 0$) or inhibitory ($J < 0$); in the following, we will consider only excitatory neurons. Moreover, η_i represents the neuronal excitability, I_B a constant background DC current (in the following we assume $I_B = 0$), $I_S(t)$ an external stimulus, and the last term on the right-hand side the synaptic current due to the recurrent connections with the pre synaptic neurons. For instantaneous post synaptic potentials (corresponding to δ-spikes), the neural activity $S_j(t)$ of neuron j reads as

$$S_j(t) = \sum_{t_j(k)<t} \delta(t - t_j(k)), \quad (2)$$

where $S_j(t)$ is the spike train produced by the j-th neuron and $t_j(k)$ denotes the k-th spike time in such sequence. We have considered a fully coupled network without autapses, therefore, the post-synaptic current will be the same for each neuron.

In the absence of synaptic input, external stimuli, and $I_B = 0$, the QIF neuron exhibits two possible dynamics, depending on the sign of η_i. For negative η_i, the neuron is excitable and for any initial condition $V_i(0) < \sqrt{-\eta_i}$, it reaches asymptotically the resting value $-\sqrt{-\eta_i}$. On the other hand, for initial values larger than the excitability threshold, $V_i(0) > \sqrt{-\eta_i}$, the membrane potential grows unbounded and a reset mechanism has to be introduced to describe the spiking behavior of a neuron. Whenever $V_i(t)$ reaches a threshold value V_p, the neuron i delivers a spike and its membrane potential is reset to V_r, for the QIF neuron $V_p = -V_r = \infty$. For positive η_i, the neuron is supra-threshold and it delivers a regular train of spikes with frequency $\nu_0 = \sqrt{\eta_i}/\pi$.

2.2. Neural Mass Model

For the heterogeneous QIF network with instantaneous synapses (Equations 1, 2), an exact neural mass model has been derived by Montbrió et al. (2015). The analytic derivation is possible for QIF spiking networks using the Ott-Antonsen Ansatz (Ott and Antonsen, 2008) applicable to phase-oscillator networks, whenever the natural frequencies are distributed according to a Lorentzian distribution. In the case of the QIF network, this corresponds to a distribution of the excitabilities $\{\eta_i\}$ given by,

$$g(\eta) = \frac{1}{\pi}\frac{\Delta}{(\eta - \bar{\eta})^2 + \Delta^2} \quad , \quad (3)$$

which is centered in $\bar{\eta}$ and has half width at half maximum (HWHM) Δ ($\Delta = 1$ throughout this study). In particular, this neural mass model allows for an exact macroscopic description of the population dynamics, in the thermodynamic limit $N \to \infty$, in terms of only two collective variables, namely the mean membrane voltage potential $v(t)$ and the instantaneous population rate $r(t)$, as follows

$$\tau_m \dot{r}(t) = \frac{\Delta}{\tau_m \pi} + 2 r(t) v(t) \quad (4a)$$

$$\tau_m \dot{v}(t) = v^2(t) + \bar{\eta} + I_B + I_S(t) - \left[\pi \tau_m r(t)\right]^2 + \tau_m \tilde{J}(t) r(t) \quad ; \quad (4b)$$

where the synaptic strength is assumed to be identical for all neurons and instantaneous synapses in absence of plasticity $\tilde{J}(t) = J$. However, by including a dynamical evolution for the synapses and, therefore, additional collective variables, this neural mass model can be extended to any generic post synaptic potential, as shown in e.g., Devalle et al. (2017) for exponential synapses or Coombes and Byrne (2019) for conductance-based synapses with α-function profile. In the following, we will consider an extension of the original model (Equations 4) to a complex topology, where multiple nodes interact with each other. By considering instantaneous post-synaptic potentials and neglecting synaptic features, we then focus on the role played by the topology in enhancing the emergence of complex dynamics.

2.3. Multipopulation Neural Mass Model

The neural mass model can be easily extended to account for multiple interconnected neuronal populations N_{pop}. In the following, we consider personalized brain models derived from structural data of Magnetic Resonance Imaging (MRI), Diffusion Weighted Imaging (DWI) and Diffusion Tensor Imaging (DTI), thus implementing different structural connectivity matrices for healthy subjects and epileptic patients. For healthy subjects cortical and volumetric parcellations were performed using the Automatic Anatomical Atlas 1 (AAL1) (Tzourio-Mazoyer et al., 2002) with $N_{\text{pop}} = 90$ brain regions: each region will be described in terms of the presented neural mass model. For epileptic subjects, cortical and volumetric parcellations were performed using the Desikan-Killiany atlas with 70 cortical regions and 17 subcortical regions (Desikan et al., 2006) (one more empty region is added in the construction of the structural connectivity for symmetry). In this case, the structural connectivity matrix is composed, for each patient with epileptic, by 88 nodes equipped with the presented region-specific neural mass model capable of demonstrating epileptiform discharges.

The corresponding multi-population neural mass model can be straightforwardly written as

$$\tau_{\text{m}}\dot{r_k} = \frac{\Delta_k}{\tau_{\text{m}}\pi} + 2r_k(t)v_k(t) \quad k = 1, 2, \ldots, N_{\text{pop}} \tag{5a}$$

$$\tau_{\text{m}}\dot{v}_k = v_k^2(t) + \bar{\eta}^{(k)} + I_{\text{B}} + I_{\text{S}}^{(k)}(t) - (\pi\tau_{\text{m}}r_k(t))^2 + \tau_{\text{m}}\sum_{l=1}^{N_{\text{pop}}} J_{kl}r_l(t), \tag{5b}$$

where $\{J_{kl}\}$ is the connectivity matrix, representing the synaptic weights among the populations. Diagonal entries J_{kk} denote intra-population and non-diagonal entries $J_{kl}, k \neq l$ inter-population connections. In this study, we have assumed that the neurons are globally coupled both at the intra- and inter-population levels, hence removing the dependency on the neuron indices.

The connectivity matrix entries J_{kl} are determined *via* a second matrix $\{\tilde{J}_{kl}\}$, which represents the topology extracted from empirical DTI. The values of $\{\tilde{J}_{kl}\}$ are normalized in the range $[0, 1]$ via rescaling with the maximal entry value, and have $\tilde{J}_{kk} = 0$ on the diagonal. To account for strong intra-coupling (recurrent synapses) and intermediate inter-coupling, we choose the entries of each structural connectivity as

$$J_{kl} = \sigma \begin{cases} 5\ \tilde{J}_{kl} & \text{if } k \neq l \\ 20 & \text{if } k = l, \end{cases} \tag{6}$$

where σ is a rescaling factor common to all synapses, that we assume to be constant and equal to 1, apart from few cases where we investigate the dependence on the synaptic weights. Hence, the synaptic weights for $k \neq l$ are in the range $J_{kl} \in [0, 5]$, while the intra coupling is set to $J_{kk} = 20$ (apart from when specified otherwise). This choice of the rescaling factor ensures that the single brain region finds itself in a bistable regime, thus being able to switch from a low-activity to a high-activity regime. The time-dependent stimulus current $I_{\text{S}}^{(k)}(t)$ is population-specific, and a single population at a time is generally stimulated during a numerical experiment. The applied stimulus $I_{\text{S}}^{(k)}(t)$ consists of a rectangular pulse of amplitude I_S and duration t_I; the dependence on these parameters is studied in this paper to support the generality of the results.

2.4. Topologies

As the first set of data, we have selected 20 diffusion-weighted MRI connectomes of healthy subjects (mean age 33 years, SD 5.7 years, 10 females, 2 left-handed) that participated in a study on schizophrenia as a control group (Melicher et al., 2015). Throughout the study we refer to the healthy subjects as H1–H20. All subjects were recruited *via* local advertisements and had none of the following conditions: Personal lifetime history of any psychiatric disorder or substance abuse established by the Mini-International Neuropsychiatric Interview (MINI) (Lecrubier et al., 1997), and any psychotic disorder in first or second-degree relatives. Further exclusion criteria included current neurological disorders, lifetime history of seizures or head injury with altered consciousness, intracranial hemorrhage, neurological sequelae, history of intellectual disability, history of substance dependence, and any contraindication for MRI scanning.

The scans were performed on a 3T Siemens scanner in the Institute of Clinical and Experimental Medicine in Prague, employing a spin-echo EPI sequence with 30 diffusion gradient directions, $TR = 8,300$ ms, $TE = 84$ ms, $2\times2\times2\ mm^3$ voxel size, and b-value 900 s/mm^2. The diffusion-weighted images (DWI) were analyzed using the Tract-Based Spatial Statistics (TBSS) (Smith et al., 2006), part of FMRIB Software Library (FSL) (Smith et al., 2004). Image conversion from DICOM to NIfTI format was accomplished using dcm2nii. With FMRIB's Diffusion Toolbox (FDT), the fractional anisotropy (FA) images were created by fitting a tensor model to the raw diffusion data and then, using the Brain Extraction Tool (BET) (Smith, 2002), brain-extracted. FA identifies the degree of anisotropy of a diffusion process, and it is a measure often used in diffusion imaging where it is thought to reflect fiber density, axonal diameter, and myelination in white matter. A value of zero means that diffusion is isotropic, i.e., it is unrestricted (or equally restricted) in all directions, while a value of one means that diffusion occurs only along one axis and is fully restricted along all other directions. Subsequently, the FA images were transformed into a common space by nonlinear registration IRTK (Rueckert et al., 1999). A mean FA skeleton, representing the centers of all tracts common to the group, was obtained from the thinned mean FA image. All FA data were projected onto this skeleton. The resulting data was fed into voxel-wise cross-subject statistics. Prior to analysis in SPM, the FA maps were converted from NIfTI format to Analyze.

The brains were segregated into 90 brain areas according to the AAL1 (Tzourio-Mazoyer et al., 2002). The anatomical names of the brain areas for each index k are shown in the **Supplementary Table 1**. In each brain network, one AAL brain area corresponds to a node of the network. The weights between the nodes were estimated through the measurement of the preferred diffusion directions, given by a set of $n_s = 5,000$ streamlines for each voxel. The streamlines are hypothesized to

correlate with the white-matter tracts. The ratio of streamlines connecting area l and area k is given by the probability coefficient p_{lk}. Then, the adjacency matrix J_{kl} is constructed from this probability coefficient. The DTI processing pipeline has been adopted from Cabral et al. (2013).

Besides the healthy connectomes, we selected 15 connectomes (9 females, 6 males, mean age 33.4, range 22–56) of patients with different types of partial epilepsy that underwent a presurgical evaluation. The scans were performed at the Centre de Résonance Magnétique et Biologique et Médicale (Faculté de Médecine de la Timone) in Marseille. Throughout the study, we refer to the epileptic patients as E1–E15. dMRI images were acquired on a Siemens Magnetom Verio 3T MR-scanner using a DTI-MR sequence with an angular gradient set of 64 directions, $TR = 10,700$ ms, $TE = 95$ ms, $2 \times 2 \times 2\ mm^3$ voxel size, 70 slices, and b-value $1,000\ s/mm^2$.

The data processing pipeline (Schirner et al., 2015; Proix et al., 2016) made use of various tools such as FreeSurfer (Fischl, 2012), FSL (Jenkinson et al., 2012), MRtrix3 (Tournier, 2010), and Remesher (Fuhrmann et al., 2010), to reconstruct the individual cortical surface and large-scale connectivity. The surface was reconstructed using 20,000 vertices. Cortical and volumetric parcellations were performed using the Desikan-Killiany atlas with 70 cortical regions and 17 subcortical regions (Desikan et al., 2006). The final atlas consists of 88 regions since one more empty region is added in the construction of the structural connectivity for symmetry. After correction of the diffusion data for eddy-currents and head motions using eddy-correct FSL functions, the fiber orientation was estimated using constrained spherical deconvolution (Tournier et al., 2007) and improved with anatomically constrained tractography (Smith et al., 2012). For tractography, 2.5×10^6 fibers were used and, for correction, spherical-deconvolution informed filtering of tractograms (Smith et al., 2013) was applied. Summing track counts over each region of the parcellation yielded the adjacency matrix. In this study, the AAL2 was employed for brain segregation leading to 88 brain areas for each patient, as shown in **Supplementary Table 2**.

2.5. EEG and SEEG Data

All 15 drug-resistant patients, mentioned in the previous section, affected by different types of partial epilepsy accounting for different EZ localizations, underwent a presurgical evaluation (as shown in **Supplementary Tables 3, 4**). For each patient, a first non invasive evaluation procedure is foreseen, which comprises of the patient clinical record, neurological examinations, PET, and EEG along with video monitoring. Following this evaluation, potential EZs are identified by the clinicians. Further elaboration on the EZ is done in a second, invasive phase, which consists of positioning SEEG electrodes in or close to the suspected regions. These electrodes are equipped with 10–15 contacts that are 1.5 mm apart. Each contact has a length of 2 mm and measures 0.8 mm in diameter. Recordings were obtained using a 128 channel DeltamedTM system with a 256 Hz sampling rate and band-pass filtered between 0.16 and 97 Hz by a hardware filter. Precise electrode positioning was performed by either a computerized tomography or MRI scan after implanting the electrodes. All patients showed seizures in the SEEG, starting in one or several localized areas (EZ), before recruiting distant regions, identified as the PZ. It is worth noticing that, among the operated patients, four of them showed a worthwhile improvement but without resulting completely seizure-free since surgery (Engel's score III), while two resulted almost seizure-free, showing rare disabling seizures since surgery (Engel's score II), thus suggesting that the EZ was correctly identified in a subset of patients only.

Two methods were used for the identification of the PZ (as shown in **Supplementary Table 4**). First, the clinicians evaluated the PZs subjectively based on of the EEG and SEEG recordings gathered throughout the two-step procedure (non invasive and invasive). Second, the PZs were identified automatically based on the SEEG recordings: For each patient, all seizures were isolated in the SEEG time series. The bipolar SEEG was considered (between pairs of electrode contacts) and filtered between 1 and 50 Hz using a Butterworth band-pass filter. An area was defined as a PZ if its electrodes detected at least 30% of the maximum signal energy over all contacts, and if it was not in the EZ. In the following, we call the PZs identified by the subjective evaluation of clinicians PZ_{Clin} and the PZs identified through SEEG data PZ_{SEEG}.

2.6. Network Measures

The topological properties of a network can be examined by using different graph measures that are provided by the general framework of graph theory. These graph metrics can be classified in terms of measures that cover three main aspects of the topology: segregation, integration, and centrality. The segregation accounts for the specialized processes that occur inside a restricted group of brain regions, usually densely connected, and it eventually reveals the presence of a dense neighborhood around a node, which results to be fundamental for the generation of clusters and cliques capable to share specialized information. Among the possible measures of segregation, we have considered the *clustering coefficient*, which gives the fraction of triangles around a node and it is equivalent to the fraction of neighbors of the node that are neighbors of each other as well. In particular, the *average clustering coefficient* C of a network gives the fraction of closed triplets over the number of all open and closed triplets, where a triplet consists of three nodes with either two edges (open triplet) or three edges (closed triplet). The *weighted clustering coefficient* c_i^w (Barrat et al., 2004) considers the weights of its neighbors:

$$c_i^w = \frac{1}{s_i(k_i - 1)} \sum_{j,h} \frac{w_{ij} + w_{ih}}{2} a_{ij} a_{ih} a_{jh}, \tag{7}$$

where s_i is the node strength (to be defined below), k_i the node degree, w_{ij} the weight of the link, and a_{ij} is 1 if the link $i \to j$ exists and 0 if node i and j are not connected. The *average weighted clustering coefficient* C_W is the mean of all weighted clustering coefficients: $C_W = \frac{1}{N} \sum_i c_i$.

The measures of integration refer to the capacity of the network to rapidly combine specialized information from not nearby, distributed regions. Integration measures are based on the concept of communication paths and path lengths, which

estimate the unique sequence of nodes and links that can carry the transmission flow of information between pairs of brain regions. The *shortest path* d_{ij} between two nodes is the path with the least number of links. The *average shortest path length* of node i of a graph G is the mean of all shortest paths from node i to all other nodes of the network: $L(G,i) = \frac{1}{N-1}\sum_{j\in\mathbb{N},j\neq i} d_{ij}$. The *average shortest path length* of all nodes is the mean of all shortest paths (Boccaletti et al., 2006): $L(G) = \frac{1}{N-1}\sum_{i,j\in\mathbb{N},i\neq j} d_{ij}$. In a weighted network, distance and weight have a reciprocal relation. If a weight between two adjacent nodes is doubled, their shortest path is cut by half: $L(G) = \frac{1}{N-1}\sum_{i,j\in\mathbb{N},i\neq j} \frac{d_{ij}}{w_{ij}}$.

Centrality refers to the importance of network nodes and edges for network functioning. The most intuitive index of centrality is the node degree, which gives the number of links connected to the node; for this measure, connection weights are ignored in calculations. In this study, we employ the network measure *node strength* s_i, which corresponds to the weighted node degree of node i and equals the sum of all its weights: $s_i = \sum_{j\in\mathbb{N}} w_{ij}$. Accordingly, the *average node strength* S corresponds to the mean of all node strengths $S = \frac{1}{N}\sum_i s_i$. All finite networks have a finite number of shortest paths $d(i,j)$ between any pair of nodes i, j. The *betweenness centrality* $c_B(s)$ of node s is equal to all pairs of shortest paths that pass through s divided by the number of all shortest paths in the network: $c_B(s) = \sum_{i,j\in\mathbb{N}} \frac{d(i,j|s)}{d(i,j)}$. For the *weighted betweenness centrality*, the *weighted shorted paths* are used.

2.7. Spectrogram Estimation

To generate the spectrograms, the *signal* package, part of the SciPy library (Virtanen et al., 2020), is used. The subroutine *stft* (short-time Fourier transform, STFT) generates Fourier transforms $\mathcal{F}[s(t)](t,f)$ of a signal $s(t)$ within a running time window of length ΔT_{win} at time t. The STFT is performed using overlapping windows (95% overlap) throughout this study. The window length is set to $\Delta T_{\text{win}} = 0.2$ s, leading to a sufficiently fine resolution in time and frequency. The colors in the spectrograms code the normalized power spectral density $|\mathcal{F}[v_k(t)](t,f)|^2/(\max|\mathcal{F}[v_k(t)](t,f)|^2)$ obtained from voltage signals v_k of different populations. For a better visibility, a log10 scale is used and values $<10^{-2}$ are set to 10^{-2}. Fourier transforms of the individual voltage signals v_k of different populations are first calculated giving rise to individual power spectral densities that are subsequently averaged over the populations to obtain the data f_{avg} shown in **Figures 2**, **9**. Finally, the spectrograms are shifted to the right by 0.1 s to preserve causality in correspondence of the stimulus onset.

3. RESULTS

The epileptic attractor is commonly described in terms of a self-sustained limit cycle that comes from the destabilization of the physiological activity while multiple types of transitions allow for the accessibility of seizure activity, status epilepticus, and depolarization block, that coexist, as verified experimentally in El Houssaini et al. (2020). The single-population firing rate (Equation 4) shows, in the absence of forcing, only fixed points as attractors. As it will become clear in the following section, a stable node and a stable focus are observable, separated by a bistability region between a high- and a low-activity state, whose boundaries are the locus of a saddle-node bifurcation (for more details see Montbrió et al., 2015). In this context are not observable self-sustained oscillations but only damped oscillations at the macroscopic level that reflect the oscillatory decay to the stable fixed point. This oscillatory decay will be considered as the representative of a seizure-like event, not being able to observe a stable limit cycle to describe the emergence of a fully developed seizure, as shown in other phenomenological mathematical models (Jirsa et al., 2014; Chizhov et al., 2018), commonly used to describe a detailed taxonomy of seizures. In particular, seizure-like events will be used as a paradigm to investigate the propagation of seizure-like activity in the network. A detailed comparison with the taxonomy of seizures described by other phenomenological models (Jirsa et al., 2014; Saggio et al., 2017; Chizhov et al., 2018) and the possible extension of the single-population firing rate (Equation 4) to show self-emergent periodic and bursting dynamics at the macroscopic level is reported in section 1 in the **Supplementary Material**.

3.1. Healthy Subjects

3.1.1. Phase and Bifurcation Diagrams

The analysis of the single-population firing rate Equations (4), performed in Montbrió et al. (2015), has revealed that there are three distinct regions, when considering the phase diagram of the system as a function of the external drive $\bar{\eta}$ and synaptic weight J, in absence of time-dependent forcing [$I(t) = 0$]: (1) a single stable node equilibrium corresponding to a low-activity state, (2) a single stable focus (spiral) generally corresponding to a high-activity state, and (3) a region of bistability between low and high firing rates. In particular, in the region where the stable focus is observable, the system undergoes damped oscillatory motion toward this fixed point. The presence of damped oscillations at the macroscopic level reflects the transitory synchronous firing of a fraction of the neurons in the ensemble. While this behavior is common in network models of spiking neurons, it is not captured by traditional firing-rate models (Schaffer et al., 2013; Devalle et al., 2017; Taher et al., 2020).

When considering the multipopulation neural mass model (5) with homogeneously set $\bar{\eta}^{(k)} = \bar{\eta}$, the corresponding phase diagram (shown in **Figures 1B,C**) is qualitatively the same as the one shown in Figure 1 in Montbrió et al. (2015), since the same attractors are observable. In the original model, these attractors are single-population states, while they reflect multipopulation states in the present case. Single-population low-activity (LA) and high-activity (HA) states translate into network LA and HA states. In the former, all populations have low, in the latter high firing rates. We observe that the single-population bistability accurately reflects the hysteretic transition in the network when changing $\bar{\eta}$. In the following, we will address how this relation between single-node and multipopulation phase diagram occurs.

The network bifurcation diagrams shown in **Figures 1A1–A3** for increasing σ values are obtained by performing an adiabatic

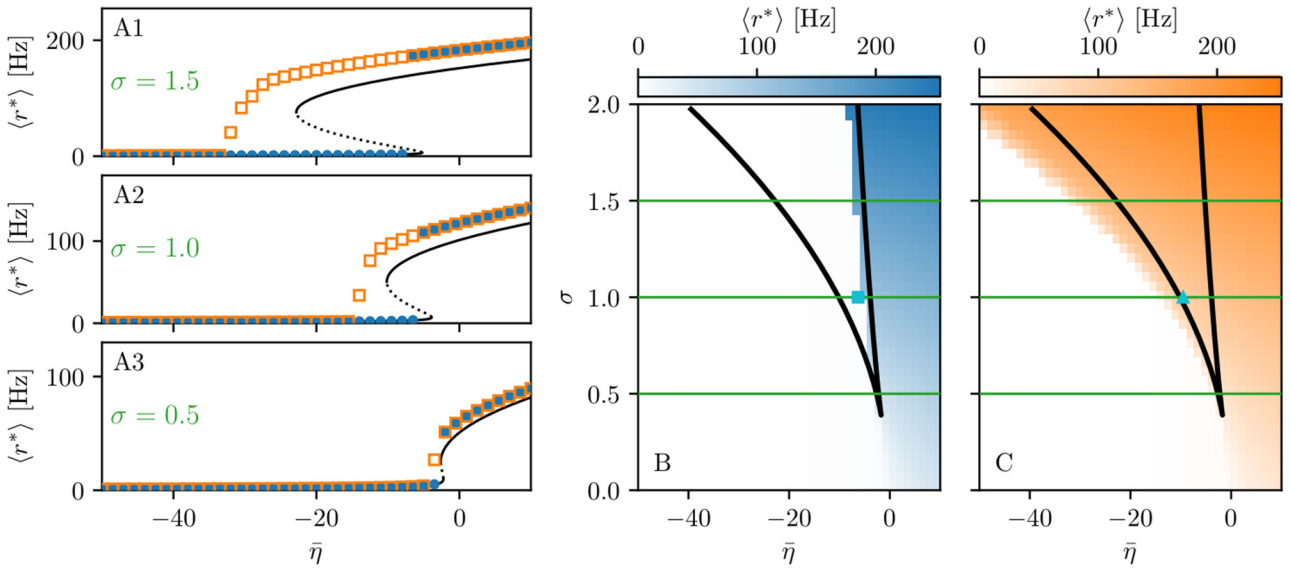

FIGURE 1 | Phase and bifurcation diagrams for subject H1. **(A1–A3)** Equilibrium firing rates $\langle r^* \rangle$ vs. $\bar{\eta}$ for the up sweep (blue dots) and down-sweep (orange squares). For each $\bar{\eta} \in [-50, 10]$ in steps of $\Delta\bar{\eta} = 1.5$, the system is initialized using the final state of the previous run and evolves for 2 s after which the average network firing rate in the equilibrium state is determined. Different panels correspond to different σ values: $\sigma = 1.5$ **(A1)**, $\sigma = 1$ **(A2)**, and $\sigma = 0.5$ **(A3)**. The solid (dashed) black line corresponds to the stable (unstable) equilibria in the single-node case. Maps of regimes as a function of σ and $\bar{\eta}$ showing the network average $\langle r^* \rangle$ color-coded for up- **(B)** and down-sweep **(C)**, obtained by following the same procedure as in **(A1–A3)** for $\sigma \in [0, 2]$ in steps of $\Delta\sigma = 0.05$. The black line indicates the single-node map of regimes like in Montbrió et al. (2015). In panels **(B,C)** the cyan square and triangle mark $\bar{\eta} = -6.3, -9.54$, respectively. Parameter values: $N_{\text{pop}} = 90$, $\tau_m = 20$ ms, $\Delta = 1$, $J_{kk} = 20$, $J_{kl} = 5\tilde{J}_{kl}$, $\forall k \neq l$.

analysis along with two different protocols such as up sweep and down-sweep. Following the up-sweep protocol, the state variables r_k, v_k of the system are initialized at $\bar{\eta} = -50$ with the values $r_k = 0$, $v_k = 0$; then the excitability is increased in steps $\Delta\bar{\eta} = 1.5$ until the maximal value $\bar{\eta} = 10$ is reached. At each step, the initial conditions for mean firing rates and mean membrane potentials correspond to the final state obtained for the previous $\bar{\eta}$ value. Note, that the average firing rate increases for increasing $\bar{\eta}$ values, both for the single node and the network. Once the maximum $\bar{\eta}$ value is reached, the reverse procedure is performed, thus following the down-sweep protocol. This time the initial conditions correspond to the high-activity state at $\bar{\eta} = 10$, while the excitability is adiabatically decreased in steps $\Delta\bar{\eta} = 1.5$ until a low-activity state at $\bar{\eta} = -50$ is approached. For both protocols, the investigation of the nature of the dynamics emerging at each $\bar{\eta}$-step is done by using the same procedure: the system is simulated for a transient time $T = 2$ s until it has reached an equilibrium state. At this time, the firing rate averaged over-all populations $\langle r^* \rangle$ is calculated and the next $\bar{\eta}$ iteration is started, using this final state as initial conditions.

The transition from LA to HA network dynamics is hysteretic: the system does not follow the same path during the up sweep and the down-sweep protocol. When the system is initialized in the low activity regime, it remains there until a critical excitability value $\bar{\eta}_{\text{HA}}$ is reached. For further increase of the excitability, the average firing rate exhibits a rapid jump to higher values. However, when the system is initialized in the high-activity regime, this regime survives for a large $\bar{\eta}$ interval until it collapses toward a low-activity state at $\bar{\eta} < \bar{\eta}_{\text{LA}}$, where $\bar{\eta}_{\text{LA}} < \bar{\eta}_{\text{HA}}$. There is a considerable difference between the critical excitability values required to lead the system to a high-activity or a low-activity regime and the difference increases for increasing coupling strength σ. While the up-sweep protocol (blue dots) is well approximated by the bifurcation diagram of the single population, represented in **Figures 1A1–A3** by the black (dashed and continuous) curve, this is no more true for the down-sweep protocol, where the coupling plays a role in determining the transition at the multipopulation level (orange squares). This results in different phase diagrams for the two protocols: the maps of regimes are dominated by the low-activity (high-activity) state when following the up-sweep (down-sweep) protocol. Merging these results, we observe that the region of bistability between LA and HA network dynamics is still identifiable by the original boundaries found for the single population in Montbrió et al. (2015) (black curve in **Figures 1B,C**), even though, for the multipopulation system, the region is wider.

We can make further use of the single-population bifurcation diagram to understand the hysteretic transition of the multipopulation model in more detail. First of all, the weight matrix $\{J_{kl}\}$ has its largest components on the diagonal ($J_{kk} = 20$), reflecting recurrent synapses. This means that synaptic inter coupling plays a minor role, as long as the firing rates of the adjacent populations are small. During the up-sweep protocol, this condition is fulfilled, as all populations are initialized in a low activity regime. Under these conditions, the dynamics of all nodes are rendered identical and equal, approximately, to the

single population dynamics. Consequently, the single-population LA branch describes the multipopulation LA behavior (in terms of $\langle r^* \rangle$) accurately as a function of $\bar{\eta}$. Second, as soon as the single-population LA state vanishes for large enough $\bar{\eta} > \bar{\eta}_{\mathrm{HA}}$, the individual nodes of the multipopulation system all transit to the HA state.

In this HA regime, deviations of the network bifurcation diagram with respect to the single-population curve are observed. The populations in the system have large firing rates, such that the inter-coupling becomes a relevant contribution to the total current on each node. This explains why the LA branch of the network is located at higher firing rates with respect to the black single-population curve: The populations in the network behave, approximately, as decoupled, irrespectively of being subject, in the HA regime, to an additional current due to the inter-coupling. This effectively shifts the single-population bifurcation diagram toward smaller $\bar{\eta}$. Moreover, this shift occurs for each population individually, depending on the matrix $\{J_{kl}\}$. During the down-sweep protocol, due to the population-dependent shift, the HA population states vanish at different values of $\bar{\eta}$. Accordingly, whenever this occurs, the network average $\langle r^* \rangle$ decreases by a small amount, such that the network LA state is reached *via* various intermediate states. We can infer, using the same type of argument, that single-population LA states disappear for increasing $\bar{\eta}$ in a region around $\bar{\eta}_{\mathrm{HA}}$. They are not observed in this study, due to the nature of the up-sweep protocol and the initialization procedure of r_k, v_k.

From the reversed viewpoint, we can hypothesize, that stable single-population HA states may take form near $\bar{\eta}_{\mathrm{LA}}$ for increasing $\bar{\eta}$ and stable LA states for decreasing $\bar{\eta}$ near $\bar{\eta}_{\mathrm{HA}}$. This implies that the network possesses complex multistability between many network states in the region $\bar{\eta}_{\mathrm{LA}} < \bar{\eta} < \bar{\eta}_{\mathrm{HA}}$. For these states, the existence of LA and HA states of individual populations are interdependent: Whether or not any given population can be in the LA or HA state is conditioned by the LA-HA configuration of all other populations. This not only demonstrates how multistability emerges in the multipopulation system but also influences the response of the network towards transient input in such a setting. Most importantly, if such an input recruits one population into high activity, other populations might follow, leading to a cascade of recruitments.

3.1.2. Seizure-Like Recruitment in Dependence of Perturbation Site and $\bar{\eta}$

To analyze the response of the multipopulation system to transient current, we stimulate one population with a step function $I_S(t)$ of amplitude $I_S = 10$ and duration $t_I = 0.4$ s. By setting $\bar{\eta} = -9.54$, the system is placed in the multistable regime (cyan triangle in **Figure 1C**), but, due to the low $\bar{\eta}$ value, it only allows for LA-HA configurations with most of the populations in LA. The stimulation with an external current $I_S(t)$ allows the system to reach a configuration with more populations in the HA. This corresponds to choosing equivalently, in the model, a higher excitability value for the single node such that it crosses the bistability region, thus reaching the HA regime. We start by initializing all nodes in the low-activity state and stimulating a single node (**Figure 2A**). During the stimulation (**Figure 2A1**), the stable states of the network change, due to the strong additional current (**Figure 2A2**). More specifically, the initial equilibrium vanishes and a new focus equilibrium of the system appears as the only stable network state. This focus is characterized by an LA-HA configuration for which only the stimulated node finds itself in HA while the rest remains in the LA regime; the focus is approached *via* damped oscillations in the time interval $0 < t < 0.4$ s (**Figures 2A3,A4**). Due to the multistability in absence of stimulation, an identical LA-HA configuration exists. Thus, when the current is removed, the system is able to maintain the LA-HA configuration. However, the position of the focus equilibrium is shifted in absence of the transient input and is reached again, *via* damped oscillations for $t > 0.4$ s.

When the perturbation of a single node has no consequences on the dynamics of the other populations, as shown in **Figures 2A2–A4**, we are in the presence of an *asymptomatic seizure-like event*, where the activity is limited to the EZ represented by the stimulated node and no propagation takes place. For higher excitability values ($\bar{\eta} = -6.3$, marked by a cyan rectangle in **Figure 1B**), the perturbation of a single node gives rise to different response dynamics. In this case, other brain areas are "recruited" and not only the perturbed node but also other populations reach the high-activity regime by showing damped oscillations (see **Figures 2B2–B4**). In terms of pathological activity, the seizure-like event originates in the EZ (as a result of the stimulation) and propagates to the PZ, identified by the other regions which rapidly propagate the oscillatory activity. The recruitment of the regions in the PZ can happen either by independent activation of the single areas or by activating multiple areas at the same time, in a *domino-like* effect (Creaser et al., 2020), until the propagation involves almost all populations (*generalized seizure-like event*).

The transition of a single population to the HA regime, upon stimulus onset, is characterized by a transient activity in the $\alpha - \beta$ band (10–14 Hz) and a sustained activity in the γ band (40–80 Hz), present throughout the stimulation, as shown in **Figures 2A5,A6**. In this study, the spectrograms show time-varying power spectral densities (PSD) of the mean membrane potentials averaged over the network (**Figure 2A5**) and for the single stimulated population (**Figure 2A6**). When more populations are recruited at higher excitability values, in addition to the former activity, it is possible to observe γ activity at higher frequencies (as shown in **Figures 2B5,B6**). High-frequency oscillations, between 80 and 500 Hz, can be recorded with EEG and reflect the seizure-generating capability of the underlying tissue, thus being used as markers of the EZ (Jacobs et al., 2012). Moreover, even for the generalized seizure-like case, the low-frequency band activity is evoked whenever a brain area gets recruited, leading to a sustained signal in the time interval $1.1\,\mathrm{s} < t < 1.8\,s$, where a majority of the populations approaches the HA state. Similar results have been obtained for all the other investigated subjects (results not shown).

In the following, we report a wide analysis of the impact of the perturbation site on the recruitment effect, for different excitability values. As before, we use a step current $I_S(t)$, with

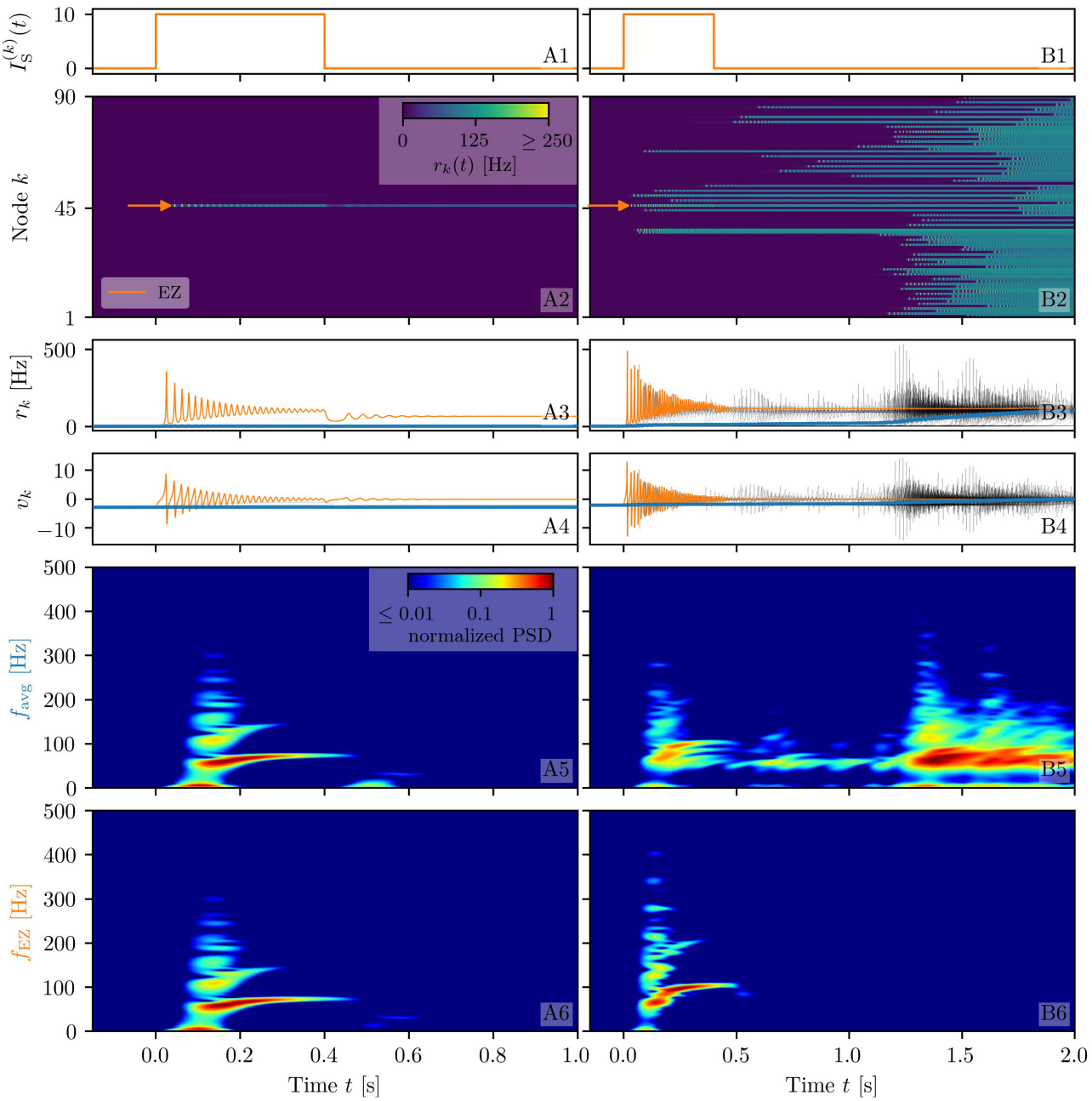

FIGURE 2 | Spectrograms of mean membrane potentials for healthy subject H1. **(A1, B1)** Stimulation current $I_S^{(k)}$, **(A3, B3)** population firing rates r_k, and **(A4, B4)** mean membrane potentials v_k for the EZ (orange) and other populations (black). The blue curves show the network average firing rate and membrane potential. Non-stimulated node dynamics are plotted as transparent gray curves: some of the nodes adapt their voltage to the stimulation of the EZ and change during stimulation. **(A2, B2)** Space-time plots of the population firing rates r_k, color-coding the value of the firing rate of each node, as a function of time. **(A5, B5)** Spectrogram of the network average membrane potential and **(A6, B6)** of the v_k of the EZ. Column A shows an asymptomatic seizure-like event for $\bar{\eta}^{(k)} = \bar{\eta} = -9.54$, column B shows a generalized seizure-like event for $\bar{\eta}^{(k)} = \bar{\eta} = -6.3$. In both cases, the EZ node 46 is stimulated. Parameter values: $N_{\text{pop}} = 90$, $\tau_m = 20$ ms, $\Delta = 1$, $J_{kk} = 20$, $\sigma = 1$, $J_{kl} = 5\tilde{J}_{kl}$, $\forall k \neq l$.

fixed amplitude $I_S = 10$ and duration $t_I = 0.4$ s, to excite a single population. In each run, the stimulating current targets a different brain area and the number of recruitments, i.e., the number of populations that pass from the LA state to the HA state is counted. The $N_{pop} = 90$ brain areas are targeted, one at a time, in 90 individual simulations. We repeat the procedure varying $\bar{\eta}$ in a range $[-15, -4]$, with steps of $\Delta\bar{\eta} = 0.1$. The results for five exemplary subjects are shown in **Figures 3A1–E1**).

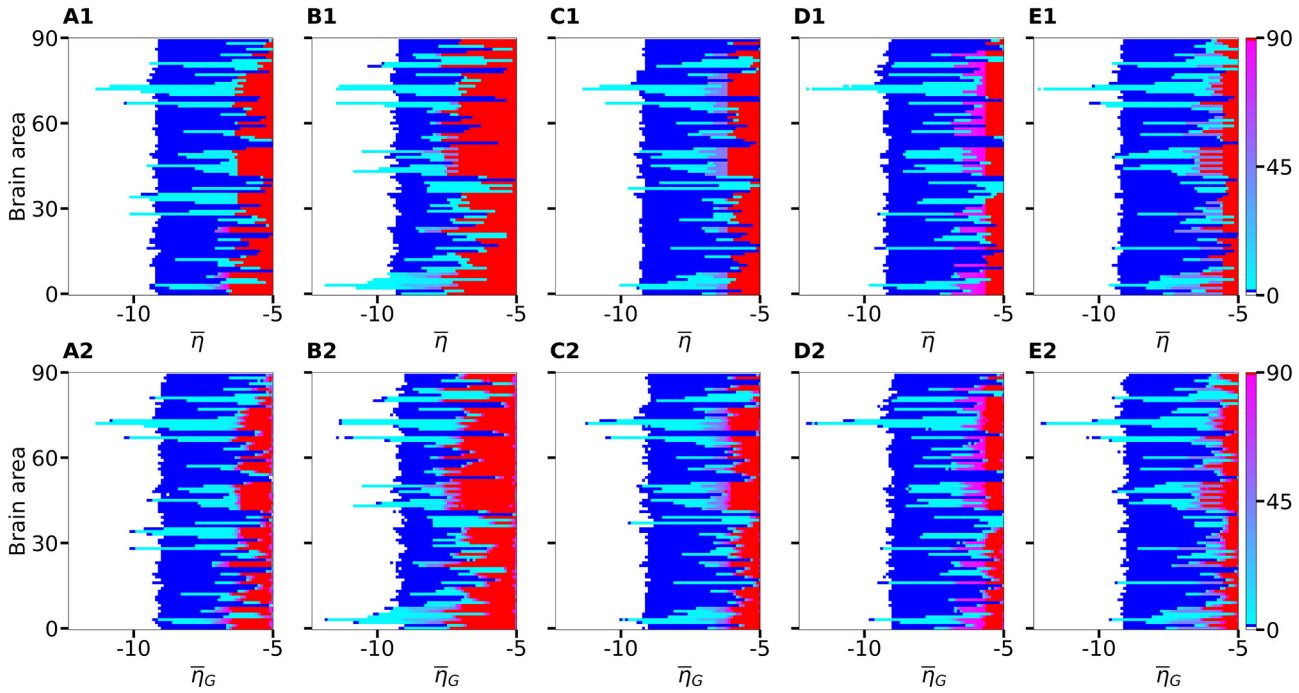

FIGURE 3 | Number of recruited brain areas as a function of the excitability parameter $\bar{\eta}$ for five exemplary healthy subject connectomes **(A–E)**. Color coding is the following: blue corresponds to the asymptomatic threshold (one area in HA regime); red represents 90 areas in HA regime (generalized threshold); cyan to purple indicate intermediate recruitment values, white marks no recruitment. When performing a vertical cut, all nodes are characterized by the same $\bar{\eta}$ for panels **(A1–E1)**. On the contrary, in panels **(A2–E2)**, $\bar{\eta}_G$ represents the mean value of a Gaussian distribution with standard deviation 0.1. Therefore, when perturbing one brain area at a time, excitabilities are distributed and not uniform in the latter case; the results are averaged over 10 repetitions with different Gaussian excitability distributions. **(A–E)** correspond to subjects H1, H5, H12, H16, and H19. Parameters: $N_{pop} = 90$, $\Delta = 1$, $\sigma = 1$, $I_S = 10$, $t_I = 0.4$ s.

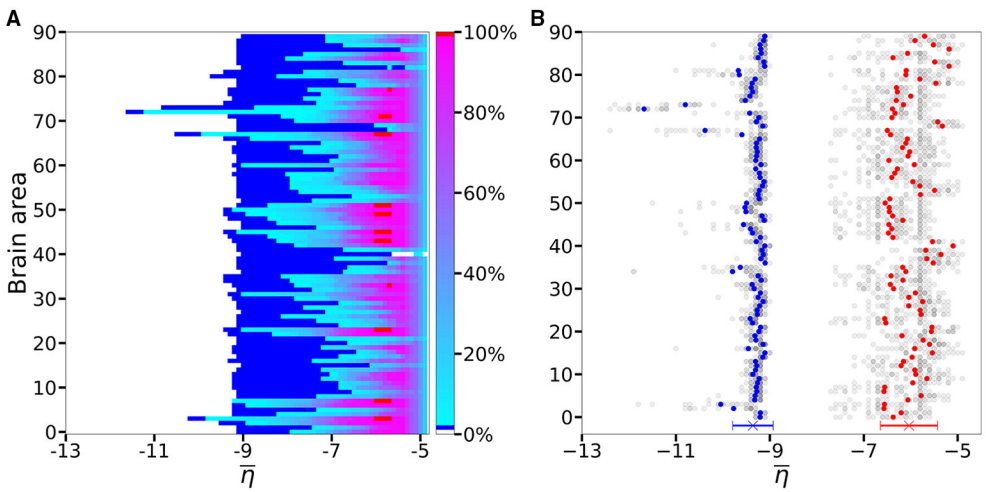

FIGURE 4 | (A) Number of recruited brain areas as a function of the excitability parameter $\bar{\eta}$, as shown in **Figures 3A1–E1**, averaged across all subjects. **(B)** $\bar{\eta}$ threshold values for asymptomatic and generalized seizure-like events. Gray dots show the thresholds for each brain area and each subject. Blue and red dots show the average over $\bar{\eta}^{(k)}_{asy}$ and $\bar{\eta}^{(k)}_{gen}$ across all subjects. The blue and red cross at the bottom shows the average value and its standard deviation for both thresholds across all subjects and all areas. Parameters as in **Figure 3**.

If the perturbed area jumps back to the LA state when the stimulation is removed and no further recruitment takes place, then the total number of recruited areas is zero, the color is coded in white. If the perturbed area remains in the HA state without recruiting other areas, we are in presence of an asymptomatic seizure-like event (blue regions). For every further recruited

brain area, the color code changes from cyan to purple. If all brain areas are recruited, we observe a generalized seizure-like event (coded as red). For $\bar{\eta} < -9$, most of the targeted brain areas goes back to the LA state, when the perturbation ends, while for $\bar{\eta} \approx -9$, we generally observe asymptomatic seizure-like events for all the subjects and most of the perturbation sites. For increasing $\bar{\eta}$ values, the probability for larger recruitment cascades increases, until the system exhibits generalized seizure-like events for $\bar{\eta} > -6$. However, some notable differences between brain areas and among the different subjects are observable. Brain area 72, for example, corresponding to the rh-CAU, exhibits asymptomatic seizure-like events at $\bar{\eta} > -11$ for most of the subjects, thus suggesting that the rh-CAU favors pathological behavior with respect to other brain areas. On the other hand, some brain areas are less likely to cause generalized seizure-like events, when stimulated, than others: brain area 40, for example, the rh-PHIP[1], causes no generalized seizure-like events for any $\bar{\eta} > -5$. Note that, for very large $\bar{\eta}$ values, the system does not exhibit multistability anymore, but instead has only one stable state, namely the network HA state, corresponding to the high firing rate of all populations. Approximately, this happens for $\bar{\eta} \in [-5.7, -4.9]$, with small variations among the subjects.

The scenario remains unchanged when we take into account heterogeneous excitabilities $\bar{\eta}^{(k)}$, as shown in **Figures 3A2–E2**. In this case, $\bar{\eta}^{(k)}$ is drawn from a Gaussian distribution with mean $\bar{\eta}_{\mathrm{G}}$, thus mimicking the variability among different brain areas present in a real brain. The populations are stimulated, as before, one at a time in individual simulation runs. However, this time the procedure is repeated for varying $\bar{\eta}_{\mathrm{G}} \in [-15, -4]$, while keeping the standard deviation of the Gaussian distribution fixed at 0.1. Larger standard deviation (≥ 1) hinder the rich multistability of the network, by eliminating the bistability between LA and HA for individual populations, due to excessively small or large $\bar{\eta}^{(k)}$, thus impeding the analysis of the impact of the stimulation, as shown in the **Supplementary Figure 1**. In particular, for larger standard deviation, an increasing amount of nodes reaches the stable focus regime, thus being able to recruit other brain areas before the stimulation is applied, while nodes whose effective excitability turns out to be very small, are too far from the bistability region to be able to reach the HA regime. The results shown in **Figure 3** are obtained averaging over 10 Gaussian distribution realizations of the $\bar{\eta}$ parameter; slightly more variability becomes apparent especially when considering the threshold in $\bar{\eta}$ to observe generalized seizures. Indeed, the excitability threshold to observe generalized seizures is the most drastically affected as the standard deviation increases, as shown in **Supplementary Figure 1**.

An overview over all the investigated subjects is possible when looking at **Figure 4A**, where is reported the average, over-all subjects, of the data shown in **Figures 3A1–E1** for five exemplary subjects only. The averaging operation smears out the transition contours, and while the region of generalized seizure-like events shrinks, it becomes wider in the region of accessibility of partial seizure-like events, where a small percentage of nodes ($\sim$ 20%) are recruited. In **Figure 4B** we report $\bar{\eta}^{(k)}_{\mathrm{asy}}$ ($\bar{\eta}^{(k)}_{\mathrm{gen}}$), i.e., the smallest $\bar{\eta}$ value for which an asymptomatic (generalized) seizure-like event occurs when stimulating population k. Gray dots indicate the individual thresholds $\bar{\eta}^{(k)}_{\mathrm{asy}}$ and $\bar{\eta}^{(k)}_{\mathrm{gen}}$ for each of the 20 subjects and 90 brain areas; the averages over all subjects are denoted by blue and red circles, respectively, for each $k \in [1, 90]$. Averaging these thresholds over all subjects and brain areas yields an asymptotic threshold of $\bar{\eta}_{\mathrm{asy}} = -9.36 \pm 0.43$ and a generalized threshold of $\bar{\eta}_{\mathrm{gen}} = -6.04 \pm 0.38$. Brain areas 72, 73, 67, and 3 have lower thresholds for asymptomatic seizure-like events, areas 40, 86, and 82 have larger thresholds for generalized seizure-like events and do not fall within a standard deviation. The variability in the response among the different areas is more evident for $\bar{\eta}^{(k)}_{\mathrm{gen}}$ values compared to the $\bar{\eta}^{(k)}_{\mathrm{asy}}$ ones: the threshold values to obtain an asymptomatic seizure-like events are very similar among the areas and among the subjects, while the threshold values to obtain a generalized seizure-like event strongly depend on the stimulated area and on the subject.

3.1.3. The Role Played by Brain Area Network Measures on Enhancing Recruitment

As shown in **Figure 4B**, $\bar{\eta}^{(k)}_{\mathrm{asy}}$ does not vary significantly among the subjects and among the brain areas; it mainly occurs in the range $\bar{\eta}^{(k)}_{\mathrm{asy}} \in [-10, -9]$, with just few nodes ($k \in [72, 73, 67, 3]$) showing smaller values. Since each brain area is characterized by its network measure, the first hypothesis that we aim to test, is the role played in the identification of the threshold, by the different network measures. We will verify in the following that connection strength and shortest path length are determinants to identify the threshold $\bar{\eta}^{(k)}_{\mathrm{gen}}$: Generalized seizure-like events are enhanced by nodes forming a clique that rapidly communicate through a dense subgraph. In particular, we investigate the dependency of $\bar{\eta}^{(k)}_{\mathrm{asy}}$ on the node strength, clustering coefficient, shortest path length, and betweenness centrality of the corresponding brain area, as shown in **Figure 5**. A very strong correlation between asymptomatic threshold and node strength becomes apparent: Brain areas that are strongly connected, need smaller excitability to pass from the LA to the HA regime (**Figure 5A1**). The same holds for the clustering coefficient, even though the relationship is less sharp (**Figure 5B1**). Moreover, it is possible to observe a direct correlation between $\bar{\eta}^{(k)}_{\mathrm{asy}}$ and shortest path length (i.e., shortest is the path and smallest is the threshold value), while betweenness is smaller for higher threshold values (**Figures 5C1,D1**, respectively).

When considering the threshold for generalized seizure-like events, we face a higher variability among different nodes (as shown in **Figure 4B**, $\bar{\eta}^{(k)}_{\mathrm{gen}}$ varies mainly between -6.5 and -5.5). The dependency of $\bar{\eta}^{(k)}_{\mathrm{gen}}$ on the node strength reveals a strong correlation: Areas with very small node strengths are characterized by large thresholds and are less likely to

[1]While the actual role of the specific regions might in reality be affected by other factors, not captured by the used structural connectivity estimate and the details of the current model, this highlights the effect of network structure on propensity to seizure-like events. The (para)hippocampal region is, in fact, one of the most commonly affected by epilepsy.

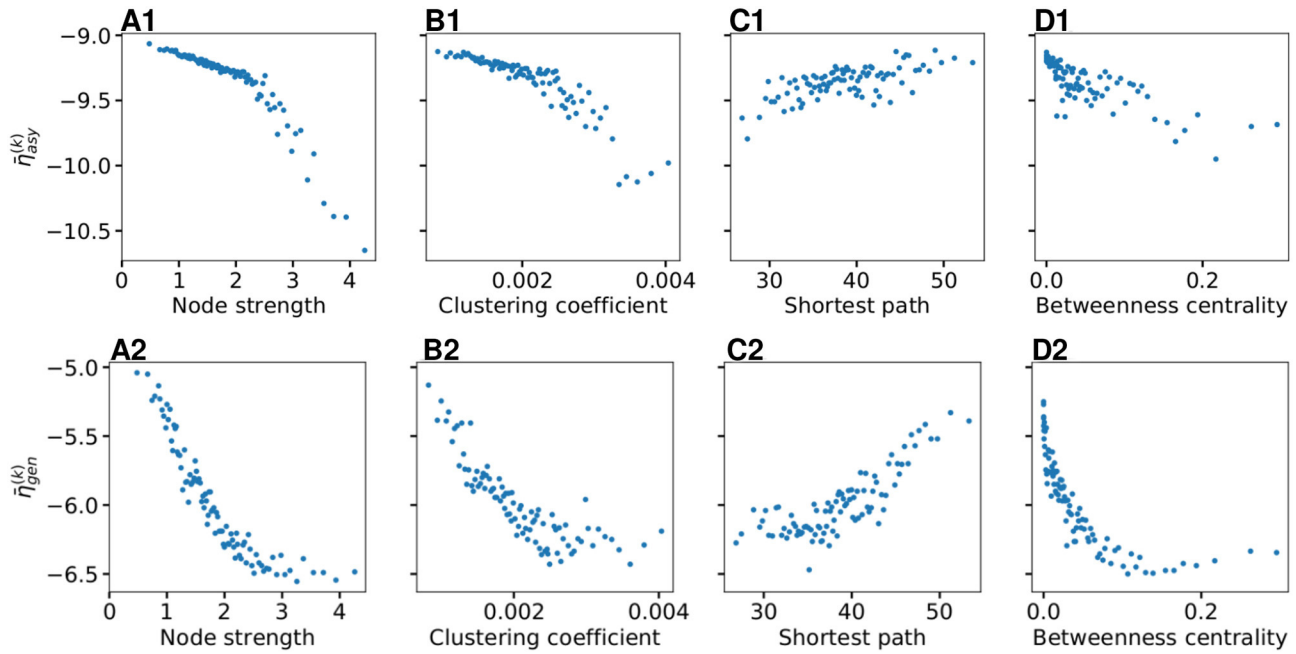

FIGURE 5 | Thresholds $\bar{\eta}^{(k)}_{\text{asy}}$ for asymptomatic seizure-like events **(A1–D1)** and $\bar{\eta}^{(k)}_{\text{gen}}$ for generalized seizure-like events **(A2–D2)** as a function of node measures: **(A)** Node strength, **(B)** clustering coefficient, **(C)** average shortest path length, and **(D)** betweenness centrality. For each panel, the thresholds $\bar{\eta}^{(k)}_{\text{asy}}$, $\bar{\eta}^{(k)}_{\text{gen}}$ are calculated for all $k \in [1, 90]$ brain areas and averaged over all 20 subjects. Parameters as in **Figure 3**.

cause generalized seizure-like events. On the other hand, for large node strengths, $\bar{\eta}^{(k)}_{\text{gen}}$ saturates at a value ≈ -6.5 (as shown in **Figure 5A2**). The clustering coefficient, shown in **Figure 5B2**), shows a similar relationship as the node strength, even though more scattered. This is not surprising since node strength and clustering coefficient are strongly correlated with each other (the Pearson correlation coefficient, in this case, is $r = 0.75$, as shown in **Supplementary Figure 2**), thus explaining the similarity between the analyses reported in **Figures 5A,B**. Moreover, regarding the integration measure, it turns out that the average shortest path length correlates positively with $\bar{\eta}^{(k)}_{\text{gen}}$ (as shown in **Figure 5C2**). Brain areas that are characterized, on average, by a short path to all the other areas are more likely to cause generalized seizure-like events. Finally, the betweenness centrality correlates negatively with $\bar{\eta}^{(k)}_{\text{gen}}$ (**Figure 5D2**). This means that brain areas that are crossed by many shortest path lengths (large betweenness centrality) are more likely to cause generalized seizure-like events. For increasing node strength, clustering coefficient, and betweenness centrality, we observe a saturation toward $\bar{\eta}^{(k)}_{\text{gen}} \approx -6.5$, that corresponds to the critical excitability value, during the up-sweep simulation, at which the system jumps to the HA network state (**Figure 1A2**).

To explore the causal mechanisms of brain dynamics and understand the sequential mechanism of node recruitment in more detail, we investigate the timing at which different brain areas are recruited. For this, the excitability parameter $\bar{\eta}$, common to all populations, is set to the threshold value $\bar{\eta}^{(k)}_{\text{gen}}$ of the perturbed brain area k, ensuring complete recruitment of all populations, when perturbing populations $k \in [1, 90]$. The results shown in **Figure 6** are obtained by averaging over k and the different subjects: in 90 individual simulations for each subject, a single brain area $k = 1, \ldots, 90$ is stimulated with an external step current $I_{\text{S}}(t)$, characterized by an amplitude $I_{\text{S}} = 10$ and a duration $t_{\text{I}} = 0.4$ s. For each k, the recruitment time of all the other areas is registered. The stimulated brain area stands in for the EZ. The brain areas and corresponding node measures are sorted by the recruitment time in ascending order. The values for recruitment time (**Figure 6A**), the weight of a connection between a single area and the EZ (**Figure 6B**) and shortest path (**Figure 6C**) is finally obtained averaging over all the stimulated nodes and all the subjects (i.e., the average is performed over 1,800 simulations across all 90 brain area perturbations times for all 20 subjects). The same averaging procedure has been employed to obtain the data shown in **Figures 6D–G**. However, in this case, the node measures are evaluated over all the connections of the recruited node minus the connection to the EZ. While ignoring the link to the exciting area (EZ), the overall network measure for connection weights (**Figure 6D**), clustering coefficient (**Figure 6E**), shortest path (**Figure 6F**), and betweenness centrality (**Figure 6G**) are reported.

On average, the first recruited brain area (labeled as 1) is connected to the EZ with a weight equal to 0.25 (1/4 of the maximum possible weight), and it is characterized by an average shortest path length to the EZ of <4.7. Moreover, the area is recruited within an average time of <156 ms (calculated after the onset of the external perturbation current). However, the first recruited area has, not only the strongest weight and the

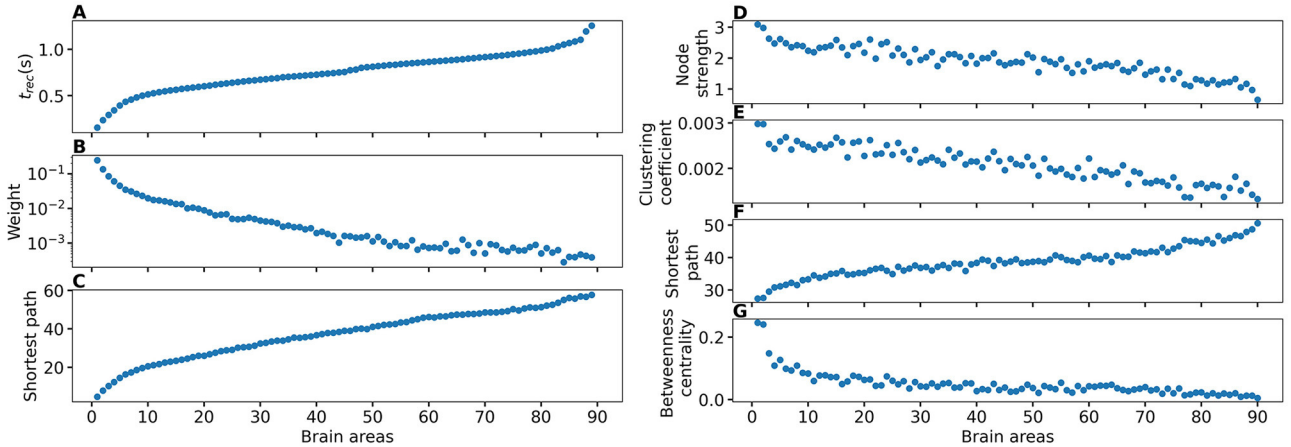

FIGURE 6 | (A) Recruitment times reported in descending order: Brain area 1 is the brain area that is recruited first and brain area 90 is the last recruited brain area. **(B)** Connection weights between the recruited brain area and the EZ, ordered according to their recruitment time, thus following the indexing of **(A)**. **(C)** Shortest path between the recruited area and the EZ, ordered according to their recruitment time. **(D)** Connection weights between the recruited brain area and all the nodes except EZ, ordered according to their recruitment time. **(E)** Clustering coefficient between the recruited brain area and all the nodes except EZ, ordered according to their recruitment time. **(F)** Shortest path between the recruited area and all the other nodes except EZ, ordered according to their recruitment time. **(G)** Betweenness centrality between the recruited brain area and all the nodes except EZ, ordered according to their recruitment time. The excitability $\bar{\eta}^{(k)}$ is set to the subject-specific threshold $\bar{\eta}^{(k)}_{\text{gen}}$, according to **Figure 3B** for each subject separately. Data are averaged over all subjects and all the stimulated areas. Parameters: $N_{\text{pop}} = 90$, $\Delta = 1$, $\sigma = 1$, $I_S = 10$, $t_I = 0.4$ s as in **Figure 3**.

shortest path to the EZ but also has, in general, the largest node strength, largest clustering coefficient, shortest average path length, and largest betweenness centrality. The seizure-like event spreads rapidly along with the brain areas with strongest connection weights outgoing from the EZ; the stronger weights are associated with the shortest paths from the EZ. Overall, a region well connected is a region well recruited; this is related to the log-normal distribution of the weights (as shown in **Supplementary Figure 3**): few connections per node have a strong weight, thus allowing for fast recruitment. Note that the results for one exemplary subject and just one perturbed brain area per time (i.e., not averaged over all the brain areas and over all subjects) are comparable, even though the corresponding relationships are characterized by more variability (data not shown).

If we vary the amplitude I_S of the perturbation current, the recruitment time will vary accordingly, decreasing for increasing I_S. In particular, in **Figure 7** we show an exemplary case, obtained from the stimulation of one brain area (45), for a specific subject (results are similar for other trials). Irrespectively of the recruitment order, the time needed by the first 10 recruited brain areas to pass from the LA to the HA state decreases slightly for increasing amplitude. However, this decrease reaches saturation at a current value $I_S \approx 40$ already. The order of recruitment varies little: we observe some exchanges between the 4-th and 5-th and between the 9-th and 10-th recruited areas. For example, for an amplitude $I_S = 15$, the 9th recruited area (dark blue circles) gets recruited earlier than the 10th area (pink dots), while, for very strong currents ($I_S = 100$), the 9th area gets recruited latest. On the other hand, we do not observe a significant change in the recruitment time and order if we increase the duration t_I of the stimulation (as shown in **Supplementary Figure 4**).

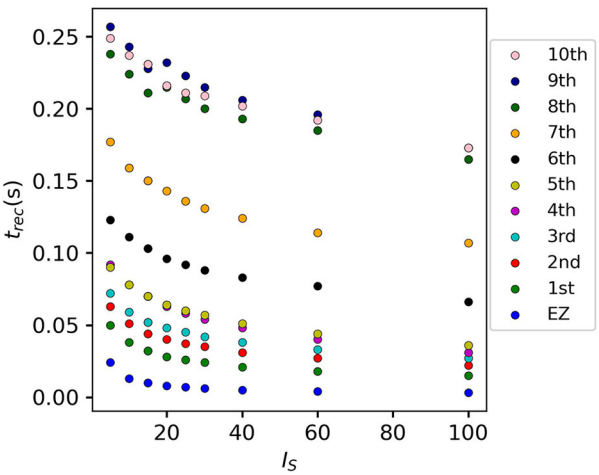

FIGURE 7 | Recruitment times of the first 10 recruited areas as a function of the input current I_S. The strength of the input current is varied between 0 and 100 on the *x*-axis. The order of the recruitment is color-coded for each current strength, and it changes slightly with different current strengths. Parameters: $N_{\text{pop}} = 90$, $\Delta = 1$, $\sigma = 1$, $t_I = 0.4$ s, $\bar{\eta}^{(k)} = \bar{\eta} = -6$, stimulation site: brain area $k = 45$ of subject H1.

3.2. Epileptic Patients

3.2.1. Phase and Bifurcation Diagrams

In this section, the structural connectivity matrices of epileptic patients are employed and an analysis, analogous to the one in section 3.1.1, is provided. We present the phase and bifurcation diagrams for the multipopulation neural mass model,

employing the structural connectivity matrices of epileptic patients. As detailed before, the bifurcation diagrams shown in **Figures 8A1–A3**, for different σ values, are obtained by performing an adiabatic scan along $\bar{\eta}^{(k)} = \bar{\eta}$, following the up- and down-sweep protocols.

As for the healthy subjects, the transition is hysteretic with $\bar{\eta}_{\mathrm{LA}} < \bar{\eta}_{\mathrm{HA}}$. However, in this case, the width of the hysteretic transition is bigger, especially for larger σ values, as testified by the comparison with the dotted red curve, reported in **Figures 8A1–A3**, that represents the results shown in **Figure 1**. This increased width can be translated in terms of the extension of the multistability region in the phase diagram (as shown in **Figures 8B,C**), which turns out to be slightly larger than before. Also in this case, the results for a healthy subject are reported for a better comparison (continuous red curve in **Figures 8B,C**). The increase in size mainly occurs due to a shift of $\bar{\eta}_{\mathrm{LA}}$, i.e., of the left boundary of the multistability regime. In this region, the transition from HA to LA, following the down-sweep, is more smooth and elongates toward smaller $\bar{\eta}$ values. This implies that, in this transition region, more single population HA states exist for epileptic patients than for healthy subjects. In other words, brain areas of epileptic subjects are more prone to recruitment[2].

While the phase diagram is obtained in the absence of time-varying input, we investigate the response of the multipopulation system to transient stimulation in the following. As for the healthy subjects, a single population is excited by injecting a step current $I_{\mathrm{S}}(t)$ of amplitude $I_{\mathrm{S}} = 10$ and duration $t_{\mathrm{I}} = 0.4$ s. Initially ($t < 0$), the system is in a multistable regime, starting in the low-activity network state. For small $\bar{\eta}$ values ($\bar{\eta} = -14$, identified by the triangle in **Figure 8C**), when a single node is stimulated, the system reacts analogously to the healthy subject case: during the stimulation, only one stable network state exists, i.e., a focus equilibrium with an LA-HA configuration for which only the stimulated node is in HA (**Figure 9A2**). This focus is approached *via* damped oscillations ($0\,\mathrm{s} < t < 0.4\,\mathrm{s}$). When the stimulation is removed, the network maintains the LA-HA configuration, but approaches the new location of the focus again *via* damped oscillations (**Figures 9A3,A4**). As a result, the stimulated node has large firing activity, while the remaining network is in a LA regime. For higher excitability values ($\bar{\eta} = -7.5$, identified by the square in **Figure 8B**), the perturbation of a single node gives rise to a cascade of recruitments, where other brain areas, initially not perturbed, reach the HA regime by showing damped oscillations (**Figures 9B2–B4**). With respect to the recruitment features shown in **Figure 2**, we observe in this study a faster emergence of the generalized seizure-like event: once a brain area is stimulated, the others react, in-substantial number, quite immediately.

Looking at the spectrograms, the transition of the stimulated population to the HA regime is characterized by a transient activity at low frequency (< 20 Hz) and a sustained activity in the γ band (50–180 Hz), observable throughout of the stimulus, as shown in **Figure 9A6**, where the spectrogram for the single stimulated population is reported. Regarding the spectrogram of the mean membrane potentials averaged over the network populations (**Figure 9A5**), it turns out that the low-frequency activity in the δ, θ bands is present, while the activity at high frequency simply reflects the activity of the stimulated area. Activity in the δ band, together with multiple types of α-like rhythms have been recently found in a network of two Jansen-Rit neural mass models, representing two cortical regions, as a result of input changes in the other region (Ahmadizadeh et al., 2018), thus confirming that the range of possible activity varies with changes in the external inputs and interconnectivity gains.

In the case of large recruitment events, at larger excitability values, it is possible to observe γ activity at higher frequencies (as shown in **Figures 9B5,B6**), which is enhanced with respect to the situation where an asymptomatic seizure-like event is present. Moreover, comparing the spectrograms in **Figure 9** and those reported in **Figure 2**, we see that the activity takes place at higher frequency ranges when considering structural connectivity matrices of epileptic patients and the activity is mainly concentrated in the EZ. A further comparison is possible, looking at **Figures 9A8–B8**, where the spectrograms for the healthy subject H2 are reported. With respect to the case shown in **Figure 2**, the excitability parameter has been increased to observe a faster *domino-like* effect, on the same temporal scale as for the epileptic patients. While high-frequency oscillations (>200 Hz) are observable for the epileptic patient case, they are not detectable in **Figure 9B8** for the healthy subject case. The last statement may be qualified, however, by recent studies proposing high-frequency oscillations (80–500 Hz) recorded not only at seizure onset but also between seizures (the interictal period), as a putative new marker of the epileptogenic focus (Jacobs et al., 2012). More specifically fast cortical ripples superimposed to interictal epileptiform discharges were correlated with the seizure onset zone and primary propagation area in neocortical epilepsy (Khadjevand et al., 2017). Neocortical ripples were also found to be more specifically confined to the seizure onset and propagation regions, and thus a better marker compared to interictal epileptiform discharges alone (Wang et al., 2013). High-frequency oscillations, as obtained *via* numerical experiments and shown in **Figures 9B5,B6**, are much more frequent in the seizure-like onset zone than outside, where they are often totally absent. The rather empty spectrograms of mean membrane potentials for patient E6 are a result of rather rapid recruitment of a majority of nodes, thus giving rise to a strong signal change, immediately upon recruitment, which suppresses the rest of the signal in the spectrogram. At the same time, the damped oscillations are all compressed within a narrow time window, and not very elongated in time, as it happens for healthy subjects (as shown in **Figure 2**). In other words, if the generalized seizure-like event is rapid, all the signals overlap, and this is especially clear looking at the strong low-frequency bands. A fast generalized seizure-like event, in absence of high-frequency oscillations outside the EZ, can be obtained for healthy subjects only increasing the excitability parameter: for higher $\bar{\eta}$ values, the recruitment is more sudden, as shown

[2]Please note that, irrespectively of the numerical results, any difference observed between the structural connectivity matrices obtained from the cohort of healthy subjects and epileptic patients may be (at least partially) ascribed to the different acquisition and processing procedures in the two research centers rather than due to disease-related causes.

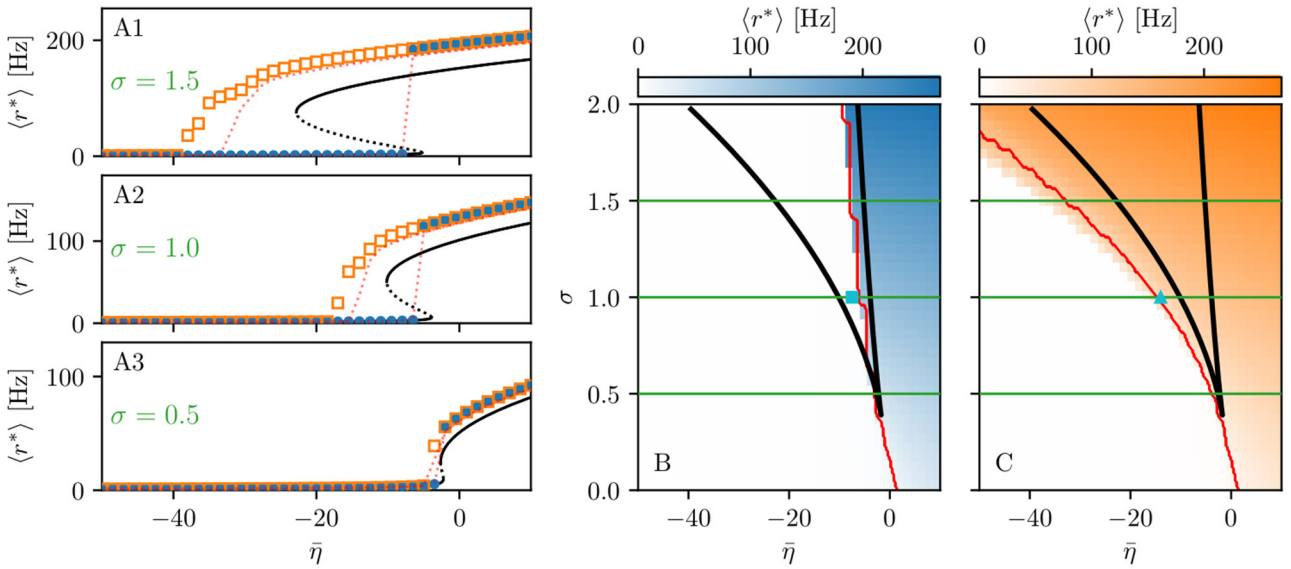

FIGURE 8 | Phase and bifurcation diagrams for patient E6. **(A1–A3)** Equilibrium firing rates $\langle r^* \rangle$ vs. $\bar{\eta}$ for the up sweep (blue dots) and down-sweep (orange squares). For each $\bar{\eta} \in [-50, 10]$ in steps of $\Delta\bar{\eta} = 1.5$, the system is initialized using the final state of the previous run and evolves for 2 s after which the average network firing rate in the equilibrium state is determined. Different panels correspond to different σ values: $\sigma = 1.5$ **(A1)**, $\sigma = 1$ **(A2)**, and $\sigma = 0.5$ **(A3)**. The solid (dashed) black line corresponds to the stable (unstable) equilibria in the single-node case. The dotted red line depicts the results for the healthy subject H1 reported in **Figure 1**. Maps of regimes as a function of σ and $\bar{\eta}$ showing the network average $\langle r^* \rangle$ color-coded for up- **(B)** and down-sweep **(C)**, obtained by following the same procedure as in **(A1–A3)** for $\sigma \in [0, 2]$ in steps of $\Delta\sigma = 0.05$. The black line indicates the single-node map of regimes like in Montbrió et al. (2015). The red solid line indicates the boundaries of the map of regimes previously as shown in **Figure 1** for the healthy subject H1. In **(B,C)** the cyan square and triangle mark $\bar{\eta} = -7.5, -14$, respectively. Parameter values: $N_{pop} = 88$, $\tau_m = 20$ ms, $\Delta = 1$, $J_{kk} = 20$, $J_{kl} = 5\tilde{J}_{kl}$, $\quad \forall k \neq l$.

in **Figure 9B8**). A difference between the signals obtained by numerically simulating the multipopulation exact neural mass model and the high-frequency oscillations observed in human intracranial EEG studies can be found in the different oscillation amplitudes: high-frequency oscillations recorded during pre-surgical evaluation in patients, both at the seizure onset and during the interictal period, are characterized by a low amplitude (Allen et al., 1992; Traub et al., 2001; Worrell et al., 2004; Zijlmans et al., 2012), while this is not the case in this study. We can conjecture that higher amplitudes are related to the nature of the coupling, which we have chosen globally coupled and fully excitatory.

3.2.2. Temporal Recruitment of Clinically and SEEG Predicted PZs

In the following, we test the clinical predictions for epileptic patients, by choosing the EZs, identified by clinical doctors *via* presurgical invasive evaluation, as perturbation sites. We investigate the recruitment times of different brain areas following such a perturbation and compare the order of recruitment with the experimental data given for each subject. A general overview of the recruitment times of all brain areas, for all patients, is shown in **Figure 10**. As perturbation sites, the clinical EZs are used for all patients. For patients with several nodes detected in the EZ, all areas were stimulated simultaneously. The perturbation step current ($I_S = 10$, $t_I = 0.4$ s) is applied, to each perturbation site, in correspondence with the dashed vertical black line. The parameters are identical for almost all patients and are chosen such that at least 90% of the brain areas are recruited while still allowing multistability among various LA-HA configurations, including the network LA state. For each patient (identified *via* his/her number on the y-axis), the recruitment time of each brain area is reported: the gray dots represent the time values for each brain area. Superimposed on the gray dots are orange and blue dots that identify the brain areas belonging to the PZ, according to the non-invasive (PZ_{Clin}) or invasive (PZ_{SEEG}) presurgical evaluation, respectively. The recruitment time-averaged over all brain areas is identified, for each patient, by a green vertical line, while the boxes contain the second and third quartile of the distribution, and the whiskers have 1.5 the length of the interquartile range (IQR) from the upper or lower quartiles. A one-sided Mann Whitney *U*-test has been performed to estimate the statistical significance of PZ_{SEEG} and PZ_{clin} recruitment times, as shown in **Supplementary Figure 5**. Remarkably, the propagation zones PZ_{Clin} and PZ_{SEEG} turn out to be among the first recruited brain areas for all patients in the numerical experiments. However, the temporal dynamics vary for all patients, with E8 and E1 having late recruitments. Looking at the set of the first 10 recruited brain areas for each patient (reported in detail in **Supplementary Tables 5–7**), we notice that most of the areas, identified by clinicians as belonging to the PZ, are actually within this set: for patients E4, E5, E6, E9, and E15, all the areas belonging to PZ_{Clin} are among the first 10 recruited areas, while

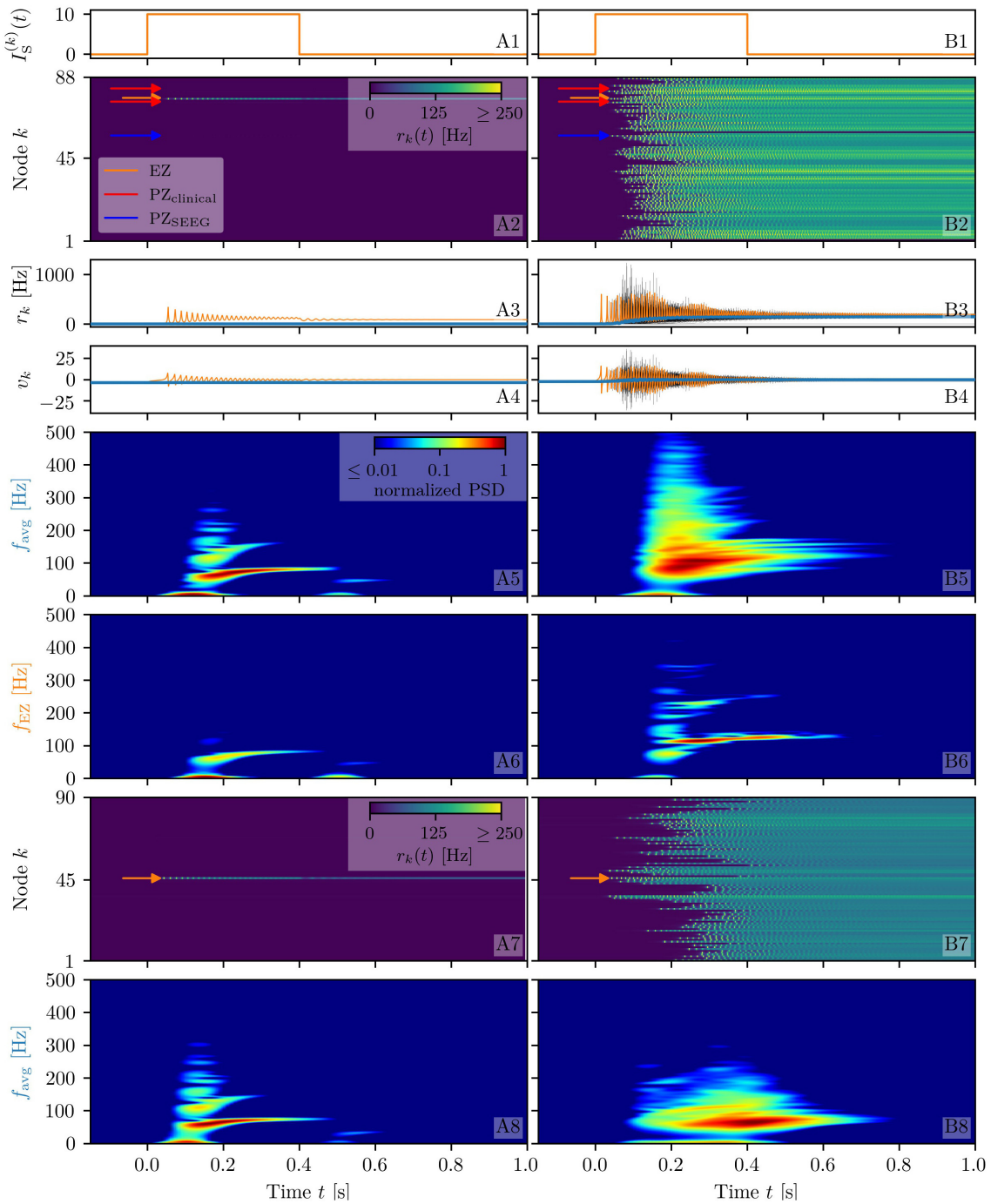

FIGURE 9 | Spectrograms of mean membrane potentials for patient E6. **(A1, B1)** Stimulation current $I_S^{(k)}$, **(A3, B3)** population firing rates r_k, and **(A4, B4)** mean membrane potentials v_k for the EZ (orange) and other populations (black). The blue curves show the network average firing rate and membrane potential. **(A2, B2)** Space-time plots of the population firing rates r_k, color-coding the value of the firing rate of each node, as a function of time. **(A5, B5)** Spectrogram of the network average membrane potential and **(A6, B6)** of the v_k of the EZ. Column A shows an asymptomatic seizure-like event for $\bar{\eta} = -14$, column B shows a generalized seizure-like event for $\bar{\eta} = -7.5$. The EZ node 77 (rh-PrG) is stimulated. Parameter values: $N_{\text{pop}} = 88$, $\tau_m = 20$ ms, $\Delta = 1$, $\sigma = 1.25$, $J_{kk} = 20$, $J_{kl} = 5\tilde{J}_{kl}$, $\forall k \neq l$. For comparison are shown the space-time plots of the population firing rates r_k **(A7, B7)** and the spectrogram of the network average membrane potential **(A8, B8)** for healthy subject H2. In accordance with the above panels, column A shows an asymptomatic seizure-like event (for $\bar{\eta} = -9.20$), column B shows a generalized seizure-like event (for $\bar{\eta} = -5.3$). The EZ node 46 is stimulated. Parameter values: $N_{\text{pop}} = 90$, $\tau_m = 20$ ms, $\Delta = 1$, $J_{kk} = 20$, $\sigma = 1$, $J_{kl} = 5\tilde{J}_{kl}$, $\forall k \neq l$.

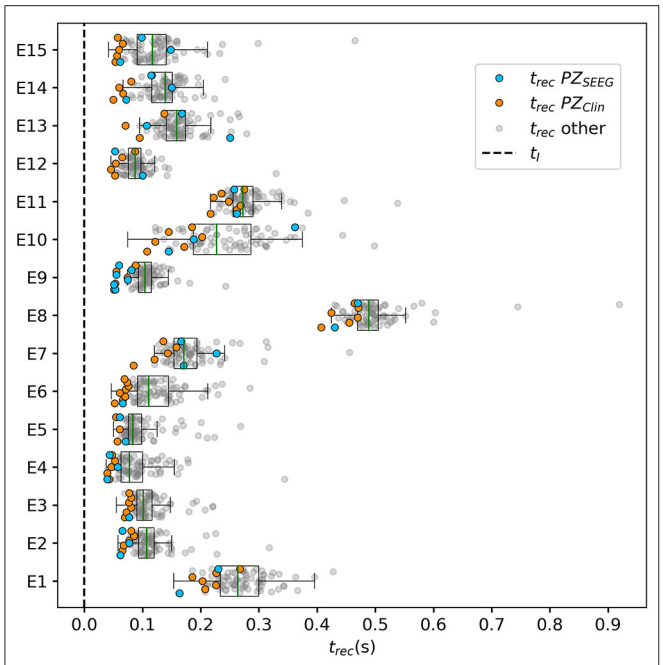

FIGURE 10 | Recruitment times of all brain areas for the cohort of epileptic patients: The recruitment time, reported on the *x*-axis, identifies the time needed by a brain area to jump to the HA regime after the application of the perturbation current. The boxplots consist of the recruitment times of all brain areas for each patient. Patients are identified according to their numbers on the *y*-axis. The median is represented as a green vertical line while the boxes contain the second and third quartile of the distribution. The whiskers are chosen with a maximum length of 1.5 × IQR (interquantile range) and show the most extreme observed values that are within 1.5 × IQR from the upper or lower quartiles. The gray dots represent the recruitment times for each brain area. The orange dots show the recruitment of a brain area clinically predicted to be part of the PZ_{Clin}. The blue dots represent the recruitment of a brain area that is part of the PZ according to the SEEG measurements PZ_{SEEG}. Parameters: $N_{pop} = 88$, $\Delta = 1$, $\sigma = 1.25$, $I_S = 10$, $t_I = 0.4$ s, $\bar{\eta}^{(k)} = \bar{\eta} = -7.5$ [except for patients E1 ($\bar{\eta} = -6$) and E11 ($\bar{\eta} = -6.5$)].

the same holds for patients E2, E3, and E6 if we consider the areas identified by the SEEG analysis as belonging to the PZ_{SEEG}. In general, a large number of the first 10 recruited areas, as revealed by the simulations, coincides with the areas that are supposed to be crucial in the seizure spreading according to the medical doctors (e.g., for patients E2, E3, E10, E12, E13, and E14). Moreover, the predictability of the model is higher if we compare the results with the predictions PZ_{Clin}, while brain areas belonging to the PZs, are in general recruited before the median recruitment time. However, the model predictions are not good for the following cases: for patients E1, E8, E11, and E14, the areas belonging to the PZ_{SEEG} are only occasionally identified (half or less than half of the times), while for patients E1, E8, and E11, other nodes are generally recruited before those belonging to the PZ_{Clin}, that are identified with a percentage <50%. In all the former bad cases, the EZ has not been correctly identified, as results from the relative surgical outcomes (as shown in **Supplementary Table 3**). Therefore, the incorrect identification of the origin of seizure-like events may lead to a misleading identification of the PZ: in other words, a different potential EZ will lead to a different recruitment order, possibly closer to the experimental data.

To evaluate the dependence of the shown results on the chosen parameters, with the idea in mind of going toward a more biologically realistic framework, we have repeated the previous numerical experiment by employing a random Gaussian distribution of the excitability parameter $\bar{\eta}^{(k)}$ (as shown in **Figure 11**). The distribution is centered at $\bar{\eta}_G = -7.5$ with standard deviation 0.1 for all patients except E1 and E11. For the latter patients, we shifted the center toward larger values, to get a sufficient number of recruitments when the EZ is stimulated. In all cases, the results are averaged over 10 different random realizations of the distribution. More details on the impact of different realizations of $\bar{\eta}^{(k)}$ are given, for one exemplary patient, in **Supplementary Figure 6**. For sufficiently larger standard deviation than the one employed (≥ 1), a too large fraction of the populations would not be able to exhibit bistability between LA and HA, highlighting the system sensitivity to finite parameter changes. However, for the chosen distribution, the results are comparable with the ones obtained with identical $\bar{\eta}^{(k)} = \bar{\eta}$, shown in **Figure 10**. For patients E2, E3, E4, E5, E6, and E9 the predicted PZ are always the first ones to be recruited. Moreover, most of the areas are usually recruited in the first half of the recruitment process, rapidly increasing in number, once the areas in the PZ have been recruited (thus giving rise to a peak in the histogram). As a general remark, in view of the distributed nature of the excitabilities, recruitments at later times, with respect to the former case with homogeneous $\bar{\eta}^{(k)} = \bar{\eta}$, may now take place.

For patients with many nodes in the EZ, the recruitment process may result to be more complex, as it happens for patients E14 and E10, for which the histograms are less narrow, but instead widely distributed. However, this cannot be taken as a general rule, since comparable histograms are obtained for patients E13 (one node in the EZ) and E8 (two nodes in the EZ), while for E15 and E12 (with both four nodes in the EZ) the histograms result to be very narrow, thus implying a fast recruitment process of most of the brain areas. The differences among the histograms can be partially justified by the fact that patients have specific connectomes with individual characteristics and by the analysis that we have proposed by choosing similar $\bar{\eta}$ values for all the patients. In this way, we have preferred to have a general look at the multiple self-emergent dynamics in a group of patients, instead of fine-tuning the excitability parameter to obtain similar collective behaviors. What we observe in this study is strongly related to what we have presented in **Figure 9**: The recruitment speed depends on the excitability parameter and the individual network structure. Faster recruitment events may be obtained for different subjects by increasing the excitability value. In the following section, we try to understand, based on network topological measures, the origin of the discrepancies among the clinical prediction of PZs and the first recruited areas predicted by the presented model.

3.2.3. Relationship Between DTI Network Structure and Temporal Seizure Recruitment

To understand the mechanism underlying the recruitment events, we evaluate the relationship between the network

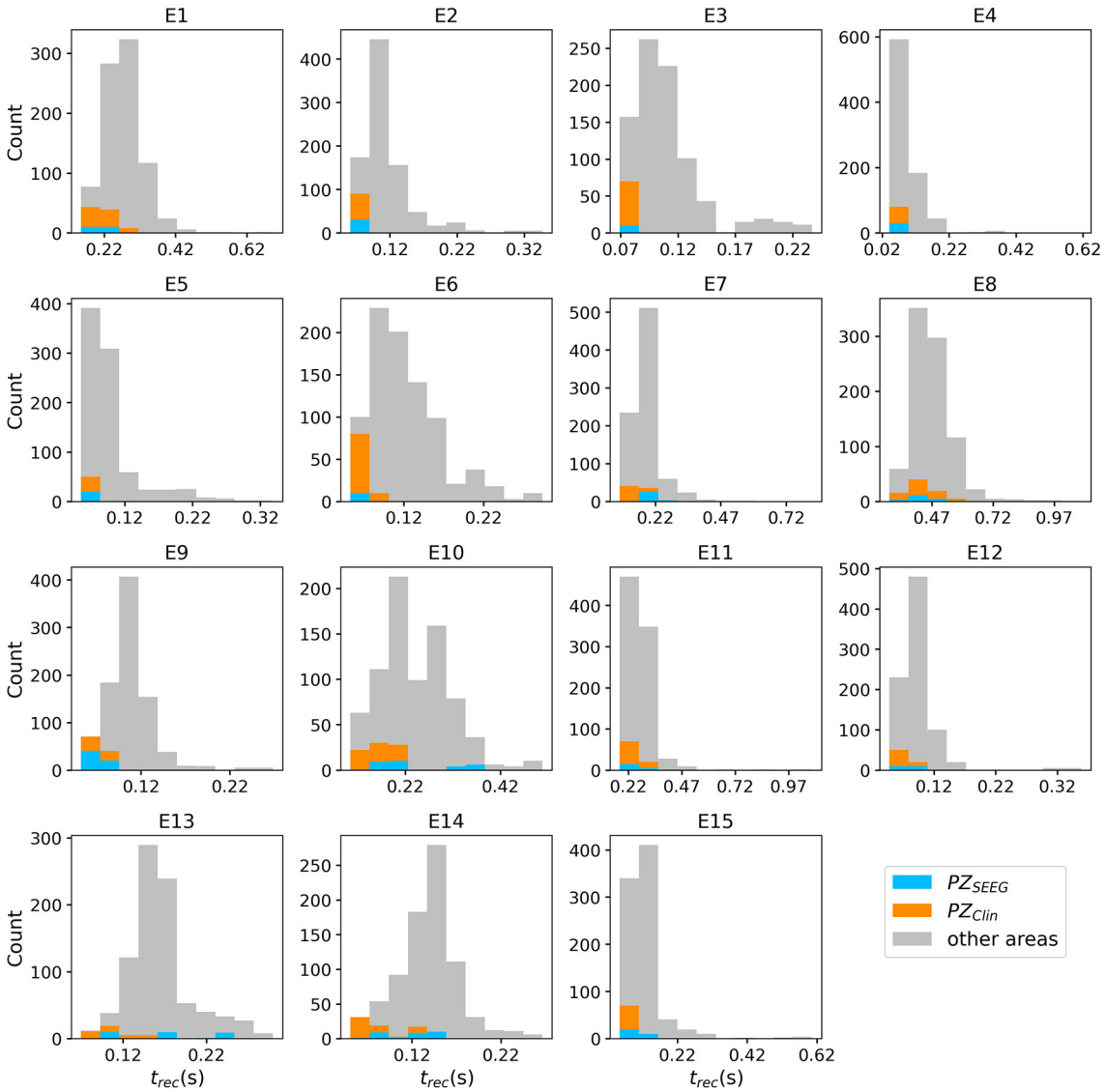

FIGURE 11 | Histograms of recruitment times for all patients with epileptic. For each patient (identified by his/her number), the recruitment times of all the brain areas are collected, once the EZ is stimulated. If several areas were identified in the EZ, they are all stimulated simultaneously. The EZ is chosen according to the presurgical evaluation (as shown in **Supplementary Table 4**) and vary from one patient to the other. Parameters as in **Figure 10** except for $\bar{\eta}^{(k)} = -7.5 \pm 0.1$ (for E1 $\bar{\eta}^{(k)} = -6 \pm 0.1$, for E11 $\bar{\eta}^{(k)} = -6.5 \pm 0.1$). Results are averaged over 10 repetitions of different random Gaussian distributions.

structure, in terms of topological measures, and the recruitment times of the first 10 recruited brain areas, as obtained through numerical experiments. For simplicity, we consider in this study patients with only one brain area in the EZ and we report, in **Figure 12**, the potential EZ (yellow circle) and the first 10 recruited areas in a graph representation. The results relative to all the other patients are reported in the **Supplementary Figures 7–9**. The first recruited areas are ordered according to their recruitment times in clockwise order. Moreover, we indicate in blue the areas belonging to the PZ, as identified according to the presurgical invasive evaluation (PZ_{SEEG}). Black lines identify the weighted connections between all areas and their thickness is proportional to their weight. The sizes of the circles representing each brain area are proportional to their inverse recruitment time (**Figures 12A1–D1**), to their weight connecting each area to the EZ (**Figures 12A2–D2**), and to their inverse shortest path length between each node and the EZ (**Figures 12A3–D3**), while the size of the yellow EZ circle remains fixed.

Since in (**Figures 12A1–D1**) the node size is proportional to the inverse recruitment time, large circles indicate early recruitment while small circles indicate late recruitments; hence, the circles become smaller clockwise. In panels (**Figures 12A2–D2**) the node size is proportional to the

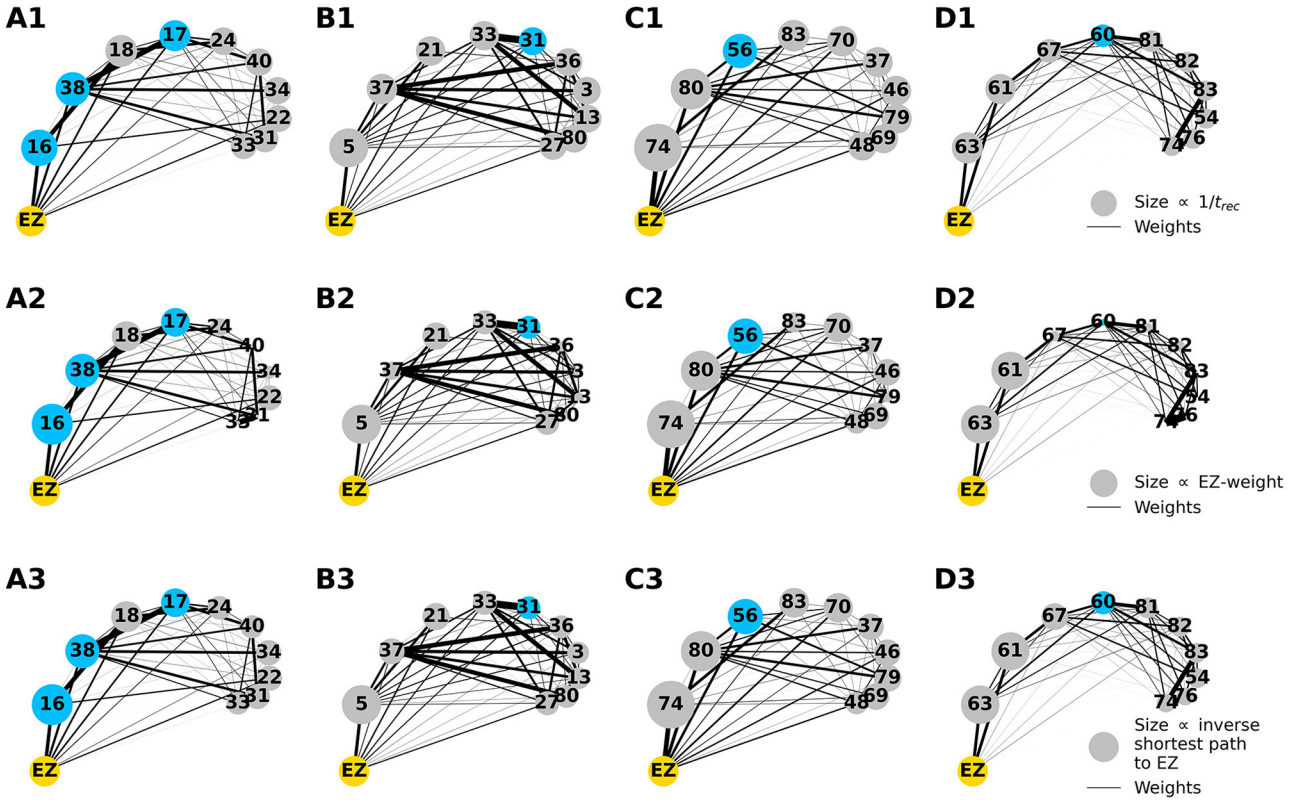

FIGURE 12 | Graph plot of the first 10 recruited areas, ordered clockwise according to their recruitment times, as found *via* numerical experiments. Node circle size corresponds to the inverse recruitment time **(A1–D1)**, to the connection strength to the EZ **(A2–D2)**, and the inverse shortest path length to the EZ **(A3–D3)**. The size of the yellow EZ remains fixed. Blue dots distinguish a recruited area to belong to the PZ_{SEEG}, i.e., the PZ identified according to the presurgical invasive evaluation. Results are obtained for patients E2 **(A1–A3)**, E3 **(B1–B3)**, E6 **(C1–C3)**, and E13 **(D1–D3)**. Parameters as in **Figure 10**.

weight connecting each area to the EZ and it turns out that, for all patients, the first recruited area has the strongest connecting weight. However, after a few recruitments, this does not hold anymore. There are many examples in which areas with a strong weight to the EZ (as shown in e.g., area 46 or 48 for patient E6) are recruited much later than areas with very small weights (e.g., area 83 for FB). The seizure-like event propagates as a chain reaction and, therefore, the strongest connecting weight to the EZ is only decisive for the very first recruited area. Later, strong connections to other early recruited areas play a decisive role, as it is the case for area 83 in E6 which has a weak connection weight to the EZ. However, through its strong connection to area 74, its weighted shortest path length to the EZ is quite short, thus meaning that the weighted shortest path length to the EZ cannot be underestimated to find the recruitment order. Indeed, in (**Figures 12A3–D3**) one can see the good predictability of the shortest path: the node size, proportional to the inverse shortest path length to EZ, decreases in general with later recruitment. This is expected, given the fact that the average shortest path to the EZ considers all connections in the network, not just the connections subgraph outgoing the EZ. An example of the high predictability of the shortest path is given by node 38 in patient E2, which has a shorter path length to the EZ than node 18. Node 38 is recruited before node 18 irrespectively of its strong connection to node 16 and a connection strength to the EZ comparable with the one of node 38. However, it is worth noticing that, in general, the nodes that are recruited before the areas belonging to the PZ, show either stronger connecting weights, or shortest path length to EZ.

For later recruitments, the prediction becomes even more difficult because one needs to account for the temporal order of the seizing brain areas. As shown before, the area which is first recruited is the one with the strongest connection to the EZ. However, depending on the strength of the connection, the recruitment time changes and it increases for decreasing strength. In the case of patient E2, the recruitment of the second area is determined, more by the strength of the connections to the EZ (i.e., area 20) than by the connection to area 16, while for the recruitments of the third and fourth areas, the strong connections of node 18 to 16 and of node 17–38, i.e., the first and second recruited nodes, are fundamental. On the other hand, when the first recruited areas have strong connections to the EZ, for example area 74 in patient E6, the successive recruitments are strongly influenced by the first recruited area, whose outgoing graph reveals areas that are recruited with high probability. Thus, the connection to area 74 turns out to be, for

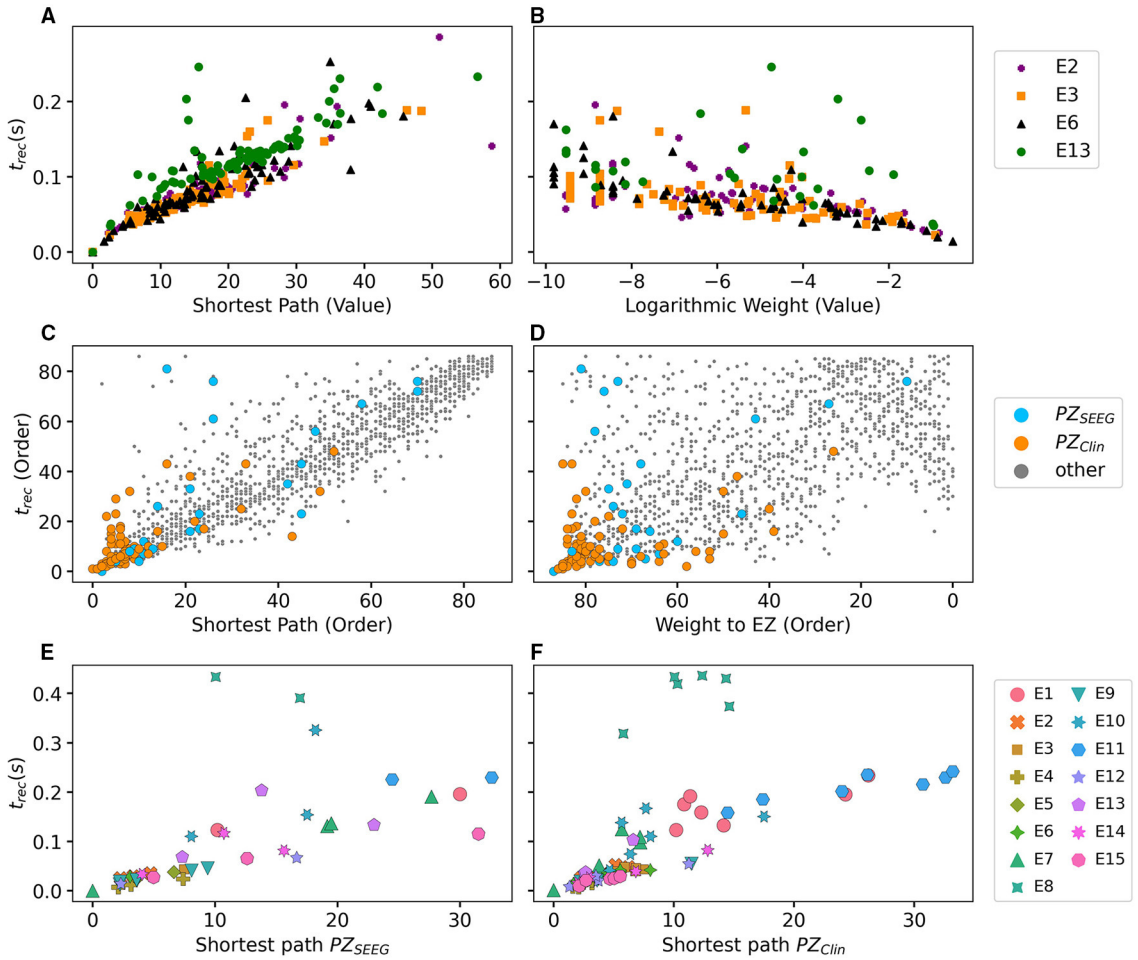

FIGURE 13 | Relationship between network measure and recruitment time, as found *via* numerical experiments. **(A)** Shortest path to EZ; **(B)** Logarithmic value of the weight to the EZ for the four patients with a single-node EZ. In **(A)** all four EZs are shown at (0, 0), while in **(B)** the EZs are omitted. The recruitment time is calculated in seconds after the perturbation current has started. In **(C,D)** the recruitment time values are plotted according to their order, as a function of the shortest path to EZ **(C)** and weight to EZ **(D)** for all 15 patients. In **(D)** the *x*-axis was inverted for better comparison. **(E)** Recruitment times t_{rec} of the areas belonging to PZ_{SEEG} and **(F)** PZ_{Clin} as a function of the shortest path length to EZ, for all 15 patients. For patients with several nodes detected in the EZ, all areas were stimulated simultaneously. Parameters as in **Figure 10**.

the second, third, and fourth recruitment almost as important as the connection to the EZ (i.e., area 76). Finally, if we compare two late recruited areas that are characterized by the same shortest path length to the EZ but with a path to the EZ that crosses very different nodes, we observe that the area with the path going through earlier recruited nodes is recruited earlier. The longer the seizure-like event propagates, the less important the shortest path length to the EZ becomes and the more important the path lengths to other recruited nodes become. This underlines the difficulty of predicting the seizure propagation in complex networks, however, it is possible to summarize some findings that hold for almost all patients (including those shown in the **Supplementary Figures 7–9**): The first recruited node is, in general, the one with the strongest connection to the EZ and the shortest path; strong connections to early recruited areas are fundamental to determine the recruitment order; nodes belonging to the PZ_{SEEG}, that are not identified by the simulations as first recruited nodes, show intermediate values of connection strength and shortest path, while the nodes that are recruited before are either more strongly connected the EZ or to the previously recruited nodes.

To confirm the importance of the shortest path length and the strength of the connections outgoing the EZ in determining recruitment events, we report in **Figure 13** the recruitment time values as a function of the shortest path and the connection weights for the patients with a single node as potential EZ (**Figures 13A,B**) and for all 15 epileptic patients (**Figures 13C,D**). While in **Figure 13B**, the recruitment time is plotted over the logarithm of the weight, in **Figures 13C,D** the values of the recruitment time, plotted as a function of the shortest path (connection weight), are ordered according to their recruitment order. In particular, the order for recruitment,

shortest path, and weight to EZ is ascending from small values to large values. This means that, in **Figure 13D**, the areas with the strongest weights (87th, 86th, etc.) correspond to the areas that are recruited earliest (1st, 2nd, etc.). The ordering has been preferred to the specific values of the shortest path and connection weight when reporting data for all 15 patients, to obtain a better visualization. For patients E2, E3, E13, and E6, the recruitment time grows almost linearly with the shortest path, while it decreases for increasing weights. This analysis is confirmed in **Supplementary Figure 10**, where a regression fit is performed over the data shown in **Figure 13A**, thus underlying the approximately linear relationship between the shortest path length and the recruitment time for larger t_{rec}. The relationship is not anymore so evident when we consider different cases of potential EZs, that is composed of more that one area. However, in this case, it is still possible to affirm than the earliest recruitments are associated with the shortest path lengths and the strongest weights, while the nodes corresponding to PZ_{SEEG} or PZ_{Clin} that, according to the simulations, were recruited late, have very long shortest path lengths to the EZs or very small weights.

In general, the recruitment mechanism is not completely defined by the shortest path length and the connection weight, therefore, it is not possible to match the pre-surgical predictions in terms of PZ_{SEEG} and PZ_{Clin} if we try to identify the nodes belonging to the PZ by calculating the first recruited nodes according to their shortest paths length or their connection weights. In particular, it turns out that the PZ_{SEEG} areas are well predicted by the investigated model if the shortest path length between the predicted PZ and the EZ is short, as shown in **Figure 13E**. However, for patients E8 and E10, the recruitments of the nodes belonging to PZ_{SEEG} happen much later when compared to brain areas of other patients with a similar shortest path length. Equivalently in **Figure 13F** it is possible to observe that, for short values of the shortest path length (<5), there is a linear correspondence between short recruitment times and PZ_{Clin} areas that are characterized by small values of the shortest path. However, the areas belonging to PZ_{Clin} are still not identifiable, in terms of topological measures, for patient E8.

To conclude this section on the influence of single connectome topology in determining activity spreading and area recruitment, we elaborate the data reported in **Figure 10** by sorting, from top to bottom, the patients according to their median shortest path length, calculated on all areas with respect to the EZ. In **Figure 14** are shown the recruitment times of all brain areas for all patients. Since patients are ordered according to their median shortest path length, the brain areas of E4 have, on average, the shortest paths to the EZ and the areas of E1 the longest. In general, it is possible to detect a slight trend, for the overall recruitment events, to delay with longer average shortest path lengths. More in detail, E10 and E8 show both very long and very short recruitment times, thus confirming the results obtained in **Figure 11** for Gaussian-distributed excitabilities. The scattering of the recruitment times for these patients reflects that, on average, their recruitment times are longer with respect to the other patients. However, the mean recruitment times are comparable with those of E11, E1, which show comparatively late recruitments irrespectively of the fact that are characterized by a longer median shortest path. A common characteristic that brings together patients E10, E8, E11, and E1 is the weak connection among the EZ and the first recruited area, that slows down the recruitment time (as already mentioned when discussing **Figure 12**), thus suggesting that is the interplay between connection strength and shortest path to determine the efficacy of seizure spreading and not the single topology measure alone.

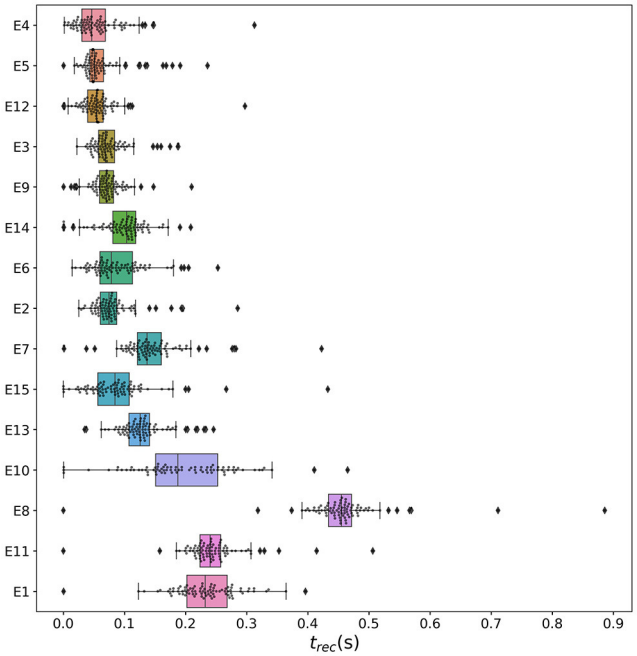

FIGURE 14 | Recruitment times of all brain areas and all patients. The patients are sorted from top to bottom according to their median shortest path length, calculated by listing all the shortest path lengths of all areas to the EZ and then locating the number in the center of that distribution. Gray dots and diamonds show individual recruitments (we use two different symbols to highlight those values that are beyond the boxplot whiskers); boxes cover the 2nd and 3rd quartile and whiskers extend 1.5 times the IQR (whiskers are asymmetric, comprising the most extreme observed values that are within 1.5×IQR from the upper or lower quartiles). Parameters as in **Figure 10**.

3.2.4. The Impact of the Input Current Strength on the Recruitment Time

Following the same approach used to obtain the results shown in **Figure 7** for a healthy subject, we present here an analysis on the impact of the stimulation strength on the recruitment mechanism. **Figure 15** displays the recruitment times of the first 10 recruited areas using different amplitudes I_S of the step current $I_S(t)$, while fixing the duration $t_I = 0.4$ s. The analysis has been performed for patients E2 (**Figure 15A**), E3 (**Figure 15B**), E6 (**Figure 15C**), and E13 (**Figure 15D**), thus integrating the information on the dependency on topological measures presented in the previous section. As expected, the recruitment times decrease for larger amplitudes. However, the order of recruitment does not substantially change. This implies that, whenever we increase the amplitude, the recruitment

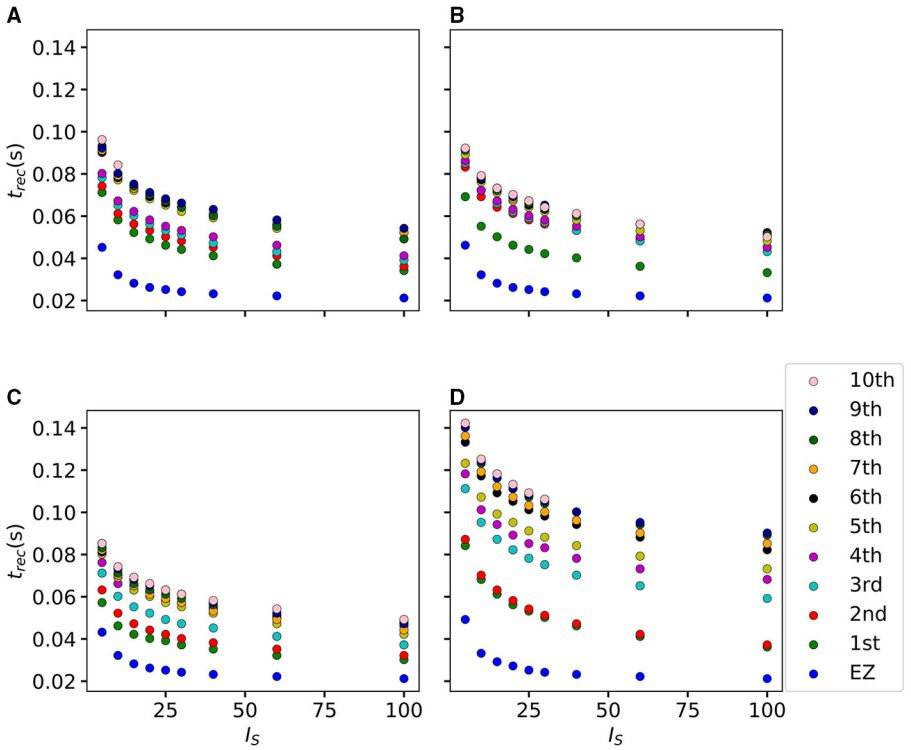

FIGURE 15 | Recruitment times of the first 10 recruited areas as a function of the input current I_S for the epileptic patients **(A)** E2, **(B)** E3, **(C)** E6, and **(D)** E13. The strength of the input current is varied between 0 and 100 on the *x*-axis, while its duration is kept unchanged at $t_I = 0.4$ s with respect to the previous numerical experiments. The order of the recruitment is color-coded for each current strength (i.e., blue dots indicate the recruitment of the EZ, green dots indicate the first recruited area, red the second, etc.), and it holds the same for all investigated patients. Parameters as in **Figure 10**.

mechanism remains unaffected: the same populations are involved in the seizure spreading and in the same order. What changes is the speed of the spreading and the time necessary to observe a generalized seizure-like event, which is smaller for stronger currents. As a general remark, the brain areas that are recruited after the first ones (i.e., the 5th, 6th,...,10th recruited areas), tend to be recruited more simultaneously for increasing I_S, thus leading to possible changes in the recruitment order. This can be appreciated especially for patient E2: for an amplitude $I_S = 10$, for example, the 10th brain area (pink) gets recruited later than the 9th area (dark blue), while for very strong currents ($I_S = 100$), the dark blue area gets recruited latest whereas the pink area gets recruited earlier.

On the other hand, if we vary the step current duration t_I keeping the amplitude $I_S = 15$ fixed, we do not observe any change in the recruitment times of the first 10 recruited areas, analogously to the healthy subject case presented in **Supplementary Figure 4**. Results are shown in the **Supplementary Figure 11**.

4. DISCUSSION

Neural mass models have been actively used since the 1970s to model the coarse-grained activity of large populations of neurons and synapses (Wilson and Cowan, 1972; Zetterberg et al., 1978). They have proven especially useful in understanding brain rhythms (Da Silva et al., 1974, 1976; Sotero et al., 2007), epileptic dynamics (Jirsa et al., 2014; Wendling et al., 2016), brain resonance phenomena (Spiegler et al., 2011), resting state (Ghosh et al., 2008; Deco et al., 2011), task activity (Huys et al., 2014; Kunze et al., 2016), and neurological and psychiatric disorders (Bhattacharya and Chowdhury, 2015) and are very popular in the neuroimaging community (Valdes-Sosa et al., 2009; Moran et al., 2013). Moreover, the desire to understand large scale brain dynamics as observed using EEG, MEG, and fMRI has prompted the increasing use of computational models (Bojak and Breakspear, 2014). Large-scale simulators such as The Virtual Brain (Sanz-Leon et al., 2015) and research infrastructures such as EBRAINS (http://ebrains.eu) make heavy use of networks of interconnected neural mass models and enable non-expert users to gain access to expert state-of-the-art brain network simulation tools.

Although motivated by neurobiological considerations, neural mass models are phenomenological in nature, and cannot hope to recreate some of the rich repertoires of responses seen in real neuronal tissue. In particular, their state variables track coarse-grained measures of the population firing rate or synaptic activity. At best they are expected to provide appropriate levels of description for many thousands of near, identical interconnected

neurons with a preference to operate in synchrony, but they cannot reproduce the variation of synchrony within a neuronal population which is believed to underlie the decrease or increase of power seen in given EEG frequency bands. Importantly, unlike its phenomenological counterpart, the next-generation neural mass model we have implemented in this study, is an exact macroscopic description of an underlying microscopic spiking neurodynamics, and is a natural candidate for use in future large scale human brain simulations. In addition to this, the inability of a single neural mass model to support event-related desynchronization/synchronization (Pfurtscheller and Da Silva, 1999) or to capture the onset of synchronous oscillations in networks of inhibitory neurons (Devalle et al., 2017), reminds us that these phenomenological models could be improved upon. While building more detailed biophysically realistic models of neurons would increase the computational complexity and the difficulties to interpret the behavior of very high dimensional models in a meaningful way, the next-generation neural mass models applied in this study, are very much in the original spirit of neural mass modeling, yet importantly they can be interpreted directly in terms of an underlying spiking model. This exact derivation is possible for networks of quadratic integrate-and-fire neurons, representing the normal form of Hodgkin's class I excitable membranes (Ermentrout and Kopell, 1986), thanks to the analytic techniques developed for coupled phase oscillators (Ott and Antonsen, 2008). This new generation of neural mass models has been recently used to describe the emergence of collective oscillations in fully coupled networks (Devalle et al., 2017; Laing, 2017; Coombes and Byrne, 2019; Dumont and Gutkin, 2019) and in balanced sparse networks (di Volo and Torcini, 2018). Furthermore, it has been successfully employed to reveal the mechanisms at the basis of theta-nested gamma oscillations (Ceni et al., 2020; Segneri et al., 2020) and the coexistence of slow and fast gamma oscillations (Bi et al., 2020). Finally, it has been recently applied to modeling electrical synapses (Montbrió and Pazó, 2020), working memory (Taher et al., 2020), the influence of transcranial magnetic stimulation on brain dynamics (Byrne et al., 2020), and brain resting state activity (Rabuffo et al., 2020).

In this, we have extended the single next-generation neural mass model derived in Montbrió et al. (2015) to a network of interacting neural mass models, where the topology is determined by structural connectivity matrices of healthy and epilepsy-affected subjects. In this way, we can take into account both the macroscopic dynamics, self-emergent in the system due to the interactions among nodes, and the differences related to the patient-specific analyses. However, the single population neural mass model does not take into account neither the synaptic kinetics nor the dynamics of the synaptic field characterizing the considered synapses, which is simply modeled as the linear superposition of δ-shaped post-synaptic potentials. Moreover, when extending the (excitatory) neural mass model derived in Montbrió et al. (2015) to a multipopulation network, we have considered only excitatory coupling to build a minimal model for the investigation of topologically-induced dynamical features. Therefore, the presented neural mass model is not able to reproduce depth-EEG epileptic signals, which represents one of the best successes of heuristic neural mass models (Wendling et al., 2002).

In absence of external forcing, the phase diagram of the system as a function of the mean external drive $\bar{\eta}$ and synaptic strength σ resembles that of the single neural mass model, since the same distinct regions can be observed: (1) a single stable node corresponding to a low-activity state, (2) a single stable focus (spiral) generally corresponding to a high-activity state, and (3) a region of bistability between low and high firing rates. However, when the system is subject to a transient external current, the scenario changes and is ruled by the interactions among different nodes. In this case, for low excitability values, a single stimulated node abandons the bistable region due to the applied current and it approaches, with damped oscillations, the high-activity state, which is a stable focus. On the other hand, for sufficiently high excitabilities, the single node stimulation leads to the recruitment of other brain areas that reach, as the perturbed node, the high-activity regime by showing damped oscillations. This activity mimicks a seizure-like event and enables the modeling of propagation and recruitment: the seizure-like event originates in the EZ (as a results of the stimulation) and propagates to the PZ, identified by the other regions where fast propagates the oscillatory activity. It is distinct from an actual seizure, which would require the emergence of self-sustained activity in the high-activity state (Jirsa et al., 2014; Saggio et al., 2017, 2020).

However, transient activity, like the proposed seizure-like events, can play a potentially important role in localizing tissue involved in the generation of seizure activity, if read in the framework of stimulation of human epileptic tissue with consequent induction of rhythmic, self-terminating responses on the EEG or electrocorticogram (ECoG) (Valentin et al., 2002; Flanagan et al., 2009; Jacobs et al., 2010). From the dynamical systems perspective, one can hypothesize that complex stimulus responses are due to a space-dependent induction of self-terminating, spatio temporal transients that are caused by brief perturbations in an excitable medium (Goodfellow et al., 2012). Accordingly, considering epileptic seizure dynamics as spatio-temporal patterns (Goodfellow et al., 2011; Baier et al., 2012) shifts attention on the self-organizing capabilities of spatio temporal brain networks, thus proposing an alternative explanatory framework for epileptiform EEG to the time-dependent modulation in system parameters (Kramer et al., 2005; Breakspear and Jirsa, 2007; Kim et al., 2009; Marten et al., 2009; Lopour and Szeri, 2010).

Moreover, perturbation experiments, like the stimulation of human tissue, turns out to be fundamental in the context of functional brain mapping, as an integral part of contemporary neurosurgery (Sagar et al., 2019). Surgical planning of the resection procedure depends substantially on the delineation of abnormal tissue, e.g., epileptic foci or tumor tissue, and on the creation of a functional map of eloquent cortex in the area close to the abnormal tissue. Traditionally, different methodologies have been used to produce this functional map: electrical cortical stimulation (Hara et al., 1991; Ojemann, 1991; Uematsu et al., 1992), functional MRI (Chakraborty and McEvoy, 2008), PET (Bittar et al., 1999; Meyer et al., 2003), magnetoencephalography (Ganslandt et al., 1999), evoked potentials (Dinner et al.,

1986), or passive recordings of electrocorticographic signals (Brunner et al., 2009). In particular, ECoG activity recorded from subdural electrodes, placed during surgical protocols, reflect task-related changes (Crone et al., 1998a,b, 2001; Aoki et al., 1999, 2001; Sinai et al., 2005; Leuthardt et al., 2007; Miller et al., 2007): ECoG amplitudes in specific frequency bands carry substantial information about movement or language tasks and they usually increase with the task in the gamma (>40 Hz) band. Extending the presented multipopulation model, *via* the addition of synaptic dynamics and an inhibitory pool, to reproduce task-related change in ECoG activity, would be essential to extend its predictive power.

The spectrogram analysis has revealed that the recruitment process is characterized by high frequency γ oscillations, thus reproducing the high-frequency (γ-band) EEG activity typical of electrophysiological patterns in focal seizures of human epilepsy. Many hypotheses have been formulated on the origin of this fast activity: (i) the behavior of inhibitory interneurons in hippocampal or neocortical networks in the generation of gamma frequency oscillations (Jefferys et al., 1996; Whittington et al., 2000); (ii) the nonuniform alteration of GABAergic inhibition in experimental epilepsy (reduced dendritic inhibition and increased somatic inhibition) (Cossart et al., 2001; Wendling et al., 2002); (iii) the possible depression of $GABA_{A,fast}$ circuit activity by $GABA_{A,slow}$ inhibitory postsynaptic currents (Banks et al., 2000; White et al., 2000); (iv) the out of phase patterns of depolarizing GABAergic post-synaptic potentials onto pyramidal cells, generated by feed-forward activation of cortical interneurons (Shamas et al., 2018). In any case, high-frequency EEG waves originating from one or several brain regions are the most characteristic electrophysiological pattern in focal seizures of human epilepsy and can be observed, in the numerical experiments, both for healthy subjects and epileptic patients, though with a distinction: for the same excitability value, the activity takes place at higher frequency ranges in epileptic patients and it is mainly concentrated in the EZ. Moreover, high-frequency γ oscillations (>200 Hz) are observable in the spectrogram of epileptic patients only. Even though it is not possible to exclude discrepancies partially imputable to the different scanning and preparation procedure of the structural connectivity matrices for the cohort of healthy and epilepsy-affected subjects, it turns out that the recruitment process is faster in epileptic patients, for which it is possible to observe generalized seizure-like events for smaller values of the excitability parameter $\bar{\eta}$. In particular, when comparing the results obtained for healthy subjects and epileptic patients, it turns out that the time necessary to recruit areas in the PZ is usually smaller for epileptic patients. However, the first recruited area is, in general, the area with the stronger connection to the EZ, independently of the considered structural connectivity matrix. The recruitment time in both cases is influenced by the strength of the external perturbation I_S, and decreases for increasing strength, while no dependence is shown on the duration of the external perturbation.

More specifically for healthy subjects, we have investigated the dependence of the recruitment mechanism on the single subject, in terms of the position of the eventual EZ and the topological measures of the single connectome. Brain network models of healthy subjects comprise 90 nodes equipped with region-specific next-generation neural mass models and each subject is characterized by a specific structural large-scale connectivity amongst brain areas. The smallest excitability values for which an asymptomatic seizure-like event occurs ($\bar{\eta}^{(k)}_{\mathrm{asy}}$) do not vary significantly from one subject to the other and do not show a relevant dependence on the stimulated area, while the smallest excitability values for which a generalized seizure-like event occurs, ($\bar{\eta}^{(k)}_{\mathrm{gen}}$), show fluctuations in the interval $(-7, -5)$ for all stimulated nodes and for all the subjects. Nonetheless, we have found many similarities at the level of topological measures, since there is always a strong correlation between $\bar{\eta}^{(k)}_{\mathrm{asy}}$ ($\bar{\eta}^{(k)}_{\mathrm{gen}}$) and node strength, clustering coefficient and shortest path, thus meaning that a region well connected is a region well recruited.

For epileptic patients, we have systematically simulated the individual seizure-like propagation patterns and validated the numerical predictions of the PZ against clinical diagnosis and SEEG signals. Patient-specific brain network models of epileptic patients comprise 88 nodes equipped with region-specific next-generation neural mass models, and for this set up, we have studied the role of the large-scale connectome based on dMRI, in predicting the recruitment of distant areas through seizure-like events originating from a focal epileptogenic network. We have demonstrated that simulations and analytical solutions approximating the large-scale brain network model behavior significantly predict the PZ as determined by SEEG recordings and clinical expertise, with performances comparable to previous analyses on this set of data (Proix et al., 2017; Olmi et al., 2019), thus confirming the relevance of using a large-scale network modeling to predict seizure recruitment networks. However, some false positives are still observable, where populations not belonging to PZ_{SEEG} or PZ_{Clin} are first recruited. In these cases, the analysis on topological properties has revealed that nodes are easily recruited whenever they show strong connections to the EZ or too early recruited areas and that are closer to the EZ in terms of the shortest path length. Therefore, nodes belonging to the PZ_{SEEG} (PZ_{Clin}), that are not identified by the simulations as first recruited nodes, are characterized by intermediate values of connection strength and shortest path. Predictions are particularly not good for those patients whose EZ has not been correctly identified, as results from the relative surgical outcomes reported in **Supplementary Table 3**. For these patients, the incorrect identification of the origin of seizure-like events may lead to a misleading identification of the PZ, since we are not able to identify, numerically, the recruitment of nodes not directly connected with the real EZ. Finally, comparing the results obtained for epileptic patients with those for healthy subjects, we infer a strong correlation between fast recruitment events and node strength, which is due to the fact that structural connectomes, both for healthy subjects and epileptic patients, are characterized by a log-normal distribution of the weights, where some connections, for each node, have a much stronger weight than the others. Moreover, the strong correlation between fast recruitment and clustering coefficient/shortest path suggests that we are in the presence of hierarchical connectivities, which are important for the spreading of activity (Kaiser et al., 2007;

Luccioli et al., 2014) and the enhancement of the network susceptibility to seizure activity (Morgan and Soltesz, 2008).

Most computational models of seizure propagation focus on small continuous spatial scales (Ursino and La Cara, 2006; Kim et al., 2009; Hall and Kuhlmann, 2013) or population of neurons (Miles et al., 1988; Golomb and Amitai, 1997; Compte et al., 2003; Bazhenov et al., 2008; Chouzouris et al., 2018; Lopes et al., 2019; Gerster et al., 2020), while only small networks are commonly used to investigate the role of the topology and localization of the EZ (Terry et al., 2012). However, functional, volumetric and electrographic data suggest a broad reorganization of the networks in epileptic patients (Lieb et al., 1987, 1991; Cassidy and Gale, 1998; Rosenberg et al., 2006; Bettus et al., 2009), thus laying the foundations for a different approach based on large-scale connectomes to identify the recruitment networks. The large-scale character of partial seizure propagation in the human brain has been only recently investigated, using patient-specific dMRI data to systematically test the relevance of the large-scale network modeling, in predicting seizure recruitment networks (Proix et al., 2014, 2017, 2018; Olmi et al., 2019). In this framework of large-scale network modeling we can also place the results presented in this study, since we have confirmed the importance of patient-specific connectomes to identify the recruitment process. As shown above, the topological characteristics of connection strength and shortest path play a non-trivial role in determining the spreading of seizure-like events, together with the localization of the EZ, while the next-generation neural mass model, employed for the first time to study seizure spreading, allows us to construct patient-specific brain models *via* a multiscale approach: the variability of brain regions, as extracted from the human brain atlas, can be introduced in the mean-field parameters, thanks to the exact correspondence between microscopic and macroscopic scales guaranteed by the model itself. The possibility to exactly move through the scales has not been fully exploited in this study, since we have focused the analysis on the extension of the single neural mass model to a multipopulation model, without adding other relevant features to the original model. However, it is possible to easily introduce, in the multipopulation model, biologically relevant characteristics, keeping intact the exact correspondence between microscopic and macroscopic scales, such as short-term synaptic plasticity (Taher et al., 2020), synaptic delays (Devalle et al., 2018), electrical coupling *via* gap junctions (Montbrió and Pazó, 2020), chemical synapses (Coombes and Byrne, 2019), and extrinsinc and endogenous noise (Goldobin et al., 2021). By adding short-term synaptic plasticity we expect to be able to reproduce the emergence of self-sustained activity in the high-activity state and, therefore, to describe a fully developed seizure. The introduction of synaptic delays and noise guarantees the possibility to observe chaotic dynamics, therefore, allowing for the reproduction of more complex signals, like depth-EEG epileptic signals. Improving the predictive power of the model by the means of more biologically relevant characteristics and anatomical data (3D T1-weighted images, high angular and spatial dMRI data, ion, and energetic and neurotransmitter measurements available e.g., in the BigBrain and human brain atlas) will be the scope of further research.

DATA AVAILABILITY STATEMENT

All relevant data are within the paper and its **Supplementary Material** files. The simulated data supporting the conclusions of this article will be made available by the authors, without undue reservation. Numerical codes can be found on the open platform https://github.com/moritz-gerster/seizure_propagation. The healthy subject structural connectivity matrices used in this paper correspond to the first 20 subjects in a larger dataset. See https://osf.io/yw5vf/ for the data and a related paper describing the dataset in detail. Structural connectivity data for epileptic patients can be made available upon request following individual institutional requirements.

ETHICS STATEMENT

The patients/participants provided their written informed consent to participate in research studies. For healthy subjects: The study design was approved by the local Ethics Committee of IKEM, Prague, Czech Republic. For epileptic patiens: Additional ethical review and approval was not required for this particular study in accordance with the local legislation and institutional requirements.

AUTHOR CONTRIBUTIONS

MGe and HT performed the simulations and data analysis, writing original software, and investigating the results. Data Curation is contributed by VJ, MGu, FB, AŠ, and JH. All the authors validated the research and participated in the drafting process. SO was responsible for conceptualization, supervision, state-of-the-art review (together with VJ), and the paper write-up.

FUNDING

SO received financial support from Campus France, programme. PHC PROCOPE 2019-Numéro de project: 42511TA. AZ received financial support from the Deutscher Akademischer Austauschdienst (DAAD, German Academic Exchange Service), Project No. 57445304, PPP Frankreich Phase I, and by the Deutsche Forschungsgemeinschaft (DFG, German Research Foundation), Project No. 163436311-SFB 910. JH was supported by the Ministry of Health Czech Republic - DRO 2021 ("National Institute of Mental Health - NIMH, IN: 00023752") and the Czech Science Foundation project No. 21-32608S. AŠ was supported by the Ministry of Health, Czech Republic - DRO 2021 ("Institute for Clinical and Experimental Medicine - IKEM, IN: 00023001"). VJ and MGu received financial support from the European Union's Horizon 2020 Framework Programme for Research and Innovation under the Specific Grant Agreement No. 945539 (Human Brain Project SGA3).

SUPPLEMENTARY MATERIAL

The Supplementary Material for this article can be found online at: https://www.frontiersin.org/articles/10.3389/fnsys.2021.675272/full#supplementary-material

REFERENCES

Ahmadi, M. E., Hagler, D., McDonald, C. R., Tecoma, E., Iragui, V., Dale, A. M., et al. (2009). Side matters: diffusion tensor imaging tractography in left and right temporal lobe epilepsy. *Am. J. Neuroradiol.* 30, 1740–1747. doi: 10.3174/ajnr.A1650

Ahmadizadeh, S., Karoly, P. J., Nešić, D., Grayden, D. B., Cook, M. J., Soudry, D., et al. (2018). Bifurcation analysis of two coupled jansen-rit neural mass models. *PLoS ONE*. 13:e0192842. doi: 10.1371/journal.pone.0192842

Allen, P., Fish, D., and Smith, S. (1992). Very high-frequency rhythmic activity during seeg suppression in frontal lobe epilepsy. *Electroencephalogr. Clin. Neurophysiol.* 82, 155–159. doi: 10.1016/0013-4694(92)90160-J

Aoki, F., Fetz, E., Shupe, L., Lettich, E., and Ojemann, G. (1999). Increased gamma-range activity in human sensorimotor cortex during performance of visuomotor tasks. *Clin. Neurophysiol.* 110, 524–537. doi: 10.1016/S1388-2457(98)00064-9

Aoki, F., Fetz, E., Shupe, L., Lettich, E., and Ojemann, G. (2001). Changes in power and coherence of brain activity in human sensorimotor cortex during performance of visuomotor tasks. *Biosystems* 63, 89–99. doi: 10.1016/S0303-2647(01)00149-6

Baier, G., Goodfellow, M., Taylor, P. N., Wang, Y., and Garry, D. J. (2012). The importance of modeling epileptic seizure dynamics as spatio-temporal patterns. *Front. Physiol.* 3:281. doi: 10.3389/fphys.2012.00281

Banks, M. I., White, J. A., and Pearce, R. A. (2000). Interactions between distinct gabaa circuits in hippocampus. *Neuron* 25, 449–457. doi: 10.1016/S0896-6273(00)80907-1

Barrat, A., Barthélemy, M., Pastor-Satorras, R., and Vespignani, A. (2004). The architecture of complex weighted networks. *Proc. Natl. Acad. Sci. U.S.A.* 101, 3747–3752. doi: 10.1073/pnas.0400087101

Bartolomei, F., Guye, M., Gavaret, M., Regis, J., Wendling, F., Raybaud, C., et al. (2002). The presurgical evaluation of epilepsies. *Revue Neurol.* 158(5 Pt 2):4S55–4S64.

Bartolomei, F., Guye, M., and Wendling, F. (2013). Abnormal binding and disruption in large scale networks involved in human partial seizures. *EPJ Nonlinear Biomed. Phys.* 1, 4. doi: 10.1140/epjnbp11

Bartolomei, F., Lagarde, S., Wendling, F., McGonigal, A., Jirsa, V., Guye, M., et al. (2017). Defining epileptogenic networks: contribution of seeg and signal analysis. *Epilepsia* 58, 1131–1147. doi: 10.1111/epi.13791

Bartolomei, F., Wendling, F., Bellanger, J.-J., Régis, J., and Chauvel, P. (2001). Neural networks involving the medial temporal structures in temporal lobe epilepsy. *Clin. Neurophysiol.* 112, 1746–1760. doi: 10.1016/S1388-2457(01)00591-0

Basser, P. J., Pajevic, S., Pierpaoli, C., Duda, J., and Aldroubi, A. (2000). In vivo fiber tractography using dt-mri data. *Magn. Reson. Med.* 44, 625–632. doi: 10.1002/1522-2594(200010)44:4andlt;625::AID-MRM17andgt;3.0.CO;2-O

Bazhenov, M., Timofeev, I., Fröhlich, F., and Sejnowski, T. J. (2008). Cellular and network mechanisms of electrographic seizures. *Drug Discov. Today Dis. Models* 5, 45–57. doi: 10.1016/j.ddmod.2008.07.005

Bernhardt, B., Hong, S.-J., Bernasconi, A., and Bernasconi, N. (2013). Imaging structural and functional brain networks in temporal lobe epilepsy. *Front. Hum. Neurosci.* 7:624. doi: 10.3389/fnhum.2013.00624

Besson, P., Bandt, S. K., Proix, T., Lagarde, S., Jirsa, V. K., Ranjeva, J.-P., et al. (2017). Anatomic consistencies across epilepsies: a stereotactic-eeg informed high-resolution structural connectivity study. *Brain* 140, 2639–2652. doi: 10.1093/brain/awx181

Besson, P., Dinkelacker, V., Valabregue, R., Thivard, L., Leclerc, X., Baulac, M., et al. (2014). Structural connectivity differences in left and right temporal lobe epilepsy. *Neuroimage* 100:135–144. doi: 10.1016/j.neuroimage.2014.04.071

Bettus, G., Guedj, E., Joyeux, F., Confort-Gouny, S., Soulier, E., Laguitton, V., et al. (2009). Decreased basal fmri functional connectivity in epileptogenic networks and contralateral compensatory mechanisms. *Hum. Brain Mapp.* 30, 1580–1591. doi: 10.1002/hbm.20625

Bhattacharya, B. S., and Chowdhury, F. N. (2015). *Validating Neuro-Computational Models of Neurological and Psychiatric Disorders*, Vol. 14. Cham: Springer.

Bi, H., Segneri, M., di Volo, M., and Torcini, A. (2020). Coexistence of fast and slow gamma oscillations in one population of inhibitory spiking neurons. *Phys. Rev. Res.* 2, 013042. doi: 10.1103/PhysRevResearch.2.013042

Bittar, R. G., Olivier, A., Sadikot, A. F., Andermann, F., Comeau, R. M., Cyr, M., et al. (1999). Localization of somatosensory function by using positron emission tomography scanning: a comparison with intraoperative cortical stimulation. *J Neurosurg.* 90, 478–483. doi: 10.3171/jns.1999.90.3.0478

Boccaletti, S., Latora, V., Moreno, Y., Chavez, M., and Hwang, D.-U. (2006). Complex networks: Structure and dynamics. *Phys. Rep.* 424, 175–308. doi: 10.1016/j.physrep.2005.10.009

Bojak, I., and Breakspear, M. (2014). *Neuroimaging, Neural Population Models for*. New York, NY: Springer.

Bonilha, L., Nesland, T., Martz, G. U., Joseph, J. E., Spampinato, M. V., Edwards, J. C., et al. (2012). Medial temporal lobe epilepsy is associated with neuronal fibre loss and paradoxical increase in structural connectivity of limbic structures. *J. Neurol. Neurosurg. Psychiatry* 83, 903–909. doi: 10.1136/jnnp-2012-302476

Breakspear, M., and Jirsa, V. K. (2007). "Neuronal dynamics and brain connectivity," in *Handbook of Brain Connectivity*, eds V. K. Jirsa and A. McIntosh (Berlin; Heidelberg: Springer), 3–64.

Brocke, E., Bhalla, U. S., Djurfeldt, M., Hellgren Kotaleski, J., and Hanke, M. (2016). Efficient integration of coupled electrical-chemical systems in multiscale neuronal simulations. *Front. Comput. Neurosci.* 10:97. doi: 10.3389/fncom.2016.00097

Brunner, P., Ritaccio, A. L., Lynch, T. M., Emrich, J. F., Wilson, J. A., Williams, J. C., et al. (2009). A practical procedure for real-time functional mapping of eloquent cortex using electrocorticographic signals in humans. *Epilepsy Behav.* 15, 278–286. doi: 10.1016/j.yebeh.2009.04.001

Byrne, Á., O'Dea, R. D., Forrester, M., Ross, J., and Coombes, S. (2020). Next-generation neural mass and field modeling. *J. Neurophysiol.* 123, 726–742. doi: 10.1152/jn.00406.2019

Cabral, J., Fernandes, H., Van Hartevelt, T., James, A., and Kringelbach, M. (2013). Structural connectivity in schizophrenia and its impact on the dynamics of spontaneous functional networks. *Chaos* 23, 046111. doi: 10.1063/1.4851117

Cassidy, R. M., and Gale, K. (1998). Mediodorsal thalamus plays a critical role in the development of limbic motor seizures. *J. Neurosci.* 18, 9002–9009. doi: 10.1523/JNEUROSCI.18-21-09002.1998

Ceni, A., Olmi, S., Torcini, A., and Angulo-Garcia, D. (2020). Cross frequency coupling in next generation inhibitory neural mass models. *Chaos* 30, 053121. doi: 10.1063/1.5125216

Chakraborty, A., and McEvoy, A. W. (2008). Presurgical functional mapping with functional mri. *Curr. Opin. Neurol.* 21, 446–451. doi: 10.1097/WCO.0b013e32830866e2

Chizhov, A. V., Zefirov, A. V., Amakhin, D. V., Smirnova, E. Y., and Zaitsev, A. V. (2018). Minimal model of interictal and ictal discharges "epileptor-2". *PLoS Comput. Biol.* 14:e1006186. doi: 10.1371/journal.pcbi.1006186

Chouzouris, T., Omelchenko, I., Zakharova, A., Hlinka, J., Jiruska, P., and Schöll, E. (2018). Chimera states in brain networks: empirical neural vs. modular fractal connectivity. *Chaos* 28, 045112. doi: 10.1063/1.5009812

Compte, A., Sanchez-Vives, M. V., McCormick, D. A., and Wang, X.-J. (2003). Cellular and network mechanisms of slow oscillatory activity (< 1 hz) and wave propagations in a cortical network model. *J. Neurophysiol.* 89, 2707–2725. doi: 10.1152/jn.00845.2002

Coombes, S., and Byrne, A. (2019). "Next generation neural mass models," in *Nonlinear Dynamics in Computational Neuroscience*, eds F. Corinto and A. Torcini (Cham: Springer), 1–16.

Cossart, R., Dinocourt, C., Hirsch, J., Merchan-Perez, A., De Felipe, J., Ben-Ari, Y., et al. (2001). Dendritic but not somatic gabaergic inhibition is decreased in experimental epilepsy. *Nat. Neurosci.* 4, 52–62. doi: 10.1038/82900

Creaser, J., Lin, C., Ridler, T., Brown, J. T., D'Souza, W., Seneviratne, U., et al. (2020). Domino-like transient dynamics at seizure onset in epilepsy. *PLoS Comput. Biol.* 16:e1008206. doi: 10.1371/journal.pcbi.1008206

Cressman, J. R., Ullah, G., Ziburkus, J., Schiff, S. J., and Barreto, E. (2009). The influence of sodium and potassium dynamics on excitability, seizures, and the stability of persistent states: I. single neuron dynamics. *J. Comput. Neurosci.* 26, 159–170. doi: 10.1007/s10827-008-0132-4

Crone, N. E., Boatman, D., Gordon, B., and Hao, L. (2001). Induced electrocorticographic gamma activity during auditory perception. *Clin. Neurophysiol.* 112, 565–582. doi: 10.1016/S1388-2457(00)00545-9

Crone, N. E., Miglioretti, D. L., Gordon, B., and Lesser, R. P. (1998a). Functional mapping of human sensorimotor cortex with electrocorticographic spectral

analysis. ii. event-related synchronization in the gamma band. *Brain* 121, 2301–2315. doi: 10.1093/brain/121.12.2301

Crone, N. E., Miglioretti, D. L., Gordon, B., Sieracki, J. M., Wilson, M. T., Uematsu, S., et al. (1998b). Functional mapping of human sensorimotor cortex with electrocorticographic spectral analysis. i. alpha and beta event-related desynchronization. *Brain* 121, 2271–2299. doi: 10.1093/brain/121.12.2271

Da Silva, F. L., Hoeks, A., Smits, H., and Zetterberg, L. (1974). Model of brain rhythmic activity. *Kybernetik* 15, 27–37. doi: 10.1007/BF00270757

Da Silva, F. L., Van Rotterdam, A., Barts, P., Van Heusden, E., and Burr, W. (1976). Models of neuronal populations: the basic mechanisms of rhythmicity. *Progr. Brain Res*. 45, 281–308.

David, O., Blauwblomme, T., Job, A.-S., Chabardès, S., Hoffmann, D., Minotti, L., et al. (2011). Imaging the seizure onset zone with stereo-electroencephalography. *Brain* 134, 2898–2911. doi: 10.1093/brain/awr238

De Tisi, J., Bell, G. S., Peacock, J. L., McEvoy, A. W., Harkness, W. F., Sander, J. W., et al. (2011). The long-term outcome of adult epilepsy surgery, patterns of seizure remission, and relapse: a cohort study. *Lancet* 378, 1388–1395. doi: 10.1016/S0140-6736(11)60890-8

Deco, G., Jirsa, V. K., and McIntosh, A. R. (2011). Emerging concepts for the dynamical organization of resting-state activity in the brain. *Nat. Rev. Neurosci*. 12, 43–56. doi: 10.1038/nrn2961

DeSalvo, M. N., Douw, L., Tanaka, N., Reinsberger, C., and Stufflebeam, S. M. (2014). Altered structural connectome in temporal lobe epilepsy. *Radiology*. 270, 842–848. doi: 10.1148/radiol.13131044

Desikan, R. S., Ségonne, F., Fischl, B., Quinn, B. T., Dickerson, B. C., Blacker, D., et al. (2006). An automated labeling system for subdividing the human cerebral cortex on mri scans into gyral based regions of interest. *Neuroimage*. 31, 968–980. doi: 10.1016/j.neuroimage.2006.01.021

Destexhe, A., and Sejnowski, T. J. (1995). G protein activation kinetics and spillover of gamma-aminobutyric acid may account for differences between inhibitory responses in the hippocampus and thalamus. *Proc. Natl. Acad. Sci. U.S.A*. 92, 9515–9519. doi: 10.1073/pnas.92.21.9515

Devalle, F., Montbrió, E., and Pazó, D. (2018). Dynamics of a large system of spiking neurons with synaptic delay. *Phys. Rev. E* 98, 042214. doi: 10.1103/PhysRevE.98.042214

Devalle, F., Roxin, A., and Montbrió, E. (2017). Firing rate equations require a spike synchrony mechanism to correctly describe fast oscillations in inhibitory networks. *PLoS Comput. Biol*. 13:e1005881. doi: 10.1371/journal.pcbi.1005881

di Volo, M., and Torcini, A. (2018). Transition from asynchronous to oscillatory dynamics in balanced spiking networks with instantaneous synapses. *Phys. Rev. Lett*. 121, 128301. doi: 10.1103/PhysRevLett.121.128301

Dinner, D., Lüders, H., Lesser, R., and Morris, H. (1986). Invasive methods of somatosensory evoked potential monitoring. *J. Clin. Neurophysiol*. 3, 113–130. doi: 10.1097/00004691-198604000-00002

Dumont, G., and Gutkin, B. (2019). Macroscopic phase resetting-curves determine oscillatory coherence and signal transfer in inter-coupled neural circuits. *PLoS Comput. Biol*. 15:e1007019. doi: 10.1371/journal.pcbi.1007019

Duncan, J. S., Winston, G. P., Koepp, M. J., and Ourselin, S. (2016). Brain imaging in the assessment for epilepsy surgery. *Lancet Neurol*. 15, 420–433. doi: 10.1016/S1474-4422(15)00383-X

El Houssaini, K., Bernard, C., and Jirsa, V. K. (2020). The epileptor model: a systematic mathematical analysis linked to the dynamics of seizures, refractory status epilepticus and depolarization block. *eNeuro*. 7:ENEURO.0485-18.2019. doi: 10.1523/ENEURO.0485-18.2019

Ermentrout, G. B., and Kopell, N. (1986). Parabolic bursting in an excitable system coupled with a slow oscillation. *SIAM J. Appl. Math*. 46, 233–253. doi: 10.1137/0146017

Fischl, B. (2012). Freesurfer. *Neuroimage* 62, 774–781. doi: 10.1016/j.neuroimage.2012.01.021

Flanagan, D., Valentín, A., García Seoane, J. J., Alarcón, G., and Boyd, S. G. (2009). Single-pulse electrical stimulation helps to identify epileptogenic cortex in children. *Epilepsia* 50, 1793–1803. doi: 10.1111/j.1528-1167.2009.02056.x

Freestone, D., Kuhlmann, L., Chong, M., Nešić, D., Grayden, D. B., Aram, P., et al. (2013). "Patient-specific neural mass modeling-stochastic and deterministic methods," in *Recent Advances in Predicting and Preventing Epileptic Seizures* (Singapore: World Scientific), 63–82.

Fuchs, A., Jirsa, V. K., and Kelso, J. S. (2000). Theory of the relation between human brain activity (meg) and hand movements. *Neuroimage*. 11, 359–369. doi: 10.1006/nimg.1999.0532

Fuhrmann, S., Ackermann, J., Kalbe, T., and Goesele, M. (2010). "Direct resampling for isotropic surface remeshing," in *Proc. Int. Workshop Vision, Modeling, and Visualization,* 9–16.

Ganslandt, O., Fahlbusch, R., Nimsky, C., Kober, H., Möller, M., Steinmeier, R., et al. (1999). Functional neuronavigation with magnetoencephalography: outcome in 50 patients with lesions around the motor cortex. *J. Neurosurg*. 91, 73–79. doi: 10.3171/jns.1999.91.1.0073

Gerster, M., Berner, R., Sawicki, J., Zakharova, A., Škoch, A., Hlinka, J., et al. (2020). Fitzhugh-nagumo oscillators on complex networks mimic epileptic-seizure-related synchronization phenomena. *Chaos* 30, 123130. doi: 10.1063/5.0021420

Ghosh, A., Rho, Y., McIntosh, A. R., Kötter, R., and Jirsa, V. K. (2008). Noise during rest enables the exploration of the brain's dynamic repertoire. *PLoS Comput. Biol*. 4:e1000196. doi: 10.1371/journal.pcbi.1000196

Goldman, J., Kusch, L., Hazalyalcinkaya, B., Depannemaecker, D., Nghiem, T.-A., Jirsa, V., et al. (2020). Brain-scale emergence of slow-wave synchrony and highly responsive asynchronous states based on biologically realistic population models simulated in the virtual brain. *bioRxiv*. doi: 10.1101/2020.12.28.424574

Goldobin, D. S., Di Volo, M., and Torcini, A. (2021). A reduction methodology for fluctuation driven population dynamics. *arXiv preprint arXiv*:2101.11679. doi: 10.1101/2021.01.28.428565

Golomb, D., and Amitai, Y. (1997). Propagating neuronal discharges in neocortical slices: computational and experimental study. *J. Neurophysiol*. 78, 1199–1211. doi: 10.1152/jn.1997.78.3.1199

Goodfellow, M., Rummel, C., Abela, E., Richardson, M., Schindler, K., and Terry, J. (2016). Estimation of brain network ictogenicity predicts outcome from epilepsy surgery. *Sci Rep*. 6, 1–13. doi: 10.1038/srep29215

Goodfellow, M., Rummel, C., Abela, E., Richardson, M. P., Schindler, K., and Terry, J. R. (2017). Computer models to inform epilepsy surgery strategies: prediction of postoperative outcome. *Brain* 140, e30–e30. doi: 10.1093/brain/awx067

Goodfellow, M., Schindler, K., and Baier, G. (2011). Intermittent spike-wave dynamics in a heterogeneous, spatially extended neural mass model. *Neuroimage* 55, 920–932. doi: 10.1016/j.neuroimage.2010.12.074

Goodfellow, M., Schindler, K., and Baier, G. (2012). Self-organised transients in a neural mass model of epileptogenic tissue dynamics. *Neuroimage* 59, 2644–2660. doi: 10.1016/j.neuroimage.2011.08.060

Hall, D., and Kuhlmann, L. (2013). Mechanisms of seizure propagation in 2-dimensional centre-surround recurrent networks. *PLoS ONE*. 8:e71369. doi: 10.1371/journal.pone.0071369

Hara, K., Uematsu, S., Lesser, R., Gordon, B., Hart, J., and Vining, E. (1991). Representation of primary motor cortex in humans: studied with chronic subdural grid. *Epilepsia* 32(Suppl.):23–24.

Hutchings, F., Han, C. E., Keller, S. S., Weber, B., Taylor, P. N., and Kaiser, M. (2015). Predicting surgery targets in temporal lobe epilepsy through structural connectome based simulations. *PLoS Comput. Biol*. 11:e1004642. doi: 10.1371/journal.pcbi.1004642

Huys, R., Perdikis, D., and Jirsa, V. K. (2014). Functional architectures and structured flows on manifolds: a dynamical framework for motor behavior. *Psychol Rev*. 121, 302. doi: 10.1037/a0037014

Jacobs, J., Staba, R., Asano, E., Otsubo, H., Wu, J., Zijlmans, M., et al. (2012). High-frequency oscillations (hfos) in clinical epilepsy. *Progr. Neurobiol*. 98, 302–315. doi: 10.1016/j.pneurobio.2012.03.001

Jacobs, J., Zijlmans, M., Zelmann, R., Olivier, A., Hall, J., Gotman, J., et al. (2010). Value of electrical stimulation and high frequency oscillations (80-500 hz) in identifying epileptogenic areas during intracranial eeg recordings. *Epilepsia* 51, 573–582. doi: 10.1111/j.1528-1167.2009.02389.x

Jefferys, J. G., Traub, R. D., and Whittington, M. A. (1996). Neuronal networks for induced '40 hz' rhythms. *Trends Neurosci*. 19, 202–208. doi: 10.1016/S0166-2236(96)10023-0

Jenkinson, M., Beckmann, C. F., Behrens, T. E., Woolrich, M. W., and Smith, S. M. (2012). Fsl. *Neuroimage* 62, 782–790. doi: 10.1016/j.neuroimage.2011.09.015

Jirsa, V., Sporns, O., Breakspear, M., Deco, G., and McIntosh, A. R. (2010). Towards the virtual brain: network modeling of the intact and the damaged brain. *Arch. Ital. Biol*. 148, 189–205. doi: 10.4449/aib.v148i3.1223

Jirsa, V. K. (2008). Dispersion and time delay effects in synchronized spike-burst networks. *Cogn. Neurodyn*. 2, 29–38. doi: 10.1007/s11571-007-9030-0

Jirsa, V. K., Jantzen, K. J., Fuchs, A., and Kelso, J. S. (2002). Spatiotemporal forward solution of the eeg and meg using network modeling. *IEEE Trans. Med. Imaging* 21, 493–504. doi: 10.1109/TMI.2002.1009385

Jirsa, V. K., Stacey, W. C., Quilichini, P. P., Ivanov, A. I., and Bernard, C. (2014). On the nature of seizure dynamics. *Brain* 137, 2210–2230. doi: 10.1093/brain/awu133

Kaiser, M., Goerner, M., and Hilgetag, C. C. (2007). Criticality of spreading dynamics in hierarchical cluster networks without inhibition. *New J. Phys*. 9, 110. doi: 10.1088/1367-2630/9/5/110

Kalitzin, S. N., Velis, D. N., and da Silva, F. H. L. (2010). Stimulation-based anticipation and control of state transitions in the epileptic brain. *Epilepsy Behav*. 17, 310–323. doi: 10.1016/j.yebeh.2009.12.023

Karoly, P. J., Kuhlmann, L., Soudry, D., Grayden, D. B., Cook, M. J., and Freestone, D. R. (2018). Seizure pathways: a model-based investigation. *PLoS Comput. Biol*. 14:e1006403. doi: 10.1371/journal.pcbi.1006403

Khadjevand, F., Cimbalnik, J., and Worrell, G. A. (2017). Progress and remaining challenges in the application of high frequency oscillations as biomarkers of epileptic brain. *Curr. Opin. Biomed. Eng*. 4, 87–96. doi: 10.1016/j.cobme.2017.09.006

Khambhati, A. N., Davis, K. A., Lucas, T. H., Litt, B., and Bassett, D. S. (2016). Virtual cortical resection reveals push-pull network control preceding seizure evolution. *Neuron* 91, 1170–1182. doi: 10.1016/j.neuron.2016.07.039

Kim, J., Roberts, J., and Robinson, P. (2009). Dynamics of epileptic seizures: evolution, spreading, and suppression. *J. Theor. Biol*. 257, 527–532. doi: 10.1016/j.jtbi.2008.12.009

Kramer, M. A., Kirsch, H. E., and Szeri, A. J. (2005). Pathological pattern formation and cortical propagation of epileptic seizures. *J. R. Soc. Interface* 2, 113–127. doi: 10.1098/rsif.2004.0028

Kramer, M. A., Szeri, A. J., Sleigh, J. W., and Kirsch, H. E. (2007). Mechanisms of seizure propagation in a cortical model. *J. Comput. Neurosci*. 22, 63–80. doi: 10.1007/s10827-006-9508-5

Kramer, M. A., Truccolo, W., Eden, U. T., Lepage, K. Q., Hochberg, L. R., Eskandar, E. N., et al. (2012). Human seizures self-terminate across spatial scales via a critical transition. *Proc. Natl. Acad. Sci. U.S.A*. 109, 21116–21121. doi: 10.1073/pnas.1210047110

Kringelbach, M. L., Cruzat, J., Cabral, J., Knudsen, G. M., Carhart-Harris, R., Whybrow, P. C., et al. (2020). Dynamic coupling of whole-brain neuronal and neurotransmitter systems. *Proc. Natl. Acad. Sci. U.S.A*. 117, 9566–9576. doi: 10.1073/pnas.1921475117

Kunze, T., Hunold, A., Haueisen, J., Jirsa, V., and Spiegler, A. (2016). Transcranial direct current stimulation changes resting state functional connectivity: a large-scale brain network modeling study. *Neuroimage* 140:174–187. doi: 10.1016/j.neuroimage.2016.02.015

Kwan, P., and Brodie, M. J. (2000). Early identification of refractory epilepsy. *New Engl. J. Med*. 342, 314–319. doi: 10.1056/NEJM200002033420503

Laing, C. R. (2017). Phase oscillator network models of brain dynamics. *Comput. Models Brain Behav*. 505:517. doi: 10.1002/9781119159193.ch37

Lecrubier, Y., Sheehan, D. V., Weiller, E., Amorim, P., Bonora, I., Sheehan, K. H., et al. (1997). The Mini International Neuropsychiatric Interview (MINI). A short diagnostic structured interview: reliability and validity according to the CIDI. *Eur. Psychiatry* 12, 224–231. doi: 10.1016/S0924-9338(97)83296-8

Leuthardt, E. C., Miller, K., Anderson, N. R., Schalk, G., Dowling, J., Miller, J., et al. (2007). Electrocorticographic frequency alteration mapping: a clinical technique for mapping the motor cortex. *Operat. Neurosurg*. 60(Suppl_4):ONS-260. doi: 10.1227/01.NEU.0000255413.70807.6E

Leyden, K. M., Kucukboyaci, N. E., Puckett, O. K., Lee, D., Loi, R. Q., Paul, B., et al. (2015). What does diffusion tensor imaging (dti) tell us about cognitive networks in temporal lobe epilepsy? *Quant. Imaging Med. Surg*. 5, 247. doi: 10.3978/j.issn.2223-4292.2015.02.01

Lieb, J. P., Dasheiff, R. M., Engel, J., Genton, P., and Genton, P. (1991). Role of the frontal lobes in the propagation of mesial temporal lobe seizures. *Epilepsia* 32, 822–837. doi: 10.1111/j.1528-1157.1991.tb05539.x

Lieb, J. P., Hoque, K., Skomer, C. E., and Song, X.-W. (1987). Inter-hemispheric propagation of human mesial temporal lobe seizures: a coherence/phase analysis. *Electroencephalogr. Clin. Neurophysiol*. 67, 101–119. doi: 10.1016/0013-4694(87)90033-2

Lindroos, R., Dorst, M. C., Du, K., Filipović, M., Keller, D., Ketzef, M., et al. (2018). Basal ganglia neuromodulation over multiple temporal and structural scales simulations of direct pathway msns investigate the fast onset of dopaminergic effects and predict the role of kv4. 2. *Front. Neural Circ*. 12:3. doi: 10.3389/fncir.2018.00003

Lopes, M. A., Goodfellow, M., and Terry, J. R. (2019). A model-based assessment of the seizure onset zone predictive power to inform the epileptogenic zone. *Front. Comput. Neurosci*. 13:25. doi: 10.3389/fncom.2019.00025

Lopes, M. A., Junges, L., Woldman, W., Goodfellow, M., and Terry, J. R. (2020). The role of excitability and network structure in the emergence of focal and generalized seizures. *Front. Neurol*. 11:74. doi: 10.3389/fneur.2020.00074

Lopes, M. A., Richardson, M. P., Abela, E., Rummel, C., Schindler, K., Goodfellow, M., et al. (2017). An optimal strategy for epilepsy surgery: disruption of the rich-club? *PLoS Comput. Biol*. 13:e1005637. doi: 10.1371/journal.pcbi.1005637

Lopour, B. A., and Szeri, A. J. (2010). A model of feedback control for the charge-balanced suppression of epileptic seizures. *J. Comput. Neurosci*. 28, 375–387. doi: 10.1007/s10827-010-0215-x

Luccioli, S., Ben-Jacob, E., Barzilai, A., Bonifazi, P., and Torcini, A. (2014). Clique of functional hubs orchestrates population bursts in developmentally regulated neural networks. *PLoS Comput. Biol*. 10:e1003823. doi: 10.1371/journal.pcbi.1003823

Marten, F., Rodrigues, S., Benjamin, O., Richardson, M. P., and Terry, J. R. (2009). Onset of polyspike complexes in a mean-field model of human electroencephalography and its application to absence epilepsy. *Philos. Trans. R. Soc. A Math. Phys. Eng. Sci*. 367, 1145–1161. doi: 10.1098/rsta.2008.0255

Melicher, T., Horacek, J., Hlinka, J., Spaniel, F., Tintera, J., Ibrahim, I., et al. (2015). White matter changes in first episode psychosis and their relation to the size of sample studied: a DTI study. *Schizophr. Res*. 162, 22–28. doi: 10.1016/j.schres.2015.01.029

Meyer, P., Sturz, L., Sabri, O., Schreckenberger, M., Spetzger, U., Setani, K., et al. (2003). Preoperative motor system brain mapping using positron emission tomography and statistical parametric mapping: hints on cortical reorganisation. *J. Neurol. Neurosurg. Psychiatry* 74, 471–478. doi: 10.1136/jnnp.74.4.471

Miles, R., Traub, R. D., and Wong, R. (1988). Spread of synchronous firing in longitudinal slices from the ca3 region of the hippocampus. *J. Neurophysiol*. 60, 1481–1496. doi: 10.1152/jn.1988.60.4.1481

Miller, K. J., Leuthardt, E. C., Schalk, G., Rao, R. P., Anderson, N. R., Moran, D. W., et al. (2007). Spectral changes in cortical surface potentials during motor movement. *J. Neurosci*. 27, 2424–2432. doi: 10.1523/JNEUROSCI.3886-06.2007

Montbrió, E., and Pazó, D. (2020). Exact mean-field theory explains the dual role of electrical synapses in collective synchronization. *Phys. Rev. Lett*. 125:248101. doi: 10.1103/PhysRevLett.125.248101

Montbrió, E., Pazó, D., and Roxin, A. (2015). Macroscopic description for networks of spiking neurons. *Phys. Rev. X* 5:021028. doi: 10.1103/PhysRevX.5.021028

Moran, R. J., Pinotsis, D. A., and Friston, K. J. (2013). Neural masses and fields in dynamic causal modeling. *Front. Comput. Neurosci*. 7:57. doi: 10.3389/fncom.2013.00057

Morgan, R. J., and Soltesz, I. (2008). Nonrandom connectivity of the epileptic dentate gyrus predicts a major role for neuronal hubs in seizures. *Proc. Natl. Acad. Sci. U.S.A*. 105, 6179–6184. doi: 10.1073/pnas.0801372105

Najm, I., Jehi, L., Palmini, A., Gonzalez-Martinez, J., Paglioli, E., and Bingaman, W. (2013). Temporal patterns and mechanisms of epilepsy surgery failure. *Epilepsia* 54, 772–782. doi: 10.1111/epi.12152

Ojemann, G. A. (1991). Cortical organization of language. *J. Neurosci*. 11, 2281–2287. doi: 10.1523/JNEUROSCI.11-08-02281.1991

Olmi, S., Petkoski, S., Guye, M., Bartolomei, F., and Jirsa, V. (2019). Controlling seizure propagation in large-scale brain networks. *PLoS Comput. Biol*. 15:e1006805. doi: 10.1371/journal.pcbi.1006805

Ott, E., and Antonsen, T. M. (2008). Low dimensional behavior of large systems of globally coupled oscillators. *Chaos* 18:037113. doi: 10.1063/1.2930766

Pazó, D., and Montbrió, E. (2016). From quasiperiodic partial synchronization to collective chaos in populations of inhibitory neurons with delay. *Phys. Rev. Lett*. 116, 238101. doi: 10.1103/PhysRevLett.116.238101

Petkoski, S., and Jirsa, V. (2020). Renormalization of the brain connectome: Duality of particle and wave. *bioRxiv*. doi: 10.1101/2020.12.02.408518

Pfurtscheller, G., and Da Silva, F. L. (1999). Event-related eeg/meg synchronization and desynchronization: basic principles. *Clin. Neurophysiol*. 110, 1842–1857. doi: 10.1016/S1388-2457(99)00141-8

Proix, T., Bartolomei, F., Chauvel, P., Bernard, C., and Jirsa, V. K. (2014). Permittivity coupling across brain regions determines seizure recruitment in partial epilepsy. *J. Neurosci.* 34, 15009–15021. doi: 10.1523/JNEUROSCI.1570-14.2014

Proix, T., Bartolomei, F., Guye, M., and Jirsa, V. K. (2017). Individual structural connectivity defines propagation networks in partial epilepsy. *Brain* 140, 641–654. doi: 10.1093/brain/awx004

Proix, T., Jirsa, V. K., Bartolomei, F., Guye, M., and Truccolo, W. (2018). Predicting the spatiotemporal diversity of seizure propagation and termination in human focal epilepsy. *Nat. Commun.* 9, 1–15. doi: 10.1038/s41467-018-02973-y

Proix, T., Spiegler, A., Schirner, M., Rothmeier, S., Ritter, P., and Jirsa, V. K. (2016). How do parcellation size and short-range connectivity affect dynamics in large-scale brain network models? *Neuroimage* 142, 135–149. doi: 10.1016/j.neuroimage.2016.06.016

Rabuffo, G., Fousek, J., Bernard, C., and Jirsa, V. (2020). Neuronal cascades shape whole-brain functional dynamics at rest. *bioRxiv*. doi: 10.1101/2020.12.25.424385

Richardson, M. P. (2012). Large scale brain models of epilepsy: dynamics meets connectomics. *J. Neurol. Neurosurg. Psychiatry* 83, 1238–1248. doi: 10.1136/jnnp-2011-301944

Rosenberg, D. S., Mauguière, F., Demarquay, G., Ryvlin, P., Isnard, J., Fischer, C., et al. (2006). Involvement of medial pulvinar thalamic nucleus in human temporal lobe seizures. *Epilepsia* 47, 98–107. doi: 10.1111/j.1528-1167.2006.00375.x

Rosenow, F., and Lüders, H. (2001). Presurgical evaluation of epilepsy. *Brain* 124, 1683–1700. doi: 10.1093/brain/124.9.1683

Rueckert, D., Sonoda, L. I., Hayes, C., Hill, D. L., Leach, M. O., and Hawkes, D. J. (1999). Nonrigid registration using free-form deformations: application to breast MR images. *IEEE Trans. Med. Imaging* 18, 712–721. doi: 10.1109/42.796284

Sagar, S., Rick, J., Chandra, A., Yagnik, G., and Aghi, M. K. (2019). Functional brain mapping: overview of techniques and their application to neurosurgery. *Neurosurg. Rev.* 42, 639–647. doi: 10.1007/s10143-018-1007-4

Saggio, M. L., Crisp, D., Scott, J. M., Karoly, P., Kuhlmann, L., Nakatani, M., et al. (2020). A taxonomy of seizure dynamotypes. *Elife* 9:e55632. doi: 10.7554/eLife.55632

Saggio, M. L., Spiegler, A., Bernard, C., and Jirsa, V. K. (2017). Fast-slow bursters in the unfolding of a high codimension singularity and the ultra-slow transitions of classes. *J. Math. Neurosci.* 7, 1–47. doi: 10.1186/s13408-017-0050-8

Sanz-Leon, P., Knock, S. A., Spiegler, A., and Jirsa, V. K. (2015). Mathematical framework for large-scale brain network modeling in the virtual brain. *Neuroimage* 111, 385–430. doi: 10.1016/j.neuroimage.2015.01.002

Schaffer, E. S., Ostojic, S., and Abbott, L. F. (2013). A complex-valued firing-rate model that approximates the dynamics of spiking networks. *PLoS Comput. Biol.* 9:e1003301. doi: 10.1371/journal.pcbi.1003301

Schirner, M., McIntosh, A. R., Jirsa, V., Deco, G., and Ritter, P. (2018). Inferring multi-scale neural mechanisms with brain network modelling. *Elife* 7:e28927. doi: 10.7554/eLife.28927

Schirner, M., Rothmeier, S., Jirsa, V. K., McIntosh, A. R., and Ritter, P. (2015). An automated pipeline for constructing personalized virtual brains from multimodal neuroimaging data. *Neuroimage* 117:343–357. doi: 10.1016/j.neuroimage.2015.03.055

Segneri, M., Bi, H., Olmi, S., and Torcini, A. (2020). Theta-nested gamma oscillations in next generation neural mass models. *Front. Comput. Neurosci.* 14:47. doi: 10.3389/fncom.2020.00047

Shamas, M., Benquet, P., Merlet, I., Khalil, M., El Falou, W., Nica, A., et al. (2018). On the origin of epileptic high frequency oscillations observed on clinical electrodes. *Clin. Neurophysiol.* 129, 829–841. doi: 10.1016/j.clinph.2018.01.062

Sinai, A., Bowers, C. W., Crainiceanu, C. M., Boatman, D., Gordon, B., Lesser, R. P., et al. (2005). Electrocorticographic high gamma activity versus electrical cortical stimulation mapping of naming. *Brain* 128, 1556–1570. doi: 10.1093/brain/awh491

Sinha, N., Dauwels, J., Kaiser, M., Cash, S. S., Brandon Westover, M., Wang, Y., et al. (2017). Predicting neurosurgical outcomes in focal epilepsy patients using computational modelling. *Brain* 140, 319–332. doi: 10.1093/brain/aww299

Smith, R. E., Tournier, J., Calamante, F., and Connelly, A. (2012). Anatomically-constrained tractography: improved diffusion MRI streamlines tractography through effective use of anatomical information. *Neuroimage* 62, 1924–1938. doi: 10.1016/j.neuroimage.2012.06.005

Smith, R. E., Tournier, J., Calamante, F., and Connelly, A. (2013). SIFT: Spherical-deconvolution informed filtering of tractograms. *Neuroimage* 67, 298–312. doi: 10.1016/j.neuroimage.2012.11.049

Smith, S. (2002). Fast robust automated brain extraction. *Hum. Brain Mapp.* 17, 143–155. doi: 10.1002/hbm.10062

Smith, S., Jenkinson, M., Johansen-Berg, H., Rueckert, D., Nichols, T. E., Mackay, C. E., et al. (2006). Tract-based spatial statistics: voxelwise analysis of multi-subject diffusion data. *Neuroimage* 31, 1487–1505. doi: 10.1016/j.neuroimage.2006.02.024

Smith, S., Jenkinson, M., Woolrich, M., Beckmann, C., Behrens, T., Johansen-Berg, H., et al. (2004). Advances in functional and structural MR image analysis and implementation as FSL. *Neuroimage* 23, S208–S219. doi: 10.1016/j.neuroimage.2004.07.051

Sotero, R. C., Trujillo-Barreto, N. J., Iturria-Medina, Y., Carbonell, F., and Jimenez, J. C. (2007). Realistically coupled neural mass models can generate eeg rhythms. *Neural Comput.* 19, 478–512. doi: 10.1162/neco.2007.19.2.478

Spencer, S. S. (2002). Neural networks in human epilepsy: Evidence of and implications for treatment. *Epilepsia* 43, 219–227. doi: 10.1046/j.1528-1157.2002.26901.x

Spiegler, A., Knösche, T. R., Schwab, K., Haueisen, J., and Atay, F. M. (2011). Modeling brain resonance phenomena using a neural mass model. *PLoS Comput. Biol.* 7:e1002298. doi: 10.1371/journal.pcbi.1002298

Taher, H., Torcini, A., and Olmi, S. (2020). Exact neural mass model for synaptic-based working memory. *PLoS Comput Biol.* 16:e1008533. doi: 10.1371/journal.pcbi.1008533

Talairach, J., and Bancaud, J. (1966). Lesion," irritative" zone and epileptogenic focus. *Stereotact. Funct. Neurosurg.* 27, 91–94. doi: 10.1159/000103937

Taylor, P. N., Goodfellow, M., Wang, Y., and Baier, G. (2013). Towards a large-scale model of patient-specific epileptic spike-wave discharges. *Biol. Cybern.* 107, 83–94. doi: 10.1007/s00422-012-0534-2

Terry, J. R., Benjamin, O., and Richardson, M. P. (2012). Seizure generation: the role of nodes and networks. *Epilepsia* 53, e166–e169. doi: 10.1111/j.1528-1167.2012.03560.x

Touboul, J., Wendling, F., Chauvel, P., and Faugeras, O. (2011). Neural mass activity, bifurcations, and epilepsy. *Neural Comput.* 23, 3232–3286. doi: 10.1162/NECO_a_00206

Tournier, J. (2010). *Mrtrix Package*. Melbourne, VIC:Brain Research Institute. Available online at: https://github.com/jdtournier/mrtrix3

Tournier, J., Calamante, F., and Connelly, A. (2007). Robust determination of the fibre orientation distribution in diffusion MRI: non-negativity constrained super-resolved spherical deconvolution. *Neuroimage* 35, 1459–1472. doi: 10.1016/j.neuroimage.2007.02.016

Toyoda, I., Bower, M. R., Leyva, F., and Buckmaster, P. S. (2013). Early activation of ventral hippocampus and subiculum during spontaneous seizures in a rat model of temporal lobe epilepsy. *J. Neurosci.* 33, 11100–11115. doi: 10.1523/JNEUROSCI.0472-13.2013

Traub, R. D., Whittington, M. A., Buhl, E. H., LeBeau, F. E., Bibbig, A., Boyd, S., et al. (2001). A possible role for gap junctions in generation of very fast eeg oscillations preceding the onset of, and perhaps initiating, seizures. *Epilepsia* 42, 153–170. doi: 10.1046/j.1528-1157.2001.4220153.x

Turrigiano, G. G. (2008). The self-tuning neuron: synaptic scaling of excitatory synapses. *Cell* 135, 422–435. doi: 10.1016/j.cell.2008.10.008

Tyulkina, I. V., Goldobin, D. S., Klimenko, L. S., and Pikovsky, A. (2018). Dynamics of noisy oscillator populations beyond the ott-antonsen ansatz. *Phys. Rev. Lett.* 120, 264101. doi: 10.1103/PhysRevLett.120.264101

Tzourio-Mazoyer, N., Landeau, B., Papathanassiou, D., Crivello, F., Etard, O., Delcroix, N., et al. (2002). Automated anatomical labeling of activations in SPM using a macroscopic anatomical parcellation of the MNI MRI single-subject brain. *Neuroimage* 15, 273–289. doi: 10.1006/nimg.2001.0978

Uematsu, S., Lesser, R., Fisher, R. S., Gordon, B., Hara, K., Krauss, G. L., et al. (1992). Motor and sensory cortex in humans: topography studied with chronic subdural stimulation. *Neurosurgery* 31, 59–72. doi: 10.1227/00006123-199207000-00009

Ullah, G., Cressman Jr, J. R., Barreto, E., and Schiff, S. J. (2009). The influence of sodium and potassium dynamics on excitability, seizures, and the stability of persistent states: Ii. network and glial dynamics. *J. Comput. Neurosci.* 26, 171–183. doi: 10.1007/s10827-008-0130-6

Ursino, M., and La Cara, G.-E. (2006). Travelling waves and eeg patterns during epileptic seizure: analysis with an integrate-and-fire neural network. *J. Theo. Biol.* 242, 171–187. doi: 10.1016/j.jtbi.2006.02.012

Valdes-Sosa, P. A., Sanchez-Bornot, J. M., Sotero, R. C., Iturria-Medina, Y., Aleman-Gomez, Y., Bosch-Bayard, J., et al. (2009). Model driven eeg/fmri fusion of brain oscillations. *Hum. Brain Mapp.* 30, 2701–2721. doi: 10.1002/hbm.20704

Valentin, A., Anderson, M., Alarcon, G., Seoane, J. G., Selway, R., Binnie, C., et al. (2002). Responses to single pulse electrical stimulation identify epileptogenesis in the human brain *in vivo*. *Brain* 125, 1709–1718. doi: 10.1093/brain/awf187

Van Drongelen, W., Lee, H. C., Hereld, M., Chen, Z., Elsen, F. P., and Stevens, R. L. (2005). Emergent epileptiform activity in neural networks with weak excitatory synapses. *IEEE Trans. Neural Syst. Rehabil. Eng.* 13, 236–241. doi: 10.1109/TNSRE.2005.847387

Virtanen, P., Gommers, R., Oliphant, T. E., Haberland, M., Reddy, T., Cournapeau, D., et al. (2020). SciPy 1.0: fundamental algorithms for scientific computing in python. *Nat. Methods* 17, 261–272. doi: 10.1038/s41592-019-0686-2

Wang, S., Wang, I. Z., Bulacio, J. C., Mosher, J. C., Gonzalez-Martinez, J., Alexopoulos, A. V., et al. (2013). Ripple classification helps to localize the seizure-onset zone in neocortical epilepsy. *Epilepsia* 54, 370–376. doi: 10.1111/j.1528-1167.2012.03721.x

Wendling, F., Bartolomei, F., Bellanger, J., and Chauvel, P. (2002). Epileptic fast activity can be explained by a model of impaired gabaergic dendritic inhibition. *Eur. J. Neurosci.* 15, 1499–1508. doi: 10.1046/j.1460-9568.2002.01985.x

Wendling, F., Benquet, P., Bartolomei, F., and Jirsa, V. (2016). Computational models of epileptiform activity. *J. Neurosci. Methods* 260, 233–251. doi: 10.1016/j.jneumeth.2015.03.027

White, J. A., Banks, M. I., Pearce, R. A., and Kopell, N. J. (2000). Networks of interneurons with fast and slow γ-aminobutyric acid type a (gabaa) kinetics provide substrate for mixed gamma-theta rhythm. *Proc. Natl. Acad. Sci. U.S.A.* 97, 8128–8133. doi: 10.1073/pnas.100124097

Whittington, M. A., Traub, R., Kopell, N., Ermentrout, B., and Buhl, E. (2000). Inhibition-based rhythms: experimental and mathematical observations on network dynamics. *Int. J. Psychophysiol.* 38, 315–336. doi: 10.1016/S0167-8760(00)00173-2

Wilson, H. R., and Cowan, J. D. (1972). Excitatory and inhibitory interactions in localized populations of model neurons. *Biophys. J.* 12, 1–24. doi: 10.1016/S0006-3495(72)86068-5

World Health Organization (2005). *Atlas: Epilepsy Care in the World 2005.* Geneva: World Health Organization, International Bureau for Epilepsy and the International League against Epilepsy.

Worrell, G. A., Parish, L., Cranstoun, S. D., Jonas, R., Baltuch, G., and Litt, B. (2004). High-frequency oscillations and seizure generation in neocortical epilepsy. *Brain* 127, 1496–1506. doi: 10.1093/brain/awh149

Zetterberg, L., Kristiansson, L., and Mossberg, K. (1978). Performance of a model for a local neuron population. *Biol. Cybern.* 31, 15–26. doi: 10.1007/BF00337367

Zijlmans, M., Jiruska, P., Zelmann, R., Leijten, F. S., Jefferys, J. G., and Gotman, J. (2012). High-frequency oscillations as a new biomarker in epilepsy. *Ann. Neurol.* 71, 169–178. doi: 10.1002/ana.22548

Conflict of Interest: The authors declare that the research was conducted in the absence of any commercial or financial relationships that could be construed as a potential conflict of interest.

frontiers in Systems Neuroscience

ORIGINAL RESEARCH
published: 19 November 2021
doi: 10.3389/fnsys.2021.720744

Complexity Collapse, Fluctuating Synchrony, and Transient Chaos in Neural Networks With Delay Clusters

S. Kamyar Tavakoli and André Longtin*

Department of Physics and Centre for Neural Dynamics, University of Ottawa, Ottawa, ON, Canada

Neural circuits operate with delays over a range of time scales, from a few milliseconds in recurrent local circuitry to tens of milliseconds or more for communication between populations. Modeling usually incorporates single fixed delays, meant to represent the mean conduction delay between neurons making up the circuit. We explore conditions under which the inclusion of more delays in a high-dimensional chaotic neural network leads to a reduction in dynamical complexity, a phenomenon recently described as multi-delay complexity collapse (CC) in delay-differential equations with one to three variables. We consider a recurrent local network of 80% excitatory and 20% inhibitory rate model neurons with 10% connection probability. An increase in the width of the distribution of local delays, even to unrealistically large values, does not cause CC, nor does adding more local delays. Interestingly, multiple small local delays can cause CC provided there is a moderate global delayed inhibitory feedback and random initial conditions. CC then occurs through the settling of transient chaos onto a limit cycle. In this regime, there is a form of noise-induced order in which the mean activity variance decreases as the noise increases and disrupts the synchrony. Another novel form of CC is seen where global delayed feedback causes "dropouts," i.e., epochs of low firing rate network synchrony. Their alternation with epochs of higher firing rate asynchrony closely follows Poisson statistics. Such dropouts are promoted by larger global feedback strength and delay. Finally, periodic driving of the chaotic regime with global feedback can cause CC; the extinction of chaos can outlast the forcing, sometimes permanently. Our results suggest a wealth of phenomena that remain to be discovered in networks with clusters of delays.

Keywords: dynamical system, transient chaos, delayed differential equation, synchrony, neural network, neural dynamics

OPEN ACCESS

Edited by:
Viktor Jirsa,
Aix-Marseille Université, France

Reviewed by:
Jason N. MacLean,
University of Chicago, United States
Matteo Di Volo,
Université de Cergy-Pontoise, France

****Correspondence:***
S. Kamyar Tavakoli
stava089@uottawa.ca

Received: *04 June 2021*
Accepted: *20 September 2021*
Published: *19 November 2021*

Citation:
Tavakoli SK and Longtin A (2021) Complexity Collapse, Fluctuating Synchrony, and Transient Chaos in Neural Networks With Delay Clusters. Front. Syst. Neurosci. 15:720744. doi: 10.3389/fnsys.2021.720744

1. INTRODUCTION

Biological neural networks can involve delays below the millisecond time scale up to several tens of milliseconds (Madadi Asl et al., 2018). A wide array of delays are involved in inter-areal communication (Deco et al., 2009). A redundancy cancellation circuit in the cerebellum of the weakly fish involves delay distributions between 10 and 70 ms (Bol et al., 2011). Local circuitry also involves delays, which are often neglected in modeling studies due to the added dynamical complexity they bring to the problem. But they have been shown to promote oscillations (Belair et al., 1996; Brunel and Hakim, 1999; Bimbard et al., 2016), and play important roles in

synchronization phenomenon (Coombes and Laing, 2009) and learning phenomenon (Gerstner et al., 1996). They are of course omnipresent in large scale neural control systems where they can reach many hundreds of milliseconds, e.g., in reflex arcs (Longtin et al., 1990).

What are the dynamical consequences of the existence of multiple delays, either centered around a single mean delay, or clustered into different groups? There is widespread belief that systems with many delays can be treated as ones with a single distribution of delays, i.e., a delay-differential equation with discrete delays can be replaced by an integro-differential equation with a suitably chosen delay or memory kernel. Accordingly, the presence of many delays with a sufficiently broad distribution should decrease the dynamical complexity (Longtin, 1990; Jirsa and Ding, 2004; Eurich et al., 2005; Tavakoli and Longtin, 2020).

Recently it has been shown, using numerical experiments of simple model physical systems along with a novel Lyapunov spectrum estimation method for multi-delay non-linear systems, that this complexity reduction can happen quite abruptly, and therefore be more aptly named complexity collapse (Tavakoli and Longtin, 2020). The effect has been investigated by adding delays to standard one-delay systems in one variable, such as the Mackey-Glass equation and the electro-optic model, or the three-variable Lang-Kobayashi laser model. Our work here raises and provides first answers to the question of whether this multi-delay complexity collapse (MDCC) can occur in chaotic neural networks with multiple neurons, i.e., with many state variables.

Note that we are distinguishing here between the number of state variables that describe the time-varying quantities in these models, and the infinite number of variables that relate to the delay *per se*; all differential-delay systems are infinite-dimensional by definition, regardless of the number of delays. Beyond this distinction, it therefore remains to be seen how a cluster of delays around some mean delay affects the chaotic properties of a neural network, and whether additional clusters further cause increases or decreases in dynamical complexity. While our previous study allowed for a more precise diagnostic of attractor properties, using permutation entropy and Lyapunov spectrum estimation, here the large number of state variables (around 1,000) make such computations prohibitively expensive. We thus resort to other simpler metrics that focus on the time-dependent mean and standard deviation of the activity variable averaged across the network.

Of particular interest to us is the question of under which conditions and with respect to which phenomena do delays matter in realistic neural systems. The particular aspect of this question that we focus on is the distribution of discrete delays. Such delays, even acting alone, are notorious for causing simple oscillations and, with the right shape and strength of non-linearities, chaotic fluctuations; yet distributed delays are known to counteract some effects of non-linearity (Longtin, 1990; Herrmann et al., 2016). At which point should one think in terms of continuous delay distributions, and what is expected in the remaining vast domain between single and distributed delays? And how are these issues at play in chaotic neural nets? One expects that bifurcations can occur, but also novel forms of multistability and susceptibility to rhythms impinging from other brain areas. Such effects are indeed highlighted in the results presented below, along with their robustness to noise.

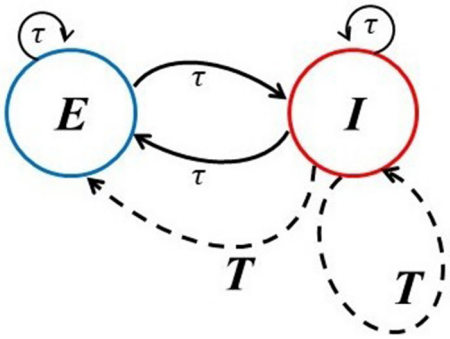

FIGURE 1 | Network architectures. The solid lines provide the schematic of the basic excitatory-inhibitory (EI) network in which the connections can have multiple smaller delays (denoted here by τ) characteristic of local circuitry. The dashed lines account for an extra global inhibitory feedback with longer delay T from population I to itself and to the E population.

In section 2, we introduce the model of interest, namely, a standard 80/20 excitatory-inhibitory (EI) model that has often been used to mimic the cortex. It has local delays between the E and I cells, but can also account for a global delayed inhibitory feedback to both populations with a larger delay (see **Figure 1**, dashed lines). This global feedback mimics a longer route for inhibition that possibly involves other populations that are not explicitly modeled. It is considered here because the complexity collapse phenomenon (CC) does not occur in the EI network on its own, but does in this slightly more complex dynamical system with two delay clusters. In the section 3, we thus first probe how a single delay within and between these sub-populations affect the dynamics. In this network, neurons behave in a much more complex manner as the time delay becomes smaller. Next, we examine the activity and complexity of dynamics generated by neurons under the influence of the global inhibitory feedback term. We will present a novel form of behavior that is reminiscent of a chimera (Larger et al., 2013; Majhi et al., 2019; Sawicki et al., 2019), but with space replaced by time. In order words, we report an alternation of asynchronous and synchronous epochs which seem to follow Poisson statistics. We further show a paradoxical effect in which the activity fluctuations are more constrained the higher the noise is, which is a form of noise-induced order (Matsumoto and Tsuda, 1983). As a consequence of the inclusion of the additive noise with sufficiently large intensity, synchronous activity can be suppressed.

We further provide preliminary observations of the effect of periodic driving of the excitatory sub-population during synchronous epochs, finding that it can alter the dynamics of the whole network. Post-stimulation dynamics can be unpredictable, leading either to transient high-frequency oscillations followed by a return to chaotic dynamics with synchronous epochs, or to CC with periodic behavior. The possibility of observing CC in the presence of the global inhibitory feedback and external stimuli led us to finally study the dynamics of these sub-networks

in the presence of multiple local time delays. The non-linear characteristic of this network prevents CC in the absence of the global inhibitory delayed feedback. However, this non-linearity is seemingly weaker when distributed delays in the local recurrent EI circuitry co-occur with a global delay. For a larger width of the distribution of delays, the transient chaos is replaced by a simple oscillation.

Note that, for the sake of brevity, none of the phenomena reported here are analyzed individually in great detail. We have rather opted for a presentation of a few novel effects related to CC that will hopefully guide future studies; all our results are linked by the existence of multiple delays in various clustered configurations.

2. MODELS AND METHODS

We consider an excitatory and an inhibitory sub-network of rate model neurons, each coupled within itself and to the other sub-network. The architecture corresponding to this network is shown in **Figure 1**. The potential of an excitatory neuron is designated as u, and an inhibitory neuron as v. A similar model without local delay and global inhibitory feedback delay has been studied in Rich et al. (2020). In parts of our work, we go beyond this model by assuming that each of these sub-networks is also affected by global delayed inhibitory feedback from the inhibitory cells, with a global feedback strength κ; this global feedback delay is made longer than the local recurrent feedback delay. The delayed feedback aspects of our model are similar to those in Herrmann et al. (2016) and Hutt et al. (2016). The dynamical equations for the potential of each unit in the network are:

$$\alpha_e^{-1}\frac{du_j}{dt} = -u_j + \frac{1}{n_e}\frac{1}{M}\sum_{l=1}^{M}\sum_{k=1}^{N_e} w_{jk}^{ee}\phi(u_k(t-\tau_l)) + \frac{1}{n_i}\frac{1}{M}\sum_{l=1}^{M}\sum_{k=1}^{N_i} w_{jk}^{ie}\phi(v_k(t-\tau_l)) + \frac{\kappa}{N_i}\sum_{k=1}^{N_i}\phi(v_k(t-T)) + \sigma\xi_E + S(t) \quad (1a)$$

$$\alpha_i^{-1}\frac{dv_j}{dt} = -v_j + \frac{1}{n_e}\frac{1}{M}\sum_{l=1}^{M}\sum_{k=1}^{N_e} w_{jk}^{ei}\phi(u_k(t-\tau_l)) + \frac{1}{n_i}\frac{1}{M}\sum_{l=1}^{M}\sum_{k=1}^{N_i} w_{jk}^{ii}\phi(v_k(t-\tau_l)) + \frac{\kappa}{N_i}\sum_{k=1}^{N_i}\phi(v_k(t-T)) + \sigma\xi_I \quad (1b)$$

where the τ_l's are the local conduction delays which may all be the same, or be taken from a discrete probability density. $\xi_{E,I}(t)$ denote Gaussian white noises, chosen for simplicity here as having the same strength $\sigma = \sqrt{2D}$ with $< \xi_{E,I}(t) > = 0$ and $< \xi_i(t)\xi_j(t') > = \delta_{ij}\delta(t-t')$.

The firing rate function ϕ follows a sigmoidal function defined as:

$$\phi(u) = \frac{1}{1+e^{-\beta u}}\,. \quad (2)$$

TABLE 1 | Parameters of the two-population model.

Symbol	Definition A	Value
N_e	Number of excitatory units	800
N_i	Number of inhibitory units	200
α_i	Dendritic rate constant—inhibitory	200 Hz
α_e	Dendritic rate constant—excitatory	100 Hz
β	Response function gain	100
n_e	Number of excitatory connections for each neuron	80
n_i	Number of inhibitory connections for each neuron	20
w^{ee}	$e \to e$ Synaptic connection strength	15
w^{ei}	$e \to i$ Synaptic connection strength	15
w^{ie}	$i \to e$ Synaptic connection strength	−15.375
w^{ii}	$i \to i$ Synaptic connection strength	−15.375
κ	Global feedback strength	Variable
M	Number of delays	Variable
D	Intrinsic noise level	Variable
dt	Integration timestep	0.1 ms

All parameters are described in **Table 1**. Some of our last results consider the effect of a periodic input $S(t)$ of different frequencies to the excitatory population. In some of our simulations below, we will consider multiple delays chosen from a discrete density. This means that each unit is connected to all other units with these multiple delays.

We assume that there are $N_e = 800$ excitatory units and $N_i = 200$ inhibitory units in the whole network, and that the probability of connection of any two neurons is 10%. Thus each neuron is connected on average to 100 other neurons. The weight matrix can be seen in **Figure 2** in which the excitatory connection weights are fixed at 15 and the inhibitory weights at −15.375 (the mean of the network and mean of the non-zero connections in the network are approximately zero). The initial conditions are picked randomly from a Gaussian distribution with zero mean and unit variance. This choice of values gives a slightly unbalanced network: there are 4 times more excitatory neurons than inhibitory neurons, but the inhibitory weight divided by the number of inhibitory connections ($\frac{w^{ii}}{n_i} = \frac{w^{ie}}{n_i}$) is 4.1 times the excitatory weight divided by the number of excitatory connections ($\frac{w^{ei}}{n_e} = \frac{w^{ee}}{n_e}$). We have checked that the phenomena reported here are robust in the sense that they are qualitatively the same when the network is set up with similar weight ratios, and in particular for the balanced case where the ratio is equal to 4, i.e., with $w^{ii} = w^{ie} = -15$. The results below are also qualitatively similar for the case where elements of the weight matrices are picked randomly from Gaussian distributions such that the mean of the excitatory neurons is 15 and the mean of the inhibitory neurons is −15.375. Also, in the absence of any delays, our network is in a chaotic state, as it is with small local delays in the absence of global feedback and noise. In the thermodynamic limit, the complexity of the dynamics decreases; however, complex dynamics can still be observed provided that smaller delay values are used (at least for the parameters $N = 10000$, $n_e = 800$, and $n_i = 200$ that we tested).

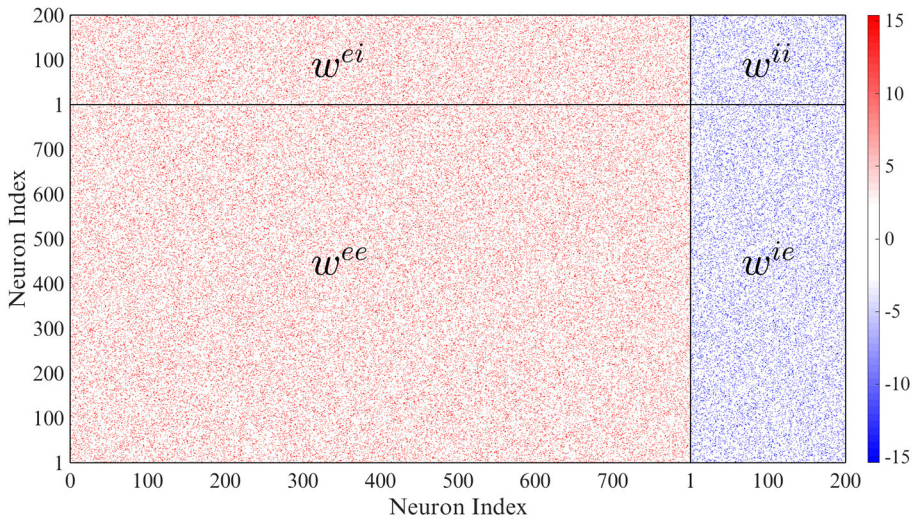

FIGURE 2 | Network connectivity. Only 10 percent of the weights are non-zero.

3. RESULTS

The mean of the activity of the excitatory sub-network for different time delays between interacting neurons can be seen in **Figure 3**. For $\tau = 2$ ms, chaotic behavior can be observed, with no clear peak in the power spectrum, which in fact has power-law characteristics. As the time delay increases to 5 ms, a peak arises in the power spectrum at 70 Hz. This peak further shifts toward the lower frequency of 55 Hz as the delay increases. When the time delay between neurons in the local recurrent circuitry is increased to 10 ms, chaotic dynamics can no longer be seen, and harmonics appear in the power spectrum at integer multiples of 25.6 Hz. For this latter case, when the dynamic is affected by noise, one can use the mean-field method introduced in Hutt et al. (2016) to study the dynamical property of the network. It can be concluded that in this system, a larger delay leads to more coherence between the neurons' activities. We should mention that when we increase connection numbers n_e to 800 and n_i to 200, and the total number of units to 10,000 for this set of parameters, the dynamical behavior becomes simpler; but chaotic behavior can still be achieved for smaller time delays.

In the next step, we examined how delayed global inhibitory feedback from inhibitory units influences network dynamics. In **Figure 4**, the dynamical behavior of the excitatory network for different global feedback time delays and the smaller fixed local time delay is shown. Without local delayed interactions, the activity is a regular oscillation as is expected from purely inhibitory networks with delay. Here we took the local time delay $\tau = 2$ ms and did the simulation for the fixed value of the global feedback coefficient $\kappa = -5$ and variable global feedback time delay T. The global feedback tends to align the dynamical behavior of all units together, while the influence of the local time delays leads to chaotic fluctuations.

The existence of the global feedback, along with the small local delay, causes the appearance of a pattern of very low activity punctuated by random, sudden and brief jumps to larger values. We call these behaviors "dropout activities." They can be characterized by the time-dependent standard deviation (SD) of the activity across the units in the excitatory sub-network (**Figure 4**, middle panels). A stronger global feedback tends to weaken the chaotic nature of the units. Each time that the dynamics enter the state of deficient firing rate activity, the standard deviation becomes very close to zero, meaning that the whole network is highly synchronized in this low activity state. Below we will see the paradoxical implications of this behavior for spiking activity using a spiking rule on top of the activities; spikes will be associated with the state of lower mean activity because they are caused by strong fluctuations, i.e., it is a fluctuation-driven spiking regime.

We can gain more insight by looking at the mean of the power spectrum of the excitatory sub-network's activity. As a result of increasing the global feedback time delay, we can observe that the peak around the 3–8 Hz low-frequency component becomes sharper, and thus that there is enhanced more regular low-frequency activity, a feature that stands out from the time series. Furthermore, it can be seen in the insets that these dropout activities are associated with high-frequency oscillations with very low amplitude, which are also evident in the power spectrum. As the global feedback time delay increases, the higher frequency components become more prominent, such that for $T = 30$ ms there are more high-frequency peaks that are positioned approximately $30 - 40$ Hz from each other.

We illustrate in **Figure 5** the influence of the global feedback strength and assume that the local and global feedback time delays are fixed. As for the previous case where the delay was increased, we observe that increasing the strength of the global feedback also promotes synchrony between units. In the power spectra, similar to the case of increasing delay, the high-frequency components become more evident as the units are more synchronized. The enhanced standard deviation outside

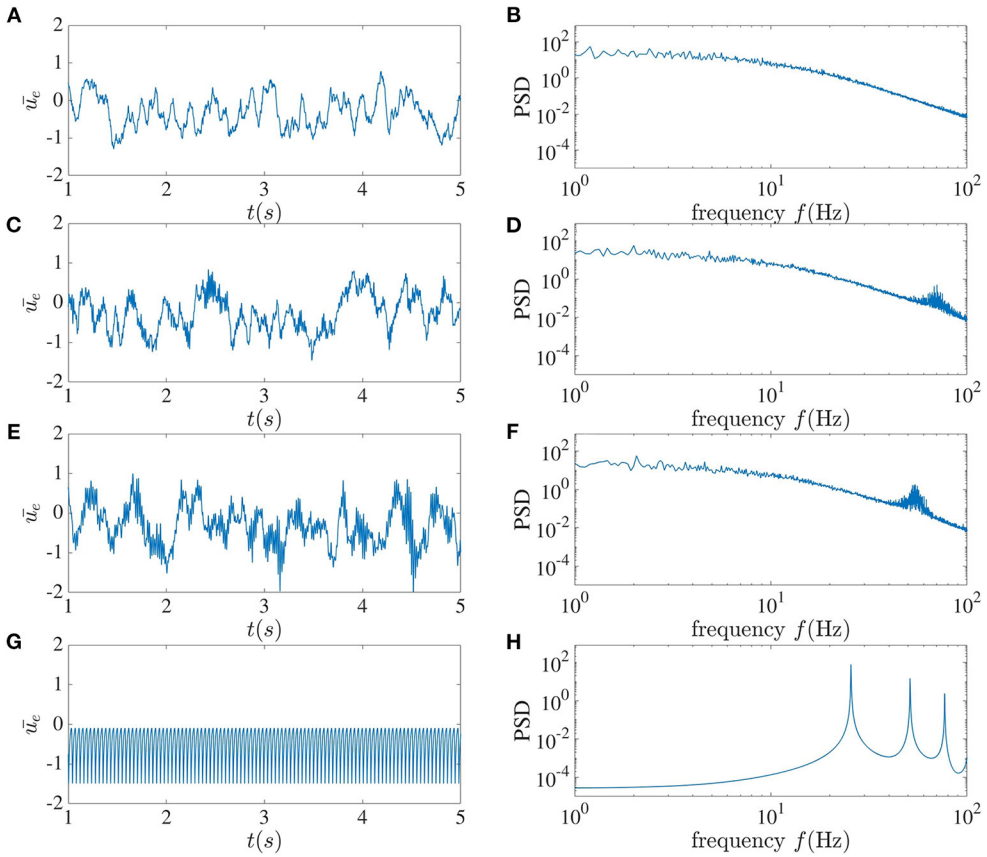

FIGURE 3 | Local dynamics alone. The left column shows the mean activity of the excitatory sub-network, and the right column plots the corresponding power spectrum averaged over the activities in this sub-network. From top to bottom, the local time delay corresponds to **(A,B)** 2 ms, **(C,D)** 5 ms, **(E,F)** 7 ms, and **(G,H)** 10 ms.

dropouts raises the possibility for spiking, a fact that will be confirmed below.

So far, we have seen that either increasing the delay or the strength of the global feedback, the degree of complexity decreases. One difference between the two cases is that at large global feedback coupling, the dynamic will be stuck in a regime of high-frequency low-amplitude oscillation (not shown), while for large global feedback time delay, oscillation with low frequency is the dominant behavior of the sub-networks. The phase diagram for different κ and different global feedback time delay T is shown in **Figure 6**. For this computation, we counted the number of activity drop-outs during 35 s following a 2-s transient, repeating the simulation for different $\kappa - T$ pair.

The pattern of sudden low activities caused by the global feedback appears to be highly vulnerable as it can not be sustained in most cases, and asynchronous fluctuations may be reinstated. In **Figure 7**, these patterns are still found for small noise intensities, while the standard deviation fluctuations in these cases are more constrained. As the noise intensity increases, these dropouts are less likely to occur. It can be noticed that for significant noise intensity, the variations of the time-dependent standard deviation become more confined around 0.5; thus at higher noise, both the mean and the standard deviation seem to stabilize. This appears to be a form of noise-induced order from a chaotic state (Matsumoto and Tsuda, 1983). A simple picture here is that the noise in fact breaks up the synchronous periods and makes the dynamics more homogeneously asynchronous. Despite the decreasing occurrence of activity dropouts, the power spectrum still shows peaks around the high-frequency component, although they are reduced in size. The power spectrum at low frequency also becomes flatter as D increases, with a clear transition to a power-law regime at higher frequencies.

From the raster plots in **Figure 8**, we can understand better the dynamics of all the neurons in the two different sub-networks for different cases. In the absence of the global feedback (left column), the mean network activity fluctuates more around the zero value, and it occurs with higher amplitude. In this case, high spiking activity can be observed, where this spiking activity of individual neurons is based on the assumption that firing follows an inhomogeneous Poisson process with the rate $\phi(x)$ (x is either u or v) and the probability of firing in an interval $(t, t + dt)$ is given by (Rich et al., 2020):

$$p(x) = 1 - e^{-\phi(x(t))dt}. \tag{3}$$

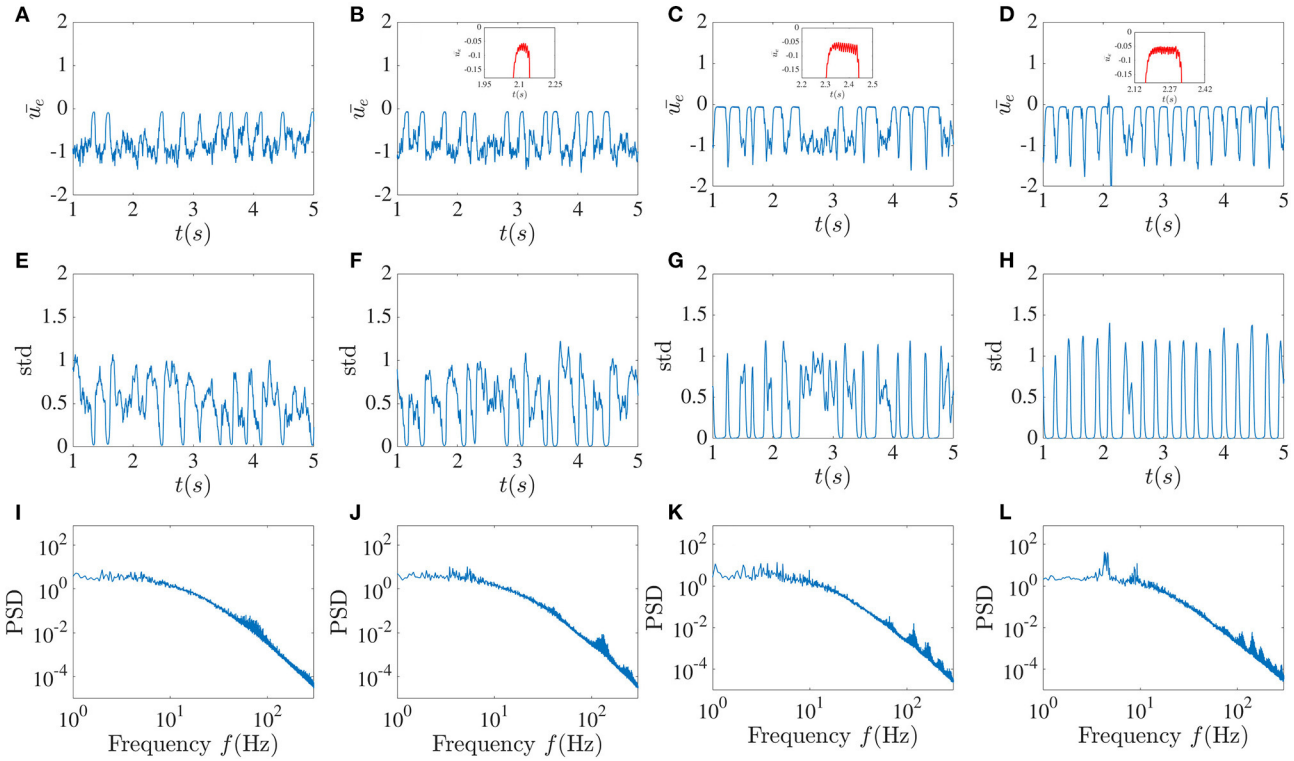

FIGURE 4 | Higher global feedback delay causes activity dropouts. Mean of the excitatory sub-network activity **(A–D)**, the standard deviation of the activities of its units **(E–H)**, and the power spectrum averaged over the units in the excitatory sub-network **(I–L)** in the presence of global inhibitory feedback with fixed strength $\kappa = -5$ without noise. From left to right, the global feedback time delay T equals 5, 10, 20, and 30 ms. The pulse-like epochs in the solution correspond to "activity dropouts" where the sub-network is synchronized with a low firing probability. Paradoxically, between these dropouts, the time-dependent mean activity is lower but its time-dependent fluctuations are stronger. Insets in the figures in the first row show the high-frequency low-amplitude oscillations that occur during the dropouts. The more regular pulsing in **(D)** is associated with a low frequency peak and its harmonics riding on top of the broadband background.

By taking into account the global delayed feedback (three right columns), activity dropouts can be seen in yellow bars in the activity rasters at the top. With a strong enough global feedback coefficient, and sufficiently long delay, the amplitude of the fluctuations decreases and the mean of network activity shifts down to more negative values. This makes sense given that the global feedback is inhibitory. As a consequence, the network spiking activity decreases. We can see clearly that the dropouts are associated with epochs of high mean activity but low standard deviation of activity—hence the name "dropout." For stronger noise intensity, the probability of dropouts decreases, resulting in slightly more widespread spiking activity.

In the middle row, it can be seen that for this set of parameters, spiking activity is slightly higher in the inhibitory sub-network compared to the excitatory sub-network, and there would rarely be a spike during an epoch of dropout. With the decreasing of the amplitude of the fluctuations of the standard deviation through increasing noise intensity, we see that somehow the spiking activity spreads out, especially in the inhibitory sub-network.

The histogram of the time difference between the two dropout activities is shown in **Figure 9**. The statistic is calculated in the following way. We first take the arbitrary threshold value of 0.06 for the standard deviation. We store the data for a duration between the time the standard deviation falls below 0.06 and the time that it rises above 0.1. During this interval, we record the time corresponding to the minimum value of standard deviation. This process is repeated up to $t = 1,500$ s.

First, we only varied the global feedback strength κ from -4 to -6, and the effect of noise was only considered in the last panel of **Figure 9**. Increasing the impact of global feedback on the dynamics coincides with the increase in the probability of these events in a shorter interval, and the statistic tends to be more Poissonian. Due to the noise, the fluctuation around the arbitrary threshold value increases and consequently, the time difference between these events decreases significantly. In general, however, greater noise levels tend to suppress dropout activity.

Externally applied stimuli can have a wide range of dynamical effects, including suppression of chaos, entrainment, etc (Rajan et al., 2010; Park et al., 2018). Of particular interest is the effect of external periodic stimuli (chosen here with an amplitude of 0.2) on the dynamics in the presence of dropout activities. In **Figure 10**, the noise is turned off, and only the sinusoidal external input with different frequencies is applied for a duration of 1 s. It can be seen that after a low-frequency stimulus such as 5

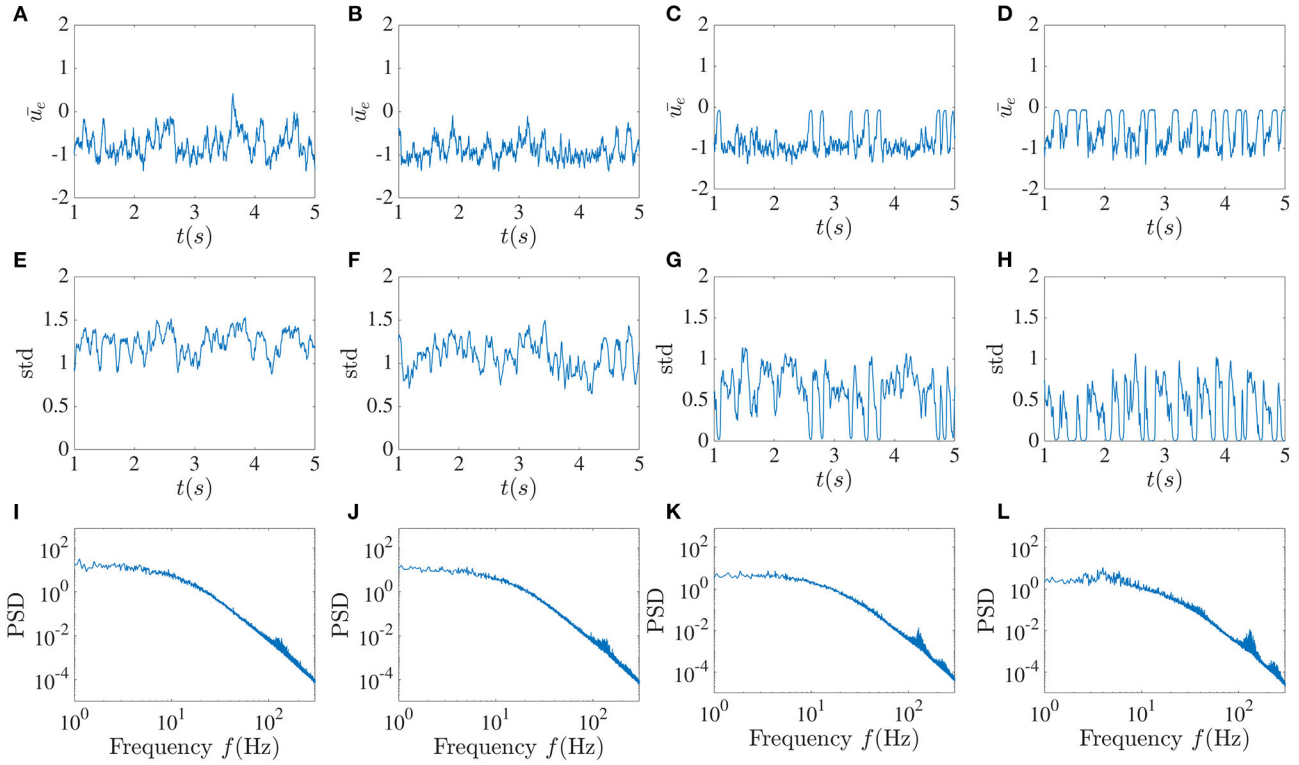

FIGURE 5 | Higher global feedback strength causes activity dropouts. Mean **(A–D)** and standard deviation **(E–H)** of the excitatory sub-network activities, with the corresponding mean power spectrum **(I–L)** in the presence of global inhibitory feedback without noise. From left to right the global feedback strength κ equals -1, -2, -4, and -6 and in all cases, the global feedback time delay is $T = 10$ ms. Higher feedback strength causes more dropouts. As for the increased delay case, between dropouts the standard deviation increases.

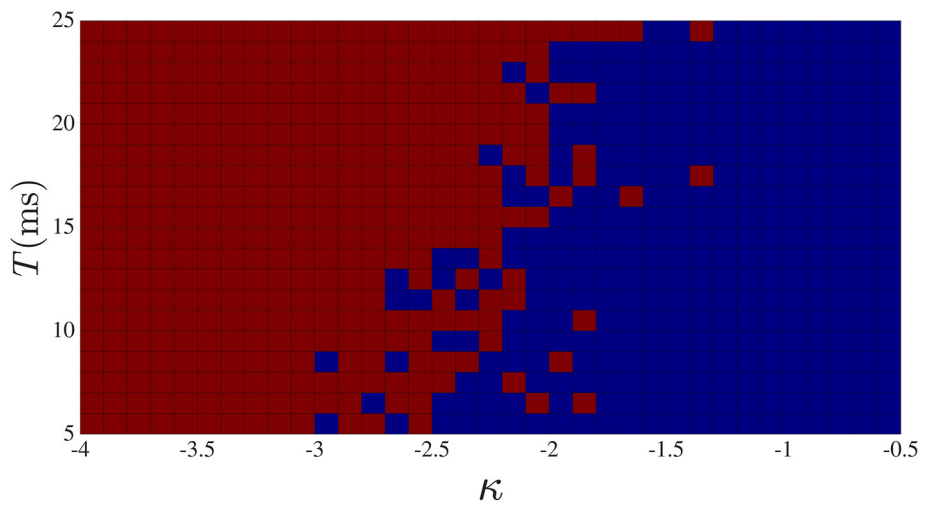

FIGURE 6 | Activity drop-out phase diagram in κ-T space. Red squares correspond to the cases where at least one activity drop-out was observed during 35 s, and blue squares for the cases with no activity drop-out. Stronger and/or longer delay global feedback are seen to promote drop-outs.

Hz ceases, the chaotic network activity prior to stimulation is replaced by a high frequency oscillation of 130 Hz. The duration of these simplified dynamics beyond the stimulation is found to vary as a function of stimulation frequency. For example, for a 15Hz stimulus, the duration elongates a little, but eventually the system recovers its natural dynamical properties. As seen third

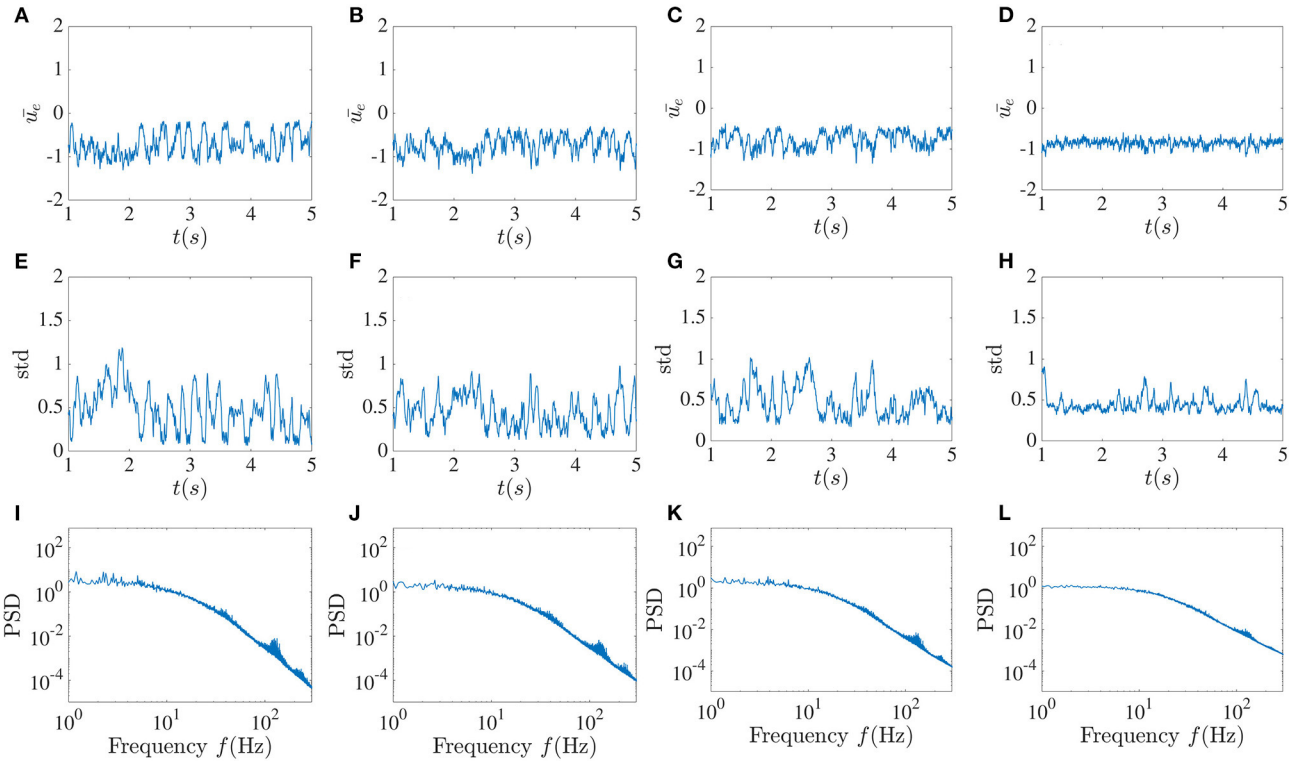

FIGURE 7 | Noise suppresses activity dropouts. Mean activity **(A–D)**, standard deviation **(E–H)**, and power spectrum **(I–L)** averaged over the excitatory sub-network for increasing noise intensity D and fixed global inhibitory feedback with time delay $T = 10$ ms and strength $\kappa = -5$. From left to right, $D = 10^{-5}$, 5×10^{-5}, 10^{-4} and 5×10^{-4}. The dropouts seen in **Figure 4B** are no longer seen, and the fluctuations of the standard deviation decrease at higher noise intensity.

column in **Figure 10**, when the stimulation frequency is relatively higher, the chaotic dynamics may not be recovered at all, or at least not for a much longer time. Because timing and duration of stimulation are crucial in applications, how the network responds to stimulation appears highly complex, and a full investigation is beyond the scope of this paper.

It has been shown (Tavakoli and Longtin, 2020) for many dynamical systems from lasers to biological feedback system that upon adding a sufficient number of delays to the dynamics, a transition from chaos to simpler behavior such as periodic motion, or even fixed-point behavior, can occur, provided that the range of delays is sufficiently broad. In **Figure 11**, we show the behavior of the network activity when multiple local delays are included. Here we set the noise to zero, as well as the periodic stimulation and the global feedback. We assume that the minimum delay is equal to 2 ms, and more delays added at $\Delta\tau = 0.2ms$ increments up to a maximum delay of $[2 + 0.2(M - 1)]$ ms.

We carried out the simulation for $M = 6$, $M = 11$, $M = 16$, and $M = 21$. **Figure 11** shows that, in contrast to the aforementioned delayed dynamical systems, the dynamical properties are not affected so drastically upon adding more delays. This is likely due to the fact that the local EI recurrent dynamics have sufficient intrinsic non-linearity to support chaos without relying on the delay. Our simulations for unrealistically large local delays (with large spacing between delays, and up to a largest delay of 242 ms for 21 delays) revealed no dropout activity or complexity collapse when there was no delayed global feedback (not shown).

It is interesting that for a single delay case, as we saw in **Figure 3**, and for large enough delay, dynamics are simple oscillatory. However, the presence of smaller local delays makes the oscillatory dynamics chaotic. As we saw earlier, global feedback delay can decrease the degree of complexity in the chaotic dynamics. Therefore, we consider the dynamics of the network with multiple local delays in the presence of the global delayed feedback to see whether we can observe the complexity reduction with multiple delays. Parameters used in **Figure 12** are the same as those used for **Figure 11**.

A key finding is that in the presence of both local recurrent delayed feedback and global inhibitory delayed feedback, the dynamics are significantly affected by the multiple local delay times. Indeed, **Figure 12** reveals that, as the distribution of the time delays broadens, the system manifests transient chaos, which eventually converges to a periodic limit cycle attractor with the low amplitude oscillations. Hence, in the presence of a global inhibitory delayed feedback, the system exhibits CC; but it requires a longer delay inhibition to occur. The new feature with respect to the previously reported MDCC is that here the transition to simpler dynamical behavior involves transient chaos.

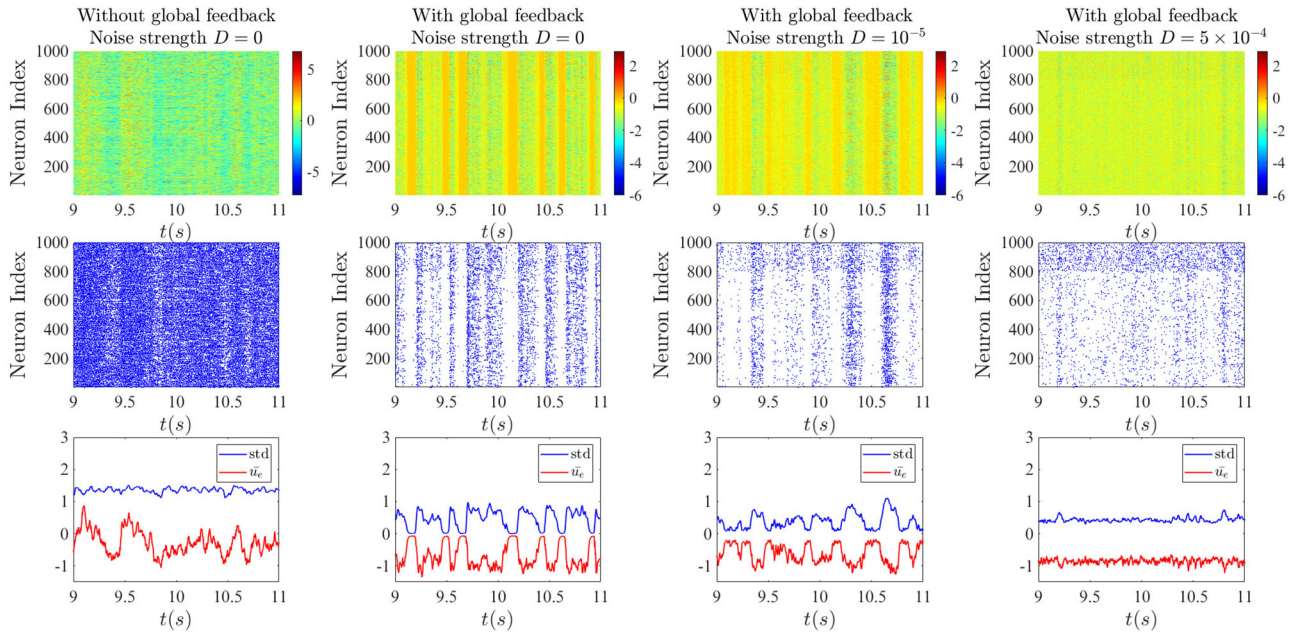

FIGURE 8 | Effect of noise on chaotic global activity dropouts. **Top**: Raster plots of neuron activities from simulations of Equations (1a) and (1b). **Middle**: Raster plots of neuron spiking obtained by applying the Poisson spiking rule Equation (3) to simulations in the top row. **Bottom**: time-dependent mean and standard deviation of the activities of units in the excitatory sub-network. In the left column, the noise and the global feedback are set to zero. In the second column, the global inhibitory feedback is added, leading to the random occurrence of epochs of strong synchrony due to activity dropouts. The last two columns correspond to the cases with additive weak and strong noise on the dynamics of the units. The global inhibitory feedback delay T is 10 ms and its strength κ is -5. The top rows show that the inhibitory sub-network exhibits qualitatively the same behavior as the excitatory one, but with a slightly higher spiking rate.

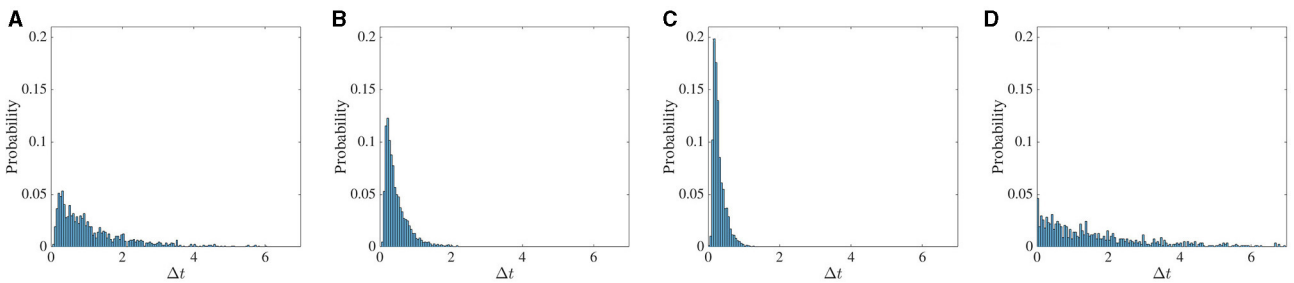

FIGURE 9 | Frequency of chaotic activity dropouts increases with stronger feedback. The probability of intervals between successive low firing activity dropout events. In the first three columns **(A–C)**, the noise strength is $D = 0$ and the global feedback strength κ changes from -4 to -5 to -6. In **(D)**, separate noise terms, each with intensity $D = 10^{-5}$, are added to the excitatory and inhibitory dynamics. In all cases the global feedback time delay T is 10ms.

4. DISCUSSION

We have focused on the properties of a rate-based neural network with a small number of short delays in the local sparsely connected EI recurrent circuitry, and how this is altered by a longer delay that acts globally through all-to-all feedback inhibition. Our goal was to investigate under which conditions, if any, a broadening of the local delay distribution can lead to a simplification of the chaotic dynamics seen for a single delay. By construction, the setup of this problem also allows a preliminary analysis of the effect of clusters of delays on local recurrent EI dynamics, although we have limited our study to two clusters, one of which contains only a single delay. But the means of these clusters are related by a factor of 2-3. Apart from being relevant to neural circuitry, the inclusion of the global feedback was found to be necessary to see CC in a chaotic EI neural network, if the local delays are not allowed to take on values that are too large.

Specifically, we first showed that an increase in the local time delay could lead to a drastic change in the deterministic dynamics. When this delay is unique and is increased from 2 ms to 10 ms, chaotic dynamics are abruptly replaced by regular periodic synchronized network firing (**Figure 3**). This is a first instance in which the complexity collapses in our network, although in a manner that does not rely on the inclusion of

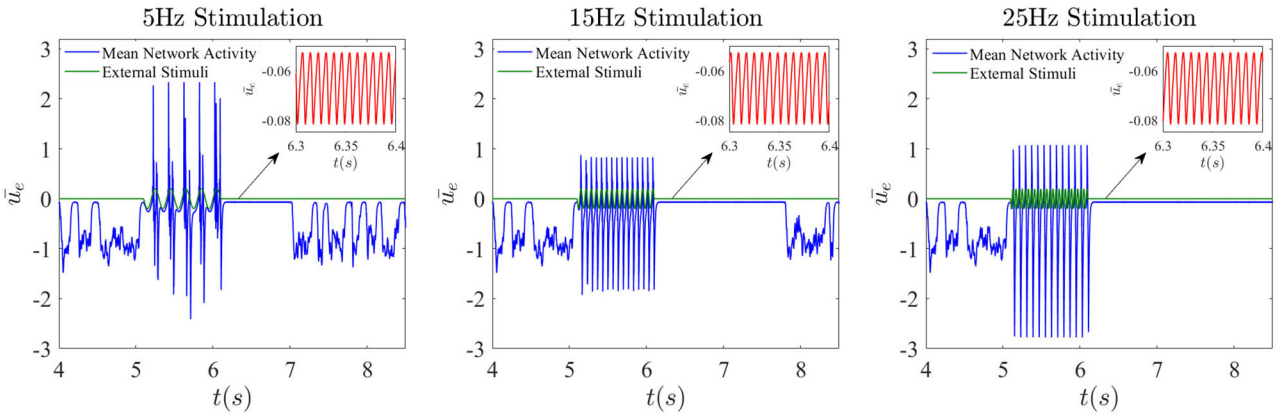

FIGURE 10 | Frequency-dependent complexity collapse. Network dynamics when an external sinusoidal stimulation is activated for 1 s from $t = 5.1$ s until $t = 6.1$ s. Here the global feedback strength is $\kappa = -5$ and the corresponding time delay is 10 ms.

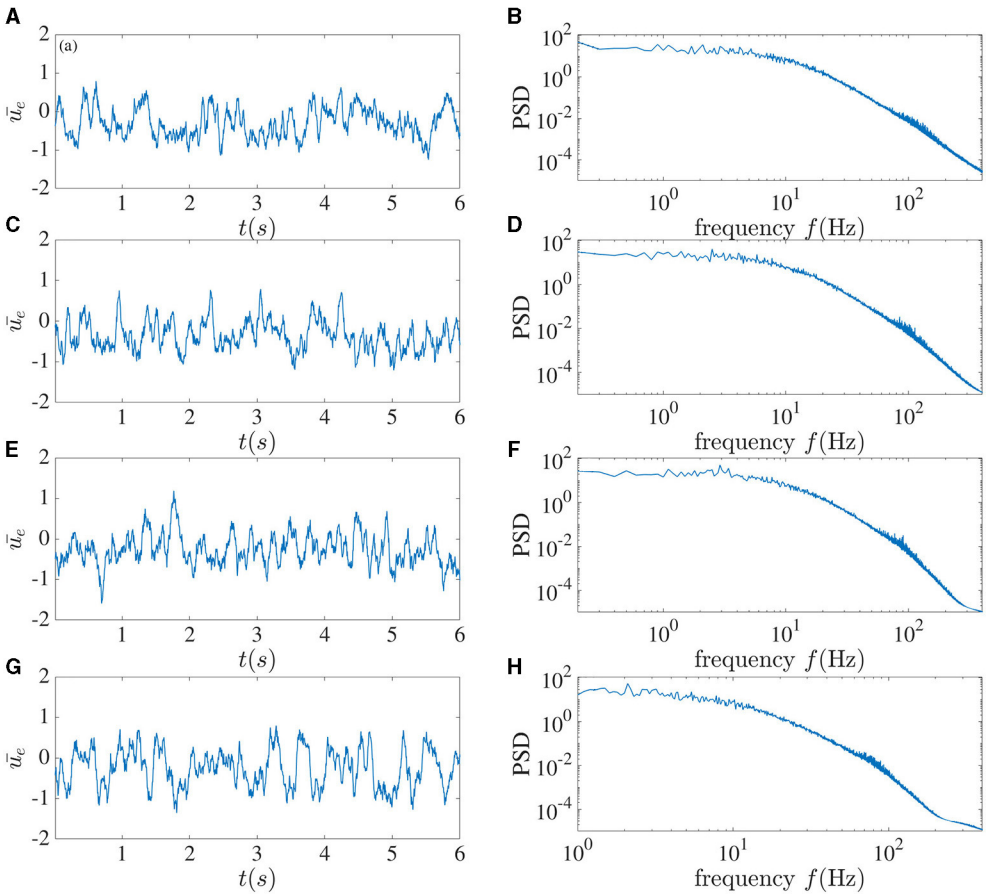

FIGURE 11 | Broadening the local recurrent delay distribution has little effect in the absence of global delayed inhibition. Mean excitatory sub-network activity for different number of delays M. From top to bottom, $M = 6$ **(A,B)**, 11 **(C,D)**, 16 **(E,F)**, and 21 **(G,H)**. Here the global feedback and the noise are set to zero. The delays are confined to the interval $[2 + 0.2(M - 1)]$ ms. No complexity collapse is seen, and the spectra are difficult to tell apart.

more delays (Tavakoli and Longtin, 2020); rather it appears to simply arise from a bifurcation when the single delay parameter is increased.

Adding a delayed global inhibitory feedback can however lead to different interesting phenomena. The main one, show in **Figures 4**, **5**, features chaotic dynamics that exhibit sudden

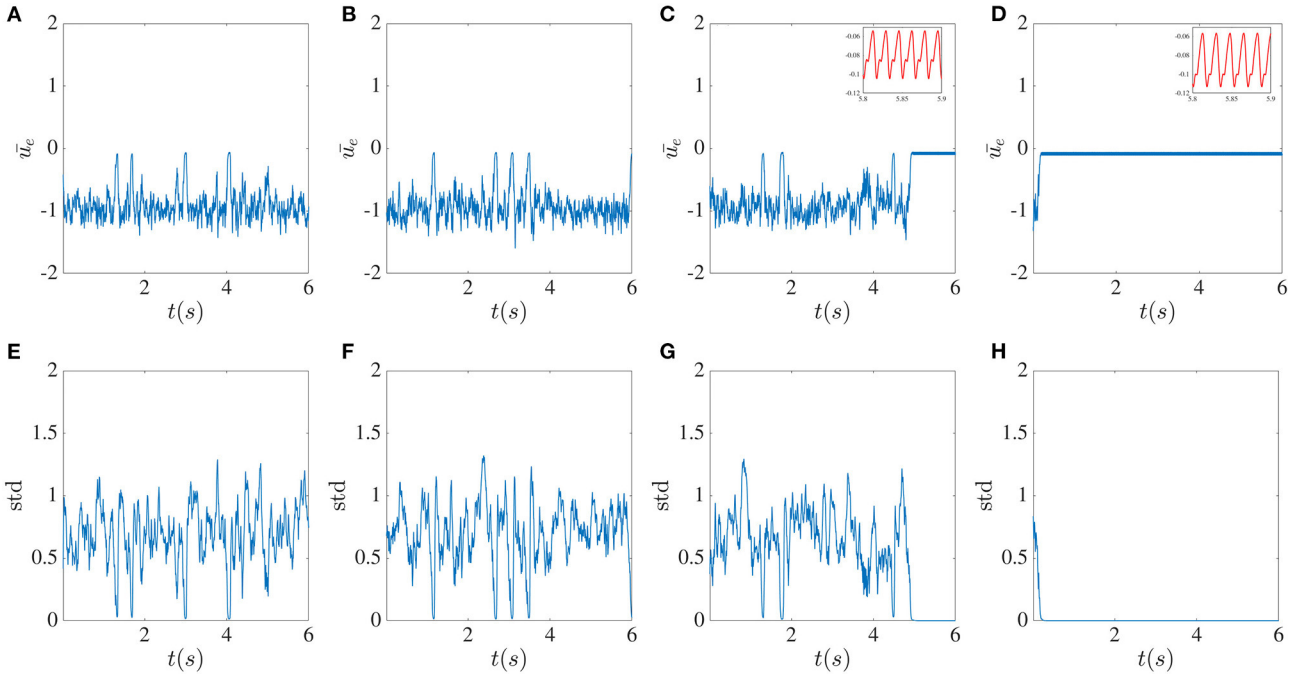

FIGURE 12 | Broadening the local delay distribution initiates complexity collapse in the presence of global delayed feedback. Mean excitatory sub-network activity for different numbers M of local delays. From top to bottom, $M = 6$ **(A,E)**, 11 **(B,F)**, 16 **(C,G)**, and 21 **(D,H)**. The global feedback time delay T is 10ms and the feedback strength κ is -4. The delays are confined to the interval $[2 + 0.2(M - 1)]$ ms. The CC occurs faster the stronger the delay is.

pulses which we have termed "activity dropouts." This effect is more pronounced when the global feedback is strong or its delay is large. Interestingly it is also associated with a power law behavior of the mean activity over three orders of magnitude (only 2.5 orders are shown). These activities contain a high-frequency component that is embedded possibly an unstable orbit in the chaotic attractor due to the local time delay. This property becomes essential when other simplification factors are added to the system, such as increasing the number of local delayed interactions (**Figure 12**) or correlated input. While adding uncorrelated input, such as white noise, does not destroy this component completely, it helps maintain the activity's chaotic nature due to the recurrent local interaction (**Figure 7**). But paradoxically, additive noise on the dynamics also leads to a reduction in the size of the fluctuations in the time-varying standard deviation. This is a form of noise-induced order from a chaotic state first reported by Matsumoto and Tsuda (1983).

The activity dropouts are interesting because the global feedback makes the standard deviation (SD) of the solution on the attractor vary randomly (in fact, Poisson-distributed—see **Figure 9**). The mean of the activity is higher during the periods of low SD, yielding minimal spikes—thus the term "dropout." During the periods of high SD, the mean activity is even lower, but the few cells that fluctuate the most are able to fire during the higher portions of these fluctuations, and their spikes drive the whole network activity. Note that the model does not explicitly run on spiking; the spikes are a derived quantity from Equation (3).

The more regularly aspects of the activity that involves dropouts is reminiscent of the stabilization of unstable periodic orbits using delayed feedback (Pyragas control), although the precise form of the global feedback used here differs from the one used in that chaos-control scheme. Nevertheless this global feedback may create or reveal an underlying slower rhythm embedded in the chaos and which becomes manifest as a lower frequency peak and its harmonics in the power spectra (see **Figure 4L**).

Complexity collapse in the sense of that in Tavakoli and Longtin (2020) does appear in our work through the broadening of the local delay distribution as seen in **Figure 12**; but for the parameter range where we found this effect, the global inhibitory feedback with longer delay must be present. It is possible that other regimes occur in which CC does not rely on the presence of this global feedback.

The novel behavior in **Figure 8** is striking in that there is a temporally random appearance of epochs of dropouts. The time between these dropouts are reminiscent of up-states seen experimentally in neuroscience, and the dropouts as down states. This appears to be a novel deterministic behavior that is synchronized across the network, i.e., it is not a chimera. It survives the presence of moderate noise. There is a sense in which the global inhibitory feedback introduces longer time scales in the network dynamics - the stronger it is, the less power there is at low frequencies (**Figure 5**). This might share features and origins with the long time scales that arise from introducing population

clusters—instead of delay clusters as done here - into EI networks in Litwin-Kumar and Doiron (2012).

Delayed inhibitory feedback has also been reported to elicit transitions between quasi-periodic partial synchronization and collective chaos (Pazó and Montbrió, 2016). Our dynamics here appear to differ from that scenario in that the collective behavior here is not periodic (our network also has E and I coupling). Another point of comparison is the work in Luccioli et al. (2019) where inhibition with long delay can bring on collective oscillations as we see here in **Figures 4**, **5**; it remains to be seen whether a winner-take-all mechanism is at work in our system as reported there.

The final point of interest is the fact that the broadening of the local delay distribution brings on a collapse from chaos to simple (limit cycle) dynamics in a time inversely proportional to the width of that distribution (**Figure 12**). This is a form of transient chaos in neural networks (Zillmer et al., 2009) that relies here on delay clusters. It warrants a deeper investigation, especially of its dependence on the initial state of the network. It reflects special properties of the underlying attractor that are emphasized also in response to external inputs. Indeed we have uncovered a frequency-dependent silencing of the network activity, or frequency-dependent CC that can be temporary or even likely permanent, depending on the frequency. It is a different form of persistence from stimulation reported in Park et al. (2018); in particular, the silencing time seems to depend on the timing of when the stimulus is applied (not shown). This will be investigated elsewhere. This may bear on the reaction of the activity of a neural network with delay clusters to extraneous rhythms or artificial stimulation.

DATA AVAILABILITY STATEMENT

The raw data supporting the conclusions of this article will be made available by the authors under request, without undue reservation.

AUTHOR CONTRIBUTIONS

ST and AL conceived the principle idea of the work and structured the manuscript. ST carried out the numerical simulation. All authors have written the manuscript.

FUNDING

This work was supported by Natural Sciences and Engineering Research Council of Canada under Grant No. RGPIN/06204-2014.

ACKNOWLEDGMENTS

AL thank the Natural Sciences and Engineering Research Council of Canada for financial support.

REFERENCES

Belair, J., Campbell, S. A., and van den Driessche, P. (1996). Frustration, stability, and delay-induced oscillations in a neural network model. *SIAM J. Appl. Math.* 56, 245–255. doi: 10.1137/S0036139994274526

Bimbard, C., Ledoux, E., and Ostojic, S. (2016). Instability to a heterogeneous oscillatory state in randomly connected recurrent networks with delayed interactions. *Phys. Rev. E* 94:062207. doi: 10.1103/PhysRevE.94.062207

Bol, K., Marsat, G., Harvey-Girard, E., Longtin, A., and Maler, L. (2011). Frequency-tuned cerebellar channels and burst-induced ltd lead to the cancellation of redundant sensory inputs. *J. Neurosci.* 31, 11028–11038. doi: 10.1523/JNEUROSCI.0193-11.2011

Brunel, N., and Hakim, V. (1999). Fast global oscillations in networks of integrate-and-fire neurons with low firing rates. *Neural Comput.* 11, 1621–1671. doi: 10.1162/089976699300016179

Coombes, S., and Laing, C. (2009). Delays in activity-based neural networks. *Philos. Trans. R. Soc. A Math. Phys. Eng. Sci.* 367, 1117–1129. doi: 10.1098/rsta.2008.0256

Deco, G., Jirsa, V., McIntosh, A. R., Sporns, O., and Kötter, R. (2009). Key role of coupling, delay, and noise in resting brain fluctuations. *Proc. Natl. Acad. Sci. U.S.A.* 106, 10302–10307. doi: 10.1073/pnas.0901831106

Eurich, C. W., Thiel, A., and Fahse, L. (2005). Distributed delays stabilize ecological feedback systems. *Phys. Rev. Lett.* 94:158104. doi: 10.1103/PhysRevLett.94.158104

Gerstner, W., Kempter, R., van Hemmen, J. L., and Wagner, H. (1996). A neuronal learning rule for sub-millisecond temporal coding. *Nature* 383, 76–78. doi: 10.1038/383076a0

Herrmann, C. S., Murray, M. M., Ionta, S., Hutt, A., and Lefebvre, J. (2016). Shaping intrinsic neural oscillations with periodic stimulation. *J. Neurosci.* 36, 5328–5337. doi: 10.1523/JNEUROSCI.0236-16.2016

Hutt, A., Mierau, A., and Lefebvre, J. (2016). Dynamic control of synchronous activity in networks of spiking neurons. *PLoS ONE* 11:e0161488. doi: 10.1371/journal.pone.0161488

Jirsa, V. K., and Ding, M. (2004). Will a large complex system with time delays be stable? *Phys. Rev. Lett.* 93:070602. doi: 10.1103/PhysRevLett.93.070602

Larger, L., Penkovsky, B., and Maistrenko, Y. (2013). Virtual chimera states for delayed-feedback systems. *Phys. Rev. Lett.* 111:054103. doi: 10.1103/PhysRevLett.111.054103

Litwin-Kumar, A., and Doiron, B. (2012). Slow dynamics and high variability in balanced cortical networks with clustered connections. *Nat. Neurosci.* 15, 1498–1505. doi: 10.1038/nn.3220

Longtin, A. (1990). "Oscillation onset in neural delayed feedback," in *Advances in Neural Information Processing Systems 3 (NIPS 1990)* (Denver), 130–136.

Longtin, A., Milton, J. G., Bos, J. E., and Mackey, M. C. (1990). Noise and critical behavior of the pupil light reflex at oscillation onset. *Phys. Rev. A* 41, 6992–7005. doi: 10.1103/PhysRevA.41.6992

Luccioli, S., Angulo-Garcia, D., and Torcini, A. (2019). Neural activity of heterogeneous inhibitory spiking networks with delay. *Phys. Rev. E* 99:052412. doi: 10.1103/PhysRevE.99.052412

Madadi Asl, M., Valizadeh, A., and Tass, P. A. (2018). Dendritic and axonal propagation delays may shape neuronal networks with plastic synapses. *Front. Physiol.* 9:1849. doi: 10.3389/fphys.2018.01849

Majhi, S., Bera, B. K., Ghosh, D., and Perc, M. (2019). Chimera states in neuronal networks: a review. *Phys. Life Rev.* 28, 100–121. doi: 10.1016/j.plrev.2018.09.003

Matsumoto, K., and Tsuda, I. (1983). Noise-induced order. *J. Stat. Phys.* 31, 87–106. doi: 10.1007/BF01010923

Park, S. H., Griffiths, J. D., Longtin, A., and Lefebvre, J. (2018). Persistent entrainment in non-linear neural networks with memory. *Front. Appl. Math. Stat.* 4:31. doi: 10.3389/fams.2018.00031

Pazó, D., and Montbrió, E. (2016). From quasiperiodic partial synchronization to collective chaos in populations of inhibitory neurons with delay. *Phys. Rev. Lett.* 116:238101. doi: 10.1103/PhysRevLett.116.238101

Rajan, K., Abbott, L. F., and Sompolinsky, H. (2010). Stimulus-dependent suppression of chaos in recurrent neural networks. *Phys. Rev. E* 82:011903. doi: 10.1103/PhysRevE.82.011903

Rich, S., Hutt, A., Skinner, F. K., Valiante, T. A., and Lefebvre, J. (2020). Neurostimulation stabilizes spiking neural networks by disrupting seizure-like oscillatory transitions. *Sci. Rep.* 10:15408. doi: 10.1038/s41598-020-72335-6

Sawicki, J., Ghosh, S., Jalan, S., and Zakharova, A. (2019). Chimeras in multiplex networks: interplay of inter- and intra-layer delays. *Front. Appl. Math. Stat.* 5:19. doi: 10.3389/fams.2019.00019

Tavakoli, S. K., and Longtin, A. (2020). Multi-delay complexity collapse. *Phys. Rev. Res.* 2:033485. doi: 10.1103/PhysRevResearch.2.033485

Zillmer, R., Brunel, N., and Hansel, D. (2009). Very long transients, irregular firing, and chaotic dynamics in networks of randomly connected inhibitory integrate-and-fire neurons. *Phys. Rev. E* 79:031909. doi: 10.1103/PhysRevE.79.031909

Conflict of Interest: The authors declare that the research was conducted in the absence of any commercial or financial relationships that could be construed as a potential conflict of interest.

frontiers in Systems Neuroscience

ORIGINAL RESEARCH
published: 10 December 2021
doi: 10.3389/fnsys.2021.752261

Asynchronous and Coherent Dynamics in Balanced Excitatory-Inhibitory Spiking Networks

Hongjie Bi[1,2], *Matteo di Volo*[1] *and Alessandro Torcini*[1,3]*

[1] CY Cergy Paris Université, Laboratoire de Physique Théorique et Modélisation, CNRS, UMR 8089, Cergy-Pontoise, France, [2] Neural Coding and Brain Computing Unit, Okinawa Institute of Science and Technology, Okinawa, Japan, [3] CNR-Consiglio Nazionale delle Ricerche, Istituto dei Sistemi Complessi, Sesto Fiorentino, Italy

Dynamic excitatory-inhibitory (E-I) balance is a paradigmatic mechanism invoked to explain the irregular low firing activity observed in the cortex. However, we will show that the E-I balance can be at the origin of other regimes observable in the brain. The analysis is performed by combining extensive simulations of sparse E-I networks composed of N spiking neurons with analytical investigations of low dimensional neural mass models. The bifurcation diagrams, derived for the neural mass model, allow us to classify the possible asynchronous and coherent behaviors emerging in balanced E-I networks with structural heterogeneity for any finite in-degree K. Analytic mean-field (MF) results show that both supra and sub-threshold balanced asynchronous regimes are observable in our system in the limit $N >> K >> 1$. Due to the heterogeneity, the asynchronous states are characterized at the microscopic level by the splitting of the neurons in to three groups: silent, fluctuation, and mean driven. These features are consistent with experimental observations reported for heterogeneous neural circuits. The coherent rhythms observed in our system can range from periodic and quasi-periodic collective oscillations (COs) to coherent chaos. These rhythms are characterized by regular or irregular temporal fluctuations joined to spatial coherence somehow similar to coherent fluctuations observed in the cortex over multiple spatial scales. The COs can emerge due to two different mechanisms. A first mechanism analogous to the pyramidal-interneuron gamma (PING), usually invoked for the emergence of γ-oscillations. The second mechanism is intimately related to the presence of current fluctuations, which sustain COs characterized by an essentially simultaneous bursting of the two populations. We observe period-doubling cascades involving the PING-like COs finally leading to the appearance of coherent chaos. Fluctuation driven COs are usually observable in our system as quasi-periodic collective motions characterized by two incommensurate frequencies. However, for sufficiently strong current fluctuations these collective rhythms can lock. This represents a novel mechanism of frequency locking in neural populations promoted by intrinsic fluctuations. COs are observable for any finite in-degree K, however, their existence in the limit $N >> K >> 1$ appears as uncertain.

Keywords: balanced spiking neural populations, sparse inhibitory-excitatory networks, asynchronous dynamics, collective oscillations, neural mass model, quadratic integrate and fire neuron, structural heterogeneity, coherent chaos

OPEN ACCESS

Edited by:
Wen-Jun Gao,
Drexel University, United States

Reviewed by:
Yu-Guo Yu,
Fudan University, China
Rune W. Berg,
University of Copenhagen, Denmark

***Correspondence:**
Alessandro Torcini
alessandro.torcini@cyu.fr

Received: *01 August 2021*
Accepted: *27 October 2021*
Published: *10 December 2021*

Citation:
Bi H, di Volo M and Torcini A (2021) Asynchronous and Coherent Dynamics in Balanced Excitatory-Inhibitory Spiking Networks. Front. Syst. Neurosci. 15:752261. doi: 10.3389/fnsys.2021.752261

1. INTRODUCTION

Cortical neurons are subject to a continuous bombardment from thousands of presynaptic neurons, mostly pyramidal ones, evoking postsynaptic potentials of sub-millivolt or millivolt amplitudes (Destexhe and Paré, 1999; Bruno and Sakmann, 2006; Lefort et al., 2009). This stimulation would induce an almost constant depolarization of the neurons leading to a regular firing, However, cortical neurons fire quite irregularly and with low firing rates (Softky and Koch, 1993). This apparent paradox can be solved by introducing the concept of a balanced network, where excitatory and inhibitory synaptic currents are approximately balanced and the neurons are kept near their firing threshold crossing it at random times (Shadlen and Newsome, 1994, 1998). However, the balance should naturally emerge in the network without fine-tuning of the parameters and the highly irregular firing observed *in vivo* should be maintained also for a large number of connections (in-degree) $K >> 1$. This is possible by considering a sparse excitatory-inhibitory (E-I) neural network composed of N neurons and characterized by an average in-degree $K << N$ and by synaptic couplings scaling as $1/\sqrt{K}$ (van Vreeswijk and Sompolinsky, 1996). This scaling as well as many other key predictions of the theory developed in (van Vreeswijk and Sompolinsky, 1996) have been recently confirmed by experiments on a neural culture (Barral and Reyes, 2016). Furthermore, Barral and Reyes (2016) have shown that the major predictions of the seminal theory (van Vreeswijk and Sompolinsky, 1996) also hold under conditions far from the asymptotic limits where K and N are large.

The dynamics usually observable in balanced neural networks is asynchronous and characterized by irregular neural firing joined to stationary firing rates (van Vreeswijk and Sompolinsky, 1996; Monteforte and Wolf, 2010; Renart et al., 2010; Litwin-Kumar and Doiron, 2012; Ullner et al., 2020). However, other asynchronous regimes characterized by sub-Poissonian and super-Poissonian statistics have been reported in balanced homogenous and heterogeneous networks (Lerchner et al., 2006; Ullner et al., 2020). Furthermore, regular and irregular collective oscillations (COs) have been shown to emerge in balanced networks composed of rate models (van Vreeswijk and Sompolinsky, 1996) and of spiking neurons (Brunel, 2000; Ostojic, 2014; di Volo and Torcini, 2018; Ullner et al., 2018; Bi et al., 2020). The balanced asynchronous irregular state has been experimentally observed both *in vivo* and *in vitro* (Shu et al., 2003; Haider et al., 2006) and dynamic balance of excitation and inhibition is observable in the neocortex across all states of the wake-sleep cycle, in both human and monkey (Dehghani et al., 2016). However, this is not the unique balanced state observable in neural systems. In particular, balancing of excitation and inhibition appears to be crucial for the emergence of cortical oscillations (Okun and Lampl, 2008; Isaacson and Scanziani, 2011; Le Van Quyen et al., 2016) as well as for the instantaneous modulation of the frequency of gamma oscillations in the hippocampus (Atallah and Scanziani, 2009). Moreover, balancing of excitation and inhibition is essential for the generation of respiratory rhythms in the brainstem (Ramirez and Baertsch, 2018) and the rhythmic activity of irregular firing motoneurons in the spinal cord of the turtle (Berg et al., 2007, 2019).

In this work, we characterize in detail the asynchronous regimes and the emergence of COs (population rhythms) in E-I balanced networks with structural heterogeneity. In particular, we consider sparse random networks of quadratic integrate-and-fire (QIF) neurons (Ermentrout and Kopell, 1986) pulse coupled *via* instantaneous post synaptic potentials. We compare numerical findings with analytical results obtained in the mean-field (MF) limit by employing an effective low-dimensional neural mass model recently developed for sparse QIF networks (Montbrió et al., 2015; di Volo and Torcini, 2018; Bi et al., 2020).

In the asynchronous regime, our analytical MF predictions are able to reproduce the mean membrane potentials and the population firing rates of the structurally heterogeneous network for any finite K value. Furthermore, in the limit $N >> K >> 1$, we analytically derive the asymptotic MF values of the population firing rates and the effective input currents. This analysis shows that the system always achieves balanced dynamics, whose supra or sub-threshold nature is determined by the model parameters. Detailed numerical investigations of the microscopic dynamics allow identifying three different groups of neurons, whose activity is essentially controlled by their in-degrees and by the effective input currents.

In the balanced network, we have identified three types of COs depending on the corresponding solution displayed by the neural mass model. The first type, termed O_P emerges in the MF *via* a Hopf bifurcation (HB) from a stable focus solution. These COs gives rise to collective chaos *via* a period-doubling sequence of bifurcations. Another type of CO, already reported for pure inhibitory networks (di Volo and Torcini, 2018), denoted as O_F corresponds in the MF to a stable focus characterized by relaxation oscillations toward the fixed point which in the sparse network become noise sustained oscillations due to fluctuations in the input currents. The last type of COs identified in the finite network are named O_S and characterized by abnormally synchronized dynamics among the neurons, and the high level of synchronization prevents their representation in the MF formulation (Montbrió et al., 2015).

O_P and O_S emerge as sustained oscillations in the network *via* a mechanism resembling that invoked for pyramidal-interneuron gamma (PING) rhythms (Whittington et al., 2011) despite the frequency of these oscillations is not restricted to the γ band. Excitatory neurons start to fire followed by the inhibitory ones and the peak of activity of the excitatory population precedes that of the inhibitory one of a time delay Δt. Furthermore, Δt tends to vanish when the amplitude of the current fluctuations in the network increases. Indeed, for O_F oscillations, which cannot emerge in absence of current fluctuations, no delay has been observed between the activation of excitatory and inhibitory populations. The last important question that we tried to address in our study was whether the COs, observable for any finite K, are still present in the limit $N >> K >> 1$.

The study is organized as follows. Section 2 is devoted to the introduction of the network model and of the corresponding effective neural mass model, as well as of the microscopic and macroscopic indicators employed to characterize the neural dynamics. In the same section, the stationary solutions for the balanced neural mass model are analytically obtained as finite in-degree expansion and their range of stability is determined.

The macroscopic dynamical regimes emerging in our network are analyzed in section 3. In particular, we report bifurcation phase diagrams obtained from the neural mass model displaying the possible dynamical states and network simulations. The focus of this section is on the analysis of the asynchronous balanced state for structurally heterogeneous networks and the emergence of the different types of COs observable at finite in-degrees. A discussion of the obtained results and conclusions are reported in section 4.

2. MODELS AND DYNAMICAL INDICATORS

2.1. Network Model

We consider two sparsely coupled excitatory and inhibitory populations composed of $N^{(e)}$ and $N^{(i)}$ QIF neurons, respectively (Ermentrout and Kopell, 1986). The evolution equation for the membrane potentials $v_j^{(e)}$ and $v_j^{(i)}$ of the excitatory and inhibitory neurons can be written as:

$$\tau_m \dot{v}_j^{(e)} = \left(v_j^{(e)}\right)^2 + I^{(e)} + 2\tau_m \Bigg[g^{(ee)} \sum_{l|t_l^{(n)}<t} \epsilon_{jl}^{(ee)} \delta(t - t_l^{(n)}) - g^{(ei)} \sum_{k|t_k^{(m)}<t} \epsilon_{jk}^{(ei)} \delta(t - t_k^{(m)}) \Bigg] \tag{1a}$$

$$\tau_m \dot{v}_j^{(i)} = \left(v_j^{(i)}\right)^2 + I^{(i)} + 2\tau_m \Bigg[g^{(ie)} \sum_{l|t_l^{(n)}<t} \epsilon_{jl}^{(ie)} \delta(t - t_l^{(n)}) - g^{(ii)} \sum_{k|t_k^{(m)}<t} \epsilon_{jk}^{(ii)} \delta(t - t_k^{(m)}) \Bigg] \tag{1b}$$

where $\tau_m = 20$ ms is the membrane time constant that we set identical for excitatory and inhibitory neurons, $I^{(e)}$ ($I^{(i)}$) is the external direct current (DC) acting on excitatory (inhibitory) population, $g^{(\alpha\beta)}$ represents the synaptic coupling strengths between post synaptic neurons in the population α and pre synaptic ones in population β, with $\alpha, \beta \in \{e, i\}$. The elements of the adjacency matrices $\epsilon_{jk}^{(\alpha\beta)}$ are equal to 1 (0) if a connection from a pre synaptic neuron k of population β toward a post synaptic neuron j of population α, exists (or not). Furthermore, $k_j^{(\alpha\beta)} = \sum_k \epsilon_{jk}^{(\alpha\beta)}$ is the number of pre synaptic neurons in the population β connected to neuron j in population α, or in other terms, its in-degree restricted to population β. The emission of the n-th spike emitted by neuron l of the population α occurs at time $t_l^{(n)}$ whenever the membrane potential $v_l^{(\alpha)}(t_l^{(n)^-}) \to \infty$, while the reset mechanism is modeled by setting $v_l^{(\alpha)}(t_l^{(n)^+}) \to -\infty$ immediately after the spike emission. The postsynaptic potentials are assumed to be δ-pulses and the synaptic transmissions to be instantaneous. The Equations (1) can be formally rewritten as

$$\tau_m \dot{v}_j^{(e)} = \left(v_j^{(e)}\right)^2 + i_{eff,j}^{(e)} \quad , \quad \tau_m \dot{v}_j^{(i)} = \left(v_j^{(i)}\right)^2 + i_{eff,j}^{(i)} \quad ; \tag{2}$$

where $i_{eff,j}^{(e)}$ ($i_{eff,j}^{(i)}$) represents the instantaneous excitatory (inhibitory) effective currents, which include the external DC current and the synaptic currents due to the recurrent connections.

We consider the neurons within the excitatory and inhibitory populations as randomly connected, with in-degrees $k^{(\alpha\alpha)}$ distributed according to a Lorentzian distribution

$$P(k^{(\alpha\alpha)}) = \frac{\Delta_k^{(\alpha\alpha)}}{(k^{(\alpha\alpha)} - K^{(\alpha\alpha)})^2 + \Delta_k^{(\alpha\alpha)^2}} \cdot \frac{1}{\pi} \tag{3}$$

peaked at $K^{(\alpha\alpha)}$ and with a half-width half-maximum (HWHM) $\Delta_k^{(\alpha\alpha)}$, this latter parameter measures the level of structural heterogeneity in each population. For simplicity, we set $K^{(ee)} = K^{(ii)} \equiv K$. Furthermore, we assume that also neurons from a population α are randomly connected to neurons of a different population $\beta \neq \alpha$. However, in this case, we consider no structural heterogeneity with in-degrees fixed to a constant value $K^{(ei)} = K^{(ie)} = K$. We have verified that by considering Erdös-Renyi distributed in-degrees $K^{(ei)}$ and $K^{(ie)}$ with average K does not modify the observed dynamical behavior.

The DC current and the synaptic coupling are rescaled with the median in degree as $I^{(\alpha)} = \sqrt{K} I_0^{(\alpha)}$ and $g^{(\alpha\beta)} = g_0^{(\alpha\beta)}/\sqrt{K}$, as done in previous studies to obtain a self-sustained balanced dynamics for $N >> K >> 1$ (van Vreeswijk and Sompolinsky, 1996; Renart et al., 2010; Litwin-Kumar and Doiron, 2012; Kadmon and Sompolinsky, 2015). The structural heterogeneity parameters are rescaled as $\Delta_k^{(\alpha\alpha)} = \Delta_0^{(\alpha\alpha)}\sqrt{K}$ in analogy to Erdös-Renyi networks. The choice of the Lorentzian distribution for the $k^{(\alpha\alpha)}$ is needed in order to obtain an effective MF description for the microscopic dynamics (di Volo and Torcini, 2018; Bi et al., 2020) as detailed in the next section.

The microscopic activity can be analyzed by considering the inter-spike interval (ISI) distribution as characterized by the coefficient of variation cv_i for each neuron i, which is the ratio between the SD and the mean of the ISIs associated with the train of spikes emitted by the considered neuron. To characterize the macroscopic dynamics of each population α, we measure the average coefficient of variation $CV^{(\alpha)} = \sum_{i=1}^{N^{(\alpha)}} cv_i/N^{(\alpha)}$, the mean membrane potential $V^{(\alpha)}(t) = \sum_{i=1}^{N^{(\alpha)}} v_i^{(\alpha)}(t)/N^{(\alpha)}$, and the population firing rate $R^{(\alpha)}(t)$, corresponding to the number of spikes emitted within the population α per unit of time and per neuron.

Furthermore, the level of coherence in the neural activity of the population α can be quantified in terms of the following indicator (Golomb, 2007),

$$\rho^{(\alpha)} = \left(\frac{\sigma^2_{V^{(\alpha)}}}{\sum_{i=1}^{N^{(\alpha)}} \sigma_i^2/N^{(\alpha)}} \right)^{1/2} \tag{4}$$

where $\sigma_{V^{(\alpha)}}$ is the SD of the mean membrane potential, $\sigma_i^2 = \left\langle (v_i^{(\alpha)})^2 \right\rangle - \left\langle v_i^{(\alpha)} \right\rangle^2$ and $\langle \cdot \rangle$ denotes a time average. A perfect synchrony corresponds to $\rho^{(\alpha)} = 1$, while an asynchronous dynamics to a vanishing small $\rho^{(\alpha)} \approx O(1/\sqrt{N^{(\alpha)}})$.

The frequencies associated with collective motions can be identified by measuring the power spectra $S(\nu)$ of the mean membrane potentials $V(t)$ of the whole network. In the case of a periodic motion, the position of the main peak ν_{CO} represents the frequency of the COs, while for quasi-periodic motions, the spectrum is characterized by many peaks that can be obtained as a linear combination of two fundamental frequencies (ν_1, ν_2). The spectra obtained in the present case, always exhibit a continuous background due to the intrinsic fluctuations present in the balanced network. The power spectra have been obtained by calculating the temporal Fourier transform of $V(t)$ sampled at time intervals of 10 ms. Time traces composed of 10,000 consecutive intervals have been considered to estimate the spectra, which are obtained at a frequency resolution of $\Delta\nu = 0.01$ Hz. Finally, the power spectra have been averaged over five independent realizations of the random network.

The network dynamics are integrated by employing an Euler scheme with time step $dt = 0.0001$ ms, while time averages and fluctuations are usually estimated on time intervals $T_s \simeq 100$ s, after discarding transients $T_t \simeq 10$ s. Usually, we consider networks composed of $N^{(e)} = 10,000$ excitatory and $N^{(i)} = 2,500$ inhibitory neurons.

2.2. Effective Neural Mass Model

In this sub-section, we derive a low dimensional effective neural mass formulation for the spiking network (Equation 1) by following Montbrió et al. (2015). In such an article, the authors obtained an exact MF model for a globally coupled heterogeneous population of QIF neurons by generalizing to neural systems using a reduction methodology previously developed for phase-coupled oscillators by Ott and Antonsen (2008). In particular, the neural mass model can be obtained by performing a rigorous mathematical derivation from the original spiking network in the limit $N \to \infty$ by assuming that the heterogeneity present in the network, which can be either neuronal excitabilities or synaptic couplings, are distributed as Lorentzians. This MF reduction methodology gives rise to a neural mass model written in terms of only two collective variables: the mean membrane potential V and the instantaneous population rate R. For sufficiently large network size, the agreement between the simulation results and the neural mass model is impressive as shown in Montbrió et al. (2015) and in several successive publications.

The detailed derivation of the neural mass models from the corresponding spiking networks can be found in Montbrió et al. (2015), in this study, we limit to report its expression for a fully coupled homogeneous network of QIF neurons with synaptic couplings randomly distributed according to a Lorentzian:

$$\tau_m \dot{R} = 2RV + \frac{\Gamma}{\pi} R \tag{5a}$$

$$\tau_m \dot{V} = V^2 + I + \bar{g}\tau_m R - (\pi \tau_m R)^2 \tag{5b}$$

where $\bar{g}$ is the median and Γ the HWHM of the Lorentzian distribution of the synaptic couplings.

Such formulation can be applied to the random sparse network studied in this article, in this paper. Indeed, as shown for a single sparse inhibitory population (di Volo and Torcini, 2018; Bi et al., 2020), the quenched disorder associated to the in-degree distribution can be rephrased in terms of random synaptic couplings. Namely, each neuron i in population α is subject to currents of amplitude $g_0^{(\alpha\beta)} k_i^{(\alpha\beta)} R^{(\beta)}/(\sqrt{K})$ proportional to their in-degrees $k_i^{(\alpha\beta)}$, with $\beta \in \{e, i\}$. Therefore, we can consider the neurons as fully coupled but with random values of the couplings distributed as Lorentzian of median $g_0^{(\alpha\beta)}\sqrt{K}$ and HWHM $g_0^{(\alpha\beta)}\Delta_0^{(\alpha\beta)}$.

The neural mass model corresponding to the spiking network (Equation 1) can be written as follows:

$$\tau_m \dot{R}^{(e)} = R^{(e)} \left[2V^{(e)} + g_0^{(ee)} \frac{\Delta_0^{(ee)}}{\pi} \right] \tag{6a}$$

$$\tau_m \dot{V}^{(e)} = \left[V^{(e)} \right]^2 - \left[\pi R^{(e)} \tau_m \right]^2 + \sqrt{K} \left[I_0^{(e)} + (g_0^{(ee)} R^{(e)} - g_0^{(ei)} R^{(i)}) \tau_m \right] \tag{6b}$$

$$\tau_m \dot{R}^{(i)} = R^{(i)} \left[2V^{(i)} + g_0^{(ii)} \frac{\Delta_0^{(ii)}}{\pi} \right] \tag{6c}$$

$$\tau_m \dot{V}^{(i)} = \left[V^{(i)} \right]^2 - \left[\pi R^{(i)} \tau_m \right]^2 + \sqrt{K} \left[I_0^{(i)} + (g_0^{(ie)} R^{(e)} - g_0^{(ii)} R^{(i)}) \tau_m \right] \quad ; \tag{6d}$$

where we have set $\Delta_0^{(ei)} = \Delta_0^{(ie)} = 0$, since we have assumed that the connections among neurons of different populations are random but with a fixed in-degree $K^{(ei)} = K^{(ie)} = K$.

2.2.1. Stationary Solutions

The stationary solutions $\{\overline{V}^{(e)}, \overline{V}^{(i)}, \overline{R}^{(e)}, \overline{R}^{(i)}\}$ of Equation (6) can be explicitly obtained for the mean membrane potentials as

$$\overline{V}^{(e)} = -\frac{g_0^{(ee)} \Delta_0^{(ee)}}{2\pi} \quad , \quad \overline{V}^{(i)} = -\frac{g_0^{(ii)} \Delta_0^{(ii)}}{2\pi} \quad ; \tag{7}$$

while the instantaneous population rates are the solutions of the following quadratic system

$$g_0^{(ee)} \overline{R}^{(e)} \tau_m - g_0^{(ei)} \overline{R}^{(i)} \tau_m = -I_0^{(e)} + \varepsilon \left\{ \left[\pi \overline{R}^{(e)} \tau_m \right]^2 - \left[\overline{V}^{(e)} \right]^2 \right\} \tag{8a}$$

$$g_0^{(ie)} \overline{R}^{(e)} \tau_m - g_0^{(ii)} \overline{R}^{(i)} \tau_m = -I_0^{(i)} + \varepsilon \left\{ \left[\pi \overline{R}^{(i)} \tau_m \right]^2 - \left[\overline{V}^{(i)} \right]^2 \right\} \tag{8b}$$

where $\varepsilon = 1/\sqrt{K}$ is a smallness parameter taking in to account finite in-degree corrections. It is interesting to notice that the parameters controlling the structural heterogeneity $\Delta_0^{(ii)}$ and $\Delta_0^{(ee)}$ fix the stationary values of the mean membrane potentials

reported in Equation (7). The solutions of Equation (8) can be exactly obtained and the associated bifurcations analyzed by employing the software XPP AUTO developed for orbit continuation (Ermentrout, 2007).

For sufficiently large K, one can obtain analytic approximations of the solution of Equation (8) by expanding the population rates as follows:

$$\overline{R}^{(\alpha)} = \overline{R}_0^{(\alpha)} + \varepsilon \overline{R}_1^{(\alpha)} + \varepsilon^2 \overline{R}_2^{(\alpha)} + \varepsilon^3 \overline{R}_3^{(\alpha)} + \dots \qquad \alpha \in \{e, i\}, \quad (9)$$

by inserting these expressions in Equation (8), and finally by solving order by order in ε.

The solutions at any order can be written as follows:

$$\begin{aligned} \overline{R}_k^{(e)} \tau_m &= \frac{N_k^{(e)} g_0^{(ii)} - N_k^{(i)} g_0^{(ei)}}{g_0^{(ei)} g_0^{(ie)} - g_0^{(ee)} g_0^{(ii)}}, \\ \overline{R}_k^{(i)} \tau_m &= \frac{N_k^{(e)} g_0^{(ie)} - N_k^{(i)} g_0^{(ee)}}{g_0^{(ei)} g_0^{(ie)} - g_0^{(ee)} g_0^{(ii)}}; \end{aligned} \quad (10)$$

where,

$$N_0^{(\alpha)} = I_0^{(\alpha)} \ , \ N_1^{(\alpha)} = \left[\overline{V}^{(\alpha)}\right]^2 - \left[\pi \overline{R}_0^{(\alpha)} \tau_m\right]^2 \quad (11a)$$

$$N_{2j}^{(\alpha)} = -2 \left[\pi \tau_m\right]^2 \sum_{k=1}^{j} \left[\overline{R}_{k-1}^{(\alpha)} \overline{R}_{2j-k}^{(\alpha)}\right] \quad (11b)$$

$$N_{2j+1}^{(\alpha)} = -2 \left[\pi \tau_m\right]^2 \left\{ \left[\sum_{k=1}^{j} \overline{R}_{k-1}^{(\alpha)} \overline{R}_{2j+1-k}^{(\alpha)} \right] + \frac{1}{2} \left[\overline{R}_j^{(\alpha)}\right]^2 \right\} \quad \text{for } j \geq 1 \quad (11c)$$

The systems (Equation 10) with parameters given by Equation (11) can be resolved recursively for any order and the final solution obtained from the expression (Equation 9). The zeroth-order approximation, valid in the limit $K \to \infty$, corresponds to the usual solution found for rate models in the balanced state (van Vreeswijk and Sompolinsky, 1996; Rosenbaum and Doiron, 2014), such solution is physical whenever one of the following inequalities is satisfied

$$\frac{I_0^{(e)}}{I_0^{(i)}} > \frac{g_0^{(ei)}}{g_0^{(ii)}} > \frac{g_0^{(ee)}}{g_0^{(ie)}} \quad , \quad \frac{I_0^{(e)}}{I_0^{(i)}} < \frac{g_0^{(ei)}}{g_0^{(ii)}} < \frac{g_0^{(ee)}}{g_0^{(ie)}} \quad ; \quad (12)$$

which ensure the positive sign of $\overline{R}_0^{(e)}$ and $\overline{R}_0^{(i)}$. The zeroth-order solution does not depend on the structural heterogeneity, since the ratio $\Delta^{(\alpha\alpha)}/K$ vanishes in the limit $K \to \infty$. It should be stressed that this ratio does not correspond to the coefficient of variation introduced in Landau et al. (2016) to characterize the in-degree distribution. This is because we are considering a Lorentzian distribution, where the average and the SD are not even defined. Moreover, already the first-order corrections depend on $\Delta_0^{(\alpha\alpha)}$.

To characterize the level of balance in the system, one usually estimates the values of the effective input currents $i_{eff,j}^{(e)}$ and $i_{eff,j}^{(i)}$ driving the neuron dynamics. These at a population level can be rewritten as

$$\begin{aligned} I_{eff}^{(e)} &= \sqrt{K} \left[I_0^{(e)} + \tau_m (g_0^{(ee)} R^{(e)} - g_0^{(ei)} R^{(i)}) \right] \ , \\ I_{eff}^{(i)} &= \sqrt{K} \left[I_0^{(i)} + \tau_m (g_0^{(ie)} R^{(e)} - g_0^{(ii)} R^{(i)}) \right]. \end{aligned} \quad (13)$$

In a balanced state, these quantities should not diverge with K, instead, they should approach some constant value. For an asynchronous state we can estimate analytically, within our MF formulation, the values of the effective currents in the limit $K \to \infty$. These read as

$$\begin{aligned} I_a^{(e)} &= \tau_m \left[g_0^{(ee)} \overline{R}_1^{(e)} - g_0^{(ei)} \overline{R}_1^{(i)} \right], \\ I_a^{(i)} &= \tau_m \left[g_0^{(ie)} \overline{R}_1^{(e)} - g_0^{(ii)} \overline{R}_1^{(i)} \right] \ . \end{aligned} \quad (14)$$

It should be noticed that these asymptotic values depend on the first-order corrections to the balanced solution (Equation 10). Therefore, they depend not only on the synaptic couplings $g_0^{(\alpha\beta)}$ and on the external DC currents but also on the parameters $\Delta_0^{(\alpha\alpha)}$ controlling the structural heterogeneities.

Depending on the parameter values, the currents $I_a^{(\alpha)}$ can be positive or negative, thus, indicating a balanced dynamics where most parts of the neurons are supra or below the threshold, respectively. Usually, in order to obtain a stationary state characterized by a low rate and a Poissonian statistic, as observed in the cortex, one assumes that the excitation and inhibition nearly cancel. So that the mean membrane potential remains slightly below the threshold, and the neurons can fire occasionally due to the input current fluctuations (van Vreeswijk and Sompolinsky, 1996; Brunel, 2000). However, as pointed out in Lerchner et al. (2006), this is not the only possible scenario for a balanced state. In particular, the authors have developed a self-consistent MF theory for balanced Erdös-Renyi networks made of heterogeneous Leaky Integrate-and-Fire (LIF) neurons. In this context, they have shown that Poisson-like dynamics are visible only at intermediate synaptic couplings. While mean driven dynamics are expected for low couplings, and at large couplings bursting behaviors appear in the balanced network. Recently, analogous dynamical behaviors have been reported also for a purely inhibitory heterogeneous LIF network (Angulo-Garcia et al., 2017). These findings are consistent with the results in Lerchner et al. (2006), where the inhibition is indeed predominant in the balanced regime.

2.2.2. Lyapunov Analysis

To analyze the linear stability of generic solutions of Equation (6), we have estimated the corresponding Lyapunov spectrum (LS) $\{\lambda_k\}$ (Pikovsky and Politi, 2016). This can be done by considering the time evolution of the tangent vector $\delta = \left\{\delta R^{(e)}, \delta V^{(e)}, \delta R^{(i)}, \delta V^{(i)}\right\}$, that is ruled by the linearization of the

Equation (6), namely

$$\tau_m \delta\dot{R}^{(e)} = \left[2V^{(e)} + g_0^{(ee)}\frac{\Delta_0^{(ee)}}{\pi}\right]\delta R^{(e)} + 2R^{(e)}\delta V^{(e)} \quad (15a)$$

$$\tau_m \delta\dot{V}^{(e)} = 2V^{(e)}\delta V^{(e)} - 2(\pi\tau_m)^2 R^{(e)}\delta R^{(e)} + \sqrt{K}\tau_m\left[g_0^{(ee)}\delta R^{(e)} - g_0^{(ei)}\delta R^{(i)}\right] \quad (15b)$$

$$\tau_m \delta\dot{R}^{(i)} = \left[2V^{(i)} + g_0^{(ii)}\frac{\Delta_0^{(ii)}}{\pi}\right]\delta R^{(i)} + 2R^{(i)}\delta V^{(i)} \quad (15c)$$

$$\tau_m \delta\dot{V}^{(i)} = 2V^{(i)}\delta V^{(i)} - 2(\pi\tau_m)^2 R^{(i)}\delta R^{(i)} + \sqrt{K}\tau_m\left[g_0^{(ie)}\delta R^{(e)} - g_0^{(ii)}\delta R^{(i)}\right] \quad . \quad (15d)$$

In this case, the LS is composed of four Lyapunov exponents (LEs) $\{\lambda_k\}$ with $k = 1, \ldots, 4$, which quantify the average growth rates of infinitesimal perturbations along the orthogonal manifolds. The LEs can be estimated as follows:

$$\lambda_k = \lim_{t\to\infty}\frac{1}{t}\log\frac{|\delta_k(t)|}{|\delta_k(0)|} \quad , \quad (16)$$

where the tangent vectors δ_k are maintained ortho-normal during the time evolution by employing a standard technique introduced in Benettin et al. (1980). The autonomous system will be chaotic for $\lambda_1 > 0$, while a periodic (two frequency quasi-periodic) dynamics will be characterized by $\lambda_1 = 0$ ($\lambda_1 = \lambda_2 = 0$) and a fixed point by $\lambda_1 < 0$.

In order to estimate the LS for the neural mass model, we have integrated the direct and tangent space evolution with a Runge-Kutta 4th order integration scheme with $dt = 0.01$ ms, for a duration of 200 s, after discarding a transient of 10 s.

2.2.3. Linear Stability of Stationary Solutions

The linear stability of the stationary solutions $\{\overline{V}^{(e)}, \overline{V}^{(i)}, \overline{R}^{(e)}, \overline{R}^{(i)}\}$ can be analyzed by solving the eigenvalue problem for the linear Equations (15) estimated for stationary values of the mean membrane potentials and of the population firing rates. This approach gives rise to a fourth-order characteristic polynomial of the complex eigenvalues $\Lambda^{(k)} = \Lambda_R^{(k)} + i\Lambda_I^{(k)}$ with $k = 1, \ldots, 4$. The stability of the fixed point is controlled by the maximal $\Lambda_R^{(k)}$, whenever it is positive (negative), the stationary solution is unstable (stable). The nature of the fixed point is determined by $\Lambda_I^{(k)}$, if the imaginary parts of the eigenvalues are all zero, we have a node, otherwise a focus. Due to the fact that the coefficients of the characteristic polynomial are real, the eigenvalues are real or if complex they appear in complex conjugates couples $\Lambda_R^{(j)} \pm i\Lambda_I^{(k)}$. Therefore, the relaxation toward the fixed point is characterized by one or two frequencies $\nu_k = \Lambda_I^{(k)}/(2\pi)$. These latter quantities, as discussed in detail in the following, can give good predictions for the frequencies ν_{CO} of fluctuation driven COs observable for the same parameters in the network dynamics.

In the limit $K >> 1$, we can approximate the linear stability (Equations 15) as follows:

$$\tau_m \delta\dot{R}^{(e)} = 2\overline{R}_0^{(e)}\delta V^{(e)} \quad (17a)$$

$$\tau_m \delta\dot{V}^{(e)} = \sqrt{K}\tau_m\left[g_0^{(ee)}\delta R^{(e)} - g_0^{(ei)}\delta R^{(i)}\right] \quad (17b)$$

$$\tau_m \delta\dot{R}^{(i)} = 2\overline{R}_0^{(i)}\delta V^{(i)} \quad (17c)$$

$$\tau_m \delta\dot{V}^{(i)} = \sqrt{K}\tau_m\left[g_0^{(ie)}\delta R^{(e)} - g_0^{(ii)}\delta R^{(i)}\right] \quad ; \quad (17d)$$

where we have considered the zeroth-order approximation for the population rates $\overline{R}_0^{(e)}$ and $\overline{R}_0^{(i)}$.

In this case, the complex eigenvalues $\Lambda^{(k)}$ are given by the following expression:

$$\left[\Lambda^{(k)}\right]^2 = \frac{\sqrt{K}}{\tau_m}\left[\left(g_0^{(ee)}\overline{R}_0^{(e)} - g_0^{(ii)}\overline{R}_0^{(i)}\right) \pm\sqrt{\left(g_0^{(ee)}\overline{R}_0^{(e)} + g_0^{(ii)}\overline{R}_0^{(i)}\right)^2 - 4g_0^{(ei)}g_0^{(ie)}\overline{R}_0^{(e)}\overline{R}_0^{(i)}}\right] \quad . \quad (18)$$

From Equation (18), it is evident that $\Lambda^{(k)} \propto (K)^{1/4}$, and by assuming $I_0^{(i)} \propto I_0^{(e)}$, as we will do in this study, we also have that $\Lambda^{(k)} \propto (I_0^{(e)})^{1/2}$. Therefore, for a focus solution, we will have the following scaling relation for the relaxation frequencies for sufficiently large K:

$$\nu_k^R = \frac{\Lambda_I^{(k)}}{2\pi} \propto \sqrt{I_0^{(e)}K^{1/2}} \quad ; \quad (19)$$

This scaling is analogous to that found for purely inhibitory QIF networks in di Volo and Torcini (2018). In van Vreeswijk and Sompolinsky (1996), it has been found that the eigenvalues, characterizing the stability of the asynchronous state, scale proportionally to $\sqrt{K}$, therefore, the convergence (divergence) from the stationary stable (unstable) solution is somehow slower with K in our model. This is due to the presence in our MF of an extra macroscopic variable, the mean membrane potential, with respect to the usual rate models.

3. RESULTS

3.1. Phase Diagrams

In this sub-section, we will investigate the possible dynamical regimes emerging in our model by employing its neural mass formulation. In particular, the dynamics of the neural mass model (Equation 6) take place in a four-dimensional space $\left\{R^{(e)}, V^{(e)}, R^{(i)}, V^{(i)}\right\}$ and it depends on nine parameters, namely on the four synaptic coupling strengths $\left\{g_0^{(ee)}, g_0^{(ei)}, g_0^{(ii)}, g_0^{(ie)}\right\}$, the two external stimulation currents $\left\{I_0^{(e)}, I_0^{(i)}\right\}$, the median in-degree K, and the HWHM of the two distributions of the in-degrees $\left\{\Delta_0^{(ee)}, \Delta_0^{(ii)}\right\}$.

However, in order to reduce the space of parameters to investigate and at the same time to satisfy the inequalities

(Equation 12) required for the existence of a balanced state in the large K limit, we fix the inhibitory DC current as $I_0^{(i)} = I_0^{(e)}/1.02$ and the synaptic couplings as $g_0^{(ee)} = 0.27$, $g_0^{(ii)} = 0.953939$, $g_0^{(ie)} = 0.3$, and $g_0^{(ei)} = 0.96286$ analogously to what was done in Monteforte and Wolf (2010). Therefore, we are left with four control parameters, namely $\Delta_0^{(ee)}$, $\Delta_0^{(ii)}$, $I_0^{(e)}$, and K, that we will vary to investigate the possible dynamical states.

Three bidimensional bifurcation diagrams for the neural mass model (Equation 6) are reported in **Figure 1** for the couple of parameters $(I_0^{(e)}, \Delta_0^{(ee)})$, $(K, \Delta_0^{(ee)})$, and $(\Delta_0^{(ii)}, \Delta_0^{(ee)})$. From the bifurcation analysis, we have identified five different dynamical states for the excitatory population: namely, (I) an unstable focus; (II) a stable focus coexisting with an unstable limit cycle (LC); (III) a stable node; (IV) a stable limit cycle coexisting with an unstable focus; and (V) a chaotic regime. For the analysis reported in the following, it is important to remark that the stable foci are usually associated with four complex eigenvalues arranged in complex conjugate couples, therefore, the relaxation toward a stable focus is characterized by two frequencies (ν_1, ν_2) corresponding to the complex parts of the eigenvalues. In region (III), the macroscopic fixed point is characterized by two real eigenvalues and a couple of complex conjugated ones. Thus, the relaxation toward the macroscopic node is, in this case, guided by a single relaxation frequency. The inhibitory population, reveals the same bifurcation structure as the excitatory one, apart from an important difference: the inhibitory population never displays stable nodes. Therefore, the region (III) for the inhibitory population is also a region of type (II).

As shown in **Figures 1A,B**, for fixed $\Delta_0^{(ii)}$ and for low values of the structural heterogeneity $\Delta_0^{(ee)}$ and of the excitatory DC current $I_0^{(e)}$, one observes a stable node (III) that becomes a stable focus (II) by increasing $\Delta_0^{(ee)}$, these transitions are signaled as green solid lines in **Figure 1**. By further increasing the degree of heterogeneity $\Delta_0^{(ee)}$, the stable focus gives rise to COs (IV) *via* a super-critical HB (blue solid lines). Depending on the values of K and $I_0^{(e)}$, one can have the emergence of chaotic behaviors (V) *via* a period doubling (PD) cascade (yellow solid lines). For sufficiently large $\Delta_0^{(ee)}$, the COs disappear *via* a saddle-node (SN) bifurcation of limit cycles (LC) (red solid lines) and above the SN line, the only remaining solution is an unstable focus (I).

As shown in **Figure 1A**, for fixed structural heterogeneities, the increase of $I_0^{(e)}$ leads to the disappearance of the stable focus (II) *via* a sub-critical HB (dashed blue line). The dependence of the observed MF solutions on the in-degree K is reported in **Figure 1B** for a current $I_0^{(e)} = 0.001$, and it is not particularly dramatic apart from for the emergence of a chaotic region (V) from a CO regime (IV).

In order to observe the emergence of COs (IV) from the destabilization of a node solution (III), we should vary the structural inhibitory heterogeneity $\Delta_0^{(ii)}$, as shown in **Figure 1C**. Indeed, for sufficiently low $\Delta_0^{(ii)}$ and $\Delta_0^{(ee)}$, we can observe a super-critical bifurcation line from a node to a stable LC. From this analysis, it emerges that the excitatory heterogeneity has an opposite effect with respect to the inhibitory one, indeed by increasing $\Delta_0^{(ee)}$, the value of $\rho^{(e)}$ increases indicating the presence of more synchronized COs. This effect is due to the fact that the increase of $\Delta_0^{(ee)}$ leads to more and more neurons with large $k_j^{(ee)} >> K$, therefore, receiving higher and higher levels of recurrent excitation. These neurons are definitely supra-threshold and drive the activity of the network toward coherent behaviors.

In order to understand the limits of our MF formulation, it is of particular interest to compare the network simulations with the MF phase diagram. To this aim, we report in **Figure 1C**, the coherence indicator $\rho^{(e)}$ (Equation 4) estimated from the network dynamics. The indicator $\rho^{(e)}$ reveals that no COs are present in the region (III), where the MF displays a stable node, however, COs emerge in all the other MF regimes for sufficiently low $\Delta_0^{(ii)} < 1$. The presence of COs is expected from the MF analysis only in the regions (IV) and (V), but neither in (II) where the MF forecasts the existence of a stable focus nor in (I) where no stable solutions are envisaged. The origin of the discrepancies among the MF and the network simulations in the region (II) is due to the fact that the considered neural mass neglects the dynamical fluctuations in the input currents present in the original networks, which can give rise to noise induced COs (Goldobin et al., 2021). However, as shown in di Volo and Torcini (2018) and Bi et al. (2020) for purely inhibitory populations, the analysis of the neural mass model can still give relevant information on the network dynamics. In particular, the frequencies of the fluctuation induced COs observable in the network simulations can be well estimated from the frequencies (ν_1, ν_2) of the relaxation oscillations toward the stable MF focus. The lack of agreement between MF and network simulations in the region (I) is due to finite size effects, indeed in this case, the system tends to fully synchronize. Therefore, in the network, one observes highly synchronized COs characterized by population firing rates that diverge for increasing K and N and the MF is unable to reproduce these unrealistic solutions (Montbrió et al., 2015).

On the basis of these observations, we can classify the COs observable in the network in three different types accordingly to the corresponding MF solutions: O_P, when in the MF we observe periodic, quasi-periodic, or chaotic collective solutions in regions (IV) and (V); O_F, when the MF displays relaxation oscillations toward the stable focus in regions (II) and (III), that in the sparse network become noise sustained oscillations due to fluctuations in the input currents; O_S, when the MF fully synchronizes as in region (I).

In the following sub-sections, we will analyze the macroscopic dynamics of the E-I network of QIF neurons in order to test the predictions of the effective neural mass mode for asynchronous and coherent dynamics. In this latter case, we will focus on the three types of identified COs: namely, O_P, O_F, and O_S. These can manifest as periodic, quasi-periodic, and chaotic solutions as we will see by examining two main scenarios indicated as dashed horizontal lines in **Figure 1A** corresponding to the transition to chaos (black dashed line) and the emergence of abnormal synchronization from a stable focus (purple dashed line).

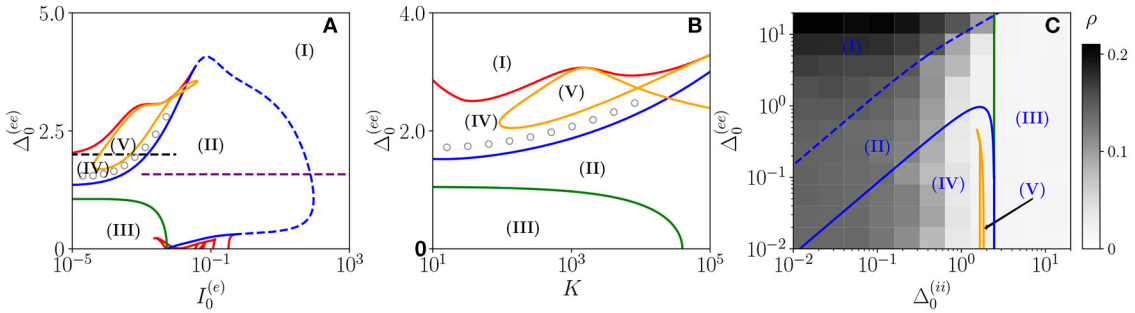

FIGURE 1 | Bifurcation diagrams of the neural mass model. The bifurcation diagrams concern the dynamical state exhibited by the excitatory population in the bidimensional parameter spaces ($I_0^{(e)}$, $\Delta_0^{(ee)}$) **(A)**, (K, $\Delta_0^{(ee)}$) **(B)**, and ($\Delta_0^{(ii)}$, $\Delta_0^{(ee)}$) **(C)**. The regions marked by Roman numbers correspond to the following collective solutions: (I) an unstable focus; (II) a stable focus coexisting with an unstable limit cycle (LC); (III) a stable node; (IV) an unstable focus coexisting with a stable LC; (V) a chaotic dynamics. The green solid line separates the regions with a stable node (III) and a stable focus (II). The blue solid (dashed) curve is a line of super-critical (sub-critical) Hopf bifurcations (HBs), and the red one of saddle-node (SN) bifurcations of LCs. The yellow curve denotes the period doubling (PD) bifurcation lines. In **(C)**, we also report the coherence indicator $\rho^{(e)}$ (Equation 4) estimated from the network dynamics with $N^{(e)}$ =10,000 and $N^{(i)}$ = 2,500. The dashed lines in **(A)** indicate the parameter cuts we will consider in **Figures 4**, **5** (black) and **Figure 7** (purple), while the open circles in **(A,B)** denote the set of parameters employed in **Figure 11**. In the three panels, the inhibitory DC current and the synaptic couplings are fixed to $I_0^{(i)} = I_0^{(e)}/1.02$, $g_0^{(ee)} = 0.27$, $g_0^{(ii)}$ =0.953939, $g_0^{(ie)} = 0.3$, $g_0^{(ei)}$ =0.96286; other parameters: **(A)** K =1,000, $\Delta_0^{(ii)} = 0.3$, **(B)** $I_0^{(e)}$ =0.001, $\Delta_0^{(ii)} = 0.3$, **(C)** K = 1,000, and $I_0^{(e)} = 0.1$.

3.2. Asynchronous Regimes

We will first consider a situation where the network dynamics remains asynchronous for any value of the median in-degree K, this occurs for sufficiently high structural inhibitory heterogeneities $\Delta_0^{(ii)}$ and external DC currents as shown in **Figures 1B,C** for E-I networks and as reported in di Volo and Torcini (2018) for purely inhibitory populations. If the population dynamics are asynchronous, we expect that at an MF level, the system will converge toward a stationary state corresponding to a stable equilibrium. Therefore, we have compared the results of the network simulations with the stationary rates ($\overline{R}^{(e)}$,$\overline{R}^{(i)}$) solutions of Equation (6). As shown in **Figures 2A,B**, the macroscopic activity of the excitatory and inhibitory populations is well reproduced by the fixed point solutions (Equation 8) in a wide range of values of the in-degrees $10 \leq K \leq 10^4$. This is particularly true for the inhibitory population, while at low $K < 100$, the excitatory firing rate is slightly underestimated by the macroscopic solution $\overline{R}^{(e)}$. Due to our choice of parameters, the average inhibitory firing rate is larger than the excitatory one for $K > 100$. This is consistent with experimental data reported for the barrel cortex of behaving mice (Gentet et al., 2010) and other cortical areas (Mongillo et al., 2018). Moreover, the rates have a non-monotonic behavior with K with a maximum at $K \simeq 450$ ($K \simeq 2{,}500$) for excitatory (inhibitory) neurons. As expected, the balanced state solutions $\overline{R}_0^{(e)} = 3.18$ Hz and $\overline{R}_0^{(i)} \simeq 11.28$ Hz (dashed horizontal lines) are approached only for sufficiently large $K >> 1$. In **Figures 1A,B** are reported also the first (second) order approximation $\overline{R}_0^{(e)} + \varepsilon\overline{R}_1^{(e)}$ ($\overline{R}_0^{(e)} + \varepsilon\overline{R}_1^{(e)} + \varepsilon^2\overline{R}_2^{(e)}$) given by Equation (10). These approximations reproduce quite well the complete solutions already at $K \geq 10^4$.

Let us now consider the effective input currents (Equation 13), these are reported in **Figure 2C** vs. the median in-degree. As expected, for increasing K, the MF estimations of the effective currents (solid lines) converge to the asymptotic values $I_a^{(e)} \simeq 0.0284$ and $I_a^{(i)} \simeq 0.4791$ (dashed lines) for our choice of parameters. For the excitatory population, the asymptotic value of the effective input current is essentially zero, while for the inhibitory population it is positive. These results suggest that for the considered choice of parameters the dynamics of both populations will be balanced, since the quantities $I_a^{(e)}$ and $I_a^{(i)}$ do not diverge with K, however, at a macroscopic level, the excitatory population will be at the threshold, while the inhibitory one will be supra-threshold. For comparison, we have estimated $I_{eff}^{(\alpha)}$ also from the direct the network simulations (circles) for $16 \leq K \leq 16{,}384$. These estimations disagree with the MF results already for $K > 1{,}000$. This is despite the fact that the population firing rates in the network are very well captured by the MF estimations at large K, as shown in **Figures 2A,B**. These large differences in the effective input currents are the effect of small discrepancies at the level of firing rates enhanced by the multiplicative factor $\sqrt{K}$ appearing in Equations (13). However, from the network simulations, we observe that the effective currents approach values smaller than the asymptotic ones $I_a^{(e)}$ and $I_a^{(i)}$ obtained from the neural mass model. In particular, despite the fact that from finite K simulations, it is difficult to extrapolate the asymptotic behaviors, it appears that $I_{eff}^{(e)}$ approaches a small negative value for $K >> 1$, while $I_{eff}^{(i)}$ converges to some finite positive value. In the following, we will see the effect of these different behaviors on microscopic dynamics. The origin of the reported discrepancies should be related to the presence of current fluctuations in the network that are neglected in the MF formulation.

The relevance of the current fluctuations for the network dynamics can be appreciated by estimating their amplitudes

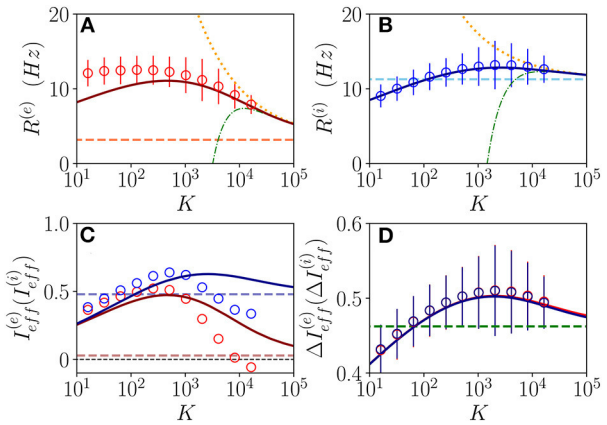

FIGURE 2 | Asynchronous dynamics: Instantaneous population rate $R^{(e)}$ ($R^{(i)}$) of excitatory (inhibitory) neurons in function of the median in-degree K are shown in **(A,B)**. The effective input currents $I^{(e)}_{eff}$ ($I^{(i)}_{eff}$) given by Equations (13) are reported in **(C)** and the fluctuations of the input currents $\Delta I^{(e)}_{eff}$ ($\Delta I^{(i)}_{eff}$), as obtained from Equations (20), in **(D)**. Red (blue) color refers to excitatory inhibitory population. The solid continuous lines represent the value obtained by employing the exact MF solutions $\overline{R}^{(x)}$ of Equation (8), the dotted (dash-dotted) lines correspond to the first (second) order approximation $\overline{R}^{(x)}_0 + \varepsilon \overline{R}^{(x)}_1$ ($\overline{R}^{(x)}_0 + \varepsilon \overline{R}^{(x)}_1 + \varepsilon^2 \overline{R}^{(x)}_2$) and the dashed horizontal lines to the zeroth-order one $\overline{R}^{(x)}_0$ in **(A,B,D)**, and to $I^{(x)}_a$ in **(C)** with $x = e, i$. The circles correspond to data obtained from numerical simulations of $N^{(e)} = N^{(i)}$ =10,000 neurons for $K < 4{,}096$, $N^{(e)} = N^{(i)}$ =20,000 for K =4,096,8,192 and $N^{(e)} = N^{(i)}$ =30,000 for $K > 8{,}192$, averaging the population rates over a window of $T = 40\ s$, after discarding a transient of $T = 60\ s$. The error bars in **(A,B)** are obtained as the SD (over the time window T) of the population rates, while the average CV of neurons is around 0.15 for all the reported simulations. Synaptic couplings and the ratio between the currents are fixed as stated in sub-section 3.1, other parameters are $\Delta^{(ii)}_0 = 1$, $\Delta^{(ee)}_0 = 2.5$, and $I^{(e)}_0 = 0.2$. The values of the asymptotic solutions (dashed lines) are : in **(A,B)** $\overline{R}^{(e)}_0 = 3.18$ Hz and $\overline{R}^{(i)}_0 = 11.28$ Hz, respectively; in **(C)** $I^{(e)}_a = 0.0284$ and $I^{(i)}_a \simeq 0.4791$; in **(D)** $\Delta I^{(e)}_{eff} = 0.4623$ and $\Delta I^{(i)}_{eff} = 0.4593$.

within a Poissonian approximation, as follows

$$\Delta I^{(e)}_{eff} = \sqrt{\tau_m \left[\left(g^{(ee)}_0\right)^2 R^{(e)} + \left(g^{(ei)}_0\right)^2 R^{(i)} \right]}$$
$$\Delta I^{(i)}_{eff} = \sqrt{\tau_m \left[\left(g^{(ie)}_0\right)^2 R^{(e)} + \left(g^{(ii)}_0\right)^2 R^{(i)} \right]} \qquad (20)$$

These have been evaluated by assuming that each neuron receives on average K excitatory and inhibitory spike trains characterized by Poissonian statistics with average rates $R^{(e)}$ and $R^{(i)}$. However, we have neglected in the above estimation the variability of the in-degrees of each neuron. As shown in **Figure 2D**, these fluctuations are essentially identical for excitatory and inhibitory neurons and coincide with the MF results. In the limit $K >> 1$, they converge to the asymptotic values $\Delta I^{(e)}_{eff} \simeq 0.4623$ and $\Delta I^{(i)}_{eff} \simeq 0.4593$ (green dashed lines). It is evident that already for $K > 1{,}000$, the amplitudes of the fluctuations are of the same order or larger than the effective input currents. Thus, suggesting that the fluctuations have indeed a relevant role in determining the network dynamics and that one would observe Poissonian or sub-Poissonian dynamics for the neurons, whenever $I^{(\alpha)}_a$ is sub-threshold or supra-threshold (Lerchner et al., 2006).

In order to understand how the in-degree heterogeneity influences the network dynamics at a microscopic level, we examine the dynamics of active neurons in the function of their total in-degree $k^{(tot)}_j$. This is defined for excitatory (inhibitory) neurons as $k^{(tot)}_j = k^{(ee)}_j + k^{(ei)}_j$ ($k^{(tot)}_j = k^{(ii)}_j + k^{(ie)}_j$). Furthermore, a neuron is considered as active if it has fired at least once during the whole simulation time $T_t + T_s = 100$ s, therefore, if it has a firing rate larger than 0.01 Hz. As shown in **Figures 3A,B**, the probability distribution function (PDF) of active neurons is skewed toward values $k^{(tot)}_j > 2K$ ($k^{(tot)}_j < 2K$) for excitatory (inhibitory) neurons. These results reflect the fact that the excitatory (inhibitory) neurons with low (high) recurrent in-degrees $k^{(ee)}_j << K$ ($k^{(ii)}_j >> K$) are driven below the threshold by the inhibitory activity, that is predominant in the network since $R^{(i)} > R^{(e)}$, $g^{(ei)}_0 > g^{(ee)}_0$, and $g^{(ii)}_0 > g^{(ie)}_0$. The number of silent neurons for $K >$1,024 is of the order of 6-10% for both inhibitory and excitatory populations, in agreement with experimental results for the barrel cortex of mice (O'Connor et al., 2010), where a fraction of 10% of neurons was identified as silent with a firing rate slower than 0.0083 Hz. It should be remarked that all the population averages we report include the silent neurons.

Let us now examine how the firing rates of active neurons will modify by increasing the value of the median in-degree K. The single neuron firing rates as a function of their total in-degrees $k^{(tot)}_j$ are reported in **Figures 3C,D** for K =1,024, 4,096 and 16,384. A common characteristic is that the bulk neurons, those with $k^{(tot)}_j \simeq 2K$, tend to approach the firing rate values $(\overline{R}^{(e)}_0, \overline{R}^{(i)}_0)$ (magenta dashed lines) corresponding to the expected solutions for a balanced network in the limit $N >> K \to \infty$ (van Vreeswijk, 1996). This is confirmed by the analysis of their coefficient of variations cv_j, whose values are of order one, as expected for fluctuation driven dynamics. On the other hand, the outlier neurons, i.e., those with $k^{(tot)}_j$ far from $2K$, are all characterized by low values of the coefficient of variation cv_j indicating a mean driven dynamics. However, there is a striking difference between excitatory and inhibitory neurons. For the excitatory ones, we observe that the firing rates of the outliers with $k^{(tot)}_j >> 2K$ decrease for increasing K, while for the inhibitory population the increase of K leads to the emergence of outliers at $k^{(tot)}_j << 2K$ with higher and higher firing rates (refer to the inset in **Figure 3D**). This difference can be explained by the different values measured for $I^{(e)}_{eff}$ and $I^{(i)}_{eff}$ in the network (refer to **Figure 2C**). The increase of K leads for the excitatory (inhibitory) population to the emergence of neurons with very large $k^{(ee)}_j >> K$ (very small $k^{(ii)}_j << K$) whose dynamics should be supra-threshold. However, this is compensated in the excitatory case by the rapid drop of $I^{(e)}_{eff}$ toward zero or negative values, while for the inhibitory population $I^{(i)}_{eff}$ remains positive even at the largest K we have examined.

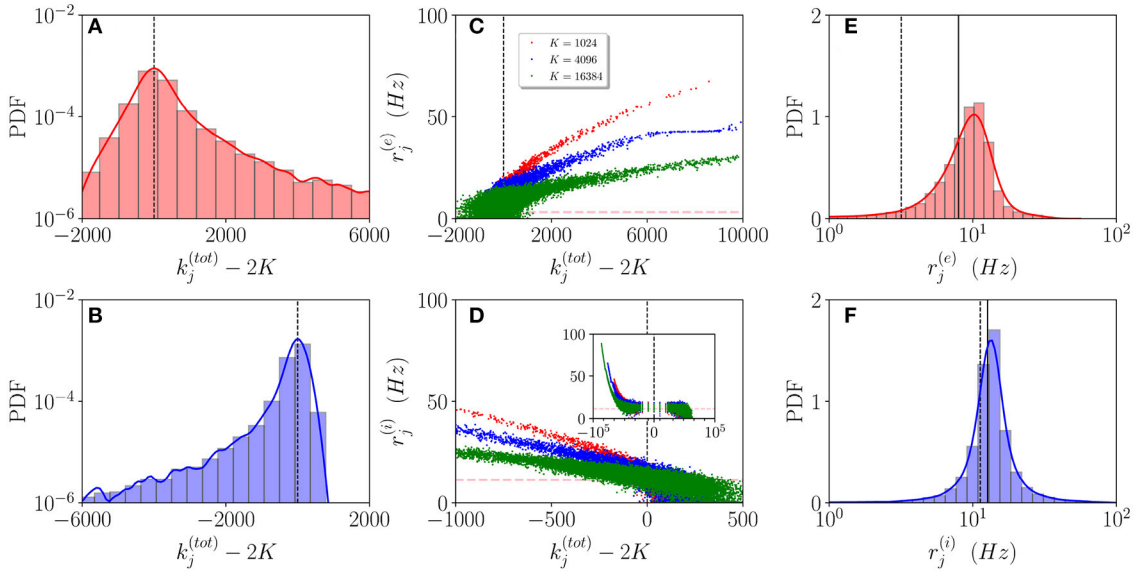

FIGURE 3 | Asynchronous dynamics: Probability distribution functions (PDFs) of the total in-degrees $k_j^{(tot)}$ for excitatory **(A)** and inhibitory **(B)** active neurons for $K = 16,384$. **(C,D)** Firing rates of the excitatory (inhibitory) neurons $r_j^{(e)}$ ($r_j^{(i)}$) vs. their total in-degrees $k_j^{(tot)} - 2K$ symbols refer to K =1,024 (red), K =4,096 (blue), and K =16,384 (green). The inset in **(D)** is an enlargement of the panel displaying the firing rates over the entire scale $k_j^{(tot)} - 2K$. The magenta dashed lines in **(C,D)** represent the balanced state solution ($\overline{R}_0^{(e)}, \overline{R}_0^{(i)}$). **(E,F)** PDF of the excitatory (inhibitory) firing rates $r_j^{(e)}$ ($r_j^{(i)}$) for $K = 16,384$, the solid (dashed) line refers to the MF results $\overline{R}^{(x)}$ ($\overline{R}_0^{(x)}$) with $x = e, i$. The red (blue) solid line refers to a log-normal fit to the excitatory (inhibitory) PDF with mean 8.8 Hz (17.5 Hz) and SD of 3.8 Hz (2.3 Hz). The parameters are the same as in **Figure 1**, the firing rates have been estimated by simulating the networks for a total time $T_s = 60$ s, after discarding a transient $T_t = 40$ s.

These outliers seem to have a negligible influence on the population dynamics, as suggested by the fact that the mean firing rates are reasonably well approximated by the balanced solutions $\overline{R}_0^{(e)}$ and $\overline{R}_0^{(i)}$ and as also confirmed by examining the PDFs of the firing rates for K =16,384. As shown in **Figures 3E,F**, the excitatory (inhibitory) PDF can be well fitted by a log-normal distribution with a mean 8.8 Hz (17.5 Hz) and SD of 3.8 Hz (2.3 Hz). This is considered a clear indication that the network dynamics is fluctuation driven (Roxin et al., 2011) as confirmed by recent investigations in the hippocampus and the cortex (Wohrer et al., 2013; Buzsáki and Mizuseki, 2014; Mongillo et al., 2018), as well as in the spinal motor networks (Petersen and Berg, 2016). However, the relative widths of our distributions are narrower than those reported in Mongillo et al. (2018). This difference can find an explanation in the theoretical analysis reported in Roxin et al. (2011), where the authors have shown that quite counter intuitively a wider distribution of the synaptic heterogeneities can lead to a narrower distribution of the firing rates. Indeed, in this study, we consider Lorentzian distributed in-degrees, while in Mongillo et al. (2018) Erdös-Renyi networks have been analyzed. As a further aspect, we have estimated the number of inhibitory neurons firing faster than a certain threshold ν_{th}, this number does not depend on the median in-degree for sufficiently large K >5,000, however, it grows proportionally to N. In the considered cases, the fraction of these neurons is $\simeq$ 1% for $\nu_{th} = 50$ Hz.

From this analysis, we can conclude that at any finite K and for finite observation times, we have at a macroscopic scale an essentially balanced regime sustained by the bulk of active neurons, whose dynamics are fluctuation-driven. Furthermore, we also have a large body of silent neurons and a small fraction of mean driven outliers. These should be considered as typical features of finite heterogeneous neural circuits as shown in various experiments (O'Connor et al., 2010; Landau et al., 2016). Moreover, in the present case, we report quite different behaviors for outliers whose macroscopic effective input currents are supra- or sub-threshold.

3.3. Collective Oscillations

We will now characterize the different types of COs observable by first following a route to coherent chaos for the E-I balanced network and successively we will examine how oscillations exhibiting an abnormal level of synchronization, somehow similar to those observable during an ictal state in the brain (Lehnertz et al., 2009), can emerge in our system. Furthermore, we will consider the phenomenon of quasi-periodicity and frequency locking occurring for fluctuation driven oscillations. As the last issue, the scaling of the frequencies and amplitudes of COs with the in-degree and as a function of the external DC current is reported.

3.3.1. A Period Doubling Route to Coherent Chaos

As a first case, we will follow the path in the parameter space denoted as a dashed black line in **Figure 1A**. In particular,

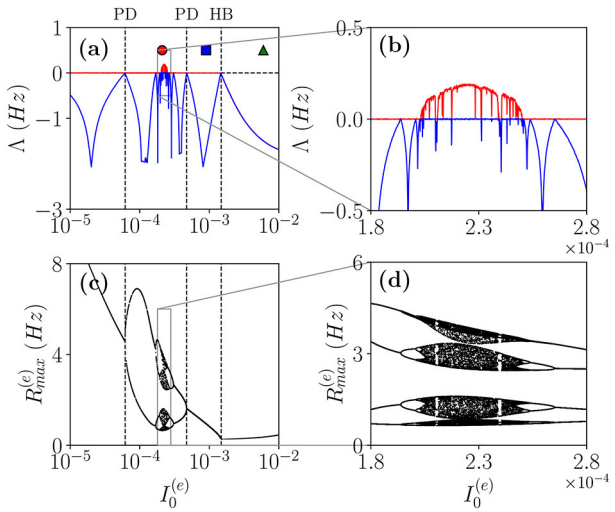

FIGURE 4 | Coherent chaos. **(a,b)** First (red) λ_1 and second λ_2 (blue) (LEs) for the MF vs. the DC current $I_0^{(e)}$ for the parameter cut corresponding to the dashed black line in **Figure 1A**. The dashed vertical lines in **(a)** indicate a super-critical Hopf bifurcation (HB) from a stable focus to periodic COs and the region of the period doubling (PD) cascade. The symbols denote three different types of MF solutions: namely, stable focus (green triangle); periodic oscillations (blue square) and chaotic oscillations (red circle). **(c,d)** Bifurcation diagrams for the same region obtained by reporting the maximal value of the instantaneous firing rate $R^{(e)}$ measured from MF simulations. The parameters are the same as in **Figure 1**, other parameters set as $\Delta_0^{(ii)} = 0.3$, $\Delta_0^{(ee)} = 2.0$, $K = 1{,}000$.

in order to characterize the different dynamical regimes, we have estimated the LS $\{\lambda_i\}$ associated the MF equations. As shown in **Figure 4**, this analysis has allowed us to identify a period doubling cascade toward a chaotic region, characterized by periodic and chaotic windows. In particular, we observe a focus region (II) for $0.0015 < I_0^{(e)} < 50.6105$, the focus loses stability *via* a super-critical HB at $I_0^e \simeq 0.0015$ giving rise to COs. One observes a period doubling cascade [regime (V)] taking place in the interval $I_0^{(e)} \in [0.00006177; 0.00047297]$ followed by a regime of COs at lower values of $I_0^{(e)}$. The chaotic dynamics refer to the MF evolution, and it can be, therefore, definitely identified as collective chaos (Nakagawa and Kuramoto, 1993; Shibata and Kaneko, 1998; Olmi et al., 2011). A peculiar aspect of this period doubling cascade is that the chaotic dynamics remain always confined in four distinct regions without merging in a unique interval as it happens e.g., for the logistic map at the Ulam point (Ott, 2002). This is due to the fact that the population dynamics display period four oscillations characterized by four successive bursts, whose amplitudes (measured by $R^{(e)}_{max}$) varies chaotically but each one remains restricted in an interval not overlapping with the other ones.

Let us now examine the network dynamics for the three peculiar MF solutions indicated in **Figure 4a** corresponding to a stable focus (II) characterized by LE ($\lambda_1 = \lambda_2 = -0.0299, \lambda_3 = \lambda_4 = -0.101$) for $I_0^{(e)} = 0.006$ (green triangle), to a stable oscillation (IV) with ($\lambda_1 = 0.0, \lambda_2 = -0.0343, \lambda_3 = -0.0555, \lambda_4 = -0.1732$) for $I_0^{(e)} = 0.0009$ (blue square), and to collective chaos (v) with ($\lambda_1 = 0.0033, \lambda_2 = 0.0, \lambda_3 = -0.0809, \lambda_4 = -0.1855$) for $I_0^{(e)} = 0.00021$ (red circle). As shown in **Figure 5**, for all these three cases, the network dynamics is always characterized by oscillations: namely, O_P for the regimes (IV) and (V) and fluctuation induced O_F for to the stable MF focus.

A typical feature of the O_P oscillations is that the excitatory neurons start to fire followed by the inhibitory ones, furthermore, the peak of activity of the excitatory population usually precedes that of the inhibitory neurons of a time interval Δt. Then the inhibitory burst silences the excitatory population for the time needed to recover toward the firing threshold. This recovering time sets the frequency ν_{CO} of the COs. In our set-up, the excitatory bursts are wider than the inhibitory ones due to the fact that $\Delta_0^{(ee)} > \Delta_0^{(ii)}$. All these features are quite evident from the population firing rates shown in **Figures 5a1,b1** and the raster plots in panels **Figures 5a3,b3**. These are typical characteristics of a PING-like mechanism reported for the generation of γ oscillations in the cortex (Tiesinga and Sejnowski, 2009), despite the fact that the frequencies of the COs shown in panels (a) and (d) are of the order of few Hz. Fluctuation driven oscillations O_F emerging in the network are radically different, as shown in **Figure 5c1**, in this case, the excitatory and inhibitory populations deliver almost simultaneous bursts. Further differences among O_P and O_F oscillations can be identified at the level of single neuron activity. These can be appreciated by considering the PDFs of the excitatory firing rates $r_j^{(e)}$ reported in the fourth column of **Figure 5**. As shown in **Figure 5c4** these firing rates are log-normally distributed for O_F oscillations, thus, confirming their fluctuation driven origin (Roxin et al., 2011; Petersen and Berg, 2016). On the other hand, for O_P oscillations, we observe with respect to a log-normal distribution an excess of high firing neurons and a lack of low firing ones (refer to **Figures 5a4,b4**). This seems to indicate the presence of a larger number of mean driven excitatory neurons. Indeed this is the case, for $I_0^{(e)} = 0.00021$ and $I_0^{(e)} = 0.0009$, the percentage of active excitatory neurons driven by average effective currents supra-threshold $i_{eff,j}^{(e)}$ is $\simeq 1.7 - 1.2\%$, while for $I_0^{(e)} = 0.006$, it drops to $\simeq 0.6\%$. The percentage of active inhibitory neurons on average supra-threshold is quite limited in both cases being of the order of 0.25–0.13%. Another interesting feature distinguishing the two kinds of oscillations is the fact that for O_P, the excitatory supra-threshold neurons have a firing rate $r_j^{(e)} > \nu_{CO}$ and that the few neurons with firing rates locked to ν_{CO} are on average exactly balanced, i.e., they have $i_{eff,j}^{(e)} \simeq 0$. The situation is different for the O_F oscillations, where we observe a group of sub-threshold excitatory and inhibitory neurons firing locked with the population bursts. In both cases, most parts of neurons are definitely sub-threshold firing at frequencies smaller than ν_{CO}, as expected for an E-I balanced network displaying fast network

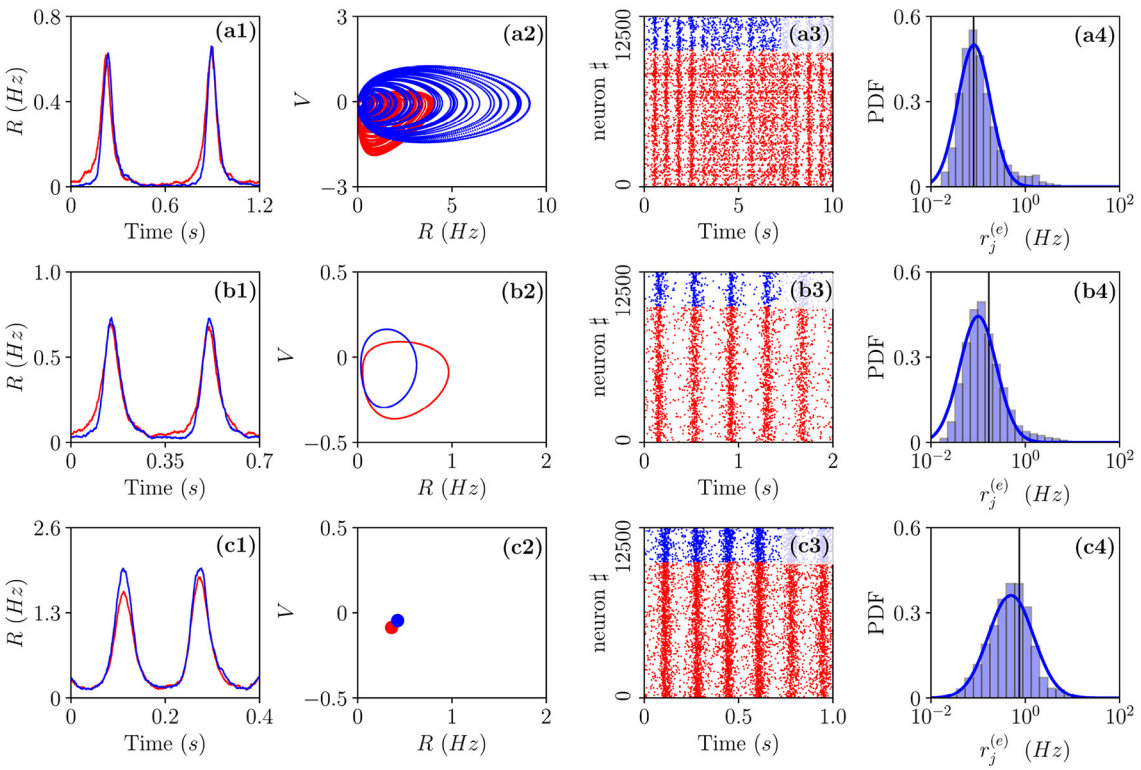

FIGURE 5 | Different types of collective oscillations(COs). Row **(a)** refers to the chaotic state observable for $I_0^{(e)} = 0.00021$ in the MF denoted by a red circle in **Figure 4a**; row **(b)** to the oscillatory state of the MF observable for $I_0^{(e)} = 0.0009$ denoted by a blue square in **Figure 4a**; row **(c)** to the stable focus for the MF observable for $I_0^{(e)} = 0.006$ denoted by a green triangle in **Figure 4a**. The first column displays the population firing rates vs. time obtained from the network dynamics, the second, the corresponding MF attractors in the planes identified by $(R^{(e)}, V^{(e)})$ and $(R^{(i)}, V^{(i)})$, the third, the raster plots, and the fourth, the PDFs of the excitatory firing rates $r_j^{(e)}$. Red (blue) color refers to excitatory (inhibitory) populations, the solid vertical lines in column 4 to the mean firing rate and the blue solid line to a fit to a log-normal distribution. Parameters as in **Figure 2**, apart from $\Delta_0^{(ii)} = 0.3$, $\Delta_0^{(ee)} = 2.0$, K =1,000. For the estimation of the firing rates we employed $N^{(e)}$=40,000 and $N^{(i)}$=10,000, while for the raster plots, $N^{(e)}$=10,000 and $N^{(i)}$=2,500. The total integration time has been of 120 s after discarding a transient of 80 s.

oscillations associated with irregular neural discharges (Brunel and Wang, 2003).

In order to understand the different mechanisms at the basis of O_P and O_F oscillations, let us examine how the delay Δt between excitatory and inhibitory bursts, observed for O_P oscillations, modifies as a function of the membrane time constant of the inhibitory population $\tau_m^{(i)}$. An increase of $\tau_m^{(i)}$ of $\simeq$ 5 ms has the effect of reducing the delay of almost a factor six from $\Delta t \simeq 28$ ms to $\Delta t \simeq 5$ ms, as shown in **Figure 6A**. The increase of $\tau_m^{(i)}$ leads to an enhanced inhibitory action since the integration of the inhibitory membrane potentials occurs on longer time scales, and this promotes a higher activity of the inhibitory population. Indeed, this is confirmed from the drop of the effective input currents from an almost balanced situation where the average $I_{eff}^{(e)}$ and $I_{eff}^{(i)}$ are almost zero to a situation where they are definitely negative (refer to **Figure 6B**). Thus, for increasing $\tau_m^{(i)}$, the percentage of neurons below threshold also increases and as a consequence the dynamics become more and more noise driven, as testified by the increase of the current fluctuations $\Delta I_{eff}^{(e,i)}$ as shown in **Figure 6C**. In summary, the delay is due to the fact that despite the effective inhibitory and excitatory currents are essentially equal, as shown in **Figure 6B**, the wider distribution of the excitatory in-degrees promotes the presence of excitatory neurons supra-threshold that are the ones igniting the excitatory burst before the inhibitory one. The delay Δt decreases whenever the number of these supra-threshold neurons decreases, and it will vanish when the dynamics will become essentially fluctuation driven as in the case of O_F oscillations.

3.3.2. From Fluctuation Driven to Abnormally Synchronized Oscillations

As the second range of parameters, we consider the cut in the parameter plane shown in **Figure 1A** as a purple dashed line. For these parameters, we report in **Figures 7a,b** the average in time of the excitatory and inhibitory population rate as a function of the excitatory DC current $I_0^{(e)}$. In particular, we compare network simulations (red and blue circles) with the MF results (red and blue lines). These predict a stable focus (solid lines) up to $I_0^{(e)} = 74.1709$, where a sub-critical HB destabilizes such solution giving

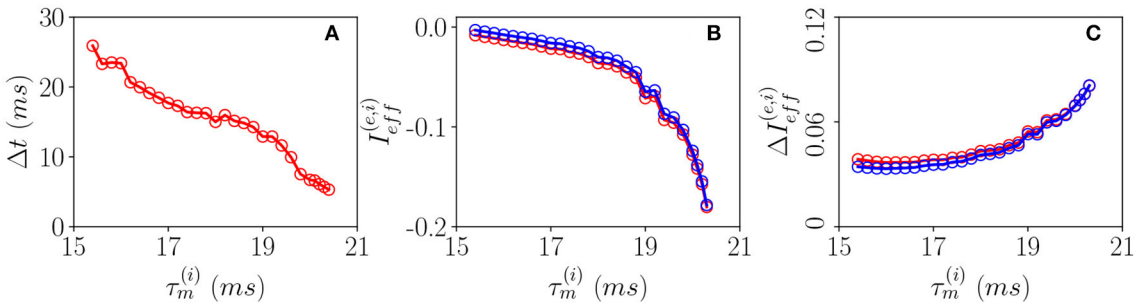

FIGURE 6 | Pyramidal-interneuron gamma (PING)-like O_P COs. **(A)** Firing delays Δt between the excitatory population peak and the inhibitory one vs. $\tau_m^{(i)}$. Effective mean input currents (Equation 13) **(B)** and current fluctuations (Equation 20) **(C)** vs. $\tau_m^{(i)}$, the excitatory (inhibitory) population are denoted by red (blue) circles. All the data reported in this study refer to MF simulations. The parameters are $I_0^{(e)} = 0.0009$, $\Delta_0^{(ii)} = 0.3$, $\Delta_0^{(ee)} = 2.0$, K =1,000, and $\tau_m^{(e)} = 20$ ms.

rise to an unstable focus (dashed lines). In panel (a), and (b), we have also reported as green dot-dashed lines the extrema of $R^{(e)}$ and $R^{(i)}$ corresponding to the unstable oscillations emerging at the HB. For currents below the HB, we observe a good agreement among the average network activity and the MF results.

In particular, below the HB, while the MF predicts only the existence of a stable focus, the network dynamics reveals quite interesting features. As shown in **Figure 7d1**, the system dynamics is indeed asynchronous for intermediate current values, in this study, $I_0^{(e)} = 1.024$, however, at lower currents, we observe fluctuation driven oscillations O_F as evident from the raster plot displayed in **Figure 7c1** for $I_0^{(e)} = 0.128$. As shown in **Figures 7c2,d2**, both these regimes are characterized by log-normal distributions of the firing rates, thus, indicating that the dynamics are fluctuation driven.

As reported in Montbrió et al. (2015), when the network dynamics become strongly synchronous (as expected for very high excitatory DC external current), the MF formulation fails since the population rates predicted within the MF formulation diverge. However, as shown in **Figures 7e1,e2**, due to finite size effects, we observe in the network a strong synchronous COs of type O_S corresponding to the MF region (I) where the MF model predicts no stable solution. These abnormally synchronized oscillations are also characterized by a quite fast frequency of oscillation $\nu_{CO} \simeq 800-1{,}000$ Hz. Furthermore, similarly to the O_P oscillations, they emerge due to a PING-like mechanism. This is evident from the raster plot in **Figure 7e1**, where excitatory neurons fire almost synchronously followed, after an extremely short delay, by the inhibitory ones whose activity silence all the network until the next excitatory burst. Quite astonishingly, the mean population rates measured in the network are reasonably well captured by the MF solutions associated with the unstable focus even beyond the HB, despite the network is now displaying COs (as shown in **Figures 7a,b**).

The emergence of COs in the network can be characterized in terms of the coherence indicator ρ (Equation 4) for the whole population of neurons. This indicator is reported in **Figure 8A** as a function of $I_0^{(e)}$ for the same parameters previously discussed in **Figure 7** and for two different values of the median in-degree : $K = 100$ (red circles) and K =4,000 (blue circles). For both values of K, we observe an almost discontinuous transition in the value of the coherence indicator at the sub-critical HB from $\rho \simeq 1/\sqrt{N}$, expected for an asynchronous dynamics, to values $\rho \simeq 1$ corresponding to full synchronization. This discontinuous transition leads to the emergence of abnormally synchronized oscillations O_S in the network. Moreover, at sufficiently high in-degrees, we observe the emergence of a new coherent state for low DC currents $I_0^{(e)} < 1.024$ characterized by a finite value of the coherence indicator, namely, $\rho \simeq 0.3$. The origin of these oscillations can be better understood by examining the coefficient of variation CV averaged over the whole population, this is reported in **Figure 8C** for the same interval of excitatory DC current and the same in-degrees as in **Figure 8A**. It is evident that the CV assumes finite values only for small input currents, namely $I_0^{(e)} < 1.024$, indicating the presence of not negligible fluctuations in the network dynamics. Furthermore, by increasing K, these fluctuations, as measured by the CV, increase as expected for a balanced network. This analysis suggests that these oscillations cannot exist in absence of fluctuations in the network, and therefore, they are of the O_F type. Furthermore, the network should be sufficiently connected in order to sustain these COs, as one can understand from **Figures 8B,D**, where ρ and CV are reported as a function of K for three different values of $I_0^{(e)}$. Indeed, for these parameter values, no O_F oscillation is observable for $K < 400$, even in presence of finite values of the CV.

As previously discussed in di Volo and Torcini (2018), the balance between excitation and inhibition generates endogenous fluctuations that modify the collective dynamics with respect to that predicted by the MF model, where the heterogeneity of the input currents, due to distributed in-degrees, is taken in account only as a quenched form of disorder and not as a dynamical source of the noise. However, also from this simplified MF formulation, one can obtain relevant information on the O_F oscillations, indeed as we will see in the next sub-section, the relaxation frequencies toward the stable MF focus represent a good estimation of the oscillation frequencies measured in the network. This suggests that the fluctuations present at the

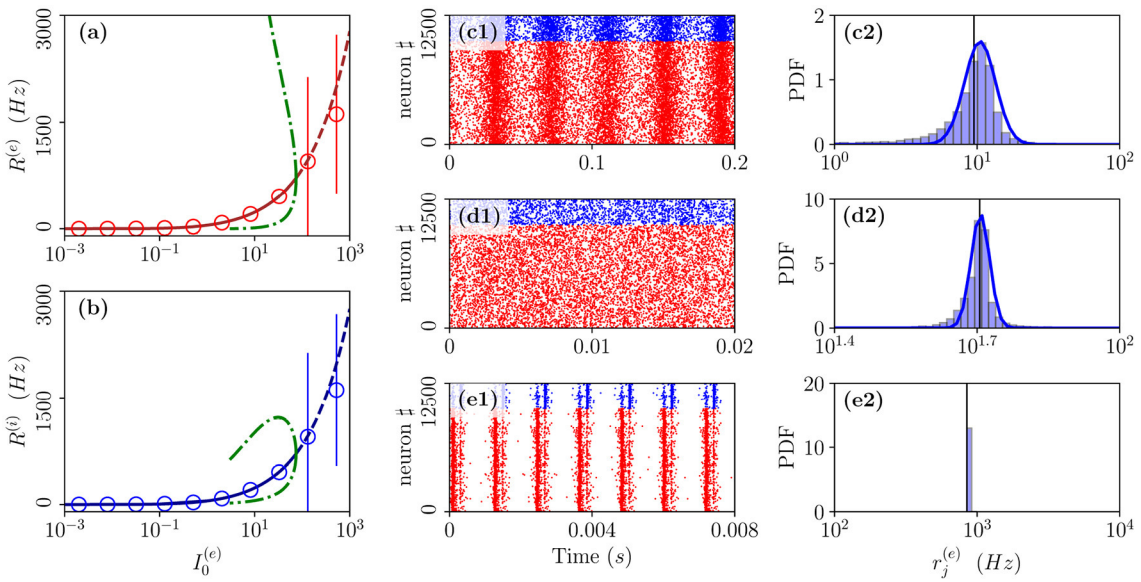

FIGURE 7 | From fluctuation driven to abnormally synchronized oscillations. Firing rates $R^{(e)}$ **(a)** and $R^{(i)}$ **(b)** as a function of $I_0^{(e)}$ for E-I network (circles) and neural mass model (lines) for the parameter cut corresponding to the dashed purple line in **Figure 1A**. For the neural mass model: solid (dashed) line shows stable (unstable) focus solution $\overline{R}^{(e)}$ and $\overline{R}^{(i)}$; green dot-dashed lines refer to the extrema of $R^{(e)}(R^{(i)})$ for the unstable LC present in region (II). The unstable LC emerges at the sub-critical HB for $I_0^{(e)} = 74.1709$ separating region (II) from (I), where the focus becomes unstable. Raster plots and PDFs of the excitatory firing rates $r_j^{(e)}$ are reported for specific cases: namely, $I_0^{(e)} = 0.128$ **(c1,c2)**, $I_0^{(e)} = 1.024$ **(d1,d2)**, and $I_0^{(e)} = 100$ **(e1,e2)**. The solid vertical lines in **(c2,d2,e2)** refer to the mean firing rate. Parameters as in **Figure 1**, other parameters are set as $\Delta_0^{(ii)} = 0.3$, $\Delta_0^{(ee)} = 1.58$, K =1,000 $N^{(e)}$ =10,000, and $N^{(i)}$ =2,500.

network level can sustain COs by continuously exciting the focus observed in the effective MF model with quenched disorder.

3.3.3. Fluctuation Driven Oscillations: From Quasi-Periodicity to Frequency Locking

As announced, this sub-section will be devoted to the characterization of the fluctuation driven oscillations O_F emerging in the region (II) reported in **Figure 1**. As the MF is now characterized by a stable focus with two couples of complex conjugate eigenvalues, there are two frequencies that can be excited by the irregular firing of neurons. Accordingly, as reported in di Volo and Torcini (2018), we expect the collective dynamics to be characterized by quasi-periodic dynamics with two (incommensurable) frequencies. These frequencies can be estimated by computing the power spectrum $S(\nu)$ of global quantities, e.g., the mean membrane potential $V(t)$. In the case of periodic dynamics, $S(\nu)$ is characterized by one main peak in correspondence of the CO frequency and minor peaks at its harmonics, while in the quasi-periodic case, the power spectrum shows peaks located at the two fundamental frequencies and all their linear combinations. Indeed, as shown in **Figure 9A**, the power spectrum exhibit several peaks over a continuous profile and the peak frequencies can be obtained as a linear combination of two fundamental frequencies (ν_1, ν_2). As already mentioned, the noisy background is due to the fluctuations present in the balanced network. It is evident from **Figure 9B**, that these two fundamental frequencies are well reproduced by the two relaxation frequencies ν_1^R and ν_2^R toward the MF focus, in particular for $I_0^{(e)} \geq 0.256$. At smaller currents, while the first frequency is well reproduced by ν_1^R, the second one is underestimated by ν_2^R. This is due to the phenomenon of frequency locking among the two collective rhythms present in the system: when the two frequencies become commensurable, we observe a common periodic CO. The locking order can be estimated by plotting the ratio between the two frequencies, indeed for low currents and $K = 8,192$, the ratio is almost constant and equal to four denoting a 1:4 frequency locking (see **Figure 9C**). Furthermore, by fixing $I_0^{(e)} = 0.128$ and by varying K the ratio ν_1/ν_2 can display different locked states, passing from locking of type 1 : 2 at low K, to 1 : 4 at larger values, as shown in the inset of **Figure 9C**.

As evident from **Figures 9B,C**, the locking phenomenon arises only in the network simulations and is not captured by the MF model. Furthermore, frequency locking occurs at low currents $I_0^{(e)} < 0.1$ where the dynamics of the neurons are driven by the intrinsic current fluctuations present in the network but not in the MF. Indeed for low DC currents the level of synchronization within the populations measured by ρ decreases with $I_0^{(e)}$, while the CV increases (as shown in **Figure 9D**). These features suggest that this phenomenon is somehow similar to what was reported in Meng and Riecke (2018) for two coupled inhibitory neural populations subject to external uncorrelated noise. Meng and Riecke (2018) observed an increase of the locking region among collective rhythms by increasing the amplitude of the additive noise terms, this joined to a counter-intuitive decrease of the level of synchronization among the neurons within each

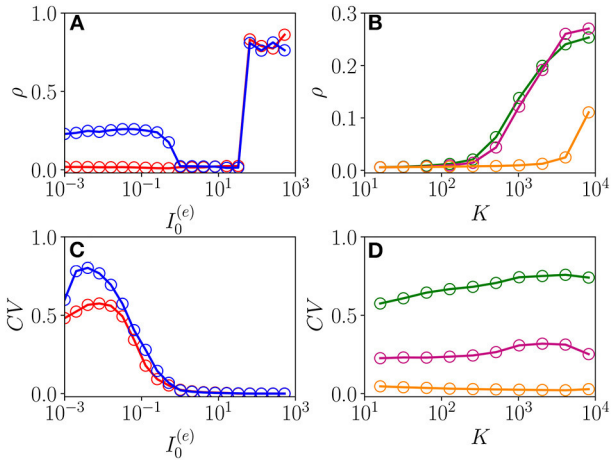

FIGURE 8 | From fluctuation driven to abnormally synchronized oscillations. Coherence indicator ρ (Equation 4) for the whole network of excitatory and inhibitory neurons vs. the excitatory DC current $I_0^{(e)}$ **(A)** and the median in-degree K **(C)**. Coefficient of variation CV for the whole network vs. $I_0^{(e)}$ **(B)** and K **(D)**. In **(A,C)**, the symbols refer to different values of the median in-degree:namely, $K = 100$ (red circles) and K=4,000 (blue circles). In **(B,D)**, the symbols refer to different excitatory DC currents: namely, $I_0^{(e)} = 0.01$ (green circles), $I_0^{(e)} = 0.1$ (purple circles), and $I_0^{(e)} = 1.0$ (orange circles). Parameters as in **Figure 1**, other parameters $\Delta_0^{(ii)} = 0.3$, $\Delta_0^{(ee)} = 1.58$, $N^{(e)}$ =40,000, and $N^{(i)}$ =10,000.

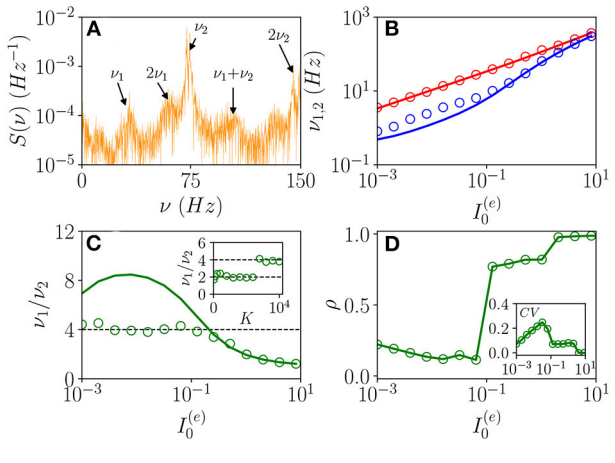

FIGURE 9 | From quasi-periodicity to frequency locking. **(A)** Power spectra $S(\nu)$ of the mean membrane potential obtained from network simulations. **(B)** The two fundamental frequencies $\nu_1(\nu_2)$ vs. $I_0^{(e)}$. **(C)** Frequency ratio ν_1/ν_2 vs. $I_0^{(e)}$, in the inset ν_1/ν_2 is shown vs. K. **(D)** Coherence parameter ρ vs. $I_0^{(e)}$, in the inset the corresponding CV is reported. In **(B,C)**, the symbols (solid lines) refer to ν_1 and ν_2 as obtained from the peaks of the power spectra $S(\nu)$ for $V(t)$ obtained from the network dynamics (to the two relaxation frequencies ν_1^R and ν_2^R associated to the stable focus solution for the MF). Parameters as in **Figure 1**, other parameters are set as $\Delta_0^{(ii)} = 0.3$, $\Delta_0^{(ee)} = 1.58$, $N^{(e)}$ =80,000, $N^{(i)}$ =20,000, K =8,192, and $I_0^{(e)} = 0.128$ in the inset of **(C)**.

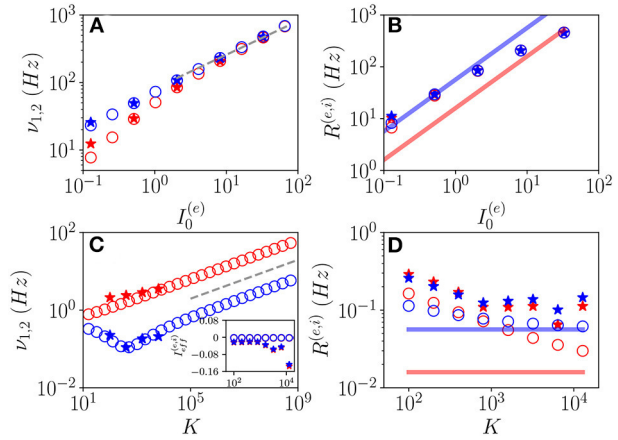

FIGURE 10 | Frequencies and amplitudes of O_F oscillations. The two fundamental frequencies ν_1 and ν_2 vs. $I_0^{(e)}$ **(A)** and K **(C)** and the average firing rates vs. $I_0^{(e)}$ **(B)** and K **(D)** for the excitatory (red) and inhibitory (blue) populations. In the inset in **(C)**, the effective mean input currents $I_{eff}^{(e)}$ ($I_{eff}^{(i)}$) of the excitatory (inhibitory) population are shown vs. K. The dashed line in **(A,C)** corresponds to a power law-scaling $\propto {I_0^{(e)}}^{1/2}$ ($\propto K^{1/4}$) for the frequencies of the COs. The solid red (blue) line in **(B,D)** denotes the asymptotic MF result $\overline{R}^{(e)}$ ($\overline{R}^{(i)}$). Network (MF) simulations are denoted as stars (circles). The MF data refer to the stable focus, in particular, in **(A,C)**, these are the two relaxation frequencies ν_1^R and ν_2^R. Parameters as in **Figure 1**, other parameters: **(A,B)** $K = 1,000$, $\Delta_0^{(ee)} = 1.58$, $\Delta_0^{(ii)} = 0.3$; **(C,D)** $I_0^{(e)} = 0.001$, $\Delta_0^{(ee)} = 1.3$, $\Delta_0^{(ii)} = 0.3$; for the network simulations, we employed $N^{(e)}$ =80,000 and $N^{(i)}$ =20,000.

population. However, in Meng and Riecke (2018), the neurons are subject to independent external noise sources, while in our case, the sources of fluctuations are intrinsic to the system and induced by the structural heterogeneity. Due to the network sparseness, the current fluctuations experienced by each neuron can be assumed to be indeed uncorrelated (Brunel and Hakim, 1999). Therefore, we are facing a new phenomenon that we can identify as a frequency locking of collective rhythms promoted by self-induced uncorrelated fluctuations. Indeed, the locking disappears for increasing external DC currents $I_0^{(e)} > 0.1$, when the coherence parameter ρ displays an abrupt jump toward higher values and the $CV \simeq 0$, thus, indicating that in this regime, the neuron dynamics becomes essentially mean driven and highly synchronized.

3.3.4. Features of COs for Large In-degrees and DC Currents

The dynamics of balanced networks are usually characterized in the limit $N >> K >> 1$ by the emergence of a self-sustained asynchronous regime. However, LC solutions have been already reported for balanced networks in the seminal article van Vreeswijk and Sompolinsky (1996). These solutions can be either unbalanced or balanced, however, in this latter case, they were characterized by oscillations of vanishing small amplitude. van Vreeswijk and Sompolinsky (1996) have shown that balanced COs are not observable in their model in the limit $N >> K \to \infty$ but only for finite K. Therefore, it is important to address in our case if COs can still be observable in the limit $N >> K >> 1$. Thus, in the following, we will investigate the dependence of COs features on the median in-degree K and the external DC currents.

Let us first consider fluctuation driven O_F oscillations, in this case, we have an analytical prediction (Equation 19) for the scaling of the fundamental frequencies ν_k^R associated with the relaxation toward the macroscopic focus, which should grow proportionally to $\sqrt{I^{(e)}}$. As shown in **Figures 10A,C**, indeed this scaling is observable for sufficiently large K and $I_0^{(e)}$. It is also evident the extreme good agreement between results obtained from the network simulations and the theoretical predictions (Equation 19), at least for the values of K reachable with our simulations. Furthermore, the frequencies of COs cover an extremely large range of values from few Hz to KHz, and this range of frequencies can be spanned by varying either K or the external DC current $I_0^{(e)}$ as shown in **Figures 10A,C**.

To better characterize these regimes, we have also evaluated the average firing rates $R^{(e)}$ and $R^{(i)}$. These quantities are displayed for O_F oscillations in **Figures 10B,D** as a function of $I_0^{(e)}$ and K, respectively. From the network simulations (stars), we observe that $R^{(e)}$ and $R^{(i)}$ grow with $I_0^{(e)}$, and they are astonishingly quite well reproduced by the MF data (circles) for sufficiently large DC currents, despite the MF results refer to a stable focus and not to COs. Instead, at smaller currents (namely, $I_0^{(e)} = 0.001$), the network data overestimates the MF results and the excitatory and inhibitory firing rates for $K >> 1$ seem to converge to a common constant value larger than those corresponding to the asynchronous regimes. For sufficiently large K, due to the prevalence of inhibition over excitation in the present model, we expect that the system will be sub-threshold, since the average excitatory and inhibitory firing rates are essentially coincident. Indeed this is confirmed by the analysis of the mean effective input currents $I_{eff}^{(e)}$ and $I_{eff}^{(i)}$ shown in the inset of **Figure 10C**. While for the MF focus, the dynamics appear as almost exactly balanced for all the considered median in-degree K since $I_{eff}^{(e)} \simeq I_{eff}^{(i)} \simeq 0$, for the network dynamics $I_{eff}^{(e)}$ and $I_{eff}^{(i)}$ are definitely negative for $K > 1,000$. This does not prevent the emergence of COs driven by fluctuations at large K, as indeed observed.

These results seem to indicate that for $N >> K \to \infty$, the network will not converge in this case toward a balanced regime characterized by constant effective input currents. On the contrary from our analysis, it emerges that the system will become more and more sub-threshold for increasing $K > 1{,}000$. However, the system always exhibits fluctuation driven dynamics, since we measured $CV \simeq 0.6$-0.8 at least in the range $K \simeq 100 - 10000$ accessible to network simulations.

Let us now examine the O_P oscillations. As shown in **Figures 11A,C**, the frequencies ν_{CO} as estimated from the MF model (open circles) reveal an almost perfect increase proportional to $\sqrt{I^{(e)}}$ analogous to the one reported for O_F oscillations. The data obtained from network simulations (stars) converge toward the MF results for sufficiently large K and $I_0^{(e)}$.

The mean firing rates $R^{(e)}$ and $R^{(i)}$ grow with $I_0^{(e)}$ for fixed K and appear to converge toward a constant value for sufficiently large K for fixed $I_0^{(e)}$, refer to **Figures 11B,D**. Moreover, the network simulations (stars) approach the MF results (open circles) at large DC currents and median in-degrees. However, while in the MF the asymptotic values of $R^{(e)}$ and $R^{(i)}$ remain distinct even at large K, these seem to become identical in the network simulations. This reflects in the fact that while the MF is perfectly balanced in the whole range of examined in-degrees, since $I_{eff}^{(e)} \simeq I_{eff}^{(i)} \simeq 0$, the network simulations reveal almost balanced effective input currents up to $K \simeq 1{,}000$ and above such median in-degree a prevalence of the inhibitory drive (refer to inset of **Figure 11C**).

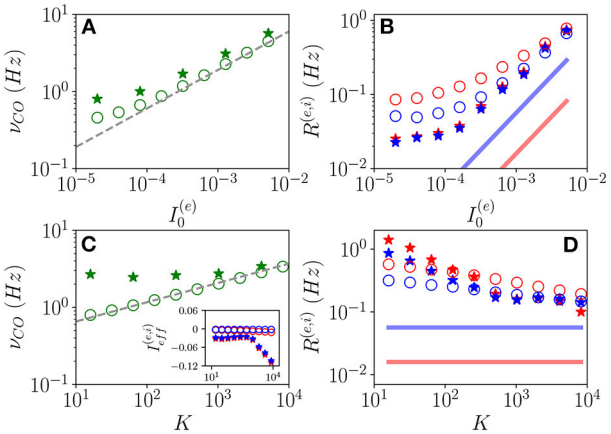

FIGURE 11 | Frequencies and amplitudes of O_P oscillations. COs' frequency ν_{CO} vs. $I_0^{(e)}$ **(A)** and K **(C)** and mean firing rates vs. $I_0^{(e)}$ **(B)** and K **(D)** for the excitatory (red) and inhibitory (blue) populations. The dashed line in **(A,C)** corresponds to a power law-scaling $\propto {I_0^{(e)}}^{1/2}$ ($\propto K^{1/4}$) for the frequencies. In the inset in (c), the effective mean input currents $I_{eff}^{(e)}$ ($I_{eff}^{(i)}$) of the excitatory (inhibitory) population are shown vs. K. The solid red (blue) line in **(B,D)** denotes the asymptotic MF result $\overline{R}^{(e)}$ ($\overline{R}^{(i)}$). The data obtained from network (MF) simulations are denoted as stars (circles). The data reported in **(A–D)** refer to the open circles in **Figures 1A,B**, respectively. For network simulations, we employed $N^{(e)}$ =80,000 and $N^{(i)}$ =20,000.

For both kinds of COs, we observe that while ν_{CO} diverges with K, the mean firing rates approach a constant value, thus, suggesting that the percentage of neurons participating in each population burst should vanish in the limit $K \to \infty$. This result indicates that COs will finally disappear, however, more refined analyses are needed to derive the asymptotic behavior of the system in the large K limit, ref to di Volo et al. (2021) for a detailed discussion of this aspect for purely inhibitory networks.

4. DISCUSSION

We have extensively characterized the macroscopic regimes emerging in a sparse balanced E-I network made of spiking QIF neurons with Lorentzian distributed in-degrees. The considered neuronal model joined to the peculiar choice of the distribution has allowed us to derive an exact low dimensional neural mass model describing the MF dynamics of the network in terms of the mean membrane potentials and of the population rates of the two populations (Montbrió et al., 2015; di Volo and Torcini, 2018). The low-dimensionality of the MF equations enabled us to study

analytically the stationary solutions and their stability as well as to obtain the bifurcation diagrams associated with the model and to identify the possible macroscopic states.

4.1. Asynchronous Regimes

The stationary solutions of the MF correspond to the asynchronous regime, which is the regime usually analyzed in the context of balanced dynamics (van Vreeswijk and Sompolinsky, 1996; Renart et al., 2010; Litwin-Kumar and Doiron, 2012). In the present case, we have analytically obtained the stationary solutions for the mean membrane potentials and average firing rates for Lorentzian distributed in-degrees for any finite value of the median K and an HWHM scaling as $\Delta_k^{(\alpha\alpha)} = \Delta_0^{(\alpha\alpha)}(K)^\eta$ with $\eta = 1/2$. The MF estimations for the population firing rates are pretty well reproduced by the network simulations in the examined range of in-degrees K. Furthermore, from the analytic expression of the stationary firing rates (Equation 8), it is evident that for $K >> 1$, the asymptotic rates would not depend on the structural heterogeneity and correspond to those usually found for balanced homogeneous or Erdös-Renyi networks (van Vreeswijk and Sompolinsky, 1996; Monteforte and Wolf, 2010). This is due to the fact that the ratio $\left(\Delta_k^{(\alpha\alpha)}\right)^2/K$ remains constant for $K \to \infty$. The final scenario will depend on the scaling exponent η, in particular, by assuming $\eta = 3/4$, the asymptotic firing rates $\overline{R}_0^{(\alpha)}$ will explicitly depend on the parameters $\Delta_0^{(\alpha\alpha)}$ controlling the structural heterogeneity. Whenever $\eta > 3/4$, the balanced state breaks down, and we face a situation similar to those investigated in Landau et al. (2016) and Pyle and Rosenbaum (2016)[1].

However, despite the system approaching a balanced state, as testified by the fact that the effective input currents converge to finite values $I_a^{(\alpha)}$, and the current fluctuations stay finite for $K \to \infty$, the balanced regime is not necessarily a sub-threshold one. Indeed, we have observed that we can have either sub-threshold or supra-threshold situations depending on the model parameters in agreement with the results previously reported in Lerchner et al. (2006). Moreover, the excitatory and inhibitory populations can achieve balanced regimes characterized by different asymptotic dynamics, where $I_a^{(i)}$ and $I_a^{(e)}$ have opposite signs.

While at a macroscopic level, the population activity for $N >> K >> 1$ approach is essentially that of a homogeneous balanced system, as shown in **Figures 2A,B**, the structural heterogeneity has a large influence on the single neuron dynamics, at least at finite K and finite investigation times. In particular, in analogy with experiments (Gentet et al., 2010; Mongillo et al., 2018), we considered a situation where the inhibitory drive prevails on the excitatory one. In this condition, microscopically the neural populations split into three groups: silent neurons, definitely sub-threshold; bulk neurons, which are fluctuation driven; and mean driven outlier neurons. In particular, excitatory (inhibitory) neurons with low (high) intra-population in-degrees are silenced due to the prevalence of synaptic inhibition. The silent neurons represent 6-10% of the whole population in agreement with experimental results for the mice cortex (O'Connor et al., 2010). Bulk neurons have in-degrees in the proximity of the median, and their firing rates approach the MF solution $\overline{R}_0^{(\alpha)}$ for increasing K. Outlier neurons represent a minority group almost disconnected from their own population, whose asymptotic behavior for $K >> 1$ is controlled by the sign of the effective mean input current.

4.2. Coherent Dynamics

The emergence of COs is observable in this balanced network whenever the level of heterogeneity in the inhibitory population is not too large, thus, suggesting that the coherence among inhibitory neurons is fundamental to support collective rhythms (Whittington et al., 2000). Indeed we observed two main mechanisms leading to COs: one that can be identified as PING-like and another one as fluctuation driven. The PING-like mechanism is present whenever the excitatory neurons are able to deliver an almost synchronous excitatory volley that in turn elicits a delayed inhibitory one. The period of the COs is determined by the recovery time of the excitatory neurons from the stimulus received from the inhibitory population. This mechanism is characterized by a delay between the firing of the pyramidal cells and the interneuronal burst as reported also in many experiments (Buzsáki and Wang, 2012). We have shown that this delay tends to vanish when the inhibitory action increases leading the system from a balanced situation to a definitely sub-threshold condition where the neural activity is completely controlled by fluctuations. In this latter case, the excitatory and inhibitory neurons fire almost simultaneously driven by the current fluctuations. These transform the relaxation dynamics toward a stable focus, observable in the MF, to sustained COs *via* a mechanism previously reported for inhibitory networks (di Volo and Torcini, 2018; Bi et al., 2020).

The PING-like COs undergo period doubling cascades by varying K and/or $I_0^{(e)}$ finally leading to collective chaos (Nakagawa and Kuramoto, 1993; Shibata and Kaneko, 1998). The nature of this chaotic behavior is definitely macroscopic since it is captured by the neural mass model obtained within the MF formulation, as shown by analyzing the corresponding LS. This kind of chaos implies irregular temporal fluctuations joined to coherence at the spatial level over a large part of the network resembling coherent fluctuations observed across spatial scales in the neocortex (Smith and Kohn, 2008; Volgushev et al., 2011; Okun et al., 2012; Achermann et al., 2016). Collective (or coherent) chaos has been previously shown to be a ubiquitous feature for balanced random spiking neural networks massively coupled, where K is proportional to N (Politi et al., 2018; Ullner et al., 2018). In this study, we have generalized such results to balanced random networks with sparse connectivity, where K is independent by N. Recently, it has been claimed that the presence of structured feed-forward connectivity in a random network is needed to observe coherent chaos (Landau and Sompolinsky, 2018). However, as evident from our results and those reported

[1]In such cases, balance has been recovered either by rewiring the post-synaptic connections (Pyle and Rosenbaum, 2016) or by introducing some sort of homeostatic plasticity or of spike-frequency adaptation (Landau et al., 2016).

in Ullner et al. (2018) and Politi et al. (2018), coherent chaos can naturally emerge in a recurrent neural network in absence of any structured connectivity introduced *ad hoc* to promote collective behaviors. Furthermore, we have shown that collective chaos can emerge in random balanced networks with instantaneous synapses and the absence of any delay, refer to Ullner et al. (2018).

Fluctuation driven COs are usually observable in our system as quasi-periodic collective motions characterized by two incommensurate frequencies. However, whenever the current fluctuations become sufficiently strong, the two frequencies can lock and give rise to a collective periodic motion. Furthermore, the locking region is characterized by a low level of synchrony in the network. These results resemble those reported in Meng and Riecke (2018) for two interconnected inhibitory neural networks subject to external uncorrelated noise. In particular, the authors have shown that uncorrelated noise sources enhance synchronization and frequency locking among the COs displayed by the two networks, despite the reduced synchrony among neurons within each network. At variance with Meng and Riecke (2018), in our case, the noise sources are intrinsic to the neural dynamics, but they can be as well considered as uncorrelated due to the sparseness in the connections (Brunel and Hakim, 1999; Brunel, 2000). Therefore, we are reporting a new example of frequency locking among collective rhythms promoted by self-induced uncorrelated fluctuations.

According to analytical arguments, the frequencies of the COs grow proportionally to the square root of the excitatory DC current. This on one side allows simply by varying the parameters $I_0^{(e)}$ or K, to cover with our model a broad range of COs' frequencies analogous to those found experimentally in the cortex (Chen et al., 2017). On another side, it implies that the frequencies of COs diverge as $K^{1/4}$, while the average firing rates seem to converge to a common value for sufficiently large K. These results seem to indicate that for large K, the network will become more and more unbalanced, with a prevalence of inhibition, while the amplitude of COs will tend to vanish. However, this analyses is not conclusive and more detailed analysis are required to capture the asymptotic behavior of the system in the limit $N >> K >> 1$.

4.3. Future Developments

The examined neural mass model has been derived by taking into account the random fluctuations due to the sparseness in the network connectivity only as a quenched disorder affecting the distribution of the effective synaptic couplings (Montbrió et al., 2015; di Volo and Torcini, 2018). The current fluctuations can be correctly incorporated in an MF formulation by developing a Fokker-Planck formalism for the problem, however, this will give rise to high (infinite) dimensional MF models (Brunel and Hakim, 1999; Brunel, 2000). We are currently developing reduction formalisms for the Fokker-Planck equation to obtain low dimensional neural mass models which will include the intrinsic current fluctuations (di Volo et al., 2021; Goldobin et al., 2021).

Relevant topics to investigate in the future to assess the generality of the reported results are their dependence on the chosen spiking neuron model and network architecture. In particular, for random networks, it is important to understand the role played by the distribution of the in-degrees, this is also in view of the recent findings reported in Klinshov et al. (2021).

DATA AVAILABILITY STATEMENT

The raw data supporting the conclusions of this article will be made available by the authors, without undue reservation.

AUTHOR CONTRIBUTIONS

HB and MV performed the simulations and data analysis. MV and AT were responsible for the state-of-the-art review and the article write-up. All the authors conceived and planned the research.

FUNDING

AT received financial support by the Excellence Initiative I-Site Paris Seine (grant no. ANR-16-IDEX-008) (together with HB), by the Labex MME-DII (grant no. ANR-11-LBX-0023-01), by the ANR Project ERMUNDY (grant no. ANR-18-CE37-0014) (together with MV), and all part of the French programme Investissements d'Avenir.

ACKNOWLEDGMENTS

The authors acknowledge extremely useful discussions with D. G. Goldobin, G. Mongillo, E. Montbrió, S. Olmi, and A. Politi.

REFERENCES

Achermann, P., Rusterholz, T., Dürr, R., König, T., and Tarokh, L. (2016). Global field synchronization reveals rapid eye movement sleep as most synchronized brain state in the human eeg. *R. Soc. Open Sci.* 3:160201. doi: 10.1098/rsos.160201

Angulo-Garcia, D., Luccioli, S., Olmi, S., and Torcini, A. (2017). Death and rebirth of neural activity in sparse inhibitory networks. *New J. Phys.* 19:053011. doi: 10.1088/1367-2630/aa69ff

Atallah, B. V., and Scanziani, M. (2009). Instantaneous modulation of gamma oscillation frequency by balancing excitation with inhibition. *Neuron* 62, 566–577. doi: 10.1016/j.neuron.2009.04.027

Barral, J., and Reyes, A. D. (2016). Synaptic scaling rule preserves excitatory-inhibitory balance and salient neuronal network dynamics. *Nat. Neurosci.* 19:1690. doi: 10.1038/nn.4415

Benettin, G., Galgani, L., Giorgilli, A., and Strelcyn, J.-M. (1980). Lyapunov characteristic exponents for smooth dynamical systems and for hamiltonian systems; a method for computing all of them. part 1: Theory. *Meccanica* 15, 9–20. doi: 10.1007/BF02128236

Berg, R. W., Alaburda, A., and Hounsgaard, J. (2007). Balanced inhibition and excitation drive spike activity in spinal half-centers. *Science* 315, 390–393. doi: 10.1126/science.1134960

Berg, R. W., Willumsen, A., and Lindén, H. (2019). When networks walk a fine line: balance of excitation and inhibition in spinal motor

circuits. *Curr. Opin. Physiol.* 8, 76–83. doi: 10.1016/j.cophys.2019.01.006

Bi, H., Segneri, M., di Volo, M., and Torcini, A. (2020). Coexistence of fast and slow gamma oscillations in one population of inhibitory spiking neurons. *Phys. Rev. Res.* 2:013042. doi: 10.1103/PhysRevResearch.2.013042

Brunel, N. (2000). Dynamics of sparsely connected networks of excitatory and inhibitory spiking neurons. *J. Comput. Neurosci.* 8, 183–208. doi: 10.1023/A:1008925309027

Brunel, N., and Hakim, V. (1999). Fast global oscillations in networks of integrate-and-fire neurons with low firing rates. *Neural Comput.* 11, 1621–1671. doi: 10.1162/089976699300016179

Brunel, N., and Wang, X.-J. (2003). What determines the frequency of fast network oscillations with irregular neural discharges? i. synaptic dynamics and excitation-inhibition balance. *J. Neurophysiol.* 90, 415–430. doi: 10.1152/jn.01095.2002

Bruno, R. M., and Sakmann, B. (2006). Cortex is driven by weak but synchronously active thalamocortical synapses. *Science* 312, 1622–1627. doi: 10.1126/science.1124593

Buzsáki, G., and Mizuseki, K. (2014). The log-dynamic brain: how skewed distributions affect network operations. *Nat. Rev. Neurosci.* 15, 264–278. doi: 10.1038/nrn3687

Buzsáki, G., and Wang, X.-J. (2012). Mechanisms of gamma oscillations. *Annu. Rev. Neurosci.* 35:203–225. doi: 10.1146/annurev-neuro-062111-150444

Chen, G., Zhang, Y., Li, X., Zhao, X., Ye, Q., Lin, Y., et al. (2017). Distinct inhibitory circuits orchestrate cortical beta and gamma band oscillations. *Neuron* 96, 1403–1418. doi: 10.1016/j.neuron.2017.11.033

Dehghani, N., Peyrache, A., Telenczuk, B., Le Van Quyen, M., Halgren, E., Cash, S. S., et al. (2016). Dynamic balance of excitation and inhibition in human and monkey neocortex. *Sci. Rep.* 6:23176. doi: 10.1038/srep23176

Destexhe, A., and Paré, D. (1999). Impact of network activity on the integrative properties of neocortical pyramidal neurons *in vivo*. *J. Neurophysiol.* 81, 1531–1547. doi: 10.1152/jn.1999.81.4.1531

di Volo, M., Segneri, M., Goldobin, D. S., Politi, A., and Torcini, A. (2021). Coherent oscillations in balanced neural networks driven by endogenous fluctuations. *bioRxiv [Preprint]*. doi: 10.1101/2021.10.18.464823

di Volo, M., and Torcini, A. (2018). Transition from asynchronous to oscillatory dynamics in balanced spiking networks with instantaneous synapses. *Phys. Rev. Lett.* 121:128301. doi: 10.1103/PhysRevLett.121.128301

Ermentrout, B. (2007). XPPAUT. *Scholarpedia* 2:1399. revision #136177. doi: 10.4249/scholarpedia.1399

Ermentrout, G. B., and Kopell, N. (1986). Parabolic bursting in an excitable system coupled with a slow oscillation. *SIAM J. Appl. Math.* 46, 233–253. doi: 10.1137/0146017

Gentet, L. J., Avermann, M., Matyas, F., Staiger, J. F., and Petersen, C. C. (2010). Membrane potential dynamics of gabaergic neurons in the barrel cortex of behaving mice. *Neuron* 65, 422–435. doi: 10.1016/j.neuron.2010.01.006

Goldobin, D. S., Di Volo, M., and Torcini, A. (2021). A reduction methodology for fluctuation driven population dynamics. *Phys. Rev. Lett.* 127:038301. doi: 10.1103/PhysRevLett.127.038301

Golomb, D. (2007). Neuronal synchrony measures. *Scholarpedia* 2, 1347. doi: 10.4249/scholarpedia.1347

Haider, B., Duque, A., Hasenstaub, A. R., and McCormick, D. A. (2006). Neocortical network activity in vivo is generated through a dynamic balance of excitation and inhibition. *J. Neurosci.* 26, 4535–4545. doi: 10.1523/JNEUROSCI.5297-05.2006

Isaacson, J. S., and Scanziani, M. (2011). How inhibition shapes cortical activity. *Neuron* 72, 231–243. doi: 10.1016/j.neuron.2011.09.027

Kadmon, J., and Sompolinsky, H. (2015). Transition to chaos in random neuronal networks. *Phys. Rev. X* 5:041030. doi: 10.1103/PhysRevX.5.041030

Klinshov, V., Kirillov, S., and Nekorkin, V. (2021). Reduction of the collective dynamics of neural populations with realistic forms of heterogeneity. *Phys. Rev. E* 103:L040302. doi: 10.1103/PhysRevE.103.L040302

Landau, I. D., Egger, R., Dercksen, V. J., Oberlaender, M., and Sompolinsky, H. (2016). The impact of structural heterogeneity on excitation-inhibition balance in cortical networks. *Neuron* 92, 1106–1121. doi: 10.1016/j.neuron.2016.10.027

Landau, I. D., and Sompolinsky, H. (2018). Coherent chaos in a recurrent neural network with structured connectivity. *PLoS Comput. Biol.* 14:e1006309. doi: 10.1371/journal.pcbi.1006309

Le Van Quyen, M., Muller, L. E., Telenczuk, B., Halgren, E., Cash, S., Hatsopoulos, N. G., et al. (2016). High-frequency oscillations in human and monkey neocortex during the wake-sleep cycle. *Proc. Natl Acad. Sci. U.S.A.* 113, 9363–9368. doi: 10.1073/pnas.1523583113

Lefort, S., Tomm, C., Sarria, J.-C. F., and Petersen, C. C. (2009). The excitatory neuronal network of the {C2} barrel column in mouse primary somatosensory cortex. *Neuron* 61, 301–316. doi: 10.1016/j.neuron.2008.12.020

Lehnertz, K., Bialonski, S., Horstmann, M.-T., Krug, D., Rothkegel, A., Staniek, M., et al. (2009). Synchronization phenomena in human epileptic brain networks. *J. Neurosci. Methods* 183, 42–48. doi: 10.1016/j.jneumeth.2009.05.015

Lerchner, A., Ursta, C., Hertz, J., Ahmadi, M., Ruffiot, P., and Enemark, S. (2006). Response variability in balanced cortical networks. *Neural Comput.* 18, 634–659. doi: 10.1162/neco.2006.18.3.634

Litwin-Kumar, A., and Doiron, B. (2012). Slow dynamics and high variability in balanced cortical networks with clustered connections. *Nat. Neurosci* 15, 1498–1505. doi: 10.1038/nn.3220

Meng, J. H., and Riecke, H. (2018). Synchronization by uncorrelated noise: interacting rhythms in interconnected oscillator networks. *Sci. Rep.* 8, 1–14. doi: 10.1038/s41598-018-24670-y

Mongillo, G., Rumpel, S., and Loewenstein, Y. (2018). Inhibitory connectivity defines the realm of excitatory plasticity. *Nat. Neurosci.* 21, 1463–1470. doi: 10.1038/s41593-018-0226-x

Montbrió, E., Pazó, D., and Roxin, A. (2015). Macroscopic description for networks of spiking neurons. *Phys. Rev. X* 5:021028. doi: 10.1103/PhysRevX.5.021028

Monteforte, M., and Wolf, F. (2010). Dynamical entropy production in spiking neuron networks in the balanced state. *Phys. Rev. Lett.* 105:268104. doi: 10.1103/PhysRevLett.105.268104

Nakagawa, N., and Kuramoto, Y. (1993). Collective chaos in a population of globally coupled oscillators. *Progr. Theor. Phys.* 89, 313–323. doi: 10.1143/ptp/89.2.313

O'Connor, D. H., Peron, S. P., Huber, D., and Svoboda, K. (2010). Neural activity in barrel cortex underlying vibrissa-based object localization in mice. *Neuron* 67, 1048–1061. doi: 10.1016/j.neuron.2010.08.026

Okun, M., and Lampl, I. (2008). Instantaneous correlation of excitation and inhibition during ongoing and sensory-evoked activities. *Nat. Neurosci.* 11, 535. doi: 10.1038/nn.2105

Okun, M., Yger, P., Marguet, S. L., Gerard-Mercier, F., Benucci, A., Katzner, S., et al. (2012). Population rate dynamics and multineuron firing patterns in sensory cortex. *J. Neurosci.* 32, 17108–17119. doi: 10.1523/JNEUROSCI.1831-12.2012

Olmi, S., Politi, A., and Torcini, A. (2011). Collective chaos in pulse-coupled neural networks. *EPL* 92, 60007. doi: 10.1209/0295-5075/92/60007

Ostojic, S. (2014). Two types of asynchronous activity in networks of excitatory and inhibitory spiking neurons. *Nat. Neurosci.* 17, 594–600. doi: 10.1038/nn.3658

Ott, E. (2002). *Chaos in Dynamical Systems*. Cambridge: Cambridge University Press.

Ott, E., and Antonsen, T. M. (2008). Low dimensional behavior of large systems of globally coupled oscillators. *Chaos* 18, 037113. doi: 10.1063/1.2930766

Petersen, P. C., and Berg, R. W. (2016). Lognormal firing rate distribution reveals prominent fluctuation-driven regime in spinal motor networks. *Elife* 5:e18805. doi: 10.7554/eLife.18805

Pikovsky, A., and Politi, A. (2016). *Lyapunov Exponents: A Tool to Explore Complex Dynamics*. Cambridge: Cambridge University Press.

Politi, A., Ullner, E., and Torcini, A. (2018). Collective irregular dynamics in balanced networks of leaky integrate-and-fire neurons. *Eur. Phys. J. Special Top.* 227, 1185–1204. doi: 10.1140/epjst/e2018-00079-7

Pyle, R., and Rosenbaum, R. (2016). Highly connected neurons spike less frequently in balanced networks. *Phys. Rev. E* 93:040302. doi: 10.1103/PhysRevE.93.040302

Ramirez, J.-M., and Baertsch, N. A. (2018). The dynamic basis of respiratory rhythm generation: one breath at a time. *Annu. Rev. Neurosci.* 41,475–499. doi: 10.1146/annurev-neuro-080317-061756

Renart, A., de la Rocha, J., Bartho, P., Hollender, L., Parga, N., Reyes, A., et al. (2010). The asynchronous state in cortical circuits. *Science* 327, 587–590. doi: 10.1126/science.1179850

Rosenbaum, R., and Doiron, B. (2014). Balanced networks of spiking neurons with spatially dependent recurrent connections. *Phys. Rev. X* 4:021039. doi: 10.1103/PhysRevX.4.021039

Roxin, A., Brunel, N., Hansel, D., Mongillo, G., and van Vreeswijk, C. (2011). On the distribution of firing rates in networks of cortical neurons. *J. Neurosci.* 31, 16217–16226. doi: 10.1523/JNEUROSCI.1677-11.2011

Shadlen, M. N., and Newsome, W. T. (1994). Noise, neural codes and cortical organization. *Curr. Opin Neurobiol.* 4, 569–579. doi: 10.1016/0959-4388(94)90059-0

Shadlen, M. N., and Newsome, W. T. (1998). The variable discharge of cortical neurons: implications for connectivity, computation, and information coding. *J. Neurosci.* 18, 3870–3896. doi: 10.1523/JNEUROSCI.18-10-03870.1998

Shibata, T., and Kaneko, K. (1998). Collective chaos. *Phys. Rev. Lett.* 81:4116. doi: 10.1103/PhysRevLett.81.4116

Shu, Y., Hasenstaub, A., and McCormick, D. A. (2003). Turning on and off recurrent balanced cortical activity. *Nature* 423, 288–293. doi: 10.1038/nature01616

Smith, M. A., and Kohn, A. (2008). Spatial and temporal scales of neuronal correlation in primary visual cortex. *J. Neurosci.* 28, 12591–12603. doi: 10.1523/JNEUROSCI.2929-08.2008

Softky, W. R., and Koch, C. (1993). The highly irregular firing of cortical cells is inconsistent with temporal integration of random epsps. *J. Neurosci.* 13, 334–350. doi: 10.1523/JNEUROSCI.13-01-00334.1993

Tiesinga, P., and Sejnowski, T. J. (2009). Cortical enlightenment: are attentional gamma oscillations driven by ing or ping? *Neuron* 63, 727–732. doi: 10.1016/j.neuron.2009.09.009

Ullner, E., Politi, A., and Torcini, A. (2018). Ubiquity of collective irregular dynamics in balanced networks of spiking neurons. *Chaos* 28:081106. doi: 10.1063/1.5049902

Ullner, E., Politi, A., and Torcini, A. (2020). Quantitative and qualitative analysis of asynchronous neural activity. *Phys. Rev. Res.* 2:023103. doi: 10.1103/PhysRevResearch.2.023103

van Vreeswijk, C. (1996). Partial synchronization in populations of pulse-coupled oscillators. *Phys. Rev. E* 54:5522. doi: 10.1103/PhysRevE.54.5522

van Vreeswijk, C., and Sompolinsky, H. (1996). Chaos in neuronal networks with balanced excitatory and inhibitory activity. *Science* 274, 1724–1726. doi: 10.1126/science.274.5293.1724

Volgushev, M., Chauvette, S., and Timofeev, I. (2011). Long-range correlation of the membrane potential in neocortical neurons during slow oscillation. *Prog Brain Res.* 193, 181–199. doi: 10.1016/B978-0-444-53839-0.00012-0

Whittington, M. A., Cunningham, M. O., LeBeau, F. E., Racca, C., and Traub, R. D. (2011). Multiple origins of the cortical gamma rhythm. *Dev. Neurobiol.* 71, 92–106. doi: 10.1002/dneu.20814

Whittington, M. A., Traub, R. D., Kopell, N., Ermentrout, B., and Buhl, E. H. (2000). Inhibition-based rhythms: experimental and mathematical observations on network dynamics. *Int. J. Psychophysiol.* 38, 315–336. doi: 10.1016/S0167-8760(00)00173-2

Wohrer, A., Humphries, M. D., and Machens, C. K. (2013). Population-wide distributions of neural activity during perceptual decision-making. *Progr. Neurobiol.* 103, 156–193. doi: 10.1016/j.pneurobio.2012.09.004

Conflict of Interest: The authors declare that the research was conducted in the absence of any commercial or financial relationships that could be construed as a potential conflict of interest.

Publisher's Note: All claims expressed in this article are solely those of the authors and do not necessarily represent those of their affiliated organizations, or those of the publisher, the editors and the reviewers. Any product that may be evaluated in this article, or claim that may be made by its manufacturer, is not guaranteed or endorsed by the publisher.

Advantages of publishing in Frontiers

OPEN ACCESS
Articles are free to read for greatest visibility and readership

FAST PUBLICATION
Around 90 days from submission to decision

HIGH QUALITY PEER-REVIEW
Rigorous, collaborative, and constructive peer-review

TRANSPARENT PEER-REVIEW
Editors and reviewers acknowledged by name on published articles

Frontiers
Avenue du Tribunal-Fédéral 34
1005 Lausanne | Switzerland

Visit us: www.frontiersin.org
Contact us: frontiersin.org/about/contact

REPRODUCIBILITY OF RESEARCH
Support open data and methods to enhance research reproducibility

DIGITAL PUBLISHING
Articles designed for optimal readership across devices

FOLLOW US
@frontiersin

IMPACT METRICS
Advanced article metrics track visibility across digital media

EXTENSIVE PROMOTION
Marketing and promotion of impactful research

LOOP RESEARCH NETWORK
Our network increases your article's readership